



UNIVERSIDAD NACIONAL AUTÓNOMA DE MÉXICO
PROGRAMA DE POSGRADO EN ASTROFÍSICA

INSTITUTO DE RADIASTRONOMÍA Y ASTROFÍSICA

EXISTENCE OF AGN IN THE NEARBY UNIVERSE AND X-RAY
PROPERTIES OF THE TORUS FOR LLAGN

TESIS

QUE PARA OPTAR POR EL GRADO DE :
DOCTORA EN CIENCIAS (ASTROFÍSICA)

PRESENTA:

NATALIA OSORIO CLAVIJO

TUTORES:

DRA. OMAIRA GONZÁLEZ MARTÍN
INSTITUTO DE RADIOASTRONOMÍA Y ASTROFÍSICA
DR. SEBASTIÁN FRANCISCO SÁNCHEZ SÁNCHEZ
INSTITUTO DE ASTRONOMÍA

Morelia, Michoacán, México, Febrero 2024



Universidad Nacional
Autónoma de México

Dirección General de Bibliotecas de la UNAM

Biblioteca Central



UNAM – Dirección General de Bibliotecas
Tesis Digitales
Restricciones de uso

DERECHOS RESERVADOS ©
PROHIBIDA SU REPRODUCCIÓN TOTAL O PARCIAL

Todo el material contenido en esta tesis esta protegido por la Ley Federal del Derecho de Autor (LFDA) de los Estados Unidos Mexicanos (México).

El uso de imágenes, fragmentos de videos, y demás material que sea objeto de protección de los derechos de autor, será exclusivamente para fines educativos e informativos y deberá citar la fuente donde la obtuvo mencionando el autor o autores. Cualquier uso distinto como el lucro, reproducción, edición o modificación, será perseguido y sancionado por el respectivo titular de los Derechos de Autor.

A las mujeres de mi familia que me han traído hasta aquí...

Agradecimientos

Esta tesis no hubiera sido posible sin el apoyo incondicional de las personas que me acompañaron de alguna u otra manera durante este proceso. Sin lugar a dudas, este es un trabajo que refleja lo afortunada que he sido de contar con personas valiosas en mi vida.

Quisiera empezar agradeciendo a mi mamá, por apoyarme a lo largo de todo este camino académico. Por contenerme y siempre decirme que todo estaría bien. A mis hermanas por alegrarse de cada uno de mis logros.

Gracias a mi pareja, Jaime, por hacer parte de mi camino desde hace más de cinco años. Por escucharme incansable y repetidamente sobre el día a día, por acompañarme en los momentos difíciles y por celebrar conmigo los momentos felices. Gracias por tomar la decisión de caminar juntos en un momento tan importante para los dos.

Esta tesis no hubiera sido posible sin el acompañamiento incansable de mi asesora, la Dra. Omaira González Martín, que creyó en mi siendo apenas una pronto-astrónoma y enseñarme el increíble mundo de los Núcleos Activos. No solamente por acompañarme en la vida académica, si no por aconsejarme y apoyarme también en las decisiones personales. Gracias por la paciencia y la confianza en que podría desarrollar un proyecto importante por mi misma, por guiarme a lo largo del doctorado, y por darme la libertad de tomar decisiones relevantes. Gracias también por creer en mi cuando aún yo no creía en mi misma y por defenderme siempre. Sin duda decidir trabajar con usted, ha sido una de las mejores decisiones que he podido tomar. Me llevo enseñanzas para toda la vida.

Gracias también al Dr. Sebastián Sánchez que decidió embarcarse en esta aventura y asesorar de igual manera la tesis. Por todos los consejos y las charlas profundas en nuestras reuniones, y también por enseñarme sobre los procesos galácticos desde una perspectiva diferente. Gracias por creer en el proyecto sin apenas conocerme. Me alegra mucho poder

haber compartido conocimientos. Mi vida en México no hubiera sido lo mismo sin el acompañamiento de las personas que me abrieron los brazos. Gracias a Alex, Palmira, Vianey, Gely, Rudy, Geovanni, Rubén, Miguel, Dani, Gris y aquellas que han ido llegando a lo largo de mi estancia, Erick, Ulises, Fer, Sandy, Pedro, Raúl, Karla, Sandino y demás. Gracias a Camila y Laura por estar siempre ahí, dándome palabras de aliento cuando sentía que no iba a librar este objetivo. Por las llamadas durante el encierro y por los recuerdos de toda una vida que nos acompañan. Gracias a Valen y a Lau por hacer de mi estancia en Europa una excelente experiencia, y por acompañarme en la distancia durante esta importante etapa de mi vida. Gracias a todos quienes de alguna u otra manera han influido en mi vida y me han ayudado llegar hasta acá. Gracias al jurado de esta tesis por sus aportes para mejorar esta tesis y ayudarme a entender aspectos que no eran tan claros para mí.

Gracias también a todo el personal administrativo por ayudarme con todos los trámites burocráticos y hacerlos más llevaderos. Para finalizar, gracias al Consejo Nacional de Ciencia y Tecnología (CONACyT) por haberme permitido llevar a cabo esta tesis y apoyar mi investigación.

Resumen

Entender los procesos de acreción en torno a los agujeros negros supermasivos es importante para determinar qué papel juegan en la evolución de las galaxias. El escenario más aceptado para la actividad nuclear es que esta ocurre cuando hay un disco de acreción que alimenta al agujero negro. Dicho fenómeno se conoce como Núcleo Activo de Galaxia (AGN por sus siglas en inglés). Además de este disco de acreción, un AGN se encuentra compuesto por diversas estructuras compuestas de gas y polvo que generan trazas en la distribución espectral de energía, de entre las cuales se encuentra lo que se conoce como toro, y que se supone que es el principal responsable de la distinción observacional entre las distintas clases ópticas de AGNs. Sin embargo los AGNs emiten en todas las longitudes de onda. En esta tesis nos enfocamos en el estudio de los espectros que se producen en rayos X y su comparación con ciertas propiedades del gas ionizado en el rango óptico. Esta región espectral traza la corona de rayos X. Particularmente, nos enfocamos en los AGNs de baja luminosidad, debido a que en estos se espera que la actividad nuclear sea mucho menor y que algunas de sus componentes hayan desaparecido, en particular el toro, debido a que la presión de radiación ya no es capaz de contrarrestar a la gravedad producida por el agujero negro. Adicionalmente, debido a su baja luminosidad, estos objetos podrían pasar desapercibidos en algunas longitudes de onda, que son más susceptibles a efectos de la galaxia huésped.

Esta tesis se encuentra dividida en dos objetivos esenciales. El primero de ellos es determinar la existencia y propiedades del toro en los AGNs de baja luminosidad, a través de la espectroscopía en rayos X, con el fin de determinar si esta estructura desaparece o cambia a bajas tasas de acreción. El segundo objetivo trata de determinar la población total de AGNs en una muestra de objetos cercanos que previamente ha sido estudiada

en el rango óptico, con el fin de determinar cuáles son las limitaciones de estudiar estos objetos a través de una sola longitud de onda, y cuáles son los objetos que se encuentran de manera óptima en rayos X, en contraste con aquellos que se encuentran en el óptico. Nuestra meta final es ofrecer una muestra más completa de objetos AGNs en el Universo local, que nos pueda ayudar a entender de qué manera co-evolucionan los AGNs con su galaxia huésped.

Para llevar a cabo el primer objetivo, nos centramos en la información provista por el satélite en rayos X *NuSTAR*, que ofrece información a altas energías (> 10 keV), donde la joroba Compton tiene su pico de emisión, por lo que resulta indispensable esta región espectral para estudiar el material reprocesado por el toro. Nuestra muestra consiste en 81 fuentes, todas ellas a una distancia $D < 200$ Mpc, con luminosidades bolométricas $L_{\text{bol}} < 10^{42}$ erg s $^{-1}$, y con tasas de Eddington $\lambda_{\text{Edd}} < 10^{-3}$ con el fin de tener información de lo que ocurre en el Universo local. En nuestra muestra, 18 fuentes son clasificadas en el óptico como LINERs, y las 63 restantes como Seyferts, de las cuales la gran mayoría son Seyfert 2. El análisis espectral se centra en estudiar diferentes modelos, que pueden o no tener en cuenta la reflexión por parte del toro. Para este trabajo encontramos que incluso para bajas tasas de acreción hay una cantidad significativa de objetos en los que el toro todavía se encuentra presente. De hecho encontramos que únicamente para el 14% de la muestra (11 fuentes) el toro parece haber desaparecido con base en las observaciones en rayos X. Además encontramos que la contribución del toro es de $\sim 40\%$ de la emisión del disco de acreción y que pareciera haber una evolución en la química del toro. Este escenario está de acuerdo con modelos teóricos que predicen que la desaparición del toro no depende únicamente de la tasa de acreción del AGNs. Esperamos que la desaparición total del toro se de para tasas de acreción incluso más bajas que las estudiadas en este trabajo (es decir, incluso debajo de 10^{-5}).

Para el segundo objetivo nos centramos en el estudio de los rayos X a través del satélite *Chandra*. Este satélite provee la mejor resolución espacial en rayos X a la fecha, lo que permite aislar la emisión del AGN de la de la galaxia huésped. Partimos de la muestra de galaxias observadas por el proyecto CALIFA, que cuenta con 941 fuentes en el Universo local estudiadas a través del óptico con espectroscopía espacialmente resuelta. Resultados

previos estimaban que el porcentaje de actividad nuclear en CALIFA era del 4% utilizando clasificaciones puramente ópticas (cocientes de líneas de emisión del gas ionizado). Nuestro trabajo consiste en un estudio morfológico y espectroscópico de las fuentes en rayos X. Para ello, estudiamos 138 fuentes con observaciones disponibles en *Chandra*. Del estudio morfológico, encontramos que 66 de las 138 fuentes cuentan con emisión puntual coincidente con el núcleo, lo cual podría ser indicio de un AGN. De estas 66 fuentes, 49 tienen al menos 50 cuentas en el espectro de rayos X para estudiar su espectro. Usamos modelos simples que recrearan la emisión AGN y también modelos asociados a otros procesos. Encontramos 34 objetos que no habían sido caracterizados como AGN previamente en CALIFA mediante información extraída de los datos en el rango óptico. Estudiamos cuál es la ubicación de los objetos clasificados en rayos X en los diagramas de diagnóstico, ampliamente usados para caracterizar procesos de ionización, lo que nos permitió determinar cuáles son las limitaciones de usar una sola longitud de onda para caracterizar este tipo de objetos. El porcentaje de AGNs en la muestra de CALIFA se eleva del 4% al 7-10% con el estudio multi-frecuencia combinando la información en rayos X y óptico. Sin embargo, nuestro trabajo está restringido a información de *Chandra*, por lo que estas estimaciones podrían ser límites inferiores. Con esto, brindamos el conteo más completo de AGNs en CALIFA hasta la fecha. Utilizando esta muestra de AGNs, revisamos las exploraciones anteriores que proponen una conexión entre la presencia de actividad nuclear y el estado de formación estelar de la galaxia. Estudios anteriores habían planteado que galaxias con AGNs se encuentran mayoritariamente en una zona de transición entre galaxias con formación estelar activa y galaxias retiradas. Con la muestra descrita anteriormente, encontramos que nuestros AGNs se encuentran distribuidos en ambas regiones de este (es decir, en la nube azul y en la secuencia roja).

Esta tesis se presenta por medio del compendio de dos artículos que fueron publicados en la revista *Monthly Notices of the Royal Astronomical Society*: Osorio-Clavijo et al. (2022) y Osorio-Clavijo et al. (2023) en los que la autora principal es la misma que presenta este documento.

Abstract

Understanding the accretion processes around supermassive black holes (SMBH) is important for determining their role in the evolution of galaxies. The most widely accepted scenario for nuclear activity is that it occurs when there is an accretion disk feeding the SMBH. This phenomenon is known as an Active Galactic Nucleus (AGN). In addition to this accretion disk, an AGN is composed of various gas and dust structures that leave traces in the spectral energy distribution (SED), among which there is the torus. This structure is thought to be the main responsible for the observational differences between optical classes of AGN. One particularity of these sources is the fact that they emit across all electromagnetic spectrum. In this thesis, we focus on studying the spectra produced in X-rays and comparing them with certain properties of ionized gas in the optical range. This spectral region traces the gas feeding the black hole through photon Comptonization in a region known as the X-ray corona. Specifically, we focus on low-luminosity AGN (LLAGN), as in these cases nuclear activity is expected to be much lower, and some components, particularly the torus, may have disappeared due to radiation pressure no longer countering the gravity from the SMBH. Additionally, due to their low luminosity, these objects might be undetected in some wavelengths that are more susceptible to host galaxy effects.

This thesis is divided into two main objectives. The first one is to determine the existence and properties of the torus in LLAGN through X-ray spectroscopy, in order to establish whether this structure disappears or changes at low accretion rates. The second objective aims to determine the total population of AGN in a sample of nearby objects previously studied in the optical range, to understand the limitations of studying these objects using a single wavelength, and to identify objects that are optimally observed

in X-rays compared to those observed in the optical. Our ultimate goal is to provide a more comprehensive sample of AGN in the local Universe to better understand how AGN co-evolve with their host galaxies.

To achieve the first objective, we focus on data provided by the X-ray satellite *NuSTAR*, which offers information at high energies (> 10 keV) where the Compton hump has its peak of emission, therefore this spectral region is crucial for studying the material reprocessed by the torus. Our sample consists of 81 sources, all within a distance of $D < 200$ Mpc, with bolometric luminosities $L_{\text{bol}} < 10^{42}$ erg s $^{-1}$ and Eddington rates $\lambda_{\text{Edd}} < 10^{-3}$, in order to understand the torus evolution in the local Universe. Our sample consists of 18 sources optically classified as LINERs and the remaining 63 as Seyferts, out of which most of them are Seyfert 2 galaxies. The spectral analysis involves studying different models, some of which account for torus reflection and others that do not. In this work, we find that even at low accretion rates, a significant number of objects still have traces of reflection associated with the torus. In fact, we determine that only for 14% of the sample (11 sources), the torus seems to have disappeared based on X-ray observations. Furthermore, we discover that the torus contributes around 40% of the intrinsic continuum emission associated with the accretion disk, and that there seems to be an evolution in the torus chemistry. This scenario aligns with theoretical models predicting that torus disappearance does not solely depend on AGN accretion rates. Furthermore, the complete disappearance of the torus might occur at lower accretion rates than those studied here i.e., even below $\lambda_{\text{Edd}} \sim 10^{-5}$.

For the second objective, we focus on X-ray studies using the *Chandra* satellite, which provides the best X-ray spatial resolution to date, allowing us to isolate AGN emission from that of the host galaxy. We begin with the sample of galaxies observed by the CALIFA project, which includes 941 sources in the local Universe studied through optically resolved spectroscopy. Previous results estimated that the nuclear activity percentage in CALIFA was 4% using purely optical classifications (ratios of ionized gas emission lines). Our work involves a morphological and spectroscopic study through X-ray energies. For this purpose, we study 138 sources with available *Chandra* observations. From the morphological study, we identify that 66 of the 138 sources exhibit coincident point-like emission with the nucleus, which could be indicative of an AGN. Among these 66 sources, 49 have sufficient X-

ray counts (i.e., more than 50) for spectral analysis. We use simple models that reproduce AGN emission as well as models associated with other processes. We identify 34 objects not previously characterized as AGN in CALIFA through optical data alone. We study the location of X-ray-classified objects in diagnostic diagrams, commonly used to characterize ionization processes, allowing us to determine the limitations of using a single wavelength to classify these objects. The percentage of AGN in the CALIFA sample increases from 4% to 7-10% with multi-frequency study combining X-ray and optical data. Note, however, that we restrict our analysis to *Chandra*. Thus, these numbers might still be lower limits of the population. This provides the most comprehensive count of AGN in CALIFA to date. Using this sample, we study the connection between nuclear activity and the star formation in the host galaxies. Earlier studies had suggested that AGN-hosting galaxies are mostly in a transition zone between actively star-forming and retired galaxies. With the above-described sample, we find that our AGN are distributed in both regions of this diagram (i.e., the blue cloud and the red sequence).

This thesis is presented as a compilation of two articles published in the journal *Monthly Notices of the Royal Astronomical Society*: Osorio-Clavijo et al. (2022) and Osorio-Clavijo et al. (2023), where the primary author is the same presenting this document.

Contents

Agradecimientos	ii
Resumen	iv
Abstract	vii
1 Introduction	1
§1.1 Active Galactic Nuclei	1
§1.2 AGN - host galaxy connection	5
§1.3 AGN components	8
§1.4 AGN fundamental quantities	11
§1.5 Unification Scheme	15
§1.6 Complementary scenarios	17
§1.7 Spectral energy distribution	18
§1.8 AGN at X-rays	20
§1.9 AGN at optical	24
§1.9.1 Diagnostic diagrams	26
§1.10 Low Luminosity AGN	29
2 State of the art and aims of the thesis	32
§2.1 AGN torus behaviour for LLAGN	32
§2.2 AGN demographics	36
3 Methodology	41
§3.1 X-ray satellites used in this work	41
§3.2 Integral Field Spectroscopy	45

§3.2.1	CALIFA survey	47
§3.3	Statistical methods	50
§3.3.1	Chi-squared statistic	50
§3.3.2	Cash statistic	51
§3.3.3	F-test	51
§3.3.4	Bayesian Information Criterion	52
4	Behaviour of the reflection component for LLAGN	53
5	AGN in the CALIFA sample	72
6	Summary and conclusions	92
7	Future work	101
8	Appendix	107
§8.1	Catalogue of X-ray spectral fittings: Behaviour of the reflection component for LLAGN.	107
§8.2	Statistical values of the models used: Behaviour of the reflection component for LLAGN.	147
§8.3	Catalogue of morphological analysis: AGN in the CALIFA survey	149
§8.4	Catalogue of spectral fittings: AGN in the CALIFA survey	182

List of Figures

1.1	Artist representation of an AGN. Credit: ESA/NASA, AVO project and Paolo Padovani.	2
1.2	AGN family as seen from the radio wavelength regime. Image credit: Alan Roy.	4

1.3 Black hole mass (M_{BH} vs stellar velocity dispersion (σ diagram. Taken from McConnell & Ma (2013). 5

1.4 Color (u-r) vs stellar mass for galaxies in the Galaxy Zoo project. Green dots correspond to AGN hosts. Figure taken from Schawinski et al. (2010). 6

1.5 SFR vs stellar mass diagram for the galaxies in the MaNGA survey. Star symbols represent AGN hosts. The colors represent the equivalent width of the $H\alpha$ emission line. AGN hosts seem to be located in the so-called GV or a transition zone between SFGs and RGs. 7

1.6 Left: Theoretical SED of a BH with $M_{\text{BH}} = 10M_{\odot}$, with a RIAF accretion flow, and for different accretion rates (from bottom to top, the accretion rates are: $\log(\dot{M}_{\text{BHR}}) = -3, -2.5, -2, -1.5, -1, -0.5$) Figure taken from Narayan et al. (1996). Right: Schematic representation of ADAF model for accretion disks. The disk becomes geometrically thick and geometrically thin towards inner radii. Figure taken from Nemmen (2013). 9

1.7 Disk-wind model proposed by Elvis (2000) to explain the different classes of QSOs, which can be extended to the rest of AGN classes. The green area corresponds to the wind that is expelled from the accretion disk in specific directions, which explains the differences in observational properties. . . . 11

1.8 Illustration of the time-delay (or lag) between the emission from the disk and that of the BLR. With this information, we can obtain the radius of the BLR and M_{BH} . Image credit: Janie Hoorman 14

1.9 Unified Model of AGN. Taken from Zackrisson (2005). 15

1.10 SED of an AGN. Each color represents the individual component that is emitting at a certain wavelength as indicated in the label. Taken from the review by Hickox & Alexander (2018). Credit: C. M. Harrison. 19

1.11 Illustration of how the X-rays are emitted and reflected in AGN. Taken from Ricci 2011. PhD thesis. 20

1.12 AGN X-ray spectra. Each component is represented in the colors as follows:
 Red represents the intrinsic continuum modeled as a power-law which can be
 affected by obscuration. Magenta is the reflection component, represented
 by the FeK α line and the Compton hump. The soft excess (blue) which may
 be related to host galaxy emission or scattered emission from the corona.
 Image credit: Laura Di Gesu 2016 PhD thesis. 21

1.13 Effect of the obscuration in the X-ray spectra of AGN. For larger values
 of column density, the X-ray photons start to be down-scattered until the
 CT limit for which the X-ray spectrum is completely suppressed over the
 complete range. Figure taken from Gilli et al. (2007). 23

1.14 Optical spectra of different types of AGN, in contrast with the emission
 from a normal galaxy (bottom panel). The labels on each panel represent
 the type of AGN. All spectra have been retrieved from the NASA/IPAC
 Extragalactic Database (NED). 24

1.15 BPT and VO87 diagrams for the AGN diagnostic. The red line corresponds
 to the delimitation line defined by Kewley et al. (2001), while the dashed
 blue line is the demarcation line proposed by Kauffmann et al. (2003) and
 the blue solid line corresponds to the demarcation line proposed by Kewley
 et al. (2006). Figure taken from Kewley et al. (2006). 27

1.16 BPT and VO87 diagrams for a sample of galaxies as presented by Sánchez
 et al. (2018). The colorbar represents the EW(H α) with higher values repre-
 senting harder ionization. The stars represent the AGN candidates in their
 sample. 29

2.1	AGN bolometric luminosity vs M_{BH} for a sample of LINER and Seyfert objects in González-Martín et al. (2017). The grey area is the region in which the torus may or may not disappear depending on the wind parameters as predicted by Elitzur & Ho (2009), while the red area is the region in which the torus is expected to disappear regardless of M_{BH} . Objects with a black dot are the sources without any hints of the presence of the torus through mid-IR information.	33
2.2	Effects on the FeK α emission line due to the proximity of the emissor to the SMBH. Adapted from Fabian & Iwasawa (2000).	35
2.3	Diagnostic diagrams applied to the CALIFA survey. The star symbols correspond to the 34 AGN candidates provided by Lacerda et al. (2020) (10 type-I and 24 Type-II).	37
2.4	SFR vs stellar mass for the eCALIFA sample and in particular, the AGN. Figure taken from Lacerda et al. (2020). The colors and symbols are the same as in Fig 2.3.	38
3.1	Timeline of X-ray satellites in Astronomy. The blue arrow indicates the beginning of X-ray astronomy. Missions in black have been already launched, while missions in red are still under planning. The start date is marked with the bullet on the left of each mission, while the end date is marked with a bulled on the right.	41
3.2	Schematics of the configuration of mirrors for X-ray telescopes. X-ray photons are incident from the left part and redirected through the mirrors towards the focal point. Image credit: NASA/CXC/S. Lee.	42
3.3	Illustration of the <i>Chandra</i> X-ray satellite used in this project. Particularly, we use the ACIS camera. Image credit: NASA	43
3.4	Mean temperature of the ACIS focal plane through the years. Each point corresponds to a single observation, therefore the exposure time is not the same in all data points. Image credit: Grant et al. (2016).	44

3.5	Artist’s illustration of the <i>NuSTAR</i> X-ray satellite which was used for the development of this project. Image credit: NASA/JPL.	44
3.6	Different types of IFUs. Figure taken from C. López-Cobá’s PhD. Thesis. Adapted from Allington-Smith & Content (1998).	46
6.1	SFR vs. stellar mass diagram for the sources studied in our work. The semi-translucent squares at the back correspond to the total CALIFA sample (941 sources). The solid squares and white-bordered circles correspond to X-ray detected and non-detected sources. The black and white pentagons correspond to bona fide AGN and non-AGN sources, respectively. Finally, the yellow dots correspond to sources in common with Lacerda et al. (2020).	95
6.2	Bolometric luminosity versus M_{BH} for our sample. The red triangles are the candidates for the torus disappearance through the X-ray analysis, while the green squares are sources with signatures of reflection associated with the torus and the small empty stars correspond to the BASS sample (Koss et al., 2017). The semi-translucent circles represent the candidates for torus disappearance found by González-Martín et al. (2017) using mid-IR data. The black dashed lines represent $\log(L_{\text{Edd}}) = [0, -1, -2, -3, -4, -5, -6]$ from top to bottom, respectively. The two red lines enclose the region in which the torus may or may not exist depending on the wind parameters, as proposed by Elitzur & Ho (2009). The gray-shaded area corresponds to the Eddington rates from the sample not biased by the selection criteria. Note that those sources with Eddington rates above $\log \lambda_{\text{Edd}} \sim -2.5$ are not shown in this plot since at those Eddington rates our sample is not complete. The figure was published in Osorio-Clavijo et al. (2022).	98

- 7.1 Surface density luminosity of the [OIII] emission line vs surface X-ray luminosity in the 0.5-10 keV band for NGC0833. The grey contours correspond to the full image at the physical scale for both images. The blue diamonds, green squares and red triangles correspond to the pixels at the central 3, 2 and 1 kpc, respectively. The black solid, blue dot-dashed, green dashed and red dotted lines correspond to the best linear fit between both quantities for the full image, and at the central 3,2 and 1 kpc, respectively. 103
- 7.2 Surface luminosity of the [OIII] emission line vs surface X-ray luminosity in the 0.5-10 keV band for the sources with extended emission classified as AGN candidates (left panel) and non-AGN sources (right panel). The colors are associated with the inclination of the galaxy obtained from the CALIFA dataproducts. Each dotted line represents the individual correlation for the sources. **The dashed line in each panel corresponds to the average correlation of the sample in each case, while the sold line corresponds to the 1:1 relation.** 104
- 7.3 X-ray spectra of NGC 1129. The black line corresponds to the *XMM-Newton*105
- 8.1 *NuSTAR* spectra of M 51. The red and green areas correspond to the FMPA and FPMB detectors. The green solid line corresponds to the total model, while the long-dashed red, dotted-dashed blue, dashed green, and short-dashed cyan lines correspond to the absorbed power-law, pexmon component, and emission lines, correspondingly. 107
- 8.2 Morphological decomposition for ARP 220. Panel (a), (b), (c), (d), (e), and (f) correspond to the total emission, Gaussian of the extended emission, Gaussian of the nuclear emission, extended emission only, nuclear emission only and residuals, respectively. 149
- 8.3 *Chandra* spectrum of the nuclear region of NGC 0023. The green area corresponds to the spectra, while the red and blue lines correspond to a power-law and thermal models, respectively. The bottom panels represent the residuals of the fits for each model version. 182

Chapter 1

Introduction

1.1 Active Galactic Nuclei

Active Galactic Nuclei (AGN, Fig. 1.1) are one of the most energetic persistent phenomena in the Universe, with luminosities that can be as high as $L_{\text{bol}} \sim 10^{48} \text{ erg s}^{-1}$, emitting in small physical scales ($< 1\text{pc}^3$) (Netzer, 2015; Padovani et al., 2017, and references therein). The light emitted by these phenomena is of the order of several million of stars, which in such a small region can only be attributed to the existence of an accretion disk surrounding a super-massive black hole (SMBH) (Rees, 1984) that resides at the center of all the galaxies (or at least those with well developed bulges Gebhardt et al., 2000; Ferrarese & Merritt, 2000).

The study of AGN dates back to the beginning of the 20th century, with the doctoral dissertation by Fath (1909), who by taking a look at the optical spectrum of the now very well studied AGN, NGC 1068, realized that the galaxy presented strong and broad optical emission lines at the center, in comparison with galaxies with active star formation. However, it was until Seyfert (1943) that the first compendium of objects with similar nuclear properties was presented, known as Seyfert galaxies. Later on, with the development of radio astronomy, the AGN field became more studied with the discovery of quasi-stellar objects (QSOs) which due to their point-like shape were misclassified as stars, however the optical the spectra diverged from those of stars. The two first radio catalogue containing these sources were published in 1959 and 1962 (Edge et al., 1959; Bennett, 1962), which



Figure 1.1: Artist representation of an AGN. Credit: ESA/NASA, AVO project and Paolo Padovani.

were compared to the counterparts in optical (Zwicky, 1964) and UV (Markarian, 1967). It was the work by Matthews & Sandage (1963) that began the great interest for AGN, with the discovery of 3C 48, classified as a star, but with strong broad optical emission lines, with velocities of at least 700 km s^{-1} . 3C 273 was identified in 1963 (Hazard et al., 1963) and it was Schmidt (1963) who identified Balmer and MgII redshifted lines. Both Seyfert and QSOs were classified as part of the AGN family. However, along with these sources there are other types of AGN, which can be classified according to their observed properties:

- Seyferts: Sources of this type emit nuclear energy which is comparable to that of the host galaxy, with luminosities of $L_{\text{bol}} \sim 10^{42} - 10^{45} \text{ erg s}^{-1}$. The optical spectrum is characterized by forbidden emission lines ($[\text{OI}]\lambda 4861$, $[\text{OIII}]\lambda\lambda 4959, 5007$, $[\text{NII}]\lambda 6583$, and $[\text{SII}]\lambda\lambda 6716, 6731$) as well as the Balmer transition lines, such as $\text{H}\alpha$ and $\text{H}\beta$. In this family, there are two main types of AGN: Type-I (showing both broad and narrow emission lines) and Type-II (showing narrow emission lines only). There are also some intermediate types as defined by Osterbrock (1989): type 1.5 (with strong broad and narrow emission lines), type 1.8 (with weak broad emission lines and

strong narrow emission lines) and type 1.9 (with broad $H\alpha$ and narrow $H\beta$ emission lines).

- Quasars: These objects are the most luminous among the AGN family, with luminosities as high as $L_{\text{bol}} \sim 10^{48} \text{ erg s}^{-1}$ (Blandford et al., 2019) outshining the host galaxy and are seen as point-like sources. The optical spectrum shows both narrow and broad permitted emission lines and narrow forbidden emission lines. They present variability and in some cases emit at radio frequencies.
- Blazars: These objects are similar to quasars, with luminosities as high as $L_{\text{bol}} \sim 10^{48} \text{ erg s}^{-1}$ (Blandford et al., 2019), although they show a prominent radio jet, strong variability and present weak or even lack of emission lines. Their extreme properties are associated with the small angle of the jet with respect to the line-of-sight.
- Radio galaxies: These sources are characterized by their radio luminosity being of the order of that of the host galaxy ($L_{\text{bol}} > 10^{42} \text{ erg s}^{-1}$ Blandford et al., 2019). They can be divided, similarly to Seyferts, between broad-line and narrow-line radio galaxies (BLRGs and NLRGs, respectively).
- Low luminosity AGN (LLAGN): They were first identified by Heckman (1980). The spectral energy distribution (SED) of these sources is different from their more luminous pairs (e.g., Seyferts, Nemmen, 2013), suggesting a different accretion mechanism. LLAGN dominate the AGN population in the nearby Universe (Ho, 2008). The nuclear X-ray luminosity of these sources can be as low as $L_X = 10^{38} \text{ erg s}^{-1}$ (Roberts & Warwick, 2000)¹, making them the least luminous sources among the AGN families. Although, not all of them, a significant fraction of LLAGN are dominated by low ionization emission lines in their optical spectra. These sources are known as Low-Ionization Nuclear Emission Regions (LINERs Heckman, 1980), and while not all LINERs correspond to LLAGN, in this thesis, we focus on those who

¹The X-ray luminosity measured at the center, is in most cases attributed to AGN emission, despite of this limit being that of X-ray binaries (XRBs) and Ultra-Luminous X-ray sources (ULXs). Indeed, this luminosity would require more than a few XRBs/ULXs located in this spatial region of the host galaxy, which is unlikely (Fabbiano, 2006; Walton et al., 2022).

are indeed LLAGN. Since these objects are particularly relevant for this thesis, They will be discussed with more detail in sec. 1.10.

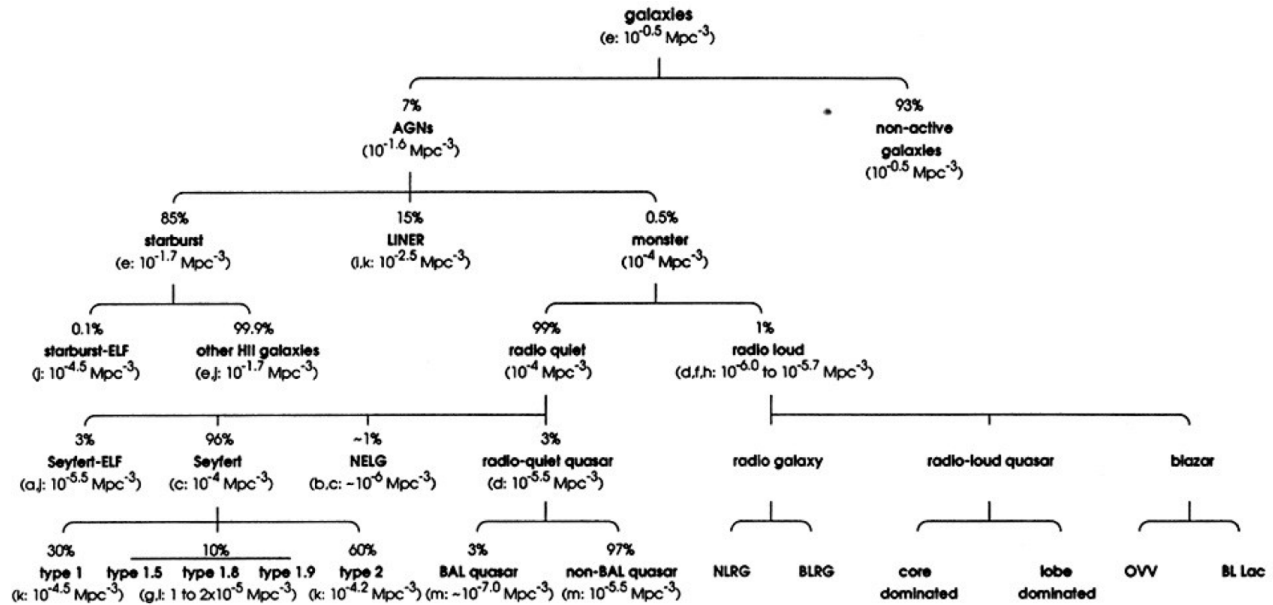


Figure 1.2: AGN family as seen from the radio wavelength regime. Image credit: Alan Roy.

However, the aforementioned types of AGN are classified through the optical wavelengths. Indeed, these objects, with the exception of Blazars, must have prominent optical emission lines to be considered as part of the AGN family. With the development of multi-wavelength astronomy, these objects were classified according to the features in the spectra. Other classifications include but are not limited to the radio band (see Fig. 1.2) in which we can find radio loud (Quasars, Blazars and Radio galaxies) to radio quiet (Seyferts and LLAGN), and even the X-ray band which divides the AGN depending on the material in the line-of-sight (LOS) between unobscured, Compton-thin and Compton-thick obscured sources (see 1.8 for details on the obscuration, see Padovani et al., 2017, for a recent review on AGN observational classification). A more physically motivated classification of AGN, is based on their accretion rate, which is associated with the black hole mass and the bolometric luminosity (see sec. 1.4). Thus, we find from quasars, the most luminous sources ($L_{\text{bol}} > 10^{45} \text{ erg s}^{-1}$ and $\dot{M}_{\text{BH}} \geq 0.1$ Dultzin-Hacyan et al., 2007), to Seyferts, which have luminosities $10^{42} < L_{\text{bol}} < 10^{45} \text{ erg s}^{-1}$ (and Eddington rates, $\dot{M}_{\text{BH}} \sim 0.01 - 0.1$ Bian &

Gu, 2007), and even the LLAGN which reside in the lowest tail of the luminosity function for AGN ($10^{38} < L_{\text{bol}} < 10^{42}$ erg s $^{-1}$, $\dot{M}_{\text{BH}} \sim 0.001$ Nemmen, 2013).

1.2 AGN - host galaxy connection

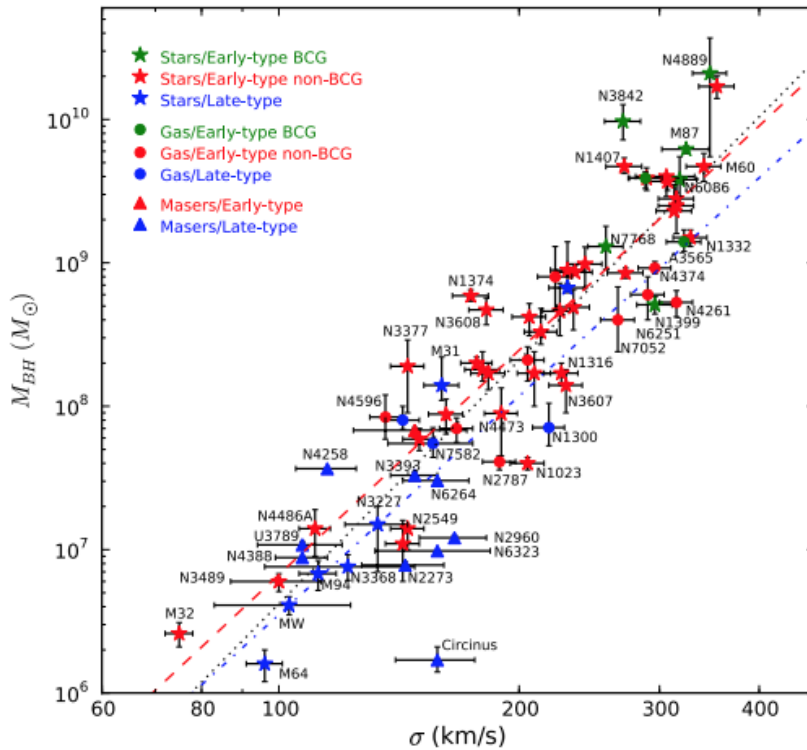


Figure 1.3: Black hole mass (M_{BH} vs stellar velocity dispersion (σ) diagram. Taken from McConnell & Ma (2013).

Within the framework of galaxy evolution, there are some irrefutable signatures that the black hole is tightly correlated with the host galaxy: i) there is a well known correlation between the velocity dispersion of the galaxy bulge and the SMBH (the $M - \sigma$ relation Ferrarese & Merritt, 2000; Gebhardt et al., 2000; Merritt & Ferrarese, 2001; Gültekin et al., 2009, see Fig. 1.3), but also on the overall characteristics of the host galaxy (such as the luminosity or mass of the bulge Kormendy & Richstone, 1995; Magorrian et al., 1998). ii) simulations and semi-analytic models show an excess of very massive galaxies, compared to observations. Thus, there must be a mechanism capable of heating or remove the gas from them, ultimately halting the star-formation rate (SFR, e.g., Sijacki et al., 2015;

Rosas-Guevara et al., 2016; Dubois et al., 2016).

One of the proposed mechanisms by which the gas is removed or heated due to AGN is known as AGN feedback. Some theoretical works suggest that AGN provides positive feedback, enhancing star formation (Ishigaki et al., 2012; Silk, 2013). Observational evidence of this effect has been seen through the correlation between the dust content in the galaxy and the AGN (Genzel et al., 1998; Kauffmann et al., 2003; Symeonidis et al., 2013; Kirkpatrick et al., 2015, among others), which could be triggered by merger events or interactive systems (Krongold et al., 2002; Kartaltepe et al., 2012) or induced by AGN jets or fast outflows (Croft et al., 2006; Ishigaki et al., 2012; Santoro et al., 2016).

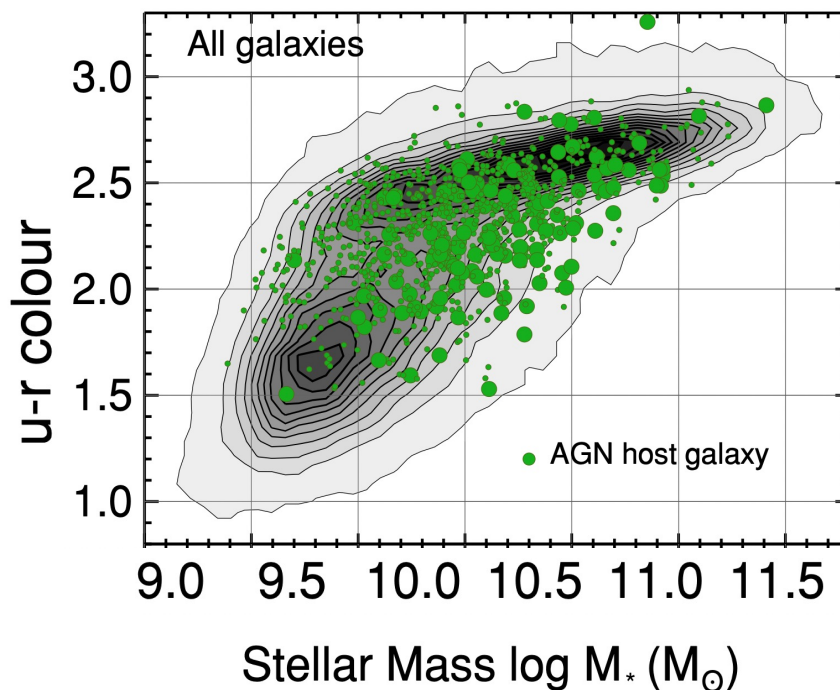


Figure 1.4: Color (u-r) vs stellar mass for galaxies in the Galaxy Zoo project. Green dots correspond to AGN hosts. Figure taken from Schawinski et al. (2010).

On the other hand, other authors propose that the AGN may quench the star formation by heating (Bower et al., 2006) or removing (Fabian, 2012; Trussler et al., 2020) the molecular gas available for star formation. Additionally, some authors suggest that the process that triggers AGN could also transform the galaxy morphology (Silk & Rees, 1998; Silk, 2005; Hopkins et al., 2010). Indeed, galaxies seem to live in two different locations

of the color-magnitude diagram (CMD, e.g., Strateva et al., 2001; Baldry et al., 2004), suggesting a mechanism responsible for this change. The transition between star forming galaxies (SFGs) and retired galaxies (RGs) invokes the necessity of either positive or negative feedback from AGN to alter the SF. Observational evidence (Sánchez et al., 2004b; Schawinski et al., 2010; Torres-Papaqui et al., 2012, 2013; Ortega-Minakata, 2015; Lacerda et al., 2020) show that galaxies hosting AGN are preferentially located in the transition region between SFGs (blue sequence) and RGs (red sequence) of the color-magnitude diagram (CMD) or the SFR- M_* (the so-called green valley (GV) Wyder et al. 2007, see Figures. 1.4, 1.5). However, it is important to note that the aforementioned results may be strongly biased to the optically-selected AGN. Moreover, the optical signatures of AGN may shift the position of galaxies in the diagram towards the GV (by altering the overall galaxy colors, see Sánchez et al., 2018) and a proper distinction between both regions is mandatory. Thus, it is also important to understand this evolutionary trend when analysing AGN at different wavelengths.

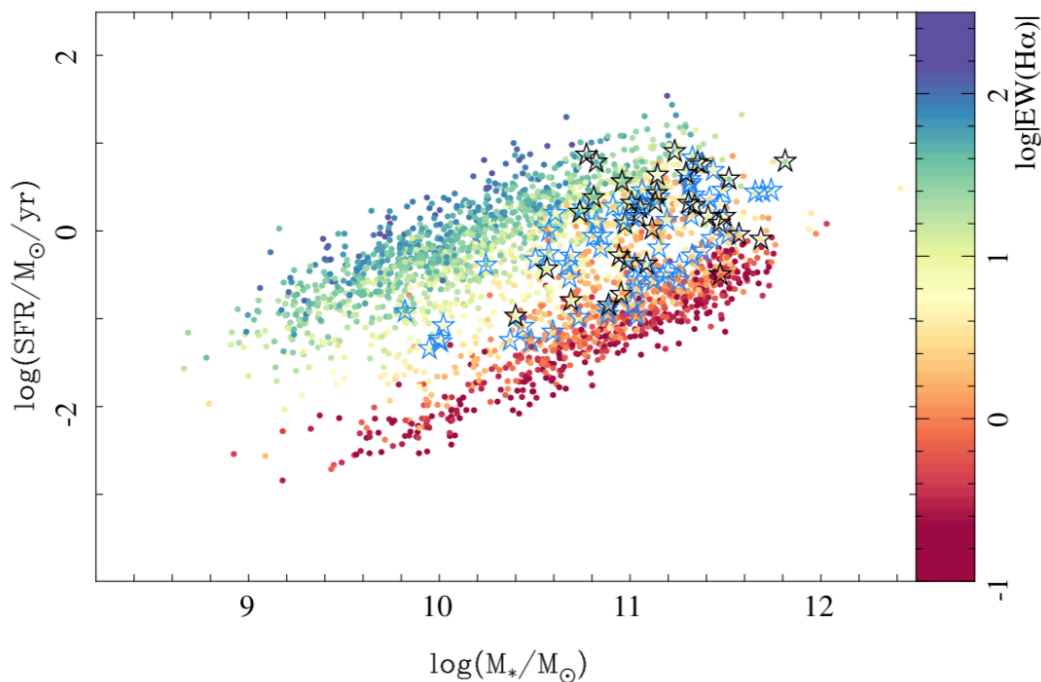


Figure 1.5: SFR vs stellar mass diagram for the galaxies in the MaNGA survey. Star symbols represent AGN hosts. The colors represent the equivalent width of the H α emission line. AGN hosts seem to be located in the so-called GV or a transition zone between SFGs and RGs.

1.3 AGN components

AGN are characterized by their large amount of energy released from a small region, based on the gravitational radius, which can be defined as:

$$r_g = \frac{GM}{c^2} \simeq 1.5 \times 10^{23} \frac{M_{BH}}{10^8} \text{cm} \quad (1.1)$$

where c is the speed of light, and G is the gravitational constant. Because of their size, AGN are mainly studied through the spectroscopic signatures of their components. In this section we enumerate the regions that compose an AGN, apart from the SMBH.

- *Accretion disk:* When the nucleus is in the active phase, the SMBH is surrounded by an accretion disk. This structure (with a size that can be $r_{\text{acc}} \sim 10 - 50r_g$, depending on the M_{BH} Netzer, 2015; Cackett et al., 2021, and references therein) is a rotating disk composed by hot gas falling onto the SMBH, with decreasing angular momentum, causing the material to spiral into the center. For a black hole of mass $M_{\text{BH}} = 10^6 M_{\odot}$ this radius would be of $r_{\text{acc}} \sim 0.02$ pc, while for a black hole of mass $M_{\text{BH}} = 10^9 M_{\odot}$, this radius would be of $r_{\text{acc}} \sim 0.04$ pc. Gravitational potential energy is then converted into electromagnetic radiation and kinetic energy. The emission from this region dominates at optical-UV wavelengths, with a peak of emission at the UV, and is characterized by a strong continuum, associated with thermal emission modelled with a modified black body and temperatures of $T \sim 10^4 - 10^5$ K (see the review by Hickox & Alexander, 2018). The accretion disk is responsible for the AGN emission that heats the rest of the components.

Moreover, the accretion disk can be divided into thin, slim and thick depending on its geometry and accretion rate, and can also be optically thick or thin depending on its column density. These two characteristics are associated with the efficiency of the disk in feeding the central source. The geometrically thin, optically thick disk is radiatively efficient (the so-called α -disk Shakura & Sunyaev, 1973) and is defined as the standard disk, and is thought to be the preferred scenario for efficient AGN (Abramowicz et al., 1988; Ohsuga & Mineshige, 2011; Netzer, 2013; Capellupo

et al., 2015, and references therein). Other types of disks include the geometrically slim and thick, optically thin accretion flows, for which the decrease of the column density causes a decrease in the disk temperature, leading to the thickening of the disk, retaining most of the energy, causing advection dominated or radiatively inefficient accretion flows (ADAF and RIAF, respectively Narayan & Yi, 1994a, see also sec. 1.10). Thus, as the disk goes from efficient to inefficient, which is estimated to happen at Eddington rates (see sec 1.4) $\lambda_{\text{Edd}} \sim 10^{-3} - 10^{-2}$ (Esin et al., 1997; Gallo et al., 2003) up to a point where the accretion disk is no longer capable of feeding the SMBH enough to produce radiation.

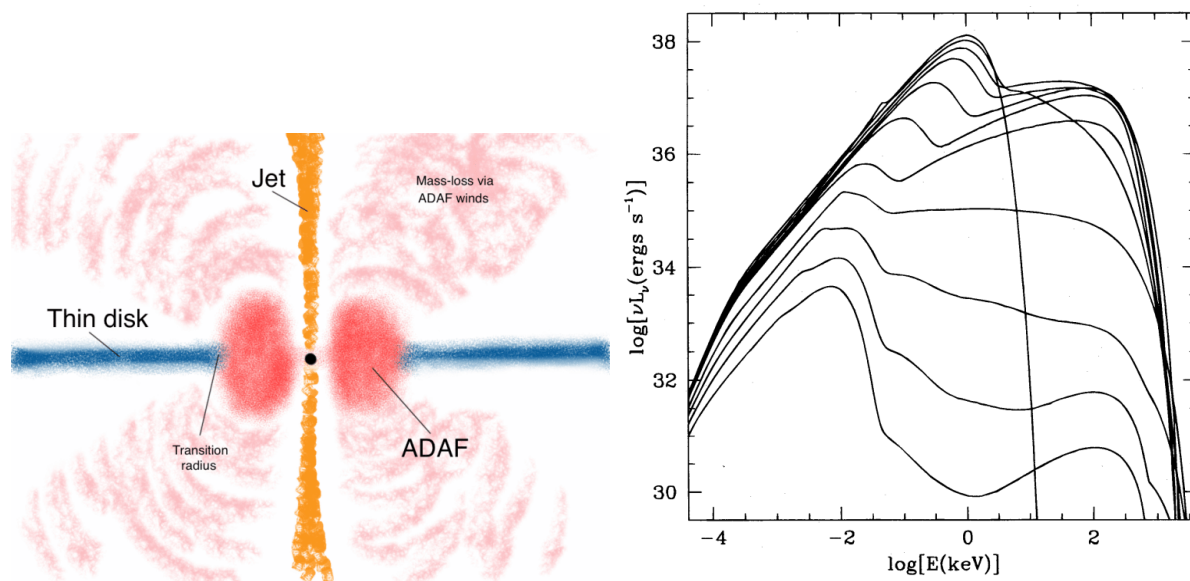


Figure 1.6: Left: Theoretical SED of a BH with $M_{\text{BH}} = 10M_{\odot}$, with a RIAF accretion flow, and for different accretion rates (from bottom to top, the accretion rates are: $\log(\dot{M}_{\text{BH}}) = -3, -2.5, -2, -1.5, -1, -0.5$) Figure taken from Narayan et al. (1996). Right: Schematic representation of ADAF model for accretion disks. The disk becomes geometrically thick and geometrically thin towards inner radii. Figure taken from Nemmen (2013).

- Broad Line Region (BLR): Beyond the accretion disk, at distances of 0.1-1 pc depending on the M_{BH} , there is a region of large column density (10^{23} cm^{-2}) and high density ($n \sim 10^{10} \text{ cm}^{-3}$) gas clouds moving at speeds of several thousands of km s^{-1} , due to its proximity to the SMBH. The size of this region is relatively small, although it is driven by the M_{BH} . For the most luminous quasars, it has been calculated to

be of $R_{\text{BLR}} \sim 0.2$ pc, although for less luminous sources is of the order of 0.1 pc (Osterbrock, 1989). Therefore it has not been resolved up to date. The large speed at which the clouds are moving, produces a broadening in the emission lines that are produced in this region, with line widths of several thousands of km s^{-1} (Netzer, 1990). This region is bounded because gravity dominates over radiation pressure. Moreover, the flux of the lines produced in this region follow the variations of the intrinsic continuum probably due to the photoionization from the central source (see Netzer, 2013).

- *Torus*: This axisymmetric structure is located further away from the central source, at distances between 1-10 pc. In the classic scheme (Unified Model, see sec. 1.5), it has a toroidal shape and is composed by dust, presenting the peak of emission at mid-infrared (mid-IR) wavelengths. However, observational works have shown that the geometry and composition are more complicated (Nikutta et al., 2009; Ramos Almeida et al., 2009, 2011; Alonso-Herrero et al., 2011; González-Martín et al., 2019, among others). For instance, it has been shown that this is a multi-phase structure, and can be separated into gas, dust and molecular phases and would emit at other wavelengths, such as X-rays, as the inner walls are composed by gas and can reprocess the X-ray photons that come from the corona above the disk (Awaki et al., 1991; Ghisellini et al., 1994). As for the geometry, it has been long debated whether the torus is an extension of the BLR and both can be seen as a wind produced by the accretion disk (Elvis, 2000, see Fig. 1.7). Part of this thesis is devoted to understand the behaviour of this component through the X-rays when the accretion rate is in the low regime.
- *Narrow Line Region (NLR)*: This region is formed by low-density ($n \sim 10^2 - 10^4 \text{ cm}^{-3}$) and low column density clouds ($10^{20-21} \sim \text{cm}^{-2}$ Netzer, 2015, and references therein). It is located outside the torus, at distances up to 1000 pc. Because of this, the clouds moving in this region have a low velocity ($< 1000 \text{ km s}^{-1}$), producing narrow line profiles. However, this region presents different states of ionization, producing both low and high ionization emission lines. Regardless of the level of

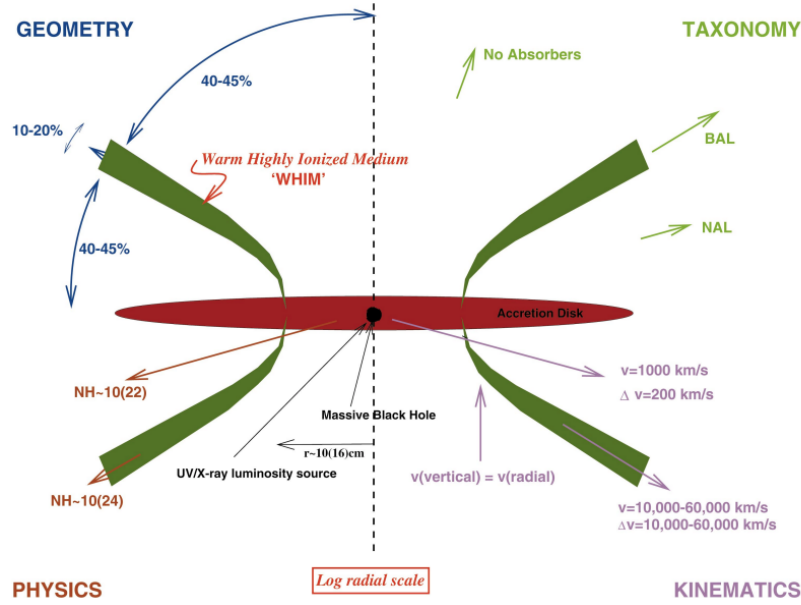


Figure 1.7: Disk-wind model proposed by Elvis (2000) to explain the different classes of QSOs, which can be extended to the rest of AGN classes. The green area corresponds to the wind that is expelled from the accretion disk in specific directions, which explains the differences in observational properties.

ionization, the emission lines produced in this region are strong (see Netzer, 2013).

- *Jet*: A collimated jet is found in $\sim 10\%$ of AGN population (Panessa et al., 2019, and references therein). While there are different physical mechanisms that can produce a jet, in the case of AGN, this structure is thought to be formed when the SMBH is spinning, producing a magnetized medium. The physical scales of these jets can go from AU to Mpc depending on the power of the source. While the radio spectra of AGN is dominated by the jet emission, these jets can also emit up to TeV energies in the case of Blazars (for a review on jets in AGN see Blandford et al., 2019, and references therein).

1.4 AGN fundamental quantities

There are three quantities that are considered fundamental to understand the variety of AGN: the black hole mass M_{BH} , the bolometric luminosity and the Eddington rate.

- Black hole mass (M_{BH}): In order to measure M_{BH} , there are several methods that can be used. The most direct method is using the orbits of stars closer to the SMBH, as was done for SgrA*² (at the center of our Galaxy Genzel et al., 1997; Ghez et al., 1998). Using the proper motion of these stars, it is possible to reproduce their orbit, and following Kepler’s laws, we can estimate the mass of the central object. Other methods include the scaling relations (such the $M - \sigma_*$ relation Ferrarese & Merritt 2000; Gebhardt et al. 2000 or the $M - L$ Magorrian et al. 1998), in which it is expected that the SMBH evolves together with the host galaxy (see sec. 1.2). Other methods include measuring the lag in the change of the emission lines from the BLR with respect to the continuum emitted at the accretion disk to estimate the size of the region and thus, the black hole mass (assuming Kepler’s third law). This method is called reverberation mapping (Peterson, 1993) and has been proven successful at measuring M_{BH} due to the proximity of the gas and the SMBH:

$$GM_{\text{BH}} = f R_{\text{BLR}} V^2 \quad (1.2)$$

Where G is the gravitational constant, f is the geometrical factor that depends on the shape of the BLR and V is the velocity at which the lines are being affected, which can be obtained through spectroscopical measurements. As for R_{BLR} it can be calculated through the lag time that the lines produced in it respond to the changes in the continuum, following:

$$R_{\text{BLR}} = \tau c \quad (1.3)$$

where the lag τ is associated with the light-crossing time between the disk and the BLR (i.e., the time-delay between the emission from the disk and the BLR, see Fig. 1.8). However, while the estimates are accurate, it has been applied to only a handful of objects³ due to the difficulties at detecting the time-lag between the continuum and the emission line (Netzer & Peterson, 1997, and references therein).

Another useful indirect method is measuring the line width of the $H\beta$ line and the

²This method has not been applied to other galaxies due to the distance (Roberts et al., 2021).

³see <http://www.astro.gsu.edu/AGNmass/>

corresponding continuum at 5100Å, as described by (Vestergaard & Peterson, 2006):

$$\log M_{BH} = \log \left[\left(\frac{FWHM(H\beta)}{1000 \text{ km s}^{-1}} \right)^2 \left(\frac{\lambda L_{\lambda 5100}}{10^{44} \text{ erg s}^{-1}} \right)^{0.5} \right] + (6.91 \pm 0.02) \quad (1.4)$$

and similarly, with the CIV line and the corresponding continuum at 1350Å, described in the same work:

$$\log M_{BH} = \log \left[\left(\frac{FWHM(CIV)}{1000 \text{ km s}^{-1}} \right)^2 \left(\frac{\lambda L_{\lambda 1350}}{10^{44} \text{ erg s}^{-1}} \right)^{0.5} \right] + (6.66 \pm 0.01) \quad (1.5)$$

Finally, X-rays are also an indirect way to measure this quantity. Using the power spectral density (PSD):

$$P(\nu) \sim \nu^{\alpha} \quad (1.6)$$

where $P(\nu)$ is the power at frequency ν and *alpha* is the slope, which is expected to change at the breaking frequency (with values around $\alpha \sim -2, -1$ Markowitz et al., 2003; McHardy et al., 2005). This break has been shown to be associated with the characteristic variability timescale, as

$$T_B = 1/\nu_B \quad (1.7)$$

which seems to correlate linearly with M_{BH} (Markowitz et al., 2003; Papadakis, 2004; McHardy et al., 2005).

- Bolometric luminosity (L_{bol}): The bolometric luminosity is that integrated over the entire SED of the source. However, obtaining information throughout the electromagnetic spectrum can be a difficult task, and different correlations have been proposed to estimate L_{bol} from a single waveband (Carballo et al., 1999). In this thesis, we obtain it through the X-ray luminosity, as it can be corrected from host galaxy and intrinsic absorption. While there are many bolometric corrections (Shankar et al., 2004; Hopkins et al., 2007; Vasudevan & Fabian, 2007; Lusso et al., 2012,

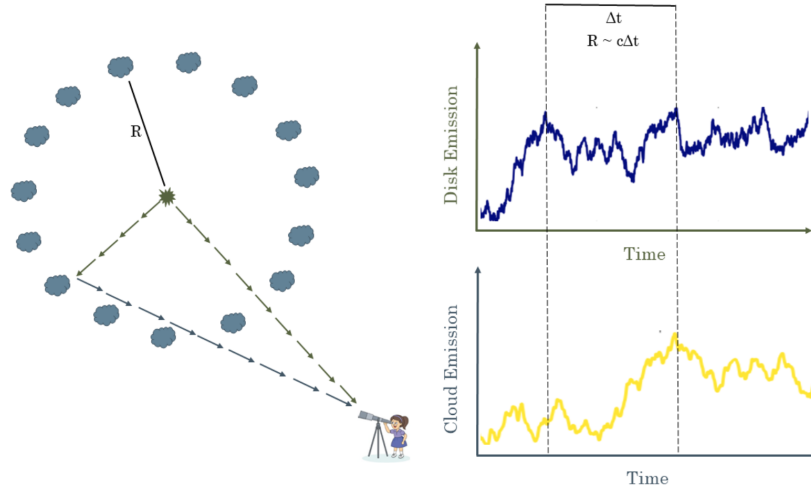


Figure 1.8: Illustration of the time-delay (or lag) between the emission from the disk and that of the BLR. With this information, we can obtain the radius of the BLR and M_{BH} . Image credit: Janie Hoorman

among others), in this work we will use the one by Marconi et al. (2004):

$$\log[L_{\text{bol}}/L_{(2-10 \text{ keV})}] = 1.54 + 0.24(\log(L_{\text{bol}}) - 12) + 0.012(\log(L_{\text{bol}}) - 12)^2 - 0.0015(\log(L_{\text{bol}}) - 12)^3. \quad (1.8)$$

where L_{bol} is in units of L_{\odot} .

- Eddington luminosity (L_{Edd}): This quantity is defined as the maximum isotropic luminosity an spherical object can emit without losing the stable equilibrium between the gravity and the radiation pressure. It can be defined as:

$$L_{\text{Edd}} = 1.5 \times 10^{38} \left(\frac{M_{\text{BH}}}{M_{\odot}} \right) \text{ erg s}^{-1} \quad (1.9)$$

- Eddington rate: This quantity is defined as the accretion rate of an astrophysical object that radiates at the Eddington luminosity

$$\dot{m}_{\text{Edd}} = \frac{L_{\text{Edd}}}{\epsilon c^2} \quad (1.10)$$

where ϵ is the efficiency and c is the speed of light.

Similarly, the Eddington ratio relates the Eddington and bolometric luminosities as :

$$\dot{M}_{BH} = \frac{L_{bol}}{L_{Edd}} \quad (1.11)$$

In this way, we can determine how efficient is the accretion disk at feeding the SMBH. Sources with $\dot{M}_{BH} > 0.1$ are super efficient, while those with $\dot{M}_{BH} < 0.01$ are classified as inefficient sources.

1.5 Unification Scheme

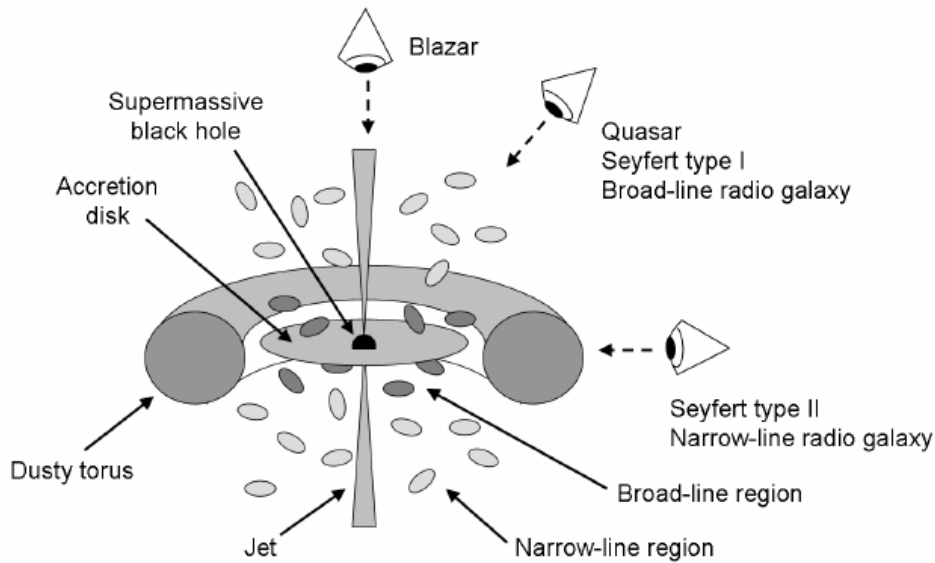


Figure 1.9: Unified Model of AGN. Taken from Zackrisson (2005).

Despite the apparent diversity of AGN from the observational point of view, a unification scheme has been proposed. The Unified Model (UM, Antonucci, 1993; Urry & Padovani, 1995) suggests that all AGN can be explained with the same scenario, which consists of the SMBH being fed by the accretion disk, surrounded by clouds composed of gas and dust at different spatial scales (as described in sec. 1.3), contributing to the overall AGN emission. The different types of AGN can be explained through different

inclinations of the AGN with respect to the observer. The simplest approximation is that the doughnut-like dusty torus adds a dependence on the viewing angle of the observer, but also the existence of the jet and the luminosity of the source. Fig. 1.9 shows a sketch of the UM. This scenario serves to distinguish among some of the different types, and explains the observational differences in different wavelengths. For instance, the difference between optically classified Type-I and Type-II objects is the existence (Type-I) or lack of (Type-II) broad emission lines, due to the obscuration of the BLR as the torus is in the LOS. The addition of the jet serves to distinguish between radio loud and radio quiet objects when the jet exists (loud) or is missing (quiet). Additionally, the luminosity of the source is able to explain the difference between Seyferts, with luminosities of the order of that of the host galaxy, and quasars, which in some cases outshine the host galaxy. In favour of the UM, X-ray observations show that in general, type-II sources have higher column densities, suggesting obscuration in the LOS, as claimed by the UM (Awaki et al., 1991; Bassani et al., 1999; Risaliti et al., 1999).

However, one of the main problems of the UM is the fact that it cannot explain all the AGN classes. One example are the LLAGN, for which another accretion mechanism rather than the standard accretion disk is proposed to explain the absence of the big-blue bump and the weak UV continuum compared to the X-rays (Ho et al., 1996), or very high luminous AGN, in which the existence of a dusty region is arguable (Jiang et al., 2010; Hao et al., 2011), and even the changing-look AGN, which have variations that cannot be explained under this model (but rather are attributed to changes in the accretion disk, see Elitzur et al., 2014; Lyu et al., 2022, and references therein). Additionally, this model does not account for the AGN-host galaxy connection and the implications that nuclear activity has on the star formation (Fabian, 2012; Heckman & Best, 2014). Therefore, it is required more information to determine which aspects of the UM should be modified or if on the contrary, the entire scenario is still valid. Thus, despite of the fact that the UM offers an appealing scheme to explaining a wide range of phenomenologies associated with AGN activity, it is clear that it is insufficient to explain all of them. Furthermore, it is clear that, as we obtain more information about AGN, it becomes more difficult to fit them all into this somehow simplistic scheme. For instance, the so-called true Type-II object for

which the BLR seems to be intrinsically missing, or the LLAGN for which the accretion disk does not reproduce the characteristic big blue bump at optical wavelengths.

1.6 Complementary scenarios

Modifications to the UM have been developed in order to understand the sources that are intrinsically different. In terms of the obscuring structure, there have been several attempts to understand the complexity of this component and its implication in the different AGN types. Indeed, observations suggest that the obscuring structure may not be the homogeneous toroidal dusty structure, disconnected from the inner AGN structures (see the reviews by Netzer, 2015; Ramos Almeida & Ricci, 2017a; Hickox & Alexander, 2018) and that this region is rather a dynamical structure which is driven by the radiation field of the disk (forming a bipolar outflow capable of sustaining the BLR and the torus under certain conditions Elitzur & Shlosman, 2006; Elitzur & Ho, 2009; Wada, 2012, 2015). In fact, observations from NGC 1068 and Circinus galaxy suggest that the material is being expelled in the form of outflows (Gallimore et al., 2016; Izumi et al., 2018).

In the scenario proposed by Elitzur & Shlosman (2006), the radiation pressure of the wind is capable of counteracting the gravity produced by the SMBH as long as the accretion disk keeps feeding it (i.e., for efficient sources), and both the BLR and the torus are part of this outflow. In this work, they find that both the BLR and the torus should disappear for sources with low bolometric luminosities ($L_{\text{bol}} < 10^{42} \text{erg s}^{-1}$). However, the reality is most probably more complex than what this scenario suggests (i.e., a pure dependence with the bolometric luminosity). Indeed, Elitzur & Ho (2009) find that there is a set of parameters that lead to the existence or disappearance of the torus, which includes: i) the efficiency of the wind, ii) the radial extent, iii) the black hole mass, iv) the density, among others, that invoke a region below which the torus disappears regardless of the black hole mass and bolometric luminosity. Indeed, such models are capable of explaining the existence of torus in some LLAGN, and the lack of obscuration in Type-II sources with high accretion rate, where the wind may sweep off the torus at very high accretion rates Elitzur & Netzer (2016), or it can even sweep off larger scale molecular gas, such as circumnuclear disks

(García-Burillo et al., 2014; Alonso-Herrero et al., 2018; García-Burillo et al., 2021).

1.7 Spectral energy distribution

One particularity of AGN is the fact that they emit throughout all the electromagnetic spectrum. Each wavelength provides information regarding the physical mechanism and the physical component (from the ones described in sec. 1.3) is emitting. Figure 1.10 shows a schematic representation of SED of an AGN and, in different colors, the component that is emitting at a certain frequency. For instance, the peak of emission from the accretion disk occurs at UV wavelengths and one of the main features of this emission is the big blue bump (BBB). However, part of this emission is scattered at X-ray energies and can produce a set of features that will be discussed in sec. 1.8. At lower frequencies, both the BLR and the NLR emit at optical wavelengths. In fact, the width of some of the lines emitted at those regions give information regarding which region emitted the line. Infrared bands are more sensible to the dust emission and the torus is expected to dominate, and while the shape of the spectrum at near-IR is still unknown, it is expected for the AGN to have a non-negligible contribution below the dominance of other contributions associated with the host galaxy. Finally, synchrotron emission from the jet and non-thermal processes dominate at radio frequencies.

Thus, AGN can be explored in all spectral bands. More importantly, the different spectral windows provide insightful information regarding these sources. With information in a single waveband, objects can be classified depending on the features on the spectra. For instance, through radio, AGN can be distinguished as radio quiet/loud depending on their radio luminosity, which is indicative of the jet power. Moreover, these jets can be distinguished between FR-I/FR-II depending on whether the peak in luminosity occurs on the core or on the lobes of the jet (Fanaroff & Riley, 1974). Also, through X-rays they can also be classified as Compton-thin/Compton-thick depending on the column density of the gas, through the line-of-sight to the observer. Finally, based on the optical information, as we indicated before, AGN can be classified as Type-I/II depending on the existence of broad lines (see above). Moreover, the different optical line ratios are useful to

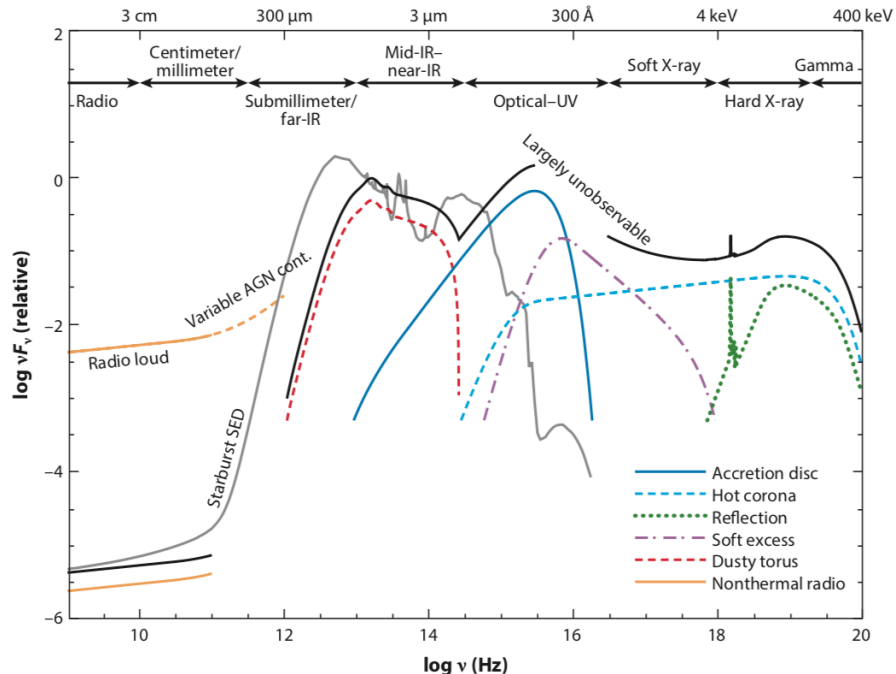


Figure 1.10: SED of an AGN. Each color represents the individual component that is emitting at a certain wavelength as indicated in the label. Taken from the review by Hickox & Alexander (2018). Credit: C. M. Harrison.

determine whether a galaxy hosts an AGN or not (see sec. 1.9.1). However, observational classification are debated due to the bias and difficulties that each regime provides. At radio wavebands, non-jetted radio-emitting sources are difficult to be identified as AGN, particularly at high redshifts, due to technical limitations (Panessa et al., 2019), while at X-rays, the detectability is subject to the column density and the intrinsic luminosity of the source, i.e., sources with large column densities may not be detected in the 2-10 keV band (Comastri, 2004, see next section). LLAGN are also subject to the sensitivity limits of the instruments used. In the case of optical detection, the fact that many of them are buried behind large amounts of material and that the host galaxy may even dilute the AGN emission (Benn et al., 1998; Richards et al., 2001; Comastri et al., 2002; Caccianiga et al., 2007; Davies et al., 2016, among others), may be preventing us from seeing the less-luminous and/or highly obscured AGN in this range. Thus, information at different wavelengths is essential to obtain a complete picture of the AGN behaviour. In this thesis, we focus our study in understanding primarily the X-ray emission of AGN

sources and compare it with what is found at optical wavelengths.

1.8 AGN at X-rays

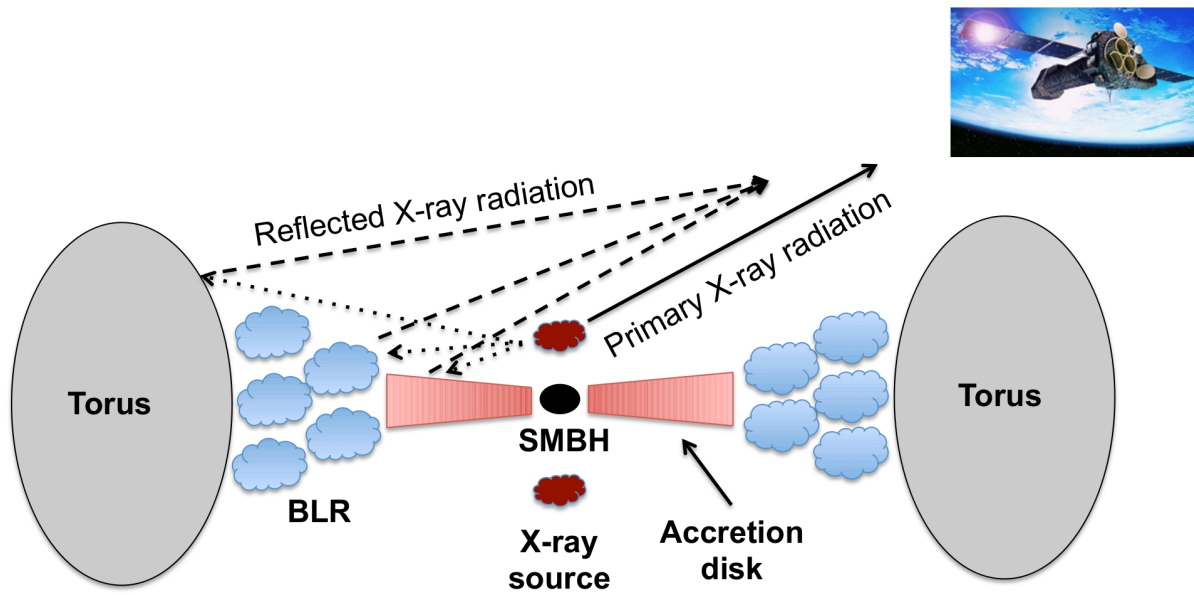


Figure 1.11: Illustration of how the X-rays are emitted and reflected in AGN. Taken from Ricci 2011. PhD thesis.

While there are several astronomical objects that emit at X-rays, most of which are associated with very energetic processes (some examples include X-ray Binaries (XRBs), evolved stars, Ultra-Luminous X-ray Sources (ULXs), etc), we are particularly interested in the X-ray information provided by AGN. The X-ray regime is classically divided into two different domains:

- Soft X-rays: $E[0.1 - 2 \text{ keV}]$
- Hard X-rays: $E > 2 \text{ keV}$

The X-ray emission associated with nuclear activity comes from the reprocessing of the soft energy photons from the accretion disk in a region known as corona. Indeed, more realistic scenarios of accretion disks show that the optical/UV photons from the accretion disk are reprocessed by a corona of high-energy electrons located close to it. These hot

electrons up-scatter the photons in X-rays, in a process known as Comptonization. The emission from the corona is known as primary X-ray continuum. While the origin and geometry of the corona is still matter of debate, its presence causes is responsible for the X-ray emission of AGN. The emission can then be scattered, obscured and reflected in other regions of the AGN Figure 1.11 shows a more recent scheme of the X-ray emission process in AGN. The X-ray spectrum of an AGN will account for these effects, as shown in Fig. 1.12.

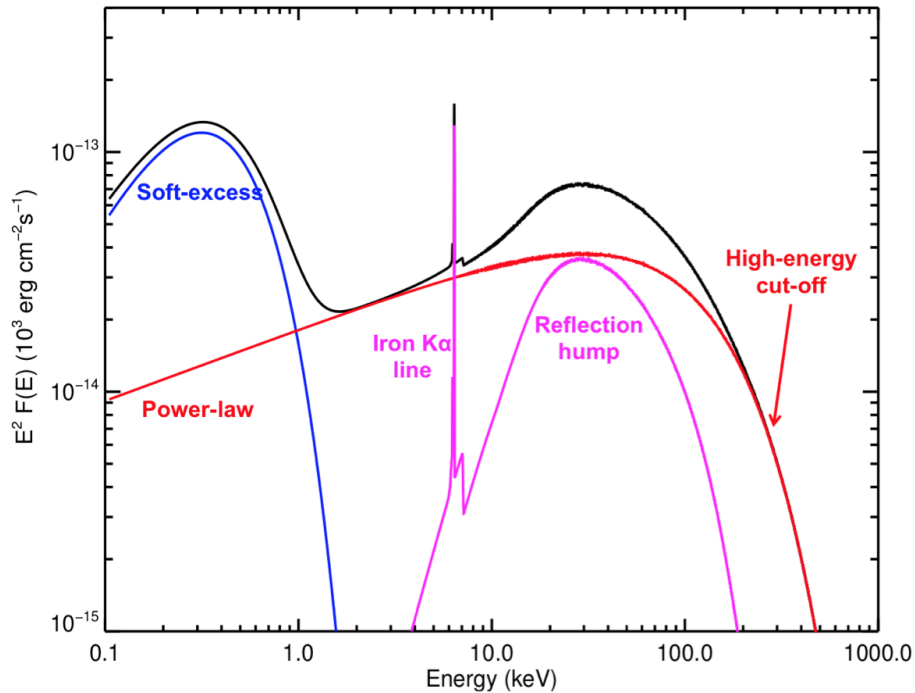


Figure 1.12: AGN X-ray spectra. Each component is represented in the colors as follows: Red represents the intrinsic continuum modeled as a power-law which can be affected by obscuration. Magenta is the reflection component, represented by the $\text{FeK}\alpha$ line and the Compton hump. The soft excess (blue) which may be related to host galaxy emission or scattered emission from the corona. Image credit: Laura Di Gesu 2016 PhD thesis.

The archetypal X-ray spectrum of AGN consists of the Comptonization of soft photons in the corona above the disk that produces a power-law continuum of the form $F(E) = AE^{-\Gamma}$ (red line of Fig. 1.12). The average value of the photon index is $\Gamma \sim 1.8$ (Nandra & Pounds, 1994; Bianchi et al., 2009). This power-law presents a high energy cut-off, associated with the temperature and the optical depth of the plasma (Haardt & Maraschi, 1991). The intrinsic emission can be affected by absorption in the line of sight,

causing a drop of the power-law at softer energies (below 2 keV). The origin of the material causing obscuration is still debated (see the reviews by Netzer, 2015; Hickox & Alexander, 2018).

While some works show evidence that it is associated with the material in the torus, as Type-II sources show in general higher column density values (in agreement with the UM scenario Awaki et al., 1991; Bassani et al., 1999), other works suggest that the clouds in the BLR can also cause obscuration, due to the fast variations in the column density, which can be attributed to clouds closer to the SMBH (Bianchi et al., 2004; Guainazzi et al., 2005, and references therein). The obscuration plays a significant role in the detection and classification of AGN, particularly below 10 keV (Comastri, 2004; Ramos Almeida & Ricci, 2017a; Hickox & Alexander, 2018). Indeed, several works suggest that the fraction of AGN in the Universe might be underestimated due to this effect (Comastri et al., 2011; Donley et al., 2012; Marchesi et al., 2018). Figure 1.13 shows the effect of the material in the LOS on the X-ray spectrum.

While for unobscured sources the intrinsic continuum is completely transmitted, for larger values of column density the powerlaw is affected. Indeed, for column densities higher than $N_{\text{H}} = 10^{24} \text{ cm}^{-2}$, the intrinsic continuum is completely suppressed below 10 keV (see the black line representing $\log(N_{\text{H}}) > 25$ dex). This regime is known as Compton-thick (CT) which is defined as *the column density that is equal to or larger than the inverse of the Thomson cross-section* (Comastri, 2004) and is mostly associated with the inner parts of the torus. However, the most accepted paradigm is that obscuration can occur in different physical scales (which includes the BLR, the torus and the host galaxy Ramos Almeida & Ricci, 2017a). Sources with column densities below this threshold are referred to as Compton-thin ($10^{22} \text{ cm}^{-2} < N_{\text{H}} < 10^{24} \text{ cm}^{-2}$) and the power-law is still detected in the X-ray spectral range Comastri (2004).

Apart from absorption, the primary X-ray photons can also suffer from reflection by gas in the AGN. This reflection (magenta line in the same figure) has two features: an iron emission line ($\text{FeK}\alpha$) at 6.4 keV and a Compton hump that peaks at 20-30 keV (see sec. 2.1). Finally, a soft excess below 2 keV (blue line in the same figure) has been attributed to different processes, also depending on the physical scales at which it is detected. For

instance, if is the result scattering by an ionized medium (such as the clouds in the NLR Guainazzi & Bianchi, 2007; Gonzalez-Martin et al., 2010; Paggi et al., 2012, attributed to type-II sources), or diffuse emission from the host galaxy (Guainazzi et al., 2005), while if it is the effect of the high energy component of the thermal comptonization from the disk produced in the optical/UV (Magdziarz et al., 1998; Middleton et al., 2009; Mehdipour et al., 2011), or ionized reflection in the inner parts of the disk (see Done et al., 2007), mostly attributed to type-I sources. Nonetheless, the origin of the soft excess is still highly debated and no concensus has been achieved, as the different scenarios proposed are statistically acceptable (Sobolewska & Done, 2007). However, the study of the spatial scales of this excess can help understand the origin of it. For instance, extended soft X-ray emission is attributed to the NLR or the host galaxy (Bianchi et al., 2006; Gonzalez-Martin et al., 2010; Gómez-Guijarro et al., 2017), while point-like soft X-ray emission is attributed to inner parts of the AGN (Czerny & Elvis, 1987; Crummy et al., 2006).

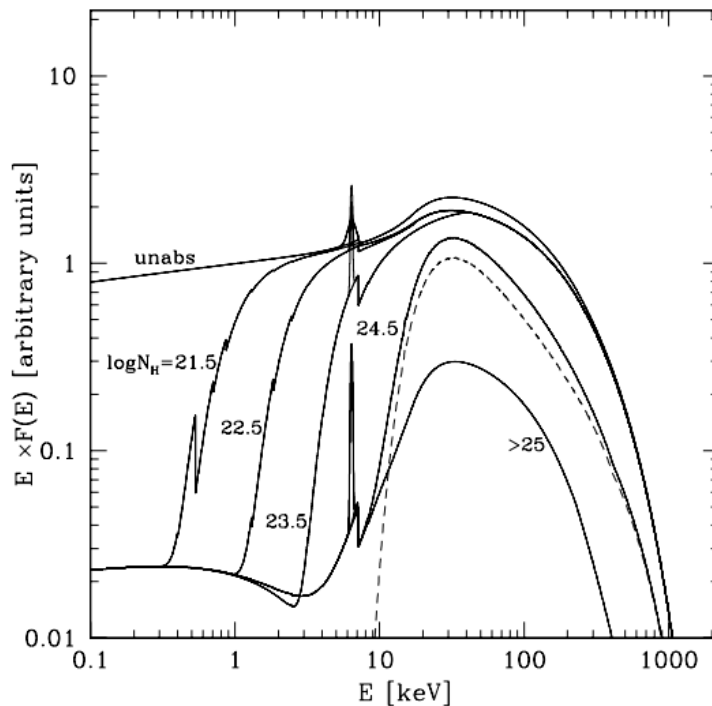


Figure 1.13: Effect of the obscuration in the X-ray spectra of AGN. For larger values of column density, the X-ray photons start to be down-scattered until the CT limit for which the X-ray spectrum is completely suppressed over the complete range. Figure taken from Gilli et al. (2007).

1.9 AGN at optical

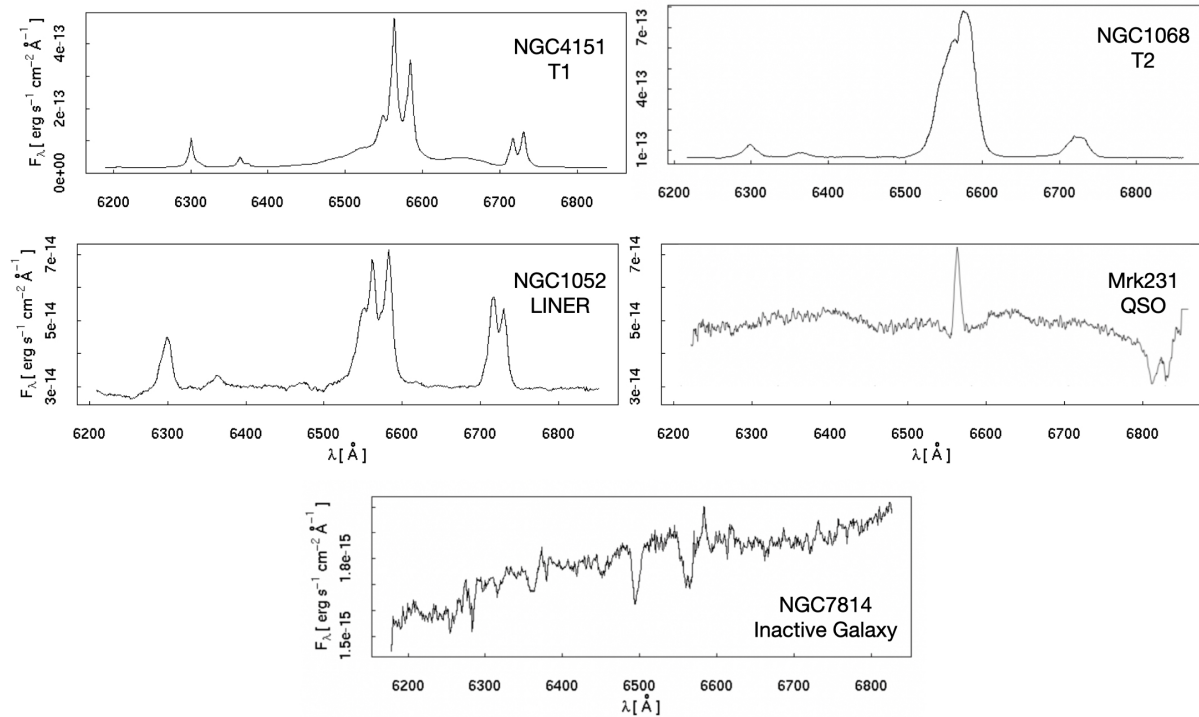


Figure 1.14: Optical spectra of different types of AGN, in contrast with the emission from a normal galaxy (bottom panel). The labels on each panel represent the type of AGN. All spectra have been retrieved from the NASA/IPAC Extragalactic Database (NED).

Different processes occurring in AGN produce emission in the optical wavelength regime. The accretion disk emits at optical/UV wavelengths, with a continuum emission and a bump located at $\sim 1 \mu\text{m}$ (the so-called big blue bump Sanders et al., 1989; Bregman, 1990) that is interpreted as the optically thick thermal radiation from it (Laor & Netzer, 1989). Additionally, the continuum emission from the disk photoionizes the the gas from the clouds around it, producing optical emission lines in the BLR and the NLR. The widths of these lines help in identifying the region of emission. As indicated before, in the case of the BLR, the line widths are of the order of thousands of km s^{-1} , and for the NLR the line widths are of the order of hundreds of km s^{-1} (Netzer, 2013). Additionally, the existence or lack of forbidden lines are indicative of the region. In the case of the BLR, there is absence of forbidden lines, while in the case of the NLR, these are produced. As discussed in previous sections, these features are important in the AGN identification.

Since the BLR has a high density ($n \geq 10^9 \text{ cm}^{-3}$, see previous sections), electron density of this region is larger than the critical density of the levels of abundant ions. Therefore, these levels are collisionally de-excited, emitting only in permitted transitions (among others from MgII, HeII, FeII, CIV and the Lyman and Balmer series of H, see Netzer, 1990; Peterson, 1997; Osterbrock & Ferland, 2006). In the case of the NLR, the medium is less dense ($n \sim 10^4 \text{ cm}^{-3}$, **the electron density is lower than that of the BLR, giving rise to both forbidden and permitted transitions (among others of the [OII], [OIII], [OIV], [NeIII], [NI], [NII], [FeVII] and [SII] emission lines, Ferland & Osterbrock 1986; Netzer 1990)**). Through the emission line spectroscopy, we can separate galaxies with nuclear activity, from those excited by young massive stars or other ionizing processes and those with both processes occurring inside (Osterbrock, 1989; Baldwin et al., 1981; Sánchez et al., 2021).

Figure 1.14 shows the optical spectrum of different AGN types, illustrating how the information obtained in this range helps differentiating the AGN emission from the emission of a galaxy with no nuclear activity. In general, the optical emission from a non-active galaxy presents absorption lines that are associated with the host galaxy, while in the case of AGN, there are also strong emission lines associated with hard ionization from the nucleus. Additionally, according to the UM described in sec. 1.5, for objects in which the torus is not in the line of sight between the observer and the AGN, the broad components of permitted lines are detected (as in the case of Seyfert 1 and Broad Line Radio Galaxies, BLRGs). In addition to those objects, there are AGN such as LINERs, in which the dominating lines are those of low ionization, such as [OI] λ 6300 and [NII] $\lambda\lambda$ 6548, 6583. On the contrary, BL Lac objects are AGN with strong jets seeing just align to the line-of-sight and therefore the emission lines are completely suppressed. Altogether, the strength and width of the lines are important to detect and characterize different AGN. Indeed, one of the most important techniques to characterize sources as AGN is through the use of line ratios between the emission lines produced in the NLR as we discuss below (Baldwin et al., 1981; Osterbrock, 1989).

1.9.1 Diagnostic diagrams

Diagnostic diagrams were developed to identify the main ionizing mechanism inside a galaxy (Osterbrock, 1989). Thus, these diagrams are broadly used to characterize AGN sources in optical wavelengths. For instance, the Baldwin, Phillips & Terlevich (BPT Baldwin et al., 1981) diagrams compare the ratios $[\text{NII}]/\text{H}\alpha$ vs $[\text{OIII}]/\text{H}\beta$. While $[\text{NII}]$ gives information mostly about the metallicity in the case of HII regions, $[\text{OIII}]$ gives information regarding the level of ionization of the medium (Osterbrock, 1989, and references therein). Additional diagrams were proposed by Veilleux & Osterbrock 1987 (commonly referred to as VO87 diagrams), which include $[\text{SII}]/\text{H}\alpha$ vs $[\text{OIII}]/\text{H}\beta$ and $[\text{OI}]/\text{H}\alpha$ vs $[\text{OIII}]/\text{H}\beta$. The $[\text{OI}]\lambda 6300$ emission line is strong when the ionizing source is considerably harder than the one produced by young stars (e.g., AGN) or when additional mechanisms enhance the ionization (for instance collisions due to shocks). Thus, this line serves a good probe of nuclear activity. Similarly, the $[\text{SII}]\lambda\lambda 6716, 6731$ (Netzer, 1990) also serves as a good probe of nuclear activity. Different ionizing sources are usually found in different regions of these diagrams. This has been used to define boundaries or demarcation lines between those regions. For instance, Kewley et al. (2001, 2006) defined a set of limits to distinguish between starburst galaxies, low-ionization narrow line emission regions (LINERs) and AGN, and Kauffmann et al. (2003), who established limits to distinguish between inactive and active galaxies within these diagrams. Thus, the location of an object in a certain region of the diagrams gives hints on the dominant ionization mechanism.

Figure 1.15 shows the work by Kewley et al. (2006) to analyze the properties of more than 85000 emission line galaxies from the SDSS with redshift < 0.1 . They propose that the Seyferts and LINER galaxies are located in two different regions of the diagnostic diagram. The solid red and dashed blue lines are the demarcation lines defined by Kewley et al. (2001); Kauffmann et al. (2003), respectively, dividing starburst from active galaxies. The solid blue line in the central and left panels, represents the demarcation lines proposed in their work, dividing pure AGN from LINER ionization.

Therefore, galaxies residing in the HII region are expected to have an ionization mechanism dominated by processes related to a recent star-formation activity, while the ioniza-

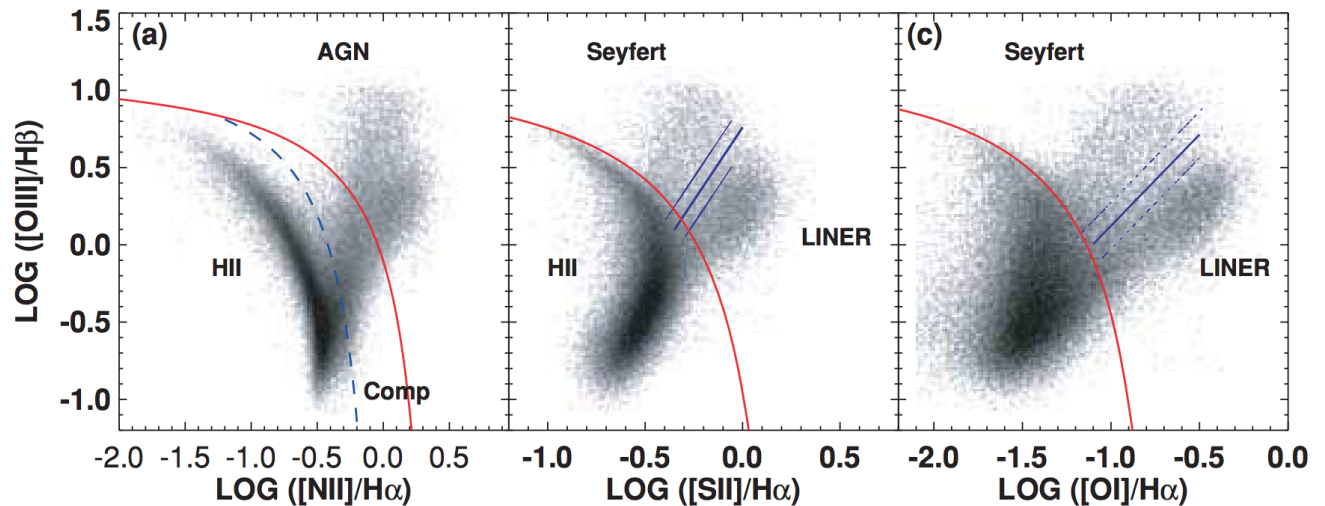


Figure 1.15: BPT and VO87 diagrams for the AGN diagnostic. The red line corresponds to the delimitation line defined by Kewley et al. (2001), while the dashed blue line is the demarcation line proposed by Kauffmann et al. (2003) and the blue solid line corresponds to the demarcation line proposed by Kewley et al. (2006). Figure taken from Kewley et al. (2006).

tion in those galaxies residing in the AGN region are expected to be dominated by nuclear activity, and galaxies in the LINER region are expected to be dominated by low ionization processes (see sec 1.10), such as in the case of LLAGN, but also in newly-born white dwarfs (Singh et al., 2013; Belfiore et al., 2016, and references therein). The composite region can be populated by post AGBs (Binette et al., 1994) or shocks (Veilleux et al., 2005). However, an object can be placed in a certain region of these diagrams without being dominated by the particular ionizing mechanism associated with that region. For instance, shocks and evolved stars (Richard et al., 2011; Singh et al., 2013; Belfiore et al., 2016; Lacerda et al., 2020; Comerford et al., 2022, and references therein), can be placed in the LINER region, even in the absence of an AGN. Thus, the interpretation of these diagrams is still under debate.

Of our particular interest, one of the main issues for detecting and classifying AGN at optical is the host galaxy emission. The dust can dilute and even completely obscure the AGN (Benn et al., 1998; Richards et al., 2001; Comastri et al., 2002; Caccianiga et al., 2007), preventing us from detecting it. Therefore, a galaxy hosting an AGN could

be located in the SF region and the AGN could be undetected, at least with optical information. This is particularly relevant for highly obscured and low luminosity AGN. Thus, separating the nucleus from the host galaxy is key in order to have a good estimate on the AGN population. Moreover, the classification of the ionization source of a galaxy should be done locally (Sánchez et al., 2021), as different ionizing mechanisms could be present in the same galaxy. This can be done through the Integral Field Spectroscopy (see sec. 3.2) which provides spatial and spectral information of a source, capable of isolating different parts of the galaxy and providing spatially resolved spectroscopy, which can help isolate AGN emission from other ionizing mechanisms in the host galaxy.

In addition, alternative diagrams have been developed including new parameters, such as the WHAN diagram (Cid Fernandes et al., 2010) which uses the Equivalent Width of the $H\alpha$ line ($EW(H\alpha)$) along with the $[NII]/H\alpha$ line ratio, as they are generally the most prominent in the spectra of galaxies. Their classification divides the ionization depending on the $\log([NII]/H\alpha)$ ratio and the $EW(H\alpha)$ as follows:

- Pure SF galaxies: $\log([NII]/H\alpha) < -0.4$ and $EW(H\alpha) > 3\text{\AA}$
- Strong AGN: $\log([NII]/H\alpha) > -0.4$ and $EW(H\alpha) > 6\text{\AA}$;
- Weak AGN: $\log([NII]/H\alpha) > -0.4$ and $3\text{\AA} < EW(H\alpha) < 6\text{\AA}$

Some authors (e.g., Sánchez et al., 2018; Lacerda et al., 2020) relax the condition on the $EW(H\alpha)$ they use an upper limit of 3\AA instead of 6\AA for weak AGN in order to include fainter AGN or measurements from instruments with lower spatial resolution. Finally, it has been proposed the combination of emission line ratios usually adopted in the VO87 diagrams with the $EW(H\alpha)$ to distinguish between different ionizing sources. Figure 1.16 shows the implementation of the BPT and VO87 diagrams combined with a restriction on the $(H\alpha)$ and the use of IFS to ensure the detection of AGN, as discussed in Sánchez et al. (2018) (see sec. 2).

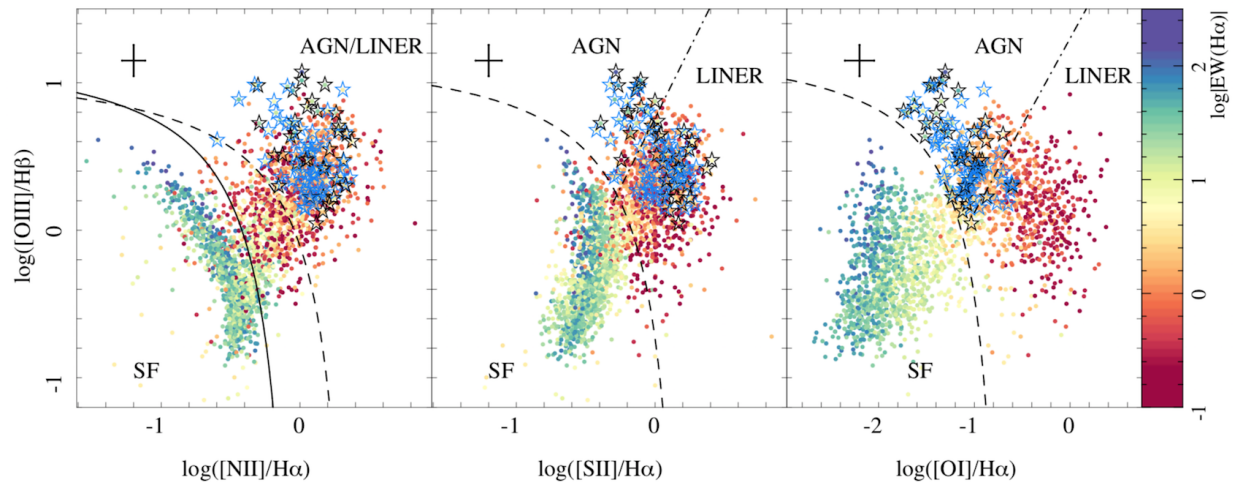


Figure 1.16: BPT and VO87 diagrams for a sample of galaxies as presented by Sánchez et al. (2018). The colorbar represents the $\text{EW}(\text{H}\alpha)$ with higher values representing harder ionization. The stars represent the AGN candidates in their sample.

1.10 Low Luminosity AGN

Low Luminosity AGN (LLAGN) were identified by Heckman (1980) to explain the observed Low Ionization Nuclear Emission Regions (LINERs). Heckman noticed that the optical spectra for these sources diverged from those of both inactive and active galaxies. The optical spectra of LINERs have very strong low ionization emission lines such as [OI] and [NII], and some of them even present a compact radio source. At the optical, a source is classified as LINER if $[\text{OIII}]\lambda 5007/\text{H}\beta < 3$, $[\text{OI}]\lambda 6300/\text{H}\alpha > 0.05$ and $[\text{NII}]\lambda 6583/\text{H}\alpha > 0.5$, (Heckman, 1980; Ho et al., 1997b; Ho, 2008; Osterbrock & Ferland, 2006). At X-rays, the extensive work by González-Martín et al. (2009) shows that around 60% of the LINERs present X-ray compact sources, indicative of its AGN nature. However, in their work, a considerable fraction of these objects ($\sim 40\%$) do not present evidence of X-ray emission. Therefore, other mechanisms can produce the observed low ionization emission lines in the optical wavelength regime. For instance, shocks (Dopita & Sutherland, 1995) and ionization by post-AGB stars (Binette et al., 1994) can also produce these optical signatures, as indicated before, as indicated before.

Thus, there is still a debate on whether the vast majority of these objects should be classified as AGN. For instance (i) they seem to lack the characteristic big blue bump

associated with the AGN photoionization (Ho, 1999), (ii) in many cases there is diffuse emission associated with old stellar populations in early-type galaxies (Singh et al., 2013), and (iii) their radial profile is incompatible with being produced by a point-like (e.g., the AGN) source in many cases (Gomes et al., 2016). In summary, a fraction of optically classified as LINER may host an AGN, but not all of them. In our work, we will focus on galaxies harbouring AGN, regardless of how these can be classified at optical.

LLAGN are classified with respect to their bolometric luminosities ($L_{\text{bol}} < 10^{42} \text{ erg s}^{-1}$ Maoz, 2007). The study of LLAGN is important due to several reasons: i) as mentioned in the sec. 1.2, there is a strong link between the host galaxy and nuclear activity. Therefore, having a correct estimate of AGN can help us understand this connection. In this sense, LLAGN might be crucial, as are mostly located in elliptical/lenticular galaxies Kauffmann et al. (2003); González-Martín et al. (2009); Tang et al. (2009). ii) throughout the life duty-cycle of AGN ($10^7 - 10^9 \text{ yr}$. Marconi et al., 2004) they are expected to spend most of its life in a low accretion state, being weak AGN (Ho, 2008). iii) they dominate the AGN population in the nearby Universe (see Ho et al., 1997b, and references therein) and are mostly located in early-type galaxies as studied by Heckman (1980). Therefore, understanding the emission mechanism and how they diverge from brighter AGN is mandatory to understand the connection between the host galaxy and the nuclear activity. In fact, they are thought to be the link between normal and active galaxies (Makishima et al., 1997; González-Martín et al., 2006).

Even when the AGN is known as the main emitter at the central regions in galaxies, the accretion mechanism is not yet understood (see Ho, 2008). However, the most accepted scenario is that the accretion flow is radiatively inefficient (i.e., RIAF or ADAF disks. See Yuan, 2007, for a review). Thus, the disk becomes geometrically thick and can even transition to an advection dominated state (ADAF). This explains why LLAGN do not show signatures of thermal emission such as the big-blue bump (see sec. 1.7 and the left panel in Fig. 1.6). Because the disk is no longer standard and does not accrete efficiently, these sources are also the least efficient within the AGN family, with accretion rates below $L_{\text{Edd}} = 10^{-2}$. Figure 1.6 (right) shows a representation of the ADAF model. In this scenario, while the accretion flow starts as a standard thin disk, it switches from

cold to hot. While the physical reasons behind this switch are unknown (Nemmen, 2013), this scenario is similar to the different spectral states of black hole binaries (Remillard & McClintock, 2006; Done et al., 2007). The rest of the AGN components are also affected. For instance, the BLR and the torus are expected to disappear as the radiation pressure from the accretion disk no longer supports the weight of the gas against gravity and these structures are expected to collapse (Elitzur & Shlosman, 2006). Indeed, the work by González-Martín et al. (2017) shows that the torus seems to change in size and contribution at mid-IR towards lower luminosities. Nonetheless, the conditions for the disappearance are still an open question. We try to understand the behaviour of the torus at X-rays through the reflection component, for a sample of LLAGN.

Despite of their importance, these sources are very difficult to detect because of their low luminosity, in particular in contrast with the luminosity of the host galaxy (Ho, 2008). Indeed, these sources might be hidden under the host galaxy emission, which can be the dominant emission in the SED (Fernández-Ontiveros et al., 2012). Therefore, the detection of these sources may strongly depend on the explored wavelength regime, as some wavelengths may be more susceptible to other physical processes, leading to an underestimation of the AGN population. Thus, having a correct demographics on the overall AGN population is important to have a clear picture of the AGN-host galaxy connection and the most complete way to do this is using information in different wavelengths.

This PhD thesis is focused on the exploration of different aspects of the LLAGN, from their detectability at different wavelengths to their inner obscuring structure.

Chapter 2

State of the art and aims of the thesis

2.1 AGN torus behaviour for LLAGN

Within the UM (Antonucci, 1993; Urry & Padovani, 1995, see sec.1.5), the torus is presented as a steady, unchanging structure. Very early on, different models were developed aiming to reproduce the AGN SED at mid-IR. On the basis of the scenario proposed by the UM, smooth models (Pier & Krolik, 1992; Granato & Danese, 1994; Efstathiou & Rowan-Robinson, 1995; van Bemmell & Dullemond, 2003; Schartmann et al., 2005; Fritz et al., 2006) assume that the torus is distributed homogeneously, with different radial and vertical density profiles. However, other models assumed that the torus was rather distributed in dust clumps (Nenkova et al., 2008; Hönig & Kishimoto, 2010). Indeed, observational works suggest intrinsic differences between different AGN types. Ramos Almeida et al. (2011) show that the covering fraction (i.e., the fraction of **sky covered by the torus as seen from the source**) is, on average, larger for type-II than for type-I sources, for a sample of 21 Seyferts, modeling their data with the clumpy torus by Nenkova et al. (2008). Their result suggests that the distribution of these clumps is not the same for different types of AGN. While their work was focused on the study at mid-IR wavelengths, this is also supported by the X-ray regime. For instance, Ricci et al. (2011) show that, for a sample of 165 nearby Seyferts, the Eddington rate might be the responsible for the difference on the obscuration and covering factor between type-I and type-II which is not in agreement with the UM. The extensive work by González-Martín et al. (2019) compared

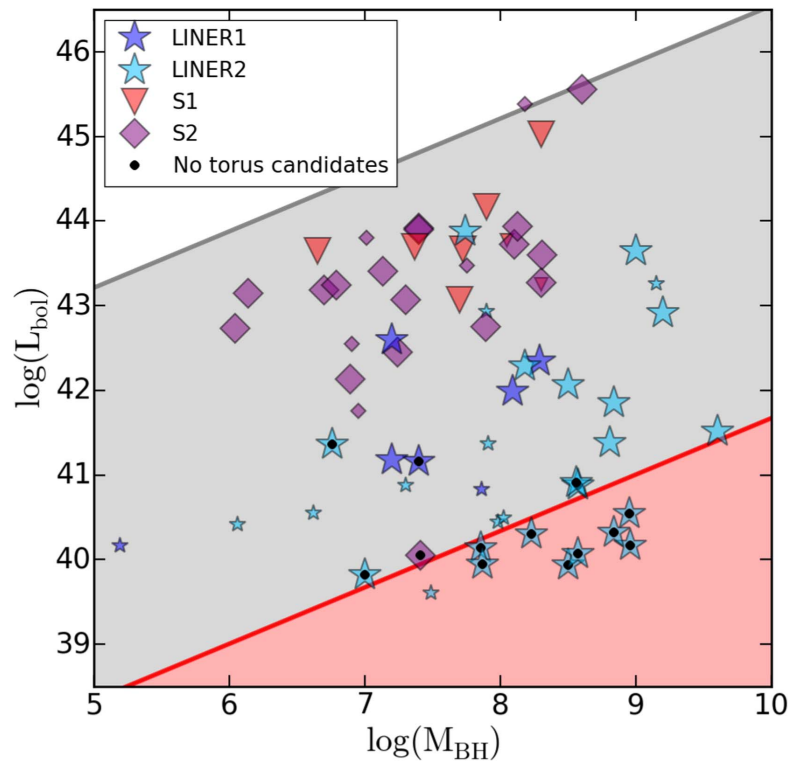


Figure 2.1: AGN bolometric luminosity vs M_{BH} for a sample of LINER and Seyfert objects in González-Martín et al. (2017). The grey area is the region in which the torus may or may not disappear depending on the wind parameters as predicted by Elitzur & Ho (2009), while the red area is the region in which the torus is expected to disappear regardless of M_{BH} . Objects with a black dot are the sources without any hints of the presence of the torus through mid-IR information.

different torus models between smooth and clumpy with the aim to determine the best model for a sample of 110 Seyferts, finding that the accretion state seems to be connected to the different geometries and distributions of the torus (see also García-Bernete et al., 2022). At larger redshifts, Martínez-Paredes et al. (2017) find that the tori of QSOs seem to be intrinsically different than those of Seyferts 1 and 2, with lower number of clouds, and less optically thick material. These results suggest that the torus may undergo a transformation through the life-cycle of AGN.

Among the AGN classes, the LLAGN play a crucial role on the understanding of the duty cycle of AGN activity, because they should be related with the switch-on/off phases (González-Martín et al., 2009). Indeed, from the theoretical disk-outflow scenario described in sec. 1.6, the torus and BLR regions should disappear for sources in which the radiation

pressure no longer counteracts the gravity from the SMBH (which is expected for LLAGN with $L_{\text{bol}} < 10^{42}$ erg s $^{-1}$ Elitzur & Shlosman, 2006; Elitzur & Ho, 2009). Observational works, such as the one presented by (Müller-Sánchez et al., 2013) suggest that the tori of LLAGN seem to be gradually disappearing, as they present lower column densities compared with their more luminous Seyfert pairs. This is supported by X-ray works on small populations of LLAGN (e.g., Ursini et al., 2015; Young et al., 2018; Younes et al., 2019). However, as suggested by Elitzur & Netzer (2016) the scenario is more complex and does not rely on the AGN bolometric luminosity only, but rather on a mix of parameters. This is supported with the work presented by (González-Martín et al., 2017, see Fig. 2.1), who show that there are AGN without any trace of the torus that fall in the region in which the torus may or not exist, in agreement with this scenario. Moreover, there are still some low-luminosity sources with reflection features in the X-ray spectra (Osorio-Clavijo et al., 2020; Baloković et al., 2021; Diaz et al., 2023).

Apart from using mid-IR information, we can study the AGN torus using X-ray information. As mentioned in the introduction, one of the X-ray features of AGN spectra is the reflection component. Traditionally, this feature has been attributed to the inner parts of the torus in which the gas is present, although the reflection can also happen inner in the AGN, for instance in the disk or in the BLR (see the review by Turner & Miller, 2009). Particularly, the shape of the FeK α line will give hints as to the region in which the reflection is produced (Fabian & Iwasawa, 2000; Yaqoob et al., 2001; Kaspi et al., 2001; Petrucci et al., 2002; Bianchi et al., 2004). Figure 2.2 shows the effects on the FeK α line due to Doppler broadening and gravitational redshifting as proposed by Fabian & Iwasawa (2000). In the first panel, both peaks represent the approaching (blue-shifted) and receding (red-shifted) material from a non-relativistic accretion disk. The second panel shows the effect of a relativistic disk (i.e., material closer to the BH) where **special relativity effects enhance the blue peak through beaming**. The third panel shows the effects of the Doppler broadening and gravitational red-shifting, **lowering the energy of the contribution at each radius**. Finally, the fourth panel shows the total effects on the emission line **convoluted by the finite resolution of the instrument, and the contribution of the line from all radii of the accretion disk**. On the other hand, if the

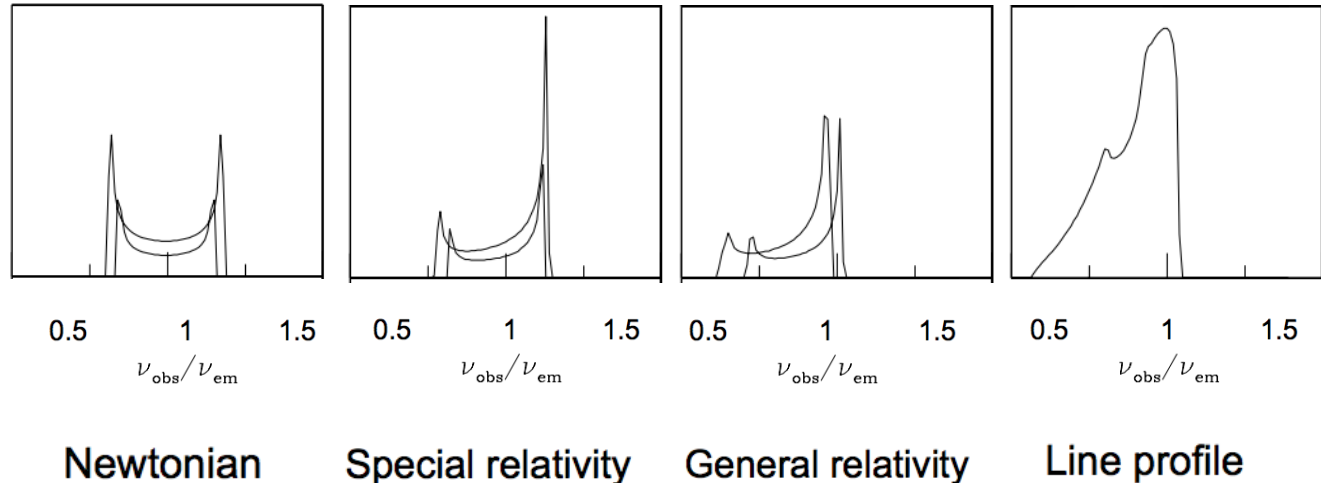


Figure 2.2: Effects on the FeK α emission line due to the proximity of the emitter to the SMBH. Adapted from Fabian & Iwasawa (2000).

line has a narrow profile, it will most probably come from further away from the accretion disk (i.e., in the torus). The Compton hump, on the other hand, is only detected when the source is highly obscured, with column densities above $N_{\text{H}} > 10^{23} \text{ cm}^{-2}$ (Ghisellini et al., 1994). Observations with satellites such as *ASCA*, *ROSAT* and even *Chandra* suggested that a tracer of reflection was a flat photon index ($\Gamma \sim 0.7$, Nandra et al., 1991; Guainazzi & Antonelli, 1999, and references therein), particularly for reflection dominated sources. However, these satellites provide information in the soft band and up to 10 keV. As presented in sec. 1.8, the reflection component is better restricted with information above 10 keV due to obscuration effects. Thus, satellites providing information above this energy range are crucial to understand the existence and nature of the reflector. Simple models, such as PEXRAV (Magdziarz & Zdziarski, 1995) or PEXMON (Nandra et al., 2007a) have been classically used to detect the reflection component (Cappi et al. 1999; Lamer et al. 2003; Brightman & Nandra 2011; Panagiotou & Walter 2019; Osorio-Clavijo et al. 2020, Victoria-Ceballos et al. (subm.), among others). In these models, the reflector is assumed to be a neutral surface (i.e., the torus). The latter is an approximation that assumes that most of the emission comes from the inner side of the torus, and that is large enough to be seen by the energy source as a plane-parallel slab. PEXMON already incorporates the

physics to produce the $\text{FeK}\alpha$, as well as the $\text{FeK}\beta$, $\text{NiK}\alpha$ emission lines. With better data of satellites reaching energies above 10 keV (such as *Suzaku*, *NuSTAR*, *Swift*, among others) more realistic reflection models have been released, which might help disentangle the geometry and distribution of this feature (such as the models MyTorus, borus, among others Murphy & Yaqoob, 2009; Baloković et al., 2018). However, due to its sensitivity, the only satellite that can provide spectra with enough signal-to-noise (SNR) to carry such detailed works is *NuSTAR*. **While *Suzaku* also provides information above 10 keV, its sensitivity might not good enough to carry a reflection study on low luminosity sources, due to the quality of the spectra.** These models aim to understand the origin of the reflector, distribution of the gas, whether the medium is clumpy, smooth or a combination of both, etc.

Within the last decade, there have been several works aiming at understanding the behaviour of the reflection component at X-rays (Ricci et al., 2011, 2014; Liu & Li, 2014; Furui et al., 2016; Kawamuro et al., 2016; Esparza-Arredondo et al., 2019, 2021; Panagiotou & Walter, 2019, 2020), testing the different geometries and distributions provided by theoretical models. All of these results suggest that the torus can have different phases throughout the AGN life. Nonetheless, the study of the reflection component has been focused on intermediate and luminous AGN, while the behaviour of the reflection for LLAGN has been little explored.

With the unprecedented sensitivity of *NuSTAR* above 10 keV, we expect to study the behaviour of the reflection component for a sample of LLAGN, in order to understand the evolution of the torus in the low-luminosity regime and compare these results with what has been studied for more luminous AGN.

2.2 AGN demographics

As mentioned in the introduction, AGN are strongly connected with the galaxy and galaxy evolution (Magorrian et al., 1998; Ferrarese & Merritt, 2000; Gebhardt et al., 2000; Merritt

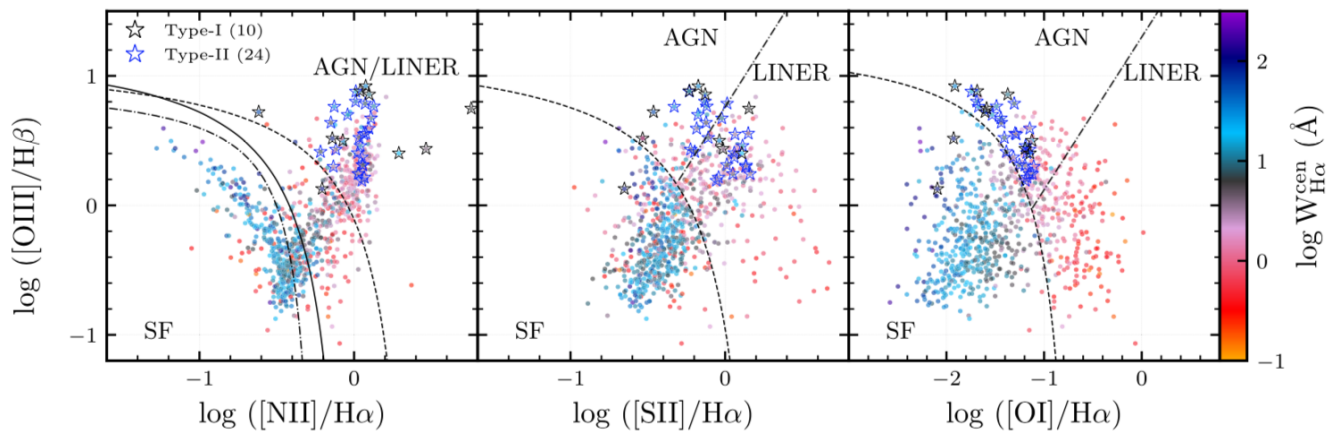


Figure 2.3: Diagnostic diagrams applied to the CALIFA survey. The star symbols correspond to the 34 AGN candidates provided by Lacerda et al. (2020) (10 type-I and 24 Type-II).

& Ferrarese, 2001, see sec. 1.2). Therefore, it is crucial to have a good estimate on the fraction of nuclear activity to understand this co-evolution. Fortunately, since AGN emit at all wavelengths, the full SED can be used to detect them. However, the AGN detection rate is dependent on the processes occurring inside the host galaxy (Benn et al., 1998; Comastri et al., 2002), on the intrinsic AGN luminosity (Ho, 2008), and on the observational limitations at each wavelength (see the review by Padovani et al., 2017).

The host galaxy contribution can be particularly tricky at optical wavelengths because it might strongly contribute to the emission lines used in BPT diagrams (see sec. 1.9.1). To try to overcome this problem, the use of IFS (see next chapter) has proven to be successful at detecting bright AGN sources, as this technique allows to isolate the nucleus from the rest of the galaxy emission. Several works have aimed at characterizing AGN sources in different samples and surveys. For instance Sánchez et al. (2018) study a sample of ~ 2700 galaxies in the MaNGA survey with $z < 0.17$, finding 98 AGN (which represents $\sim 4\%$ of their sample). In order to characterize a source as AGN, it had to be located above the demarcation line proposed by Kewley et al. (2001) in all three diagrams, and a $EW(H\alpha) > 1.5\text{\AA}$. Similarly, Albán & Wylezalek (2023) used the full MaNGA survey (corresponding to ~ 10000 galaxies) to identify AGN, reporting 399 optically selected sources (which corresponds to $\sim 4\%$ using similar criteria than Sánchez et al.). Of particular interest for our work, Lacerda et al. (2020) find 34 objects in the *Calar Alto Legacy Integral*

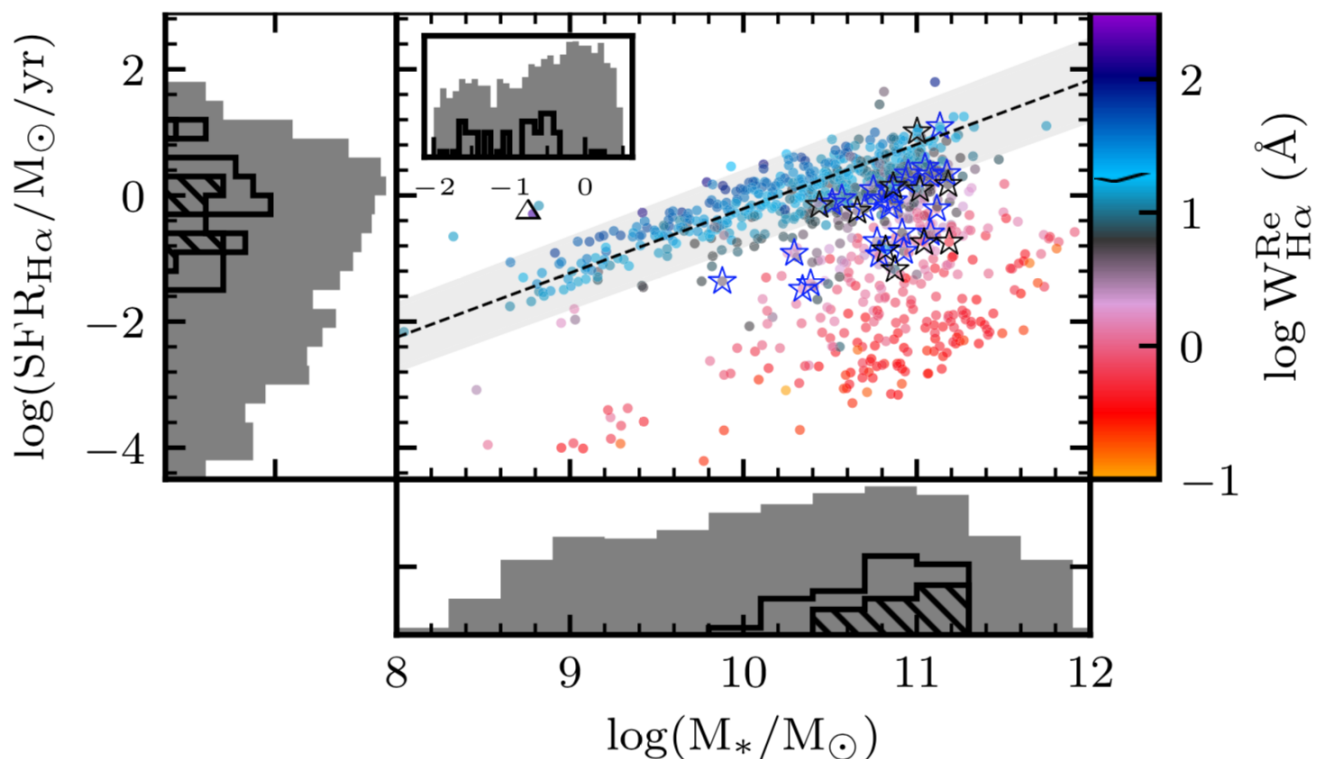


Figure 2.4: SFR vs stellar mass for the eCALIFA sample and in particular, the AGN. Figure taken from Lacerda et al. (2020). The colors and symbols are the same as in Fig 2.3.

Field Survey (CALIFA Sánchez et al., 2012, see next chapter) **hosting** an AGN. In order to define a source as AGN they establish three criteria, which included: i) that the source be located above the Kewley et al. (2001) line of all three diagrams. ii) that the $EW(H\alpha) > 3\text{\AA}$ and iii) for type-I sources, they should detect the broad component of the $H\alpha$ line (see Fig. 2.3). This ensures that they find bright AGN sources.

They also study the host-galaxy properties and find that AGN are predominantly located in a transition between galaxies with current star formation (predominantly Sab and Sb galaxies) and those in which the star formation ceased (i.e., the so-called GV, see Fig. 2.4). This suggests a link between the AGN and the SFR.

Although very effective in the high luminosity range, the host galaxy dilution at optical wavelengths might bias against the AGN detection for LLAGN in particular (Ho, 2008; Fernández-Ontiveros et al., 2012). The dust in the LOS can also obscure the AGN

emission, even preventing us from seeing any trace of nuclear activity (Moran et al., 2002; Trump et al., 2009). Alternatively, the X-rays provide a unique window to detect AGN, which suffer less from host galaxy dilution and are less affected by gas clouds that affect UV/optical wavelengths. Works focused on X-ray detection of AGN have found higher fractions of AGN compared to optical results. **Roberts & Warwick (2000) found that from the ~ 500 sources in their sample, more than 70% present a nuclear source, out of which 33% were classified as LLAGN.** Similar fractions were found by González-Martín et al. (2006, 2009) where they studied samples of ~ 50 and ~ 80 LINERs from the Palomar sample (Ho et al., 1997a), a statistically complete sample of galaxies in the nearby Universe (with a mean distance of $D \sim 17$ Mpc). They find that at least 60% and 90% of the 50 and 80 LINER sources, respectively, also present X-ray nuclear sources. All of them were classified as AGN through a spectroscopic analysis. Similarly, Zhang et al. (2009) studied a sample of 187 nearby galaxies ($D < 15$ Mpc) from the Uppsala Galaxy Catalog (UGC Nilson, 1973), and found that more than 40% of them present evidence of X-ray cores, consistent with AGN. This result is in agreement with the work by She et al. (2017), where they studied more than 700 nearby galaxies ($D < 50$ Mpc) from the *Chandra* archive, out of which more than 300 present AGN. The recent work by Williams et al. (2022) shows that in 213 galaxies within the Palomar sample, $\sim 70\%$ of them present X-ray emission consistent with the nucleus. Nonetheless, the obscuration is also important for the AGN detection at X-rays. Indeed, without information above 10 keV, compton-thick sources might be completely missed in this energy regime. Thus, the detection of AGN at X-rays is still affected by technical limitations (Padovani et al., 2017; Hickox & Alexander, 2018).

A better way to be complete in the AGN demographics is the use of multi-wavelength information that can somehow diminish the bias that each wavelength provides. Indeed, several works have succeeded at combining both optical and X-ray information for the selection of AGN in the local Universe (LaMassa et al., 2009; Vasudevan & Fabian, 2009; Yan et al., 2011; Pouliaxis et al., 2019; Agostino et al., 2023), but also at higher redshift galaxies (Malizia et al., 2012; Azadi et al., 2017; Agostino & Salim, 2019). However, little

is known about the bias on each wavelength in comparison with the other (i.e., how many sources detected at optical are lost at X-rays and vice-versa).

Using the subarcsec spatial resolution provided by *Chandra* (see next chapter) we aim to study the AGN population in the *Calar Alto Legacy Integral Field Survey* (CALIFA Sánchez et al., 2012, see next chapter), in order to compare the X-ray selected AGN with those selected based on the optical emission lines (Lacerda et al., 2020), and to determine the advantages and disadvantages of detecting AGN at optical vs X-rays. Finally, we aim provide the most complete demographics of AGN in the CALIFA survey up to date.

Chapter 3

Methodology

In this chapter, we explore the X-ray and optical instruments used throughout the thesis, as well as the statistical methods we applied in order to test our results.

3.1 X-ray satellites used in this work

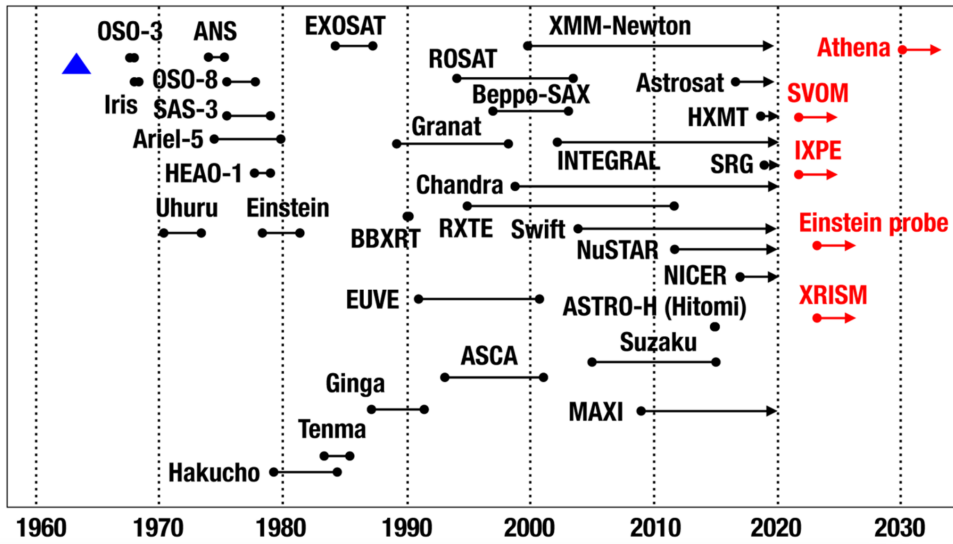


Figure 3.1: Timeline of X-ray satellites in Astronomy. The blue arrow indicates the beginning of X-ray astronomy. Missions in black have been already launched, while missions in red are still under planning. The start date is marked with the bullet on the left of each mission, while the end date is marked with a bullet on the right.

To study X-ray sources, astronomers use satellites that are in orbit, as X-ray emission

does not cross the Earth’s atmosphere. X-ray astronomy began in the 60s of the past century and it was done with the use of X-ray detectors attached to rockets and sent out to space. The first X-ray satellites, *Uhuru*, *Ariel 5*, *SAS-3*, *OSO-8* and *HEAO-1*, were developed in the next decade, and during the following years, different missions have been carried out (see Fig. 3.1). Nowadays, there are several missions in orbit, among which some of the most broadly used by the community are: *Chandra*, *XMM-Newton*, *Suzaku*, *Swift*, *NuSTAR* and more recently and *eROSITA*.

The X-ray telescopes consist of concentric paraboloid and hyperboloid mirrors (Wolter telescopes, see Fig. 3.2) coated with gold or iridium, and with a low grazing angle (i.e., the angle between the mirror and the X-ray photon is very small) to reflect the X-ray photons, which would not interact with canonical mirrors. These mirrors are nested together forming an onion-like structure in order to increase the reflecting area and thus the sensitivity. Moreover, since the wavelengths at which X-ray photons are emitted are of the size of atoms, the mirror surfaces need to be as smooth as possible to avoid blurring images. Therefore, this will impact on the angular resolution of the instrument. In this work, we use data from *Chandra* and *NuSTAR*. We briefly discuss them:

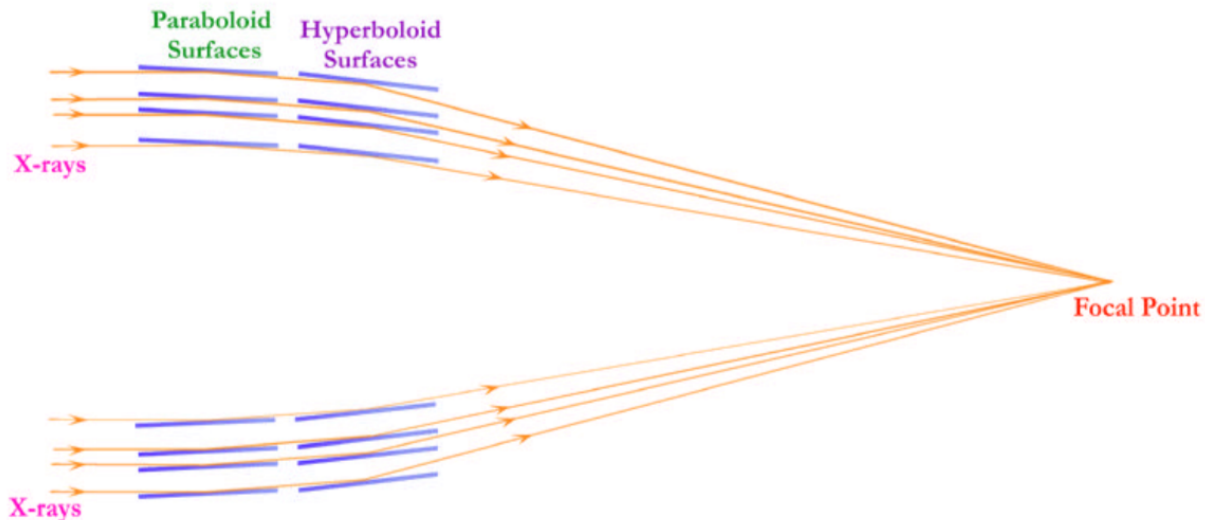


Figure 3.2: Schematics of the configuration of mirrors for X-ray telescopes. X-ray photons are incident from the left part and redirected through the mirrors towards the focal point. Image credit: NASA/CXC/S. Lee.

- *Chandra*: The Chandra X-ray Observatory (CXO) is a mission developed by NASA, launched in 1999. It consists of four pairs of nested iridium mirrors and four instruments, namely: High Resolution Camera (HRC), Advanced CCD Imaging Spectrometer (ACIS), High Energy Transmission Grating Spectrometer (HETGS), and Low Energy Transmission Grating Spectrometer (LETGS). In this work, we use the ACIS camera, as it provides high resolution images and moderate resolution spectra. *Chandra* has an angular resolution of $\sim 0.5''$ with around 1000 times better resolution than the first X-ray telescopes. Moreover, it has a spectral range that goes from 0.08 keV, to 10 keV. However, below 0.5 keV and above ~ 7 keV the effective area of the optics significantly decreases. Moreover, the *Chandra* ACIS CCD detector has suffered from degradation due to the the damage of the spacecraft thermal insulation While this has been handled through a radiation-protection program, this has increased the temperature over the last years, lastly affecting the quality of the observations (see Fig. 3.4).

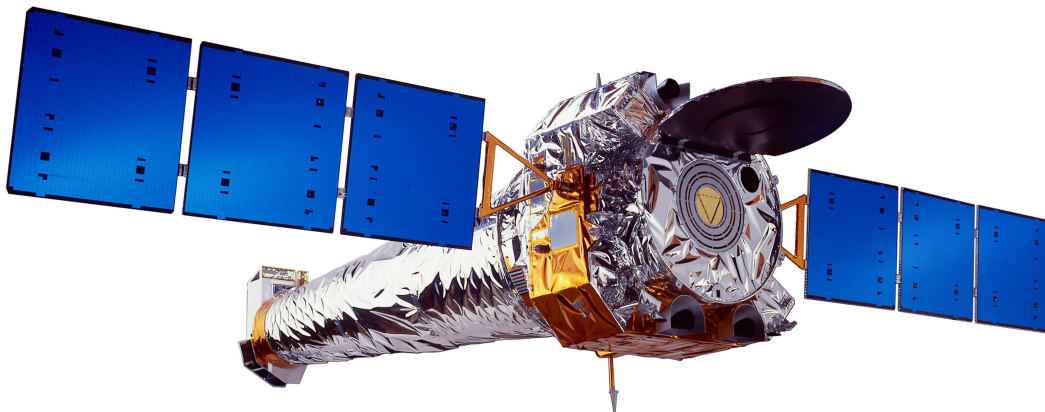


Figure 3.3: Illustration of the *Chandra* X-ray satellite used in this project. Particularly, we use the ACIS camera. Image credit: NASA

- *NuSTAR*: The Nuclear Spectroscopic Telescope Array Mission is a mission developed by NASA, launched in 2012. It consists of 133 Wolter mirrors. It has two focal plane module detectors, namely FPMA and FPMB. The spectral range covers from 3-79 keV. While the angular resolution of $18''$ is not as good as that provided by *Chandra*,

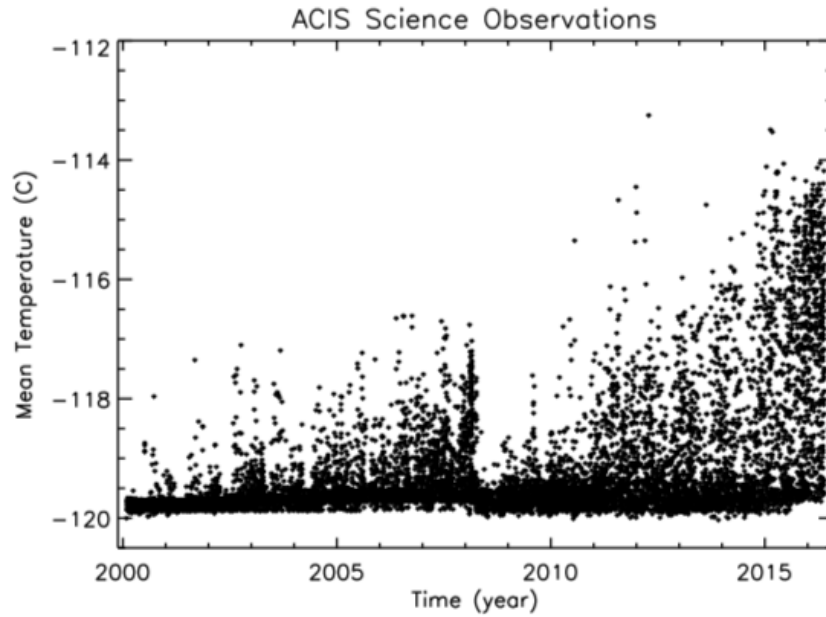


Figure 3.4: Mean temperature of the ACIS focal plane through the years. Each point corresponds to a single observation, therefore the exposure time is not the same in all data points. Image credit: Grant et al. (2016).

the sensitivity above 10 keV makes it ideal to study highly obscured AGN, for which the intrinsic continuum is suppressed under the reflection component.

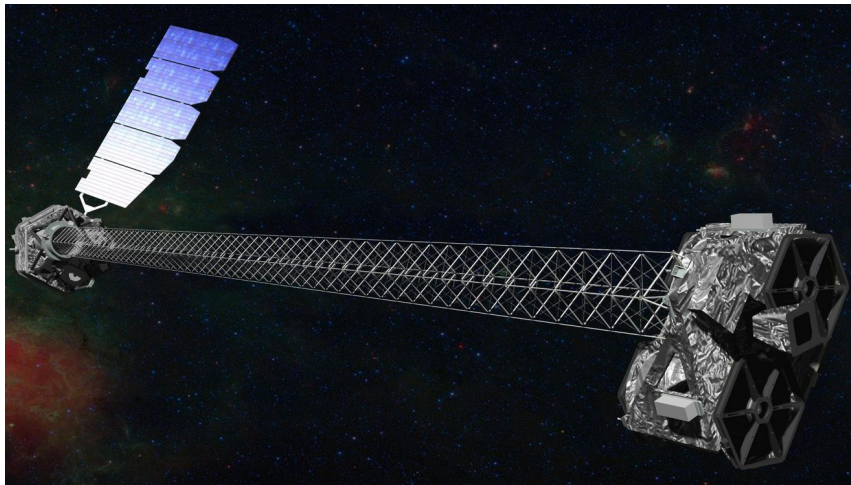


Figure 3.5: Artist's illustration of the *NuSTAR* X-ray satellite which was used for the development of this project. Image credit: NASA/JPL.

Specification	<i>Chandra</i>
Energy Range	0.1 - 10 keV
Angular resolution	0.5"
FoV	17' (0.2 - 10 keV)
Spectral resolution	95 eV at 1.49 keV, 150 eV at 5.9 keV
Sensitivity	4×10^{-15} erg cm ⁻² s ⁻¹ in 10 ⁵ s
<i>NuSTAR</i>	
Energy Range	3 - 78.4 keV
Angular resolution	18"
FoV	10' at 10 keV, 6' at 68 keV
Spectral resolution	400 eV at 10 keV, 900 eV at 68 keV
Sensitivity	2×10^{-15} erg cm ⁻² s ⁻¹ (6-10 keV) in 10 ⁶ s 1×10^{-14} erg cm ⁻² s ⁻¹ (10-30 keV) in 10 ⁶ s

Table 3.1: Technical specifications of the X-ray satellites used in this work. Note that although *Chandra* has four instruments, we only use the ACIS camera. The specifications are taken from the webpages of the satellites. See <https://chandra.harvard.edu/about/specs.html> and https://heasarc.gsfc.nasa.gov/docs/nustar/nustar_tech_desc.html. Both angular and spectral resolution correspond to the values on axis.

3.2 Integral Field Spectroscopy

The Integral Field Spectroscopy (IFS) technique was first presented in the late 80s (Vanderriest et al., 1987), although the first project to perform a survey of galaxies using this technique is considered to be the SAURON project (de Zeeuw et al., 2002). This technique allows to obtain spatial and spectral information within the Field of View (FoV) of the instrument in a quasi-continuous way (i.e. for each pair of coordinates, we also have the information along the wavelength). In this way, we can obtain spatially-resolved information of extended sources, such as in the case of galaxies.

The information is recorded in what is known as Integral Field Unit (IFU) which is attached to the spectrograph. We briefly discuss the most common types of IFUs (see Allington-Smith & Content, 1998; Allington-Smith, 2006, for a full review on IFS):

- ★ Lenslets: Using this technique, the image formed by the telescope is segmented by the array of lenslets, located at the focal plane of the telescope. The resulting images are directly formed at the entrance of the spectrograph where they are dispersed. While using this method provides a complete mapping of the FoV, it might produce some overlapping, unless the wavelength of the spectra is limited to avoid it. This system

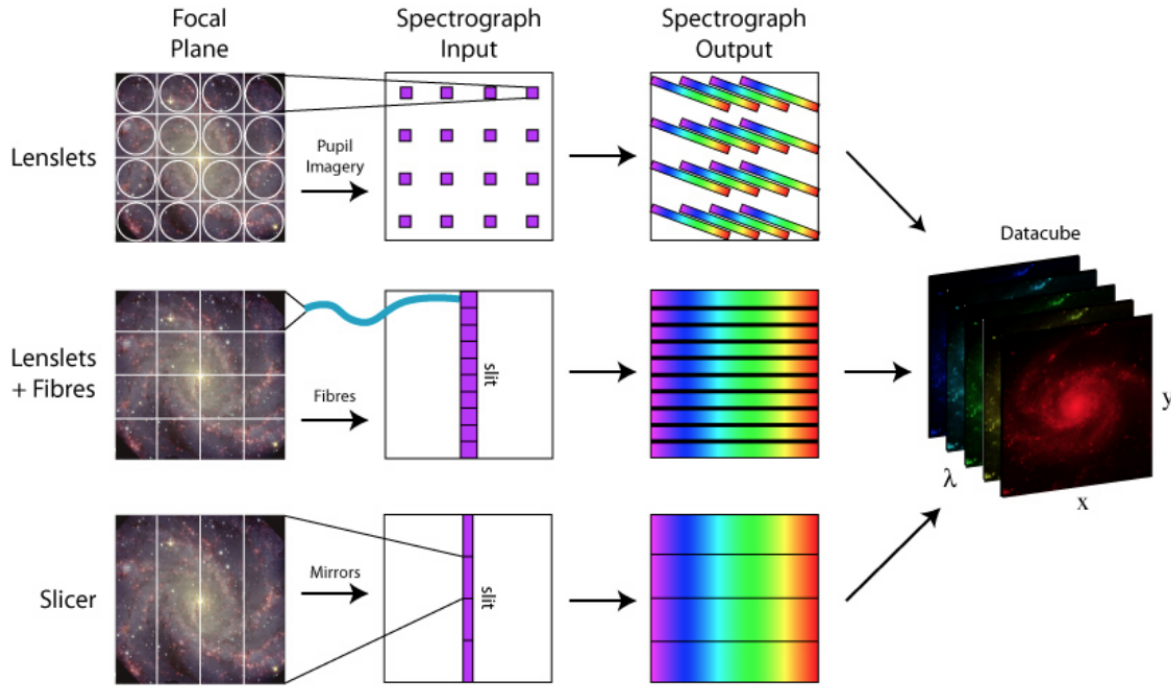


Figure 3.6: Different types of IFUs. Figure taken from C. López-Cobá's PhD. Thesis. Adapted from Allington-Smith & Content (1998).

is used in experiments where a long spectrum in physical scales is not required (i.e., low resolution and large wavelength range or high resolution and small wavelength range).

- ★ **Fibers**: The image formed by the telescope falls on a 2D array of fibers. The output of those fibers is then coupled to the long-slit spectrograph. It can be combined with a lenslet array or a dithering technique could be implemented to provide a complete mapping of the FoV. The flexibility of this technique allows for the decoupling of the focal plane with the entrance of the spectrograph. However, one of the disadvantages is the inability to operate in a cryogenic environment which limits the wavelength coverage to $< 1.6\mu m$. This is one of the most common IFUs techniques used (as in the case of CALIFA, see below).
- ★ **Slicers**: The image formed by the telescope is coincident with a segmented mirror that effectively splits the input image into narrow slices. Each slice has a slightly different angle so that the beam exists in a different direction for each segment of

the mirror, that are sent to a spectrograph. The final effect is to prevent overlapping of the spectra. This technique is most commonly used at wavelengths $> 1.8\mu\text{m}$, due to the necessity of cooling the instrument to avoid thermal emission.

While these three techniques are different, the final dataset is similar in most cases. This data set is known as datacube, which is a 3D array, with two spatial and one spectral dimensions. Each spatial element of the cube that sustains a spectrum is known as spaxel (spectral pixel). Each of them records spectral information of a small region of the object, along with the physical information of the region. This technique offers the advantage of studying individual and isolated parts of extended objects in a continuous way with a considered spatial resolution. In the case of galaxies it allows to segregate and derive the spectra of different component such as the nucleus¹, spiral arms, bars, as well as environmental processes affecting star formation, as it can be feedback, tidal forces, mergers, etc (Sánchez et al., 2012).

Several large astronomical projects use this technique. The first one was the ATLAS3D project (Cappellari et al., 2011), which compiles information of 260 galaxies within the local (42 Mpc) volume. Other projects, such as the *Sydney AAO Multiobject Integral Field* (SAMI Galaxy Survey Allen et al., 2015) which in its last data release provides information for more than 3000 low redshift galaxies ($z < 0.12$). Another project that uses this technique is the *Multi Unit Spectroscopic Explorer* (MUSE Bacon et al., 2010). Finally, largest survey up to date in terms of the number of objects, is the *Mapping Nearby Galaxies at APO* survey (MaNGA Bundy et al., 2015) which provides information for ~ 10000 galaxies in the local Universe. In the following section, we introduce the *Calar Alto Legacy Integral Field Area* survey (CALIFA Sánchez et al., 2012), used in the second part of this thesis.

3.2.1 CALIFA survey

The CALIFA survey (Sánchez et al., 2012) uses the Potsdam Multi-Aperture Spectrograph (PMAS Roth et al., 2005) instrument in the PPAK configuration (Kelz et al., 2006), at

¹Note, however, that there might be still some contribution from the host galaxy on top of the nucleus.

the Calar Alto 3.5m telescope, with a FoV of $> 1 \text{ arcmin}^2$ (i.e., one of the largest FoV for IFS), and with a resolution of $2.5''$. This survey uses two grating modes to achieve different goals: i) in the range $3750\text{--}7000\text{\AA}$ (with a resolution of $R \sim 850$, known as V500 grating) mostly used for ionized gas measurements and stellar populations. ii) In the range $3700\text{--}4700\text{\AA}$ (with a resolution of $R \sim 1650$, known as V1200 grating) used for detailed stellar populations and stellar gas kinematics. In this thesis we use observations performed in the V500 grating mode. Additionally, the exposure times go from 900s in the red band, and 1200s in the blue band.

The galaxies were drawn from the 7th release of the Sloan Digital Sky Survey (SDSS DR7 Walcher et al., 2014), spanning a large variety of morphologies, colours, luminosities and stellar masses, all located at redshifts $0.005 < z < 0.03$. The mean distribution of the r-band magnitude is $\bar{r} = 13.3$ mag. All the galaxies were diameter-selected (i.e., the optical extension should fit in the FoV of the instrument). Throughout this work, we use the extended CALIFA survey (eCALIFA) which comprises information for 941 galaxies, covering a mass range between $10^{7.6} < \log(M_*/M_\odot) < 10^{11.9}$.

The data were processed using the version 2.2 of the CALIFA reduction pipeline (Sánchez et al., 2016b). This reduction pipeline involves several steps, including fibre tracing, extraction, wavelength calibration, fibre-to-fibre corrections, flux calibration, spatial re-sampling and registration, and differential atmospheric refraction correction. As a product of this pipeline, a 3D datacube is created, in which the spatial information is recorded in the x and y axes, and the spectral information is recorded in the z axis.

After these datacubes are generated, they are analyzed using the Pipe3D pipeline Sánchez et al. (2016a,b); Lacerda et al. (2022). In summary, the code uses a multi Single Stellar Population modelling (SSP), providing a decomposition of the stellar population, accounting for the line-of-sight velocity distribution and the extinction affecting the stellar populations. In the particular implementation of Pipe3D, it is used the GSD156 SSP-library. This library, first described in Cid Fernandes et al. (2013), comprises 156 SSP templates, that sample 39 ages (1 Myr to 14 Gyr, on an almost logarithmic scale), and four different metallicities ($Z/Z_\odot = 0.2, 0.4, 1, \text{ and } 1.5$), adopting the Salpeter Initial Mass Function, IMF (Salpeter, 1955). Once the best stellar model is obtained for each spectrum

(using the χ^2 as a quality measure of the fit), it is subtracted from the original spectra, creating a cube with the ionized emission line component. The parameters of the ionized gas emission lines are estimated using two methods: a Gaussian fitting and a moment analysis. The equivalent width of the emission lines is calculated by dividing the flux of the line by its adjacent stellar continuum flux density. While only a set of stellar templates are considered, the non-stellar continuum due to the AGN is well reproduced by a young stellar template of low metallicity. Thus, the emission line fluxes and their SN are not affected by this approach. (see Cortes-Suárez et al., 2022). Along this thesis, we use measurements of the following emission lines: $H\alpha$, $H\beta$, $[\text{NII}]\lambda 6584$, $[\text{OIII}]\lambda 5007$ and $[\text{OI}]\lambda 6301$, as well as the equivalent width (EW) of $H\alpha$. We also use the $H\alpha$ -based star formation rate (SFR) using the Kennicutt (1998) relation:

$$\text{SFR} (M_{\odot} \text{ yr}^{-1}) = 0.79 \times 10^{-41} L_{H\alpha} \text{ (erg/s)} \quad (3.1)$$

where $L_{H\alpha}$ is the dust-corrected luminosity of the $H\alpha$ emission line. Finally, we use the stellar mass calculated from the SSP decomposition as:

$$M_{\star} = L_V \Sigma_{\text{ssp}} \mathcal{W}_{\text{ssp},\star,L} \Upsilon_{\text{ssp},\star} \quad (3.2)$$

where L_V is the dust-corrected luminosity in the V band, $\mathcal{W}_{\text{ssp},\star,L}$ corresponds to the coefficients of the decomposition (see Sánchez et al., 2016c; Lacerda et al., 2022, for details), and $\Upsilon_{\text{ssp},\star}$ is the mass-to-light ratio of each SSP.

The aforementioned physical parameters are (i) integrated galaxy-wide, (ii) estimated in a ring at effective radius (Re), and (iii) estimated in a central aperture of $2.5''$ /diameter. These three set of quantities provide with an estimation of (i) the integrated/total values, (ii) characteristic values and (iii) central values (roughly corresponding to ~ 1 kpc). While in this thesis we explore the values in the three regions, we focus our analysis on the central region, where the AGN should be located.

3.3 Statistical methods

3.3.1 Chi-squared statistic

The χ^2 statistic (Pearson, 1900) is commonly used as a hypothesis test (in data that can be described by a Gaussian distribution) to quantify the goodness of the best fit model. In other words, this statistic helps quantify how the model compares to the data by evaluating the distance between the observed data and the predicted value at the same data point, in the form:

$$\chi^2 = \sum_{i=1}^n \frac{(x_i - m_i)^2}{m_i} \quad (3.3)$$

where x_i are the observed values and m_i are the predicted values. Thus, the larger the value of the χ^2 , the less probable that the null-hypothesis (that both the data and the model can be drawn from the same distribution) can be accepted. Through the X-ray spectral fitting package `xspec` (Arnaud, 1996), this can be quantified by minimizing the likelihood of the form:

$$\chi^2 = \sum_{i=1}^n \frac{(x_i - m_i)^2}{\sigma_i^2} \quad (3.4)$$

where σ^2 are the errors of the data. Moreover, the reduced χ^2 , χ_r^2 accounts for the degrees-of-freedom (d.o.f) of the model in the form $\chi_r^2 = \chi^2/\text{d.o.f}$, where $\text{d.o.f} = n - k$ and k are the number of free parameters of the model. Therefore, we look for values of the $\chi_r^2 \sim 1$. Values $\chi_r^2 > 1$ reflect that the model is not accurate to describe the data, while values $\chi_r^2 < 1$ reflect that the model is too complex for the data (i.e., the model is over-fitting the observations). Apart from the χ_r^2 , we also use the *p-value* which is the statistical significance of the model, i.e., the probability that the difference between the model and the data is due to chance. In our case, we use a p-value threshold of 10^{-3} (i.e., p-value $< 10^{-3}$ means that M_2 is 1000 more likely than M_1). We make use of the χ^2 statistics in Chapter 4 due to the binning method based on the SNR of the data.

3.3.2 Cash statistic

When the data does not follow a Gaussian distribution, but rather drawn from a Poisson distribution, the likelihood, defined by Cash (1979) has the following form:

$$C = 2 \sum_{i=1}^N (tm_i) - S_i \ln(tm_i) + \ln(S_i!) \quad (3.5)$$

where S_i are the observed data counts, t is the exposure time, and m_i are the predicted values. This statistic is useful when the data are low sampled (i.e. for low values of the SNR). Similarly to the χ^2 , the larger the value of C , the less probable that the data can be described by the model. We also use the d.o.f to assess the goodness-of-fit, by estimating the $C/\text{d.o.f}$, and the p-value of the null-hypothesis. We use the C-statistics in Chapter 5 since the number of counts for the spectra were very low and can be treated as Poissonian.

3.3.3 F-test

The F-test statistical method is used to compare which out of two nested models, fits best the data. This is done by checking whether the variances of the two samples are equal or not. Moreover, it contemplates the values of the statistics (either χ^2 or C as well as their d.o.f). The assumptions to use this test is that model M_2 has at least one extra free parameter compared to model M_1 (this is the result of freeing an extra parameter, or adding an extra component).

$$F_{12} = \frac{\chi_1^2/\text{dof}_1}{\chi_2^2/\text{dof}_2} \quad (3.6)$$

The above equation (pg. 204 in Bevington & Robinson, 2003) represents the value of the F-test statistic. In this case, χ_1^2/dof_1 represents the reduced χ^2 for the simpler model (i.e., more degrees of freedom and less free parameters) while χ_2^2/dof_2 represents the complex model (i.e., less degrees of freedom and more free parameters). Low values of F represent low statistical significance for extra free parameters, while high values represent a high statistical significance. Note that this test can only be used with additive models, and will not work with multiplicative ones (Orlandini et al., 2012). Moreover, this test is not

correct to test the presence of a line (Protassov et al., 2002, see also the `xspec` manual).

3.3.4 Bayesian Information Criterion

The Bayesian Information Criterion (BIC Schwarz, 1978) is another statistical method to compare the goodness-of-fit between several models, by penalizing based on the number of parameters of each compared model. In general, models with lower values of BIC are preferred. It has the following form:

$$\text{BIC} = \chi^2 - m * \ln(n) \quad (3.7)$$

where χ^2 is the value of the statistic of the fit, m are the free parameters in the fit and n is the number of data points. Note that the χ^2 value can be replaced by the C -statistic value correspondingly. When comparing two, or more models:

$$\Delta\text{BIC} = |\text{BIC}_1 - \text{BIC}_2| \quad (3.8)$$

Following Raftery (1995), a $0 < \Delta\text{BIC} < 2$, there is *weak* evidence in favour of the model with smaller BIC. A value of ΔBIC between 2 and 6 represents *positive* evidence in favour of the model with smaller BIC, while a value between 6 and 10 represents *strong* evidence in favour of the model with smaller BIC and a value larger than 10 represents *very strong* evidence in favour of the model with smaller BIC. Note that this can be extrapolated to more than two model comparisons. Thus, in our case, we accept that a model with smaller BIC is statistically favoured if there is *very strong* evidence in favour of it (i.e., $\Delta\text{BIC} > 10$). Opposite to the F-test, the BIC can be used for both nested and non-nested models.

Chapter 4

Behaviour of the reflection component for LLAGN

As was mentioned in Sec. 2.1, the conditions under which the torus may disappear are more complex than just depending on the bolometric luminosity of the source. Moreover, the study of the torus at X-rays through the reflection component has been only recently taking place due to the development of the *NuSTAR* satellite (see Sec. 3.1) which allows the study of X-ray spectra at high energies. However, studies on the existence of the torus in LLAGN have been done only for individual or small sample of sources (see Kawamuro et al., 2016; Diaz et al., 2020, 2023). In this chapter, we explore the behaviour of the torus for a sample of LLAGN through the reflection component detected at X-rays (see sec. 1.8 and sec. 2.1). We use the X-ray satellite *NuSTAR* as it provides information above 10 keV, essential to correctly study this component. Our sample comprises 81 sources within $D < 200\text{Mpc}$ to study the nearby Universe. We select our sources based on their Eddington ratios (which should be $\lambda_{\text{Edd}} < 10^{-3}$) to evaluate the behaviour of the reflection component in the low luminosity regime. We analyze these sources using the X-ray Spectral Fitting package (XSPEC) as it provides a set of models accounting for different mechanisms emitting at X-rays, as well as different statistical tools, such as the F-test, that we use throughout the analysis.

We present four baseline models. One of them represents the power-law continuum emission affected by obscuration in the l.o.s, through the use of the partial-covering sce-


nario, which assumes that the obscuration is not uniform. Models two and three represent the combination of AGN continuum emission and the addition of a reflection component from neutral distant material, assuming that it is coming from the torus. Finally, the fourth model is a pure-reflection model, which would be the case of highly obscured, Compton-thick sources, for which the power-law continuum is not detected.

We find that sources with reflection are located in the region in which the torus may or may not disappear according to the theoretical predictions. From the 81 sources, we find that 11 objects lack of any traces of reflection, indicating that the torus is not present in them. Additionally, we find a change in the contribution of the $\text{FeK}\alpha$ line in the reflection component, indicating that there might be a change in the chemical composition of the torus towards lower luminosities. Finally, we find that the vast majority of sources in the sample ($\sim 80\%$) are obscured at X-rays. This is likely to be due to the prevalence of obscured sources in the nearby Universe, as other authors have found as well (Ricci et al., 2017b), (Marchesi et al., 2018).

As additional material, we present in Appendix 8.1 the figures corresponding to the spectral fits of the four models for the complete sample, while in Appendix 8.2 we show the values of the statistics in each model version for the complete sample.

This work was done in its majority by the main author, with the Dr. Omaira González Martín and Dr. Sebastián F. Sánchez as the advisors, contributing to the exhausting revision and discussion of the results. The rest of the authors contributed with additional revisions and comments. This work was accepted for publication by the *Monthly Notices of the Royal Astronomical Society* (MNRAS) journal in December of 2021. The electronic version of this publication can be found at: <https://ui.adsabs.harvard.edu/abs/2022MNRAS.510.51020/abstract>.

Observational hints on the torus obscuring gas behaviour through X-rays with *NuSTAR* data

N. Osorio-Clavijo ¹,¹★ O. González-Martín,¹ S. F. Sánchez,² D. Esparza-Arredondo,¹ J. Masegosa,³ C. Victoria-Ceballos,¹ L. Hernández-García^{4,5} and Y. Díaz⁵

¹*Instituto de Radioastronomía and Astrofísica (IRyA-UNAM), 3-72 (Xangari), 8701 Morelia, Mexico*

²*Instituto de Astronomía, Universidad Nacional Autónoma de México, A. P. 70-264, C.P. 04510 México, D.F., Mexico*

³*IAA - Instituto de Astrofísica de Andalucía (CSIC), Glorieta de la Astronomía, E-18008 Granada, Spain*

⁴*Millennium Institute of Astrophysics (MAS), Nuncio Monseñor Sótero Sanz 100, Providencia, Santiago, Chile*

⁵*Instituto de Física y Astronomía, Facultad de Ciencias, Universidad de Valparaíso, Gran Bretaña 1111, Playa Ancha, Valparaíso, Chile*

Accepted 2021 December 19. Received 2021 December 16; in original form 2021 March 25

ABSTRACT

According to theory, the torus of active galactic nuclei (AGN) is sustained from a wind coming off the accretion disc, and for low efficient AGN, it has been proposed that such structure disappears. However, the exact conditions for its disappearance remain unclear. This can be studied throughout the reflection component at X-rays, which is associated with distant and neutral material at the inner walls of the torus in obscured AGN. We select a sample of 81 AGNs observed with *NuSTAR* with a distance limit of $D < 200$ Mpc and Eddington rate $\lambda_{\text{Edd}} \equiv L_{\text{bol}}/L_{\text{Edd}} < 10^{-3}$. We fit the 3–70 keV spectra using a model accounting for a partial-covering absorber plus a reflection component from neutral material. We find that the existence of the reflection component spans in a wide range of black hole mass and bolometric luminosities, with only ~ 13 per cent of our sample (11 sources) lacking of any reflection signatures. These sources fall in the region in which the torus may be lacking in the L-MBH diagram. For the sources with a detected reflection component, we find that the vast majority of them are highly obscured ($\log N_{\text{H}} > 23$), with ~ 20 per cent being Compton-thick. We also find an increase in the number of unobscured sources and a tentative increase on the ratio between FeK α emission line and Compton-hump luminosities toward $\lambda_{\text{Edd}} = 10^{-5}$, suggesting that the contribution of the FeK α line changes with Eddington ratio.

Key words: galaxies: active – galaxies: nuclei – galaxies: Seyfert – X-rays: galaxies.

1 INTRODUCTION

It has been widely accepted that most galaxies with bulges host a supermassive black hole (SMBH), sometimes fed by an accretion disc, causing the release of energy in orders of magnitude that can go up to $L_{\text{bol}} \sim 10^{47}$ erg s $^{-1}$ (see Netzer 2015, for a review). Such objects are known as active galactic nuclei (AGN). The unified model (UM) of AGN (Antonucci 1993; Urry & Padovani 1995) assumes that all AGN have the same components (accretion disc, broad and narrow line regions, a dusty structure – the torus and, in some cases, a jet) and that the difference in the spectrum relies on the angle of sight to the observer. This effect may prevent the observer to see the inner parts of AGN and therefore the existence or absence of broad lines in the optical spectrum, leading to a purely observational classification (see Netzer 2015; Ramos Almeida & Ricci 2017, for recent reviews on the topic).

The cornerstone of the UM are both the obscuring structure and the inclination angle, as well as the existence of the jet. However, some observations suggest that there are objects lacking the obscuring structure (the so-called true type-2 AGN; Laor 2003). This might

be explained under the theoretical prediction that the torus should disappear below a certain luminosity, assuming that both the torus and broad-line region (BLR) are formed from a wind coming off the accretion disc (Elvis 2000). In fact, Elitzur & Shlosman (2006) state that both the torus and the BLR should disappear for bolometric luminosities below ($L_{\text{bol}} \sim 10^{42}$ erg s $^{-1}$), since the radiation pressure cannot longer counteract the gravity for both structures. Indeed, González-Martín et al. (2017) using mid-infrared (mid-IR) spectra, have found hints on the torus disappearance in inefficient AGN (see also González-Martín et al. 2015). Moreover, Elitzur & Ho (2009) find that the torus might still be absent for luminous AGN, depending on the efficiency of the accretion disc at feeding the SMBH. Therefore, not only the luminosity of the AGN gives us hints on the existence of the torus, but also the efficiency and density of the wind. Both mid-IR and X-ray studies suggest that the torus is intrinsically different in type-2 AGN than in type-1 AGN (e.g. Ramos Almeida et al. 2009; Ricci et al. 2011), and that the fraction of type-2 sources increases for AGN with Eddington rates $\lambda_{\text{Edd}} \equiv L_{\text{bol}}/L_{\text{Edd}} \simeq 0.001$ (Ricci et al. 2017). Indeed, Khim & Yi (2017) found a complex behaviour where the number of clouds and covering factor change for high-accretion sources (i.e. $0.01 < \lambda_{\text{Edd}} < 1$), forming a ridge-shaped distribution in the luminosity versus black hole mass (M_{BH}) diagram. However,

* E-mail: n.osorio@irya.unam.mx

the behaviour of the torus for low accretion AGN with $\lambda_{\text{Edd}} < 0.001$, where the torus should evolve to its disappearance, remains an open question.

Historically, the obscuring matter has been studied through the column density along the line of sight (LOS) that affects the primary X-ray continuum (e.g. Matt, Guainazzi & Maiolino 2003). Additionally, the torus can also be studied at X-rays because the inner parts of it can reflect the X-ray emission from the corona above the disc, placing a reflection component in the X-ray spectrum. This reflection component has two main signatures: the Compton hump and the FeK α line. Theoretical works have shown that the resulting reflection spectrum depends on the shape and distribution of the reflector, but also on the LOS to the observer, and all of this might have an impact on the luminosity of this component (e.g. see Furu et al. 2016). However, studies aiming to detect and characterize the torus through the reflection component at X-rays have only been recently developed (e.g. Ricci et al. 2011; Liu & Li 2014; Ricci et al. 2014; Furu et al. 2016; Kawamuro et al. 2016), but also thanks to the unprecedented sensitivity achieved above 10 keV provided by *NuSTAR* (e.g. Esparza-Arredondo et al. 2019, 2021; Panagiotou & Walter 2019, 2020, among others).

The aim of this study is to trace the behaviour of the obscuring material and plausible disappearance of the torus through X-rays for low accretion AGN, compared to what has already been found for more efficient AGN, by using *NuSTAR* data. This work is divided as follows: in Section 2 we present the sample and the data reduction. In Section 3 we present the model and the spectral analysis, while in Section 4 we present the results obtained, in Section 5 we discuss them, and finally we present the summary and conclusions of our work in Section 6. Throughout the analysis, we assume a cosmology of $H_0 = 70 \text{ km s}^{-1} \text{ Mpc}^{-1}$, $q_0 = 0$, and $\Omega_{\lambda_0} = 0.73$, and all distances are redshift independent taken from the NASA Extragalactic Data base (NED¹).

2 SAMPLE AND DATA REDUCTION

2.1 Sample selection

We search for all available galaxies within a 10 arcmin radius (using SIMBAD data base²) for all archived pointings within the *NuSTAR* data base (until 2020 July). We find a total of 1313 galaxies within a distance of 200 Mpc ($z < 0.05$) to sample the nearby universe. We then retrieve the activity type, keeping only those galaxies classified as AGN in either NED or SIMBAD data bases. We obtain a total of 463 AGN. We download all the data from the HEASARC archive³ and reduce the observations for these 463 AGN (see Section 2.2 reduction procedure), keeping only the observations with more than 30 bins after producing grouped spectra, and at least 10 bins above 10 keV. We also remove from the sample those AGN where the *NuSTAR* resolution cannot fully isolate the nuclear spectra for dual AGN. We obtain a total of 301 sources fulfilling these criteria.

We finally search for M_{BH} . These measurements are needed to obtain an estimate of the Eddington rate. We first look for M_{BH}

calculated via reverberation mapping (e.g. Laor 2001, 2003; Woo & Urry 2002; Vasudevan & Fabian 2009) and velocity dispersion otherwise (e.g. McKernan, Ford & Reynolds 2010; van den Bosch et al. 2015; van den Bosch 2016), by using the M - σ relation, M_{BH} ($\log(M_{\text{BH}}/M_{\odot}) = 8.27 + 5.1 \log(\sigma/200 \text{ km s}^{-1})$) Ferrarese & Merritt 2000; Gebhardt et al. 2000). As for the sources for which the M_{BH} is not calculated through the methods reported above, we also search for the M_{BH} in different AGN catalogues where the mass are compiled from literature (e.g. Khorunzhev et al. 2012; Koss et al. 2017; Bär et al. 2019). We obtain measurements for 231 out of the 301 AGN. This sample is now referred to as full sample.

We then fit the spectra of the 231 AGN with an unabsorbed power law to roughly calculate the bolometric luminosity, L_{bol} , from X-rays following the $L_{\text{bol}}/L_{(2-10 \text{ keV})}$ conversion from Marconi et al. (2004), where L_{bol} is in units of L_{\odot} :

$$\log[L_{\text{bol}}/L_{(2-10 \text{ keV})}] = 1.54 + 0.24(L_{\text{bol}} - 12)0.012(L_{\text{bol}} - 12)^2 - 0.0015(L_{\text{bol}} - 12)^3. \quad (1)$$

We define low accretion sources as those with $\lambda_{\text{Edd}} < 10^{-3}$, where L_{Edd} is the Eddington luminosity, defined as the maximum luminosity an object can release without losing the thermal equilibrium. Such definition is based on the assumption that the transition from the standard disc (Shakura & Sunyaev 1973) to an Advection Dominated Accretion disc (ADAF; Narayan & Yi 1995) occurs around this value (see also Constantin et al. 2009; Gu & Cao 2009; Younes et al. 2011; Gültekin et al. 2012; Jang et al. 2014; Connolly et al. 2016; Hernández-García et al. 2016). This sample contains a total of 87 sources. This corresponds to ~ 20 per cent of the total nearby available AGN observed with *NuSTAR*. Four of these sources (NGC 3310, Mrk 18, Arp 299C, and M 83) are excluded from the sample because although they are classified as AGN in SIMBAD/NED, they are also classified as starbursts. Finally, we exclude NGC 4486 due to the strong thermal and jet contribution (de Jong et al. 2015), while we exclude Centaurus A due to strong jet contribution (Hardcastle et al. 2003). Note that we also check for important thermal or jet contribution for the rest of the sample. Although in some cases there are reported thermal contribution at X-rays (see González-Martín et al. 2009), it does not contribute above 3 keV for the rest of the sources. One consequence, although not the only one, would be a very steep photon index (i.e. $\Gamma > 2$ Nemmen, Storchi-Bergmann & Eracleous 2014) as the one in M 87 ($\Gamma = 2.8 \pm 0.4$ de Jong et al. 2015), which is not the case in our sample; see Section 4). Our final sample comprises a total of 81 sources.

Fig. 1 shows the distribution (in logarithmic scale) of M_{BH} (left), L_{bol} (center), and λ_{Edd} (right) for our final sample of 81 sources, compared to the full sample of 231 sources with M_{BH} estimates. The mean of the distributions of the final sample for M_{BH} , L_{bol} , and λ_{Edd} are $\langle \log(M_{\text{BH}}) \rangle = 7.9$, $\langle \log(L_{\text{bol}}) \rangle = 42.1$, and $\log(\lambda_{\text{Edd}}) = -3.8$, compared to $\langle \log(M_{\text{BH}}) \rangle = 7.6$, $\langle \log(L_{\text{bol}}) \rangle = 43.0$, and $\langle \log(\lambda_{\text{Edd}}) \rangle = -2.6$, for the full sample. Thus, our final sample contains lower luminosity AGN with roughly the same range of M_{BH} values compared to the full sample. Note that this imposes a bias on our sample for Eddington rates above $\log(\lambda_{\text{Edd}}) > -3$. Moreover, once we correct by absorption in the LOS, Eddington rates will be higher (see Section 4.1). Thus, we might lack objects with low obscuration and intrinsically high Eddington rate above $\log(\lambda_{\text{Edd}}) > -2.5$. Another source of bias is the fact that our sample relies purely on archival data. For instance, we do not find available *NuSTAR* data for the candidates of torus disappearance in González-Martín et al. (2017). Thus, we might also be missing the least

¹The NASA/IPAC Extragalactic Database (NED) is operated by the Jet Propulsion Laboratory, California Institute of Technology, under contract with the National Aeronautics and Space Administration. <https://ned.ipac.caltech.edu/>

² The SIMBAD astronomical database <http://simbad.u-strasbg.fr/simbad/> Wenger et al. (2000)

³<https://heasarc.gsfc.nasa.gov/>

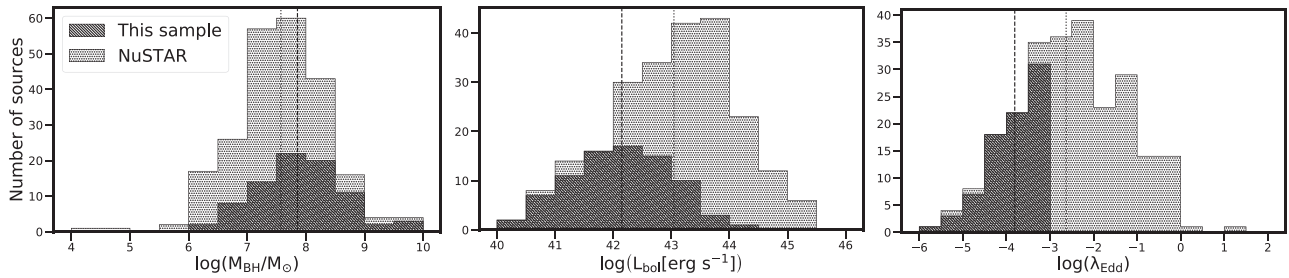


Figure 1. Histograms of the distribution of M_{BH} (left), L_{bol} (center), and λ_{Edd} (right), for the final sample (dashed, 81 sources) versus the full sample with M_{BH} measurements (dotted, 231 sources). The dashed and dotted vertical lines in each panel represent the mean value of the parameter in the X-axis for both the final and full samples, respectively. Note that in the left-hand panel, six sources fulfill the accretion criterion but are still excluded from the analysis because they are classified as starburst or because they are at the center of clusters (see the text).

luminous sources as they might not have been observed yet. We warn the reader on the fact that our sample is by no means complete, although it does cover a wide range in M_{BH} and Eddington rate.

Several works have studied samples of inefficient AGN in different wavelengths aiming to understand the nature and behaviour of the reflection component and will be used to compare with our new results along the text. Here, we report a brief summary on the matching of our sample with theirs. The largest sample using X-rays is reported by González-Martín et al. (2009), where they study a sample of 82 inefficient AGN using *Chandra* and *XMM-Newton* data. We have 12 sources in common with available *NuSTAR* observations. Kawamuro et al. (2016) also studied a sample of 10 inefficient AGN using *Suzaku* and we have five sources in common with them. On the other hand, González-Martín et al. (2017) analysed a sub-sample of those presented by González-Martín et al. (2009) together with a complementary Seyfert sample (22 sources). We have a total of 39 sources in common with the works mentioned above, which is around 50 per cent of our final sample.

Tables 1 and 2 report the observational parameters for the optically classified as low-ionization nuclear emission-line regions (LINER, 18 sources) and Seyfert (64 sources) samples, respectively.

2.2 Data reduction

All *NuSTAR* (Harrison et al. 2013) data were reduced using the data analysis software NUSTARDAS v.1.4.4. distributed by the High Energy Astrophysics Archive Research Center (HEASARC). The calibrated, cleaned, and screened event files for both FPMA and FMPB focal plane modules were generated using the NUPIPELINE task (CALDB 20160502). We automatically extracted three circular apertures with radius of 0.5, 1, and 2 arcsec centred at the NED position of the source. For each of them we produced eight backgrounds around the target. These backgrounds are located at a distance of three times the aperture radius of the target (i.e. 1.5, 3, or 6 arcsec) with position angles of 0, 45, 90, 135, 180, 225, 270, and 315 deg. We produced in this way 24 spectra for each target. The Redistribution Matrix and Auxiliary Response files (RMF and ARF) were produced with the NUPRODUCTS package available in *NUSTARDAS*. We chose the spectrum that maximizes the S/N in the 3–70 keV band, avoiding off-nuclear contributors. Tables 1 and 2 provide the best extraction radius for each target. Note the optimal extraction radius is ~ 1 arcmin ($D \simeq [1-52]$ kpc) for the vast majority of the objects, due to the relative faintness of our sources.

We then performed a binning method with a minimum S/N ratio of 3, using the FTGROUPPHA task within FTOOLS. The grouping using a minimum S/N ratio is particularly relevant for faint sources which are

probably background dominated above ~ 25 keV. Note that we also performed the standard grouping method accounting for a minimum of 30 counts per bin (the GRPPHA task) finding similar results in the spectral parameters of the sources. However, the grouping performed with a minimum S/N ratio clearly improves the error bars at high energies for faint sources as expected.

3 SPECTRAL ANALYSIS

3.1 Baseline models

In this section we present four models used in the analysis to fit the spectra, which are fitted using XSPEC (Arnaud 1996, version 12.10.0).⁴ Throughout the analysis, we use the χ^2 statistics. We begin the analysis by modelling the intrinsic continuum with a power law affected by a patchy absorber, in what is known as the partial covering scenario. We add two Gaussian profiles centred at 6.7 and 6.97 keV, to account for the Fe XXV and Fe XXVI ionized emission lines as they are the most common ionized lines present at hard X-rays for AGN. In the software terminology, this model has the following form:

$$M_1 = \text{phabs}_{\text{Gal}}((z\text{phabs}_{\text{intr}} * z\text{powerlw}) + ct * z\text{powerlw} + z\text{gauss}_{6.7 \text{ keV}} + z\text{gauss}_{6.97 \text{ keV}}), \quad (2)$$

where $(z\text{phabs}_{\text{intr}} * z\text{powerlw}) + ct * z\text{powerlw}$ represents the partial-covering scenario, in which the first power-law component is associated with the intrinsic continuum absorbed by the material along the LOS to the observer and the second power-law component is the scattered emission that reaches the observer. The parameters for both power law are linked, including the normalization, to simulate the partial-covering scenario. The free parameters for this model are the column density (N_{H}), the constant associated with the covering factor (as $ct = 1 - f_{\text{cov}}$), the photon index (Γ_{pl}), and the normalization of the power law. The free parameters of the Gaussian components, emulating the emission lines are the center, width, and normalization. The widths of the Gaussian components are fixed to be narrow (0.1 keV⁵) and the centers are fixed to 6.7 and 6.97 keV, respectively.

For the second and third models, we include an extra reflection component as follows:

$$M_2 = M_1 + \text{phabs}_{\text{Gal}}(\text{pexrav} + z\text{gauss}_{6.4 \text{ keV}}), \quad (3)$$

$$M_3 = M_1 + \text{phabs}_{\text{Gal}}(\text{pexmon}). \quad (4)$$

⁴<http://xc.heasarc.gsfc.nasa.gov/docs/xanadu/xspec/>

⁵The *NuSTAR* spectral resolution is 400 eV at 6 keV, see

https://heasarc.gsfc.nasa.gov/docs/nustar/nustar_tech_desc.html

Table 1. Observational parameters for the LINER sample. (1) Name of the source; (2) other name; (3) right ascension; (4) declination; (5) Redshift; (6) Redshift-independent distance in Mpc; (7) $\log(M_{\text{BH}}/M_{\odot})$; (8) AGN classification; (9) Galaxy type. All galaxy types were retrieved from NED; (10) date of the observation; (11) Observation ID in *NuSTAR*; (12) Exposure time of the observation in ksec; (13) is the extraction radius used in the data reduction; (14) is the number of counts in the 3–60 keV *NuSTAR* band when accounting for the background subtraction; and (15) is the number of bins. In columns (1) and (2), 2MXJ (2MXIJ) is abbreviation for 2MASXJ (2MASXIJ), 2M is the abbreviation for 2MASS and W is the abbreviation for WISE.

Name	Other name	RA deg	Dec deg	Redshift	Dist. Mpc	$\log M_{\text{BH}}$	AGN type	Galaxy type	Obs. date	Obs ID	Exp. time ks	Ext. radius arcmin	N. counts	Bins
(1)	(2)	(3)	(4)	(5)	(6)	(7)	(8)	(9)	(10)	(11)	(12)	(13)	(14)	(15)
NGC 1052	PKS0238–084	40.269 99	–8.255 76	0.0048	20.6	8.4	L2	E4	2017-01-17	60201056002	59.75	0.5	91.27	738
NGC 2655	ARP225	133.907 21	78.223 08	0.0057	24.4	8.0	L2	Sa-0	2016-11-10	60160341004	15.95	2	35.30	98
UGC5101	CGCG289–011	143.965 39	61.352 92	0.0394	168.6	8.3	L1	S?	2014-03-21	60001068002	18.29	1	24.33	51
M81	NGC 3031	148.888 22	69.065 30	0.0009	3.7	7.8	L1.8	SAab	2015-05-18	60101049002	209.09	0.5	255.69	1252
NGC 3079	UGC05387	150.490 85	55.679 79	0.0038	16.4	7.2	L2	Sbc	2013-11-12	60061097002	21.54	0.5	29.85	128
UGC5881	CGCG125–008	161.677 15	25.931 55	0.0206	88.2	8.2	L2	Sa	2015-05-17	60160409002	21.41	1	37.39	169
NGC 3628	UGC06350	170.070 91	13.589 49	0.0023	9.8	7.2	L2	SAb	2017-12-23	60371004002	50.35	1	32.46	86
NGC 3718	ARP214	173.145 22	53.067 91	0.0034	14.7	8.3	L1	SB	2017-10-27	60301031004	90.37	0.5	44.38	208
NGC 3998	UGC06946	179.483 89	55.453 59	0.0047	20.1	9.0	L1.9	Sa-0	2016-10-25	60201050002	103.94	0.5	111.02	714
NGC 4102	UGC07096	181.596 31	52.710 95	0.0046	19.5	8.2	L2	SAB	2015-11-19	60160472002	20.57	0.5	39.14	198
M106	NGC 4258	184.740 08	47.303 72	0.0017	7.3	7.5	L1.9	SBbc	2016-01-10	60101046004	103.62	0.5	71.20	466
M58	NGC 4579	189.431 65	11.818 09	0.0043	18.4	7.9	L1.9	Sb	2016-12-06	60201051002	117.84	0.5	116.60	738
NGC 5005	UGC08256	197.734 63	37.058 94	0.0047	20.1	8.1	L1.9	SABb	2014-12-16	60001162002	49.70	1	27.82	40
NGC 6240	IC4625	253.245 25	2.400 99	0.0245	104.8	9.1	L2	SO-a	2014-03-30	60002040002	30.86	0.5	55.62	444
MCG+08-31-041	ARP102B	259.810 38	48.980 40	0.0242	103.5	8.9	L1	E0	2015-11-24	60160662002	22.40	1	45.28	248
NGC 7130	IC5135	327.081 21	–34.951 31	0.0162	69.2	7.5	L2	Sa	2016-12-15	60261006002	42.12	0.5	23.86	63
NGC 7331	UGC12113	339.267 09	34.415 92	0.0031	13.4	7.8	L2	Sbc	2016-05-03	40202013002	42.97	1	38.16	153
NGC 7479	UGC12343	346.236 12	12.322 88	0.0066	28.3	7.3	L1.9	SBbc	2016-05-12	60201037002	18.45	1	27.73	82

For M_2 , we choose as reflection component the `pexrav` model (Magdziarz & Zdziarski 1995). This model assumes Compton reflection from neutral X-ray photons in an optically thick material with plane-parallel geometry. This model has as free parameters the photon index, high-energy cutoff, relative reflection (R), metal and iron abundances, inclination angle, and normalization. We have set the photon index of `pexrav` (Γ_{pex}) to be the same as that of the power law, assuming that the reflection occurs in the AGN such that both emissions are correlated. The energy cutoff is fixed to 300 keV assuming this cutoff to happen above the *NuSTAR* energy range. Note that although several works (e.g. Molina et al. 2019; Younes et al. 2019; Ezhikode et al. 2020) have aimed to find this cutoff in AGN spectra, it has only been possible for very few objects, and in most cases, it happens well above the *NuSTAR* range (e.g. Baloković et al. 2020). Therefore, we do not expect for this parameter to be constrained nor to affect the overall analysis. We have set R to -1 for `pexrav` to account for the reflection component only, without contribution from the intrinsic power-law continuum. Thus, this reflection model with the relative reflection set to -1 plus the power-law component is equivalent to the `pexrav` allowing the relative reflection to vary. However, we used with the relative reflection to -1 in order to separate both the intrinsic continuum and the reflection components.

The rest of the parameters are set to their default values except for the normalization. Note that in this model version, the addition of an extra Gaussian profile is necessary to emulate the $\text{FeK}\alpha$ line, since `pexrav` assumes reflection from a neutral material, and does not account for this line. In this model, the width of the line at 6.4 keV is also fixed to 0.1 keV.

For M_3 , we include the reflection component using `pexmon` (Nandra et al. 2007). This model is an updated version of `pexrav` that includes fluorescence lines such as $\text{FeK}\alpha$, $\text{FeK}\beta$, and $\text{NiK}\alpha$. This model also accounts for the Compton shoulder, by assuming a Gaussian line at 6.315 keV with a width of 0.35 keV. Additionally, it assumes a connection between the equivalent width (EW) of the $\text{FeK}\alpha$ line and that of the Compton shoulder. This reflection model has as free parameters the photon index (Γ_{pex}), relative reflection,

cutoff energy, metal and iron abundances, inclination angle, and normalization. Similar to M_2 , the parameter R is set to -1 , the energy cutoff is set to 300 keV and the other parameters, except the normalization, are set to their default values.

The difference between M_2 and M_3 relies on the fact that `pexmon` accounts for the abundance of iron in the medium through the inclusion of the $\text{FeK}\alpha$, $\text{FeK}\beta$, and $\text{NiK}\alpha$ lines. Indeed, these lines are correlated with the Compton-reflection as they are fixed to a fraction of the Compton-shoulder, and they also depend on the photon index of the intrinsic continuum. `pexmon` also accounts for the Compton-shoulder, while `pexrav` is a simpler model not accounting for such features. Thus, `pexmon` already incorporates the $\text{FeK}\alpha$ line at 6.4 keV while we add this line using a Gaussian profile in M_2 . We use M_2 to calculate the EW and luminosity of the 6.4 keV line, with the normalization and error of the line component and the tools `EQUIVALENT` and `LUMINOSITY` within `XSPEC`. M_2 also allows us to isolate the effect of the line from that of the Compton shoulder. Note that both models are equivalent in the analysis. However, since `pexmon` self-consistently accounts for both the continuum and line emission due to the reprocessing in neutral, distant material, the rest of the analysis is based on this model. We include M_1 to study the detection of the reflection component in our sample through the f-statistic test when comparing models (see below). Note also that regardless of the model, we account for Galactic absorption and redshift by using the `NH` tool within `FTOOLS` (retrieved from NED⁶ and fixed to the HI maps of Kalberla et al. 2005).

We also use a fourth model that accounts for reflection dominated sources, i.e. sources for which the intrinsic continuum is completely covered by the reflection component in the available X-ray data. This model has the following form:

$$M_4 = \text{phabs}_{\text{Gal}} * \text{pexmon}. \quad (5)$$

This analysis does not use sophisticated models as `BORUS` (Baloković et al. 2018) or `MYTORUS` (Murphy & Yaqoob 2009) for

⁶<https://ned.ipac.caltech.edu>

Table 2. Observational parameter for the Seyfert sample. Columns are as in Table 1.

Name	Other name	RA deg	Dec deg	Redshift	Dist. Mpc	log M _{BH}	AGN type	Galaxy type	Obs. date	Obs ID	Exp. time ks	Ext. radius arcmin	N. counts	Bins
(1)	(2)	(3)	(4)	(5)	(6)	(7)	(8)	(9)	(10)	(11)	(12)	(13)	(14)	(15)
NGC 253	ESO474–G029	11.888 06	–25.288 80	0.0008	3.2	6.9	S2	SAB	2012-09-15	50002031004	157.65	0.5	83.01	431
NGC 424	ESO296–G004	17.865 16	–38.083 45	0.0118	50.7	7.5	S1	SB0-a	2013-01-26	60061007002	15.48	1	32.14	145
IC1657	ESO352–G024	18.529 24	–32.650 90	0.0107	45.9	7.3	S2	SBbc	2017-01-15	60261007002	45.16	0.5	40.39	217
2MXJ01142491–5523497	NGC 0454NED0	18.603 88	–55.397 05	0.0121	51.9	8.5	S2	II	2016-02-14	60061009002	24.23	1	34.16	144
MCG+08-03-018	2MXJ01223442+5003180	20.643 41	50.054 96	0.0204	87.4	8.4	S2	S?	2014-01-27	60061010002	31.66	1	43.88	230
NGC 612	ESO353–G015	23.490 63	–36.493 28	0.0298	127.5	8.5	S2	SA0	2012-09-14	60061014002	16.69	0.5	31.62	158
Mrk573	UGC01214	25.990 74	2.349 87	0.0172	73.6	7.4	S2	S0	2018-01-06	60360004002	32.00	1	29.73	66
NGC 788	MCG-01-06-025	30.276 93	–6.815 87	0.0136	58.3	7.7	S2	S0-a	2013-01-28	60061018002	15.41	0.5	35.64	198
M77	NGC 1068	40.669 88	–0.013 29	0.0025	10.6	7.2	S2	SAb	2012-12-18	6002030002	57.85	0.5	82.88	657
NGC 1106	UGC02322	42.668 73	41.671 58	0.0145	62.0	7.5	S2	SA0	2019-02-22	60469002002	18.74	1	26.56	67
NGC 1125	MCG-03-08-035	42.917 92	–16.651 11	0.0109	46.8	7.2	S2	SAB0	2019-06-10	60510001002	31.74	1	36.46	123
NGC 1142	UGC02389	43.800 95	–0.183 55	0.0288	123.5	8.9	S2	Spec	2017-10-14	60368001002	20.71	0.5	28.40	119
Mrk1066	UGC02456	44.994 15	36.820 50	0.0121	51.7	7.0	S2	SBO	2014-12-06	60001154002	30.08	1	30.03	64
NGC 1194	UGC02514	45.954 63	–1.103 75	0.0136	58.2	7.8	S1.9	SA0	2015-02-28	60061035002	31.54	0.5	39.68	224
NGC 1229	ESO480–G033	47.045 13	–22.960 25	0.0363	155.4	8.3	S2	SBb	2013-07-05	60061325002	24.92	1	35.29	155
NGC 1320	MRK0607	51.202 88	–3.042 26	0.0088	37.7	6.9	S2	Sa	2013-02-10	60061036004	28.00	1	34.45	120
NGC 1358	MCG-01-10-003	53.415 35	–5.089 51	0.0134	57.5	8.1	S2	SAB0	2017-08-01	60301026002	50.00	0.5	39.72	206
NGC 1386	ESO358–G035	54.192 66	–35.999 27	0.0038	16.1	7.0	S1	S0-a	2016-05-11	60201024002	26.43	1	22.29	45
UGC3157	CGCG468–001	71.623 99	18.460 91	0.0154	66.0	8.0	S2	SBbc	2014-03-18	60061051002	20.09	1	35.16	163
2MJ05081968+1721481	CGCG468–002NED01	77.082 11	17.363 36	0.0175	75.0	8.6	S2	-	2012-07-23	60006011002	15.52	0.5	51.25	368
ES05–4	IRAS06220–8636	91.423 84	–86.631 95	0.0060	25.9	7.6	S2	Sb	2015-11-10	60061063002	24.70	1	33.74	109
NGC 2273	UGC03546	102.536 14	60.845 80	0.0068	29.0	7.0	S2	SBa	2014-03-23	60001064002	23.23	1	36.69	150
UGC3601	CGCG204–032	103.956 38	40.000 31	0.0171	73.3	8.6	S1.5	S?	2019-01-06	60160278002	19.67	1	45.70	257
ESO428–14	MCG-05-18-002	109.130 03	–29.324 69	0.0054	23.2	7.0	S2	SA0	2015-01-11	60001152002	40.25	0.5	29.46	111
2MXJ07561963–4137420	WAJ075619.61–413742.1	119.081 82	–41.628 35	0.0210	90.1	8.0	S2	-	2014-07-29	60061076002	22.75	2	38.87	62
NGC 2788A	ESO060–G024	135.664 18	–68.226 83	0.0144	61.6	8.7	S2	Sb	2019-06-14	60469001002	27.58	0.5	27.18	99
IC2560	ESO375–G004	154.077 95	–33.563 01	0.0078	33.4	7.2	S2	SBbc	2014-07-16	50001039002	49.56	1	35.56	99
NGC 3147	UGC05532	154.223 47	73.400 65	0.0092	39.6	8.7	S2	SABc	2015-12-27	60101032002	49.26	0.5	48.47	293
NGC 3393	ESO501–G100	162.097 78	–25.162 03	0.0125	53.6	7.5	S2	SBab	2013-01-28	60061205002	15.66	0.5	25.00	87
2MXJ11055897+5856456	CGCG291–028	166.495 93	58.946 03	0.0271	116.0	8.4	S2	-	2019-03-26	60160420002	15.77	2	38.17	134
NGC 3621	ESO377–G037	169.567 92	–32.812 60	0.0016	6.7	6.8	S2	SA	2017-12-15	60371002002	30.78	2	41.09	100
NGC 3786	UGC06621	174.927 14	31.909 43	0.0118	50.6	7.5	S1.8	SAB	2014-06-09	60061349002	21.99	2	36.08	103
IC751	UGC06972	179.719 15	42.570 34	0.0312	133.6	8.6	S2	Sb	2013-02-04	60061217004	52.02	0.5	25.72	63
M88	NGC 4501	187.996 73	14.420 41	0.0042	18.0	7.5	S2	SAb	2018-01-26	60375002002	62.77	1	27.45	55
IC3639	ESO381–G008	190.220 15	–36.755 85	0.0109	46.8	6.9	S2	SBbc	2015-01-09	60001164002	58.73	0.5	25.34	51
NGC 4785	ESO219–G004	193.363 82	–48.749 15	0.0116	49.6	8.1	S2	SAB	2014-08-20	60001143002	48.83	0.5	40.05	208
Mrk231	UGC08058	194.059 31	56.873 68	0.0422	180.6	8.4	S2	Sc	2017-10-19	80302608002	82.06	0.5	46.30	242
NGC 4941	PGC045165	196.054 61	–5.551 60	0.0033	14.2	6.9	S2	SABa	2016-01-19	60061236002	20.66	1	32.48	119
NGC 4939	MCG-02-33-104	196.059 70	–10.339 53	0.0085	36.4	7.9	S2	Sbc	2017-02-17	60002036002	22.04	0.5	36.10	181
NGC 4945	ESO219–G024	196.363 66	–49.467 90	0.0010	4.2	6.3	S2	SBc	2013-06-15	60002051004	54.62	0.5	129.04	1565
MCG-03-34-064	PGC046710	200.602 02	–16.728 36	0.0200	85.6	8.1	S1.8	SB?	2016-01-17	60101020002	78.50	0.5	80.69	727
NGC 5135	ESO444–G032	201.433 58	–29.833 68	0.0015	6.3	7.6	S2	Sab	2015-01-14	60001153002	33.36	1	34.28	88
M51	ARP085	202.469 57	47.195 26	0.0017	7.3	6.6	S2	-	2017-03-17	60201062003	163.06	0.5	41.19	99
NGC 5252	UGC08622	204.566 13	4.542 65	0.0195	83.6	8.9	S1.9	S0	2013-05-11	60061245002	19.01	0.5	65.88	523
NGC 5283	UGC08672	205.273 95	67.672 22	0.0106	45.3	7.7	S2	S0	2018-11-17	60465006002	33.02	0.5	42.87	234
NGC 5347	UGC08805	208.324 16	33.490 83	0.0050	21.6	6.8	S2	Sab	2015-01-16	60001163002	47.30	1	32.04	54
NGC 5643	ESO272–G016	218.169 91	–44.174 61	0.0027	11.4	7.0	S2	Sc	2014-05-24	60061362002	22.46	1	36.54	146
NGC 5695	UGC09421	219.342 23	36.567 83	0.0125	53.5	7.7	S2	SBb	2018-01-16	60368004002	41.61	1	27.60	43
NGC 5728	MCG-03-37-005	220.599 70	–17.253 17	0.0071	30.3	7.8	S2	SABa	2013-01-02	60061256002	24.36	0.5	52.02	402
NGC 5899	UGC09789	228.763 55	42.049 85	0.0090	38.6	8.7	S2	SABc	2014-04-08	60061348002	23.88	0.5	54.44	383
MCG+14-08-004	CGCG367–009	244.830 58	81.046 50	0.0239	102.4	9.8	S2	-	2014-12-21	60061270002	29.76	1	38.54	165
ESO137–34	2MXJ16351411–5804481	248.808 81	–58.080 03	0.0077	33.0	8.0	S2	SAB0	2016-06-07	60061272002	18.55	0.5	28.69	111
2MXJ16504275+0436180	NGC 6230NED01	252.678 13	4.605 08	0.0321	137.3	9.8	S2	-	2017-02-06	60061273002	21.03	0.5	56.94	409
2MXJ1802473–145454	WAJ180247.38–145454.8	270.697 08	–14.915 28	0.0034	14.6	7.8	S1	-	2016-05-01	60160680002	19.96	0.5	80.72	595
2MXJ18305065+0928414	LEDA1365707	277.710 98	9.478 30	0.0194	83.2	8.4	S2	-	2015-11-15	60061285002	22.72	1	39.73	183
IC4995	ESO186–G034	304.995 74	–52.621 92	0.0161	68.9	7.2	S2	SA0	2019-06-03	60360003002	34.00	1	32.33	70
NGC 6921	UGC11570	307.120 18	25.723 39	0.0145	62.0	8.4	S2	SA0	2013-05-18	60061300002	19.52	1	33.67	117
NGC 7213	ESO288–G043	332.317 54	–47.166 69	0.0051	22.0	7.7	S1.5	Sa	2014-10-05	60001031002	101.62	0.5	160.49	965
NGC 7319	UGC12102	339.015 01	33.975 88	0.0109	46.7	7.3	S2	SBbc	2017-09-27	60261005002	41.88	0.5	30.20	88
UGC12282	CGCG532–004	344.730 35	40.932 21	0.0169	72.4	9.8	S1.9	Sa	2019-11-18	60160812002	28.56	1	27.50	43
NGC 7582	ESO291–G016	349.598 42	–42.370 57	0.0049	21.2	7.6	S1.5	SBab	2016-04-28	60201003002	48.49	0.5	123.14	1100
2MXJ23252420–3826492	IRAS23226–3843	351.350 78	–38.447 00	0.0359	153.8	8.2	S1	-	2017-06-11	80101001002	96.61	0.5	30.57	80
NGC 7674	UGC12608	351.986 24	8.778 95	0.0174	74.5	7.6	S2	SABc	2014-09-30	60001151002	52.00	0.5	36.08	161

neutral torus reflection because the faintness of the sources in our sample may not allow us to restrict geometrical parameters for the majority of them. Indeed, we also tested the MYTORUS model, but the S/N of the data were too low for parameters to be restricted in most cases. Instead, we prefer a homogeneous analysis of the strength and general characteristics of the reflection component in our sample. This is sufficient to study the dependence of the existence of the reflection component with the AGN power, which is one of the main purposes of this analysis. Furthermore, it also avoids the use of ionized disc reflection components, such as RELXILL (Dauser et al.

2014) because disc reflection has been found only for a small fraction of AGN, all of them in the high-accretion regime (Esparza-Arredondo et al. 2021). Finally, this spectral analysis lacks the inclusion of the Compton scattering, which contributes specially for Compton-thick⁷ (CT) sources. However, the available models within XSPEC (e.g. CABS) do not properly account for it as they assume an inadequate

⁷https://ned.ipac.caltech.edu/level5/March04/Comastri/Comastri_contents.html

cross-section in the modelling (cf., Murphy & Yaqoob 2009, and MYTORUS manual.⁸). Indeed, we also try the scenario in which CABS is included but we find the intrinsic luminosity to be unrealistically high in some cases (see Appendix A). Note that the exclusion of such a component leads to a systematic uncertainty, which is translated into an underestimation of the intrinsic luminosities of CT sources. However, our baseline model has been widely used in several works aimed to find general properties of AGN and characterize the reflection component, even in CT objects (e.g. Kawamuro et al. 2016; Panagiotou & Walter 2019; Kang, Wang & Kang 2020; Panagiotou & Walter 2020). Thus, the baseline model used in this work will lead to robust results that can be easily compared with previous works (e.g. Annuar et al. 2015, 2017, 2020; Kawamuro et al. 2016).

3.2 Spectral fitting

We start the analysis by fitting the spectra to M_1 . We then fit the spectra to M_2 , and obtain the EW and the luminosity of the FeK α line as explained above. We then fit the spectra to M_3 and test if reflection is required by the data using the f-test tool within XSPEC. If the f-test throws a probability value below 10^{-3} , then the reflection component is required by the data. For those objects for which the reflection component is required, we also test the statistical need for a power law (i.e. we fit the spectra to M_4). Objects for which such component is not statistically needed will be referred as reflection dominated.

We also estimate the reflection fraction, defined in this work as $C_{\text{ref}} = L_{\text{ref}}/L_{\text{cont}}$, where L_{ref} is the luminosity of the reflection component and L_{cont} is the luminosity of the intrinsic continuum, modelled with a power law, with both luminosities calculated in the 3–70 keV energy range. They are computed using the CLUMINOSITY command within XSPEC. We estimate the 1σ errors for the best-fitting parameters. Errors in the luminosities of the different components, as well as in the EW of the FeK α line, are presented as follows: if the 3σ errors are well constrained, we present the 1σ error; upper or lower limits correspond to the 3σ estimates otherwise. This makes the analysis more conservative on the luminosity limit of the reflection component and the FeK α line for those sources where the reflection component or the FeK α line are not recovered by the data since it gives 99.6 per cent the upper limit of the distribution. As for the reflection fraction, we perform MCMC simulations to recover its value and error as follows: we choose a random number within a normal distribution centred at the actual value whenever the luminosity is well constrained. However, when there is an upper or lower limit of the luminosity, we choose a random number drawn from a uniform distribution with limits zero and the upper or lower limit. We then calculate the ratio and repeat the same procedure 1000 times. Finally, we obtain the median for the central value and the 25th and 75th quartiles as the error range. Whenever the upper limit is above 1 or the lower limit is below 0, we report the value as a lower or upper limit, respectively.

Fig. 2 shows the best fit for M_1 (upper left), M_2 (upper right), M_3 (lower left), and M_4 (lower right) for NGC 7582 as an example of the resulting spectral fits. For this particular object, we obtain for M_1 a $\chi^2/\text{dof} = 699/675$, for M_2 a $\chi^2/\text{dof} = 655/674$, while for M_3 we obtain $\chi^2/\text{dof} = 650/674$, for which the f-test gives a value of 10^{-12} . Indeed, in the upper left panel of the figure, it is possible to see the poor fit and large residuals in particular around the FeK α line, indicating the need of an extra component to fit the spectrum.

Also note that although upper right and lower left panels show different models, they both fit the data well, by accounting for the reflection component, mostly noticeable through the FeK α line. On the other hand, M_4 fits the data poorly with a $\chi^2/\text{dof} = 3115.7/677$ (see lower right panel). Indeed, although required, the line accounts only for ~ 0.9 per cent of the reflection component, while the latter only accounts for ~ 20 per cent of the 3–70 keV primary continuum luminosity. This is an example where the existence of the FeK α emission line, the f-test when comparing with the partial-covering intrinsic continuum model, and the luminosity detection limit, point out to the existence of a reflection component for this source.

4 RESULTS

Tables 3 and 4 present the best-fitting parameters for both the LINER and Seyfert samples when fitted to the M_3 model. Note that we present the best-fitting values for this model only as the analysis is based on this model version (see above). Note that for the covering factor, f_{cov} , we also test whether it is zero or free to vary. In the cases in which it is zero, the source is not covered, corresponding to unobscured or low-obscured sources or, on the contrary, it is reflection dominated, thus the partially covered continuum is not restricted. We mark the column with a dash line in these cases (six sources). However, although left free to vary, in many cases it is pegged to one (42 sources), indicating full covering of the source. As for the f-test, we conclude that when it is below 10^{-3} , the reflection component is statistically significant and is marked with the check mark symbol in this column (12). Among the 81 objects, we find that only NGC 424 is reflection dominated, i.e. the data do not require the addition of a power law and the luminosity of this component is not restricted. This object is marked with an R in the column (1) of Table 4. The N_{H} cannot be calculated for this source. Moreover, we also find 18 other sources for which the f-test comparing models M_3 and M_4 does not favour the addition of a power-law component, although their N_{H} are well constrained. These objects have a large contribution of the reflection component in the CT regime, although the power-law continuum is still reachable thanks to the wide spectral range of *NuSTAR* data. As for intrinsic luminosities, as it was previously mentioned in Section 3.2, these may be larger for CT objects as we are inducing a systematic uncertainty by excluding the Compton-scattering effect. Thus, we warn the reader that intrinsic luminosities reported here for CT objects should be treated a lower limits, even if they are well constrained by the spectral fits.

4.1 Luminosity correction

As mentioned in Section 2 we select sources with Eddington rate $L_{\text{bol,obs}}/L_{\text{Edd}} < 10^{-3}$ to study inefficient AGN with the public data available. However, we use as a proxy of the bolometric luminosity, the observed 2–10 keV X-ray luminosity (i.e. uncorrected from N_{H}). Indeed, the intrinsic luminosity, and therefore the Eddington rate, are expected to increase once we take into account the N_{H} . Fig. 3 shows the observed versus intrinsic 2–10 keV luminosity, the latter corrected from LOS obscuration according to the best fit reported in Tables 3 and 4.

The largest shift from the 1:1 relation is found for CT objects (green squares in Fig. 3), for which the luminosity can change more than a factor of 10. Note that NGC 424, classified as reflection dominated has long been studied at X-rays (e.g. Baloković et al. 2014; Hernández-García et al. 2015; Ricci et al. 2017; Marchesi et al. 2018), finding that this object has a large contribution of the reflection component, with weak signatures of the intrinsic continuum.

⁸<http://mytorus.com>

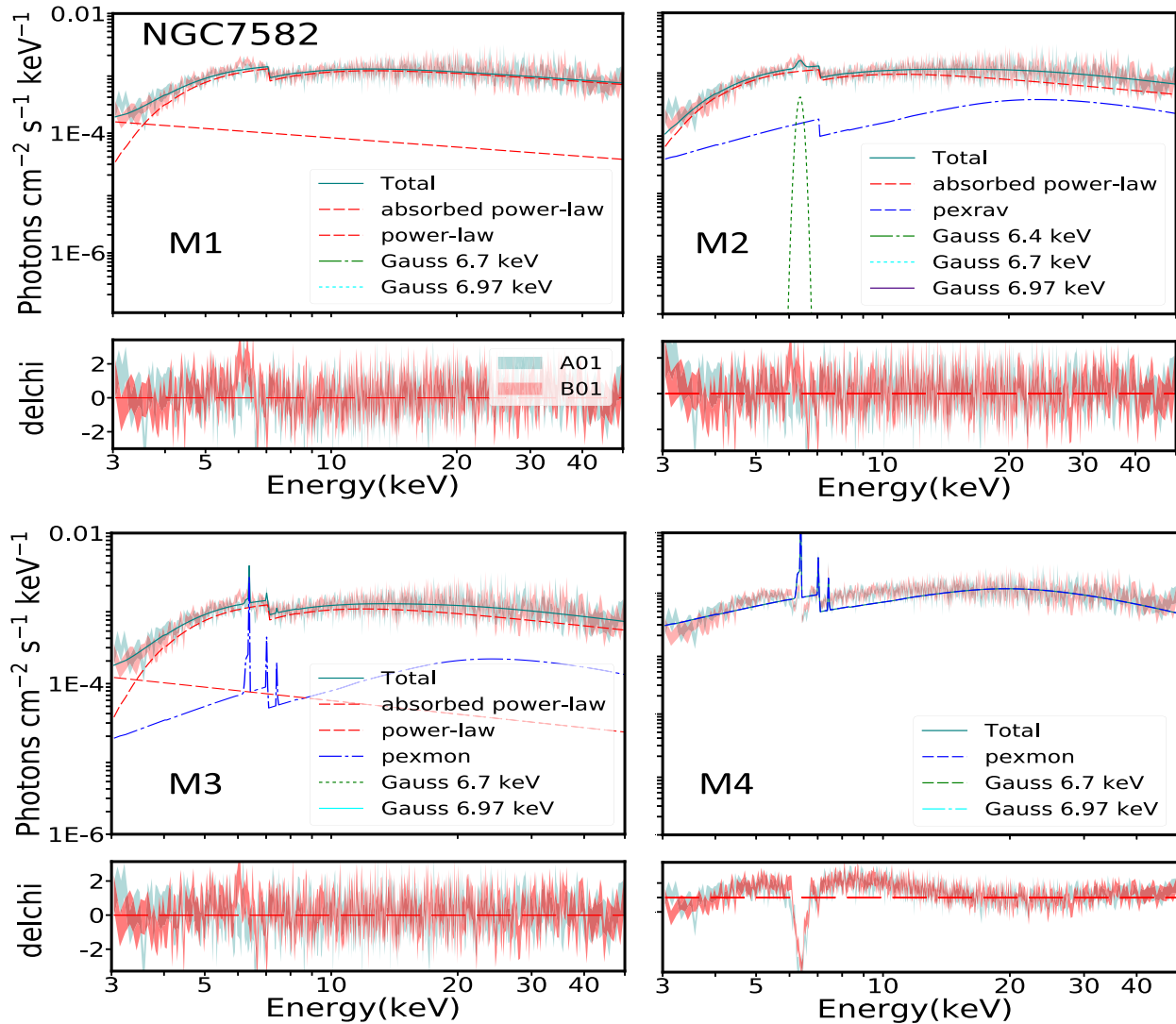


Figure 2. Spectral fits for M_1 (upper left), M_2 (upper right), M_3 (lower left), and M_4 (lower right) for NGC 7582. Each colour represents each of the components as follows: teal is the total spectrum, red is the partial-covering component, blue are pexmon (left), and pexrav (right) components, while green, cyan, and purple are the extra lines in each model version. (see Section 3.2).

However, since we are unable to account for such a component, we calculate the bolometric luminosity through the luminosity of the reflection component as follows: we assume that the correction in the intrinsic luminosity for a certain object is given in the following form: $\log(L_{\text{cont}}) = A + \log(L_{\text{refl}})$, where A can be calculated through those CT objects for which the power law is still detected in the spectra.

Moreover, by calculating the constant A for these objects, we can estimate how much the intrinsic luminosity changes for a certain amount of reflection. In practice, we estimate this factor using the green objects in Fig. 3 (i.e. 25 CT AGN). We find for our sample that $A = 1.5 \pm 0.8$. We then use this value to estimate the intrinsic luminosity for NGC 424. This extrapolation can be seen as the semitranslucent cyan triangle in Fig. 3.

Fig. 4 shows the final distribution for the Eddington rate in our sample when the obscuration is properly taken into account, compared to the initial Eddington rate, estimated through the observed X-ray luminosity. Indeed, a shift towards greater Eddington rates is seen in objects with larger N_{H} (mostly CT objects) and a decrease in objects with lower Eddington rates. The mean Eddington rate of the sample is $\langle \log(\lambda_{\text{Edd}}) \rangle = -3.3$ (dash-dotted vertical line in Fig. 4) with a

1σ range of $[-5.2, -1.49]$ (see dotted lines in the figure), roughly expanding four orders of magnitude in Eddington rate. Additionally, the lack of Compton-scattering may shift CT objects to even higher Eddington rates (as intrinsic luminosities may be even larger). As it was previously mentioned in Section 2.2, we are aware that our selection criteria bias our sample towards a large LOS obscuration for Eddington rate between $-2.5 < \log \lambda_{\text{Edd}} < -1.49$ (14 CT AGN). Thus, we will exclude these sources from the discussion as we are missing an important portion of objects residing in this range of Eddington rates (mostly highly obscured objects with intrinsically higher Eddington rates). Moreover, the discussion will be based on the remaining 67 sources.

4.2 Existence of the reflection component

We base our analysis on the existence of the reflection component in three criteria: (1) the detection of the $\text{FeK}\alpha$ line; (2) a statistical significance of the reflection component compared to the model without reflection (i.e. f -test < 0.001 when comparing models M_1 and M_3), and (3) the restriction of the reflection luminosity at 3σ .

Table 3. Spectral fit results for the LINER sample. Column (1) is the name of the source, (2) is the χ^2/dof , where dof are the degrees of freedom. Columns (3)–(7) are the column density, log NH in units of cm^{-2} , the covering factor, the photon index, Γ , the equivalent width (EW) in units of eV and the reflection fraction, respectively, while columns (8)–(11) are the continuum and reflected luminosities in units of erg s^{-1} , in the (2–10 keV) and (3–70 keV) bands, respectively. Column (12) is the f-test performed between models 1 and 3 in all cases. The checkmark (✓) symbol represents an f-test $< 1\text{E-}4$, while the x symbol represents otherwise. In Column (1), the superscript RD is for reflection-dominated sources, while those marked with CT are the Compton-thick sources in our sample, whereas in Column (4) the dash means that the covering factor is zero, therefore no emission is scattered, and the * symbol means that the parameter is frozen.

Name	χ^2/dof	log NH	f_{cov}	Γ	EW	C_{ref}	log $L_{(2-10)\text{ keV}}$		log $L_{(3-70)\text{ keV}}$		f-test
(1)	(2)	cm^{-2} (3)	(4)	(5)	eV (6)	(7)	continuum erg s^{-1} (8)	reflected erg s^{-1} (9)	continuum erg s^{-1} (10)	reflected erg s^{-1} (11)	(12)
NGC 1052	744.71/734	$23.15^{+0.03}_{-0.03}$	1*	$1.78^{+0.04}_{-0.04}$	139.30 ± 27.4	$0.15^{+0.06}_{-0.06}$	41.73 ± 0.01	40.21 ± 0.15	42.14 ± 0.01	41.32 ± 0.15	✓
NGC 2655	84.87/94	$23.41^{+0.12}_{-0.14}$	1*	$2.05^{+0.17}_{-0.15}$	$368.43 \pm 105.$	$0.56^{+0.35}_{-0.26}$	41.32 ± 0.10	40.30 ± 0.17	41.59 ± 0.07	41.23 ± 0.17	x
UGC5101	54.98/47	$23.84^{+0.06}_{-0.06}$	1*	< 1.26	$< 451.$	< 1	42.61 ± 0.09	< 41.7	43.45 ± 0.08	< 43.4	x
M81	1372.00/1246	$22.16^{+0.13}_{-0.09}$	–	$1.94^{+0.01}_{-0.01}$	33.78 ± 9.45	< 0.024	40.54 ± 0.01	< 38.2	40.88 ± 0.15	< 39.2	x
NGC 3079 ^{CT}	114.37/123	$24.41^{+0.03}_{-0.05}$	$0.98^{+0.01}_{-0.01}$	$1.68^{+0.16}_{-0.15}$	$479.64 \pm 210.$	$0.10^{+0.06}_{-0.05}$	41.59 ± 0.13	39.83 ± 0.20	42.06 ± 0.05	41.01 ± 0.20	✓
UGC5881	136.07/163	$23.43^{+0.21}_{-0.36}$	$0.52^{+0.19}_{-0.25}$	$1.75^{+0.16}_{-0.16}$	215.40 ± 75.1	$0.37^{+0.37}_{-0.26}$	42.37 ± 0.11	41.18 ± 0.33	42.80 ± 0.07	42.31 ± 0.33	x
NGC 3628	64.43/81	< 22.07	–	$2.05^{+0.09}_{-0.09}$	$< 100.$	< 0.230	40.18 ± 0.20	< 38.4	40.32 ± 0.27	< 39.3	x
NGC 3718	192.45/202	$23.79^{+0.13}_{-0.13}$	< 0.06	$2.21^{+0.06}_{-0.04}$	< 91.1	< 0.111	41.07 ± 0.25	< 39.1	41.43 ± 0.27	< 40.1	x
NGC 3998	613.34/709	$22.36^{+0.74}_{-0.49}$	–	$1.98^{+0.04}_{-0.04}$	< 18.4	$0.05^{+0.07}_{-0.03}$	41.59 ± 0.17	39.76 ± 0.27	41.89 ± 0.16	40.73 ± 0.27	x
NGC 4102	181.53/194	$23.68^{+0.06}_{-0.07}$	1*	$1.26^{+0.11}_{-0.11}$	$< 312.$	$0.29^{+0.22}_{-0.18}$	41.34 ± 0.06	40.00 ± 0.27	42.08 ± 0.04	41.50 ± 0.27	x
M106	431.61/460	$23.02^{+0.15}_{-0.03}$	> 0.87	$1.86^{+0.07}_{-0.04}$	$< 112.$	< 0.151	40.36 ± 0.03	< 38.8	40.73 ± 0.03	< 39.8	x
M58	802.22/732	$22.34^{+0.09}_{-0.11}$	1*	$2.01^{+0.04}_{-0.04}$	120.73 ± 21.4	$0.08^{+0.05}_{-0.05}$	41.52 ± 0.01	39.75 ± 0.27	41.81 ± 0.01	40.70 ± 0.27	x
NGC 5005	26.45/34	$22.96^{+0.39}_{-0.48}$	$0.68^{+0.32}_{-0.32}$	> 2.37	$348.49 \pm 145.$	> 0.05	40.39 ± 0.71	39.58 ± 0.20	40.50 ± 0.61	40.25 ± 0.20	x
NGC 6240	374.82/439	$24.12^{+0.03}_{-0.03}$	$0.95^{+0.01}_{-0.01}$	$1.63^{+0.07}_{-0.07}$	398.33 ± 74.3	$0.17^{+0.06}_{-0.05}$	43.37 ± 0.06	41.87 ± 0.12	43.87 ± 0.02	43.08 ± 0.12	✓
MCG+08-31-041	200.10/241	< 22.47	> 0.21	$1.96^{+0.09}_{-0.08}$	150.75 ± 63.9	$0.42^{+0.25}_{-0.20}$	42.64 ± 0.07	41.52 ± 0.20	42.90 ± 0.04	42.51 ± 0.20	✓
NGC 7130 ^{CT}	43.65/58	$24.27^{+0.16}_{-0.25}$	1*	< 1.50	$715.41 \pm 213.$	> 0.42	41.54 ± 0.38	40.92 ± 0.26	42.29 ± 0.19	42.44 ± 0.26	✓
NGC 7331	133.31/147	$22.39^{+0.27}_{-0.43}$	1*	$2.13^{+0.16}_{-0.05}$	$< 182.$	< 0.437	40.46 ± 0.04	< 39.4	40.69 ± 0.03	< 40.2	x
NGC 7479 ^{CT}	71.56/78	$24.78^{+0.05}_{-0.06}$	1*	$1.86^{+0.61}_{-0.34}$	$693.07 \pm 246.$	$0.20^{+0.45}_{-0.17}$	42.73 ± 0.48	40.45 ± 0.48	42.80 ± 0.24	41.51 ± 0.48	✓

We detect the FeK α emission line in 61 out of the 81 sources (~ 75 per cent of the sample). On the other hand, the inclusion of a reflection component improves the spectral fit for 46 out of the 81 sources (~ 57 per cent of the sample). Additionally, we restrict the luminosity of the reflection component for 67 out of the 81 sources (i.e. ~ 83 per cent). A total of 45 out of 81 (~ 55 per cent) sources fulfill the three criteria to establish the existence of the reflection component, while 15 (~ 19 per cent) meet two out of the three criteria, and 9 (~ 10 per cent) meet only one of the criteria (namely M 81, NGC 3998, NGC 4102, NGC 253, 2MXJ 0114–5523, UGC 3601, 2MXJ 0756–4137, IC 751, and Mrk 231).

As for the 15 sources fulfilling two criteria, one (Mrk 1066) statistically needs the reflection component and it is well constrained. However, the FeK α emission line is not well detected at a 3σ limit. Note that the spectrum is a low-quality spectrum (dof <50) which may cause a poor restriction of the three lines at 6.4, 6.7, and 6.97 keV. In order to test this possibility, we use the non-grouped spectrum of the source and check which line is present. Indeed, the line present in this object is the FeK α emission line. Once we remove both ionized lines from the fit, and calculate the EW and flux for the FeK α emission line for this source, we obtain a constrained parameter. Thus, we can safely say that this source fulfills the three criteria.

The remaining 14 objects, with two out of the three criteria, fulfill the detection of the FeK α emission line and a constrained luminosity for the reflection component. However, statistically speaking, the reflection component is not needed. Among them, all but NGC 5695 show a relatively low reflection fraction (C_{ref}) and/or N_{H} . Thus, the reflection component is present mainly through the FeK α emission

line, while the Compton hump is suppressed under the intrinsic continuum. Under this scenario, the f-statistic is not suitable to test the presence of the reflection component because it only affects a narrow range of the spectrum where the FeK α emission line is located. In the case of NGC 5695, it shows a relatively high N_{H} . In this case, the quality of the spectrum for this source might be responsible for the statistical significance of the reflection component.

As for the objects fulfilling only one criterion, seven objects (NGC 3998, NGC 4102, 2MXJ 0114–5523, UGC 3601, 2MXJ 0756–4137, IC 751, and Mrk 231) meet the restriction of the luminosity of the reflection component, and the remaining two objects (M 81 and NGC 253) meet the detection of the FeK α emission line. The detection of the reflection component without the FeK α line can be due to a combination of high absorption which can lead to the detection of a Compton hump and a low-S/N spectrum which can lead to the poor restriction of the line. The detection of the FeK α line without statistical significance for the reflection component can again be explained due to low N_{H} and/or low reflection fraction as indicated above. Moreover, the non-detection of the Compton hump may also depend on the shape of the spectrum; for highly obscured sources it may only require data up to 10 keV, while for low obscured sources, the Compton hump requires high S/N up to 30 keV.

We find that 12 objects do not present any signs of reflection (namely UGC 5101, NGC 3628, NGC 3718, M 106, NGC 7331, NGC 612, 2MXJ 1105+5856, NGC 3621, NGC 3786, M 88, NGC 5252, and 2MXJ 2325–3826). Note that five out these 12 objects are LINERs, while the remaining seven are Seyferts. However, several works have found traces for the reflection component in UGC 5101 (e.g. González-Martín et al. 2009; Oda et al. 2017; La

Table 4. Spectral fit results for the Seyfert sample. Columns are as in Table 3.

Name	χ^2/dof	log NH	f_{cov}	Γ	Eq. Width	C_{ref}	log $L_{(2-10)} \text{ keV}$		log $L_{(3-70)} \text{ keV}$		ftest
(1)	(2)	cm^{-2}	(4)	(5)	eV	(7)	continuum erg s^{-1}	reflected erg s^{-1}	continuum erg s^{-1}	reflected erg s^{-1}	(12)
NGC 253	566.66/426	$22.81^{+0.04}_{-0.07}$	>0.84	>2.50	248.08 ± 32.8	<0.008	39.69 ± 0.03	<36.9	39.76 ± 0.02	<37.6	x
NGC 424 ^R	146.96/139	–	–	$1.54^{+0.08}_{-0.08}$	$992.62 \pm 155.$	>3.52	–	41.31 ± 0.08	–	42.60 ± 0.08	✓
IC1657	224.23/213	$23.44^{+0.06}_{-0.07}$	1*	$1.52^{+0.09}_{-0.09}$	234.92 ± 82.4	$0.36^{+0.24}_{-0.20}$	41.78 ± 0.04	40.58 ± 0.23	42.35 ± 0.05	41.88 ± 0.23	x
2MXJ0114–5523	133.09/140	$23.55^{+0.09}_{-0.10}$	1*	$1.26^{+0.13}_{-0.13}$	<342.	$0.34^{+0.29}_{-0.23}$	41.73 ± 0.07	40.45 ± 0.30	42.47 ± 0.05	41.95 ± 0.30	x
MCG+08-03-018	181.87/225	$23.92^{+0.07}_{-0.08}$	$0.90^{+0.03}_{-0.04}$	$2.17^{+0.15}_{-0.13}$	412.61 ± 84.1	$0.37^{+0.25}_{-0.18}$	42.74 ± 0.12	41.62 ± 0.18	42.95 ± 0.07	42.46 ± 0.18	✓
NGC 612	138.33/153	$23.98^{+0.05}_{-0.06}$	$0.99^{+0.01}_{-0.02}$	$1.66^{+0.14}_{-0.13}$	<280.	<0.090	43.36 ± 0.09	<41.5	43.84 ± 0.03	<42.7	x
Mrk573 ^{CT}	71.03/60	$25.04^{+0.12}_{-0.24}$	>0.97	$2.30^{+0.14}_{-0.29}$	$1096.99 \pm 213.$	$0.18^{+0.26}_{-0.11}$	42.79 ± 0.26	41.39 ± 0.16	42.95 ± 0.24	42.18 ± 0.16	✓
NGC 788	179.07/194	$23.79^{+0.08}_{-0.08}$	1*	$1.65^{+0.11}_{-0.10}$	286.80 ± 97.2	$0.53^{+0.28}_{-0.23}$	42.51 ± 0.08	41.49 ± 0.16	43.00 ± 0.04	42.70 ± 0.16	✓
M77 ^{CT}	747.04/651	$25.08^{+0.03}_{-0.03}$	$0.97^{+0.01}_{-0.01}$	$2.37^{+0.04}_{-0.04}$	1224.43 ± 64.2	$0.18^{+0.04}_{-0.03}$	41.93 ± 0.05	40.57 ± 0.04	42.05 ± 0.03	41.31 ± 0.04	✓
NGC 1106 ^{CT}	88.06/62	$24.72^{+0.08}_{-0.11}$	>0.98	$1.64^{+0.29}_{-0.47}$	$1916.85 \pm 423.$	>0.11	42.31 ± 0.68	41.16 ± 0.35	42.81 ± 0.42	42.45 ± 0.35	✓
NGC 1125 ^{CT}	108.35/119	$24.42^{+0.06}_{-0.05}$	1*	$2.36^{+0.14}_{-0.39}$	$523.39 \pm 148.$	$0.13^{+0.16}_{-0.09}$	42.53 ± 0.26	40.99 ± 0.27	42.63 ± 0.14	41.73 ± 0.27	✓
NGC 1142	104.67/115	$24.07^{+0.11}_{-0.11}$	1*	$1.79^{+0.19}_{-0.16}$	$696.39 \pm 174.$	$0.54^{+0.42}_{-0.29}$	42.98 ± 0.17	41.98 ± 0.20	43.38 ± 0.08	43.07 ± 0.20	✓
Mrk1066	45.16/59	$23.79^{+0.19}_{-0.19}$	1*	<1.42	<333.	>0.51	41.27 ± 0.17	40.60 ± 0.26	42.02 ± 0.13	42.11 ± 0.26	✓
NGC 1194	148.66/219	$23.84^{+0.09}_{-0.09}$	1*	$1.53^{+0.08}_{-0.08}$	$631.45 \pm 127.$	>0.81	42.06 ± 0.09	41.43 ± 0.12	42.62 ± 0.07	42.72 ± 0.12	✓
NGC 1229	129.13/151	$23.37^{+0.12}_{-0.14}$	1*	$1.42^{+0.10}_{-0.11}$	$448.97 \pm 108.$	>0.54	42.58 ± 0.07	41.85 ± 0.18	43.22 ± 0.07	43.22 ± 0.18	✓
NGC 1320 ^{CT}	136.01/114	$24.76^{+0.08}_{-0.08}$	>0.91	>0.35	$3827.63 \pm 345.$	>0.35	41.46 ± 0.53	40.88 ± 0.25	42.09 ± 0.67	42.05 ± 0.25	✓
NGC 1358	176.34/202	$24.16^{+0.06}_{-0.06}$	1*	$1.48^{+0.11}_{-0.10}$	$886.71 \pm 165.$	$0.47^{+0.20}_{-0.17}$	42.14 ± 0.10	41.06 ± 0.12	42.73 ± 0.04	42.39 ± 0.12	✓
NGC 1386 ^{CT}	65.02/39	$25.15^{+0.20}_{-0.19}$	>0.92	$2.33^{+0.14}_{-0.16}$	$1826.11 \pm 326.$	$0.18^{+0.58}_{-0.13}$	41.37 ± 0.36	40.01 ± 0.15	41.41 ± 0.42	40.76 ± 0.15	✓
UGC3157	121.35/158	$23.57^{+0.08}_{-0.12}$	1*	$1.56^{+0.12}_{-0.12}$	181.35 ± 84.4	$0.31^{+0.22}_{-0.18}$	42.23 ± 0.07	40.95 ± 0.25	42.77 ± 0.04	42.21 ± 0.25	x
2MSJ0508+1721	354.36/363	$22.49^{+0.13}_{-0.18}$	1*	$1.91^{+0.07}_{-0.07}$	202.44 ± 54.3	$0.40^{+0.20}_{-0.17}$	42.86 ± 0.02	41.77 ± 0.17	43.20 ± 0.03	42.78 ± 0.17	✓
ESO5–4 ^{CT}	128.33/104	>25.38	>0.98	$1.92^{+0.05}_{-0.09}$	$1622.20 \pm 222.$	>0.38	41.53 ± 0.28	40.71 ± 0.07	41.92 ± 0.27	41.74 ± 0.07	✓
NGC 2273 ^{CT}	135.57/144	$25.29^{+0.11}_{-0.07}$	1*	$2.11^{+0.05}_{-0.07}$	$1950.97 \pm 179.$	$0.44^{+0.37}_{-0.19}$	42.06 ± 0.17	41.01 ± 0.07	42.26 ± 0.18	41.90 ± 0.07	✓
UGC3601	248.47/252	$22.61^{+0.76}_{-0.58}$	–	$1.89^{+0.08}_{-0.09}$	<211.	$0.16^{+0.22}_{-0.11}$	42.47 ± 0.86	41.07 ± 0.29	42.75 ± 0.17	42.10 ± 0.29	x
ESO428–14 ^{CT}	105.45/107	$24.48^{+0.13}_{-0.18}$	1*	$2.15^{+0.19}_{-0.24}$	$1100.08 \pm 178.$	>0.24	41.41 ± 0.41	40.56 ± 0.19	41.63 ± 0.31	41.43 ± 0.19	✓
2MXJ0756–4137	44.55/58	<22.55	1*	$1.83^{+0.16}_{-0.10}$	<343.	>0.32	41.91 ± 0.05	41.07 ± 0.27	42.30 ± 0.08	42.16 ± 0.27	x
NGC 2788A ^{CT}	72.35/95	$24.27^{+0.14}_{-0.19}$	1*	$1.41^{+0.19}_{-0.14}$	$1714.57 \pm 303.$	>0.55	41.90 ± 0.28	41.25 ± 0.18	42.53 ± 0.18	42.63 ± 0.18	✓
IC2560 ^{CT}	118.75/93	>25.29	1*	$2.31^{+0.04}_{-0.11}$	$2639.16 \pm 225.$	$0.19^{+0.29}_{-0.10}$	42.14 ± 0.27	40.72 ± 0.07	42.39 ± 0.30	41.51 ± 0.07	✓
NGC 3147	242.65/288	<22.65	0.10●	$1.84^{+0.08}_{-0.08}$	126.95 ± 55.3	>0.07	41.68 ± 0.54	40.31 ± 0.29	42.15 ± 0.53	41.38 ± 0.29	x
NGC 3393 ^{CT}	53.01/83	$24.37^{+0.06}_{-0.07}$	1*	$1.73^{+0.21}_{-0.19}$	$935.61 \pm 336.$	$0.17^{+0.12}_{-0.09}$	42.60 ± 0.18	41.07 ± 0.20	43.04 ± 0.07	42.21 ± 0.20	✓
2MXJ1105+5856	115.59/129	$23.17^{+0.39}_{-0.52}$	0.30●	$1.48^{+0.17}_{-0.15}$	<118.	<1	42.57 ± 0.30	<41.7	43.16 ± 0.25	<43.0	x
NGC 3621	94.55/94	$22.73^{+0.18}_{-0.19}$	0.14●	>2.46	<210.	<0.219	39.90 ± 0.32	<38.5	40.00 ± 0.38	<39.2	x
NGC 3786	86.13/98	<22.45	<0.17	$1.71^{+0.11}_{-0.11}$	<161.	<0.302	42.84 ± 0.70	<40.7	43.42 ± 0.57	<41.9	x
IC751	53.50/59	$23.73^{+0.14}_{-0.20}$	1*	<1.29	<733.	>0.25	42.06 ± 0.12	41.07 ± 0.24	42.91 ± 0.08	42.69 ± 0.24	x
M88 ^{CT}	94.56/50	$24.37^{+0.42}_{-0.34}$	$0.66^{+0.25}_{-0.34}$	>2.44	<325.	<0.344	40.87 ± 0.55	<39.2	40.94 ± 0.55	<39.9	x
IC3639 ^{CT}	43.71/46	$24.80^{+0.14}_{-0.13}$	1*	$2.19^{+0.18}_{-0.23}$	$1896.55 \pm 326.$	$0.25^{+0.32}_{-0.15}$	42.03 ± 0.27	40.75 ± 0.19	42.23 ± 0.19	41.58 ± 0.19	✓
NGC 4785	171.80/204	$23.69^{+0.05}_{-0.05}$	1*	$1.79^{+0.11}_{-0.10}$	187.29 ± 72.9	$0.19^{+0.12}_{-0.10}$	42.06 ± 0.06	40.61 ± 0.23	42.46 ± 0.03	41.71 ± 0.23	x
Mrk231	232.65/238	$22.93^{+0.09}_{-0.09}$	1*	$1.68^{+0.09}_{-0.09}$	<228.	$0.28^{+0.20}_{-0.17}$	42.76 ± 0.03	41.46 ± 0.27	43.22 ± 0.04	42.63 ± 0.27	x
NGC 4941	111.35/115	$24.03^{+0.14}_{-0.15}$	1*	$1.65^{+0.20}_{-0.17}$	$688.08 \pm 167.$	>0.11	40.81 ± 0.19	39.96 ± 0.23	41.29 ± 0.10	41.15 ± 0.23	x
NGC 4939	158.68/177	$23.63^{+0.06}_{-0.07}$	1*	$1.51^{+0.10}_{-0.10}$	204.33 ± 86.2	$0.33^{+0.22}_{-0.18}$	41.88 ± 0.06	40.63 ± 0.23	42.45 ± 0.04	41.94 ± 0.23	x
NGC 4945 ^{CT}	1477.10/1559	$24.53^{+0.01}_{-0.01}$	0.99●	$1.65^{+0.03}_{-0.03}$	707.58 ± 71.7	$0.05^{+0.01}_{-0.01}$	41.41 ± 0.02	39.40 ± 0.05	41.90 ± 0.00	40.60 ± 0.05	✓
MCG-03-34-064	765.22/722	$23.88^{+0.05}_{-0.05}$	$0.94^{+0.01}_{-0.01}$	$1.73^{+0.05}_{-0.04}$	543.42 ± 44.6	>0.69	42.74 ± 0.05	41.98 ± 0.05	43.18 ± 0.03	43.12 ± 0.05	✓
NGC 5135 ^{CT}	101.51/83	>25.29	1*	$1.65^{+0.09}_{-0.08}$	$1192.03 \pm 206.$	>0.27	40.20 ± 0.16	39.21 ± 0.10	40.77 ± 0.18	40.41 ± 0.10	✓
M51 ^{CT}	85.90/94	$24.72^{+0.13}_{-0.06}$	$0.81^{+0.07}_{-0.03}$	$1.54^{+0.24}_{-0.06}$	$1636.52 \pm 197.$	<0.047	40.93 ± 0.10	37.49 ± 0.40	41.04 ± 0.08	37.49 ± 1.07	✓
NGC 5252	551.16/518	$23.01^{+0.28}_{-0.43}$	0.38●	$1.77^{+0.07}_{-0.05}$	<114.	<0.187	43.17 ± 0.15	<41.6	43.58 ± 0.16	<42.7	x
NGC 5283	216.31/230	$23.10^{+0.07}_{-0.07}$	1*	$1.92^{+0.08}_{-0.08}$	113.85 ± 67.7	$0.42^{+0.24}_{-0.20}$	41.98 ± 0.03	40.90 ± 0.19	42.31 ± 0.04	41.91 ± 0.19	✓
NGC 5347 ^{CT}	43.70/45	$24.79^{+0.15}_{-0.13}$	>0.94	$1.74^{+0.13}_{-0.13}$	$2299.24 \pm 326.$	$0.09^{+0.12}_{-0.06}$	42.03 ± 0.27	40.06 ± 0.26	42.23 ± 0.19	41.11 ± 0.26	✓
NGC 5643 ^{CT}	156.54/142	$24.94^{+0.25}_{-0.23}$	1*	$2.47^{+0.06}_{-0.09}$	$1137.79 \pm 151.$	$0.28^{+0.24}_{-0.12}$	41.35 ± 0.21	40.24 ± 0.07	41.42 ± 0.19	40.93 ± 0.07	✓
NGC 5695	38.99/38	$23.94^{+0.39}_{-0.11}$	>0.77	<1.40	$797.16 \pm 644.$	>0.75	41.05 ± 0.31	40.45 ± 0.26	41.87 ± 0.21	42.07 ± 0.26	x
NGC 5728	336.17/398	$24.05^{+0.03}_{-0.03}$	1*	$1.45^{+0.06}_{-0.06}$	428.24 ± 83.7	$0.26^{+0.07}_{-0.07}$	42.21 ± 0.05	40.87 ± 0.09	42.83 ± 0.02	42.23 ± 0.09	✓
NGC 5899	308.81/378	$22.98^{+0.25}_{-0.16}$	$0.87^{+0.13}_{-0.32}$	$1.80^{+0.07}_{-0.07}$	95.88 ± 46.9	$0.28^{+0.22}_{-0.14}$	42.16 ± 0.08	40.90 ± 0.17	42.56 ± 0.10	41.99 ± 0.17	✓
MCG+14-08-004	130.22/161	$23.24^{+0.10}_{-0.11}$	1*	$1.87^{+0.12}_{-0.12}$	265.59 ± 81.6	$0.31^{+0.24}_{-0.19}$	42.48 ± 0.06	41.25 ± 0.27	42.84 ± 0.05	42.28 ± 0.27	x
ESO137–34 ^{CT}	96.36/106	$24.49^{+0.12}_{-0.12}$	>0.98	$1.78^{+0.20}_{-0.23}$	$1066.66 \pm 216.$	$0.31^{+0.32}_{-0.18}$	42.14 ± 0.26	40.92 ± 0.19	42.54 ± 0.15	42.02 ± 0.19	✓
2MXJ1650+0436	331.00/392	<22.45	0.52●	$1.72^{+0.06}_{-0.06}$	93.32 ± 46.1	$0.24^{+0.14}_{-0.12}$	43.29 ± 0.04	41.95 ± 0.21	43.73 ± 0.02	43.09 ± 0.21	x
2MXJ1802-1454	605.51/591	$22.45^{+0.09}_{-0.11}$	1*	$2.02^{+0.05}_{-0.05}$	97.45 ± 32.1	$0.18^{+0.08}_{-0.07}$	41.76 ± 0.01	40.35 ± 0.16	42.04 ± 0.02	41.29 ± 0.16	✓
2MXJ1830+0928	158.71/179	$23.18^{+0.07}_{-0.10}$	1*	$1.89^{+0.10}_{-0.10}$	224.05 ± 73.6	$0.35^{+0.24}_{-0.19}$	42.37 ± 0.04	41.21 ± 0.23	42.72 ± 0.04	42.23 ± 0.23	x
IC4995 ^{CT}	66.10/65	>25.30	$0.97^{+0.01}_{-0.02}$	$1.81^{+0.14}_{-0.07}</$							

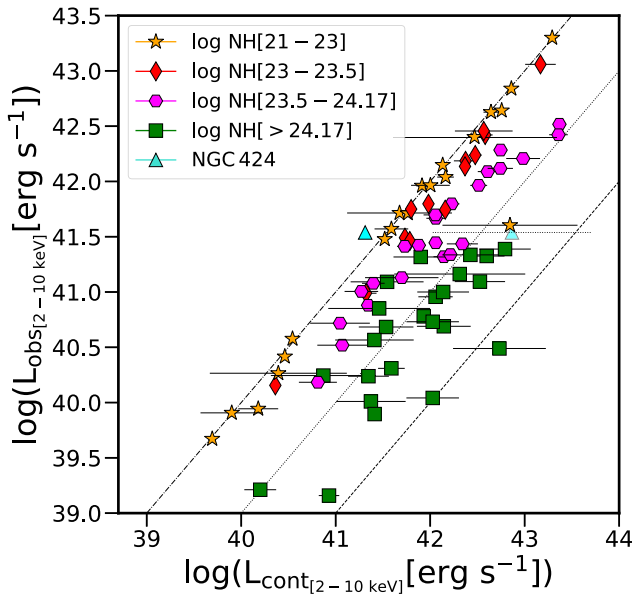


Figure 3. Observed 2–10 keV luminosity versus the intrinsic 2–10 keV luminosity. Note that the upper limits refer to the reflection dominated objects (see the text). The dash–dotted, dotted, and dashed lines represent the 1:1, 1:10, 1:100 relations, respectively, indicating the correction factor that should be applied in order to obtain the intrinsic continuum luminosity from the observed luminosity. Orange stars, red diamonds, magenta hexagons, and green squares are the N_{H} ranges shown in the figure label, while the cyan triangles are NGC 424 uncorrected (solid) and corrected (semitranslucent; see the text).

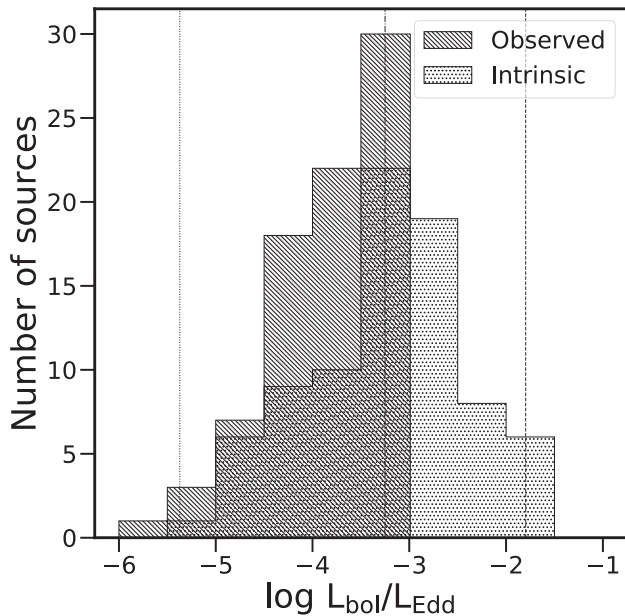


Figure 4. Comparison between the Eddington rate obtained with a rough fit to a simple power law (dashed histogram) versus the Eddington rate obtained once a proper obscuration is accounted for (dotted histogram).

Caria et al. 2019). In addition, the fact that the spectrum has a low S/N leads us to exclude it from our final sample of candidates for the disappearance of the torus. Fig. 5 shows the spectral fits for our final sample of 11 candidates to the torus disappearance (~ 12 per cent).

All but NGC 612 can be modelled with a single power law⁹ with little obscuration, supporting the idea that the reflection component is not present in these objects.

Altogether, we present 11 candidates which lack the reflection component, related to the plausible disappearance of the torus using X-rays observations. Among them, we find that eight sources have studies aiming to find the reflection component or the torus (through X-rays or mid-IR). For all of them, we find complete agreement with the idea of the absence of the reflection component associated with the torus in previous works (see Section 5).

4.3 Reflection strength

We explore here the degree of the reflection component strength for the objects in our sample. Fig. 6 shows the luminosity distribution for the intrinsic continuum (left histogram), FeK α emission line (upper right histogram), and reflection (right histogram). Note that for both the reflection and FeK α line distributions, we only show those sources for which the parameter is well constrained.

The FeK α line luminosity ranges from $\log(L_{6.4 \text{ keV}}) \sim [38. - 41.3]$, with a mean value of $\langle \log(L_{6.4 \text{ keV}}) \rangle = 40.1$, the reflection luminosity ranges from $\log(L_{\text{ref}(3-70 \text{ keV})}) \sim [37.5, 43.2]$, with a mean value of $\langle \log(L_{\text{ref}(3-70 \text{ keV})}) \rangle = 41.9$, and the intrinsic 3–70 keV luminosity ranges from $\log(L_{\text{cont}(3-70 \text{ keV})}) \sim [39.8, 43.9]$, with a mean value of $\langle \log(L_{\text{cont}(3-70 \text{ keV})}) \rangle = 42.3$ (see dashed lines in the histograms). Thus, all these three luminosities span around four orders of magnitude.

The reflection component represents, on average, 40 per cent of the intrinsic continuum luminosity of the source, (i.e. $\langle C_{\text{ref}} \rangle = 0.41^{10}$). In 20 out of the 81 sources the reflection is below 20 per cent of the intrinsic continuum (i.e. $C_{\text{ref}} < 0.2$), 28 sources fall in the range $0.2 < C_{\text{ref}} < 0.6$, and 5 fall in the range $C_{\text{ref}} > 0.6$, while the remaining 28 sources have lower limits for C_{ref} . On the other hand, around 50 per cent of the sample (41 sources) is located in the area where FeK α luminosity accounts for 1–3 per cent of the reflection component luminosity, 15 per cent (12 sources) is consistent with 3–10 per cent, and 6 per cent (five sources) sources present a weak line luminosity, accounting for less than 1 per cent of the reflection component. As for the remaining 28 per cent (23 sources), either the EW of the FeK α line and/or the luminosity of the reflection component are upper limits, therefore the fraction is an upper limit as well. Naturally, the 11 candidates lacking of reflection signatures are included in this group.

In order to study the connection between these luminosities, the large panels in Fig. 6 show the correlation between the reflection luminosity versus the intrinsic continuum (left-hand panel) and the FeK α emission line (right-hand panel) luminosities. As expected, the three quantities are well correlated. Moreover, the reflection component and the FeK α emission line are slightly better correlated (with a Pearson’s coefficient of 0.93) than the intrinsic continuum and the reflection component (with a Pearson’s coefficient of 0.89).

In order to obtain the best characterization of the relation between those parameters, we use a bootstrap method to account for possible outliers in the correlations, by choosing a random sub-sample with 80 per cent of the total sample and repeating this process a total of 100 times. For each random sub-sample, we also perform an

⁹Note that all of them present ionized emission lines.

¹⁰Note that this value is calculated for objects with both luminosities well constrained (i.e. neglecting upper or lower limits.)

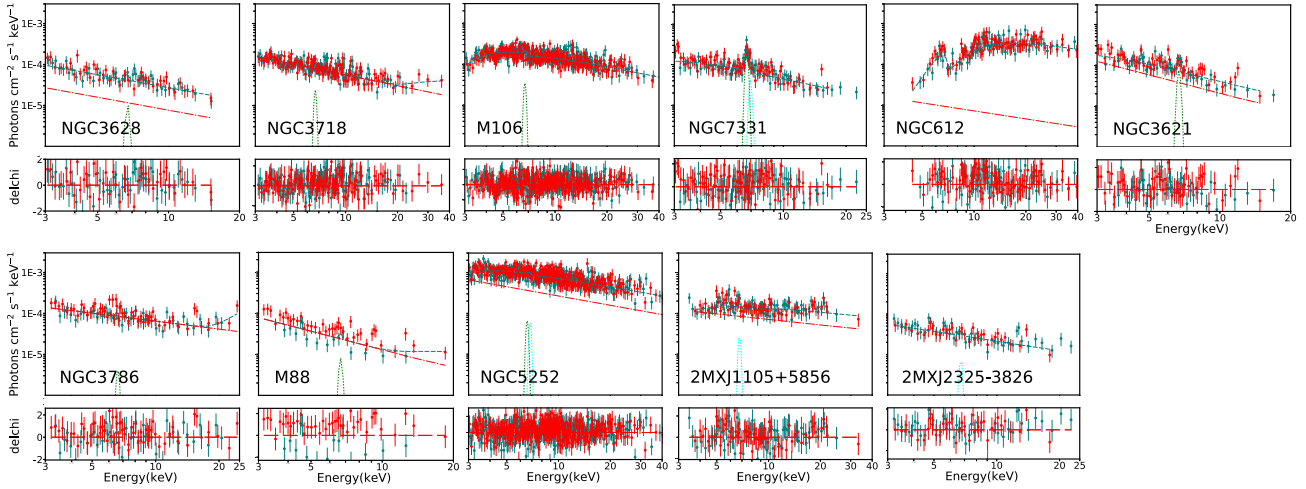


Figure 5. Spectral fits for our 11 candidates for the disappearance of the torus. Colours and axis labels are as in Fig. 2. Note that ionized lines are present in all the objects (except for NGC 612) and that we have tested the scenario in which the FeK α line could be the responsible for the line feature, finding that such line is not present in any of the spectra. Also note that for M 88 both FPMA and FPMB modules seem to be misaligned with a normalization factor of 1.99, well above the overall sample.

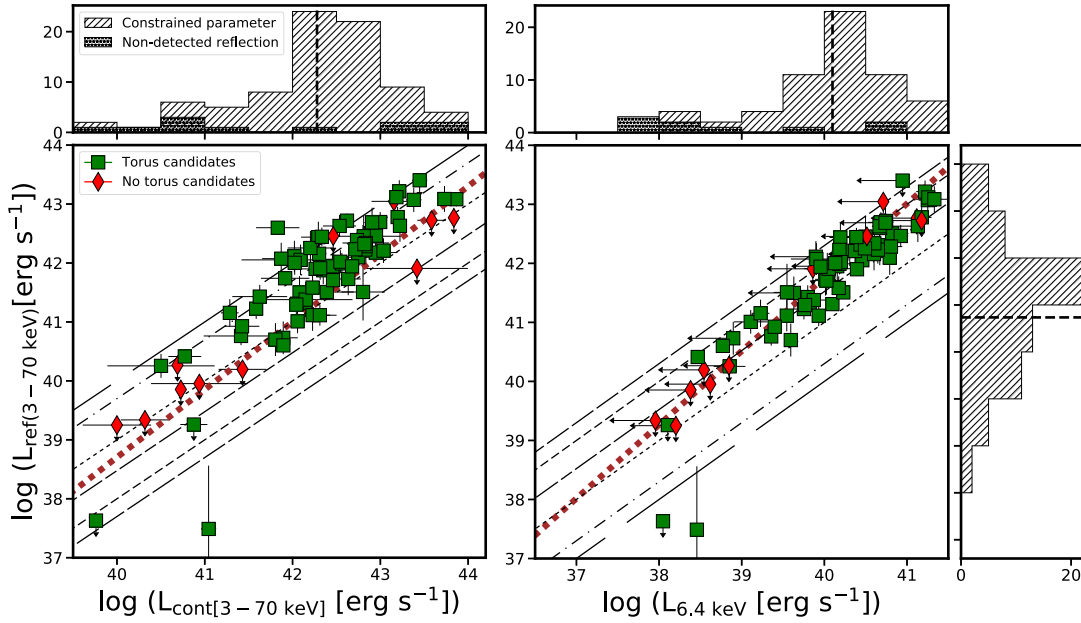


Figure 6. 3–70 keV band luminosity of the reflection component versus that of the intrinsic continuum (left) and the FeK α emission line luminosity versus the 3–70 keV reflection luminosity (right). In both cases, lines represent the percentage of the quantity in the Y-axis with respect to the X-axis. From top to bottom 100, 50, 10, 3, 1, and 0.5 per cent of the intrinsic (large left panel) and reflection (large right panel) luminosities. The red diamond and green square are objects well fitted with the power-law components (i.e. no reflection candidates) and with the combination of reflection plus power-law components, respectively. The thick dotted brown line in both panels represents the linear correlation found for the quantities in each panel when the X-axis is the independent quantity, while the black dashed line in the histograms represents the mean of each quantity. The histograms in the top and right-hand panels are the distribution of the different luminosities (see the text).

MCMC simulation similar to that mentioned in Section 3.2: for each luminosity pair, we choose a random number drawn from a normal distribution whenever the value is well constrained, and from a uniform distribution whenever there are upper or lower limits involved. We then perform a binning method in the x -axis by dividing it into bins of $dx = 0.5$ dex, and obtain the median and standard deviation along both axes. We calculate the correlation through a linear regression method and obtain the slope, intercept, and the r - and p -values. We repeat this process 100 times and then estimate

the mean values of all quantities. As for the correlation between L_{ref} and $L_{6.4 \text{ keV}}$, we also perform the linear regression analysis assuming that the luminosity of the reflection component is the independent component and the luminosity of the line is the dependent one. We present the best correlation found after performing a bisection method from both correlations. In this case the fraction of the luminosity of the FeK α line over the Compton hump increases from 1 per cent at $\log(L_{\text{ref}}) = 43$ to ~ 5 per cent at $\log(L_{\text{ref}}) = 40$ and to ~ 10 per cent at $\log(L_{\text{ref}}) = 38$. Both correlations can be represented

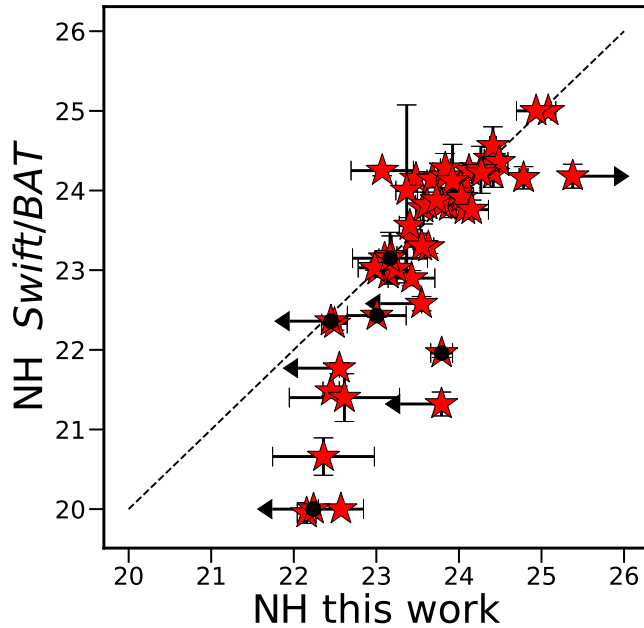


Figure 7. Comparison between our N_{H} estimates and the values reported in Ricci et al. (2017) for the common sample. Sources with a black dot inside the red star are the candidates for the torus disappearance in our sample. Note that upper limits in our analysis might be due to the fact that the sources are low-obscured or unobscured (see the text).

in the following form (represented as the thick dotted brown lines in Fig. 6):

$$\log(L_{\text{ref}}) = (1.13 \pm 0.22) \log(L_{\text{cont}}) - (6.43 \pm 9.35) \quad (6)$$

$$\log(L_{\text{ref}}) = (1.24 \pm 0.15) \log(L_{6.4 \text{ keV}}) - (8.17 \pm 6.16). \quad (7)$$

Note that we also explore if this trend is seen over the intrinsic continuum or the Eddington rate but no correlation is found.

4.4 Obscuration

The LOS obscuration and the reflection might occur in the same structure (i.e. the torus), thus both the reflection and the obscuration may be related. Therefore, a proper estimate on the N_{H} is necessary in order to place solid conclusions on the reflection component. For this purpose, Fig. 7 shows the comparison between the N_{H} found in this analysis compared to those presented in Ricci et al. (2017). They analyse the X-ray properties of the *Swift*/BAT sample for which we find 53 sources in common. We find that for most sources, the LOS obscuration found in both works are well in agreement when their column density is $N_{\text{H}} > 3 \times 10^{22} \text{cm}^{-2}$. We find discrepancies for seven objects below $N_{\text{H}} < 3 \times 10^{22} \text{cm}^{-2}$, which may be expected since *NuSTAR* does not cover energies below 3 keV, necessary to constrain low values of obscuration. Moreover, Fig. 8 (right histogram) shows the N_{H} distribution for our sample. We find a mean column density of $\langle \log(N_{\text{H}}) \rangle = 23.74$ (see dashed line in the figure). We also find that 24 sources are CT AGN (i.e. $\log N_{\text{H}} > 24.17 \text{cm}^{-2}$), while 45 out of the 81 are Compton-thin and 12 are unobscured sources. In addition, the majority of sources with no clear indication of reflection appear to be below the CT regime. On the other hand, the EW of the $\text{FeK}\alpha$ line shows a mean value of $\langle \log(\text{EW}(\text{FeK}\alpha)) \rangle = 2.89$ (Fig. 8, top histogram), with 20 sources presenting upper limits. Using *Suzaku* and *Swift*/BAT data, Kawamuro et al. (2016) also study a sample of 10 inefficient

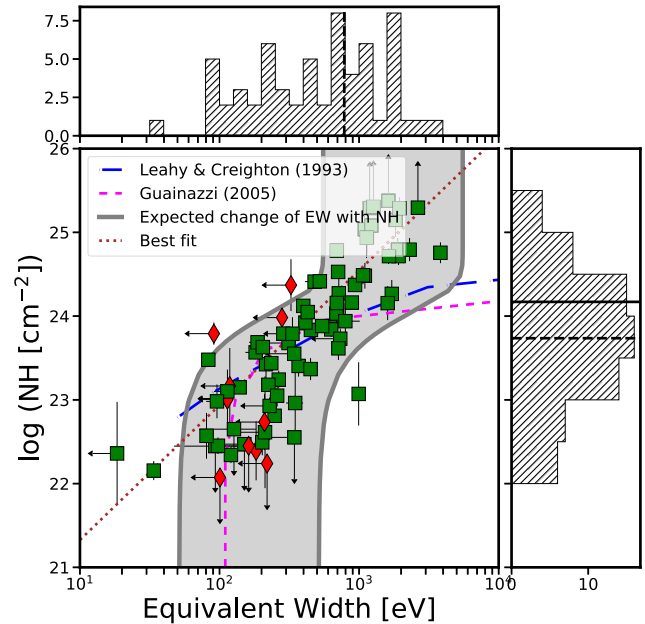


Figure 8. Equivalent width of the $\text{FeK}\alpha$ line versus the column density along the LOS. Colours and symbols are as in Fig. 6. The correlation line is drawn as the brown dotted line, while the blue long-dashed line and pink dashed lines show the expected relation according to Leahy & Creighton (1993) and Guainazzi et al. (2005), respectively. Moreover, the grey shaded area corresponds to the case in which the EW changes according to different levels of obscuration and reflection (see the text).

AGN. Among the seven objects in common with our sample, three (NGC 3718, NGC 4941, and NGC 5643) show different values for N_{H} (discrepancies around 10–20 per cent). We find higher N_{H} for the three sources, even when accounting for error bars. However, note that although the model is quite similar, they allow the reflection fraction in p_{exrav} and the constant (which they relate to the scattering fraction) free to vary in all cases. The main difference is that we test whether letting the covering fraction free to vary significantly improves the fit. This might explain the N_{H} differences found in both analyses.

Marchesi et al. (2018) analyse a sample of 26 sources classified as CT, using *NuSTAR* along with other X-ray facilities. Among those objects, we find 14 sources in common with our work, from which 10 have similar value of N_{H} compared to ours, while three have small discrepancies on the N_{H} (i.e. lower than 10 per cent), and one case (NGC 424) for which we have strong differences: they report a reflection dominated source, with $N_{\text{H}} = 24.4$, while from our analysis it should be considered as highly obscured ($\log(N_{\text{H}}) = 23.1$). Indeed, this source is also reflection dominated according to our f-test analysis. Thus, statistically speaking, the obscured power law associated with the intrinsic continuum is not required by the data. Moreover, their reflection model is different to ours, which might be responsible for the small changes in the spectral parameters.

Panagiotou & Walter (2019) also studied six sources in common with this work (M 106, NGC 1194, NGC 4941, NGC 5643, NGC 5728, and NGC 7582). All but two NGC 4941 (24.09 ± 0.15) and NGC 1194 (23.7 ± 0.1) present consistent N_{H} values. NGC 4941 and NGC 1194 present higher N_{H} compared to ours, even when accounting for error bars. Again, they classify these two sources as reflection dominated so this might be affecting the constraint of the LOS absorption due to a weak detection of the intrinsic continuum. In a second paper of the series, Panagiotou & Walter

(2020) include *NuSTAR* data for other six sources in common with our analysis (NGC 1052, NGC 2655, M 106, NGC 5252, NGC 5283, and NGC 7213), also showing consistent N_{H} . Note that Panagiotou & Walter (2020) exclude in their sample selection 21 sources in common with our sample; four (M 81, NGC 3998, NGC 7130, and NGC 7479) are excluded due to their LINER nature, two (IC 751 and NGC 7582) due to variability, and the remaining 15 are excluded for being reflection dominated (although included in Panagiotou & Walter 2019).

We plot the expected correlation between the N_{H} and the $\text{EW}(\text{FeK}\alpha)$ emission line in the large panel of Fig. 8. The equivalent width increases when the N_{H} does so, with a Pearson's linear relation coefficient of 0.85 (linear fit shown as dotted brown line in the figure). This is well explained by the predicted EW from a uniform shell of material encompassing the continuum source (blue long-dashed line in large panel of Fig. 8; see also fig. 2 in Leahy & Creighton 1993). Moreover, Guainazzi, Matt & Perola (2005) propose a slight change in this correlation when the reflection occurs in the inner walls of an optically thick matter, as seen through the unobscured LOS, while the continuum is obscured by material along the LOS (see pink dashed line in Fig. 8 and fig. 9 in Guainazzi et al. 2005). Note that the dispersion on this relation is naturally explained through the differences in geometry and composition of the reflector. Therefore, this reinforces the good estimate on the N_{H} in our analysis. This is also reproduced in more recent models with spherical and torus-like geometries (e.g. Ikeda, Awaki & Terashima 2009; Tanimoto et al. 2019). Moreover, we explore how the EW is affected by the amount of obscuration and the strength of the line (see shaded area in Fig. 8). We choose NGC 1052 as a test object and vary the normalization of the $\text{FeK}\alpha$ line (from $\text{norm}_{6.4\text{keV}} = 0.5$ to $\text{norm}_{6.4\text{keV}} = 5$), from left to right, respectively, while changing the N_{H} in order to see how the relation should change. We find that there is a value of EW above which this correlation saturates and thus we would only measure reflection (i.e. in the cases of reflection dominated sources). The main reason for the differences between this work and Guainazzi et al. (2005) is the fact that they do not have very obscured sources in their sample and thus their best fit does not cover such range. Thus, we confirm that 69 out of the 81 objects (~ 85 per cent) are obscured at X-rays (i.e. $N_{\text{H}} > 3 \times 10^{22}\text{cm}^{-2}$). This is further discussed in Section 5.

Furthermore, more than half of the sources (42) appear to be completely covered, 27 present a covering factor $f_{\text{cov}} > 0.5$, while seven show $f_{\text{cov}} < 0.5$. The remaining five AGN present either upper limits or non-constrained estimates for the covering factor. Among these objects, all of them present either low N_{H} or upper limits whereas the sources presenting full covering, also present high obscuration (with only 6 sources being mildly obscured).

5 DISCUSSION

The aim of this work is to study the behaviour of the reflection component and obscuration at X-rays (classically associated with the torus) at low accretion rates. In order to trace such a component, we selected a sample of 81 sources with *NuSTAR* observations among all the nearby AGN observed so far with available M_{BH} measurements. We performed a spectral analysis with a model that accounts for the reflection component from neutral material plus a partially absorbed intrinsic continuum.

Early X-ray observations of local AGN have served as observational proofs of the AGN unified theories, showing that most type-1 AGN are unobscured while type-2 AGN tend to show obscuration exceeding $N_{\text{H}} > 10^{22}\text{cm}^{-2}$ (Awaki et al. 1991; Bassani et al. 1999).

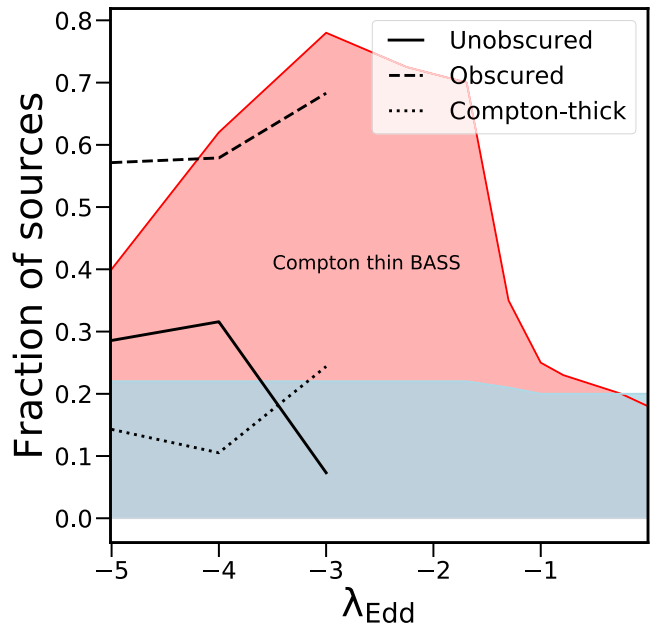


Figure 9. Fraction of Compton-thin and Compton-thick sources for the *Swift*/BAT sample reported by Ricci et al. (2017; red and blue shaded areas, respectively) compared to the unobscured, obscured, and CT (solid, dashed, and dotted lines, respectively). Note that our sample is limited above $\lambda_{\text{Edd}} > -2.5$ due to the selection criteria we use in this work.

Table 5. Number of unobscured, obscured, CT and no reflection sources per Eddington rate range. In parenthesis, it is represented the contribution percentage for each of the classifications. Note that sources with no reflection do not sum up to the total contribution in each range, since both the N_{H} classification is independent.

$\log(\lambda_{\text{Edd}})$ (total)	Unobs.	Obs	CT	No ref.
	# (per cent)	# (per cent)	# (per cent)	# (per cent)
(1)	(2)	(3) (4)	(5)	
-5 (7)	2 (28)	4 (57)	1 (14)	2 (28)
-4 (19)	6 (31)	11 (58)	2 (10)	4 (21)
-3 (41)	3 (7)	28 (68)	10 (24)	3 (7)

However, since then, several authors have shown that the fraction of obscured sources might depend on the evolutionary stage of the sources (see Ramos Almeida & Ricci 2017, for a review).

The covering factor of the gas can be estimated studying the absorption properties of large samples of AGN. In Fig. 9 we compare the results found by Ricci et al. (2017) using the BASS sample and those found in this study (numbers are reported in Table 5). Using this technique, recent hard X-ray studies have shown that the fraction of CT sources below $\lambda_{\text{Edd}} \sim 0.032$ is 23 ± 6 per cent (blue shaded area in Fig. 9). Marchesi et al. (2018) find that the fraction of CT sources decreases when using *NuSTAR* data thanks to a better covering and sensitivity above 10 keV which allows a better restriction in the LOS obscuration affecting the intrinsic continuum.

Our results indicate that the fraction of CT sources at $\lambda_{\text{Edd}} \simeq 10^{-5}$ is 15 per cent (dotted line), while Ricci et al. (2017) find it to be $\sim 20 \pm 4$ per cent. Thus, our results are statistically in agreement with them. Meanwhile, Ricci et al. (2017) find that the peak of obscured sources happens around $\lambda_{\text{Edd}} \sim 10^{-3}$, rising from 20 per cent to 80 per cent at Eddington rates $\lambda_{\text{Edd}} \simeq 10^{-1}$ and $\lambda_{\text{Edd}} \simeq 10^{-3}$, respectively (see red shaded area in Fig. 9; see also Ricci et al. 2017). Interestingly, our sample agrees well with these numbers at

$\lambda_{\text{Edd}} \simeq 10^{-3}$ for the percentage of obscured AGN (dashed line in Fig. 9). Note that our results indicate a low population of unobscured sources at $\lambda_{\text{Edd}} \simeq 10^{-3}$. Moreover, a slight decrease on the fraction of Compton-thin obscured sources is found below $\lambda_{\text{Edd}} \simeq 10^{-3}$, reaching ~ 60 per cent at $\lambda_{\text{Edd}} \simeq 10^{-5}$. Correspondingly, the fraction of unobscured sources rises from ~ 6 at $\lambda_{\text{Edd}} \simeq 10^{-3}$ to ~ 30 per cent at $\lambda_{\text{Edd}} \simeq 10^{-5}$. None the less, we are aware that this may be due to a bias in the selection criteria. Indeed, if there were more unobscured sources at these Eddington rates, they should have been included in our sample. However, we select only those sources with archival data and a minimum S/N in the spectrum. This has two main consequences: i) there may be several objects which have not yet been observed, among which there might be unobscured sources. ii) there might be more obscured sources for which the flux is so low that they do not fulfill our S/N criteria. Thus, although our results are in agreement with the complete sample by Ricci et al. (2017), we warn the reader that our sample is incomplete.

The trend found in this analysis might suggest no obscuration for a large fraction of sources at even lower accretion rates. The scenario in which both the BLR and the torus can be seen as different regions from a wind coming off the disc has long been proposed (Elvis 2000) and it naturally includes the absence of such regions in some objects (e.g. True-type 2 AGN intrinsically miss the BLR; Tran 2001; Laor 2003; Panessa et al. 2006). If the accretion disc cannot expel material in an efficient way, then the gravitational force from the SMBH will overcome the radiation pressure from the wind, causing the wind, and therefore the BLR and the torus, to collapse (Elitzur & Shlosman 2006). Therefore, as a first approach, the condition for the torus disappearance can be related to the bolometric luminosity of the source and the accretion rate. According to Elitzur & Shlosman (2006), the BLR should disappear for low-luminosity AGN (i.e. $L_{\text{bol}} < 10^{42}$ erg s $^{-1}$). 6 out of the 11 objects lacking reflection signatures in our sample are below this threshold. However, in a more recent study it has been shown that this structure can disappear even for bright sources (e.g. Elitzur & Netzer 2016), depending on the properties of the wind, such as the wind efficiency or the number/density of clouds. In fact, it requires a minimal column density, implying a minimal outflow rate, and thus a minimal accretion rate. Interestingly, three of our candidates present upper limits on the N_{H} and other five show $N_{\text{H}} \leq 10^{23}$ cm $^{-2}$. Finally, three are rather obscured (namely M 106, NGC 612, and M 88). In particular, for M 106, Kawamuro et al. (2016) find that the FeK α line is variable, proposing it might be originated in the accretion disc, while in the case of NGC 612, Ursini et al. (2018) do not find strong features of a Compton-reflection component, although like us, they find that this source presents high absorption, proposing that it might originate in an extended structure rather than the pc-scale torus. Thus, these works are still in agreement with the lack of reflection originated in the torus. Another particularly interesting object is M 88, being proposed as a True-Type 2 AGN (i.e. intrinsically missing the BLR; Brightman & Nandra 2008). We would expect for this object to be low obscured. Although we modelled this source with an obscured component, the quality of the observations¹¹ may prevent us from finding a reliable value in the N_{H} for this particular source. Thus, almost all our candidates to

¹¹The spectra of M 88 show calibration issues clearly visible in Fig. 5 and resulting in a calibration factor much larger than for the rest of the sample, with a value of $C_{\text{cross}} = 1.99 \pm 0.19$.

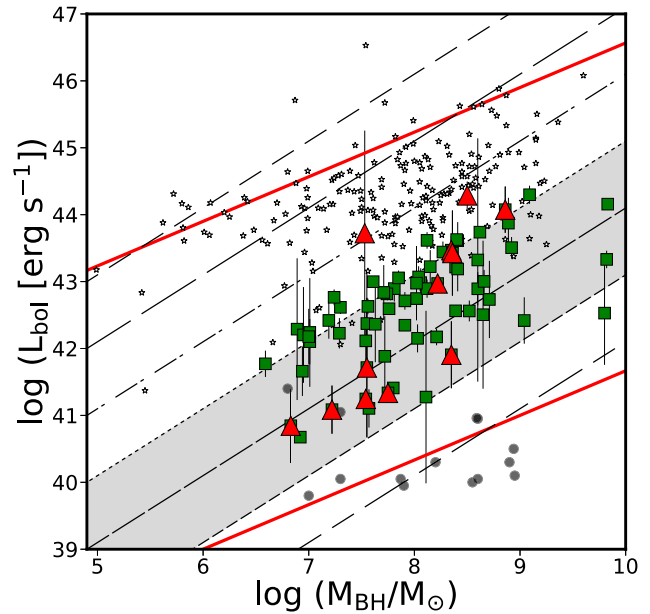


Figure 10. Bolometric luminosity versus M_{BH} for our sample (colours and symbols as in Fig. 6) and the BASS sample (small empty stars). Our 11 candidates are plotted in the larger red triangles. The semitranslucent circles represent the candidates for torus disappearance found by González-Martín et al. (2017) using mid-IR data. The black dashed lines represent $\log(L_{\text{Edd}}) = [0, -1, -2, -3, -4, -5, -6]$ from top to bottom, respectively. The two red lines enclose the region in which the torus may or may not exist depending on the wind parameters, as proposed by Elitzur & Ho (2009). The grey-shaded area corresponds to the Eddington rates from the sample not biased by the selection criteria. Note that those sources with Eddington rates above $\log \lambda_{\text{Edd}} \sim -2.5$ are not shown in this plot since at those Eddington rates our sample is not complete.

the torus disappearance are on the lower end of LOS obscuration (Fig. 8).

According to Elitzur & Netzer (2016), the BLR/torus may or may not exist in a delimited zone in the luminosity- M_{BH} diagram and both components should disappear under a certain threshold delimited by the wind parameters. Fig. 10 shows the bolometric luminosity versus M_{BH} diagram for our sample (large symbols), excluding the sources for which $\lambda_{\text{Edd}} > -2.5$. Note that although these sources are mostly CT at this Eddington rate, it is difficult to assess how many sources we may be missing due to the selection biases we have imposed and to the available data.

As a comparison sample, we also plot data from the *Swift*/BAT sample (Koss et al. 2017; plotted as the small star symbols). We selected sources from that sample such that they had some estimate on the M_{BH} , with reported values for the intrinsic 2–10 keV luminosity, to obtain the bolometric luminosity and LOS obscuration. We discarded sources without constrained $\log(N_{\text{H}})$ values and we also neglect the sources in common. We obtained a total of 195 sources for the comparison sample. Note that all our sources fall within the region in which the BLR/torus may or may not exist (red lines), according to Elitzur & Netzer (2016). We also plot with red triangles our 11 candidates for the torus disappearance. The location of our candidates is in complete agreement with the idea that the torus disappearance does not rely solely on the bolometric luminosity of the source, yet, it does disappear for inefficient sources. Moreover, González-Martín et al. (2017) study a sample of AGN using mid-IR spectra trying to understand the behaviour of the torus in what is

called the gradual resizing. We plot in Fig. 10 (grey circles) their candidates for the disappearance of the torus from a mid-IR point of view. Unlike us, they do have objects lacking the torus below the limit proposed by Elitzur & Netzer (2016), at $\lambda_{\text{Edd}} = 10^{-6} - 10^{-5}$ depending on the M_{BH} . However, they also found several candidates in the range $\lambda_{\text{Edd}} = 10^{-5} - 10^{-3}$. Our study complements theirs by the inclusion of these 11 new candidates to the torus disappearance; all together a sample of 25 AGN. Indeed, we may also be missing objects with $\lambda_{\text{Edd}} < 10^{-5.5}$, either because observations for such low-luminosity objects have not yet been performed, or because the S/N of the observations are so low that they do not fulfill our selection criteria. Moreover, highly obscured objects might be missing because they are more difficult to detect than unobscured objects.

Another interesting result on the obscurer behaviour is the increase on the narrow FeK α line luminosity compared to the reflection luminosity when the reflection luminosity decreases (Fig. 6, large right panel). This is present when we compare the reflection luminosity with the intrinsic luminosity, showing a mean contribution of 40 per cent of reflection for the full range of the intrinsic luminosity (Fig. 6, large left panel). However, the FeK α line and reflection component changes are not associated with the accretion rate, because no correlation is found between the accretion rate and the luminosity of the reflection component or the FeK α line. Although the flux of the narrow FeK α line (compared to the intrinsic X-ray flux) is generally weaker in type-2 AGN than in type-1 AGN for the same 10–50 keV continuum luminosity (Ricci et al. 2014), this is not reproduced by the low accretion AGN in our sample. Ricci et al. (2014) suggest that this difference can be explained by means of different average inclination angles with respect to the torus, as predicted by the unified model. However, our sample is mostly constituted by type-2 AGN, which might explain why we do not find such behaviour. While the FeK α line can be produced by material with column densities as low as $N_{\text{H}} \simeq 10^{21-23} \text{ cm}^{-2}$, the Compton hump can only be created by the reprocessing of X-ray photons in CT material. Thus, the increase on the fraction of FeK α line luminosity compared to the Compton hump luminosity toward low-reflection luminosities might be an indication of a higher fraction of the emission produced in Compton-thin material associated with the accretion disc. If the accretion disc contribution is responsible for this behaviour, we might expect differences on the photon index distributions that might contribute to the Compton hump and or the FeK α line differently as long as the reflection luminosity decreases. For instance, it is expected for the photon index of standard discs to be larger for higher intrinsic luminosities (softer when brighter), while it is expected to decrease with increasing luminosity in radiatively inefficient accretion discs (harder when brighter; Narayan & Yi 1995; Connolly et al. 2016, and references therein).

However, the mean of the distribution of the photon index ($\langle \Gamma \rangle = 1.81$) is similar to the average photon index found in diverse AGN samples (e.g. *Swift*/BAT; Koss et al. 2017), and we do not find any particular trend on the accretion disc that might explain this behaviour found in the strength of the line. Another alternative is a smooth transition on the average iron abundances of the X-ray reflector (i.e. torus; Ricci et al. 2014). This might imply a smooth transition on the chemistry of the torus as seen at X-rays as long as the torus luminosity decreases traced by the Compton hump. In favour, González-Martín et al. (2017) also find that a group of objects with a low contribution from the torus are not well described with the clumpy torus model at mid-IR. They suggest that this might imply that the torus chemistry may be different at low luminosities, consistent with these findings.

6 SUMMARY AND CONCLUSIONS

We have performed an analysis aimed to find the conditions for the change and plausible disappearance of the obscuring gas for low-accretion AGN. For that purpose, we used a sample of 81 sources observed with *NuSTAR* selected by having Eddington rates $\lambda_{\text{Edd}} \lesssim 10^{-3}$. We fitted the data with a model accounting for a patchy absorber and a reflection component from neutral material. We found that ~ 80 per cent of our sample is obscured, with 20 per cent of CT sources, in agreement with several works (e.g. Ricci et al. 2017; Marchesi et al. 2018).

In order to directly compare the lack of reflection component with those sources lacking of the torus at mid-IR wavelengths, fainter X-ray sources, with luminosities $L_{\text{X}} \sim 10^{38} \text{ erg s}^{-1}$ are required. However, we found that a small number of sources in our sample (~ 15 per cent) seem to lack the reflection component associated with the torus, while the rest of the sources are found to have reflection features such as the existence of the FeK α line and/or the reflection hump. The sources lacking of reflection component features are located in the region where the torus may or may not disappear according to their M_{BH} and bolometric luminosities. When the reflection component was detected, it accounts for 40 per cent of the luminosity of the intrinsic continuum. We also found tentative evidence in favour of an increase of unobscured sources and a change of the reflector chemistry toward $\lambda_{\text{Edd}} \sim 10^{-5}$. Our findings are in agreement with the scenario in which as the AGN becomes less efficient, the torus is not supported by the radiation field from the wind coming off the accretion disc and fades. As a final remark, we highlight the importance of better S/N data and a broader energy coverage in order to apply more complex models for the reflection component, which includes testing if it may also be produced in the accretion disc (i.e. ionized reflection), but also testing different geometries and matter distributions (i.e. homogeneous, clumpy, etc.).

ACKNOWLEDGEMENTS

We thank the anonymous referee for her/his useful comments which greatly improved this paper. This research has made use of the NASA/IPAC Extragalactic Data base (NED), which is operated by the Jet Propulsion Laboratory, California Institute of Technology, under contract with the National Aeronautics and Space Administration. This research has made use of data and/or software provided by the High Energy Astrophysics Science Archive Research Center (HEASARC), which is a service of the Astrophysics Science Division at NASA/GSFC and the High Energy Astrophysics Division of the Smithsonian Astrophysical Observatory. NOC would like to thank CONACyT scholarship No. 897887. CVC acknowledges support from CONACyT. We thank the UNAM PAPIIT project IN105720 (PI OGM). LHG acknowledges funds by ANID – Millennium Science Initiative Program – ICN12.009 awarded to the Millennium Institute of Astrophysics (MAS).

DATA AVAILABILITY

The data underlying this article are available in at <https://heasarc.gsfc.nasa.gov/>. The data sets were derived from sources in the public domain.

REFERENCES

- Annunzio A. et al., 2015, *ApJ*, 815, 36
Annunzio A. et al., 2017, *ApJ*, 836, 165

- Annunzi A. et al., 2020, *MNRAS*, 497, 229
- Antonucci R., 1993, *ARA&A*, 31, 473
- Arnaud K. A., 1996, Jacoby G. H., Barnes J., eds, ASP Conf. Ser. Vol. 101, Astronomical Data Analysis Software and Systems V. Astron. Soc. Pac., San Francisco, p. 17
- Awaki H., Koyama K., Inoue H., Halpern J. P., 1991, *PASJ*, 43, 195
- Baloković M. et al., 2014, *ApJ*, 794, 111
- Baloković M. et al., 2018, *ApJ*, 854, 42
- Baloković M. et al., 2020, *ApJ*, 905, 41
- Bär R. E. et al., 2019, *MNRAS*, 489, 3073
- Bassani L., Dadina M., Maiolino R., Salvati M., Risaliti G., Della Ceca R., Matt G., Zamorani G., 1999, *ApJS*, 121, 473
- Brightman M., Nandra K., 2008, *MNRAS*, 390, 1241
- Connolly S. D., McHardy I. M., Skipper C. J., Emmanoulopoulos D., 2016, *MNRAS*, 459, 3963
- Constantin A. et al., 2009, *ApJ*, 705, 1336
- Dauser T., Garcia J., Parker M. L., Fabian A. C., Wilms J., 2014, *MNRAS*, 444, L100
- de Jong S., Beckmann V., Soldi S., Tramacere A., Gros A., 2015, *MNRAS*, 450, 4333
- Elitzur M., Ho L. C., 2009, *ApJ*, 701, L91
- Elitzur M., Netzer H., 2016, *MNRAS*, 459, 585
- Elitzur M., Shlosman I., 2006, *ApJ*, 648, L101
- Elvis M., 2000, *ApJ*, 545, 63
- Esparza-Arredondo D. et al., 2019, *ApJ*, 886, 125
- Esparza-Arredondo D., Gonzalez-Martín O., Dultzin D., Masegosa J., Ramos-Almeida C., García-Bernete I., Fritz J., Osorio-Clavijo N., 2021, *A&A*, 651, A91
- Ezhikode S. H., Dewangan G. C., Misra R., Philip N. S., 2020, *MNRAS*, 495, 3373
- Ferrarese L., Merritt D., 2000, *ApJ*, 539, L9
- Furui S., Fukazawa Y., Odaka H., Kawaguchi T., Ohno M., Hayashi K., 2016, *ApJ*, 818, 164
- Gebhardt K. et al., 2000, *ApJ*, 539, L13
- González-Martín O. et al., 2015, *A&A*, 578, A74
- González-Martín O. et al., 2017, *ApJ*, 841, 37
- González-Martín O., Masegosa J., Márquez I., Guainazzi M., Jiménez-Bailón E., 2009, *A&A*, 506, 1107
- Gu M., Cao X., 2009, *MNRAS*, 399, 349
- Guainazzi M., Matt G., Perola G. C., 2005, *A&A*, 444, 119
- Gültekin K., Cackett E. M., Miller J. M., Matteo T. D., Markoff S., Richstone D. O., 2012, *ApJ*, 749, 129
- Hardcastle M. J., Worrall D. M., Kraft R. P., Forman W. R., Jones C., Murray S. S., 2003, *ApJ*, 593, 169
- Harrison F. A. et al., 2013, *ApJ*, 770, 103
- Hernández-García L., Masegosa J., González-Martín O., Márquez I., 2015, *A&A*, 579, A90
- Hernández-García L., Masegosa J., González-Martín O., Márquez I., Perea J., 2016, *ApJ*, 824, 7
- Ikeda S., Awaki H., Terashima Y., 2009, *ApJ*, 692, 608
- Jang I., Gliozzi M., Hughes C., Titarchuk L., 2014, *MNRAS*, 443, 72
- Kalberla P. M. W., Burton W. B., Hartmann D., Arnal E. M., Bajaja E., Morras R., Poeppel W. G. L., 2005, *A&A*, 440, 775
- Kang J., Wang J., Kang W., 2020, *ApJ*, 901, 111
- Kawamuro T., Ueda Y., Tazaki F., Terashima Y., Mushotzky R., 2016, *ApJ*, 831, 37
- Khim H., Yi S. K., 2017, *ApJ*, 846, 155
- Khorunzhev G. A., Sazonov S. Y., Burenin R. A., Tkachenko A. Y., 2012, *Astron. Lett.*, 38, 475
- Koss M. et al., 2017, *ApJ*, 850, 74
- La Caria M.-M., Vignali C., Lanzuisi G., Gruppioni C., Pozzi F., 2019, *MNRAS*, 487, 1662
- Laor A., 2001, *ApJ*, 553, 677
- Laor A., 2003, *ApJ*, 590, 86
- Leahy D. A., Creighton J., 1993, *MNRAS*, 263, 314
- Liu Y., Li X., 2014, *ApJ*, 787, 52
- Magdziarz P., Zdziarski A. A., 1995, *MNRAS*, 273, 837
- Marchesi S. et al., 2019, *ApJ*, 872, 8
- Marchesi S., Ajello M., Marcotulli L., Comastri A., Lanzuisi G., Vignali C., 2018, *ApJ*, 854, 49
- Marconi A., Risaliti G., Gilli R., Hunt L. K., Maiolino R., Salvati M., 2004, *MNRAS*, 351, 169
- Matt G., Guainazzi M., Maiolino R., 2003, *MNRAS*, 342, 422
- McKernan B., Ford K. E. S., Reynolds C. S., 2010, *MNRAS*, 407, 2399
- Molina M., Malizia A., Bassani L., Ursini F., Bazzano A., Ubertini P., 2019, *MNRAS*, 484, 2735
- Murphy K. D., Yaqoob T., 2009, *MNRAS*, 397, 1549
- Nandra K., O'Neill P. M., George I. M., Reeves J. N., 2007, *MNRAS*, 382, 194
- Narayan R., Yi I., 1995, *ApJ*, 452, 710
- Nemmen R. S., Storchi-Bergmann T., Eracleous M., 2014, *MNRAS*, 438, 2804
- Netzer H., 2015, *ARA&A*, 53, 365
- Oda S., Tanimoto A., Ueda Y., Imanishi M., Terashima Y., Ricci C., 2017, *ApJ*, 835, 179
- Panagiotou C., Walter R., 2019, *A&A*, 626, A40
- Panagiotou C., Walter R., 2020, *A&A*, 640, A31
- Panessa F. et al., 2006, *A&A*, 455, 173
- Ramos Almeida C. et al., 2009, *ApJ*, 702, 1127
- Ramos Almeida C., Ricci C., 2017, *Nature Astron.*, 1, 679
- Ricci C. et al., 2017, *Nature*, 549, 488
- Ricci C., Ueda Y., Paltani S., Ichikawa K., Gandhi P., Awaki H., 2014, *MNRAS*, 441, 3622
- Ricci C., Walter R., Courvoisier T. J.-L., Paltani S., 2011, *A&A*, 532, A102
- Shakura N. I., Sunyaev R. A., 1973, *A&A*, 500, 33
- Tanimoto A., Ueda Y., Kawamuro T., Ricci C., Awaki H., Terashima Y., 2018, *ApJ*, 853, 146
- Tanimoto A., Ueda Y., Odaka H., Kawaguchi T., Fukazawa Y., Kawamuro T., 2019, *ApJ*, 877, 95
- Tanimoto A., Ueda Y., Odaka H., Ogawa S., Yamada S., Kawaguchi T., Ichikawa K., 2020, *ApJ*, 897, 2
- Tran H. D., 2001, *ApJ*, 554, L19
- Urry C. M., Padovani P., 1995, *PASP*, 107, 803
- Ursini F., Bassani L., Panessa F., Bazzano A., Bird A. J., Malizia A., Ubertini P., 2018, *MNRAS*, 474, 5684
- van den Bosch R. C. E., 2016, *ApJ*, 831, 134
- van den Bosch R. C. E., Gebhardt K., Gültekin K., Yıldırım A., Walsh J. L., 2015, *ApJS*, 218, 10
- Vasudevan R. V., Fabian A. C., 2009, *MNRAS*, 392, 1124
- Wenger M. et al., 2000, *A&A*, 143, S9
- Woo J.-H., Urry C. M., 2002, *ApJ*, 581, L5
- Younes G., Porquet D., Sabra B., Reeves J. N., 2011, *A&A*, 530, A149
- Younes G., Ptak A., Ho L. C., Xie F.-G., Terashima Y., Yuan F., Huppenkothen D., Yukita M., 2019, *ApJ*, 870, 73
- Zhao X., Marchesi S., Ajello M., Marcotulli L., Cusumano G., La Parola V., Vignali C., 2019, *ApJ*, 870, 60

APPENDIX A: MODELING WITH CABS

We use a model which does not account for the Compton scattering, particularly important for Compton-thick objects (Annunzi et al. 2017; Ricci et al. 2017; Marchesi et al. 2019; Zhao et al. 2019). XSPEC has a model to account for Compton scattering called `cabs`¹². This model component has been reported to present some issues (see e.g. MYTORUS manual and Tanimoto et al. 2018), and does not emulate properly the X-ray spectra of AGN. However, `cabs` has been used in several recent works to account for Compton scattering in AGN when using *NuSTAR* data (see Oda et al. 2017; Ricci et al. 2017; Tanimoto et al. 2020). In practice, we added the `cabs` component

¹²see XSPEC manual <https://heasarc.gsfc.nasa.gov/xanadu/xspec/manual/XspecManual.html>

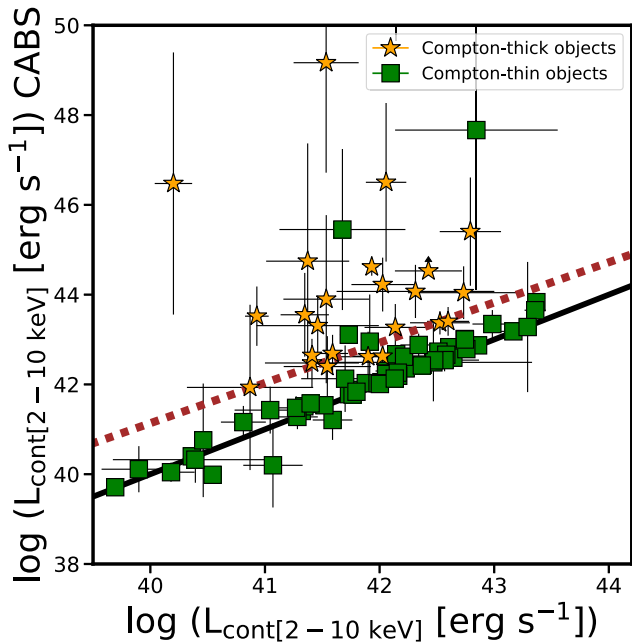


Figure A1. Intrinsic luminosity of the power-law component when including `cabs` in the spectral modelling (vertical axis) compared to the case in which it is not used (horizontal axis). The brown dotted and black solid lines are the best fit to the data and the 1:1 relation, respectively.

to the model in equation (4) as follows:

$$M_5 = phabs_{Gal}((zphabs_{intr} * cabs * zpowerlw) + ct * zpowerlw + pexmon + zgauss_{6.7\ keV} + zgauss_{6.97\ keV}) \quad (A1)$$

letting the N_H in the `cabs` component to be the same as that of the LOS obscuration. The resulting N_H values are mostly consistent with those reported in this work (see below). However, the intrinsic luminosity of the sources obtained for some objects changes by a factor of 10^4 (see Fig. A1 shows). Indeed, note that a non-negligible amount of sources fall well outside the 1:1 relation even when accounting for error bars (black solid line). Moreover, the error bars are much larger when using `CABS` than when excluding it. These luminosities result in Eddington rates close to the Eddington limit, which are unrealistic values for LLAGN.

These results imply that there is a systematic uncertainty when adding the Compton-scattering through the `cabs` component.

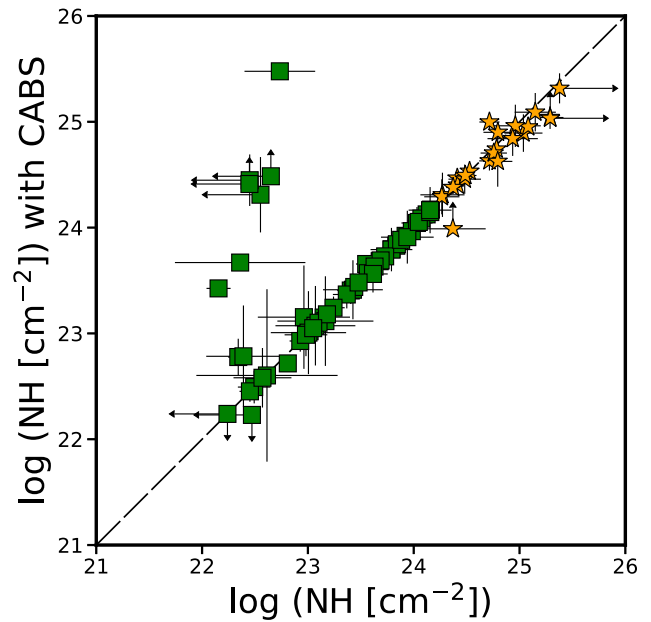


Figure A2. Column density of the sources when `cabs` is added (vertical axis) compared to the case in which it is not used (horizontal axis). The black dashed line is the 1:1 relation.

However, this does not imply that such a component does not physically exist in the X-ray spectra of AGN. In fact, the neglect of this component does add a systematic uncertainty to the general analysis. Indeed, this effect primarily affects the X-ray spectra of CT objects. Thus, although the addition of `cabs` does not lead to physically realistic results, the exclusion of the Compton-scattering effects in our analysis, imply that all intrinsic luminosities for CT sources reported here should be treated as lower limits.

We have also checked how the exclusion of this component affects the N_H measurement. Fig. A2 shows the change in this parameter. The black dashed line shows the 1:1 relation. In this case, most of the sources fall in this line, with only 8 sources falling outside the relation. Note that this is a result similar to the one by Tanimoto et al. (2018, see their Fig. 5a), where they found larger values for the intrinsic luminosity when using this model. However, the spectral parameters were not very much affected.

This paper has been typeset from a $\text{\TeX}/\text{\LaTeX}$ file prepared by the author.

Chapter 5

AGN in the CALIFA sample

In this chapter we study the existence of AGN sources in the CALIFA optical survey, introduced in section 3.2.1, through the X-ray point-of-view. Our aim is to compare the detectability of AGN sources at optical and X-ray wavelengths, in order to understand the bias that each wavelength provides when comparing to the other one. In the work by Lacerda et al. (2020), they already catalogued 34 AGN sources from the optical point of view, which corresponds to $\sim 4\%$ of the CALIFA sample with nuclear activity. We use the extended CALIFA (eCALIFA) data release, which comprises 941 objects with $z < 0.03$. For this part of the thesis, we use the X-ray satellite *Chandra* (sec. 3.1) as it provides the best spatial resolution up to date which is essential to isolate the nuclear emission. We search in the HEASARC database for observations with exposure times longer than 5ks to ensure a minimum quality of both the images and the spectra, and with a search radius of 30". Our final sample consists of 138 sources meeting the aforementioned criteria. We obtain the full band image (0.5-10 keV) and two spectra for each observation: one of the central (3") region and one for the extended emission (with an inner radius of 5" and an outer radius that relies on the extension of the emission). The outer radius is chosen such that it maximizes the SNR of the spectra. Moreover, in this part of the analysis, we perform the optimal binning technique by Kaastra & Bleeker (2016), allowing us to use the C-statistic introduced in section 3.3.2. We analyze this sample through the morphology of the emission and through the spectroscopic signatures that could be associated with AGN emission.

The morphology was quantified by performing a 2D decomposition of the X-ray images. We use the full band X-ray image (in the 0.5-10 keV band) and model it with two independent 2D Gaussian profiles (nuclear and extended Gaussians). In order to classify a source as detected, the nuclear Gaussian should have an amplitude above the detection limit of the image.

After characterizing these sources with the imaging analysis we perform a spectroscopic analysis on the nuclear spectra using models associated with AGN emission and non-AGN emission. We use four baseline models: Three of them are associated with the X-ray emission from AGN, while one is associated with thermal emission from optically thin material.

One of the main results from this analysis, is the fact that we find 34 new bona fide AGN candidates using X-ray information. Moreover, we also classify 28 extra sources as AGN candidates as their spectra did not have enough SNR to perform a spectral analysis, but the imaging analysis already hinted the existence of a nuclear source. We analyze the location of these X-ray detected sources in the classical BPT-VO87 (see sec. 1.9.1) diagrams in order to determine the restrictions imposed by these criteria. From this analysis, we find that if we classify sources based on their location, and assume that bona fide AGN are only those located in the AGN region of the diagrams, we might be missing up to 70% of X-ray detected AGN. We also find that sources detected at both wavelengths are among the brightest in the sample. Additionally, sources classified as AGN at optical and not at X-rays might be subject to intrinsically large amounts of column density in the l.o.s, which would make it hard to detect these sources with *Chandra*. Altogether, combining both optical and X-ray information, we were able to determine that there is a percentage of nuclear activity in the CALIFA survey between 7-10%.

In Appendix 8.3 we present the figures corresponding to the morphological analysis for the detected sources, while in Appendix 8.4 we present the figures corresponding to the spectral fitting performed for the sample of sources with enough SNR.

This work was done in its majority by the main author, with the Dr. Omaira González Martín and Dr. Sebastián Sánchez as the advisors, contributing to the exhausting revision and discussion of the results. The rest of the authors contributed with additional revisions

and comments. This work was published by the *Monthly Notices of the Royal Astronomical Society* (MNRAS) journal in April of 2023. The electronic version of this publication can be found at: <https://ui.adsabs.harvard.edu/abs/2023MNRAS.522.57880/abstract>.

AGNs in the CALIFA survey: X-ray detection of nuclear sources

N. Osorio-Clavijo ¹★, O. Gonzalez-Martín ¹, S. F. Sánchez ², M. Guainazzi ³
and I. Cruz-González ²

¹Instituto de Radioastronomía and Astrofísica (IRyA-UNAM), 3-72 (Xangari), 8701 Morelia, Mexico

²Instituto de Astronomía, Universidad Nacional Autónoma de México, A. P. 70-264, C.P. 04510 México, D.F., Mexico

³ESA European Space Research and Technology Centre (ESTEC), Keplerlaan 1, NL-2201 AZ Noordwijk, the Netherlands

Accepted 2023 March 28. Received 2023 March 22; in original form 2022 October 14

ABSTRACT

A complete demographic of active galactic nuclei (AGNs) is essential to understand the evolution of the Universe. Optical surveys estimate the population of AGNs in the local Universe to be of ~ 4 per cent. However, these results could be biased towards bright sources, not affected by the host galaxy attenuation. An alternative method for detecting these objects is through the X-ray emission. In this work, we aim to complement the AGN population of the optical CALIFA survey (941 sources), by using X-ray data from *Chandra*, which provides the best spatial resolution to date, essential to isolate the nuclear emission from the host galaxy. We study a total of 138 sources with available data. We find 34 new bona fide AGNs and 23 AGN candidates, which could increase the AGN population to 7–10 per cent among the CALIFA survey. X-rays are particularly useful for low-luminosity AGNs since they are excluded by the criterion of large equivalent width of the $H\alpha$ emission line when applied to optical selections. Indeed, placing such a restrictive criteria might cause a loss of up to 70 per cent of AGN sources. X-ray detected sources are preferentially located in the right side of the $[O III]/H\beta$ versus $[N II]/H\alpha$ diagram, suggesting that this diagram might be the most reliable at classifying AGN sources. Our results support the idea that multiwavelength studies are the best way to obtain a complete AGN population.

Key words: galaxies: active – galaxies: nuclei – galaxies: Seyfert – X-rays: galaxies.

1 INTRODUCTION

It has been widely accepted that most galaxies (at least those with a well-formed bulge) host a supermassive black-hole (SMBH), sometimes fed by an accretion disc, releasing energies that can go up to $L_{\text{bol}} \sim 10^{48} \text{ erg s}^{-1}$ (Netzer 2015). These are known as active galactic nuclei (AGNs). Observational results suggest that AGNs play a role in star formation and galaxy evolution, with the most accepted paradigm being that AGN may quench the star formation by heating (Bower et al. 2006) or removing (Fabian 2012; Trussler et al. 2020) the molecular gas available for star formation, ultimately also changing the galaxy morphology (Hopkins et al. 2010). Thus, complete samples of AGNs are crucial for understanding their role in galaxy evolution.

Our structural model of an AGN comprises an accretion disc, both broad and narrow emission line regions (BLR and NLR, respectively), a dusty toroidal structure called the torus, and in some cases a jet. Most of the variety of the observational properties can be explained with different observation angles and whether or not the line-of-sight (LOS) is impeded by the torus, obscuring the innermost regions. Indeed the distinction between Type I (with both broad and narrow emission lines in the optical spectrum) and Type II (with only narrow emission lines) can be explained under this scenario (Unified model Antonucci 1993; Urry & Padovani 1995). AGN

can emit throughout the complete electromagnetic spectrum. The big blue bump at optical/UV wavelengths is associated with the accretion disc (Wills, Netzer & Wills 1985), while the Compton-hump at X-rays can be associated with reflection occurring in the torus (Murphy & Yaqoob 2009) or the disc (Fabian & Iwasawa 2000). The optical emission lines can be associated with the BLR and NLR and their profiles give information about the physical characteristics of these regions (see the review by Netzer 2015). However, the AGN detection is not trivial; due to their location at the centre of galaxies, their detection strongly depends on the intrinsic luminosity but also on the amount of obscuration provided by the host galaxies. Particularly at optical wavelengths, one of the most common methods to detect and classify AGNs is through the use of diagnostic diagrams (BPT diagrams; Baldwin, Phillips & Terlevich 1981; Veilleux & Osterbrock 1987), which calculate ratios between different narrow emission lines. These diagrams can potentially identify star-forming (SF) dominated galaxies, and differentiate them from galaxies dominated by nuclear activity, shock excitation (Kewley et al. 2013), post-AGB stars (Singh et al. 2013), and low ionization nuclear emission regions (LINERs; Heckman 1980). The interpretation of these diagrams is still under debate, particularly because several of the processes mentioned above can locate a galaxy in the same region of the BPT (Richard et al. 2011; Singh et al. 2013; Belfiore et al. 2016; Lacerda et al. 2020; Comerford et al. 2022, and references therein). Additionally, the presence of dust in the host galaxy can attenuate the nuclear emission, even preventing us from detecting any trace of nuclear activity (Moran,

* E-mail: n.osorio@irya.unam.mx

Filippenko & Chornock 2002; Trump et al. 2009; Agostino & Salim 2019; Comerford et al. 2022, and references therein).

Therefore, spatially resolved spectroscopy (e.g. Singh et al. 2013; Belfiore et al. 2016; Sánchez et al. 2018; Wylezalek et al. 2018) is crucial to study all the processes occurring in galaxies and particularly, for the proper characterization of their nuclei. Indeed, several works have been performed aiming to characterize these regions and have been proven successful at detecting AGNs. For instance, Lacerda et al. (2020) found 34 objects in the The Calar Alto Legacy Integral Field Area survey (CALIFA; Sánchez et al. 2012) to host an AGN.

They followed a method proposed by Sánchez et al. (2018) which consists of two main criteria: the object should reside in the AGN region in all BPT diagrams and additionally should have an $EW(H\alpha) > 3 \text{ \AA}$. This optical classification method is particularly useful to find bright sources where the nuclear emission is not strongly affected by the host galaxy. In a similar work, Comerford et al. (2022) found 10 AGNs in the MaNGA survey, which had been previously classified as SF dominated or LINERs, thanks to the higher spatial resolution. Therefore, spatially resolved spectroscopy is essential for a correct classification of the sources. However, different works have shown that this method fails at finding low-luminosity AGNs (LLAGN Heckman 1980) where the attenuation by the host galaxy is highly significant, or galaxies with active star formation processes and AGNs residing in low-mass galaxies (Goulding & Alexander 2009; Kewley et al. 2013; Trump et al. 2015; Cann et al. 2019, and references therein).

Another way to detect AGNs is through the X-rays, which are dominated by the AGN emission above 2 keV (known as hard X-rays) with a continuum described as a power law of the form $A(E) = KE^{-\Gamma}$, where Γ can range between 0.7 and 3, with a mean of $\Gamma = 1.8$ in the local Universe (Nandra & Pounds 1994; Bianchi et al. 2009). These objects are seen as point-like sources (Netzer 2015), and constitute the bulk of the Cosmic X-ray Background (Comastri et al. 1995; Ueda et al. 2003). The brightest AGNs can even outshine the galaxy (Azadi et al. 2017) and therefore are less affected by host-galaxy attenuation (Brandt & Alexander 2015). The spectral and imaging identification of these objects strongly depend on the telescope resolution, spectral range, and sensitivity. This is particularly important for LLAGN, where the imaging identification can be difficult, but also because there are other energetic processes associated with stellar processes that can emit X-rays, such as X-ray binaries (XRBs) and Ultra-Luminous X-ray sources (ULXs), and the distinction between these objects and nuclear activity is crucial. In fact, several works have shown that these processes have a luminosity function that differs from that of AGNs (see the review by Fabbiano 2006, and references therein). Several studies have attempted to properly characterize the X-ray emission of galaxies, aiming to detect AGN sources. In particular, Roberts & Warwick (2000) use data from the *ROSAT* satellite, finding that 45 out of the 83 galaxies in their parent sample host nuclear sources associated with an AGN. Among the sample, a significant amount of sources (33 per cent) host LLAGN with luminosities as low as $L_X = 10^{38} \text{ erg s}^{-1}$. More recently, with the exceptional spatial resolution provided by *Chandra*, several works have estimated the population of AGNs in different types of galaxies. For instance, Zhang et al. (2009) study a total of 187 local galaxies, with a distance below 15 Mpc. They find that 46 per cent of their present point-like sources at the centre associated with black holes, most of them with low Eddington rates. In addition, She, Ho & Feng (2017) find a similar fraction of active galaxies in X-rays which had been previously classified as H II galaxies in optical. In a very recent work by Williams et al. (2022), they find a similar

fraction of active galaxies, with a significant amount of them in the low-luminosity regime. Heavily obscured objects (the so-called Compton-thick – CT-AGN) are also difficult to be detected at X-rays, as the material from the inner parts of the AGN can suppress the intrinsic emission (Brightman & Nandra 2008; Georgantopoulos & Akylas 2010; Comastri et al. 2011; Azadi et al. 2017; Ricci et al. 2017), and observations covering above 10 keV are necessary to properly characterize the spectra (Ricci et al. 2011; Netzer 2015; Ramos Almeida & Ricci 2017).

Thus, the use of more than one wavelength to identify AGN sources leads to a more complete statistics on the AGN population. In fact, several works have proven to be successful at identifying AGNs using optical and X-ray wavelengths for local (LaMassa et al. 2009; Vasudevan et al. 2009; Yan et al. 2011; Pouliaisis et al. 2019) and high-redshift objects (Malizia et al. 2012; Azadi et al. 2017; Agostino & Salim 2019). It is clear that the fraction of AGN sources is lower when using a single wavelength (Torbaniuk et al. 2021; Birchall et al. 2022; Comerford et al. 2022).

Our aim is to identify AGN objects in the CALIFA survey, which provides a census of the local galaxies with $z < 0.1$ using spatially resolved spectroscopy, through their X-rays properties, in order to complement the AGN census in the nearby Universe as reported through optical wavelengths by Lacerda et al. (2020). Furthermore, it allows us to compare both optical and X-ray wavelengths to understand how reliable each method is at detecting these sources, and what information is missing when only one of them is used. In this work we use data from the *Chandra* X-ray satellite (Weisskopf et al. 2002) because it provides the best spatial resolution in X-rays to date ($0.49 \text{ arcsec px}^{-1}$), crucial to properly separate our sources from emission due to gas or stellar sources in host galaxy. Moreover, we also perform a spectral analysis to characterize these sources and determine their nuclear nature and whether or not these X-ray sources can be classified as AGN.

This work is divided as follows: in Section 2 we present the parent CALIFA sample and a brief description of the data products employed for the analysis. In Section 3 we present the X-ray data reduction and imaging analysis, in Section 4 we present the spectral analysis, while in Section 5 we present the results obtained, and in Section 6 we discuss them, to finally summarize and conclude our work in Section 7. Throughout the analysis, we assume a cosmology of $H_0 = 70 \text{ km s}^{-1} \text{ Mpc}^{-1}$, $q_0 = 0$, and $\Omega_{\lambda_0} = 0.73$.

2 OPTICAL DATA SELECTION AND PROCESSING

We selected our sources from the extended CALIFA sample (eCALIFA¹; Sánchez et al. 2016c; Galbany et al. 2018). CALIFA is a survey of nearby galaxies observed at the Calar Alto 3.5m telescope, using the Potsdam MultiAperture Spectrophotometer (PMAS; Roth et al. 2005) in the PPaK configuration (Kelz et al. 2006), obtained in the low-resolution mode (V500). The sources were drawn from the 7th release of the Sloan Digital Sky Survey (SDSS DR7; Walcher et al. 2014) with most of their optical extent falling in the field-of-view (FoV) of the instrument and a spatial resolution of $\sim 1 \text{ kpc}$ ($\sim 2.5 \text{ arcsec}$ per spaxel). The final sample extends in a wide range stellar masses, and therefore a wide range of black hole masses (M_{BH}), morphological type, and colour, with redshifts $0.005 \leq z \leq 0.3$. Note, however, that restrictions on the galaxy mass are imposed in the

¹Throughout this text we will refer as CALIFA to the last available internal release of data of this project, i.e. the eCALIFA compilation.

CALIFA sample since it is known that the evolution of dwarf galaxies (i.e. $M < 10^7 M_{\odot}$) is different from that of their more massive peers. The Integral Field Unit technique (IFU) of the PMAS/PPaK allows the possibility of studying both spectroscopic and spatially resolved properties of all galaxies. Altogether, the CALIFA sample used in this work comprises 941 sources observed in the spectral range [3750–7500] Å with good quality observations in the V500 setup (Sánchez et al. 2016c, and references therein). The data have been reduced using version 2.2 of the pipeline (Sánchez et al. 2016c). This code comprises all the usual reduction steps for fibre-fed IFS (Sánchez 2006), including fibre tracing, extraction, wavelength calibration, fibre-to-fibre corrections, flux calibration, spatial re-sampling and registration, and differential atmospheric refraction correction. As a result of the reduction, a 3D cube is created, in which the spatial information is registered in the x and y axis, and the spectral one in the z axis. As reported in Sánchez et al. (2016c), the astrometry accuracy of the final datacubes is ~ 0.5 arcsec, the precision of the absolute photometric calibration is ~ 8 per cent (~ 5 per cent relative from blue to red), and the average 3σ depth of the spectra is $r \sim 23.6$ mag arcsec $^{-2}$. Further details on the data reduction and the quality of the data can be found in Sánchez et al. (2012) (see also Husemann et al. 2013; García-Benito et al. 2015; Sánchez et al. 2016c).

The Pipe3D pipeline (Sánchez et al. 2016a, b; Lacerda et al. 2022) has been applied to the CALIFA data providing a number of data base files where measurements performed in the data cubes are recorded. For the purpose of this analysis we use flux ratios of different emission lines, including the [N II] $\lambda 6584/H\alpha$, [O III] $\lambda 5007/H\beta$, [S II] $\lambda 6717/H\alpha$, and [O I] $\lambda 6301/H\alpha$, measured in three different regions of the galaxy: the inner 2.5 arcsec \times 2.5 arcsec (hereafter *centre*), effective radius, which is the radius at which half of the luminosity of the galaxy is contained (hereafter R_e) and the average across the entire galaxy (hereafter *All*). Table C1 provides these values, as well as the equivalent width (EW) of the $H\alpha$ emission line for our compiled sample when detected in the three regions mentioned above. Upper limits correspond to the 3σ limit of the corresponding flux.

3 X-RAY DATA SELECTION AND PROCESSING

We searched in the HEASARC² archive for *Chandra* observations of the 941 sources with the following criteria: we select sources that use the ACIS instrument without grating, the sources should be located within 30 arcsec from the central coordinates and the observations should have at least 5 ksec of net exposure time to impose a minimum data quality. We obtained a total of 139 sources with at least one observation. Note that in order to make sure that we select the same source in both bands, we use the coordinates from the CALIFA datacubes, which have an astrometry accuracy of 0.5 arcsec. We obtained spectra of the central 3 arcsec for these observations (in this way, we avoid possible contamination by ULXs (see Walton et al. 2011; Lehmer et al. 2020) and, for each galaxy, we keep the observation that maximizes the signal-to-noise ratio (SNR). We further discard M 87 from the analysis due to the contamination of the jet at X-rays (Prieto et al. 2016). Thus, we explore here the 138 targets (compiled sample) with the maximum number of counts observed with *Chandra*. This naturally selects observations close to the focal plane of the telescope and the longest exposures. Observational properties of the sources are indicated in Table 1.

Table 1. First 10 rows of the compiled sample of 138 sources with *Chandra* data available from the extended CALIFA sample. (1) Name of the source. (2) Observation ID in the *Chandra* data base. (3) Right ascension in degrees. (4) Declination in degrees. (5) redshift. (6) Distance in Mpc. (7) Hubble type. (8) Exposure time of the observation measured in kiloseconds. The rest of the table is available as supplementary online material.

Name	Obsid	RA (deg)	DEC (deg)	z	Dist. (Mpc)	H. T.	Exp. T. (ks)
(1)	(2)	(3)	(4)	(5)	(6)	(7)	(8)
NGC7803	6978	0.333	13.111	0.018	76.7	Sb	28.17
NGC0023	10 401	2.472	25.923	0.016	51.5	Sbc	19.98
NGC0192	8171	9.806	0.864	0.014	59.0	S0a	19.42
NGC0197	8171	9.828	0.892	0.011	58.9	E7	19.42
NGC0214	9098	10.367	25.499	0.015	51.1	Sb	5.04
NGC0384	2147	16.854	32.292	0.014	60.7	I	44.98
NGC0495	10 536	20.733	33.471	0.014	69.9	E4	18.64
NGC0499	10 536	20.798	33.46	0.015	66.8	Sbc	18.64
NGC0496	10 536	20.798	33.529	0.021	63.4	E2	18.64
NGC0504	317	20.866	33.204	0.014	64.7	Sb	27.19
NGC0507	317	20.916	33.256	0.016	69.1	Sb	27.19

3.1 X-ray data reduction

All X-ray data were reduced using the *CXC Chandra Interactive Analysis of Observations* (CIAO³) software version 3.1, following standard procedures (e.g. González-Martín et al. 2009). The exposure time was processed to exclude background flares, using the task LC_CLEAN.SL⁴ in source-free sky regions of the same observation.

We selected a circular region of 3 arcsec centred at the source coordinates. This region corresponds to the central source extraction and is used to study the existence and properties of the AGNs. We also selected an annular region with an inner radius of 3 arcsec and an outer radius that varied from 5 to 30 arcsec such that its SNR is maximized. This region corresponds to the extended emission extraction and is used to detect any possible emission associated with the host galaxy or the NLR of the AGN. Additionally, we extracted the background for both the central source and extended emission, by selecting circles around the outer radius of the annular extraction with position angles from 0 to ± 90 degrees in steps of 10 degrees. We impose a distance between the background region and the extended emission in order to avoid any possible contamination for both the central and extended regions.

We extracted the spectra of the circle, annulus, and background, as well as both ARF and RMF files, using the DMEXTRACT, MKWARF, and MKACISRMF tools. Furthermore, we produced binned spectra of both the nuclear and extended emission, with the FTGROUPPHA tool, using the optimal binning scheme by Kaastra & Bleeker (2016).

We explore possible biases in the compiled sample compared to the total CALIFA sample. The green circles and pink squares in Fig. 1 show the absolute magnitude of all the objects in the CALIFA and compiled samples, respectively, measured in the R filter compared to the cosmological distances at which they are located. Top and side histograms show the distributions of distance and magnitude, respectively, of both samples. The mean magnitude of the CALIFA sample is $\langle R \rangle = 13.76$ mag, while for the compiled sample is $\langle R \rangle = 13.08$ mag. As for the redshift, the mean value of the CALIFA sample is $\langle z \rangle = 0.019$, while for the compiled sample it is $\langle z \rangle = 0.013$. Moreover, when performing the Kolmogorov–Smirnov (KS)

³<http://asc.harvard.edu/ciao>

⁴<http://cxc.harvard.edu/ciao/download/scripts/>

²<https://heasarc.gsfc.nasa.gov>

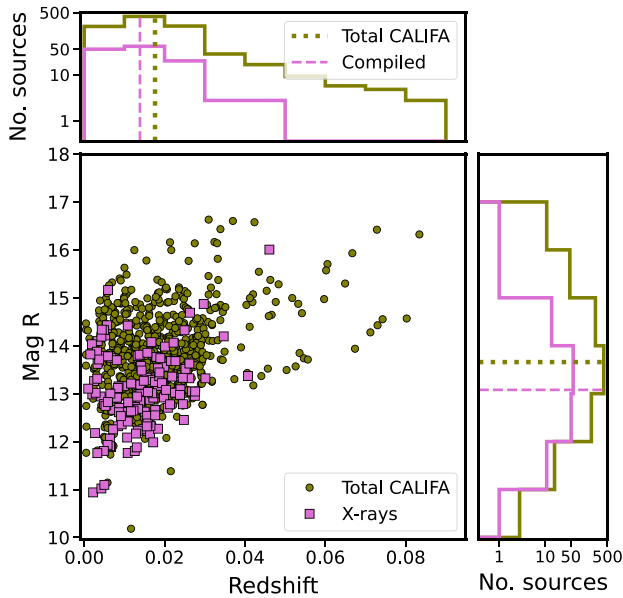


Figure 1. Magnitude in the R filter versus distance represented in redshift for the CALIFA sample (green circles) and our compiled sample (pink squares). The top and side histograms represent the distribution of redshift and magnitude, respectively, for both the CALIFA sample (green histograms) and our compiled sample (pink). Note that the axes are presented in logarithmic scale for clarity. The dotted green and dashed pink lines in both panels represent the mean value in each case for both samples (see the text).

test, we find that for the redshift, the p -value = 0.012, showing slight differences between both samples, although not very significant, while for the magnitude the p -value = 4×10^{-12} , showing much more significant differences between both samples. Therefore, our compiled sample is slightly biased towards the nearest and brightest objects, compared to the total CALIFA sample. This can be naturally explained as for a certain luminosity, sources become fainter with distance, and are harder to detect. Despite any bias, we are losing sources with shorter exposure times than 5 ks, which are discarded based on our selection criteria, although for such short exposure times, we expect for most sources to be undetected. Furthermore, we discuss possible biases on the different samples are analysed in Section 5.3.

3.2 Structural analysis of the X-ray emission

We aim to separate both the extended and nuclear X-ray emission. To do this, we start by fitting the full band image of all the 138 sources with the `Gaussian2D` model available in `PYTHON`. This model has as free parameters: amplitude a , the central coordinates (x, y) , dispersion in both directions ($dispx, dispy$), and the position angle (θ). We first fit a Gaussian profile for the central source, allowing the amplitude to vary between zero and the maximum value at the central position, which corresponds to the brightest pixel at the centre of coordinates. The x and y positions are allowed to vary ± 7 pixels (~ 1.2 arcsec), while the dispersion in both directions is allowed to vary from 0 to 4.3 pixels (i.e. ~ 1 arcsec). We minimize the values for the Gaussian profile using a least-square minimization routine included in `astropy` (`SLSQPLSQFitter`). Once we obtain the best fit for the nuclear Gaussian, we subtract it from the original image, in order to obtain a first estimate of the extended emission.

Then, to fit the extended Gaussian profile, we allow the x and y positions to vary 10 pixels (~ 1.5 arcsec), to account for the cases in which the extended emission is not in the same position of the nucleus. As for the dispersion in both directions, we visually inspect each source and depending on the extent of the diffuse emission, we allow this value to vary between 150 and 300 pixels (~ 18 – 37 arcsec). We then minimize the parameters of the extended Gaussian profile.

Once again, we subtract the modelled extended Gaussian profile from the original image. In this way, we obtain the nuclear emission. We then re-fit the nuclear emission to a Gaussian profile, subtract the corresponding nuclear Gaussian from the original image, obtaining the extended emission, and we perform a final fit on the extended emission. Note that the double loop on each component of the image allows us to properly decompose both nuclear and extended emission of the sources. In this way, we minimize the contribution of one component on the other.

We finally obtain the best-fitting parameters of the nuclear and extended Gaussian profiles, and the residuals of the fit. Our best-fitting parameters are those that minimize the residuals. Fig. 2 shows the outcome of the process for NGC 0835 as an example. The left-hand large panel (a) is the original 0.5–10.0 keV image, while (b) and (c) are the extended and nuclear Gaussians best-fitting components, respectively, (d) and (e) are the extended and nuclear emission, respectively, and (f) are the residuals of the fit.

We identify a detection of either nuclear or extended emission if the amplitude of the corresponding Gaussian profile is larger than the value of the SNR of the image at the $3\text{-}\sigma$ level. This value is determined in a source-free region in a box of 5×5 pixels. Nuclear regions with detection are referred to as detected sources in this paper. The analysis of the extended X-ray emission is the focus of a subsequent paper.

4 X-RAY SPECTRAL MODELLING

After determining the sources with nuclear detection (i.e. those for which the amplitude of the nuclear Gaussian is larger than the noise) we select those with more than 50 counts in the 0.5–7.0 keV spectra. Note that although we are able to obtain images of the full energy range, the effective area of the *Chandra* optics significantly decreases above 7 keV. Therefore, for the spectroscopic analysis we restrict the energy band to 7 keV. We model the spectra using a forward-folding approach in order to recover their physical properties.

All models used in this section are summarized in Table 2, and are motivated by previous works fitting the intrinsic continuum of AGN (González-Martín et al. 2009; Hernández-García et al. 2013, 2015; Osorio-Clavijo et al. 2020, 2022), but also by scenarios unrelated to AGN such as diffuse hot gas (perhaps from intercluster emission) among others (González-Martín et al. 2006; Yoshino et al. 2009; Ota et al. 2014). We already account for the Galactic absorption in all the models, using the `NH` tool within `FTOOLS` (retrieved from `NED`⁵ and assuming the H I maps of Kalberla et al. 2005).

For model M_1 we use a simple absorbed power law, which is the simplest approximation to the AGN intrinsic continuum at X-rays. The parameters of this model are the intrinsic absorption (material in the LOS of the AGN), photon index, and normalization. We allow

⁵<https://ned.ipac.caltech.edu>

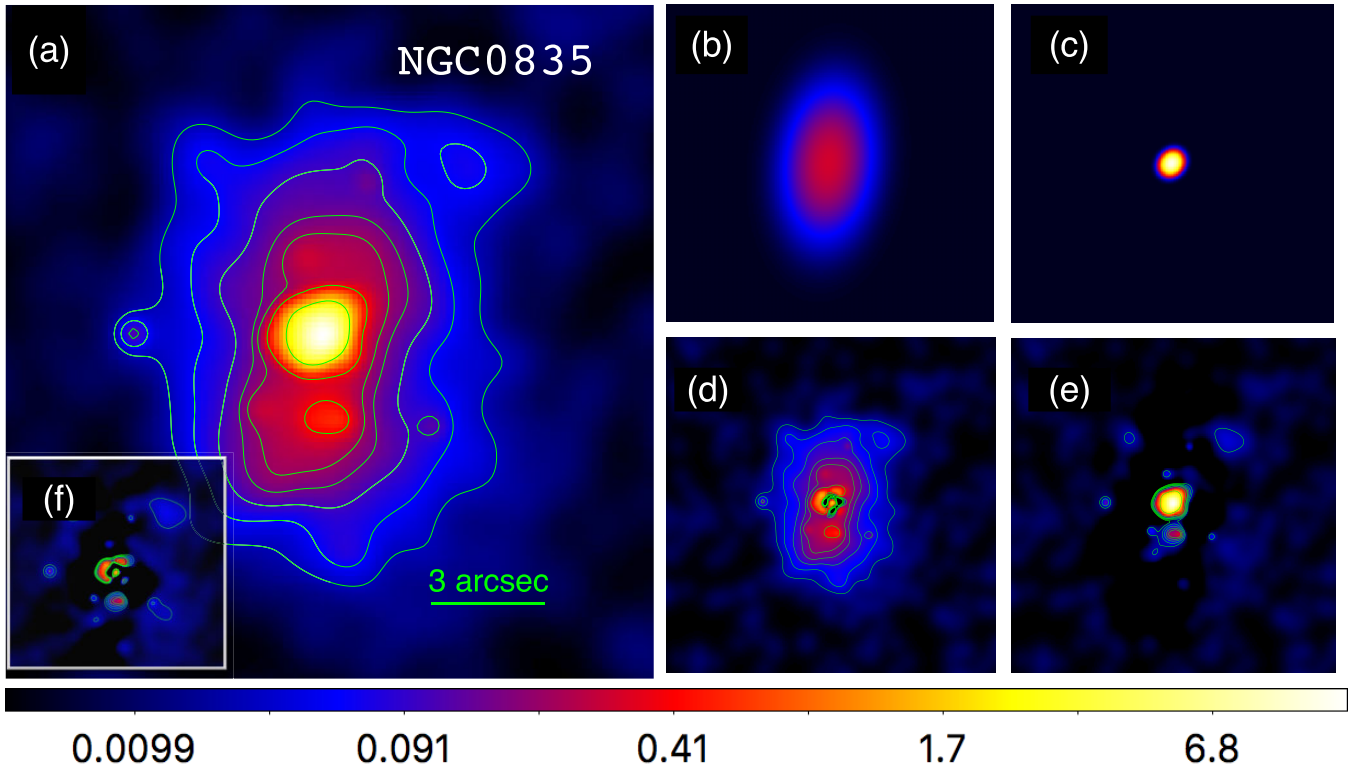


Figure 2. Gaussian fit for the extended emission in NGC 0835. (a) is the total emission, (b) is the Gaussian profile of the extended emission, (c) is the Gaussian profile of the nuclear emission, (d) corresponds to the extended emission (i.e. (a)–(c)), (e) is the nuclear emission (i.e. (a)–(b)), while (f) are the residuals of the image, once accounting for both nuclear and extended emission. The bar at the bottom corresponds to the flux range in the total emission image. Cases in which there is nuclear detection are expected to have a point-like morphology (deconvolved by the PSF of the instrument). Values in the colour-bar correspond to counts $s^{-1} \text{ pixel}^{-1}$.

Table 2. Models used in the spectroscopic analysis. In all models we already account for the Galactic absorption (see the text). Columns (2)–(6) represent the parameters used in each model version. The parameters with a dash symbol are not used in the model version. The range of variability is represented in each column. Note that each model has a normalization associated with it. For this parameter, we allow it to vary in the whole range.

(1)	$\log(N_{\text{H,int}})$ (2)	powerlaw		apec	
		Γ (3)	C_{r} (4)	kT (5)	abund (6)
M_1	22–25	0.7–3	–	–	–
M_2	–	–	–	0–1.5	1
M_3	22–25	0.7–3	0–1	–	–
M_4	22–25	0.7–3	0–1	0–1.5	1

these parameters to vary in the range presented in cols. (2), (3), and (4), respectively.

Model M_2 reproduces the spectrum of a thermal diffuse gas (apec within $x\text{SPEC}$). This model is used to represent warm thermal emission from optically thin material associated with heating, either by the AGN or any other source (e.g. stellar processes, shocks, etc). The free parameters of this model are the temperature, metal abundances, and normalization. The ranges of variation are listed in cols. (6), (7), and (8). Note that in all cases, the metal abundance is fixed to the Solar one.⁶

⁶Due to the quality of the data, the spectral fits are not sensitive to the metal abundances.

The third and fourth models are combinations of the previous two. On the one hand, M_3 represents the partial covering scenario, which has been widely used in the modelling of bona fide AGNs (González-Martín et al. 2009; Ricci et al. 2017; Osorio-Clavijo et al. 2022). In this scenario, the intrinsic absorption is not due to a uniform medium but rather is non-homogeneously distributed (in clumps/clouds or hollow cones). Note that this model can be seen as a combination of two power laws with the addition of a constant, known as the covering factor (see column (4) in Table 2). Altogether, the free parameters of M_3 are the ones listed in cols. (2)–(4) of Table 2. As for M_4 it is a combination of models 1 and 2 (i.e. $M_4 = M_1 + M_2$) and it is associated with a scenario in which the AGN is surrounded by thermal material from the host galaxy and the free parameters are all those listed in the table.

Models M_1 and M_2 are defined as *simple* models as because they are constituted by one component, while M_3 and M_4 are defined as *complex* models because they are combinations of the previous ones.

Note that we do not use more sophisticated models of AGN, first due to the quality of the data which might cause an overfitting of the data, and second because the spectral range recovered by *Chandra* is narrow and does not allow the use of such complex models. None the less, our models allow us to determine the existence of AGNs. We also tested models including a blackbody component, but they failed to reproduce any of the sources in our spectroscopic sample. In total, three out of the four models used in this work account for the AGN scenario (M_1 , M_3 , and M_4) while one model accounts for a non-AGN scenario (M_2). In the following section, we explain how we compare *simple* models to *complex*

ones and ultimately, how we choose the best-fitting model of the sources.

4.1 X-ray spectral fitting

For the spectral fitting, we use the X-ray spectral analysis software XSPEC v.12.10.0c. Due to the binning technique used in this work, we use the Cash statistic (C -statistic) throughout the analysis (Kaastra & Bleeker 2016). We start by fitting the data to the simple models (M_1 , M_2), described in the preceding section and keep the C/dof values and the number of bins. Following Buchner et al. (2014), we estimate the Bayesian Information Criterion (BIC):

$$\text{BIC} = C - m * \ln(n), \quad (1)$$

where C is the C -stat of the fit, m are the free parameters in the fit, and n is the number of data points (pha bins of the spectra). The model with the smallest BIC is the best fit one if the difference is of at least 10 when compared to the other.

If the difference between both BIC values is smaller than 10, then the two simple models produce statistically equivalent spectral fits. We then fit the data to the complex models with the following procedure:

(i) If there is only one best-fitting simple model, we fit the data with complex model including it (i.e. M_1 - M_3 , M_1 - M_4 , M_2 - M_4).

(ii) In order to test if the *complex* model is statistically significant compared to the *simple* one, we use the following criterion (in agreement with Brightman et al. 2014). For each free parameter, we require a minimum of $\delta C = 2.71$ when comparing the simple and complex models. This is equivalent to using the f -test within XSPEC.

(iii) If this condition is fulfilled, then the complex model is better than its corresponding simple one. Note that, by construction, M_3 can be compared to M_1 , and M_4 can be compared to both M_1 and M_2 . However, if both simple models are statistically equivalent, we fit the data to the corresponding complex models. In addition to using the f -test accordingly, we use the BIC value between the complex models, in order to determine if there is one preferred model over the others.

Note that this methodology allows the possibility for more than one model to be able to reproduce the observed spectra of the sources. Once we have the best-fitting model (or models) for each source, we calculate the parameters associated with it (or them) and their 1σ errors using the command `ERROR` within `xspec`.

5 RESULTS

In this section, we present the results obtained in the aforementioned morphological (Section 5.1) and spectral (Section 5.2) analyses.

5.1 Nuclear morphology

We find that 66 out of the 138 sources in the compiled sample present nuclear detection. We refer to these sources as the detected sample and it corresponds to ~ 50 per cent of the compiled sample. Table 3 shows the Gaussian parameters for the nuclei of the detected sample. To indicate that a source has nuclear detection, the amplitude of the nuclear Gaussian must be larger than the noise of the image. Moreover, the ratio between semi-axes is consistent with a point-like sources in all of the objects when accounting for the errors. Note that although we have made a thorough decomposition of the nucleus and diffuse extended emission, there might still be some contamination of thermal emission in the LOS, mostly in the soft X-ray band

Table 3. First 10 rows of the best-fitting values of the Gaussian fit for the nuclear source. Col. (1) is the name of the source, (2) is the amplitude of the nuclear Gaussian, (3) is the semimajor axis of the Gaussian, in arcsec. (4) is the ratio between the semimajor and semiminor axes, (5) is the noise of the image, calculated in a source-free region, and (6) is the contamination from the extended emission. Values with an * symbol have errors below 0.005. The rest of the table is available as supplementary online material.

Name	Amp. (cts s ⁻¹ px ⁻¹)	b (arcsec)	b/a	Noise (cts s ⁻¹ px ⁻¹)	Cont (per cent)
(1)	(2)	(3)	(4)	(5)	(6)
NGC0023	0.7 ± 0.1	0.4 ± 0.1	1*	0.039	0.33
NGC0192	0.08 ± 0.01	0.5*	1*	0.089	0.14
NGC0214	1.7 ± 0.3	0.3 ± 0.2	1.1 ± 0.2	0.009	0.04
NGC0499	0.16 ± 0.03	0.5 ± 0.1	1.1 ± 0.1	0.049	0.27
NGC0507	0.5 ± 0.6	0.2*	1*	0.058	0.27
NGC0508	0.07 ± 0.01	0.4 ± 0.3	0.9 ± 0.3	0.01	0.032
NGC0741	0.4 ± 0.1	0.6*	1*	0.09	0.31
NGC0833	0.8 ± 0.5	0.1*	1*	0.094	0.27
NGC0835	6.2 ± 7.1	0.4 ± 0.2	0.9 ± 0.2	1.636	0.015
UGC01859	0.3 ± 0.1	0.2*	1*	0.008	0.27

(i.e. below 2 keV). While for most sources this contamination is negligible, around 10 per cent of the sample (six sources) have > 50 per cent of contribution from the extended emission in the nuclear extraction. Three of these sources are spectroscopically analysed (namely NGC 2639, NGC 3842, and UGC 11958), while the remaining three do not have enough SNR in their spectra. Therefore, although the sources with nuclear detection are AGN candidates, their true nature, based on the spectroscopic analysis, is further discussed in the next section.

5.2 Spectral fits

Out of the 66 detected sources, 48 have enough quality (i.e. they have enough SNR, see Section 4) to perform a spectral fitting (hereafter spectroscopic sample). We fit them to the models described in Section 4.1 and show the C/dof for all of them in Table 4. The club-suit symbol (♣) next to the C/dof value for each model highlights the best-fitted model for the corresponding source. Out of the 48 sources, 15 prefer the M_1 model, six prefer M_2 , eight prefer M_3 , and 20 prefer M_4 . Note that one source (NGC 5675) prefers both M_3 and M_4 equally.

Table A1 shows the best-fitting parameters for the spectroscopic sample. In general terms, the photon index has a mean value of $\langle \Gamma \rangle = 1.9$, which is in agreement with the mean value for the local Universe (Nandra & Pounds 1994; Bianchi et al. 2009). The LOS column density has a mean value of $\langle \log(N_{\text{H}}) \rangle = 22.2 \text{ cm}^{-2}$, and the temperature has a mean value of $\langle kT \rangle = 0.8 \text{ keV}$. Note that all average values are determined for the best-fitting model parameters. In models with a non-negligible absorption, all but nine sources are low obscured (i.e. the obscuration has a value $N_{\text{H}} < 1 \times 10^{22} \text{ cm}^{-2}$). Additionally, the temperature in either model has average values consistent with strong thermal processes (Strickland et al. 2002), with five of them presenting temperatures above $kT > 1 \text{ keV}$.

As it was mentioned in Section 4, the simplest approximation to the AGN spectra at X-rays is a power law. Thus, objects containing a power-law component with photon index consistent with the AGN nature (i.e. $\Gamma \lesssim 3$), can be referred to as bona fide AGNs. This is the case for most objects in the sample with the exception of six (namely NGC 0507, NGC 2639, NGC 5953, NGC 6166N01, UGC 12127, and

Table 4. First 10 rows of the statistical results of the spectral fits for the nuclear extraction. Column (1) is the name of the source. Columns (2), (4), (6), and (9) are the C/dof all the models used in the analysis, respectively, while Columns (3), (5), (7), and (10) are the Bayesian Information Criterion (BIC) values for each of the models, and Columns (8) and (11) are the f-tests values for the comparison between models $M_1 - M_3$ and $M_1 - M_4/M_2 - M_4$, respectively. The club-suit (♣) symbol in each of the C/dof columns, represents the preferred model (models) for each source. The rest of the table is available as supplementary online material.

Name (1)	PL (M_1)		APEC (M_2)		2PL (M_3)		f_1 (8)	A + PL (M_4)		f_1/f_2 (11)
	C/dof (2)	BIC (3)	C/dof (4)	BIC (5)	C/dof (6)	BIC (7)		C/dof (9)	BIC (10)	
NGC0023	95.42/46	83.75	86.01/47	78.23	95.43/45	79.86	x	49.21/44♣	29.75	✓/✓
NGC0192	65.49/44	53.94	90.86/45	83.16	44.01/43♣	28.61	✓	64.21/42	44.96	x/✓
NGC0499	58.09/44	46.54	55.41/45	47.71	58.10/43	42.7	x	45.83/42♣	26.57	✓/✓
NGC0507	99.51/45	87.9	30.08/46♣	22.33	99.51/44	84.03	x	30.08/43	10.72	✓/x
NGC0741	310.20/50	298.29	91.20/51	83.25	305.01/49	289.12	✓	53.22/48♣	33.37	✓/✓
NGC0833	315.49/52	303.47	889.70/53	881.68	58.07/51♣	42.04	✓	80.84/50	60.8	✓/✓
NGC0835	989.69/60	977.26	3023.78/61	3015.5	144.52/59	127.94	✓	87.55/58♣	66.84	✓/✓
NGC1060	76.47/39	65.26	62.78/40	55.31	75.80/38	60.85	x	41.57/37♣	22.88	✓/✓
NGC1167	37.94/44♣	26.39	50.60/45	42.9	35.71/43	20.31	x	35.78/42	16.53	x/✓
NGC1277	63.91/56	51.68	95.28/57	87.12	63.91/55	47.6	x	34.83/54♣	14.44	✓/✓

NGC 7619) which are best fitted to pure-thermal models and could be in principle rejected as AGN candidates. However, these objects could also be low-luminosity sources dominated by the extended emission, or even highly obscured sources. In either case, longer exposure times are needed for the intrinsic continuum to be detected. Therefore, we treat these sources as AGN candidates, along with the rest of the detected sample, for which better SNR is needed to perform a spectral analysis. Thus, the fraction of AGN might raise when the spectroscopic sample is enlarged (such as with spectra from *XMM-Newton* and/or *NuSTAR*). Three sources (NGC 2639, NGC 3842, and UGC 11958) have a significant amount of contamination from the extended emission in the morphological decomposition. While the spectrum of NGC 2639 is described by a thermal component, NGC 3842 presents in the spectrum with both power law and thermal components, and UGC 11958 presents a second power law in the form of partial-covering. All three scenarios can explain the significant contribution of the extended emission in the nuclear region.

5.3 X-ray selection bias

After performing the morphological and spectroscopic analyses, we check if the sources within the detected (see Section 3.2) or spectroscopic (see Section 4) samples have larger exposure times and count-rate with respect to the X-ray compiled sample. Fig. 3 shows the distribution of net exposure times in the compiled X-ray sample (green histogram). Around 95 per cent of the sample (130 sources) have exposure times below 100 ks. The objects with nuclear detection have a similar distribution with the majority of them having exposure times shorter than 100 ks. Additionally, sources with enough SNR for the spectral modelling follow the same trend. Therefore, although there is a bi-modality in the distribution of sources with respect to their exposure times, we do not find a clear bias on the distribution of detected sources when compared to that of non-detected sources. Note that from the analysis in sections 3.2 and 4, around half of the sample with exposure times below 100 ks have nuclear detection (62 sources), while only 32 per cent (43 sources) have enough SNR to perform a spectral analysis. As for sources with exposure times above 100 ks, those which are detected can also be spectroscopically analysed.

On the other hand, Fig. 4 shows the distribution of count rate the different samples analysed here. Around 52 per cent of the compiled sample (72 objects, blank histogram) are not detected in the central

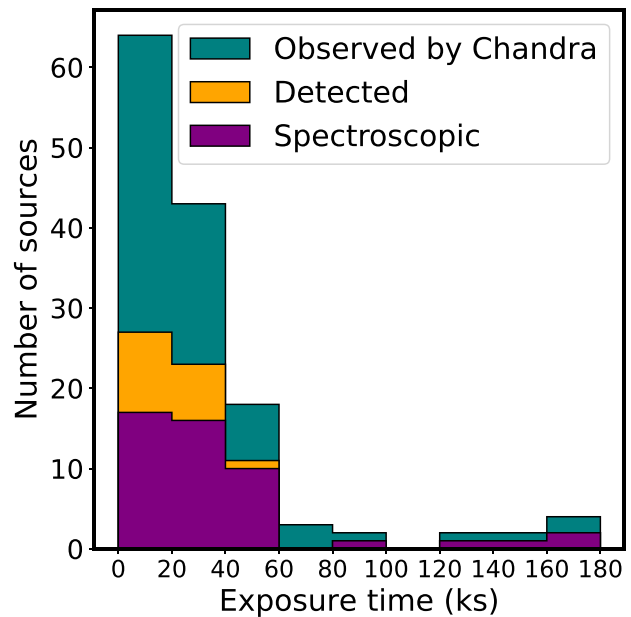


Figure 3. Histogram of the exposure times for the X-ray observations in our sample. The green, orange, and purple histograms correspond to the compiled sample (138 sources), detected sample (66 sources), and spectroscopic sample (48 sources). For detected and spectroscopic samples, see Section 3.2 and Section 4, respectively.

3 arcsec extraction, while the remaining ~ 48 per cent (66 objects) have a count rate between 10^{-5} and 1 counts s^{-1} (detected sample, see grey histogram in Fig. 4). Moreover, spectral models are applied for sources with enough SNR in the spectra (48 objects, see Section 5.2), out of which 27 are best fitted to a simple model (dashed blue histogram) and 21 are best fitted to a complex model (red dotted histogram) and have count-rates above 10^{-3} counts s^{-1} .

5.4 BPT diagrams

Once we select the AGN candidates according to the morphological (see Section 3.2) and the spectral (see Section 4) X-ray analyses, we place these objects in the three classical optical diagnostic

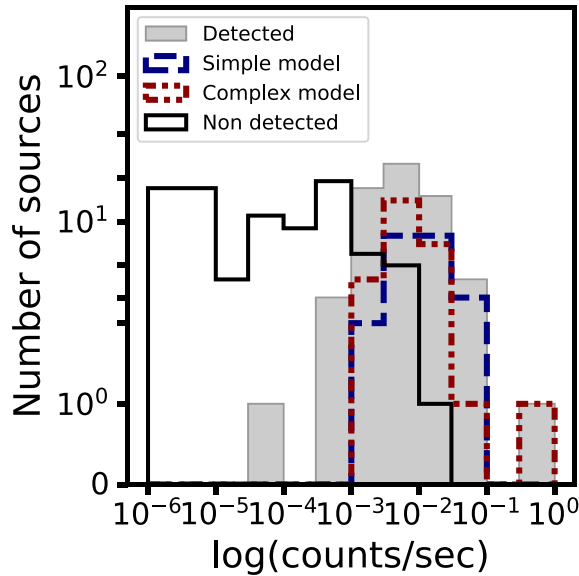


Figure 4. Distribution of count rate in the sample. The grey histogram is the distribution of sources for which there is detection in the nuclear 3 arcsec extraction, while the blue and red histograms correspond to the sources which are best fitted to simple and complex models, respectively (see Section 4). Non-detected sources are represented with the blank histogram.

diagrams: [O III]/H β versus [N II]/H α , [O III]/H β versus [S II]/H α , and [O III]/H β versus [O I]/H α . As mentioned in Section 2, the PIPE3D pipeline provides line flux measurements for three regions: *centre*, R_e , and the average across the entire galaxy. From the 138 sources in our compiled sample, 119 have constrained measurements of all the lines required for the diagnostic diagrams explored in this section, and the EW(H α) at the *centre* CALIFA region. On the other hand, 121 have complete measurements at the R_e .

The colour-coded area in both panels of Fig. 5 represent the CALIFA sample, while the white border circles and black border squares are the compiled and detected samples, respectively. The bona fide AGN are represented with a black cross symbol, while the non-AGN are marked with a black ‘x’ symbol. The colour-coded (and colour-bar at the top of both panels) represents the $\log |\text{EW}(\text{H}\alpha)|$. The yellow circles are the sources optically classified AGN in common with Lacerda et al. (2020) (namely NGC 0833, NGC 2639, NGC 5216, NGC 5675, NGC 5929, NGC 6251, NGC 3861, UGC 03995, and UGC 1859). The dot-dashed line in all panels is the Kewley et al. (2001) demarcation line between ionization from AGN and star formation. The dashed line in the [O III]/H β versus [N II]/H α panels corresponds to the one reported by Kauffmann et al. (2003) to distinguish from AGN and star forming processes. The dotted line in both [O III]/H β versus [S II]/H α and [O III]/H β versus [O I]/H α panels is the demarcation line between AGN and LINER ionization (Kewley et al. 2006).

Note that the region between the Kewley et al. (2001) and Kauffmann et al. (2003) demarcation lines is also known as mixed or composite region (although this strongly depends on the aperture/resolution of the data, e.g. Mast et al. 2014; Davies et al. 2016; Sánchez et al. 2021).

In sections 5.4.1 and 5.4.2 we explore the distribution of sources in the diagrams when the line flux ratios are measured at the *centre* and R_e CALIFA regions. Note that, irrespective of the region, we only report sources with constrained measurements of the flux line

ratios. The results found using the values at R_e and those using the average galactic value (*All*) do not present significant differences. This is expected as the values at R_e are already recovering the main characteristics of the galaxies (Sánchez et al. 2021). Fig. B1 shows the distribution of sources in the BPT diagrams for the *All* region.

5.4.1 Line flux ratios measured at the Centre

We evaluate the distribution of the objects in the BPT diagrams for all the samples. We start with the [O III]/H β versus [N II]/H α diagram (Fig. 5, left-hand panel). The distribution of objects in the CALIFA sample for this diagram has a *v* shape with two main branches (left and right), although the sources are distributed throughout all three regions (AGN/LINER, composite, and SF). Our compiled sample also reproduces this distribution. On the other hand, note that the detected sample is mostly located at the right branch of the diagram.

We start by quantifying the difference between the different samples, by performing a set of KS tests (results reported in Table 5). The *p*-value of the KS test between the CALIFA and compiled samples suggest no significant differences, while in the case of the CALIFA and detected samples, the *p*-value suggests that there are significant differences (see Table 5, Column 3), which is also the case when comparing the CALIFA and spectroscopic samples. Thus, although the compiled sample is representative of the CALIFA sample, there is a lack of X-ray detection on the left branch of this diagram. The numbers reported for the [O III]/H β versus [N II]/H α diagram (first three rows named as N II region in the panel (a) of Table 6) reinforce this result.

Indeed, around half of the CALIFA sample (426 sources) are located in the SF region of this diagram, while 24 per cent (213 sources) are located in the composite region and 28 per cent (248 sources) are located in the AGN region. As for the compiled sample, 45 sources (36 per cent) are in the SF, 36 sources (28 per cent) are in the composite region and 36 per cent are in the AGN regions. The majority of sources in the detected sample are located in either composite (29 per cent, 18 sources) or AGN (55 per cent, 34 sources) regions, with only ~ 16 per cent (10 sources) in the SF region. Interestingly, most of the sources in the non-detected sample are located in the SF region (55 per cent corresponding to 35 sources), while 27 per cent (17 sources) are located in the composite region and 18 per cent (12 sources) are located in the AGN region. This is an expected bias as X-ray observations are frequently requested for objects that a priori are expected to have a strong X-ray source. This is the case of already known AGNs, galaxy clusters and mergers and post-mergers. As for the bona fide AGN, 15 per cent (six sources) are located in the SF region, while 28 per cent (11 sources) are located in the composite region, and 57 per cent (22 sources) are located in the AGN region.

When analysing the [O III]/H β versus [S II]/H α diagram, we find that the distribution of both the CALIFA and compiled samples are very similar. This is reinforced when using KS test between these samples (see Column (4), first row of Table 5). This result is also reproduced when comparing the CALIFA sample with both the detected and spectroscopic samples (see second and third rows of Col. (4) in the same table). Fig. 5 and Table 6 (panel a) shows that ~ 60 per cent of the sources in both the CALIFA and compiled samples fall in the SF region (560 and 75, respectively), less than 10 per cent fall in the AGN region (52 and 10, respectively), while in both cases around 30 per cent of each sample fall in the LINER region (265 and 39). For the detected sample, around half of the sources (27) are located in the SF region, while around 13 per cent (8) are located

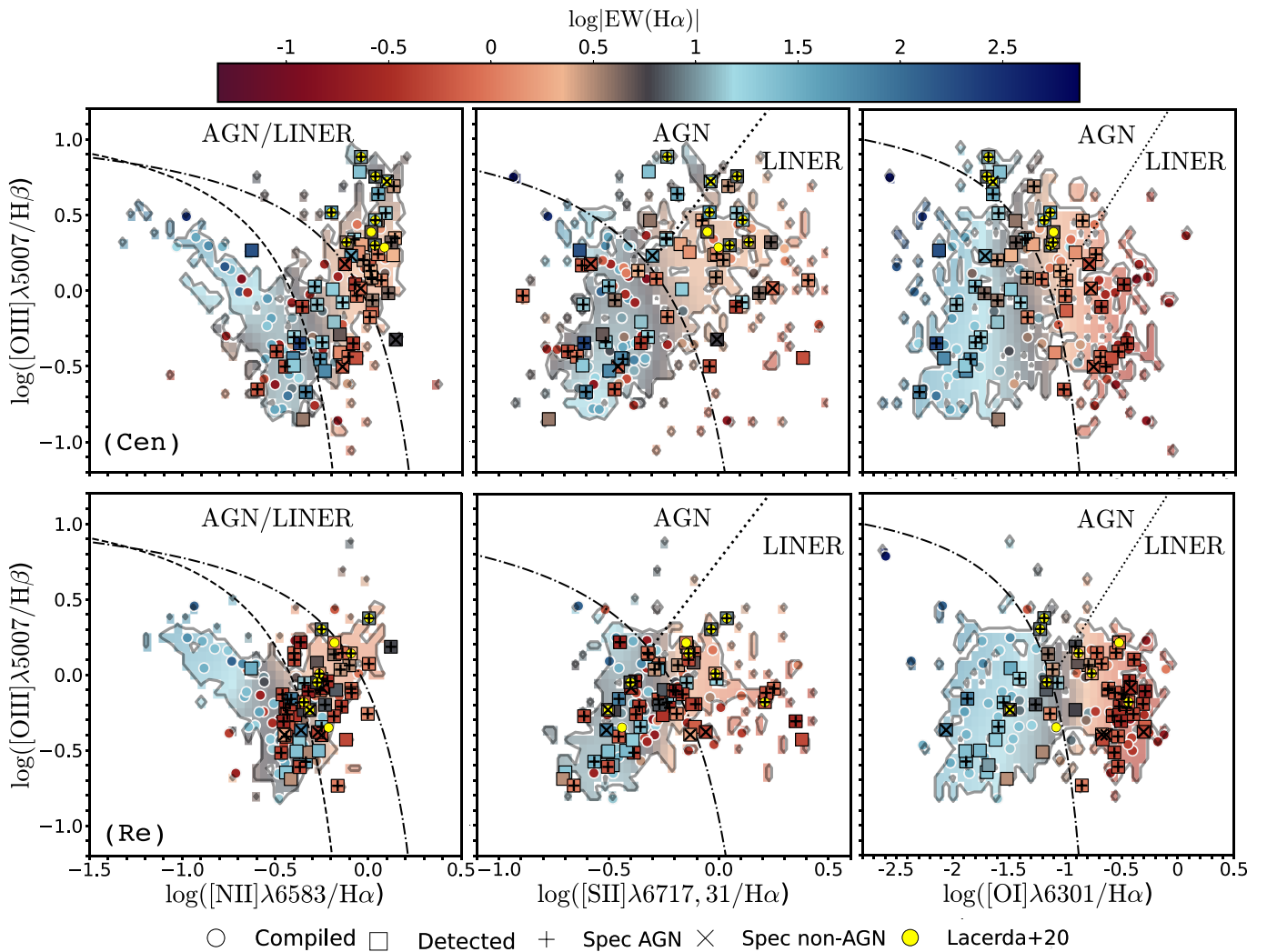


Figure 5. Top panel: diagnostic diagrams for the CALIFA measurements at the *centre* region. Bottom panel: diagnostic diagrams for the CALIFA measurements at the R_e region. In all the diagrams, the colour-coded image at the back corresponds to the CALIFA, while the white border circles, black border squares, black crosses, and \times symbols correspond to our compiled, detected, spectroscopic AGN, and non-AGN samples, respectively, and the yellow circles are the sources in common with Lacerda et al. (2020), respectively. The dot-dashed line in all panels is the Kewley et al. (2001) demarcation line between AGN and star formation ionization, the dashed line in the $[\text{O III}]/\text{H}\beta$ versus $[\text{N II}]/\text{H}\alpha$ panels is the one reported by Kauffmann et al. (2003), and the dotted line in both $[\text{O III}]/\text{H}\beta$ versus $[\text{S II}]/\text{H}\alpha$ and $[\text{O III}]/\text{H}\beta$ versus $[\text{O I}]/\text{H}\alpha$ panels is the demarcation line between AGN and LINER ionization (Kewley et al. 2006).

Table 5. KS tests performed between the CALIFA, compiled, detected, and spectroscopic samples for the BPT diagram diagnostic ratios and the distribution of the $\text{H}\alpha$ equivalent width. Column (1) is the sample compared to CALIFA, Columns (2–5) are the KS tests in each BPT diagram or $\text{EW}(\text{H}\alpha)$. The values correspond to the KS in the *centre*/ R_e region.

Sample (1)	EW (2)	O III versus N II (3)	O III versus S II (4)	O III versus O I (5)
Compiled	0.02/2e-06	0.04/0.03	0.02/0.08	0.03/2E-04
Detected	0.14/6e-06	2E-05/5E-5	0.01/0.02	0.033/0.002
Spectroscopic	–	6E-04/3E-06	0.02/0.01	0.04/4E-4

in the AGN region and 42 per cent (25) are located in the LINER region. However, when applying the KS test between the CALIFA and detected sample, they do not seem to have statistical significances (see column (4), second row of Table 5.) The behaviour of the non-detected sample is similar to both the CALIFA and compiled samples,

with most of the sources located in the SF region (48), while two are located in the AGN region and the remaining 14 sources are located in the LINER region. As for the bona fide AGN, 17 are located in the SF region, four are located in the AGN region and 17 are located in the LINER one.

In the $[\text{O III}]/\text{H}\beta$ versus $[\text{O I}]/\text{H}\alpha$ none of the KS tests performed, suggest a difference in the distribution of the samples in the *centre* measurement.

Moreover, half of the sources for the CALIFA sample fall in the SF region (549), while around 16 per cent (135) fall in the AGN region and the remaining 21 per cent (182) fall in the LINER region (Table 6, panel a). The total compiled sample is similarly distributed, with 54 per cent of the sources (66) falling in the SF region, while 17 per cent (21) fall in the AGN region and the remaining 29 per cent (34) fall in the LINER region. Non-detected and detected samples are similarly distributed, with 53 per cent and 57 per cent of the samples located in the SF region, 22 per cent and 13 per cent of the samples falling in the AGN region and 24 per cent and 32 per cent of the samples

Table 6. Number of sources for each sample in each region of the BPT diagrams. Rows 1–4 correspond to the [O III]/H β versus [N II]/H α diagram, rows 5–7 correspond to the [O III]/H β versus [S II]/H α diagram and rows 8–10 correspond to the [O III]/H β versus [O I]/H α diagram. Col. (1) is the region (i.e. SF, composite, AGN, and/or LINER) depending on the diagram. Cols. (2–7) are the CALIFA, compiled, detected, non-detected bona fide AGN, and non-AGN samples, respectively. The values in each column correspond to the number of sources, showing also between parenthesis the fraction of the corresponding sample. (a) corresponds to the measurements at the *centre* and (b) corresponds to the measurements at the R_e . Note that the fourth row in the [O III]/H β versus [N II]/H α region, corresponds to values within the AGN region which also have EW(H α) above 3 Å.

		(a)						(b)					
	(1)	CALIFA (2)	Compiled (3)	Det. (4)	Non det. (5)	AGN (6)	non-AGN (7)	CALIFA (2)	Compiled (3)	Det. (4)	Non det. (5)	AGN (6)	non-AGN (7)
N II	SF	426 (0.48)	45 (0.36)	10 (0.16)	35 (0.55)	6 (0.15)	0 (0)	595 (0.67)	72 (0.56)	24 (0.39)	48 (0.73)	12 (0.3)	2 (0.33)
	Mix	213 (0.24)	35 (0.28)	18 (0.29)	17 (0.27)	11 (0.28)	1 (0.17)	245 (0.28)	51 (0.40)	34 (0.55)	17 (0.26)	24 (0.6)	4 (0.67)
	AGN	248 (0.28)	46 (0.36)	34 (0.55)	12 (0.18)	22 (0.57)	5 (0.83)	41 (0.05)	5 (0.04)	4 (0.06)	1 (0.01)	4 (0.1)	0 (0)
	AGN + EW	83 (0.1)	21 (0.17)	18 (0.29)	3 (0.05)	12 (0.31)	3 (0.5)	11 (0.01)	2 (0.01)	2 (0.04)	0 (0)	2 (0.05)	0 (0)
S II	SF	560 (0.64)	75 (0.60)	27 (0.46)	48 (0.74)	17 (0.44)	2 (0.33)	691 (0.79)	90 (0.71)	39 (0.64)	51 (0.78)	24 (0.6)	4 (0.8)
	AGN	52 (0.06)	10 (0.09)	8 (0.13)	2 (0.03)	4 (0.12)	2 (0.33)	10 (0.01)	1 (0.01)	0 (0)	1 (0.02)	0 (0)	0 (0)
	LINER	265 (0.30)	39 (0.31)	25 (0.42)	14 (0.22)	17 (0.44)	2 (0.33)	172 (0.20)	35 (0.28)	22 (0.36)	13 (0.20)	16 (0.4)	1 (0.2)
OI	SF	549 (0.63)	66 (0.54)	31 (0.53)	35 (0.57)	20 (0.53)	1 (0.2)	504 (0.57)	48 (0.37)	19 (0.31)	29 (0.43)	8 (0.2)	2 (0.33)
	AGN	135 (0.16)	21 (0.17)	13 (0.22)	8 (0.13)	9 (0.23)	1 (0.2)	31 (0.04)	6 (0.05)	4 (0.07)	2 (0.03)	4 (0.1)	0 (0)
	LINER	182 (0.21)	34 (0.29)	14 (0.24)	20 (0.32)	9 (0.23)	3 (0.5)	346 (0.39)	75 (0.58)	38 (0.62)	37 (0.54)	28 (0.7)	4 (0.67)

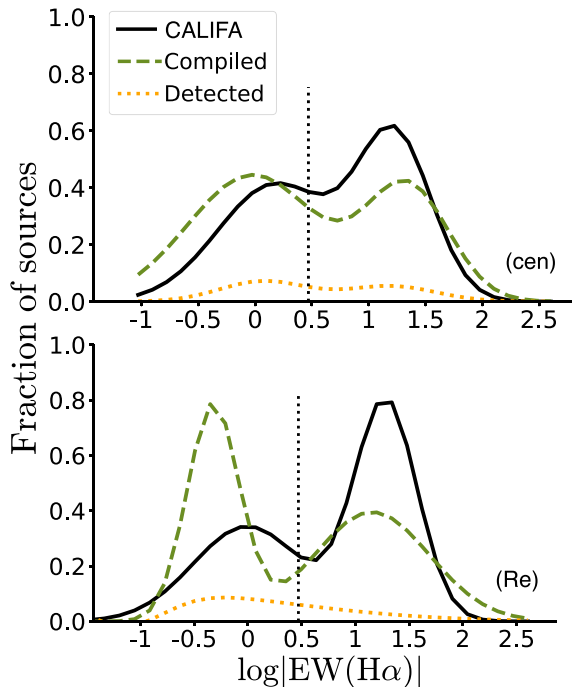


Figure 6. Top: Histogram distribution for EW(H α) measured at the *centre* region. Bottom: Histogram distribution for EW(H α) measured at the R_e region. The black, green, and orange lines correspond to the distribution of EW(H α) for the CALIFA, the X-ray compiled and detected samples, respectively, and the dotted line corresponds to the limit of EW(H α) = 3 Å imposed by Lacerda et al. (2020) for AGN sources. Both compiled and detected samples are normalized such that the integral over the range is 1. All the distributions are weighted by the total number of sources in each sample.

located in the LINER region, respectively. In the case of the bona fide AGN, 53 per cent are located in the SF region, 23 per cent are located in the AGN region and the remaining 23 per cent are located in the LINER region. As for the non-AGN, they are located evenly in all three regions of the diagram. Finally, Fig. 6 shows the distribution of the EW(H α) for the CALIFA, compiled and detected samples for sources with constrained values of flux ratios. The CALIFA sample

follows a bimodal distribution with a mean value of 0.71 ± 0.69 dex when measured at the *centre* (top panel). As for the compiled sample, the distribution has a mean value of 0.56 ± 0.83 dex. Finally, for the detected sample, the EW has a mean value of 0.57 ± 0.73 dex. Additionally, the p -value when comparing the distribution of EW in the CALIFA and compiled samples is 0.02 and 2×10^{-6} for the *centre* and R_e region (Col. 2 of the table) which suggests that the compiled sample is distributed statistically different regardless of the region when compared to the CALIFA sample. Additionally, note that the X-ray samples tend to have lower values of EW(H α), although all of the distributions have a large dispersion, i.e. span a wide set of values.

5.4.2 Line flux ratios measured at the effective radius

In the case of the [O III]/H β versus [N II]/H α diagram (panel b in Fig. 5), we find that the CALIFA and compiled samples do not have significant differences (as can be seen in Column (3), second row of Table 5). On the contrary, the CALIFA and detected samples are statistically different (see Column (3), third row of the same table), and the same happens between the CALIFA and spectroscopic samples. However, as for the number of sources in each region, most of the sources in the CALIFA, compiled and non-detected samples fall in the SF region (595, 72 and 48 sources), respectively. The second most populated region is the composite, where there are 245 sources from the CALIFA sample, 51 sources from the compiled sample, 34 sources from the detected sample, 17 sources from the non-detected sample, and 24 sources from the bona fide AGN sample. Therefore, there seems to be a preference towards the SF/composite region in all the samples. This will be further discussed in Section 6.

When analysing the [O III]/H β versus [S II]/H α diagram, the fraction of sources is similar to that at the *centre* (see panel (b) of Table 6, and there are no significant differences as seen through the KS tests between the samples (see Col. 4 in Table 5). The vast majority of sources fall in the SF region (691, 90, 39, 51, 24, and four sources from the CALIFA, compiled, detected, non-detected, bona fide AGN and non-AGN, respectively), followed by the LINER region (172, 35, 22, 13, 16, and one sources, respectively) and only few sources fall in the AGN region. Interestingly, the detected sample does not have any sources in the AGN region.

As for the [O III]/H β versus [O I]/H α diagram, 57 per cent of the CALIFA sample is located in the SF region, while 4 per cent is located in the AGN region and 39 per cent is located in the AGN region. The compiled, detected and non-detected samples follow a similar behaviour, with 37 per cent, 31 per cent, and 43 per cent of the sources in the SF region, respectively, while 5 per cent, 7 per cent, and 3 per cent are located in the AGN region, respectively, and 58 per cent, 62 per cent and 54 per cent located in the LINER region. As for the bona fide AGN sample, ~ 20 per cent fall in the SF region, 10 per cent in the AGN region and 70 per cent fall in the LINER region, while for the non-AGN, the fraction slightly changes as no source populates the AGN region. Note that in the case of the R_c measurements, the KS test suggest significant differences between the CALIFA sample and the compiled/detected/spectroscopic samples.

Finally, from the distribution of EW(H α) (Fig. 6, it is possible to see the bimodality of the CALIFA, compiled, and detected samples. The mean of the CALIFA sample is 0.75 ± 0.72 dex. As for the compiled sample, the distribution has a mean value of 0.43 ± 0.83 dex. Finally, for the detected sample, the EW has a mean value of 0.33 ± 0.70 dex. Note that in this region, there is a larger fraction of sources with EW(H α) < 0.5 dex in both the compiled and detected samples, in contrast with the fraction of sources in the CALIFA sample.

6 DISCUSSION

From the results presented in the previous section, we find that from the 138 sources studied in this analysis (i.e. ~ 15 per cent of the CALIFA) 66 present a clear nuclear emission at X-rays (~ 48 per cent of the X-ray sample and ~ 7 per cent of the CALIFA sample) out of which 42 (30 per cent of the X-ray sample and 5 per cent of the CALIFA sample) are bona fide AGN from the spectroscopic analysis. In this section, we analyse how many AGNs are in the CALIFA sample (Section 6.1), what are the differences between sources found at X-rays in contrast to those found at optical by analysing their location in the BPT diagrams (Section 6.2), and ultimately what are the benefits of studying AGN at each wavelength (Section 6.3).

6.1 AGN rate in the CALIFA

From the X-ray spectroscopic analysis, we find that 42 out of the 48 sources in the spectroscopic sample (~ 88 per cent) can be classified as bona fide AGN, while six (~ 12 per cent) can be ruled out as bona fide AGN. However, these six objects and the rest of detected nuclear sources are treated as AGN candidates.

From the 42 AGN sources classified in this analysis, six are already reported in the work by Lacerda et al. (2020) using optical wavelengths. Therefore, our work adds at least 36 extra bona fide AGN to the sample of AGN in the CALIFA survey, for a total of 70 bona fide AGNs, which raises the percentage of nuclear activity from 4 per cent to ~ 7 per cent.

Lacerda et al. (2020) found a total of 34 AGNs in the CALIFA using optical diagnostics. We find that among the nine objects classified as AGN by Lacerda et al. (2020) in common with our X-ray sample (namely NGC 0833, NGC 2639, NGC 5215, NGC 5675, NGC 5929, NGC 6251, NGC 3861, UGC 3995, and UGC 01859), all but one (NGC 3861) have clear X-ray emission based on our analysis. Interestingly, NGC 3861 presents among the shortest exposure times (see Table 1) which may be the cause for its non-

detection. Moreover, it is classified as a Type-II AGN, and therefore it might be intrinsically obscured, thus more difficult to detect. Indeed, Terashima et al. (2015) show that this object is Compton-thin obscured in X-rays. Therefore, short exposure times may also explain why we do not detect an AGN in the sources fitted to the pure-thermal scenario. This reinforces the commonly accepted scenario in which most of the X-ray detected sources are bona fide AGN.

We find in our work that six sources are not fitted to a model associated with the AGN scenario. These six sources are NGC 0507, NGC 2639, NGC 5953, NGC 6166N1, UGC 12127, and NGC 7619. NGC 2639 is the only object in common with Lacerda et al. (2020) that is not classified as bona fide AGN in our work. We find that the best-fitting model only accounts for thermal soft X-ray emission. This object is classified as a Type-II AGN in their work, which might suggest that is highly obscured and cannot be detected with the *Chandra* capabilities. This was also found by González-Martín et al. (2009); Williams et al. (2022). Additionally, Sebastian et al. (2020) finds radio emission at the core of the galaxy. Therefore, the lack of bright X-ray sources can be due to the fact that the spectral range covered by *Chandra* (only up to ~ 7 keV) might be preventing us from detecting highly obscured X-ray AGN sources (see also LaMassa et al. 2009; Yan et al. 2011; Azadi et al. 2017). Thus, information above 10 keV is crucial to ultimately ascertain the nature of this object.

None the less, other physical mechanisms can produce X-ray emission. For instance, galactic-scale outflows can produce X-ray emission in the soft X-ray band (0.5–2.0 keV). Indeed, out of the 17 galaxies in López-Cobá et al. (2019) which present galactic scale outflows seen at optical wavelengths, we have detected X-ray emission in two objects with *Chandra* (NGC 4676A and NGC 6286). Unfortunately, neither of these objects have enough SNR in the nuclear region to perform a detailed spectroscopic analysis. It should be noted, though, that these outflows can also be detected in the extended X-ray emission when they are prominent and/or very extended. From a very preliminary analysis, we note that in the case of NGC 4676A, there is a significant extended component along the major axis of the X-ray emission, which might be consistent with the outflow. In fact, the nuclear emission has a significant contribution from the extended one (~ 47 per cent). This is not the case for NGC 6286, which is not detected in the *Chandra* observation. However, this will be further explored in the following paper. Sources within the spectroscopic sample which are best-fitted with a ionized thermal component could also be candidates for outflows. This will be investigated in Paper II, aiming to understand the extended emission of these sources. X-ray binaries can also produce hard X-ray emission. In fact, their luminosities can even be up to 10^{38} erg s $^{-1}$ (see the review by Fabbiano 2006), or higher in the case of ULXs (Walton et al. 2022). Therefore, accounting for the intrinsic X-ray luminosity is an additional way to ensure the detection of AGN sources. If the central source has a luminosity above this value, a stellar process cannot account for such luminosity, and the source is most likely to be an AGN.

Thus, we explore the nature of the selected AGN when using both criteria (optical versus X-rays) based on well known correlations for $L_{(2-10 \text{ keV})}$ and $L_{[\text{O III}]}$ (Bassani et al. 1999). To do this, we estimate the luminosity of the best-fitting model for the objects in the spectroscopic sample, by adding the `clumin` component as a convolution component within XSPEC. The intrinsic luminosity is computed from the unabsorbed power-law component when the best-fit model includes it, and luminosity of the thermal component otherwise. The

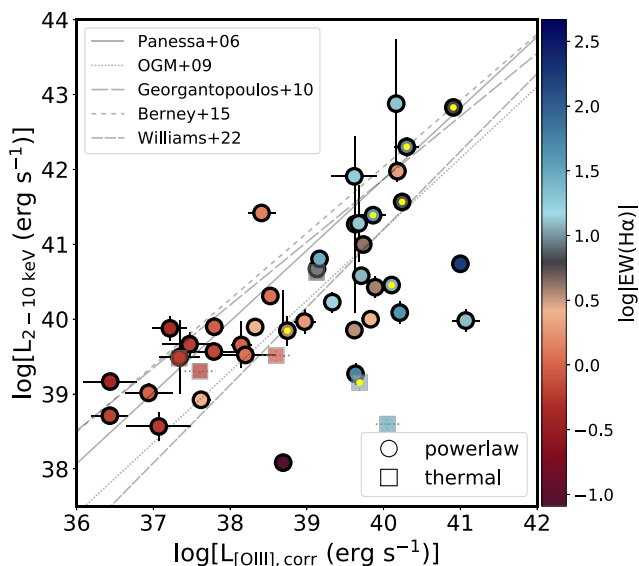


Figure 7. X-ray luminosity in the 2–10 keV band compared to the [O III] optical emission line for the spectroscopic sample. The objects are colour-coded depending on their $\text{EW}(\text{H}\alpha)$. Squares are object best-fitted to thermal models (M_2), while circles are objects best-fitted to power-law models (M_1 , M_3 , and/or M_4). The yellow dots represent sources in common with Lacerda et al. (2020). The grey solid, dotted, long-dashed, and dashed lines correspond to the correlations predicted by Panessa et al. (2006); González-Martín et al. (2009); Georgantopoulos & Akylas (2010); Berney et al. (2015) and Williams et al. (2022), respectively.

X-ray and O III^7 luminosities are reported in Columns (12) and (13) of Table A1, respectively. Note that although we fit the spectra in the 0.5–7 keV energy band, we prefer to calculate the luminosity in the 2–10 keV energy band, as it can be directly compared to the optical luminosity given the well-known correlations. We use convolution model `clumin`, which can escalate the luminosity up to 10 keV. Fig. 7 shows this relation for bona fide AGN (i.e. objects modelled as a power law, circles) and non-AGN (i.e. modelled with a thermal component, squares). We compare our results with previously found relationships between both quantities for larger samples of AGN (e.g. Panessa et al. 2006; González-Martín et al. 2009; Georgantopoulos & Akylas 2010; Berney et al. 2015; Williams et al. 2022, see caption). Although most of the sources follow the expected correlation, there are some sources that are located outside of it. This can be explained under different scenarios: high LOS obscuration, variability, the dust-correction, which might be poorly estimated for objects in which the $\text{H}\beta$ line is not constrained, and even calibration issues. This can either cause an underestimation in the X-ray luminosity or an overestimation of the [O III] luminosity.

Moreover, four of the non-AGN sources also fall along this relation, while the remaining two are clearly located outside this trend, among which is NGC 2639, optically classified as AGN. However, these six sources do not seem to follow a particular trend, opposite to what is seen with the detected sample. Indeed, four of the non-AGN sources have around the same X-ray luminosities (when accounting for errors) and different optical luminosities. However, obscuration may play an important role in these sources, for which the

⁷The $L_{[\text{O III}]}$ luminosities are corrected by dust attenuation, assuming a Balmer decrement $\text{H}\alpha/\text{H}\beta = 2.86$ and an extinction law (e.g. Cardelli, Clayton & Mathis 1989).

quality of the data might be insufficient to provide a correct estimate of the obscuration and therefore of the intrinsic X-ray luminosity. The sources in common with Lacerda et al. (2020) (yellow dots) have among the largest X-ray and optical luminosities, except for NGC 2639. This result suggests that BPT diagrams are useful to select luminous/strong AGN, but they are likely to fail at detecting most of the LLAGN. Indeed, Georgantopoulos et al. (2009) propose that for AGN with low X-ray luminosity and high [O III] luminosity, the latter might be significantly contaminated by star-formation. Similarly, Yan et al. (2011) use a sample of 146 objects at redshifts $0.3 < z < 0.8$, out of which ~ 40 per cent are classified as star-forming galaxies but their X-ray luminosity coincides with a scenario of both SF and nuclear activity, where optical emission is dominated by SF and X-ray emission is dominated by the AGN.

All put together, 42 out of 138 X-ray studied sources are bona fide AGN according to our analysis (i.e. 30 per cent), which implies an AGN population of 5 per cent among the CALIFA sample (studying X-ray data only). If all the AGN candidates are treated as AGN, this percentage will increase up to 48 per cent among the X-ray sample and 7 per cent among the CALIFA, for a total of 11 per cent of AGN sources when accounting for both optical and X-ray information. In a subsequent paper, data from *XMM-Newton* and *NuSTAR* will help us to confirm the nature of these AGN candidates and to study a larger portion of the CALIFA at X-rays. If the behaviour of the AGN candidates is similar to the spectroscopic one, we could expect up to ~ 52 AGN in the CALIFA, in addition to the 34 sources reported by Lacerda et al. (2020), which together would represent ~ 10 per cent of the CALIFA galaxies with possible nuclear activity. This might imply more than twice the AGN population compared to the optical selection (4 per cent in CALIFA according to Lacerda et al. 2020). This low percentage of 4 per cent has also been reported in the MaNGA survey (Sánchez et al. 2018), using optical information only. Indeed, Comerford et al. (2020) report a fraction of ~ 7 per cent when using multiwavelength data in that survey, which is consistent with our result when combining optical and X-ray results.

Previous X-ray censuses of AGN have shown that the fraction of AGN in the nearby Universe may be even larger. For instance, in the work by Zhang et al. (2009) where they analyse a sample of 187 nearby sources, they find that ~ 46 per cent of sources (86) present evidence of nuclear activity. They show that these sources tend to have lower Eddington rates and obscuration, which might explain why the optical fraction is lower. In addition, a similar fraction is reported by She et al. (2017) (~ 44 per cent), most of them optically classified as SF galaxies. Indeed, our lower fraction of AGN sources relies on the incompleteness that our selection criteria impose on the sample, and on the intrinsic properties with which the objects in the CALIFA sample were selected.

6.2 Location of X-ray AGN in the BPT diagrams

As indicated before, one of our main goals is to compare both optical and X-ray classification criteria. Several authors have shown that spatially resolved spectroscopy is essential to minimize the contamination from the host galaxy when exploring AGN (Singh et al. 2013; Belfiore et al. 2016; Sánchez et al. 2018; Wylezalek et al. 2018). Indeed, this can be seen in figs 5 (bottom panel) and B1, which show the position of the sources in the BPT diagrams when the line flux ratios are measured at R_e and the average value across the entire galaxy (*All*), respectively. Sources tend to group towards the centre of the diagrams and are less scattered in contrast to what is seen when the line flux ratios are measured at the 2.5 arcmin \times 2.5 arcmin *centre* aperture (Fig. 5, top panel). This effect is also

known as host galaxy dilution and can play a significant role in hiding LLAGN emission or sources hosted by galaxies with large amounts of dust (Sánchez et al. 2018; Wylezalek et al. 2018). Therefore, the R_e measurements do not seem to be as reliable to find AGN sources as the *centre* measurements.

Considering our sample of X-ray AGN candidates and bona fide AGN, the [O III]/H β versus [N II]/H α diagram is the most reliable in separating AGN candidates because the X-ray AGN candidates are clearly segregated from the main sample (see Section 5.4). On the contrary, the X-ray sources seem to be located throughout all the range of values, not showing any clear difference with the distribution of the remaining sources in the other two diagrams. Azadi et al. (2017) find that high-redshift X-ray/optical AGN are preferentially located in the right branch of the [O III]/H β versus [S II]/H α diagram, while our local AGNs are located mostly in the right branch of the [O III]/H β versus [N II]/H α diagram. However, their BPT diagrams might be similar to those when the line flux ratios are measured at R_e (see above). This is probably due to the fact that high redshift AGN are not only more severely affected by host galaxy emission (due to poorer spatial resolution) but also the redshift might cause source confusion at optical wavelengths (Azadi et al. 2017) and they might also miss heavily absorbed weak AGN at X-rays (Malizia et al. 2012).

6.3 Completeness of AGN selection criteria

In order to compare the selection at both wavelengths, and to determine which type of sources we select in each one, we determine how many objects we may lose at optical wavelengths when the different criteria are used for the BPT diagrams (i.e. completeness). In addition, we also explore how many non-AGN objects we are considering in our statistics when we relax each selection criterion as well (i.e. contamination). We only explore the [O III]/H β versus [N II]/H α diagram since it is the one providing the best separation of X-ray AGN candidates (see Section 6.2).

For both the AGN/non-AGN and detected/non-detected samples, when not applying any restriction, we obtain a total of 42 bona fide AGNs (i.e. we are 100 per cent complete) and 62 AGN candidates, although we are contaminating the sample with $\sim 13 - 51$ per cent of the non-AGN targets. This is clearly a too simplistic approach, in which it is essentially assumed that the location in the diagnostic diagrams presents no useful information regarding the presence or lack of AGN. When applying the Kauffmann et al. (2003) demarcation line, which is the less restrictive criterion to select AGN, we are lose 15 per cent of the bona fide AGN (sources that are now located at the so-called SF region of the diagram as seen in Table 6).

Additionally, by applying this criterion, the contamination decreases to a range between 13 and 36 per cent by counting non-AGN and non-detected sources, respectively. These results can be compared to those obtained by Williams et al. (2022) in which they find that 89 objects located in the AGN/LINER region of the BPT diagram have X-ray detection (which corresponds to 60 per cent of their sample). Therefore, they would be 89 per cent complete, and would have ~ 11 per cent of contamination. Furthermore, when applying the Kewley et al. (2006) line (a more restrictive selection procedure), we lose 43 per cent of the bona fide AGN, 35 per cent of the AGN candidates, and we reduce the contamination to 18–26 per cent. Therefore, we lose a significant fraction of the bona fide AGN and AGN candidates, and the contamination does not decrease significantly. This would be similar in the work by Williams et al. (2022), where there are only 13 AGN sources and the remaining

68 are LINERs. Therefore, it would correspond to ~ 14 per cent of completeness. Finally, if we impose as an additional criterion a limit on the EW of the H α line, following Lacerda et al. (2020) (i.e. considering sources with $\text{EW}(\text{H}\alpha) > 3 \text{ \AA}$ only), we miss 69 per cent of the bona fide AGN and 76 per cent of the AGN candidates, while the contamination is 16 – 20 per cent for both samples, respectively. We then miss most of the AGN and the decontamination does not improve. Thus, imposing such a restrictive criterion on the EW might be causing us to miss the weakest AGN at optical wavelengths, just detecting the brightest AGN in this spectral regime. In Fig. 7 we colour-code objects according to the $\text{EW}(\text{H}\alpha)$ to explore possible patterns with respect to this parameter. It is clear that most of the bona fide AGN at X-rays show low $\text{EW}(\text{H}\alpha)$.

It is worth noticing that using either the [O III]/H β versus [S II]/H α or the [O III]/H β versus [O I]/H α diagram, may cause a much more significant loss, up to 50 per cent AGN. This is relevant since it is usually considered that AGN selected through line ratios more sensitive to harder ionizing spectra (e.g. [S II]/H α and in particular [O I]/H α) are more reliable than those selected when using [N II]/H α . Although it should be confirmed with a larger sample, our results clearly indicate the contrary. Therefore, the strict criteria that combines the use of the Kewley demarcation line in the [O III]/H β versus [N II]/H α diagram and the $\text{EW}(\text{H}\alpha)$ are specially useful to select luminous/strong AGN, but it will clearly fail at detecting LLAGN.

Our results support the idea that the BPT diagrams, although useful at distinguishing between SF and other ionization processes, have long been misused for AGN detection (Sánchez et al. 2012; Singh et al. 2013; Cano-Díaz et al. 2016; López-Cobá et al. 2019; Lacerda et al. 2020). This is the case for the demarcation line proposed by Kewley et al. (2001), which should be used to differentiate those objects harbouring ionization processes not associated with SF. However, as most of the optically detected AGN sources are located above this line, it has been improperly used to differentiate between pure SF and pure AGN ionization. Additionally, our work reinforces the idea that a single spectral range fails at detecting all families of AGN, as each of them presents its own bias.

7 SUMMARY AND CONCLUSIONS

The AGN population in the CALIFA was previously reported to be 4 per cent by Lacerda et al. (2020) using optical emission line ratios and the diagnostic diagrams. In this work we have performed an analysis aiming to complement the fraction of AGN sources in the CALIFA (941 sources), using X-ray data from *Chandra* for the 138 sources with X-ray observations, and to compare the differences of identifying AGN sources at both spectral ranges. Here we summarize our main results:

- (i) The fraction of bona fide AGN sources in the CALIFA survey is 7 per cent when accounting for optical and X-ray spectroscopic analyses. However, this fraction could rise up to 10 per cent if AGN candidates are treated as bona fide.
- (ii) X-ray sources are mostly distributed along the right branch in the [O III]/H β versus [N II]/H α , while there is no preferential location for these sources in neither [O III]/H β versus [S II]/H α or [O III]/H β versus [O I]/H α . This suggests that [O III]/H β versus [N II]/H α is the most reliable diagram to detect AGN sources.
- (iii) Using only optical data might cause a significant loss of AGN sources that could be obscured by the host galaxy, sources which could be hosted by a high SFR galaxy and low-luminosity AGN. The

best way to get a complete statistics on the AGN population is by using multiwavelength information.

(iv) Objects classified as AGN at both wavelengths have among the largest X-ray and optical luminosities, suggesting that a strict criterion in the EW might be biased towards brighter sources.

(v) Most of our bona fide AGN follow the expected correlation between $L(2 - 10 \text{ keV})$ and $L[\text{O III}]$ which reinforces the AGN nature of these sources.

Finally, sources detected at optical wavelengths but missing at X-rays could be intrinsically obscured, unreachable by the capabilities of *Chandra*. Observations from more sensitive instruments (e.g. *XMM-Newton*) or at higher energies (e.g. *NuSTAR*) might help to disentangle this effect.

ACKNOWLEDGEMENTS

We thank the anonymous referee for her/his comments which significantly improved this work. This research has made use of data obtained from the Chandra Data Archive and the Chandra Source Catalog, and software provided by the Chandra X-ray Center (CXC) in the application packages CIAO and Sherpa. We acknowledge support from ESA through the Science Faculty – Funding reference ESA-SCI-SC-LE-083. NOC and OGM acknowledge support from DGAPA, UNAM grant IN105720. NOC would like to thank CONACyT scholarship No. 897887. ICG acknowledges support from DGAPA, UNAM grant IN119123.

DATA AVAILABILITY

The X-ray data underlying this article are available in <https://heasarc.gsfc.nasa.gov/>. The data sets were derived from sources in the public domain. The optical data underlying this article are available <https://califa.caha.es/>.

REFERENCES

- Agostino C. J., Salim S., 2019, *ApJ*, 876, 12
 Antonucci R., 1993, *ARA&A*, 31, 473
 Azadi M. et al., 2017, *ApJ*, 835, 27
 Baldwin J. A., Phillips M. M., Terlevich R., 1981, *PASP*, 93, 5
 Bassani L., Dadina M., Maiolino R., Salvati M., Risaliti G., Della Ceca R., Matt G., Zamorani G., 1999, *ApJS*, 121, 473
 Belfiore F. et al., 2016, *MNRAS*, 461, 3111
 Berney S. et al., 2015, *MNRAS*, 454, 3622
 Bianchi S., Bonilla N. F., Guainazzi M., Matt G., Ponti G., 2009, *A&A*, 501, 915
 Birchall K. L., Watson M. G., Aird J., Starling R. L. C., 2022, *MNRAS*, 510, 4556
 Bower R. G., Benson A. J., Malbon R., Helly J. C., Frenk C. S., Baugh C. M., Cole S., Lacey C. G., 2006, *MNRAS*, 370, 645
 Brandt W. N., Alexander D. M., 2015, *A&AR*, 23, 1
 Brightman M., Nandra K., 2008, *MNRAS*, 390, 1241
 Brightman M., Nandra K., Salvato M., Hsu L.-T., Aird J., Rangel C., 2014, *MNRAS*, 443, 1999
 Buchner J. et al., 2014, *A&A*, 564, A125
 Cann J. M., Satyapal S., Abel N. P., Blecha L., Mushotzky R. F., Reynolds C. S., Secrest N. J., 2019, *ApJ*, 870, L2
 Cano-Díaz M. et al., 2016, *ApJ*, 821, L26
 Cardelli J. A., Clayton G. C., Mathis J. S., 1989, *ApJ*, 345, 245
 Comastri A., Setti G., Zamorani G., Hasinger G., 1995, *A&A*, 296, 1
 Comastri A. et al., 2011, *A&A*, 526, L9
 Comerford J. M. et al., 2020, *ApJ*, 901, 159
 Comerford J. M., Negus J., Barrows R. S., Wylezalek D., Greene J. E., Müller-Sánchez F., Nevin R., 2022, *ApJ*, 927, 23
 Davies L. J. M. et al., 2016, *MNRAS*, 461, 458
 Fabbiano G., 2006, *ARA&A*, 44, 323
 Fabian A. C., 2012, *ARA&A*, 50, 455
 Fabian A. C., Iwasawa K., 2000, *Adv. Space Res.*, 25, 471
 Galbany L., Collett T. E., Méndez-Abreu J., Sánchez S. F., Anderson J. P., Kuncarayakti H., 2018, *MNRAS*, 479, 262
 García-Benito R. et al., 2015, *A&A*, 576, A135
 Georgantopoulos I., Akylas A., 2010, *A&A*, 509, A38
 Georgantopoulos I., Akylas A., Georgakakis A., Rowan-Robinson M., 2009, *A&A*, 507, 747
 González-Martín O., Masegosa J., Márquez I., Guerrero M. A., Dultzin-Hacyan D., 2006, *A&A*, 460, 45
 González-Martín O., Masegosa J., Márquez I., Guainazzi M., Jiménez-Bailón E., 2009, *A&A*, 506, 1107
 Goulding A. D., Alexander D. M., 2009, *MNRAS*, 398, 1165
 Heckman T. M., 1980, *A&A*, 87, 152
 Hernández-García L., González-Martín O., Márquez I., Masegosa J., 2013, *A&A*, 556, A47
 Hernández-García L., Masegosa J., González-Martín O., Márquez I., 2015, *A&A*, 579, A90
 Hopkins P. F. et al., 2010, *ApJ*, 715, 202
 Husemann B. et al., 2013, *A&A*, 549, A87
 Kaastra J. S., Bleeker J. A. M., 2016, *A&A*, 587, A151
 Kalberla P. M. W., Burton W. B., Hartmann D., Arnal E. M., Bajaja E., Morras R., Pöppel W. G. L., 2005, *A&A*, 440, 775
 Kauffmann G. et al., 2003, *MNRAS*, 346, 1055
 Kelz A. et al., 2006, *PASP*, 118, 129
 Kewley L. J., Dopita M. A., Sutherland R. S., Heisler C. A., Trevena J., 2001, *ApJ*, 556, 121
 Kewley L. J., Groves B., Kauffmann G., Heckman T., 2006, *MNRAS*, 372, 961
 Kewley L. J., Maier C., Yabe K., Ohta K., Akiyama M., Dopita M. A., Yuan T., 2013, *ApJ*, 774, L10
 LaMassa S. M., Heckman T. M., Ptak A., Hornschemeier A., Martins L., Sonnentrucker P., Tremonti C., 2009, *ApJ*, 705, 568
 Lacerda E. A. D., Sánchez S. F., Cid Fernandes R., López-Cobá C., Espinosa-Ponce C., Galbany L., 2020, *MNRAS*, 492, 3073
 Lacerda E. A. D., Sánchez S. F., Mejía-Narváez A., Camps-Fariña A., Espinosa-Ponce C., Barrera-Ballesteros J. K., Ibarra-Medel H., Lugo-Aranda A. Z., 2022, *New Astron.*, 97, 101895
 Lehmer B. D. et al., 2020, *ApJS*, 248, 31
 López-Cobá C., Sánchez S. F., Bland-Hawthorn J., Moiseev A. V., Cruz-González I., García-Benito R., Barrera-Ballesteros J. K., Galbany L., 2019, *MNRAS*, 482, 4032
 Malizia A., Bassani L., Bazzano A., Bird A. J., Masetti N., Panessa F., Stephen J. B., Ubertini P., 2012, *MNRAS*, 426, 1750
 Mast D. et al., 2014, *A&A*, 561, A129
 Moran E. C., Filippenko A. V., Chornock R., 2002, *ApJ*, 579, L71
 Murphy K. D., Yaqoob T., 2009, *MNRAS*, 397, 1549
 Nandra K., Pounds K. A., 1994, *MNRAS*, 268, 405
 Netzer H., 2015, *ARA&A*, 53, 365
 Osorio-Clavijo N., González-Martín O., Papadakis I. E., Masegosa J., Hernández-García L., 2020, *MNRAS*, 491, 29
 Osorio-Clavijo N., González-Martín O., Sánchez S. F., Esparza-Arredondo D., Masegosa J., Victoria-Ceballos C., Hernández-García L., Díaz Y., 2022, *MNRAS*, 510, 5102
 Ota N., Nagayoshi K., Pratt G. W., Kitayama T., Oshima T., Reiprich T. H., 2014, *A&A*, 562, A60
 Panessa F., Bassani L., Cappi M., Dadina M., Barcons X., Carrera F. J., Ho L. C., Iwasawa K., 2006, *A&A*, 455, 173
 Pouliaxis E. et al., 2019, *MNRAS*, 487, 4285
 Prieto M. A., Fernández-Ontiveros J. A., Markoff S., Espada D., González-Martín O., 2016, *MNRAS*, 457, 3801
 Ramos Almeida C., Ricci C., 2017, *Nat. Astron.*, 1, 679
 Ricci C., Walter R., Courvoisier T. J. L., Paltani S., 2011, *A&A*, 532, A102

- Ricci C. et al., 2017, *ApJS*, 233, 17
- Richard J., Jones T., Ellis R., Stark D. P., Livermore R., Swinbank M., 2011, *MNRAS*, 413, 643
- Roberts T. P., Warwick R. S., 2000, *MNRAS*, 315, 98
- Roth M. M. et al., 2005, *PASP*, 117, 620
- Sánchez S. F., 2006, *Astron. Nachr.*, 327, 850
- Sánchez S. F. et al., 2012, *A&A*, 538, A8
- Sánchez S. F. et al., 2016a, *Rev. Mex. Astron. Astrofis.*, 52, 21
- Sánchez S. F. et al., 2016b, *Rev. Mex. Astron. Astrofis.*, 52, 171
- Sánchez S. F. et al., 2016c, *A&A*, 594, A36
- Sánchez S. F. et al., 2018, *Rev. Mex. Astron. Astrofis.*, 54, 217
- Sánchez S. F., Walcher C. J., Lopez-Cobá C., Barrera-Ballesteros J. K., Mejía-Narváez A., Espinosa-Ponce C., Camps-Fariña A., 2021, *Rev. Mex. Astron. Astrofis.*, 57, 3
- Sebastian B., Kharb P., O’Dea C. P., Gallimore J. F., Baum S. A., 2020, *MNRAS*, 499, 334
- She R., Ho L. C., Feng H., 2017, *ApJ*, 842, 131
- Singh R. et al., 2013, *A&A*, 558, A43
- Strickland D. K., Heckman T. M., Weaver K. A., Hoopes C. G., Dahlem M., 2002, *ApJ*, 568, 689
- Terashima Y., Hirata Y., Awaki H., Oyabu S., Gandhi P., Toba Y., Matsuhara H., 2015, *ApJ*, 814, 11
- Torbaniuk O., Paolillo M., Carrera F., Cavuoti S., Vignali C., Longo G., Aird J., 2021, *MNRAS*, 506, 2619
- Trump J. R. et al., 2009, *ApJ*, 706, 797
- Trump J. R. et al., 2015, *ApJ*, 811, 26
- Trussler J., Maiolino R., Maraston C., Peng Y., Thomas D., Goddard D., Lian J., 2020, *MNRAS*, 491, 5406
- Ueda Y., Akiyama M., Ohta K., Miyaji T., 2003, *ApJ*, 598, 886
- Urry C. M., Padovani P., 1995, *PASP*, 107, 803
- Vasudevan R. V., Mushotzky R. F., Winter L. M., Fabian A. C., 2009, *MNRAS*, 399, 1553
- Veilleux S., Osterbrock D. E., 1987, *ApJS*, 63, 295
- Walcher C. J. et al., 2014, *A&A*, 569, A1 (W14)
- Walton D. J., Roberts T. P., Mateos S., Heard V., 2011, *MNRAS*, 416, 1844
- Walton D. J., Mackenzie A. D. A., Gully H., Patel N. R., Roberts T. P., Earnshaw H. P., Mateos S., 2022, *MNRAS*, 509, 1587
- Weisskopf M. C., Brinkman B., Canizares C., Garmire G., Murray S., Van Speybroeck L. P., 2002, *PASP*, 114, 1
- Williams D. R. A. et al., 2022, *MNRAS*, 510, 4909
- Wills B. J., Netzer H., Wills D., 1985, *ApJ*, 288, 94
- Wylezalek D., Zakamska N. L., Greene J. E., Riffel R. A., Drory N., Andrews B. H., Merloni A., Thomas D., 2018, *MNRAS*, 474, 1499
- Yan R. et al., 2011, *ApJ*, 728, 38
- Yoshino T. et al., 2009, *PASJ*, 61, 805
- Zhang W. M., Soria R., Zhang S. N., Swartz D. A., Liu J. F., 2009, *ApJ*, 699, 281

SUPPORTING INFORMATION

Supplementary data are available at *MNRAS* online.

suppl_data

Please note: Oxford University Press is not responsible for the content or functionality of any supporting materials supplied by the authors. Any queries (other than missing material) should be directed to the corresponding author for the article.

APPENDIX A: BEST-FITTING PARAMETERS OF THE SPECTRAL FITS

We present here the best-fitting parameters of the spectral fits performed in Section 4.1.

Table A1. Best-fitting values for the spectral analysis of the spectroscopic sample. In all model versions, we only list for each object, the best-fitting values, i.e. the values of the model(s) that best fit the data. Column (1) are the names of the sources, Column (2) is the AGN classification according to the spectral analysis. Columns (3), (6), (9), and (12) are the column densities (obscuration in the los) in units of cm^{-2} , while Columns (4), (7), (10), and (14) are the photon indices of the power law, Columns (5), (11), and (14) are the temperatures of the plasma or neutral material and Column (8) is the covering fraction of the source. Note that we do not list model M_3 as none of the sources are best fitted to this model.

Name	Type	M_1 $\log(N_{\text{H}})$ (cm^{-2})	Γ	M_2 kT (keV)	$\log(N_{\text{H}})$ (cm^{-2})	M_3 Γ	Cfrac	$\log(N_{\text{H}})$ (cm^{-2})	M_4 Γ	kT (keV)	$\log(L_{2-10 \text{ keV}})$ erg s^{-1}	$\log(L_{\text{OIII}})$ erg s^{-1}
(1)	(2)	(3)	(4)	(5)	(6)	(7)	(8)	(9)	(10)	(11)	(12)	(13)
NGC0023	AGN	-	-	-	-	-	-	<20.9	$1.9^{+0.3}_{-0.4}$	$0.9^{+0.1}_{-0.1}$	40.1 ± 0.1	40.21 ± 0.04
NGC0192	AGN	-	-	-	$24.3^{+0.2}_{-0.2}$	$2.4^{+0.3}_{-0.3}$	<0.003	-	-	-	42.9 ± 0.8	40.2 ± 0.1
NGC0499	AGN	-	-	-	-	-	-	<21.4	>1.6	$1.2^{+0.1}_{-0.1}$	39.7 ± 0.3	38.2 ± 0.1
NGC0507	Non-AGN	-	-	$0.9^{+0.1}_{-0.1}$	-	-	-	-	-	-	39.5 ± 0.2	37.3 ± 0.1
NGC0741	AGN	-	-	-	-	-	-	<21.2	>2.9	$0.78^{+0.03}_{-0.03}$	39.6 ± 0.1	37.8 ± 0.4
NGC0833	AGN	-	-	-	$23.49^{+0.04}_{-0.04}$	$2.2^{+0.3}_{-0.3}$	<0.01	-	-	-	41.6 ± 0.1	40.2 ± 0.1
NGC0835	AGN	-	-	-	-	-	-	$23.30^{+0.03}_{-0.03}$	<0.8	$0.84^{+0.03}_{-0.03}$	41.91 ± 0.03	39.6 ± 0.3
NGC1060	AGN	-	-	-	-	-	-	$21.6^{+0.3}_{-0.6}$	>2.4	$0.9^{+0.1}_{-0.1}$	39.9 ± 0.1	37.8 ± 0.1
NGC1167	AGN	<20.9	$2.5^{+0.3}_{-0.3}$	-	-	-	-	-	-	-	39.9 ± 0.1	41.1 ± 0.2
NGC1277	AGN	-	-	-	-	-	-	$21.1^{+0.3}_{-0.6}$	$1.6^{+0.3}_{-0.3}$	$1.1^{+0.1}_{-0.1}$	40.01 ± 0.09	<38.7
UGC03816	AGN	-	-	-	$24.1^{+0.4}_{-0.4}$	$2.4^{+0.3}_{-0.3}$	<0.12	-	-	-	41.3 ± 1.2	39.6 ± 0.1
UGC03995	AGN	-	-	-	$23.7^{+0.1}_{-0.1}$	$2.2^{+0.3}_{-0.3}$	<0.2	-	-	-	42.3 ± 0.1	40.3 ± 0.2
NGC2445	AGN	-	-	-	-	-	-	$21.9^{+0.2}_{-0.3}$	>2.4	$0.9^{+0.1}_{-0.1}$	39.3 ± 0.1	39.6 ± 0.1
NGC2484	AGN	<20.9	$2.0^{+0.3}_{-0.2}$	-	-	-	-	-	-	-	41.9 ± 0.1	40.2 ± 0.1
NGC2623	AGN	-	-	-	$23.7^{+0.3}_{-0.4}$	<1.2	$0.2^{+0.7}_{-0.2}$	-	-	-	41.3 ± 0.5	39.67 ± 0.04
NGC2639	Non-AGN	-	-	>1.5	-	-	-	-	-	-	39.1 ± 0.1	39.6 ± 0.1
NGC2787	AGN	$21.1^{+0.1}_{-0.2}$	$2.2^{+0.2}_{-0.2}$	-	-	-	-	-	-	-	38.9 ± 0.1	37.6 ± 0.1
PGC32873	AGN	-	-	-	-	-	-	<21.4	$1.6^{+0.5}_{-0.3}$	$0.9^{+0.1}_{-0.1}$	40.3 ± 0.1	<38.7
PGC033423	AGN	-	-	-	-	-	-	$21.4^{+0.4}_{-1.2}$	$1.8^{+0.5}_{-0.4}$	$0.7^{+0.1}_{-0.1}$	40.7 ± 0.1	39.13 ± 0.04
NGC3842	AGN	-	-	-	-	-	-	$21.6^{+0.3}_{-0.3}$	>2.6	$0.96^{+0.03}_{-0.03}$	39.7 ± 0.2	37.5 ± 0.4
NGC3860	AGN	$20.9^{+0.2}_{-0.5}$	$1.6^{+0.2}_{-0.2}$	-	-	-	-	-	-	-	40.6 ± 0.1	39.7 ± 0.1

Table A1 – continued

Name	Type	M ₁		M ₂		M ₃		Cfrac	M ₄		log(L _{2–10 keV})	log(L _{OIII})
		log(N _H) (cm ⁻²)	Γ	kT (keV)	log(N _H) (cm ⁻²)	Γ	log(N _H) (cm ⁻²)		Γ	kT (keV)		
(1)	(2)	(3)	(4)	(5)	(6)	(7)	(8)	(9)	(10)	(11)	(12)	(13)
NGC3945	AGN	20.8 ^{+0.3} _{-0.7}	2.4 ^{+0.2} _{-0.3}	-	-	-	-	-	-	-	39.5 ± 0.1	38.1 ± 0.4
NGC4291	AGN	-	-	-	-	-	-	21.9 ^{+0.4} _{-0.9}	>1.4	0.7 ^{+0.1} _{-0.1}	39.2 ± 0.1	36.4 ± 0.3
NGC4486B	AGN	<20.9	1.9 ^{+0.2} _{-0.2}	-	-	-	-	-	-	-	38.7 ± 0.1	36.4 ± 0.2
NGC4676B	AGN	<21.4	1.8 ^{+0.4} _{-0.4}	-	-	-	-	-	-	-	40.2 ± 0.1	39.33 ± 0.01
NGC4874	AGN	-	-	-	-	-	-	21.4 ^{+0.3} _{-0.6}	>2	1.0 ^{+0.1} _{-0.1}	39.9 ± 0.2	37.2 ± 0.2
NGC5216	AGN	<21.44	>1.94	-	-	-	-	-	-	-	39.9 ± 0.2	38.7 ± 0.1
NGC5395	AGN	<21.4	1.5 ^{+0.6} _{-0.3}	-	-	-	-	-	-	-	39.9 ± 0.2	38.9 ± 0.1
NGC5532	AGN	-	-	-	-	-	-	21.3 ^{+0.4} _{-0.4}	1.2 ^{+0.2} _{-0.1}	0.79 ^{+0.02} _{-0.02}	41.42 ± 0.03	38.4 ± 0.1
NGC5576	AGN	<21.6	>1.8	-	-	-	-	-	-	-	38.6 ± 0.2	37.1 ± 0.4
NGC5614	AGN	<20.9	2.3 ^{+0.3} _{-0.2}	-	-	-	-	-	-	-	39.9 ± 0.1	39.8 ± 0.1
NGC5623	AGN	<21.1	2.2 ^{+0.3} _{-0.3}	-	-	-	-	-	-	-	39.9 ± 0.1	38.3 ± 0.1
NGC5675	AGN	-	-	-	22.7 ^{+0.1} _{-0.2}	>1.9	0.03 ^{+0.06} _{-0.01}	22.8 ^{+0.1} _{-0.2}	>2.3	>1.4	40.4 ± 0.1	40.11 ± 0.02
NGC5845	AGN	<21.3	1.8 ^{+0.4} _{-0.3}	-	-	-	-	-	-	-	39.0 ± 0.1	36.9 ± 0.3
NGC5929	AGN	-	-	-	23.3 ^{+0.1} _{-0.1}	1.4 ^{+0.3} _{-0.3}	0.05 ^{+0.03} _{-0.02}	-	-	-	41.4 ± 0.1	39.9 ± 0.2
NGC5953	Non-AGN	-	-	1.0 ^{+0.1} _{-0.1}	-	-	-	-	-	-	38.6 ± 0.1	40.1 ± 0.2
ARP220	AGN	-	-	-	-	-	-	21.7 ^{+0.2} _{-0.2}	0.9 ^{+0.2} _{-0.2}	0.9 ^{+0.1} _{-0.1}	40.81 ± 0.03	39.2 ± 0.1
NGC6090	AGN	-	-	-	-	-	-	21.9 ^{+0.2} _{-0.5}	>2.3	0.9 ^{+0.1} _{-0.1}	40.7 ± 0.1	41.00 ± 0.05
NGC6125	AGN	-	-	-	-	-	-	<20	3*	0.9 ^{+0.1} _{-0.1}	39.5 ± 0.5	37.3 ± 0.3
NGC6166N1	Non-AGN	-	-	>1.5	-	-	-	-	-	-	40.62 ± 0.02	39.13 ± 0.03
NGC6251	AGN	-	-	-	-	-	-	21.2 ^{+0.1} _{-0.1}	1.55 ^{+0.03} _{-0.03}	0.29 ^{+0.02} _{-0.01}	42.83 ± 0.01	40.91 ± 0.04
NGC6278	AGN	21.2 ^{+0.2} _{-0.3}	1.9 ^{+0.2} _{-0.2}	-	-	-	-	-	-	-	40.3 ± 0.1	38.5 ± 0.1
NGC6338	AGN	-	-	-	-	-	-	21.3 ^{+0.2} _{-0.2}	>2.9	1.10 ^{+0.04} _{-0.05}	40.4 ± 0.1	39.89 ± 0.03
UGC11958	AGN	-	-	-	22.1 ^{+0.1} _{-0.2}	2.4 ^{+0.4} _{-0.4}	0.06 ^{+0.05} _{-0.03}	-	-	-	40.9 ± 0.1	39.74 ± 0.03
UGC12127	Non-AGN	-	-	0.8 ^{+0.1} _{-0.1}	-	-	-	-	-	-	39.5 ± 0.1	38.6 ± 0.2
NGC7457	AGN	<20.8	>2.8	-	-	-	-	-	-	-	38.1 ± 0.1	<38.7
NGC7619	Non-AGN	-	-	0.97 ^{+0.02} _{-0.03}	-	-	-	-	-	-	39.30 ± 0.03	37.6 ± 0.2
NGC7052	AGN	-	-	-	-	-	-	<21.19	2.35 ^{+0.31} _{-0.27}	0.74 ^{+0.07} _{-0.10}	39.8 ± 0.1	39.619 ± 0.001

APPENDIX B: BPT DIAGRAMS

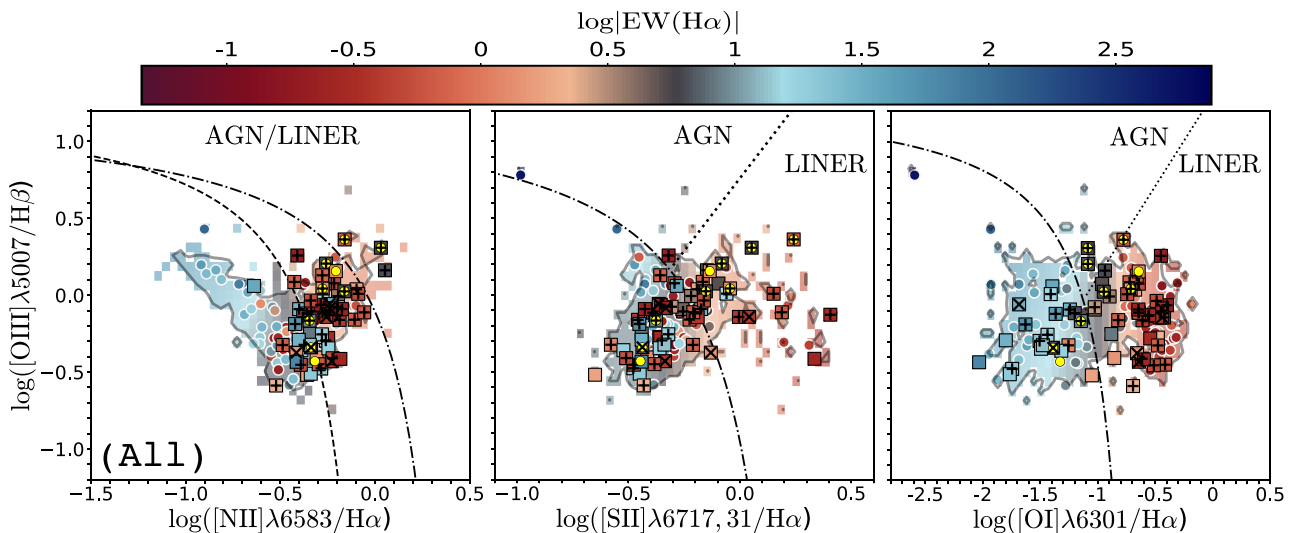


Figure B1. CALIFA measurements at the average galaxy value (All) region. The lines and symbols are as in Fig. 5.

APPENDIX C: OPTICAL EMISSION LINE FLUX RATIOS

Table C1. First 10 rows of the emission line flux ratios. Col. (1) is the name of the source. Cols. (2), (7), and (12) is the ratio between [N II] and H α for central CALIFA, R_e , and *complete galaxy*, respectively. Cols. (3), (8), and (13) is the ratio between [O III] and H β for the *centre*, R_e , and *complete galaxy*, respectively. Cols. (4), (9), and (14) is the ratio between [S II] and H α for the *centre*, R_e , and *complete galaxy*, respectively. Cols. (5), (10), and (15) is the ratio between [O I] and H α for the *centre*, R_e , and *complete galaxy*, while Cols. (6), (11), and (16) is the EW(H α) for *centre*, R_e , and *complete galaxy*, respectively. All measurements are in logarithmic scale. The rest of the table is available as supplementary online material.

Name	Centre					R_e				
(1)	[N II]/H α (2)	[O III]/H β (3)	[S II]/H α (4)	[O I]/H α (5)	EW(H α) (6)	[N II]/H α (7)	[O III]/H β (8)	[S II]/H α (9)	[O I]/H α (10)	EW(H α) (11)
NGC7803	-0.311 ± 0.047	-0.349 ± 0.137	-0.375 ± 0.047	-2.303 ± 0.164	1.181 ± 0.829	-0.347 ± 0.028	-0.468 ± 0.468	-0.404 ± 0.049	-2.265 ± 0.217	1.486 ± 1.311
NGC0023	-0.262 ± 0.028	-0.453 ± 0.062	-0.432 ± 0.047	-1.844 ± 0.140	1.610 ± 0.964	-0.250 ± 0.045	-0.346 ± 0.346	-0.356 ± 0.081	-1.593 ± 0.253	1.365 ± 1.093
NGC0192	-0.291 ± 0.040	0.027 ± 0.241	-0.496 ± 0.044	-1.802 ± 0.139	1.289 ± 0.477	-0.183 ± 0.086	0.136 ± 0.136	-0.319 ± 0.139	-1.151 ± 0.245	0.581 ± 0.269
NGC0197	-0.413 ± 0.115	-0.181 ± 0.269	-0.438 ± 0.068	<-1.240	0.995 ± 0.779	-0.559 ± 0.239	-0.047 ± 0.047	-0.197 ± 0.225	-0.447 ± 0.331	0.808 ± 0.852
NGC0214	0.047 ± 0.061	0.462 ± 0.206	-0.309 ± 0.093	-1.447 ± 0.267	0.547 ± 0.231	-0.442 ± 0.056	-0.647 ± 0.647	-0.698 ± 0.123	-1.697 ± 0.295	1.335 ± 0.950
NGC0384	-0.025 ± 0.127	0.150 ± 0.281	-0.429 ± 0.177	-1.141 ± 0.288	0.026 ± 0.567	-0.363 ± 0.226	-0.185 ± 0.185	-0.365 ± 0.287	-0.329 ± 0.329	-0.419 ± 0.525
NGC0495	-0.401 ± 0.202	-0.390 ± 0.504	-0.732 ± 0.061	-0.677 ± 0.327	-0.352 ± 0.760	-0.562 ± 0.293	-0.245 ± 0.245	-0.504 ± 0.134	-0.731 ± 0.255	-0.383 ± 0.236
NGC0499	0.016 ± 0.101	0.077 ± 0.256	-0.280 ± 0.114	-1.214 ± 0.404	-0.011 ± 0.648	-0.143 ± 0.226	-0.211 ± 0.211	-0.362 ± 0.231	-0.515 ± 0.283	-0.368 ± 0.671
NGC0496	-0.467 ± 0.015	-0.781 ± 0.139	-0.569 ± 0.025	-1.900 ± 0.194	1.474 ± 0.515	-0.526 ± 0.087	-0.427 ± 0.427	-0.432 ± 0.149	-1.462 ± 0.399	1.370 ± 1.228
NGC0504	-0.239 ± 0.156	0.174 ± 0.153	-0.488 ± 0.065	-0.353 ± 0.185	-0.598 ± 0.930	-0.267 ± 0.147	-0.505 ± 0.505	-0.138 ± 0.222	-0.402 ± 0.225	-0.429 ± 0.519

This paper has been typeset from a \LaTeX file prepared by the author.

Chapter 6

Summary and conclusions

The study of the AGN is crucial to determine how it can affect the host galaxy (see Kormendy & Ho, 2013, for a review). A pivotal step to understand this connection is having a complete estimate of the AGN population. However, the study of AGN is strongly affected by the host galaxy emission (Padovani et al., 2017), which particularly affects the detection of LLAGN, since they can be completely undetected due to their luminosity compared to that of the galaxy (Ho, 2008). Moreover, the role that LLAGN play in this connection is still an open question. For instance, the accretion mechanism of these sources, that differs from their more luminous pairs, prevents us from fully understand whether larger regions, such as the BLR or the torus, are able to survive without enough radiation pressure from the accretion disk that can counteract the gravitational force from the SMBH (Elitzur & Shlosman, 2006).

Part of this thesis is devoted to characterize the population of AGN in the CALIFA optical survey (with 941 sources in the local Universe, $z < 0.03$) through the X-rays which are less susceptible to the contamination by the host galaxy emission (see Osorio-Clavijo et al., 2023). We use the X-ray satellite *Chandra*, as it provides a sub-arcsec angular resolution, which is important to isolate the nucleus. While optical surveys estimate a 4% of AGN in the local Universe (e.g. Sánchez et al., 2018; Wylezalek et al., 2018; Lacerda et al., 2020), we find that the contribution of AGN in the CALIFA survey to be at least of 7%, when adding the spectral information given by *Chandra*, although it could rise up to 10% when taking into account only the morphological features of the sources, and to even

higher estimates when including other X-ray satellites. Indeed, while we detect a point-like source in 66 out of the 138 objects analyzed in this work, only 48 had enough SNR in the spectra to perform a spectroscopic analysis. It is possible that the 24 sources without sufficient SNR spectra could be LLAGN, providing a low number of counts in the X-ray spectral range. In fact, we find that most of the AGN found at X-rays which had not been detected previously at optical in the work by Lacerda et al. can be classified as LLAGN from their X-ray luminosities ($L_{2-10\text{keV}} < 10^{42} \text{ erg s}^{-1}$). Thus, for the undetected ones it may be the case that longer exposure times would be required. Additionally, for NGC 2639, we found the best-fit model was a thermal one, opposite to the optical classification by Lacerda et al.. Similarly, NGC 3861, also classified as AGN by Lacerda et al., is undetected at X-rays. This could be explained if they are intrinsically obscured (i.e., the material in the l.o.s comes from within the AGN), which could make them unreachable by the *Chandra* capabilities. In favour of this, several X-ray studies estimate a fraction of Compton-thick ($N_{\text{H}} > 10^{24} \text{ cm}^{-2}$) AGN in the local Universe to be $\sim 24\%$ (Risaliti et al., 1999; Ueda et al., 2014; Ricci et al., 2017a; Laloux et al., 2023). This could affect the detection of AGN sources from the X-ray point of view with the use of information below 10 keV (this was also suggested by Yan et al., 2011, although at slightly larger redshifts).

At optical, AGN are frequently classified based on the line ratios of the narrow emission lines through the diagnostic diagrams (see sec. 1.9). When analyzing the location of our sources in these diagrams, we find that most of the X-ray detected objects lie in the right branch of the [OIII]/H β vs [NII]/H α diagram, mostly populating the AGN/LINER, mixed and starburst regions of it. If we had based the analysis purely on the criteria used at the optical wavelength regime, we could miss up to 75% of the detected sources, leading to wrong estimations on nuclear activity in the nearby Universe, and therefore to an incomplete scenario in the understanding of the AGN-host galaxy connection. However, as indicated before, most of the lost AGN could be intrinsically LLAGN, with a more limited impact in the evolution of the host galaxy than the strongest ones.

With regards to this connection, several authors (Kauffmann et al., 2003; Sánchez et al., 2004a; Schawinski et al., 2007, 2014; Sánchez et al., 2018) find that AGN are located in the so-called Green Valley (GV), a transition region between star-forming and retired

galaxies (SFGs and RGs, respectively). While these studies have used optical information only, explorations using X-ray data suggest that this result might still hold for the local Universe (Nandra et al., 2007b; Pović et al., 2012).

As a first approach to understand this connection in the CALIFA sample, we use our sample of AGN classified through the X-ray properties to explore their distribution in the SFR vs. stellar mass diagram. Figure 6.1 shows the distribution of objects studied in our work. The dark squares represent the X-ray detected sources (AGN candidates throughout our work), while the white-bordered circles are non-detected sources. The black diamonds represent bona fide AGN (i.e., those sources fitted to models associated with AGN emission), while black crosses are objects fitted with pure-thermal models (i.e., non-AGN). Finally, the yellow dots correspond to the AGN classified by Lacerda et al. (2020) at optical wavelengths.

While the diagram shows a clear bimodal behaviour already discussed extensively (Brinchmann et al., 2004; Salim et al., 2007; Renzini & Peng, 2015; Sánchez et al., 2018) between SFGs and RGs, we find that our X-ray detected sources are located in both sequences, opposite to the behaviour found by Lacerda et al. (2020) for optically classified AGN. Indeed, using the demarcation limits of Lacerda et al. (2020) based on the $EW(H\alpha)$:

- Star-forming galaxies (SFGs): $EW(H\alpha) > 10 \text{ \AA}$
- Green Valley galaxies (GVGs): $3 \text{ \AA} < EW(H\alpha) \leq 10 \text{ \AA}$
- Retired galaxies (RGs): $EW(H\alpha) \leq 3 \text{ \AA}$

we find that 22/28/12 AGN candidates are in the SFG, RG and GV regions, respectively, while 25/32/9 non-detected sources are in the SFG, RG and GV regions, respectively. While there is an excess of AGN candidates in the GV compared to the non-detected sources, the former do not seem to be located in a preferential region. Moreover, from the bona fide AGN, 15/22/8 are located in the SFG, RG, and GV regions, respectively. Compared to the non-detected sources, the proportion is similar. Thus, bona fide AGN do not seem to be preferentially located in any region of the SFR-M diagram. In contrast, Lacerda et al. find that the AGN hosts are located in towards the bluer region of the red sequence.

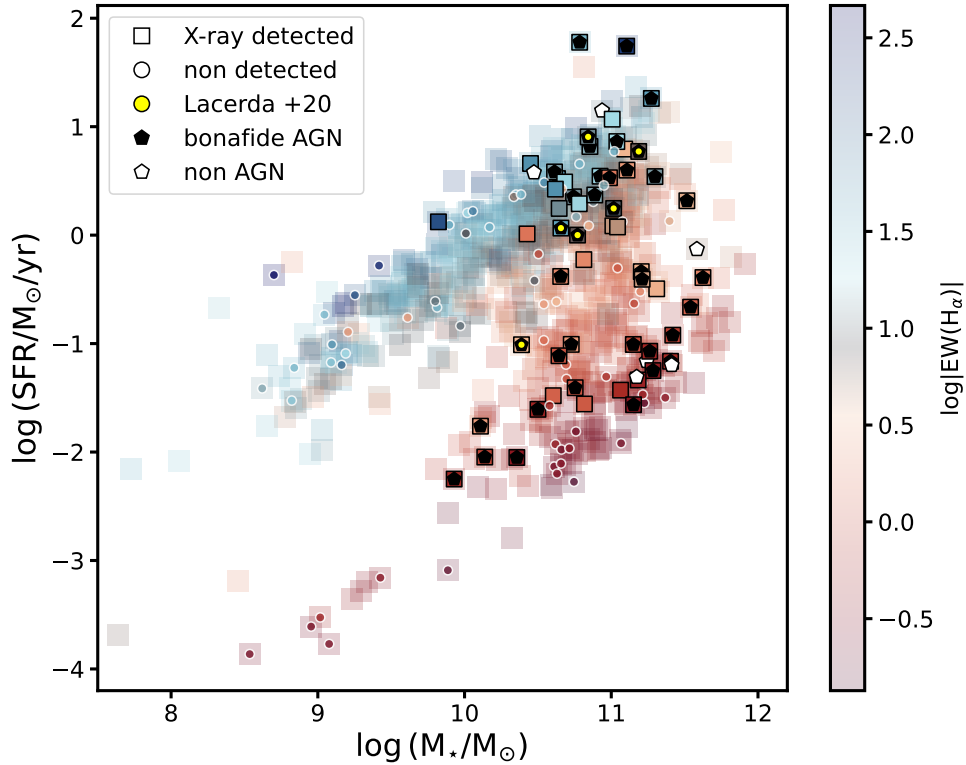


Figure 6.1: SFR vs. stellar mass diagram for the sources studied in our work. The semi-transparent squares at the back correspond to the total CALIFA sample (941 sources). The solid squares and white-bordered circles correspond to X-ray detected and non-detected sources. The black and white pentagons correspond to bona fide AGN and non-AGN sources, respectively. Finally, the yellow dots correspond to sources in common with Lacerda et al. (2020).

This contrast can be explained in terms of the luminosities of the AGN. through the X-ray approach, we are including mostly LLAGN, which might explain why these are not in a preferential location of the diagram. Note that a this part of the analysis is still under development and has not yet been published. We plan to add information from *XMM-Newton* to obtain a larger number of AGN sources in the CALIFA survey (see 7) and derive more robust conclusions on how the nuclear activity might affect SF and vice versa. On the other hand, Nandra et al. (2007b) study a sample of 68 AGN from the *Chandra* survey of the Extended Groth Strip with $0.6 < z < 1.4$, finding that most of their sources are located in luminous and redder galaxies. Nonetheless, they find a non-negligible amount of sources residing in the GV. They suggest that this result might be indicative that AGN activity does not require ongoing star formation. Additionally, Xue et al. (2010) find, for a sample of 207 galaxies with $0 < z \leq 4$, that AGN hosts do not present a preferential location on the CMD diagram, which is in agreement with our result. Moreover, they claim that AGN hosts do not seem to follow a bimodal distribution, although they agree with the fact that most AGN hosts are redder galaxies. This is similar to what was found by Pović et al. (2012) for a sample of 262 AGN observed with *Subaru/XMM-Newton* at $z \leq 2.0$. They attribute the location of AGN in the GV to a transitional population, most probably due to minor and major galaxy mergers, which might induce both star formation and nuclear activity. One caveat of the works mentioned previously, is the fact that they classify an AGN having $L_{2-10\text{keV}} > 10^{42} \text{ erg s}^{-1}$, while we do not put a restriction on the X-ray luminosity, which might be a possible source of bias towards luminous AGN in these works.

These results highlight the importance of combining different wavelengths and instruments to account for the majority of AGN sources, in order to have a better knowledge of the co-evolution between AGN and their host galaxies.

As mentioned above, the role of LLAGN in the co-evolution is still an open question. In fact, the accretion mechanism of these sources is thought to be different, going from a radiatively efficient to inefficient state and also changing the geometry of the accretion disk from optically thin to thick (Narayan & Yi, 1994b). Moreover, under the disk-wind scenario proposed by Elvis (2000), the torus and the BLR can be seen as a wind coming

off the accretion disk. Therefore, as predicted by Elitzur & Shlosman (2006), these structures should disappear once the accretion disk cannot expel enough material to counteract the gravity from the SMBH, which would be the case of LLAGN. The timescale of the disappearance of these structures is < 100 years (Ichikawa & Tazaki, 2017), which is short in contrast with the AGN duty cycle (of the order of 10^5 yr, Esparza-Arredondo et al., 2020, and references therein).

While the torus can be studied at mid-IR as it is mainly composed by dust, it can also be studied at X-rays through the reflection component. Additionally, the reflection is linked to the l.o.s obscuration in AGN, as for Compton-thick sources ($N_{\text{H}} > 10^{24.2} \text{ cm}^{-2}$), the material completely absorbs the intrinsic continuum. In relation to the obscuration, early X-ray observations showed that optically classified Type-I sources are generally less obscured than Type-II, which have $N_{\text{H}} > 10^{22} \text{ cm}^{-2}$ (Awaki et al., 1991; Bassani et al., 1999), which might be in agreement with the UM. However, recent works have suggested that, rather than an observational difference, the obscuration can be related to the evolutionary stage of the AGN (see Ramos Almeida & Ricci, 2017b, for a review). Therefore, understanding the obscuration and reflection for AGN will help us understand the overall AGN evolution and its role in that of the host galaxy. The study of the X-ray reflection component for LLAGN has only been done recently (Kawamuro et al., 2016; Diaz et al., 2020, 2023) for individual sources due to the low SNR of them. In our work, we selected a sample of 81 sources from the *NuSTAR* database for which there were M_{BH} measurements, in order to study the evolutionary trend through the Eddington rate for $\lambda_{\text{Edd}} < 10^{-3}$ (i.e., inefficient sources).

In Osorio-Clavijo et al. (2022), we found that 11 sources (namely NGC 3628, NGC 3718, M 106, NGC 7331, NGC 612, 2MXJ 1105+5856, NGC 3621, NGC 3786, M 88, NGC 5252 and 2MXJ 2325-3826) do not present an evident trace of reflection, most of them having low values for the column density. However, all the sources fall in the region in which the torus may or may not exist depending on the wind parameters as predicted by Elitzur & Ho (2009) (see Fig. 6.2). After our work was published, Diaz et al. (2023) studied nine sources in common with our work (namely NGC 3998, NGC 3718, M 106, NGC 1052, NGC 2655, NGC 3147, M 52, NGC 2273 and NGC 7674), with data from *Swift*, *XMM-Newton* and

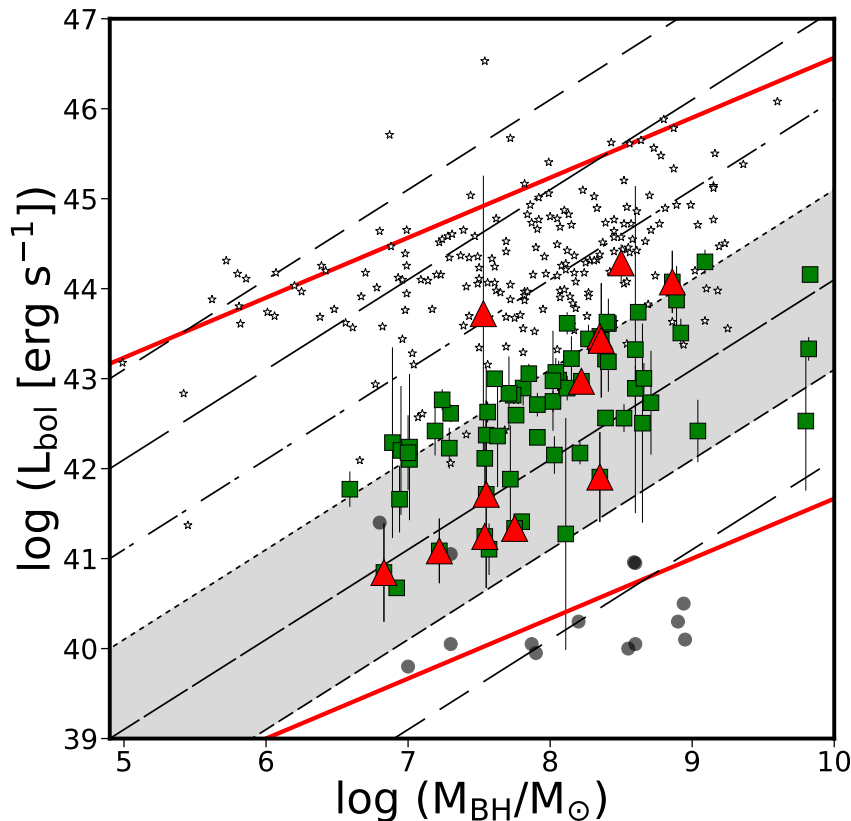


Figure 6.2: Bolometric luminosity versus M_{BH} for our sample. The red triangles are the candidates for the torus disappearance through the X-ray analysis, while the green squares are sources with signatures of reflection associated with the torus and the small empty stars correspond to the BASS sample (Koss et al., 2017). The semi-transparent circles represent the candidates for torus disappearance found by González-Martín et al. (2017) using mid-IR data. The black dashed lines represent $\log(L_{\text{Edd}}) = [0, -1, -2, -3, -4, -5, -6]$ from top to bottom, respectively. The two red lines enclose the region in which the torus may or may not exist depending on the wind parameters, as proposed by Elitzur & Ho (2009). The gray-shaded area corresponds to the Eddington rates from the sample not biased by the selection criteria. Note that those sources with Eddington rates above $\log \lambda_{\text{Edd}} \sim -2.5$ are not shown in this plot since at those Eddington rates our sample is not complete. The figure was published in Osorio-Clavijo et al. (2022).

NuSTAR. They found different reflectors in their analysis, either coming from the disk, the torus or both. Particularly, while we found no traces of reflection for NGC 3718, they found that this source presents an ionized reflector, most probably associated with the accretion disk, which is still in agreement with the scenario in which the torus is not present for this source. The reported values for the obscuration in the l.o.s are completely in agreement with our results as well. On the other hand, they found a reflector associated

with the torus for M 106, which we classify as candidate for the torus disappearance. The use of *XMM-Newton* and its spectral resolution, which is greater than that of *NuSTAR* for energies in the range 3-10 keV, might have lead to the restriction of the narrow FeK α line, indicative of reflection in the torus. However, Reynolds et al. (2009) use observations from *Suzaku*, *Swift* and *XMM-Newton* to study this source, while Kawamuro et al. (2016) use *Suzaku* observations only, and both works find that the FeK α line originates in a closer region, most probably the accretion disk, due to the variability scale of the emission line. This scenario might explain why we do not find traces of reflection in the torus for this source.

Through the mid-IR point of view, González-Martín et al. (2017) studied the evolution of the torus for a sample of 48 LINERs, 42 Seyferts and 19 Starburst galaxies, finding a total of 14 sources without traces of torus, although none of them have X-ray observations with *NuSTAR*. From the expected correlation between X-rays and mid-IR luminosities, we would expect these sources to have 2-10 keV luminosities of $L_{2-10\text{keV}} \sim 10^{38} \text{ erg s}^{-1}$ which is well below the average X-ray luminosity of our candidates. Therefore, a complete disappearance of the torus as seen through the X-ray analysis might be found for $\lambda_{\text{Edd}} < 10^{-5}$, which has also been proposed by Ricci et al. (2017b). Additionally, we also find a change in the contribution of the FeK α line with respect to the reflection component. This might indicate that the composition of the torus is changing, which is supported by González-Martín et al. (2017), where they found that sources with low contribution of the torus in the mid-IR spectral modelling, are not well fitted to clumpy distributions of the matter, which they attribute to a change in the geometry or chemical composition of the torus.

We also study the level of obscuration in our sample and compared to other studies of nearby AGN. While our sample is not complete due to our selection criteria, we see a decrease in the fraction of obscured sources towards lower Eddington rates. Indeed, we find that the level of Compton-thin obscured sources decreases from 80% at $\lambda_{\text{Edd}} \sim 10^{-3}$ to $\sim 60\%$ at $\lambda_{\text{Edd}} \sim 10^{-5}$, which is in agreement with was found by Ricci et al. (2017b) for the BASS sample DR1 (Koss et al., 2017), consisting of 731 non-blazar AGN sources. Therefore, although both samples are chosen with different selection criteria, both results are in complete agreement. Moreover, the fraction of Compton-thick sources is also in

agreement with the work by Ricci et al., with a value of $CT = 0.24$. This might indicate a transition in the reflector towards lower Eddington rates, in agreement with the evolutionary scenario.

In summary, the conditions under which the torus is expected to disappear are much more complex, as suggested by Elitzur & Ho (2009), than only depending on the bolometric luminosity. However, we expect the torus to completely disappear below $\lambda_{\text{Edd}} \sim 10^{-5}$.

Chapter 7

Future work

The results found in this thesis are of great importance in the understanding of AGN behaviour and evolution. There are different ways in which we can complement these results and answer some of the key points in the disappearance of the torus and in the co-evolution of the AGN and the host galaxy. In this section, we propose some goals to be completed in the upcoming years.

- **X-ray extended emission of AGN hosts within the CALIFA sample:** We plan to study the X-ray extended emission of the sources reported in Osorio-Clavijo et al. (2023). From the extended profile obtained in our paper, we will compare X-rays and optical tracers (e.g., [OIII], H α images) already available in the CALIFA dataproducts, in order to determine whether these two indicators are related. Indeed, as a preliminar analysis, we explore the $L_{[\text{OIII}]}$ vs $L_{2-10 \text{ keV}}$ correlation. Fig. 7.1 shows the comparison of spatially resolved distribution of both parameters. The grey area corresponds to the surface density luminosity of X-ray and [OIII] of all the spatially resolved elements considered in the galaxy NGC 0833, while the blue diamonds, green squares and red triangles correspond to the particular values in the central 3, 2 and 1 kpc, respectively. Moreover, the solid black, dot-dashed blue, dashed green and dotted red lines correspond to the correlations between both surface densities for each dataset. We determine the correlation between both quantities, and in each respective physical scales, in order to compare whether this correlation is of

the same order of magnitude as those proposed in previous works for the nuclear region (e.g., Panessa et al., 2006; González-Martín et al., 2009; Georgantopoulos & Akylas, 2010; Berney et al., 2015; Williams et al., 2022). While we see a correlation between both quantities, even for the extended emission, we still need to explore different scenarios to have a definite explanation for the similarities and differences between the correlations and distribution found for the different datasets. Moreover, we want to explore if the correlation is the same for all the galaxies or if there is a dependence on additional observational physical parameters of the galaxies (e.g., inclination, ellipticity, etc).

Furthermore, apart from studying the sources individually, we intend to study the behaviour of this relation for the complete sample of sources with extended emission, in order to determine if it is the same in all galaxies or not, and to narrow down its nature. Indeed, we have stacked all the images together in order to better understand the behaviour of both quantities (see Fig.,7.2). In this panel, we show how the inclination may affect how the correlation changes among different sources. Our preliminar explorations indicate that the scenario is more complex than a pure dependence on one single observational parameter, such as the inclination. Therefore, we still need to explore different scenarios (e.g., ellipticity, black hole mass, accretion rate, etc) to see if we can find a single relation valid for all the galaxies, or if the reported relation is different for each galaxy. In either case, we need to find a suitable explanation.

Additionally, we want to explore the connection between the reported relation and the physical properties derived from the X-ray spectroscopic analysis, in order to determine the physical process involved in its emission. Similar to what we already did with the nuclear region, we will use a set of models to identify which explains better the extended X-ray emission. This is connected to the next project.

- **Spectral analysis of AGN in the CALIFA sample with *XMM-Newton*:** Another project derived from our analysis with *Chandra* is to analyse the CALIFA sample with *XMM-Newton*. While this satellite does not have as good angular resolution as the former, it provides a better spectral resolution and a slightly larger

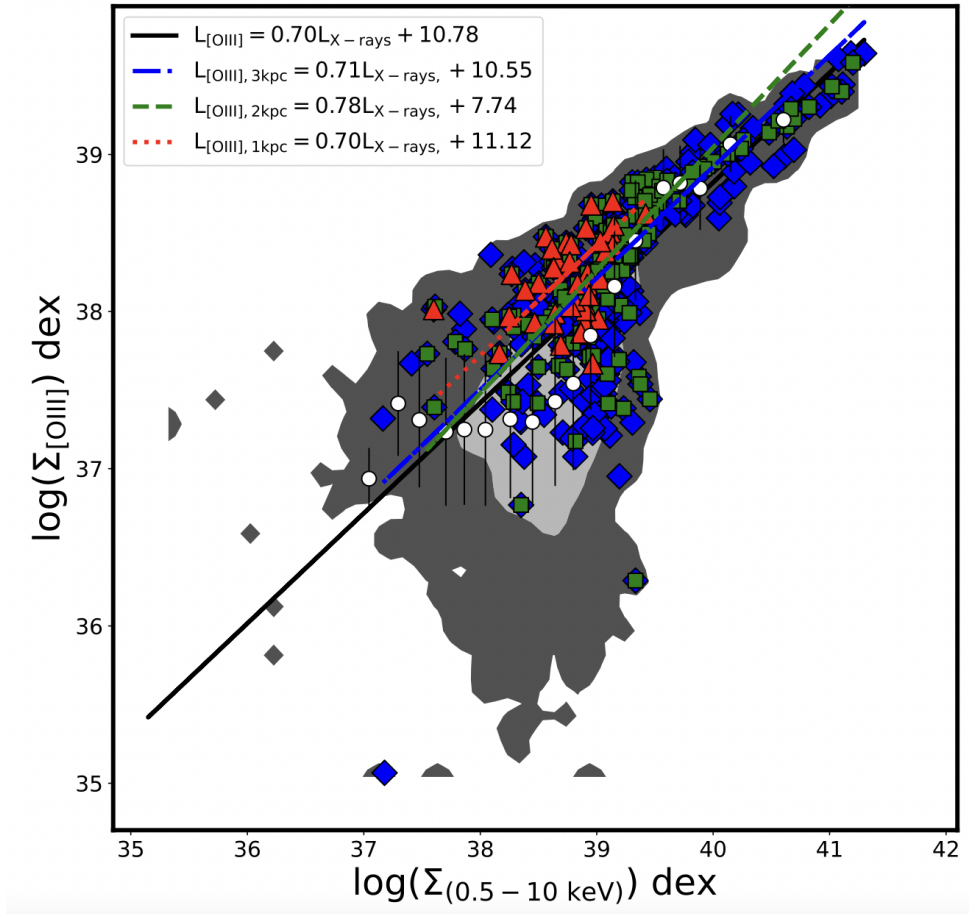


Figure 7.1: Surface density luminosity of the [OIII] emission line vs surface X-ray luminosity in the 0.5-10 keV band for NGC0833. The grey contours correspond to the full image at the physical scale for both images. The blue diamonds, green squares and red triangles correspond to the pixels at the central 3, 2 and 1 kpc, respectively. The black solid, blue dot-dashed, green dashed and red dotted lines correspond to the best linear fit between both quantities for the full image, and at the central 3,2 and 1 kpc, respectively.

energy range, which could potentially help us identify more AGN sources. Indeed, from a preliminar search in the database, we found observations for 100 sources, half of which already have observations with *Chandra*, too. We have already obtained the spectra for this sample. This allows us to use the best-fits from the X-ray extended emission found in the previous project, and isolate the extended emission from the *XMM-Newton* spectra, and to better fit the nuclear emission. For the sources without *Chandra* information, we can still perform a spectroscopic analysis based on that from Osorio-Clavijo et al. (2023). Moreover, using information from both satellites

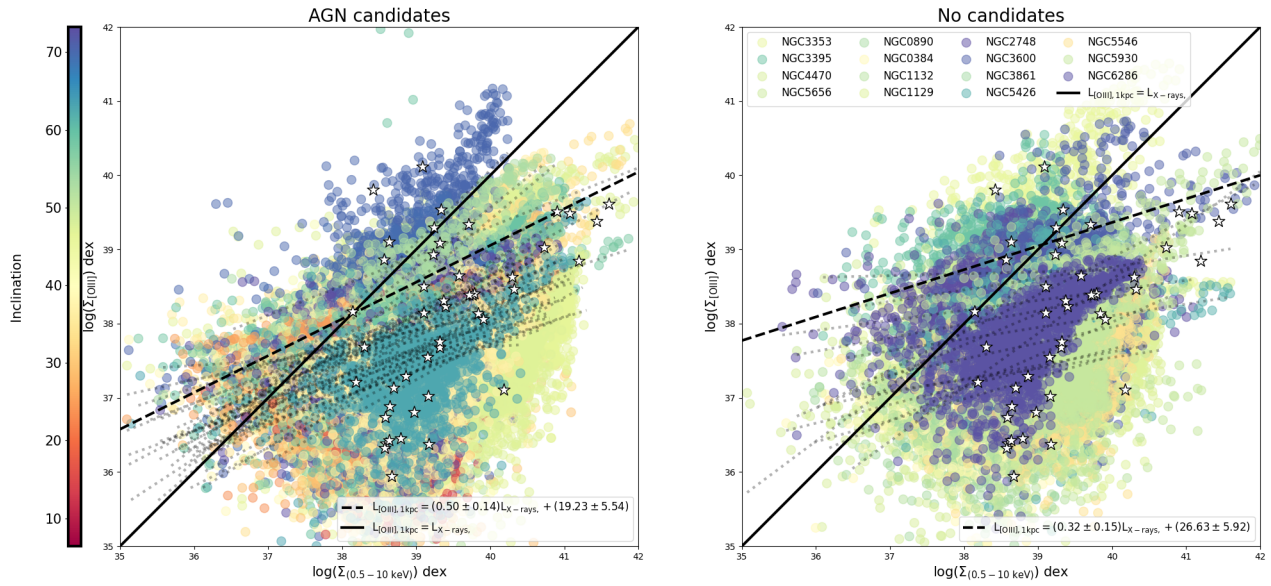


Figure 7.2: Surface luminosity of the [OIII] emission line vs surface X-ray luminosity in the 0.5-10 keV band for the sources with extended emission classified as AGN candidates (left panel) and non-AGN sources (right panel). The colors are associated with the inclination of the galaxy obtained from the CALIFA dataproducts. Each dotted line represents the individual correlation for the sources. **The dashed line in each panel corresponds to the average correlation of the sample in each case, while the solid line corresponds to the 1:1 relation.**

will provide insightful information and better constrained parameters for the sources that have observations from both satellites. Figure 7.3 shows a comparison of both spectra for NGC 1129. It is possible to see how the quality of the *XMM-Newton* spectrum is better (black line), specially at energies above 5 keV. However, note that the spectrum of the extended emission as studied by *Chandra* (red line) will help us decontaminate once we have a best fit of this component. Moreover, there is a significant excess of *XMM-Newton* with comparison to the *Chandra* spectra, and this is something we also need to understand better. Using both satellites will allow us to fully constrain the emission from both the extended and nuclear regions in *XMM-Newton* for which both regions are in the same spectrum.

- **Study of the accretion state of sources in the SFR-M diagram:** A way to better understand how the AGN can affect the star formation in the host galaxy, is

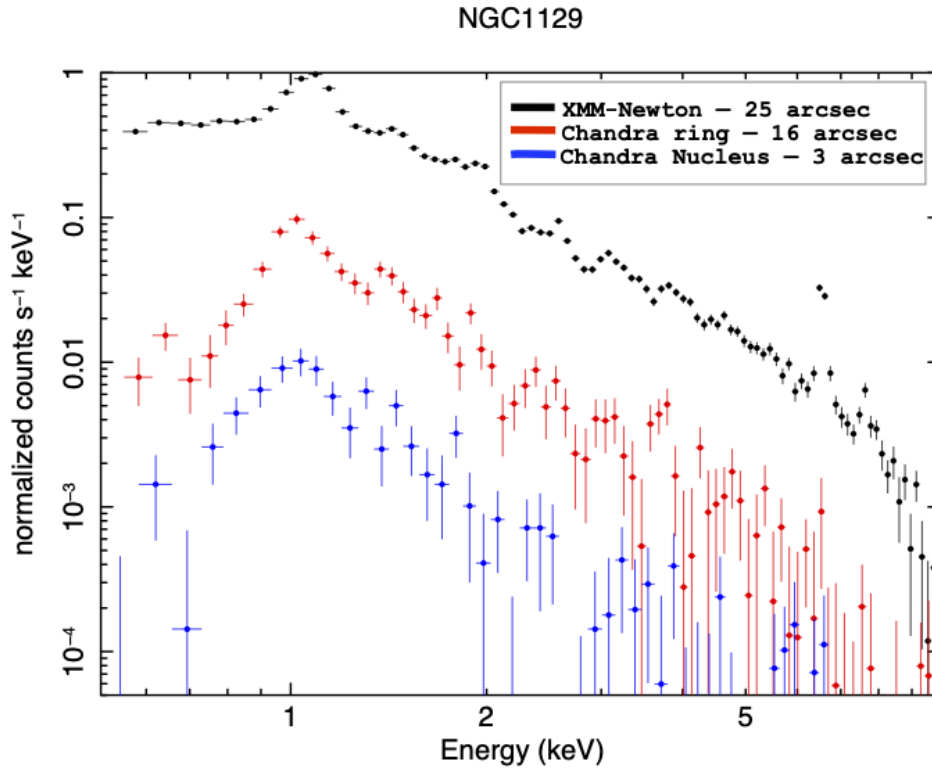


Figure 7.3: X-ray spectra of NGC 1129. The black line corresponds to the *XMM-Newton* spectra for a circular extraction of 25 arcsec, while the red and blue lines correspond to the annular and circular extractions in the *Chandra* spectrum for 16 and 3 arcsec, respectively. Note that for the ring, the inner radius corresponds to 5 arcsec to avoid nuclear contamination.

through the study of the accretion of these AGN sources and how it correlates with the location in the diagram (i.e., if inefficient sources are located in the red sequence and more efficient sources are located in the blue region). One way to do this, would be to obtain the accretion rate from the relation between L_{bol} (obtained from $L_{\text{X-rays}}$, see sec. 1.4) and the M_{BH} . With the data provided by *XMM-Newton*, we can better constrain the X-ray luminosity in order to have a good estimate on the accretion rate. This could then be compared to other X-ray studies from different samples at different redshifts and mass ranges to see if there are any differences depending on these parameters.

- **Multi-frequency study of the torus for LLAGN:** From the work in Osorio-

Clavijo et al. (2022) a case of study would be to search for information about the star formation rate for the eleven sources without traces of torus as seen through the X-ray spectral analysis, to see if the torus could also be supported by the spectral winds of regions with star formation (Wada & Norman, 2002). Another scenario can be to search the sources found to be AGN in the CALIFA survey in Osorio-Clavijo et al. (2023), for available data in *NuSTAR* to see what are the traces of torus in this case. A very preliminary investigation indicates that there are 92 sources from the CALIFA survey with *NuSTAR* information. Using this information can help us better understand the formation and disappearance of the torus.

We will try to attempt all these new partially started explorations in the upcoming years.

Chapter 8

Appendix

8.1 Catalogue of X-ray spectral fittings: Behaviour of the reflection component for LLAGN.

In this section, we present the figures corresponding to the spectral fits performed on all the sources for the study of the behaviour of the reflection component in LLAGN using *NuSTAR* data. In all the figures, the components are shown in the labels.

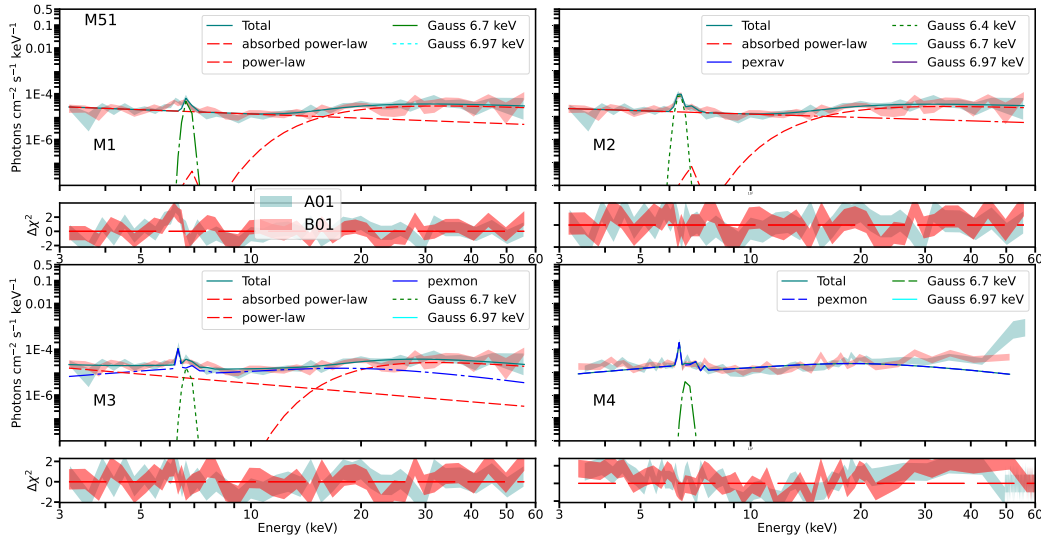


Figure 8.1: *NuSTAR* spectra of M51. The red and green areas correspond to the FMFA and FPMB detectors. The green solid line corresponds to the total model, while the long-dashed red, dotted-dashed blue, dashed green, and short-dashed cyan lines correspond to the absorbed power-law, pexmon component, and emission lines, correspondingly.

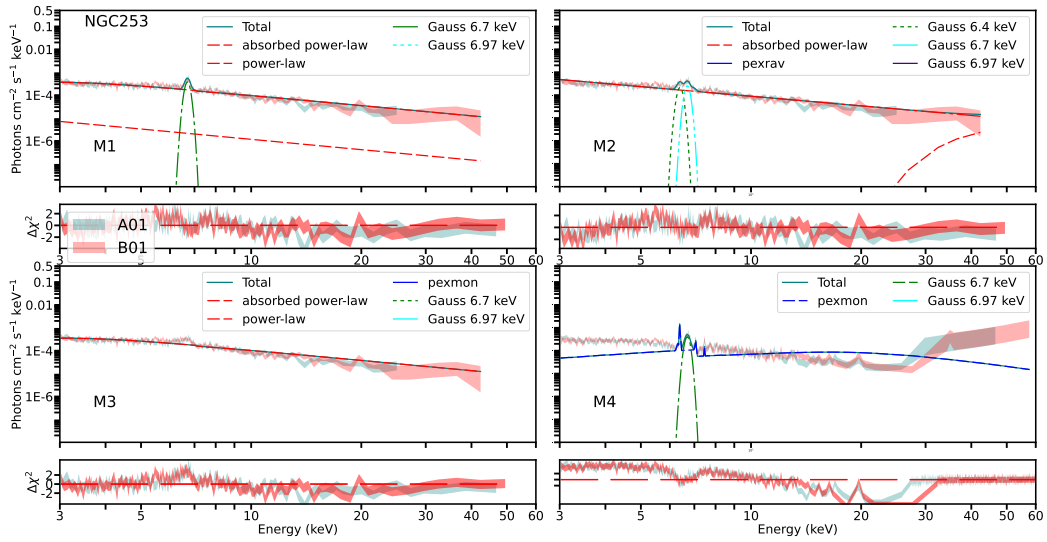


Figure 1: *NuSTAR* X-ray spectra of NGC253. Labels as in Fig. 8.1.

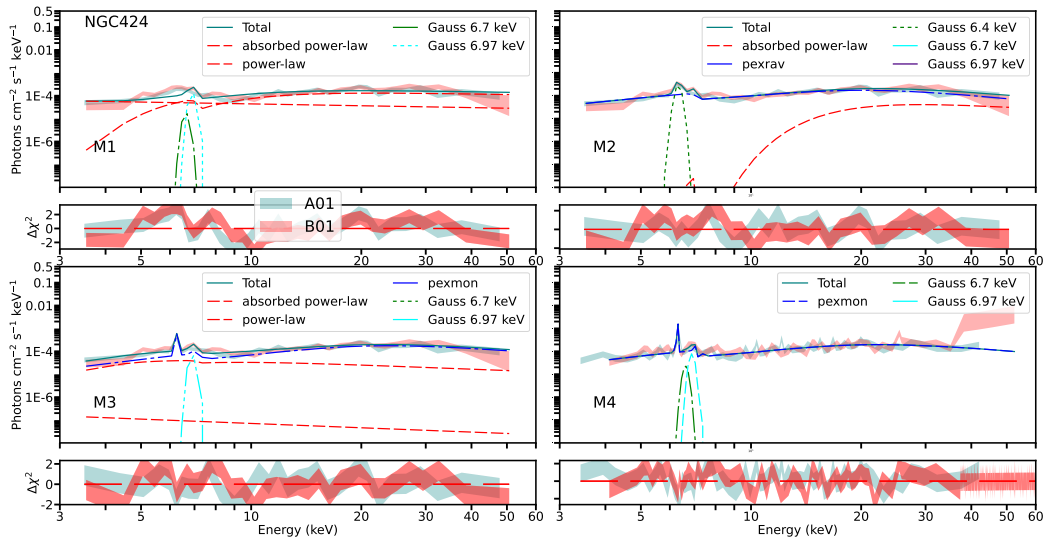


Figure 2: *NuSTAR* X-ray spectra of NGC424. Labels as in Fig. 8.1.

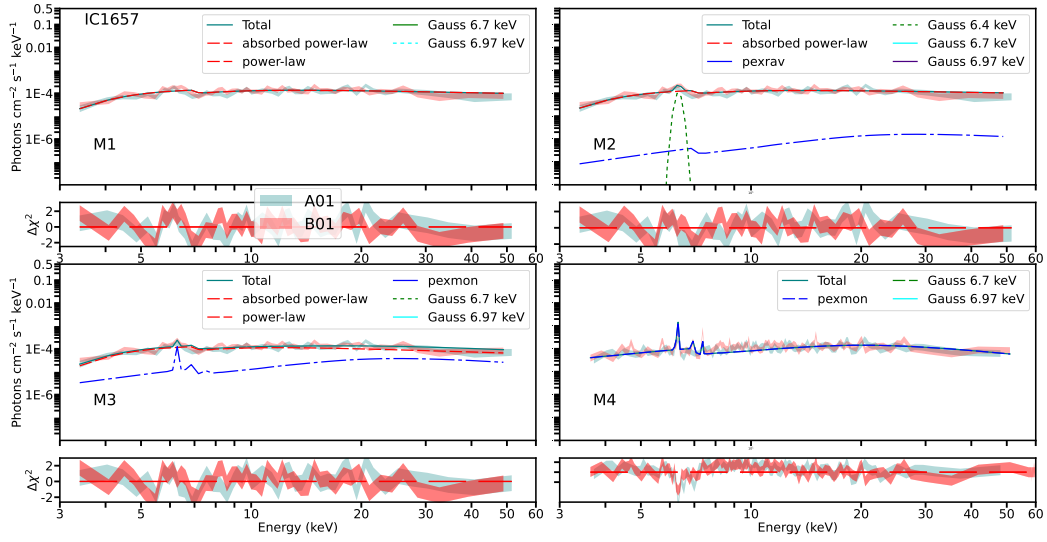


Figure 3: *NuSTAR* X-ray spectra of IC1657. Labels as in Fig. 8.1.

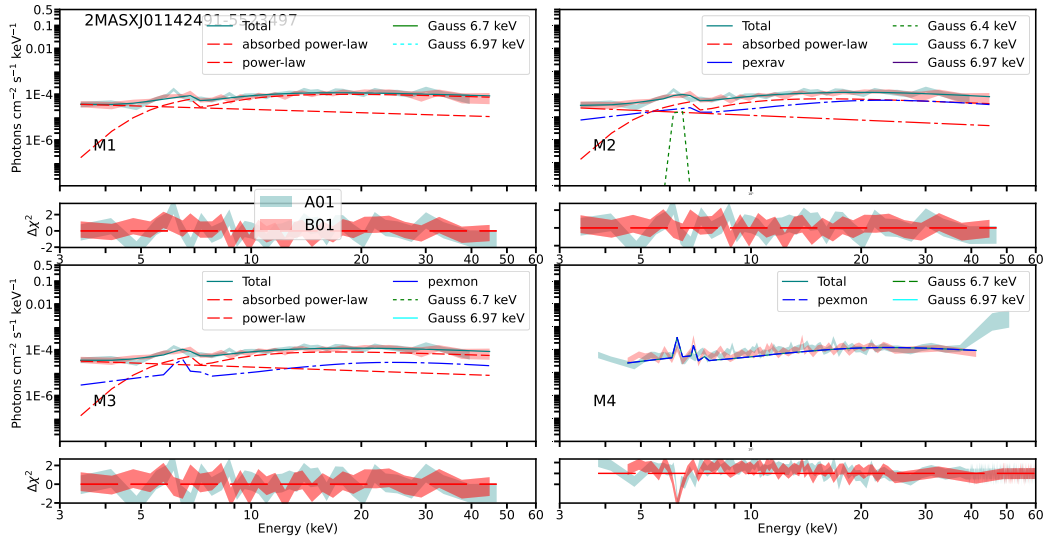


Figure 4: *NuSTAR* X-ray spectra of 2MASXJ01142491-5523497. Labels as in Fig. 8.1.

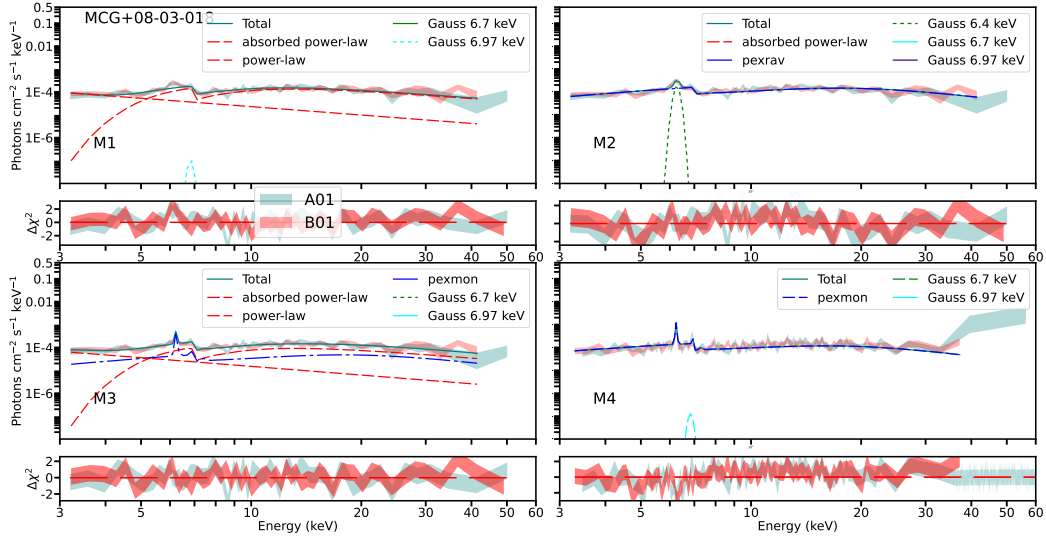


Figure 5: *NuSTAR* X-ray spectra of MCG+08-03-018. Labels as in Fig. 8.1.

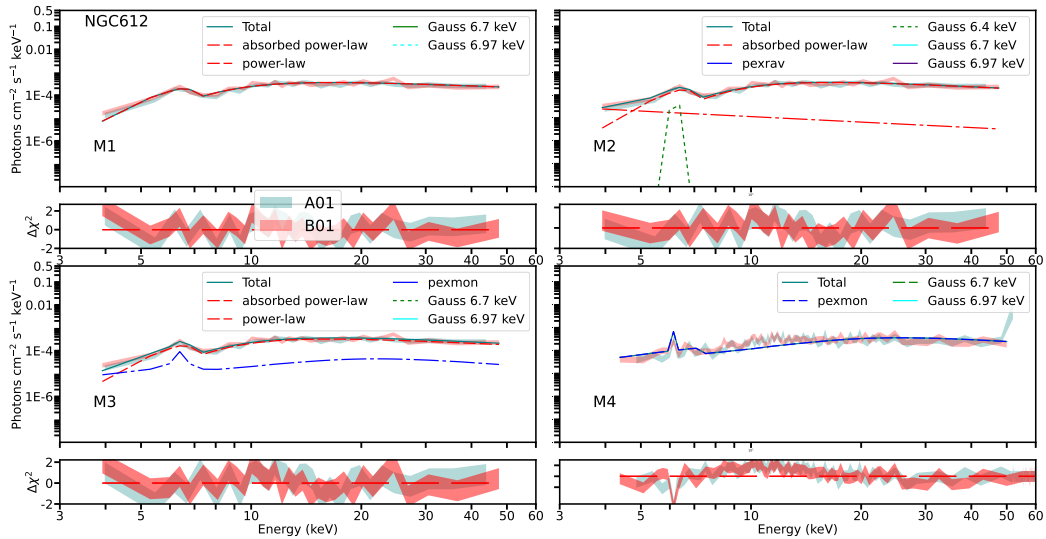


Figure 6: *NuSTAR* X-ray spectra of NGC612. Labels as in Fig. 8.1.

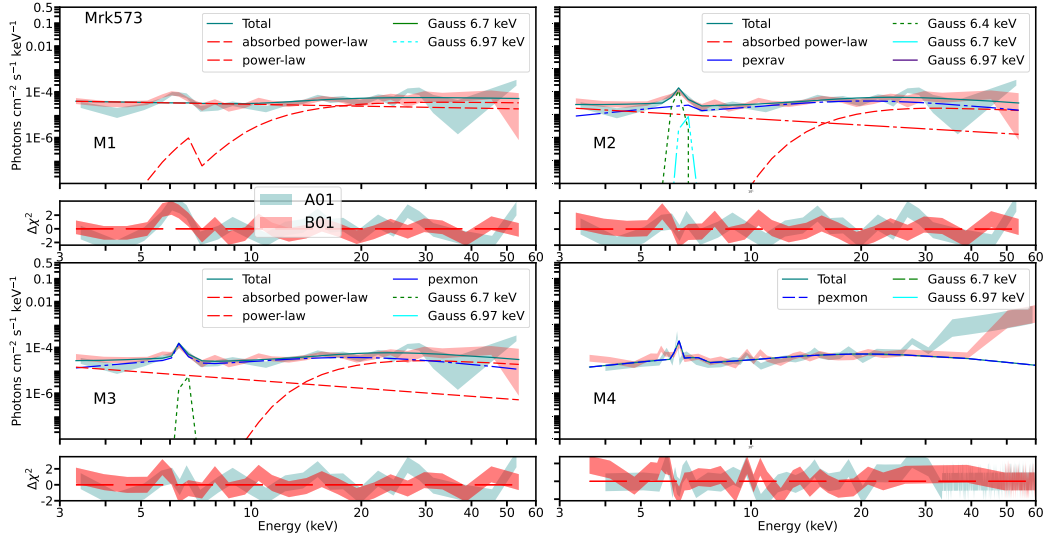


Figure 7: *NuSTAR* X-ray spectra of Mrk573. Labels as in Fig. 8.1.

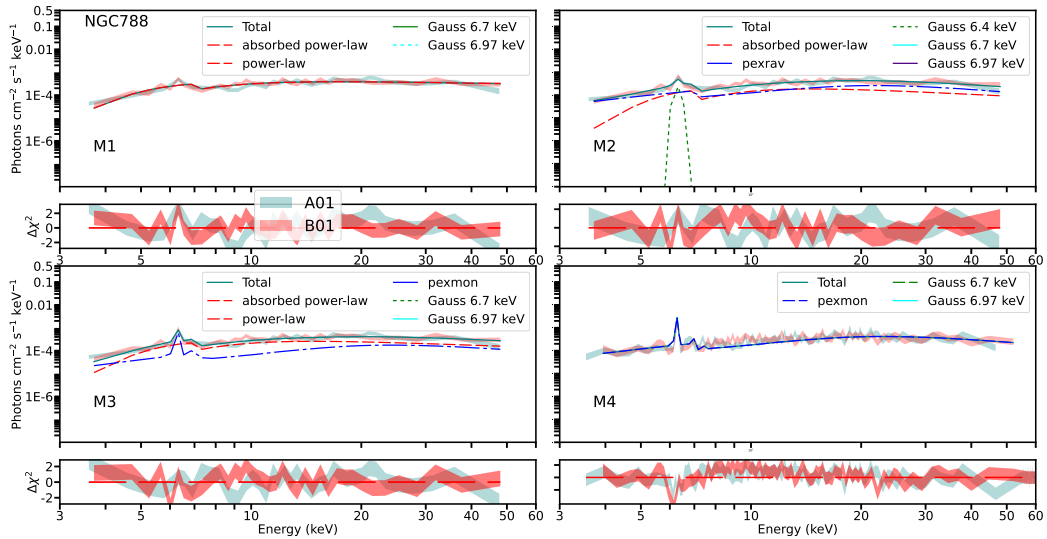


Figure 8: *NuSTAR* X-ray spectra of NGC788. Labels as in Fig. 8.1.

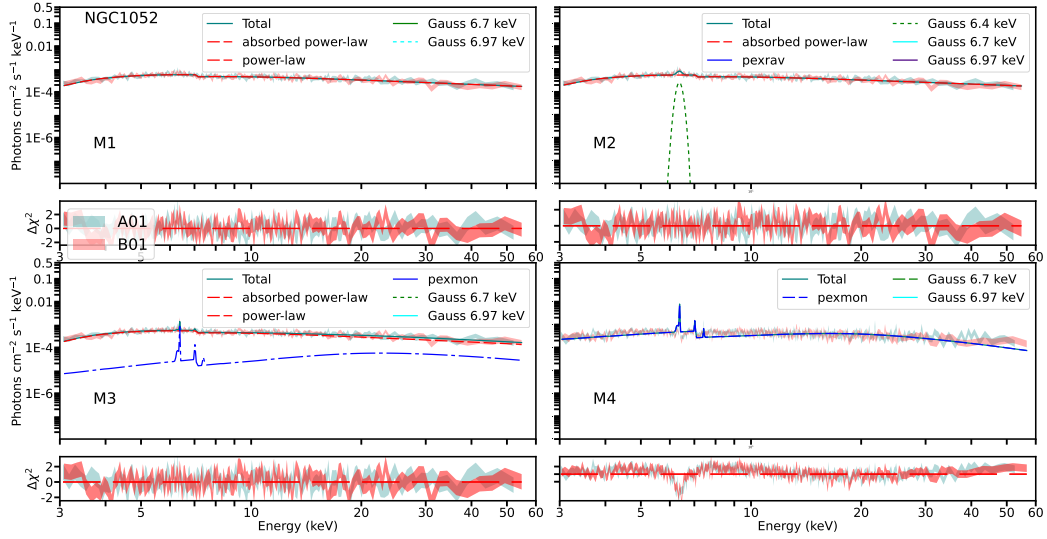


Figure 9: *NuSTAR* X-ray spectra of NGC1052. Labels as in Fig. 8.1.

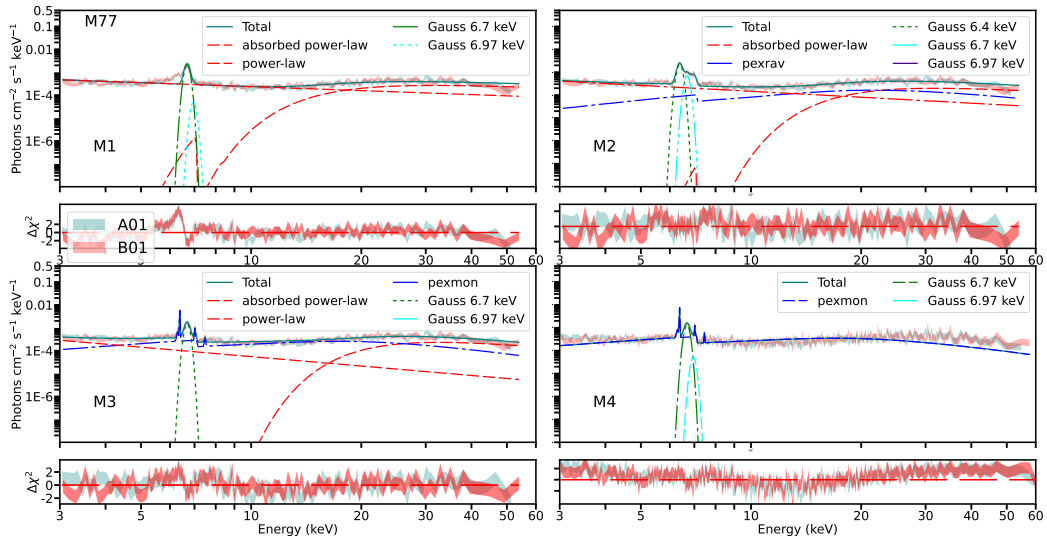


Figure 10: *NuSTAR* X-ray spectra of M77. Labels as in Fig. 8.1.

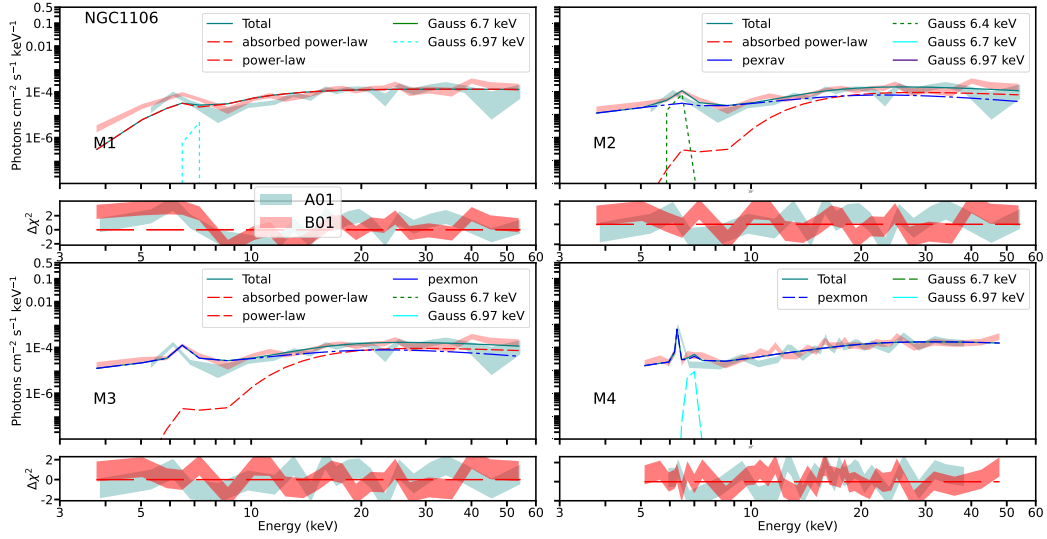


Figure 11: *NuSTAR* X-ray spectra of NGC1106. Labels as in Fig. 8.1.

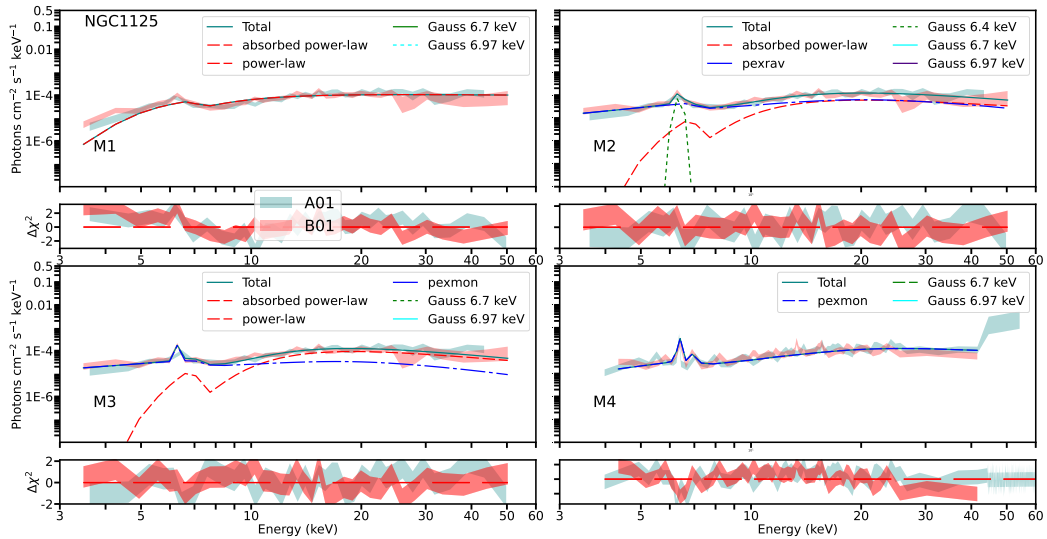


Figure 12: *NuSTAR* X-ray spectra of NGC1125. Labels as in Fig. 8.1.

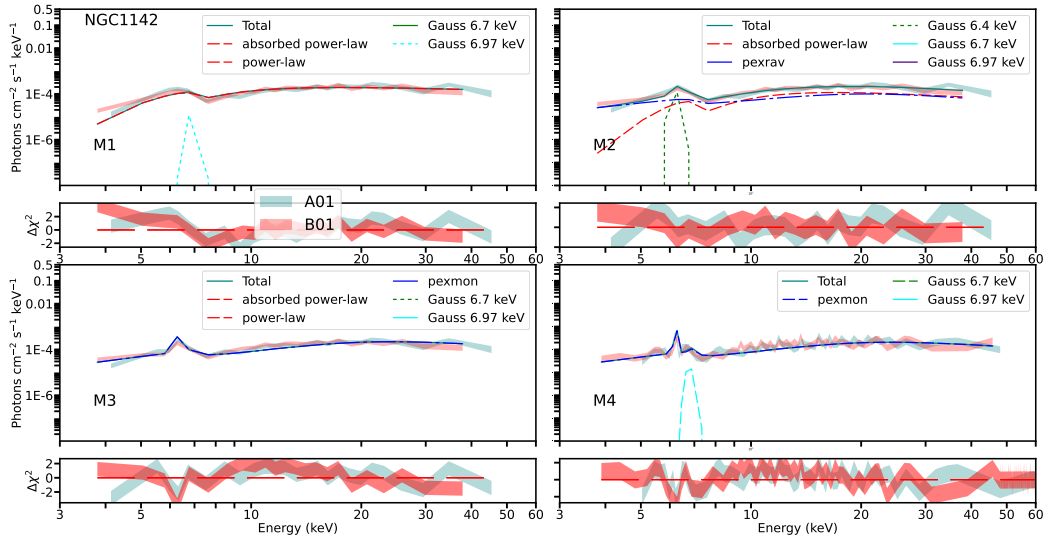


Figure 13: *NuSTAR* X-ray spectra of NGC1142. Labels as in Fig. 8.1.

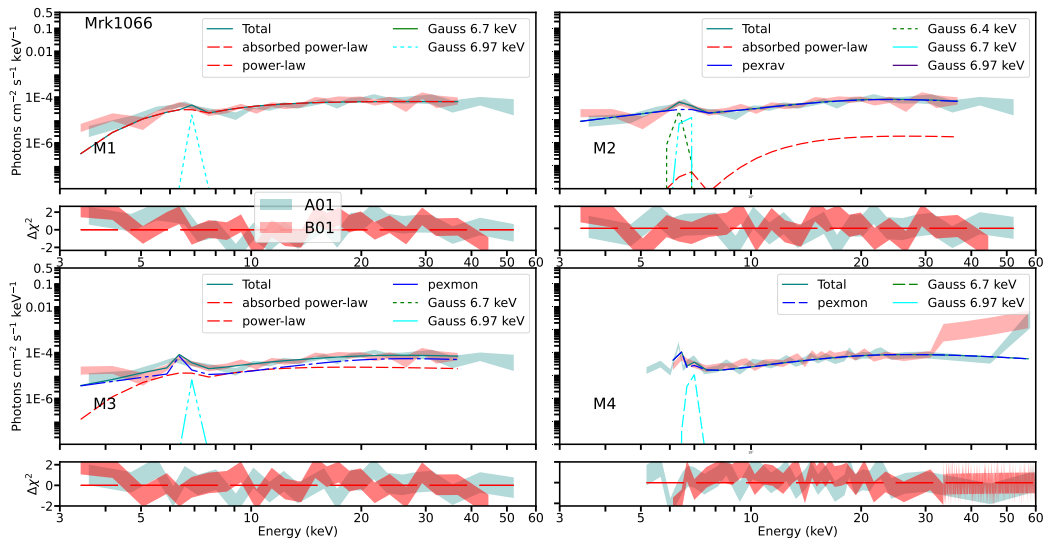


Figure 14: *NuSTAR* X-ray spectra of Mrk1066. Labels as in Fig. 8.1.

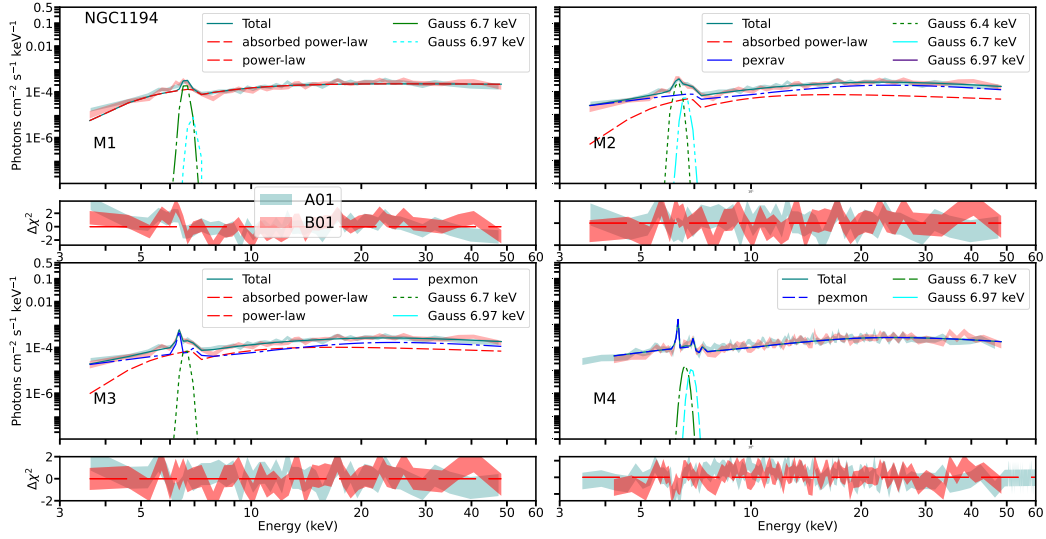


Figure 15: *NuSTAR* X-ray spectra of NGC1194. Labels as in Fig. 8.1.

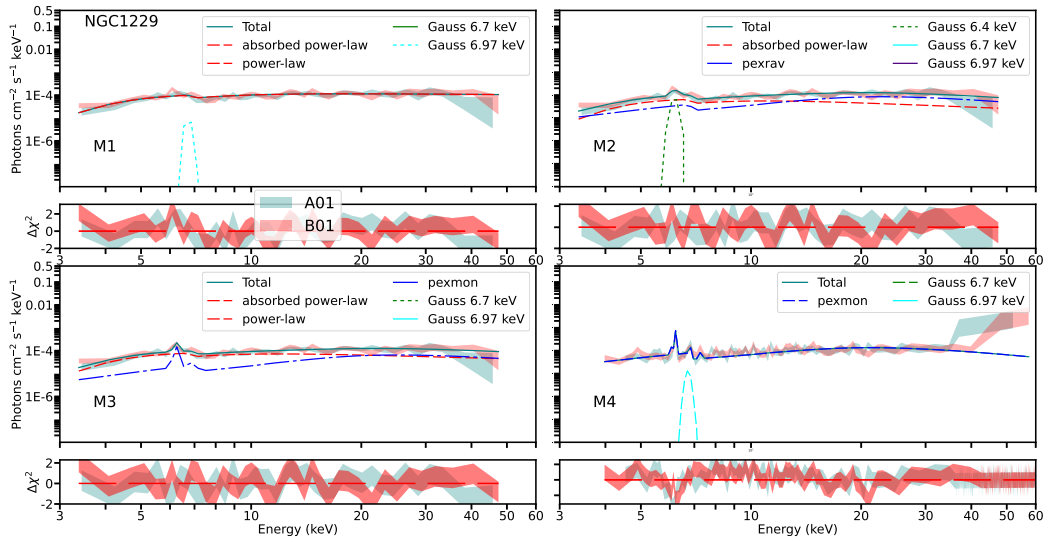


Figure 16: *NuSTAR* X-ray spectra of NGC1229. Labels as in Fig. 8.1.

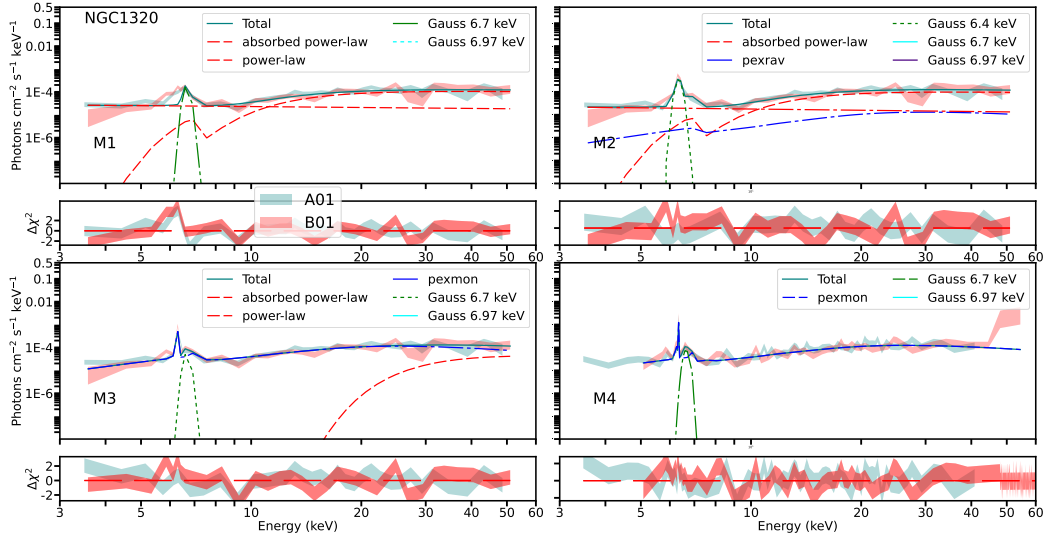


Figure 17: *NuSTAR* X-ray spectra of NGC1320. Labels as in Fig. 8.1.

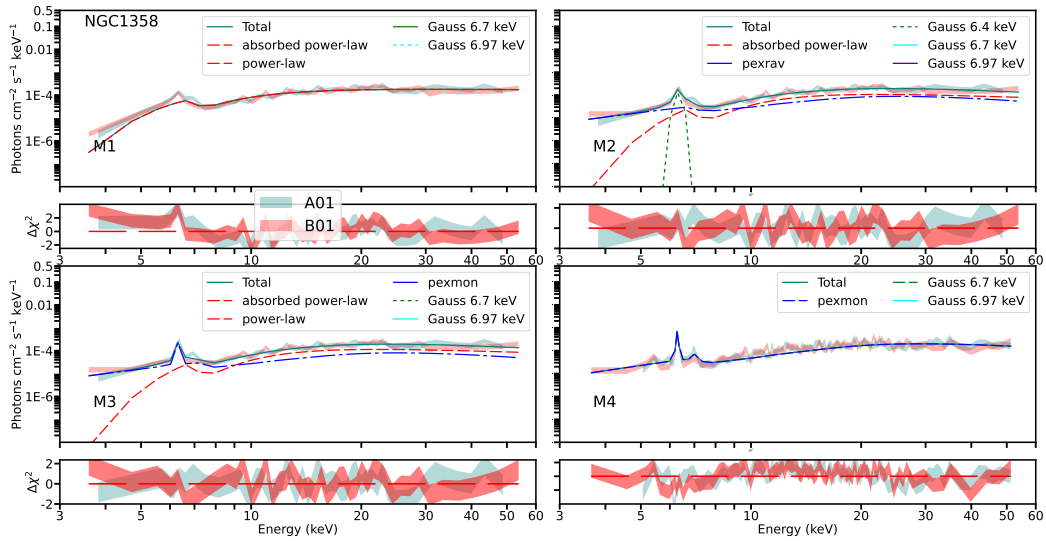


Figure 18: *NuSTAR* X-ray spectra of NGC1358. Labels as in Fig. 8.1.

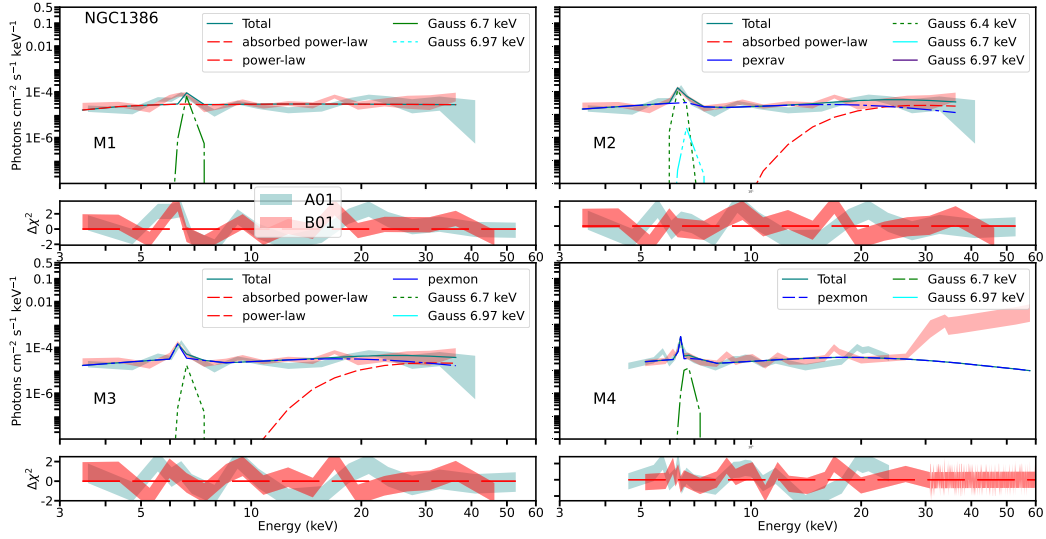


Figure 19: *NuSTAR* X-ray spectra of NGC1386. Labels as in Fig. 8.1.

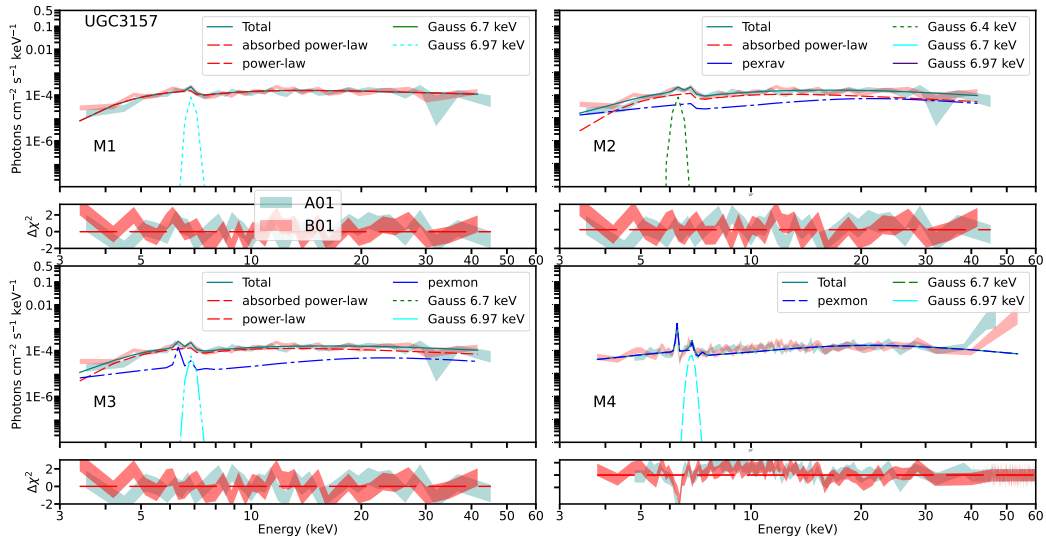


Figure 20: *NuSTAR* X-ray spectra of UGC3157. Labels as in Fig. 8.1.

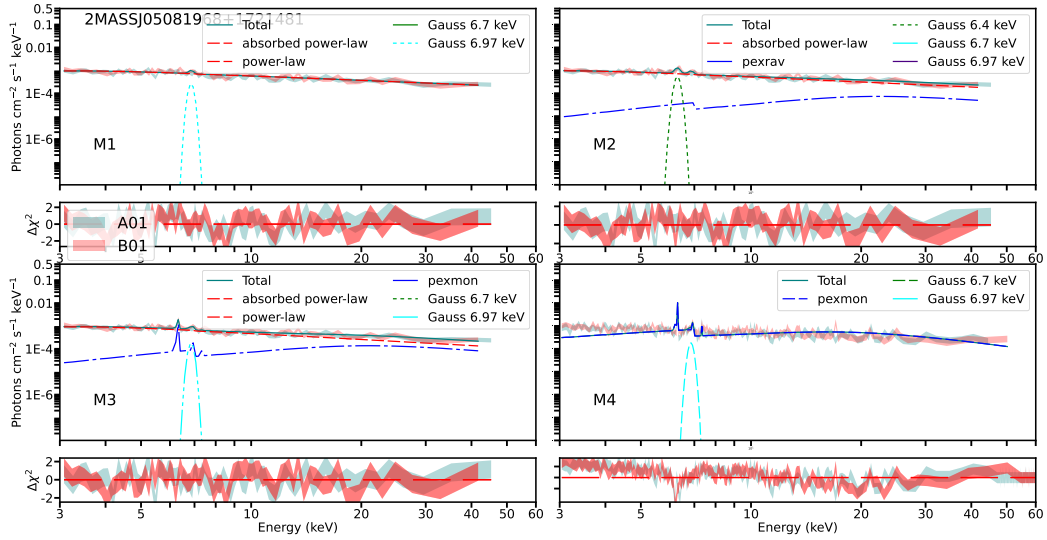


Figure 21: *NuSTAR* X-ray spectra of 2MASSJ05081968+1721481. Labels as in Fig. 8.1.

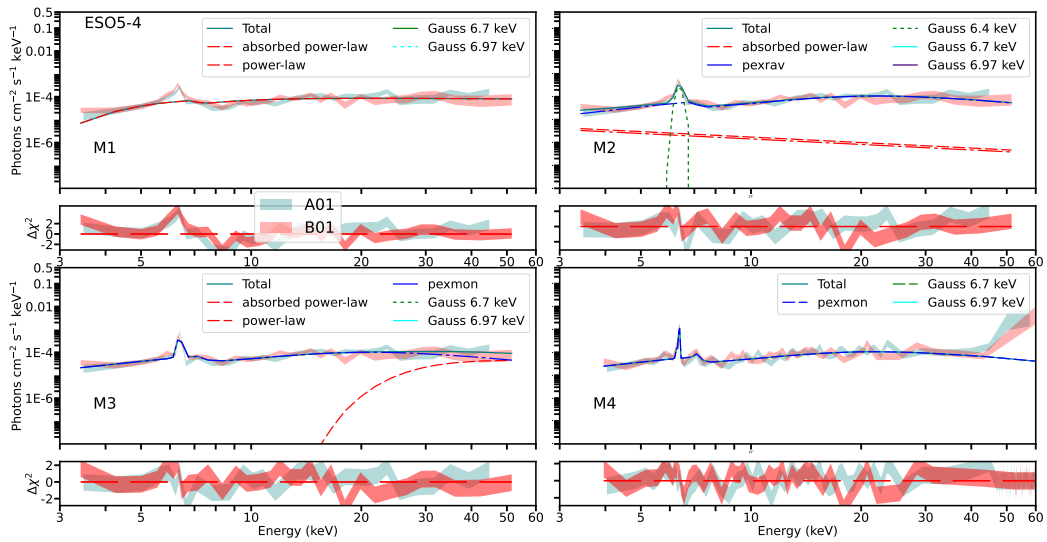


Figure 22: *NuSTAR* X-ray spectra of ESO5-4. Labels as in Fig. 8.1.

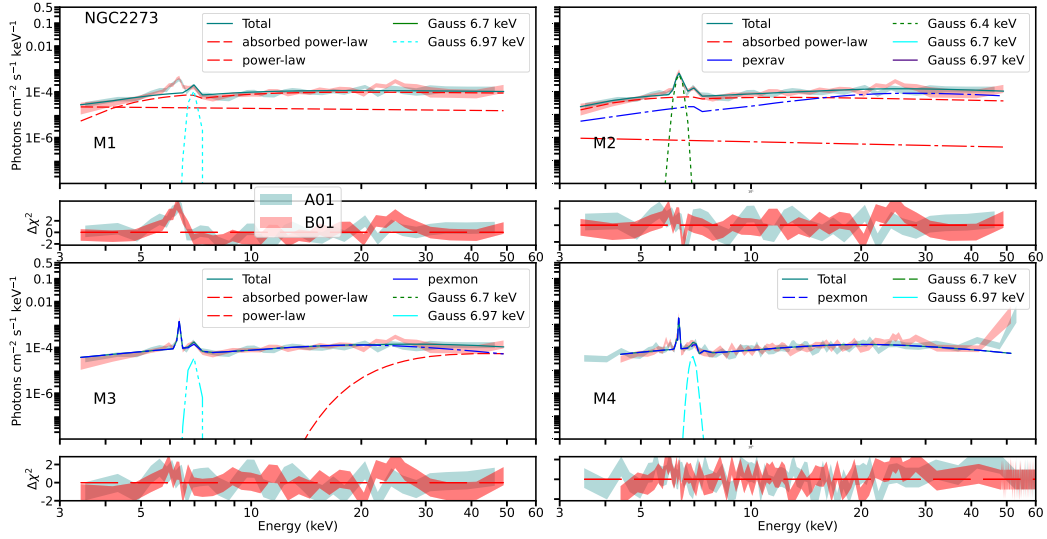


Figure 23: *NuSTAR* X-ray spectra of NGC2273. Labels as in Fig. 8.1.

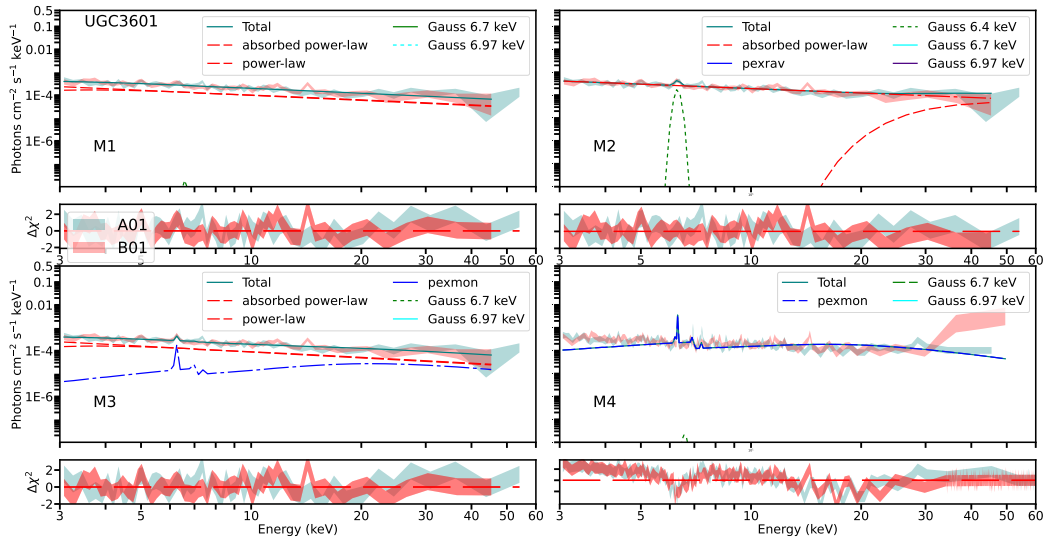


Figure 24: *NuSTAR* X-ray spectra of UGC3601. Labels as in Fig. 8.1.

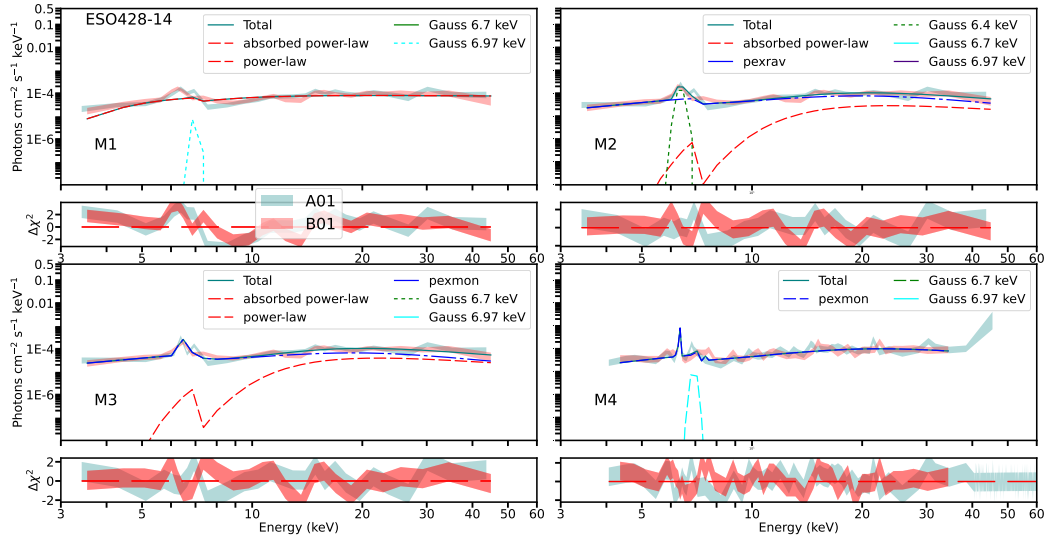


Figure 25: *NuSTAR* X-ray spectra of ESO428-14. Labels as in Fig. 8.1.

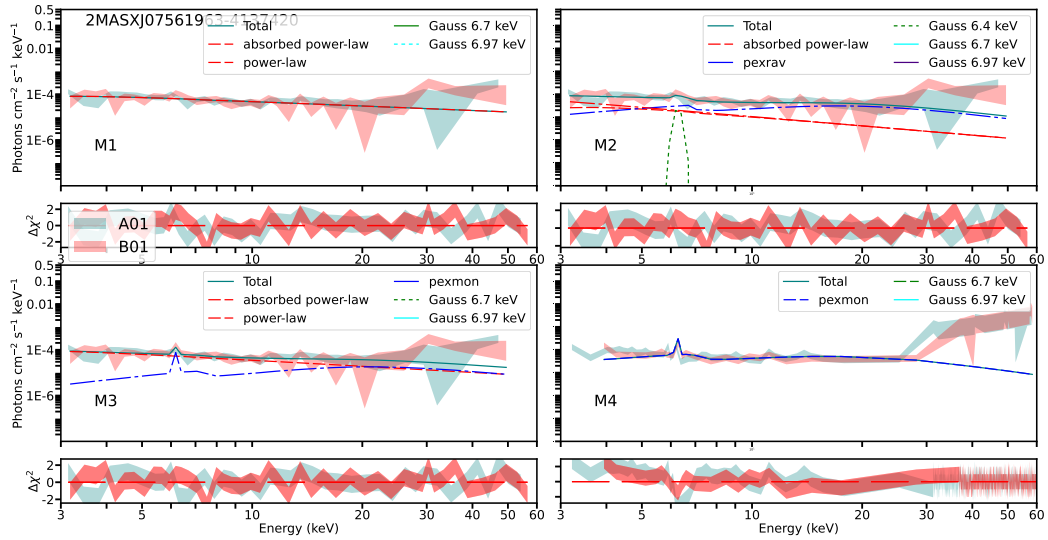


Figure 26: *NuSTAR* X-ray spectra of 2MASXJ07561963-4137420. Labels as in Fig. 8.1.

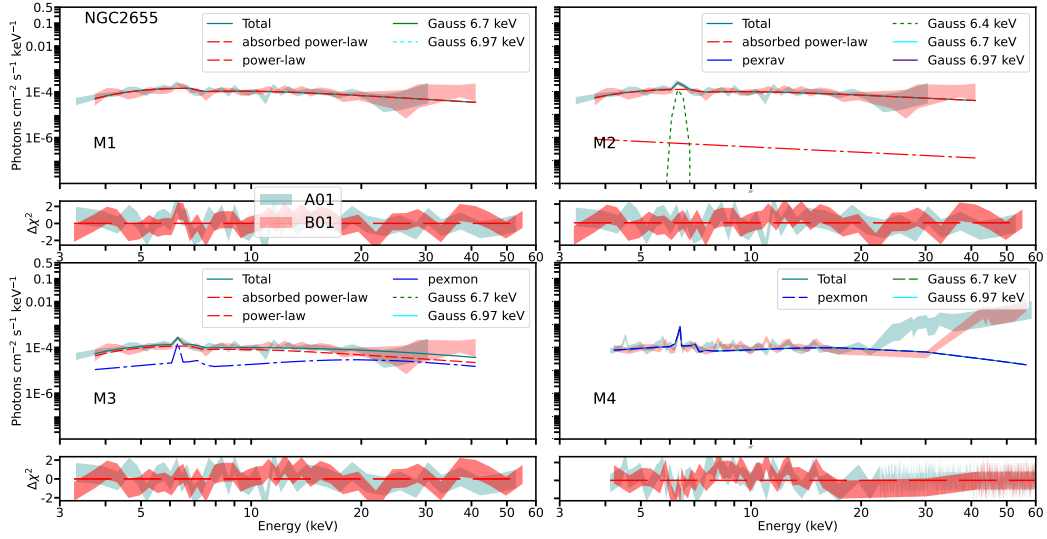


Figure 27: *NuSTAR* X-ray spectra of NGC2655. Labels as in Fig. 8.1.

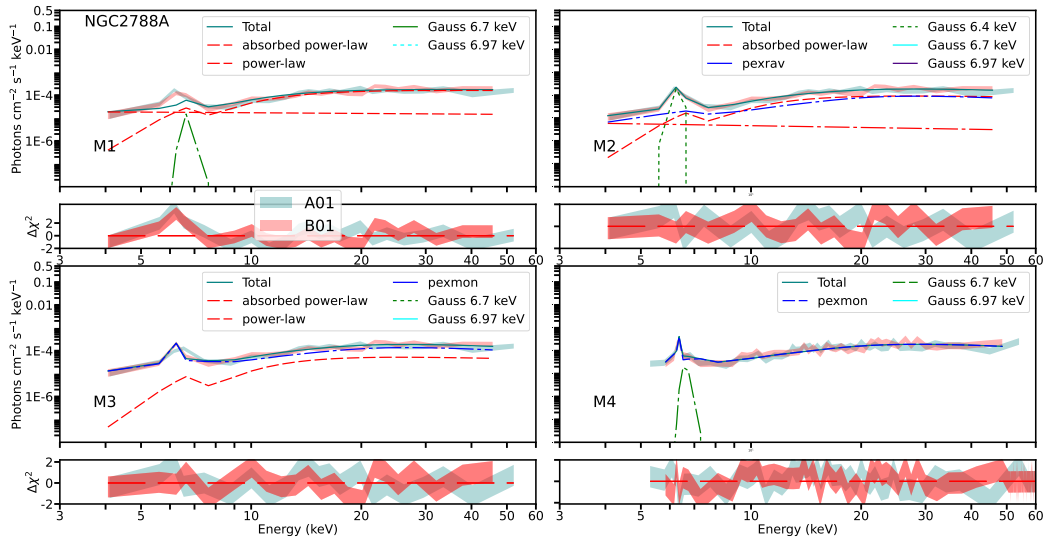


Figure 28: *NuSTAR* X-ray spectra of NGC2788A. Labels as in Fig. 8.1.

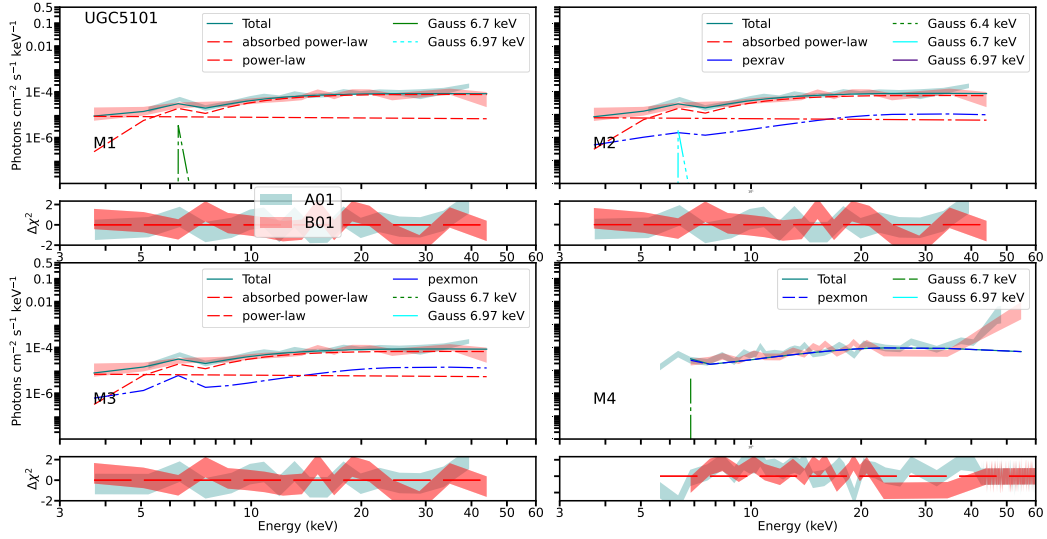


Figure 29: *NuSTAR* X-ray spectra of UGC5101. Labels as in Fig. 8.1.

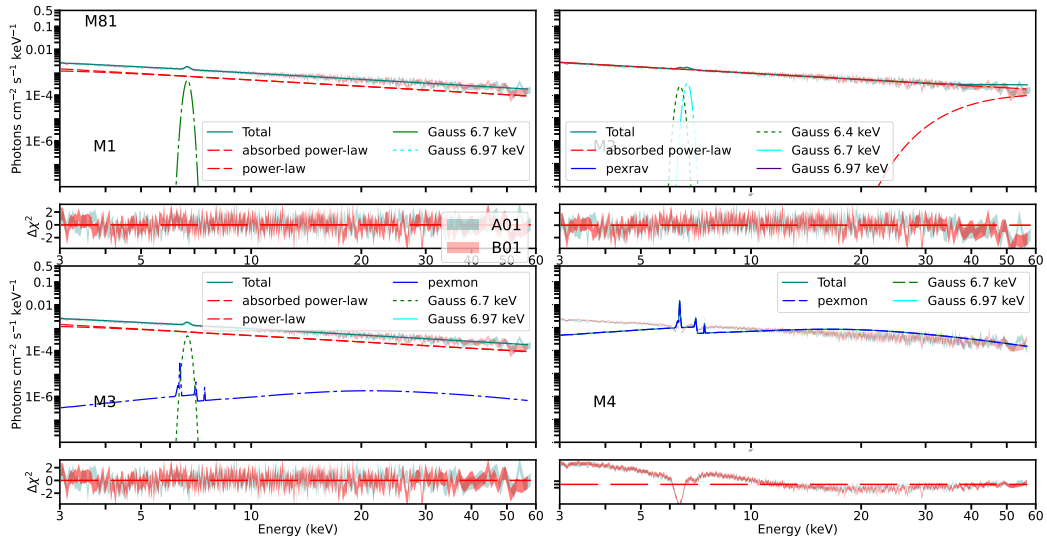


Figure 30: *NuSTAR* X-ray spectra of M81. Labels as in Fig. 8.1.

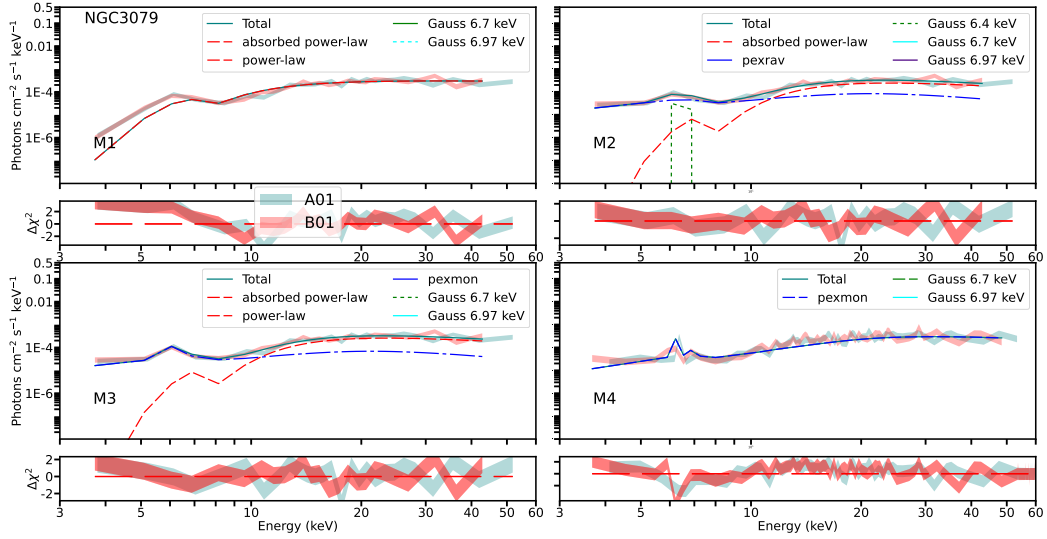


Figure 31: *NuSTAR* X-ray spectra of NGC3079. Labels as in Fig. 8.1.

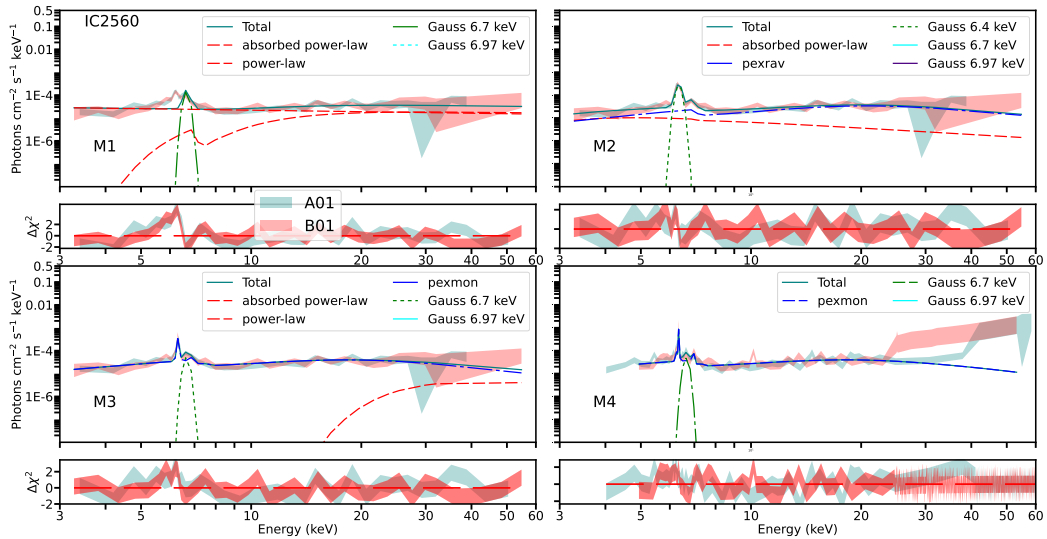


Figure 32: *NuSTAR* X-ray spectra of IC2560. Labels as in Fig. 8.1.

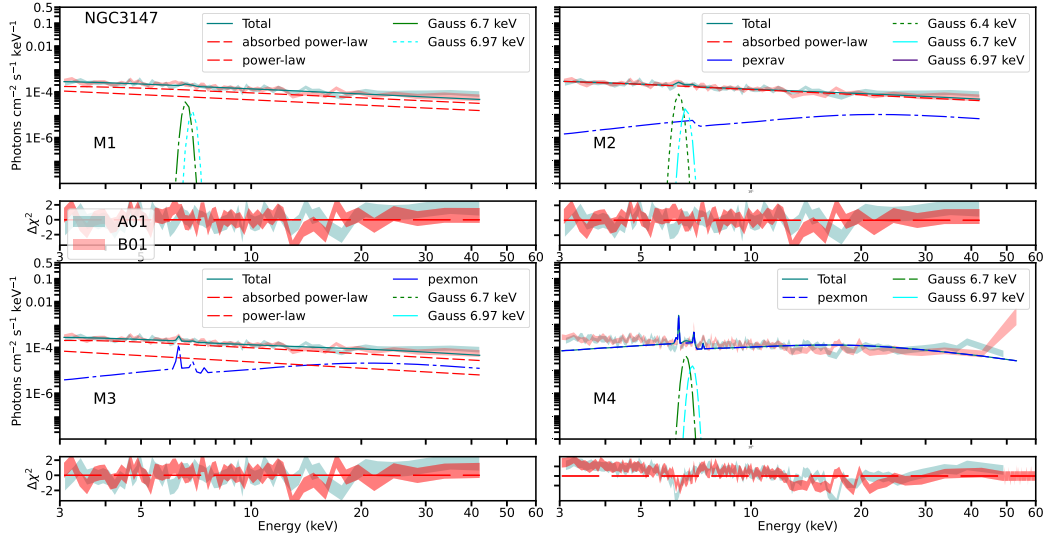


Figure 33: *NuSTAR* X-ray spectra of NGC3147. Labels as in Fig. 8.1.

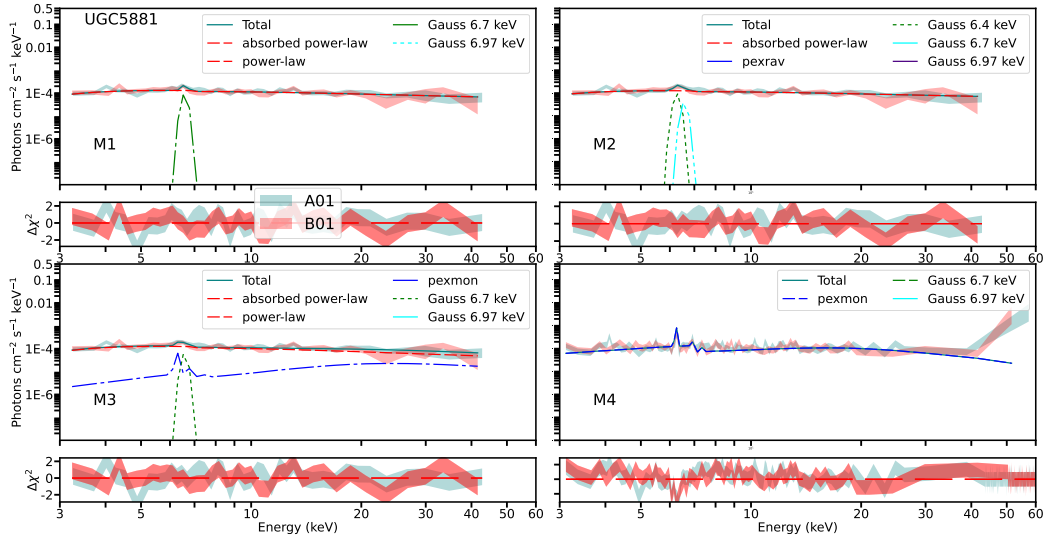


Figure 34: *NuSTAR* X-ray spectra of UGC5881. Labels as in Fig. 8.1.

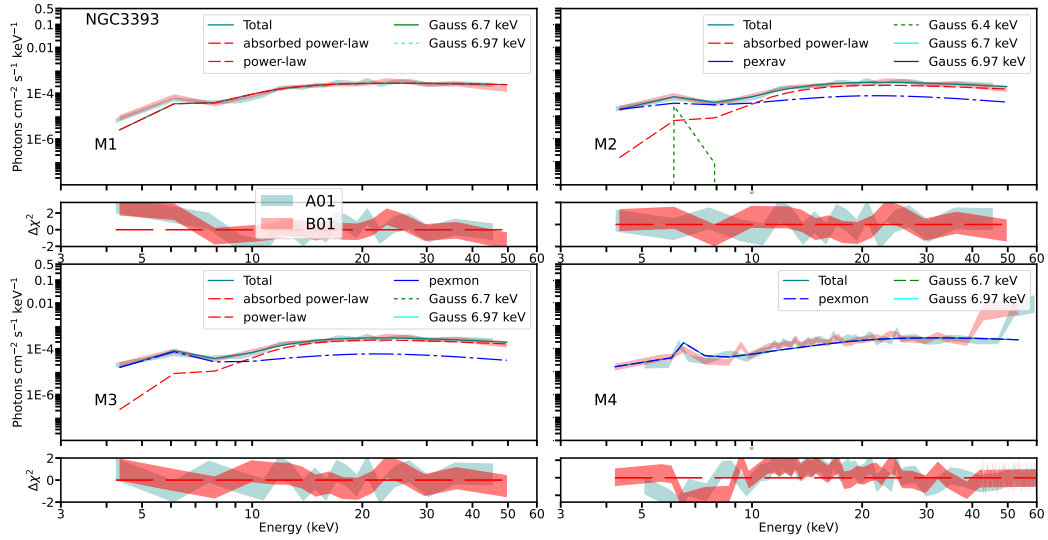


Figure 35: *NuSTAR* X-ray spectra of NGC3393. Labels as in Fig. 8.1.

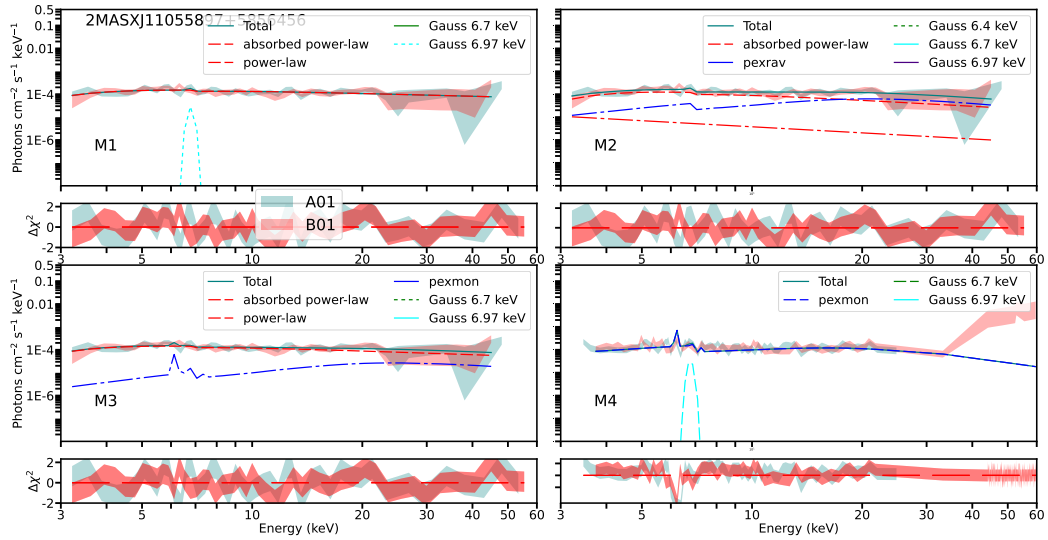


Figure 36: *NuSTAR* X-ray spectra of 2MASXJ11055897+5856456. Labels as in Fig. 8.1.

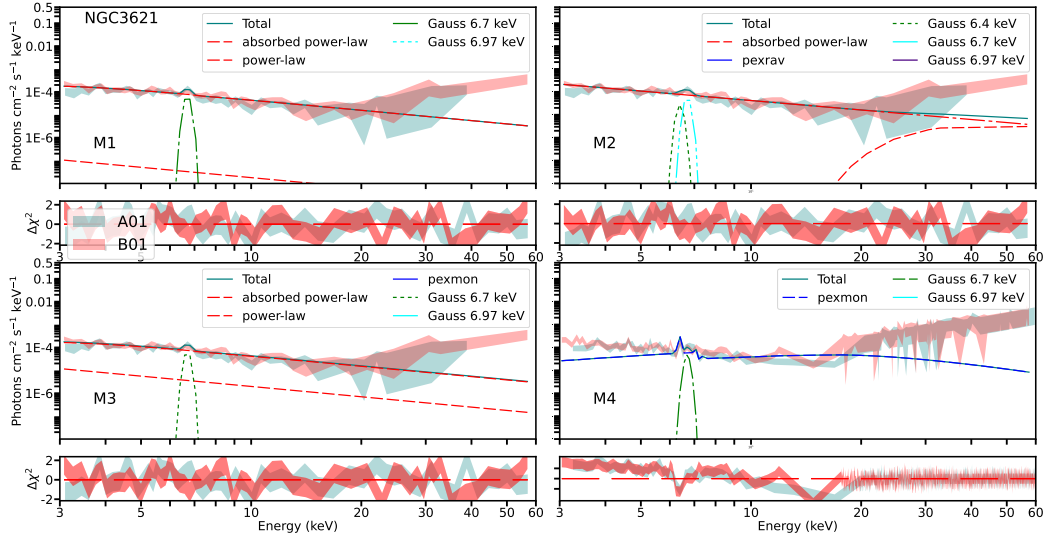


Figure 37: *NuSTAR* X-ray spectra of NGC3621. Labels as in Fig. 8.1.

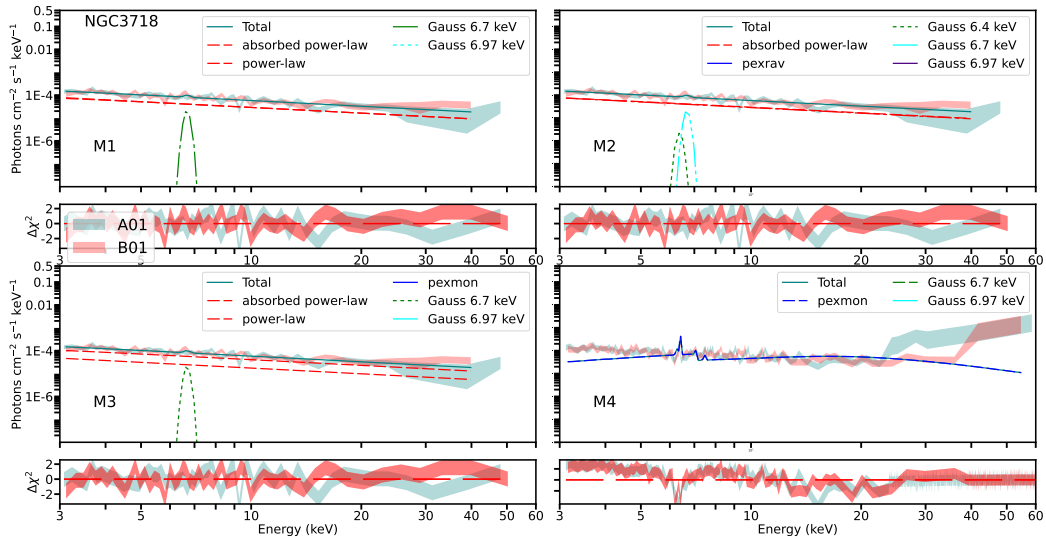


Figure 38: *NuSTAR* X-ray spectra of NGC3718. Labels as in Fig. 8.1.

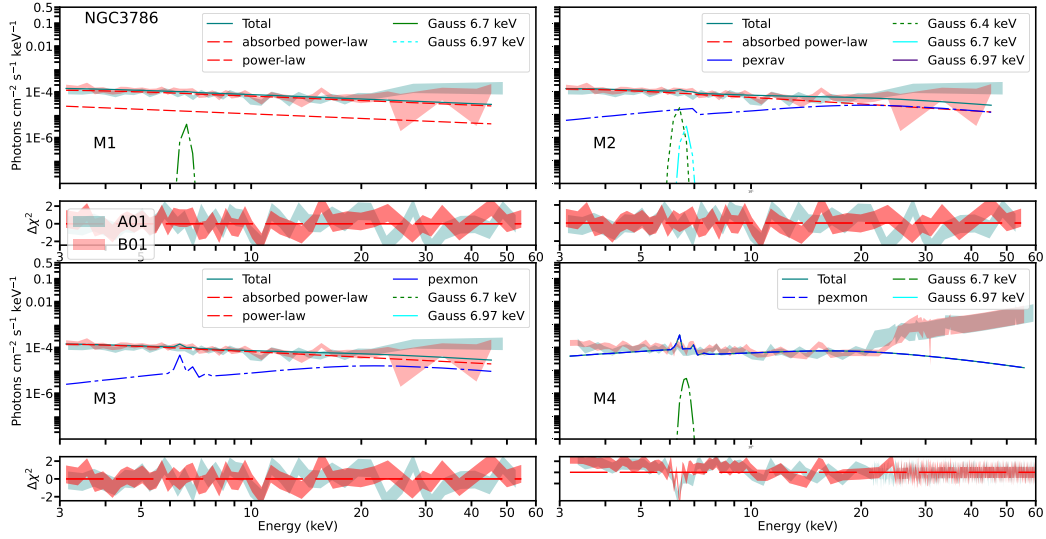


Figure 39: *NuSTAR* X-ray spectra of NGC3786. Labels as in Fig. 8.1.

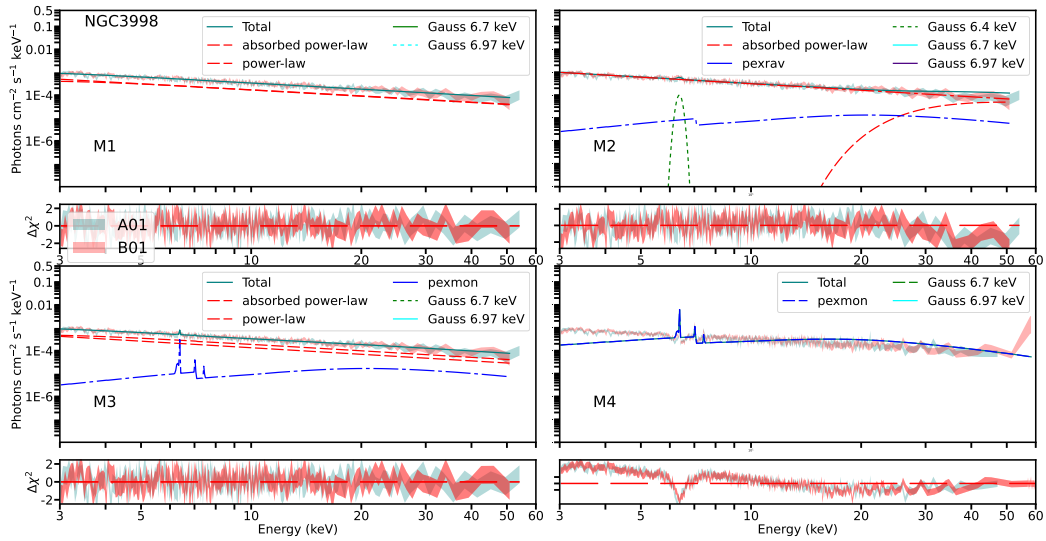


Figure 40: *NuSTAR* X-ray spectra of NGC3998. Labels as in Fig. 8.1.

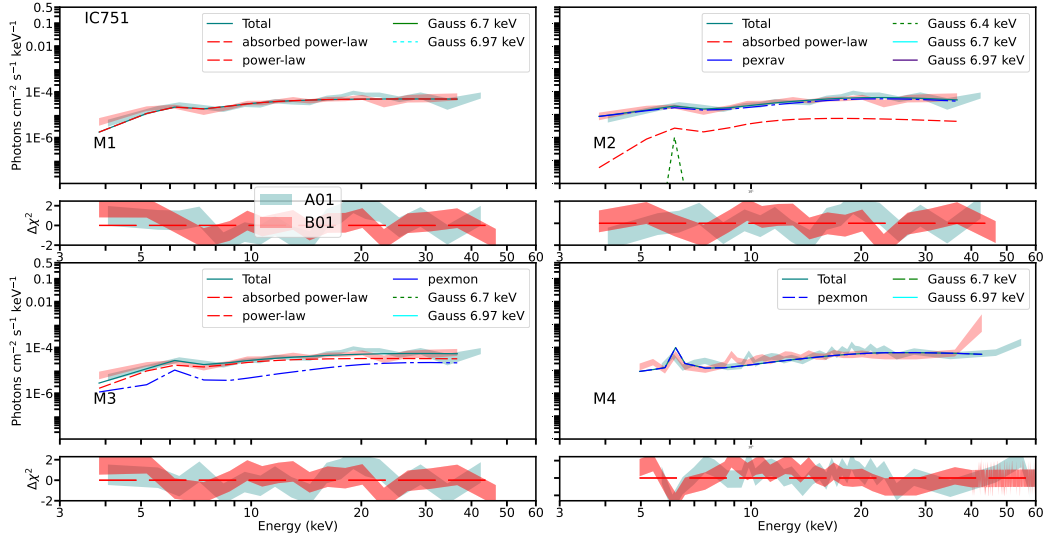


Figure 41: *NuSTAR* X-ray spectra of IC751. Labels as in Fig. 8.1.

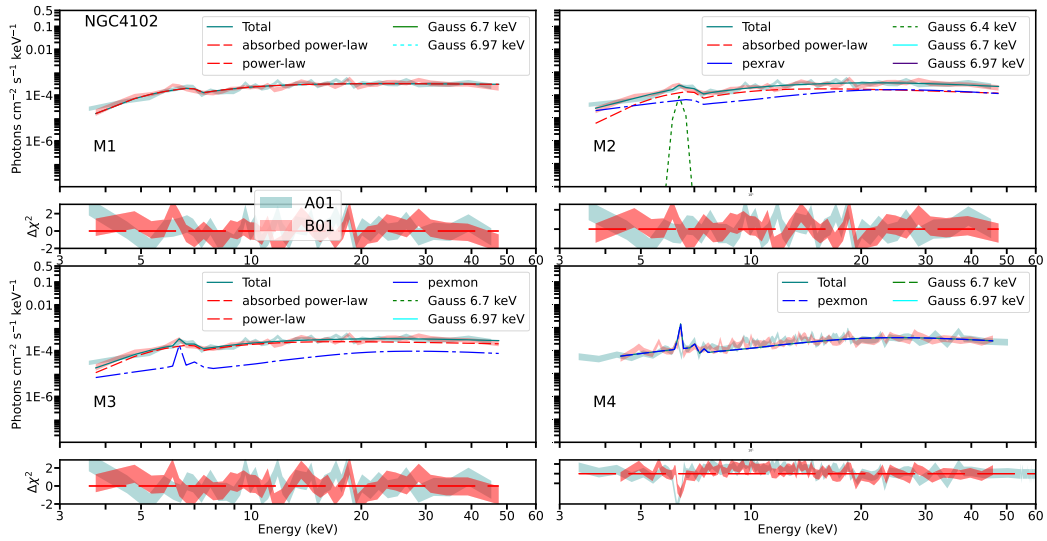


Figure 42: *NuSTAR* X-ray spectra of NGC4102. Labels as in Fig. 8.1.

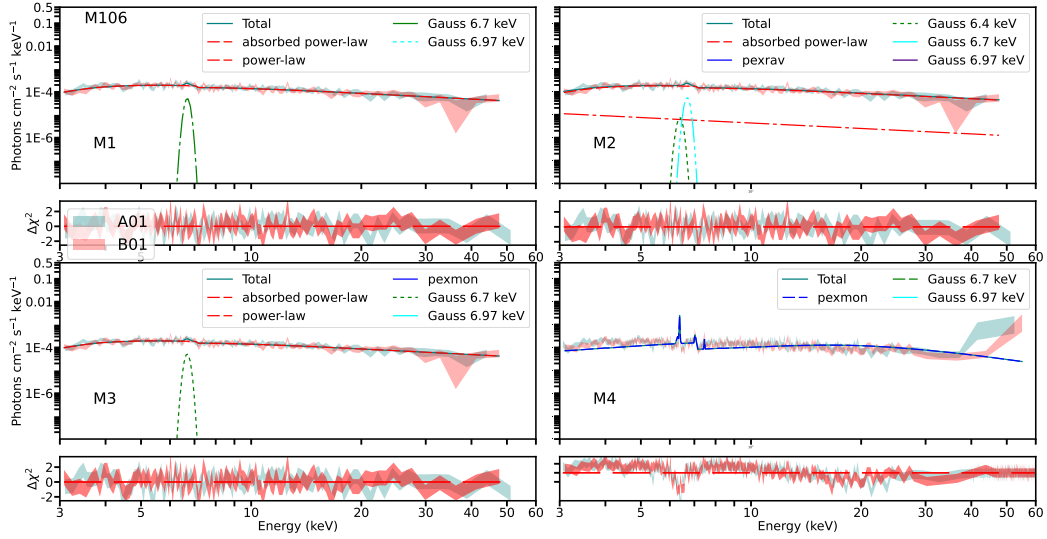


Figure 43: *NuSTAR* X-ray spectra of M106. Labels as in Fig. 8.1.

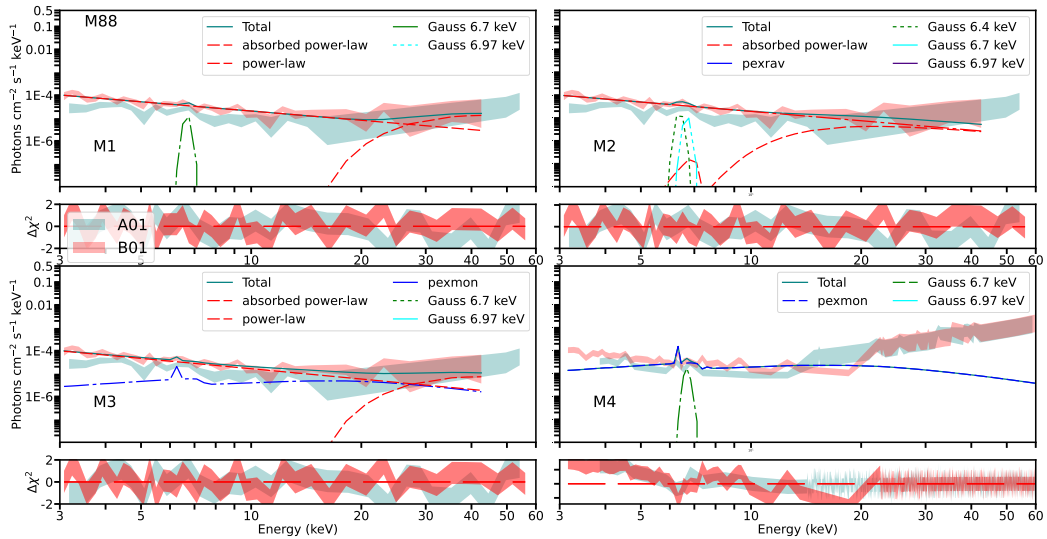


Figure 44: *NuSTAR* X-ray spectra of M88. Labels as in Fig. 8.1.

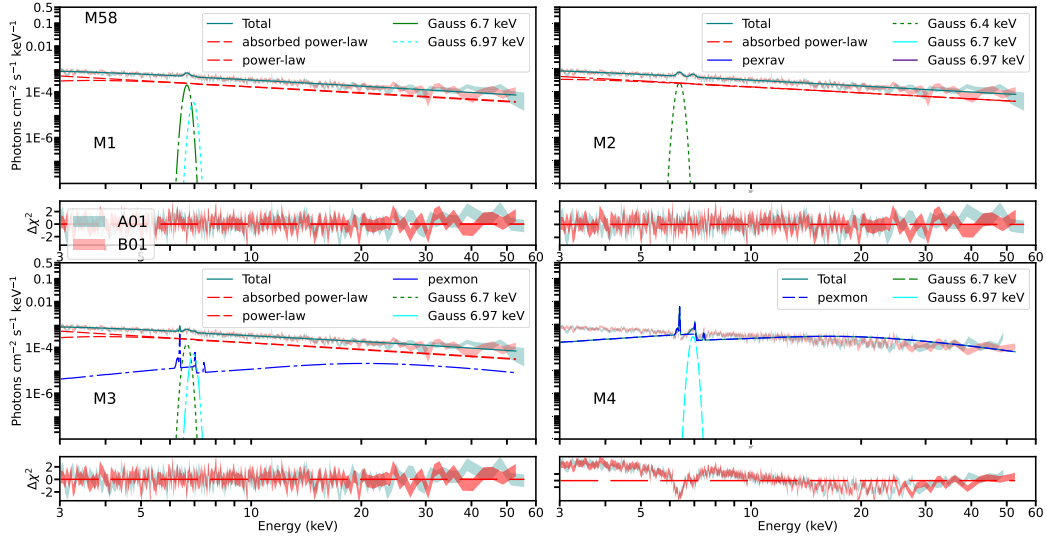


Figure 45: *NuSTAR* X-ray spectra of M58. Labels as in Fig. 8.1.

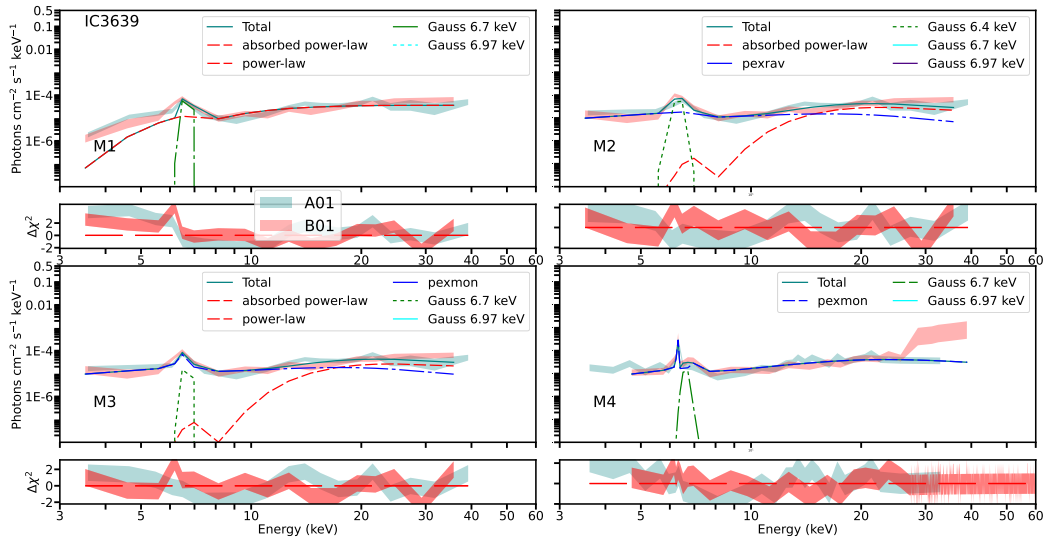


Figure 46: *NuSTAR* X-ray spectra of IC3639. Labels as in Fig. 8.1.

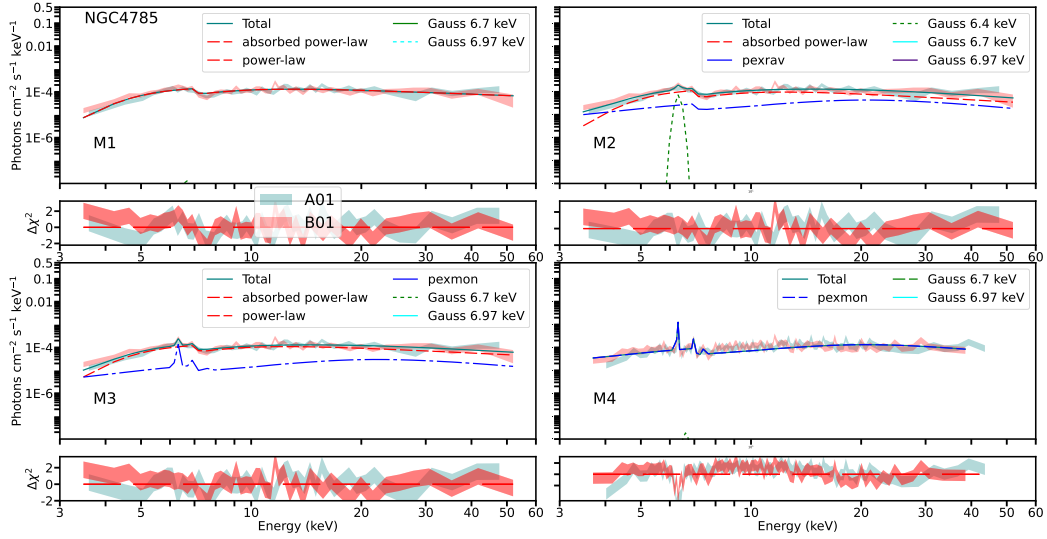


Figure 47: *NuSTAR* X-ray spectra of NGC4785. Labels as in Fig. 8.1.

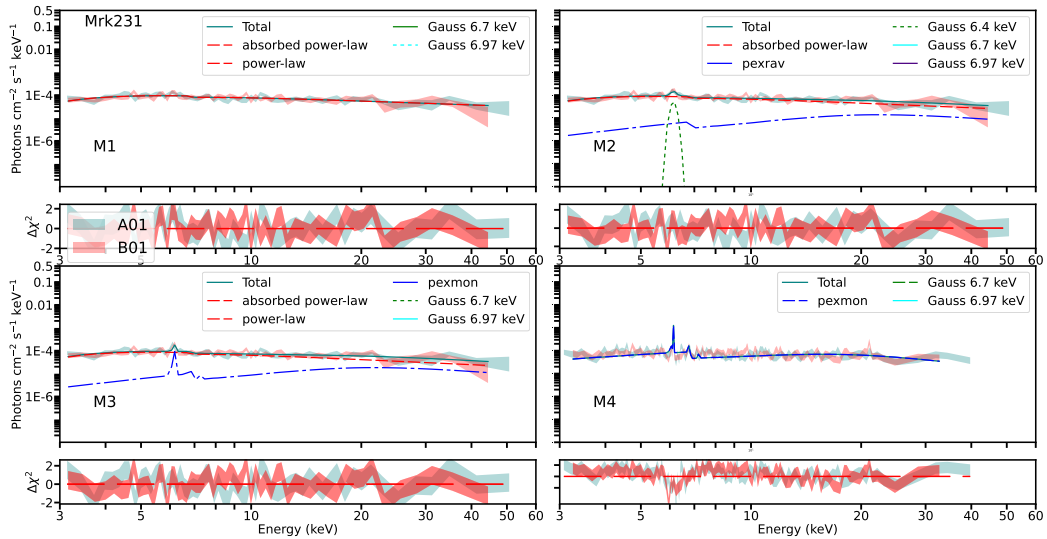


Figure 48: *NuSTAR* X-ray spectra of Mrk231. Labels as in Fig. 8.1.

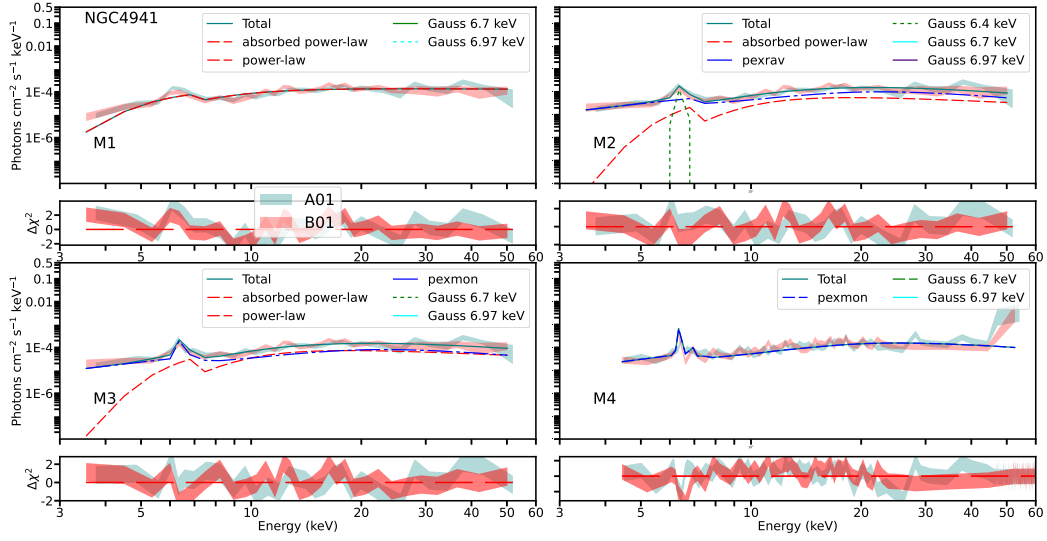


Figure 49: *NuSTAR* X-ray spectra of NGC4941. Labels as in Fig. 8.1.

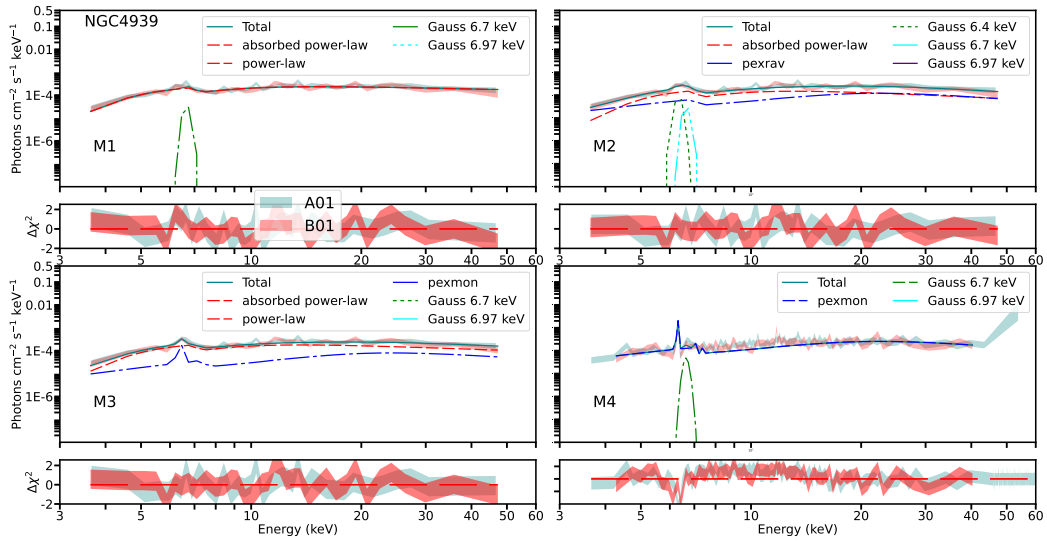


Figure 50: *NuSTAR* X-ray spectra of NGC4939. Labels as in Fig. 8.1.

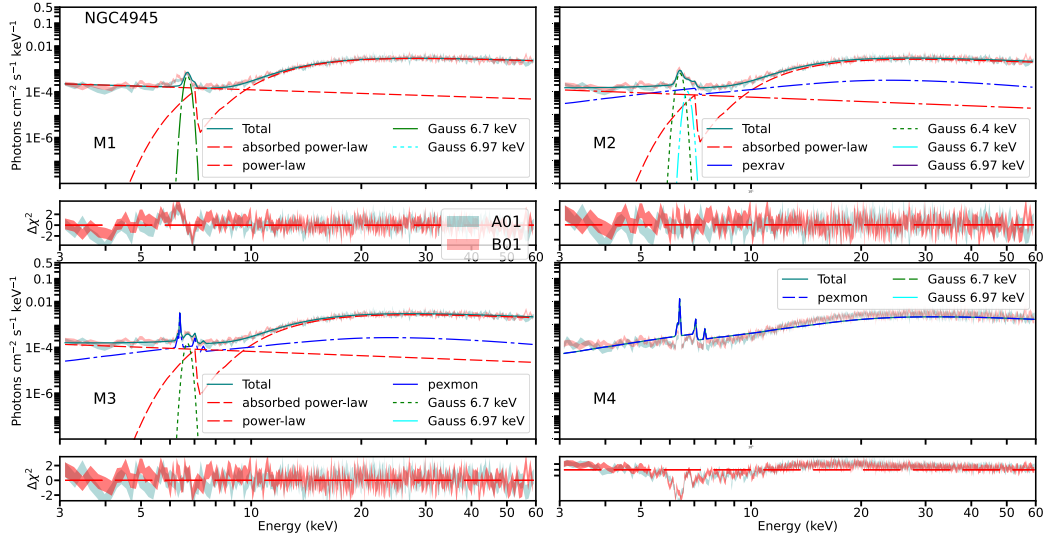


Figure 51: *NuSTAR* X-ray spectra of NGC4945. Labels as in Fig. 8.1.

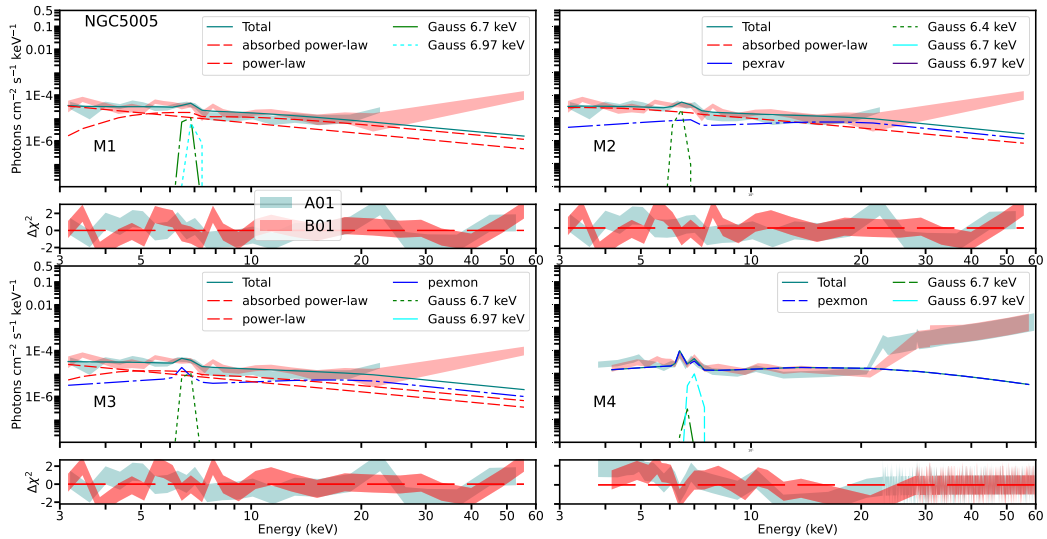


Figure 52: *NuSTAR* X-ray spectra of NGC5005. Labels as in Fig. 8.1.

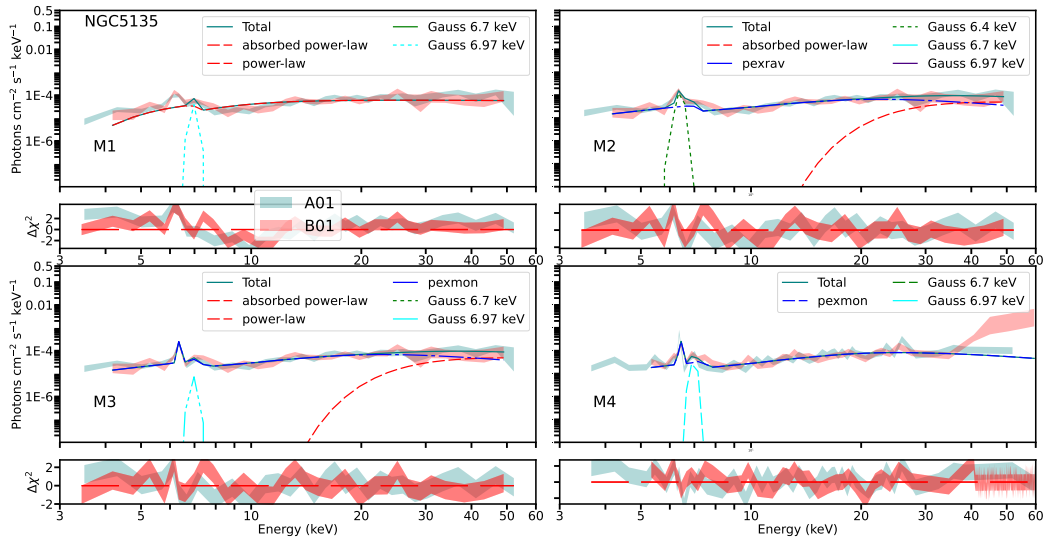


Figure 54: *NuSTAR* X-ray spectra of NGC5135. Labels as in Fig. 8.1.

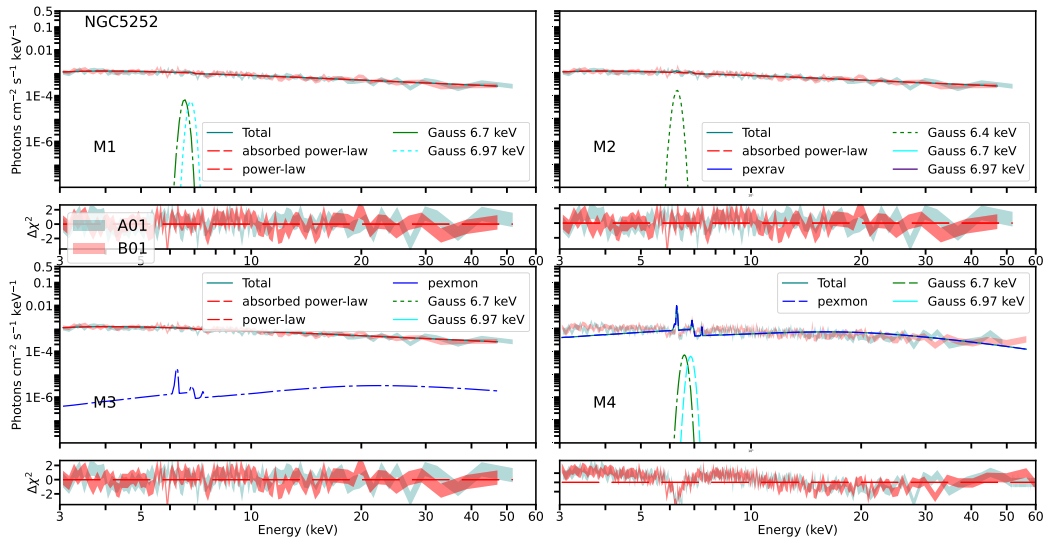


Figure 55: *NuSTAR* X-ray spectra of NGC5252. Labels as in Fig. 8.1.

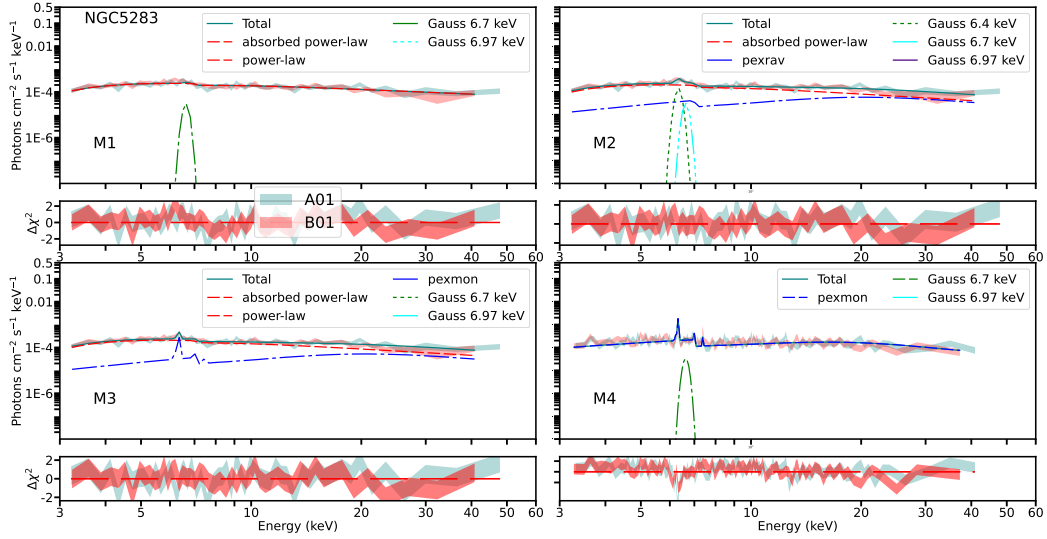


Figure 56: *NuSTAR* X-ray spectra of NGC5283. Labels as in Fig. 8.1.

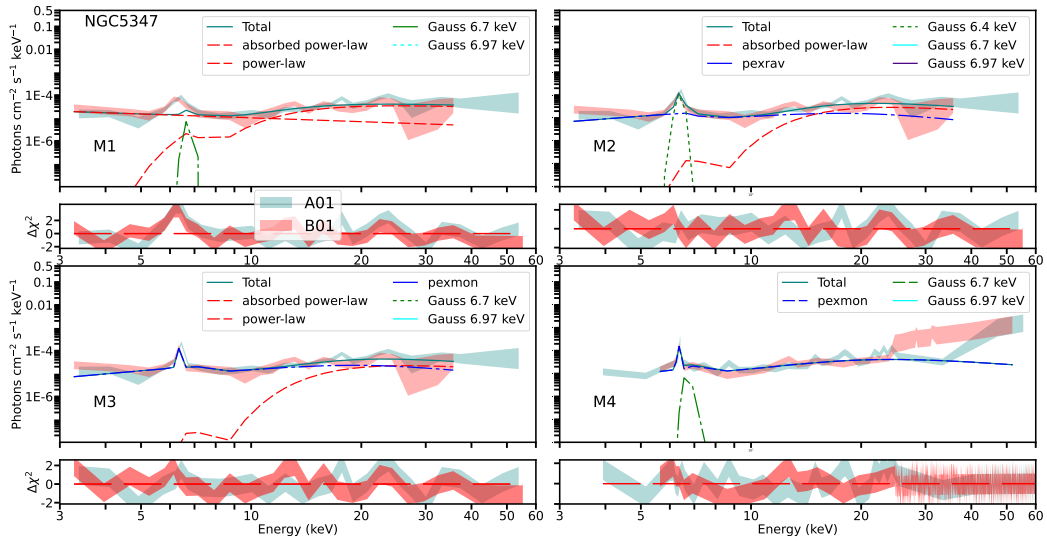


Figure 57: *NuSTAR* X-ray spectra of NGC5347. Labels as in Fig. 8.1.

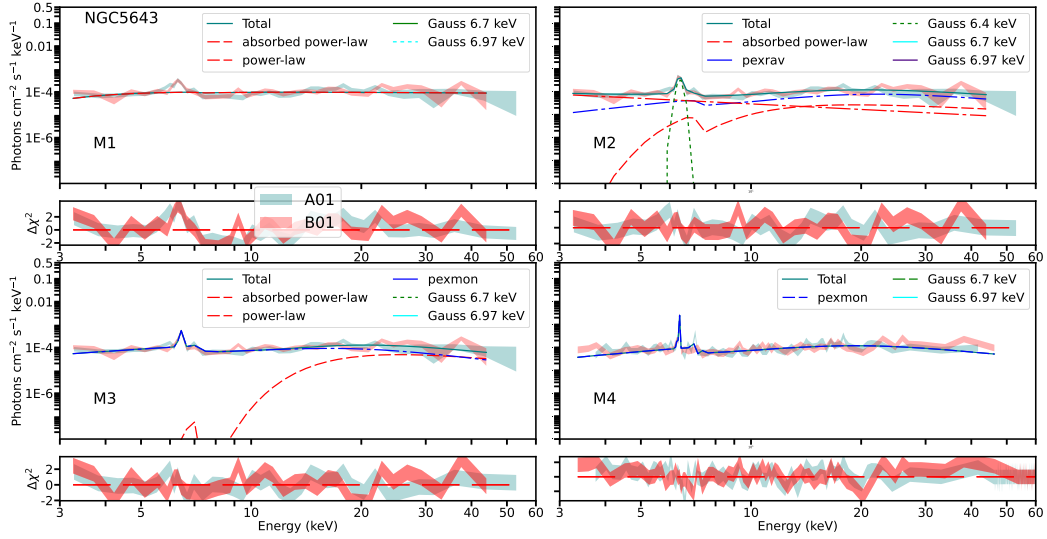


Figure 58: *NuSTAR* X-ray spectra of NGC5643. Labels as in Fig. 8.1.

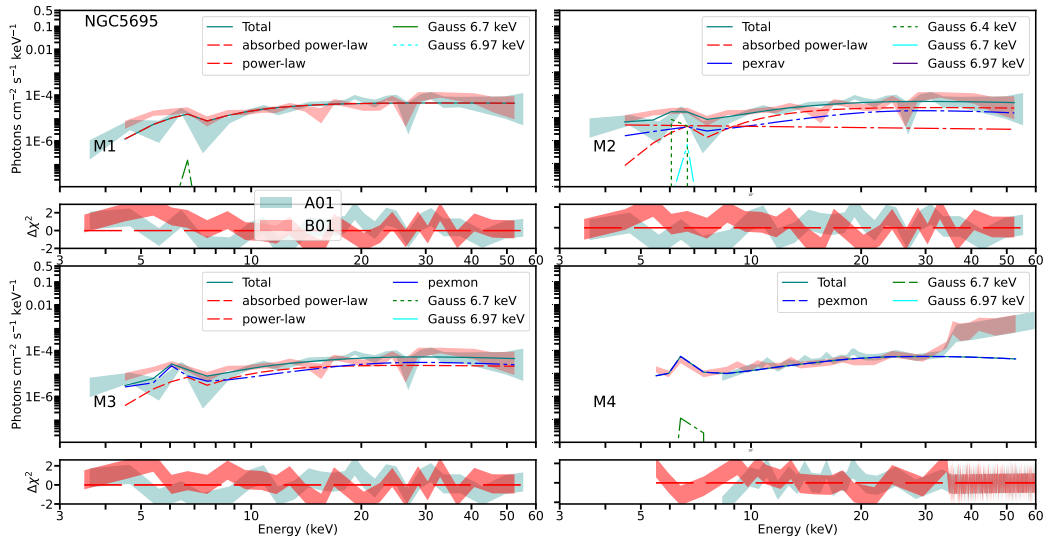


Figure 59: *NuSTAR* X-ray spectra of NGC5695. Labels as in Fig. 8.1.

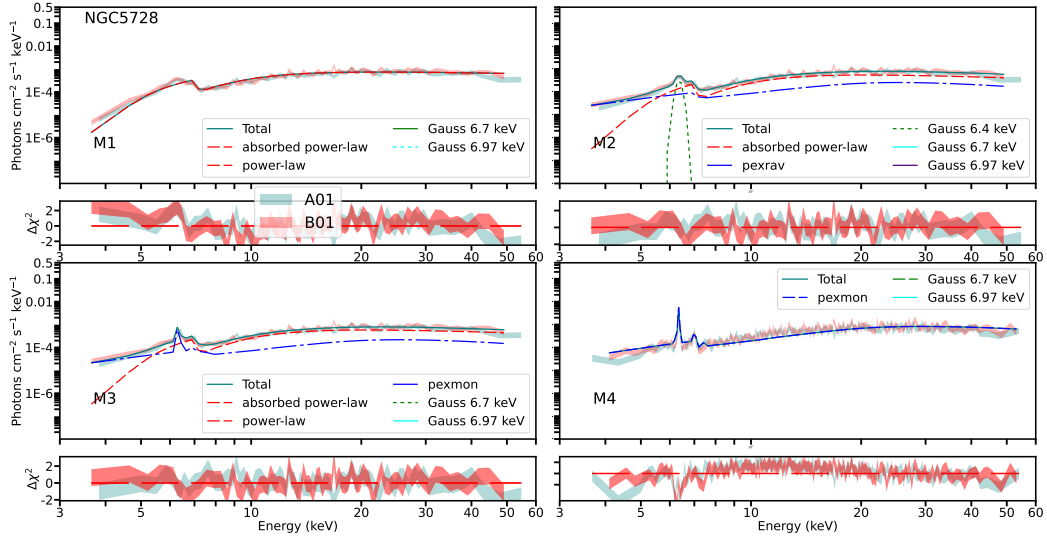


Figure 60: *NuSTAR* X-ray spectra of NGC5728. Labels as in Fig. 8.1.

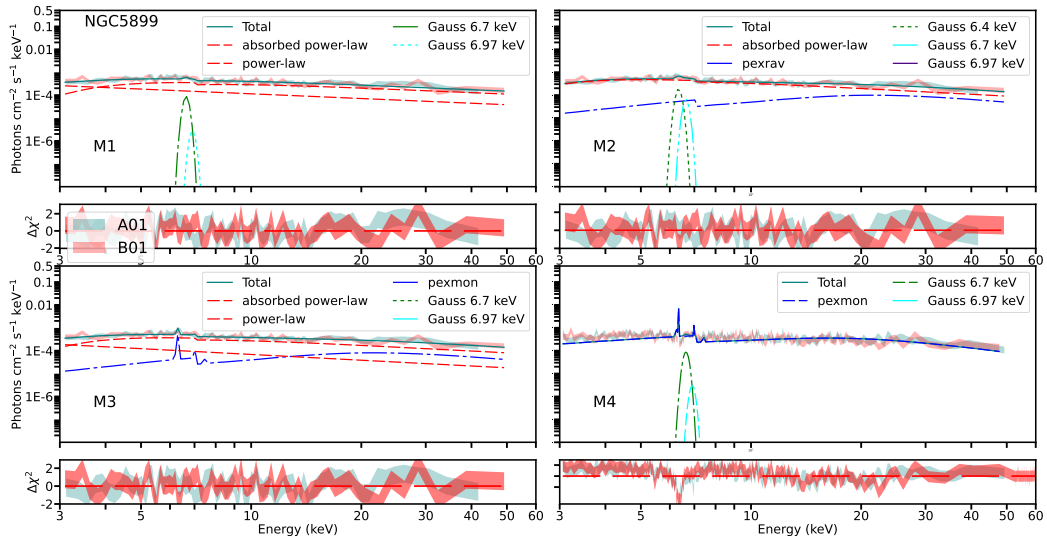


Figure 61: *NuSTAR* X-ray spectra of NGC5899. Labels as in Fig. 8.1.

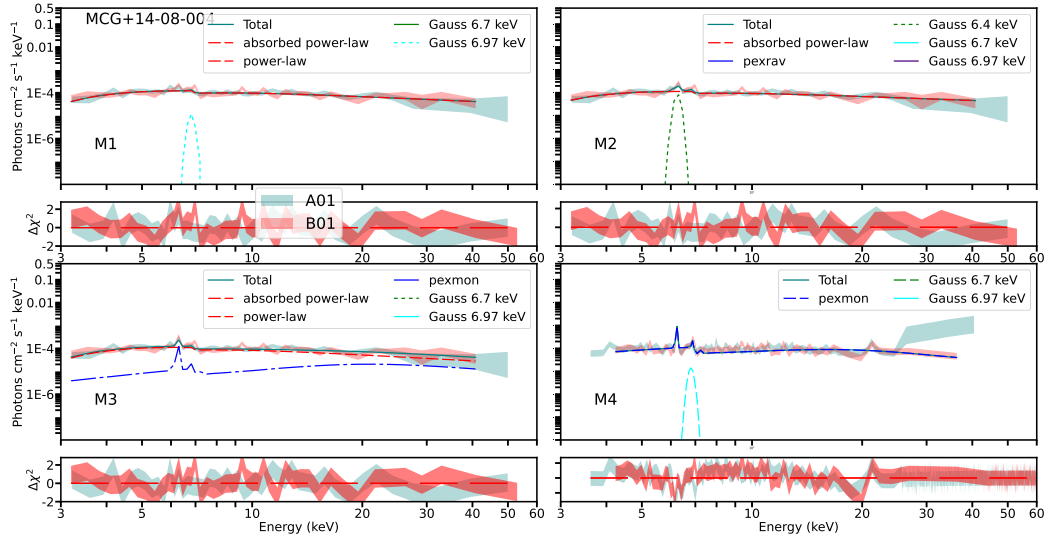


Figure 62: *NuSTAR* X-ray spectra of MCG+14-08-004. Labels as in Fig. 8.1.

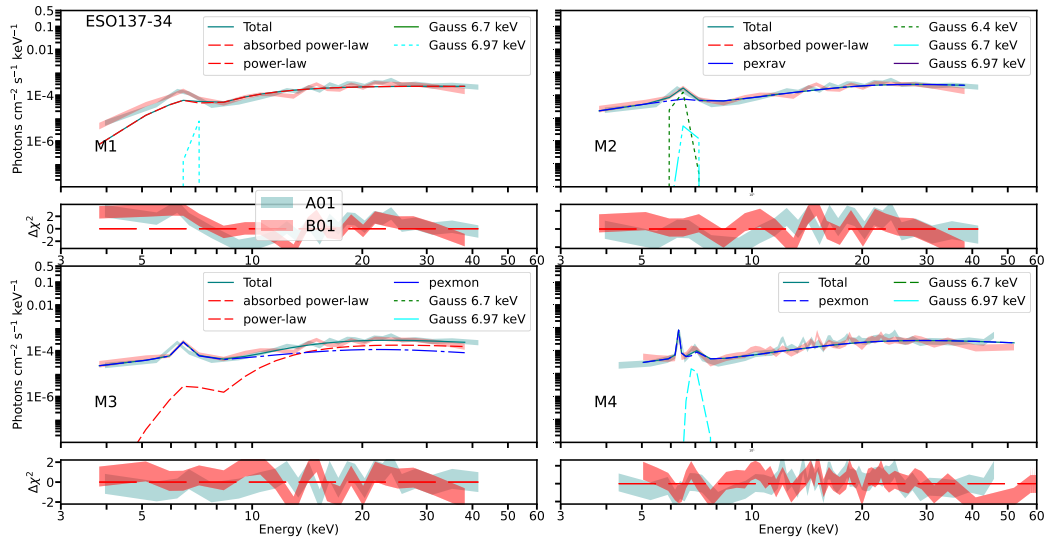


Figure 63: *NuSTAR* X-ray spectra of ESO137-34. Labels as in Fig. 8.1.

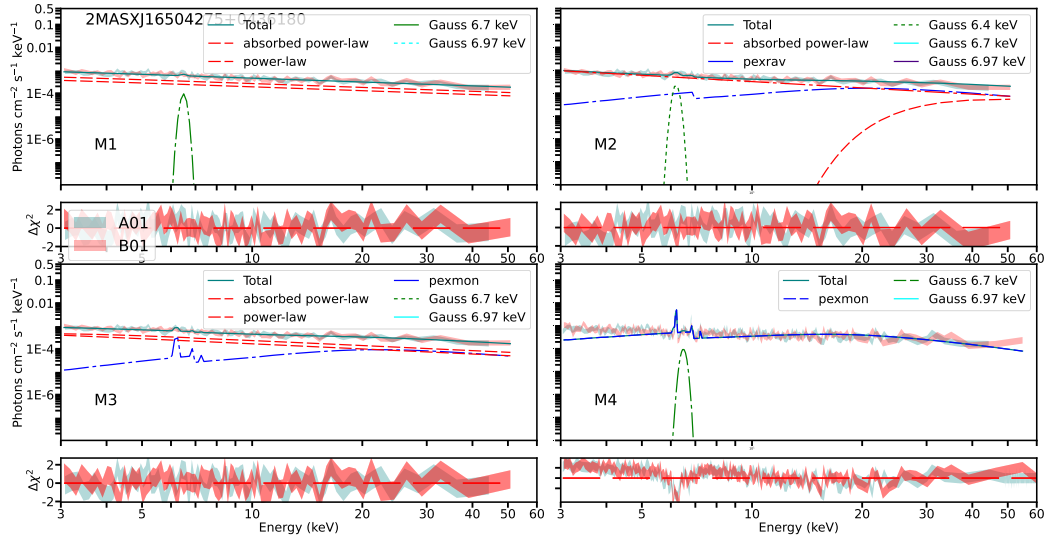


Figure 64: *NuSTAR* X-ray spectra of 2MASXJ16504275+0436180. Labels as in Fig. 8.1.

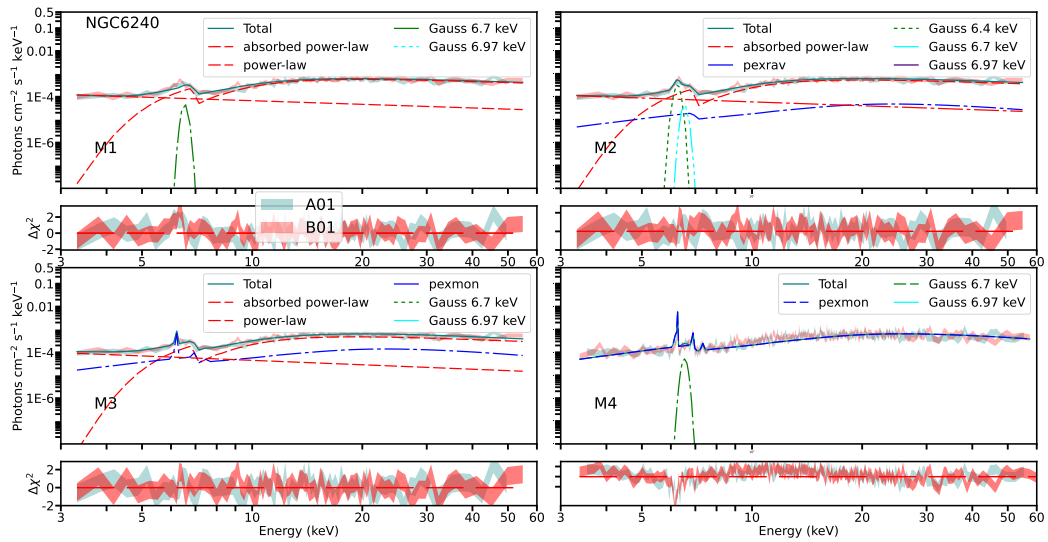


Figure 65: *NuSTAR* X-ray spectra of NGC6240. Labels as in Fig. 8.1.

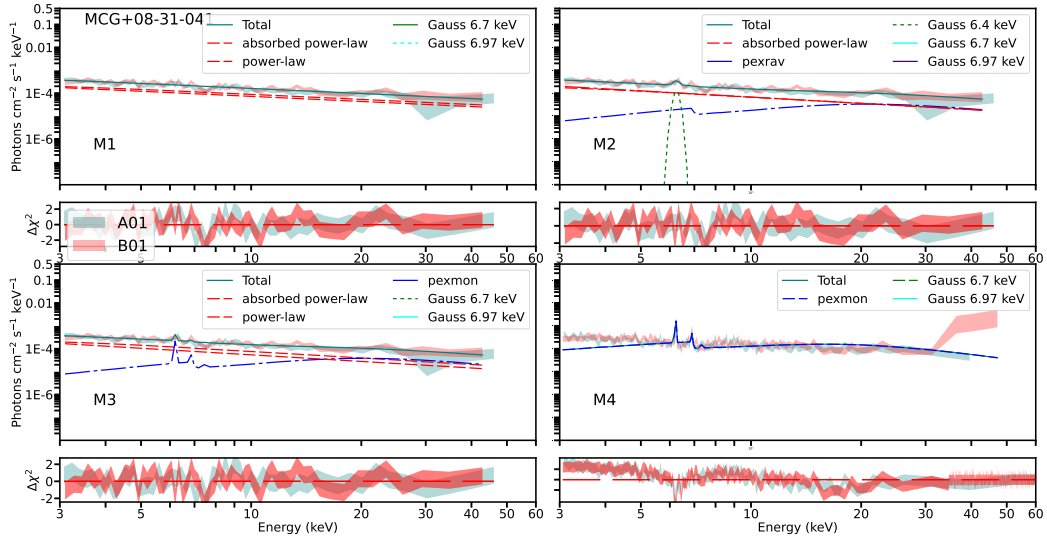


Figure 66: *NuSTAR* X-ray spectra of MCG+08-31-041. Labels as in Fig. 8.1.

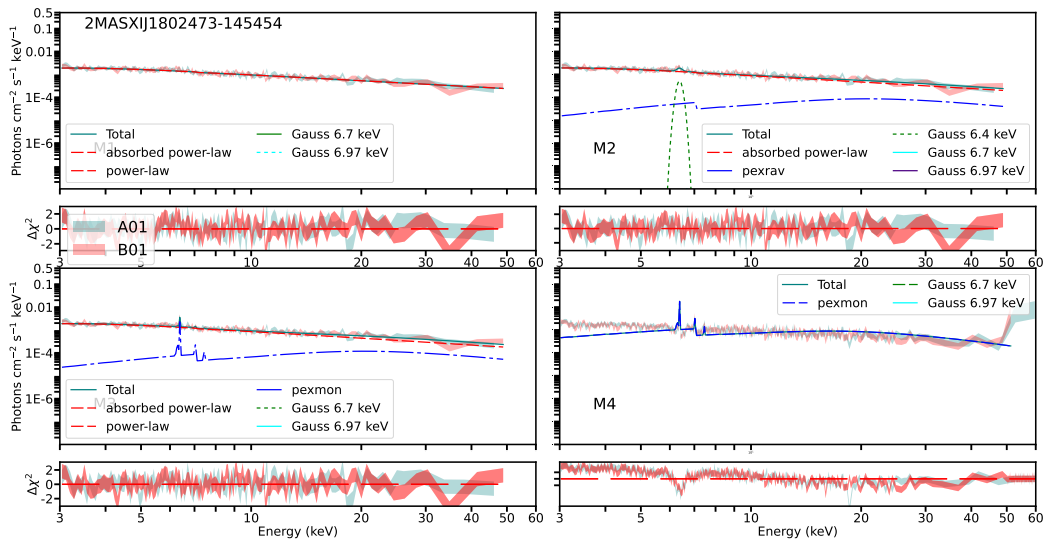


Figure 67: *NuSTAR* X-ray spectra of 2MASXIJ1802473-145454. Labels as in Fig. 8.1.

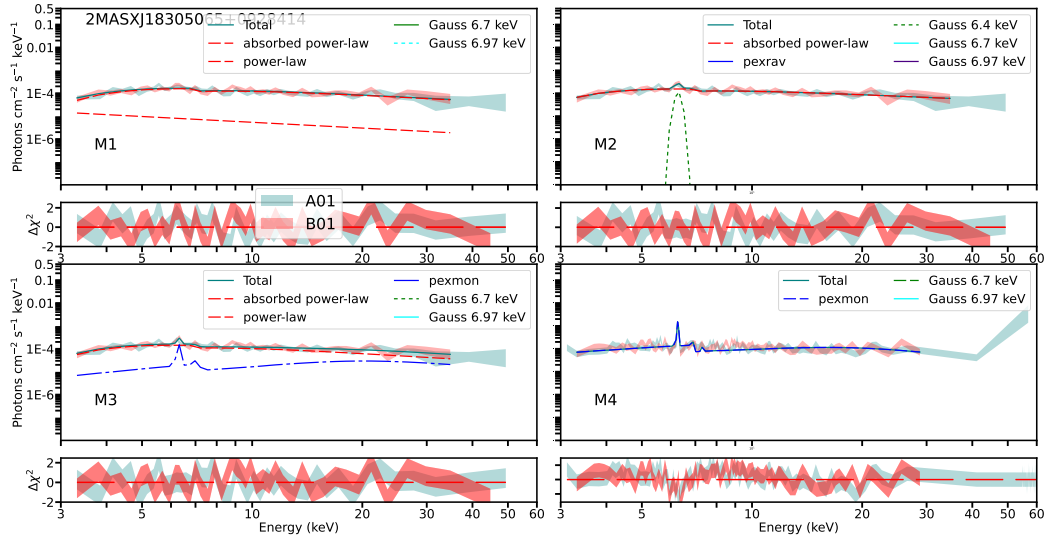


Figure 68: *NuSTAR* X-ray spectra of 2MASXJ18305065+0928414. Labels as in Fig. 8.1.

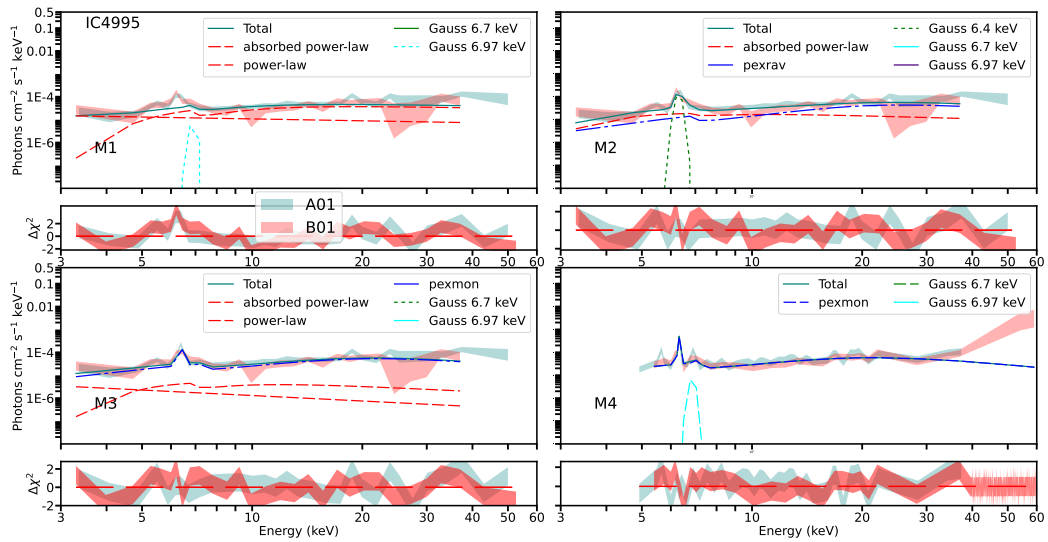


Figure 69: *NuSTAR* X-ray spectra of IC4995. Labels as in Fig. 8.1.

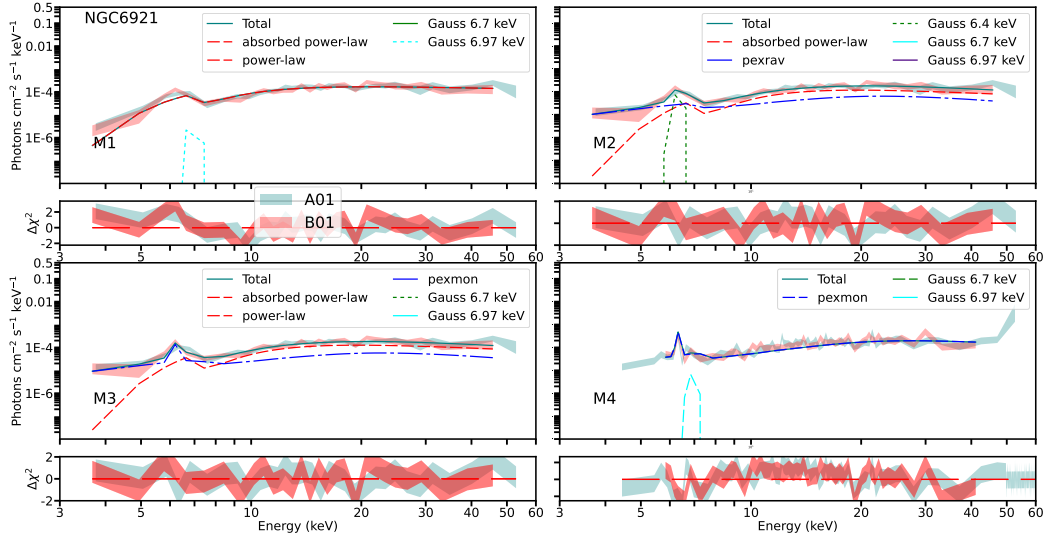


Figure 70: *NuSTAR* X-ray spectra of NGC6921. Labels as in Fig. 8.1.

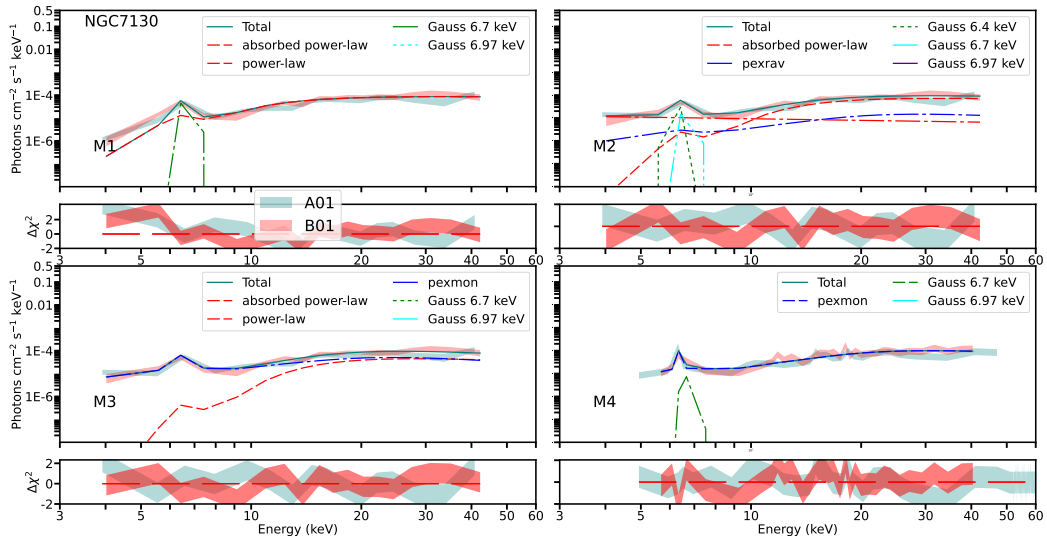


Figure 71: *NuSTAR* X-ray spectra of NGC7130. Labels as in Fig. 8.1.

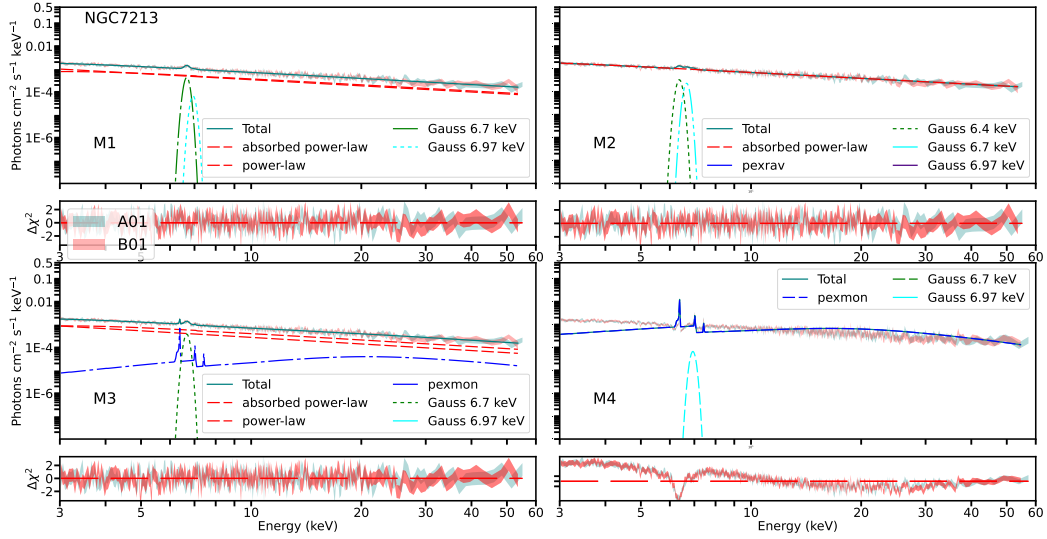


Figure 72: *NuSTAR* X-ray spectra of NGC7213. Labels as in Fig. 8.1.

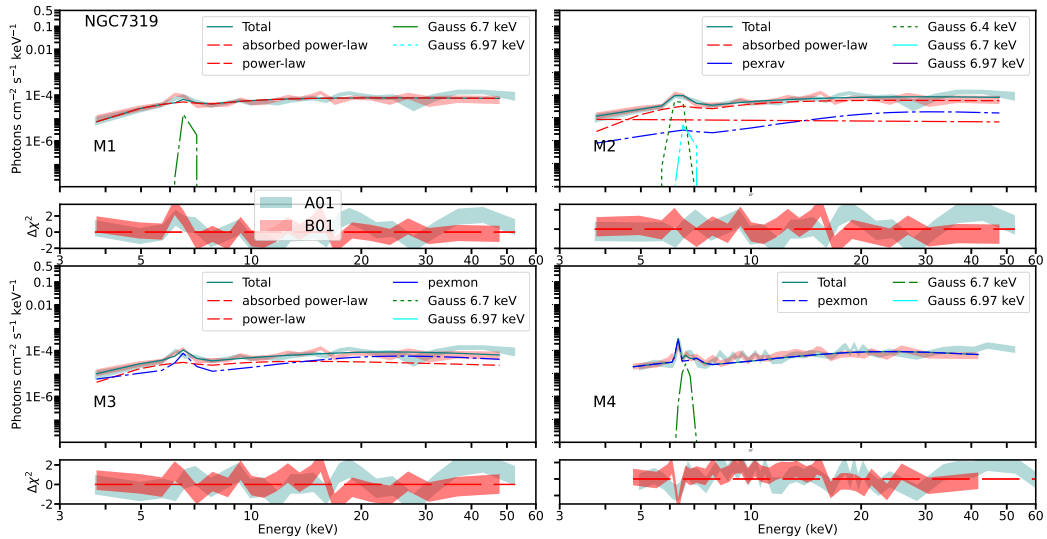


Figure 73: *NuSTAR* X-ray spectra of NGC7319. Labels as in Fig. 8.1.

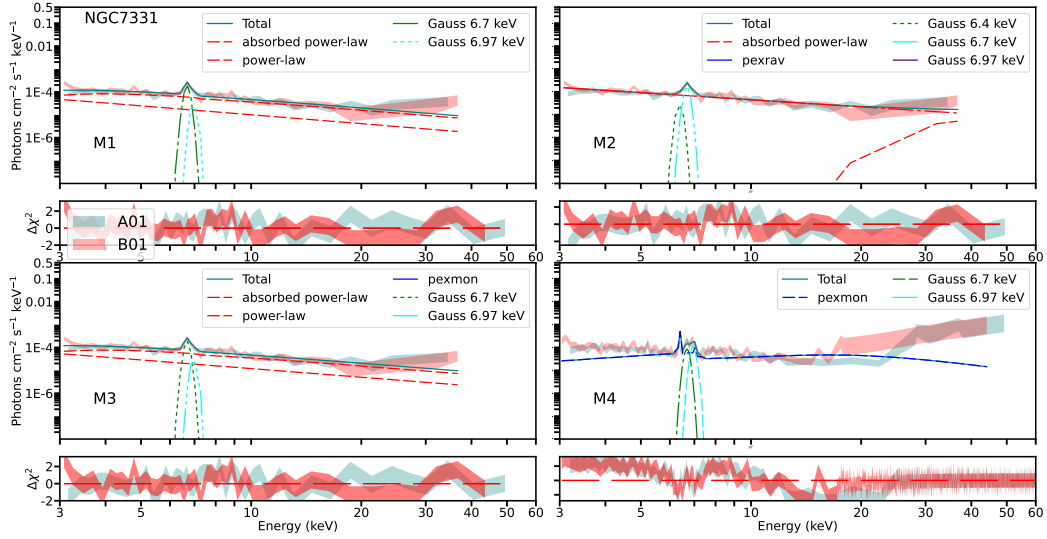


Figure 74: *NuSTAR* X-ray spectra of NGC7331. Labels as in Fig. 8.1.

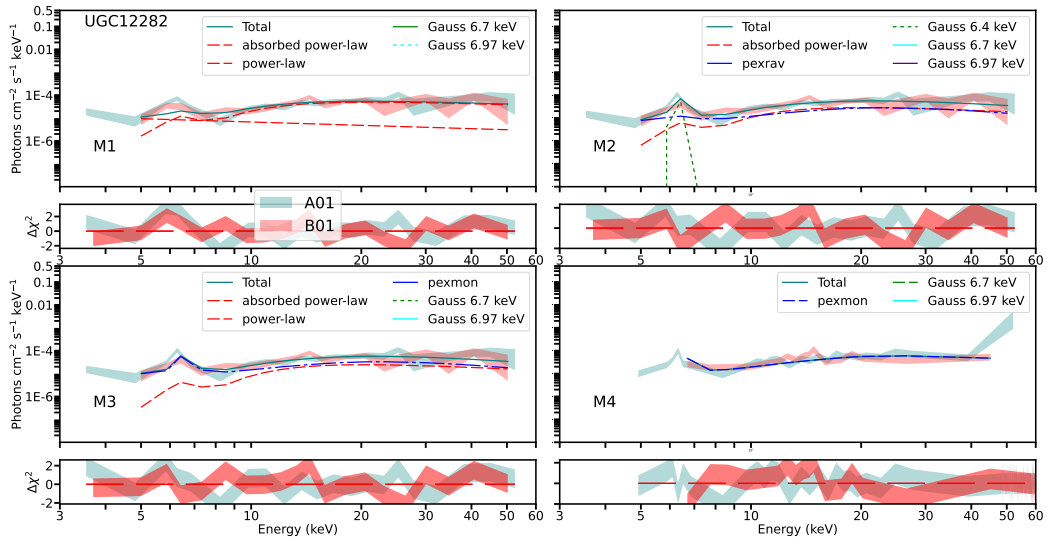


Figure 75: *NuSTAR* X-ray spectra of UGC12282. Labels as in Fig. 8.1.

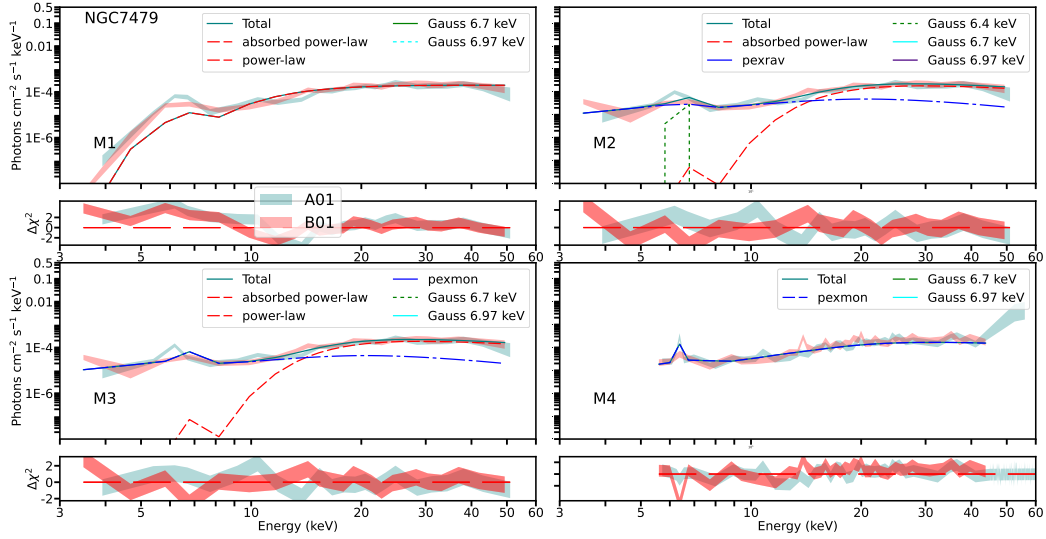


Figure 76: *NuSTAR* X-ray spectra of NGC7479. Labels as in Fig. 8.1.

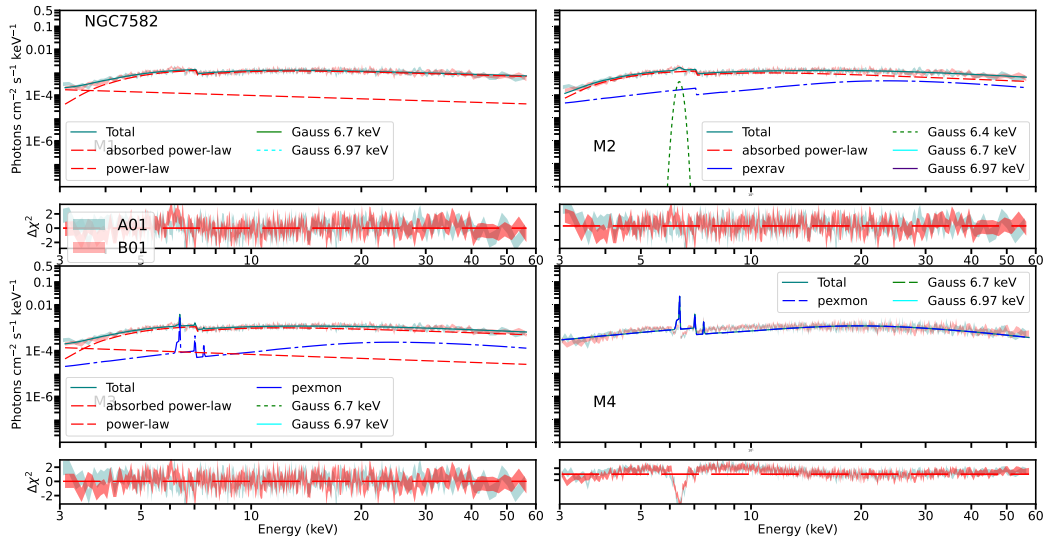


Figure 77: *NuSTAR* X-ray spectra of NGC7582. Labels as in Fig. 8.1.

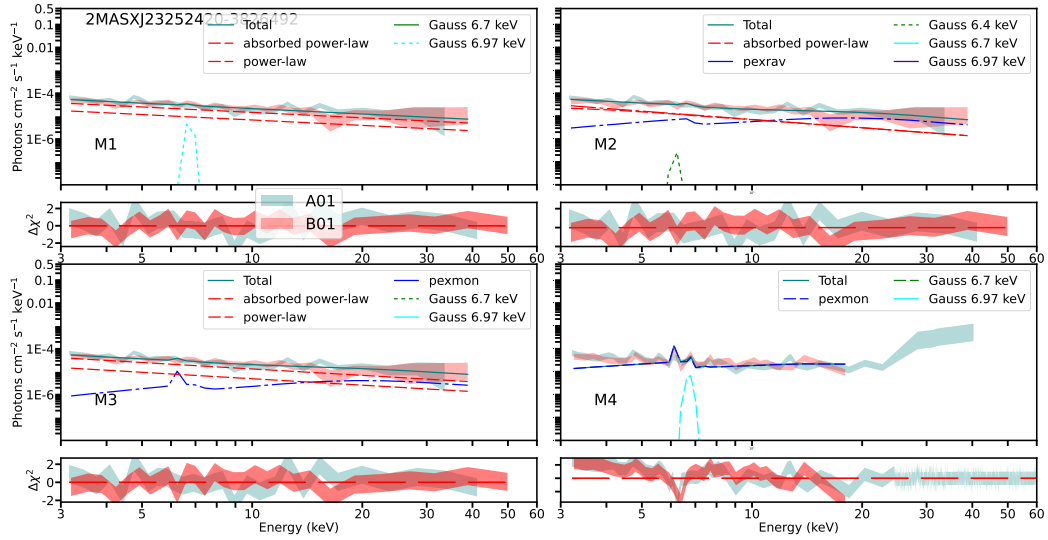


Figure 78: *NuSTAR* X-ray spectra of 2MASXJ23252420-3826492. Labels as in Fig. 8.1.

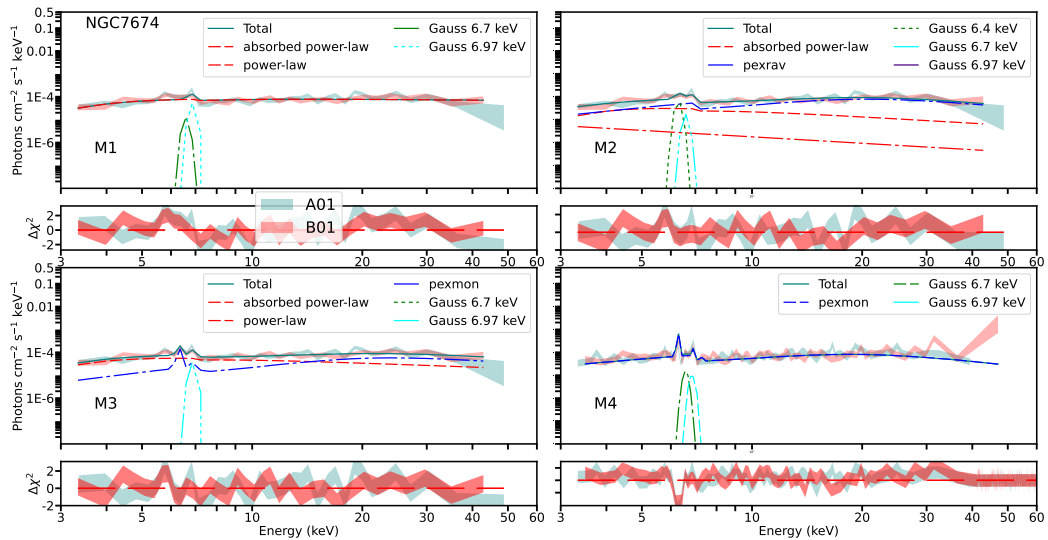


Figure 79: *NuSTAR* X-ray spectra of NGC7674. Labels as in Fig. 8.1.

8.2 Statistical values of the models used: Behaviour of the reflection component for LLAGN.

In this section, we present the χ^2 -statistics of each model version for all the sources, separated into the LINER and Seyfert samples, as presented in the paper.

Name (1)	χ^2_1/dof_1 (2)	χ^2_2/dof_2 (3)	χ^2_3/dof_3 (4)	χ^2_4/dof_4 (5)
NGC1052	757.32/735	734.85/732	744.71/734	1605.31/736
NGC2655	93.98/95	81.80/91	84.87/94	118.20/96
UGC5101	55.37/48	52.37/44	54.98/47	85.25/49
M81	1372.18/1247	1364.80/1243	1372.19/1246	24950.56/1249
NGC3079	125.15/124	118.24/122	114.37/123	230.75/126
UGC5881	140.96/164	135.05/163	136.07/163	223.05/166
NGC3628	64.43/82	65.41/80	64.43/81	291.28/84
NGC3718	175.87/203	182.58/200	176.12/202	673.27/205
NGC3998	617.02/710	648.51/707	613.34/709	4681.88/712
NGC4102	187.59/195	179.17/192	181.53/194	344.05/196
M106	431.62/461	427.98/458	431.61/460	1122.49/463
M58	806.18/733	783.68/730	802.22/732	4964.53/734
NGC5005	31.53/35	24.11/33	26.48/34	60.70/37
NGC6240	401.33/440	366.94/437	374.82/439	733.12/442
MCG+08-31-041	213.89/243	200.45/241	201.13/242	589.82/245
NGC7130	66.44/59	41.30/56	43.65/58	48.65/60
NGC7331	133.27/148	132.83/144	133.30/147	470.69/149
NGC7479	165.23/79	65.42/76	71.81/78	109.83/80

Table 8.1: Values of the χ^2 -statistics for each model version for the LINER sample. Column (1) is the name of the source. Col. (2) is the value of the statistics for M_1 , Col. (3) is the value of the statistics for M_2 , Col. (4) is the value of the statistics for M_3 and Col. (5) is the value of the statistics for M_5 .

Name (1)	χ^2_1/dof_1 (2)	χ^2_2/dof_2 (3)	χ^2_3/dof_3 (4)	χ^2_4/dof_4 (5)
NGC253	566.56/427	600.56/422	566.56/426	4243.68/429
NGC424	216.99/140	143.20/138	146.96/139	162.38/142
IC1657	231.99/214	215.44/211	224.23/213	387.02/215
2MXJ0114-5523	138.35/141	126.43/137	133.09/140	258.09/142
MCG+08-03-018	211.99/226	206.63/223	181.87/225	277.53/228
NGC612	138.55/154	133.46/151	138.33/153	340.52/156
Mrk573	125.82/61	67.40/59	71.02/60	79.66/63
NGC788	203.63/195	172.44/192	179.07/194	281.68/196
M77	1174.02/652	635.87/648	747.04/651	1214.01/654
NGC1106	111.86/63	81.48/61	88.05/62	90.62/65
NGC1125	156.87/120	100.98/116	108.35/119	157.36/121
NGC1142	135.82/116	97.76/112	104.67/115	147.74/117
Mrk1066	62.54/60	37.99/57	45.16/59	61.66/61
NGC1194	212.01/220	145.67/215	148.66/219	198.16/221
NGC1229	154.78/152	126.92/149	129.13/151	198.72/153
NGC1320	207.50/115	124.55/112	135.83/114	136.97/117
NGC1358	231.08/203	174.59/200	176.34/202	277.21/204
NGC1386	92.66/40	59.73/39	65.00/39	68.45/42
UGC3157	128.25/159	119.20/156	121.35/158	266.86/160
2MSJ0508+1721	371.51/364	341.84/361	354.36/363	850.29/365
ESO5-4	222.40/105	137.46/102	128.20/104	131.52/107
NGC2273	286.52/145	131.70/142	135.55/144	144.60/147
UGC3601	252.67/253	238.69/250	248.47/252	674.37/255
ESO428-14	193.93/108	106.85/104	105.45/107	108.57/109
2MXJ0756-4137	51.97/59	42.31/55	44.55/58	99.08/60
NGC2788A	125.10/96	70.21/92	72.35/95	82.87/97
IC2560	227.91/94	98.07/91	118.54/93	121.75/96
NGC3147	247.03/289	241.91/287	242.65/288	771.71/291
NGC3393	80.37/84	52.18/81	53.01/83	127.26/85
2MXJ1105+5856	118.36/130	111.32/127	115.59/129	223.43/132
NGC3621	94.62/95	93.73/92	94.62/94	424.86/97
NGC3786	86.79/99	82.93/97	86.52/98	234.92/101
IC751	61.93/60	48.74/56	53.50/59	83.87/61
M88	94.56/51	37.30/48	94.56/50	211.82/53
IC3639	112.02/46	39.23/45	43.71/45	49.54/47
NGC4785	178.44/205	169.54/202	171.80/204	377.13/206
Mrk231	238.33/239	232.72/236	232.65/238	397.25/240
NGC4941	143.67/116	109.82/113	111.35/115	146.30/117
NGC4939	167.07/178	155.88/175	158.68/177	302.96/179
NGC4945	1631.71/1560	1465.57/1557	1477.10/1559	5837.98/1562
MCG-03-34-064	1017.65/723	710.63/720	765.22/722	1021.06/725
NGC5135	194.92/84	105.15/81	101.55/83	108.32/85
M51	85.86/92	155.08/85	85.88/91	828.82/94
NGC5252	551.26/519	538.62/517	551.15/518	1484.06/521
NGC5283	229.51/231	213.28/228	216.31/230	345.59/232
NGC5347	115.48/50	51.60/48	57.15/49	58.19/52
NGC5643	245.80/142	151.78/139	156.44/141	170.78/143
NGC5695	44.74/39	39.11/36	38.99/38	44.36/41
NGC5728	386.17/399	329.90/395	336.17/398	722.36/400
NGC5899	321.16/379	305.83/377	308.81/378	684.70/381
MCG+14-08-004	135.92/162	126.43/158	130.22/161	209.33/163
ESO137-34	143.06/107	107.86/104	96.36/106	116.15/109
2MXJ1650+0436	351.83/405	355.79/402	343.84/404	955.28/407
2MXIJ1802-1454	618.05/592	603.00/589	605.51/591	2444.92/593
2MXJ1830+0928	166.79/180	158.22/176	158.71/179	252.42/181
IC4995	104.74/66	68.87/64	66.12/65	72.56/68
NGC6921	138.94/114	113.66/111	113.83/113	179.35/115
NGC7213	885.21/960	867.83/957	879.92/959	9122.28/962
NGC7319	89.99/84	72.06/81	74.57/83	108.95/86
UGC12282	56.07/40	36.25/37	38.97/39	43.87/41
NGC7582	1036.85/1096	994.77/1094	993.71/1095	3442.38/1098
2MXJ2325-3826	64.25/77	61.33/73	62.89/76	190.09/78
NGC7674	189.15/157	144.69/153	154.67/156	239.64/158

Table 8.2: Values of the χ^2 -statistics for each model version for the Seyfert sample. Column (1) is the name of the source. Col. (2) is the value of the statistics for M_1 , Col. (3) is the value of the statistics for M_2 , Col. (4) is the value of the statistics for M_3 and Col. (5) is the value of the statistics for M_5 .

8.3 Catalogue of morphological analysis: AGN in the CALIFA survey

In this section, we show the morphological decomposition for the sources corresponding to the CALIFA sample (66) sources with nuclear detection.

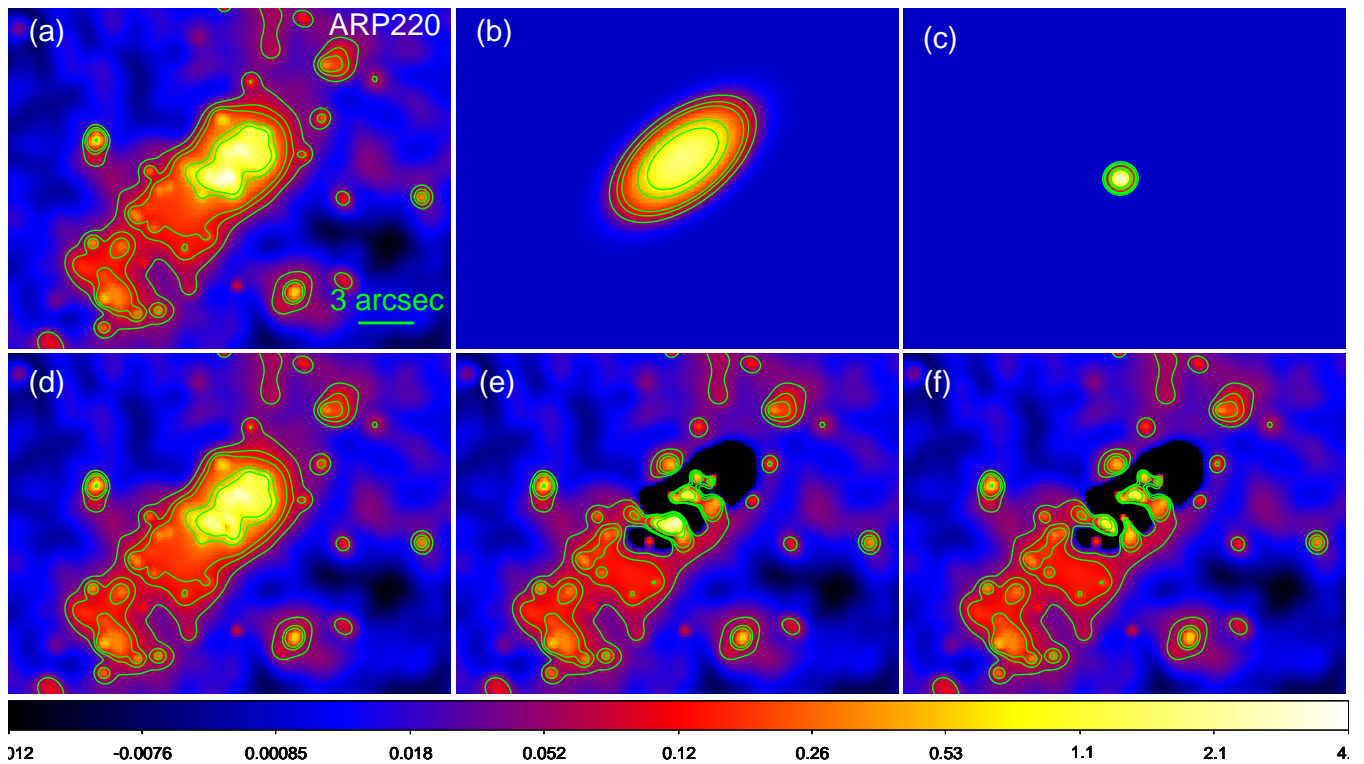


Figure 8.2: Morphological decomposition for ARP 220. Panel (a), (b), (c), (d), (e), and (f) correspond to the total emission, Gaussian of the extended emission, Gaussian of the nuclear emission, extended emission only, nuclear emission only and residuals, respectively.

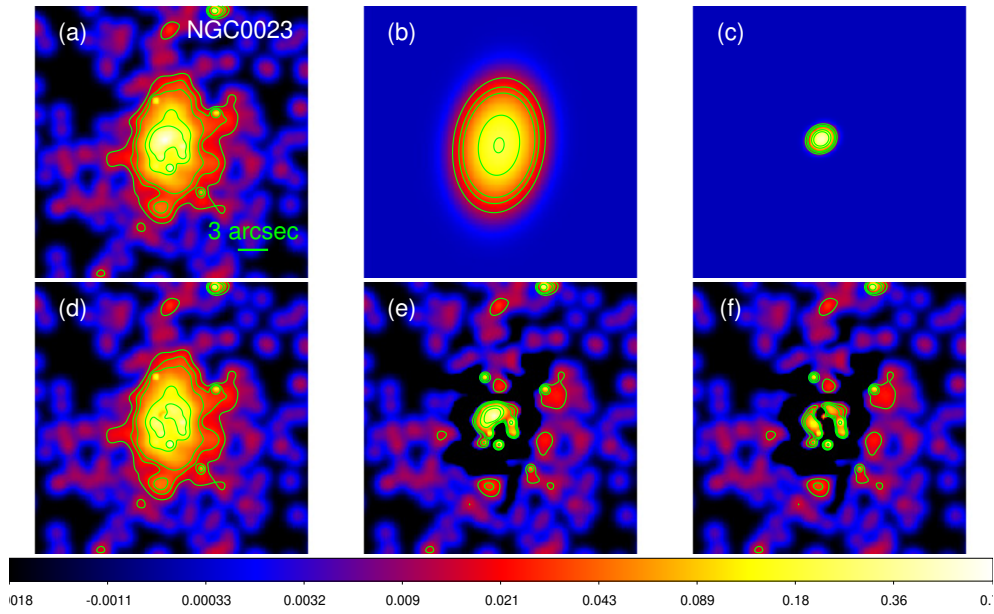


Figure 1: Morphological decomposition for NGC0023. Panels as in the Figure 2 of the paper.

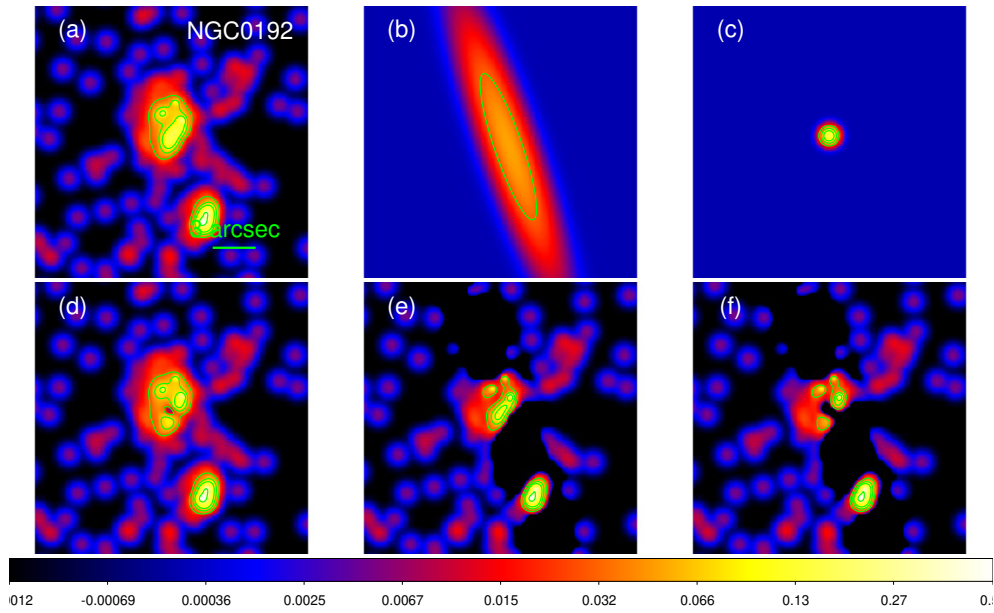


Figure 2: Morphological decomposition for NGC0192. Panels as in the Figure 2 of the paper.

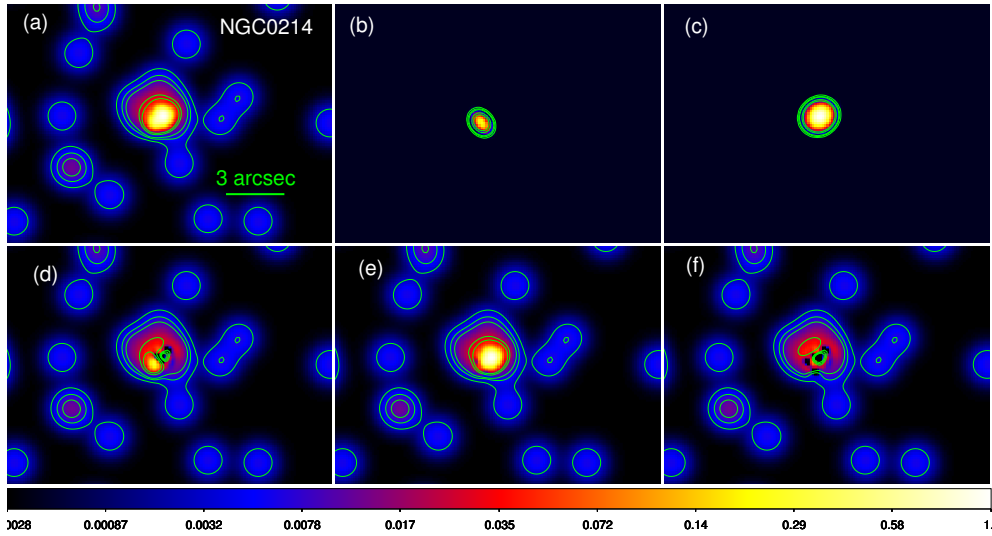


Figure 3: Morphological decomposition for NGC0214. Panels as in the Figure 2 of the paper.

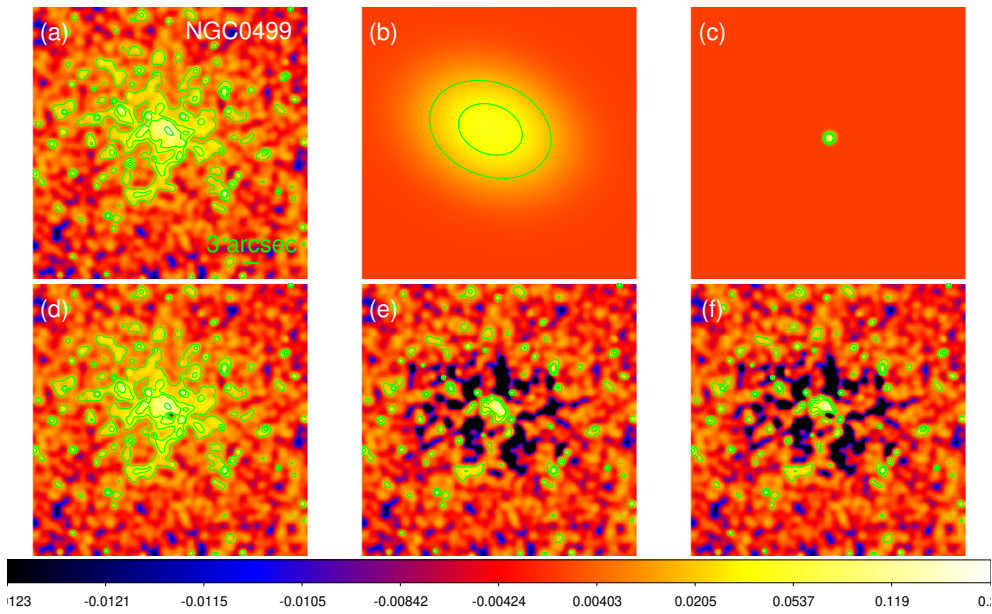


Figure 4: Morphological decomposition for NGC0499. Panels as in the Figure 2 of the paper.

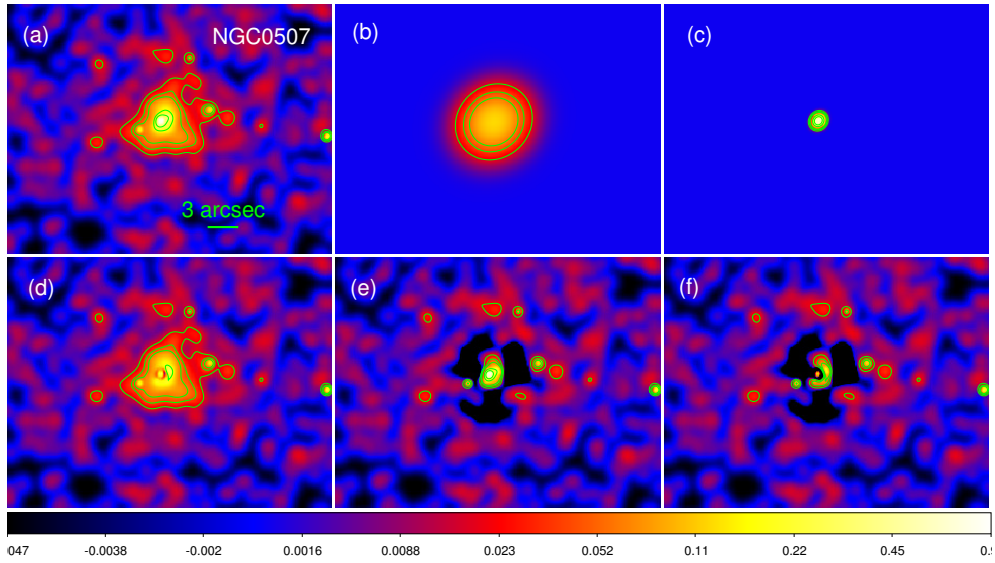


Figure 5: Morphological decomposition for NGC0507. Panels as in the Figure 2 of the paper.

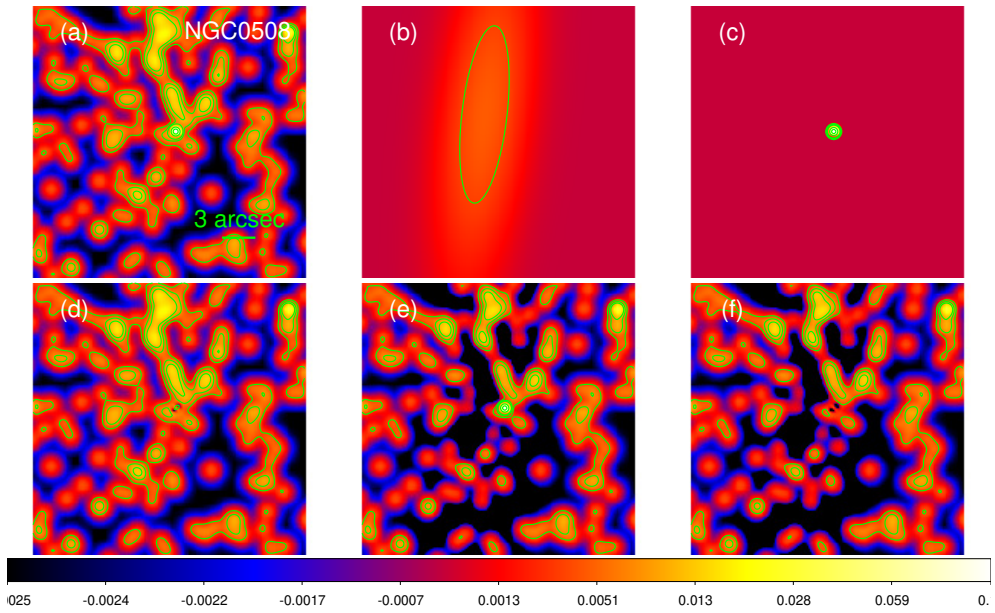


Figure 6: Morphological decomposition for NGC0508. Panels as in the Figure 2 of the paper.

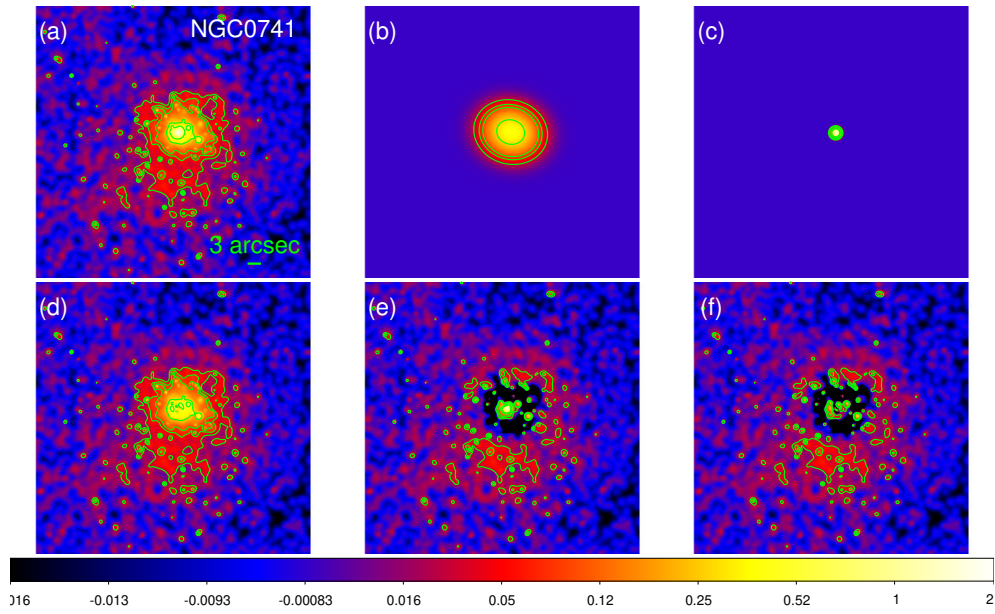


Figure 7: Morphological decomposition for NGC0741. Panels as in the Figure 2 of the paper.

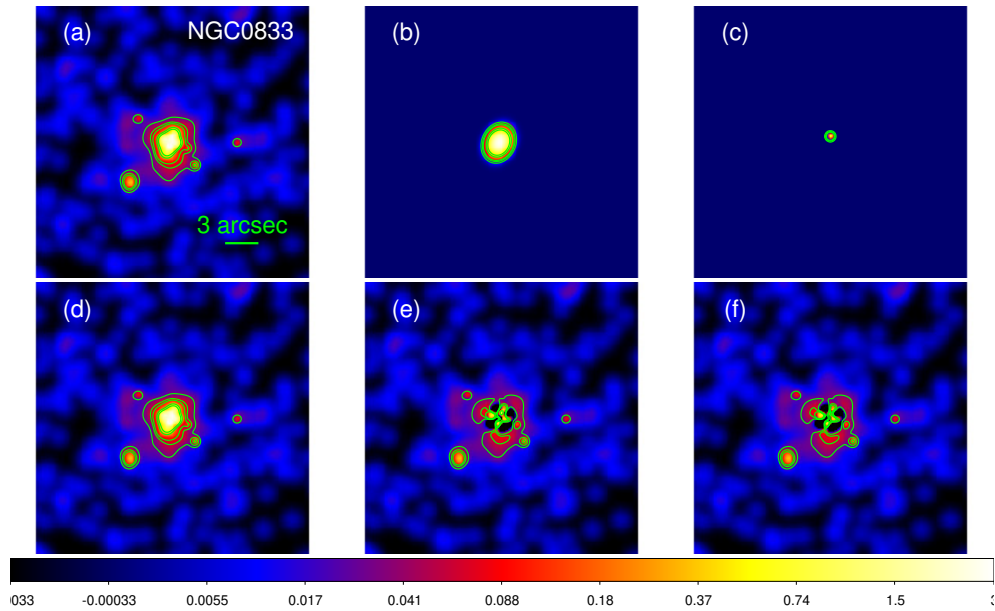


Figure 8: Morphological decomposition for NGC0833. Panels as in the Figure 2 of the paper.

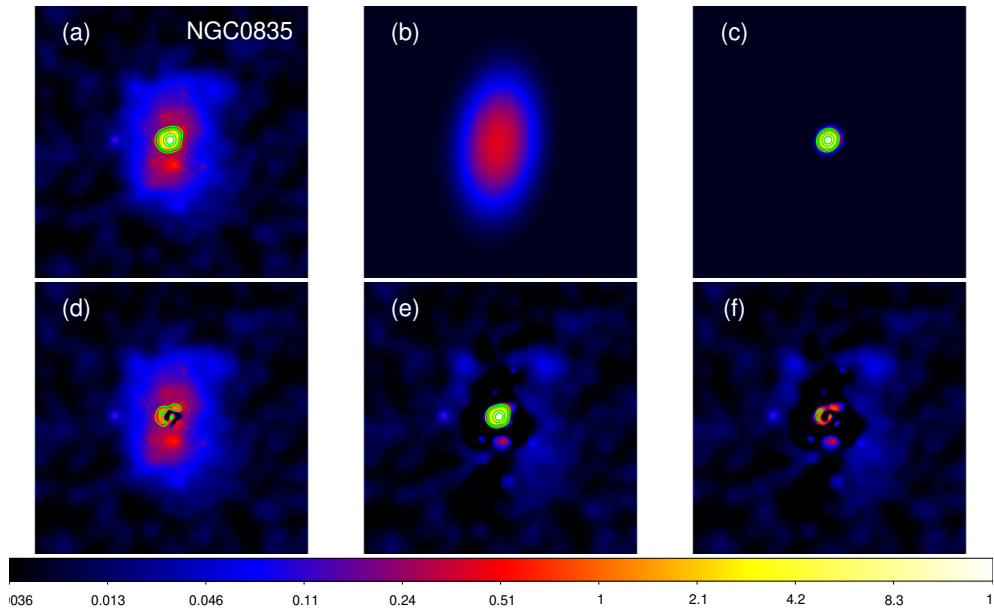


Figure 9: Morphological decomposition for NGC0835. Panels as in the Figure 2 of the paper.

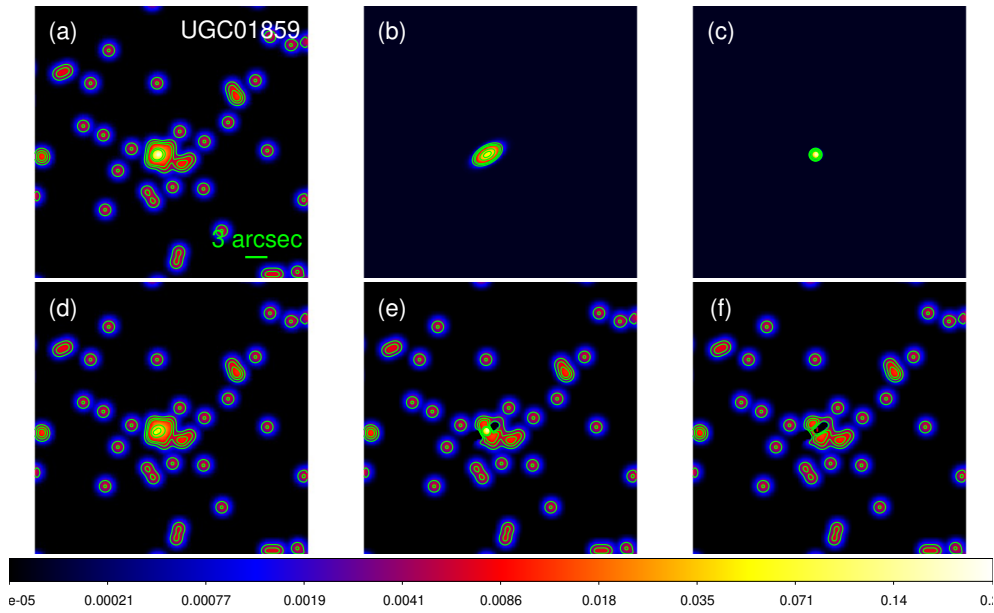


Figure 10: Morphological decomposition for UGC01859. Panels as in the Figure 2 of the paper.

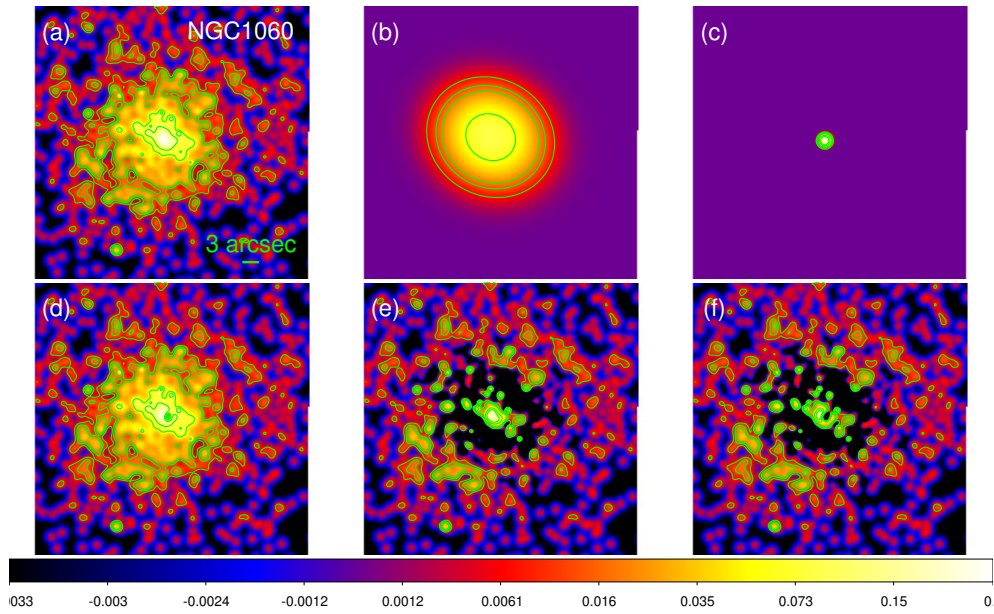


Figure 11: Morphological decomposition for NGC1060. Panels as in the Figure 2 of the paper.

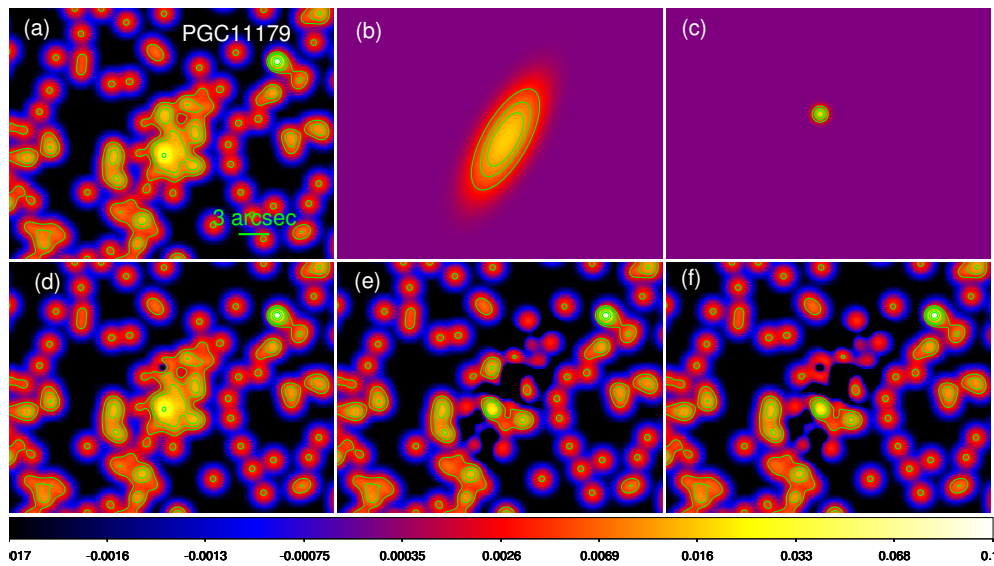


Figure 12: Morphological decomposition for PGC11179. Panels as in the Figure 2 of the paper.

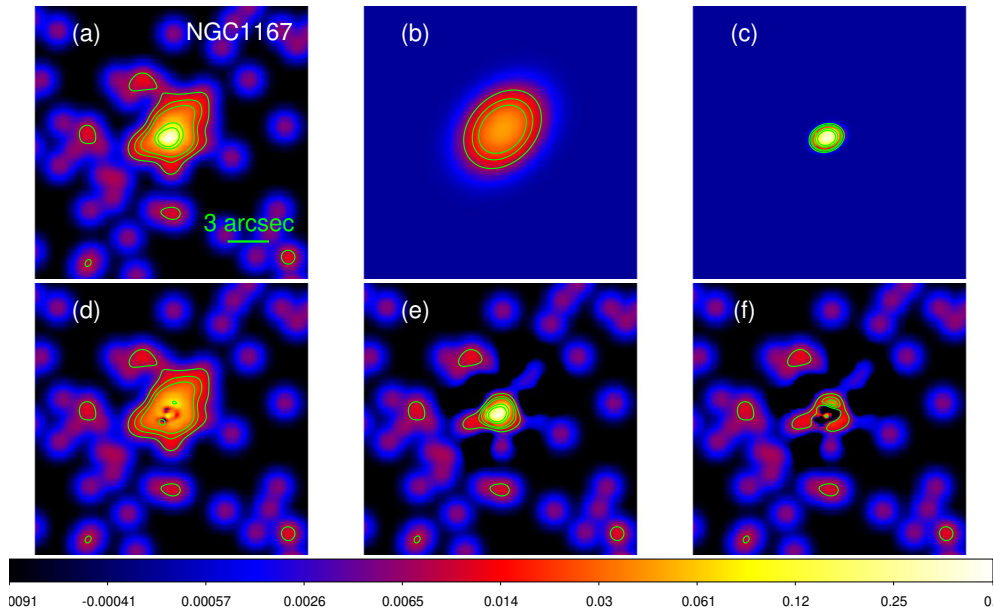


Figure 13: Morphological decomposition for NGC1167. Panels as in the Figure 2 of the paper.

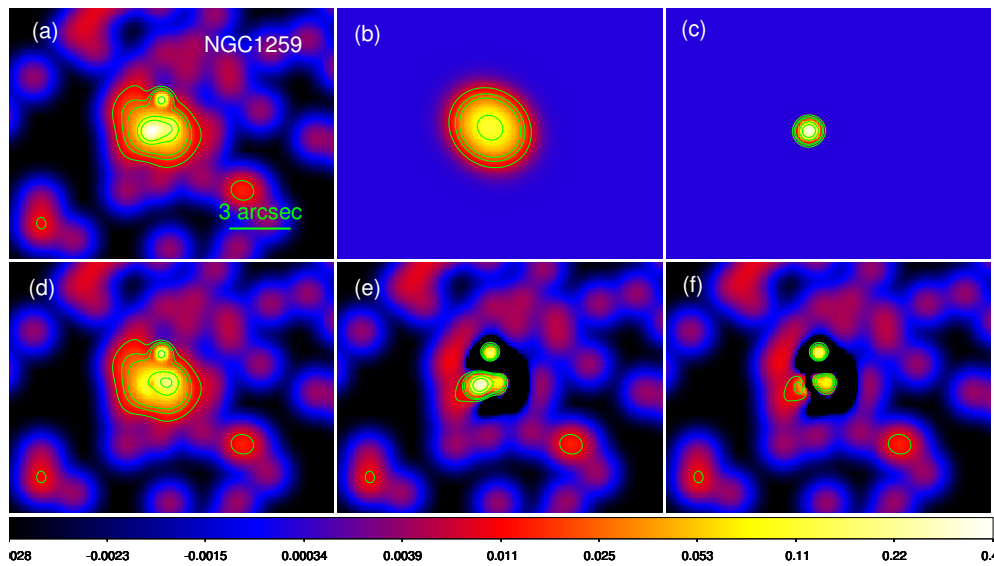


Figure 14: Morphological decomposition for NGC1259. Panels as in the Figure 2 of the paper.

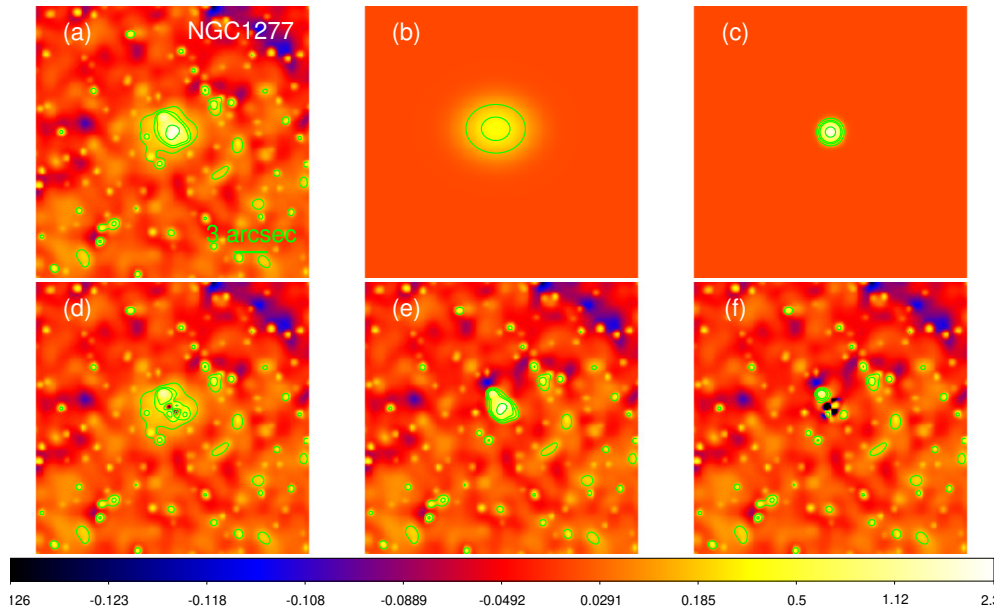


Figure 15: Morphological decomposition for NGC1277. Panels as in the Figure 2 of the paper.

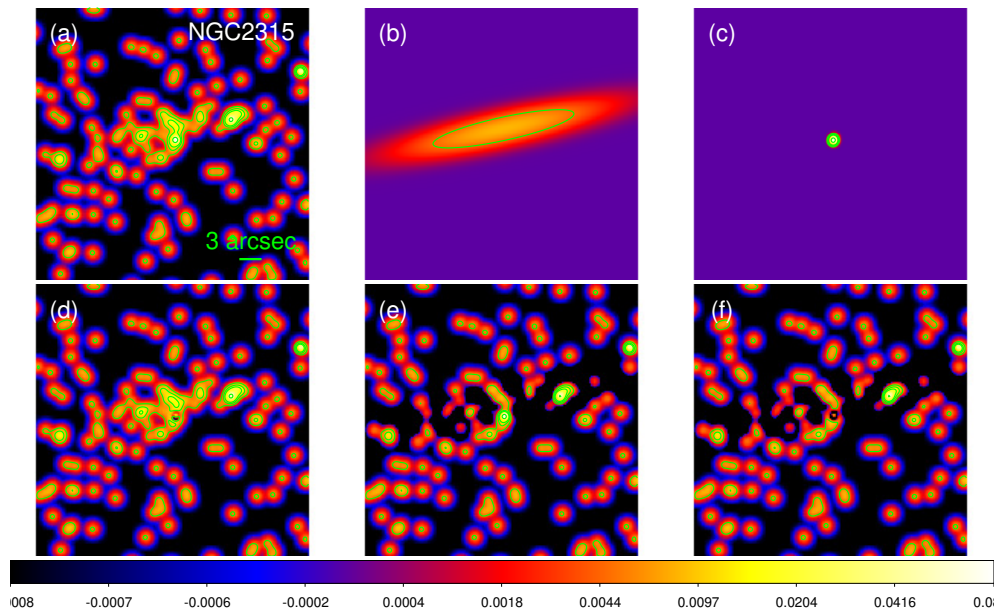


Figure 16: Morphological decomposition for NGC2315. Panels as in the Figure 2 of the paper.

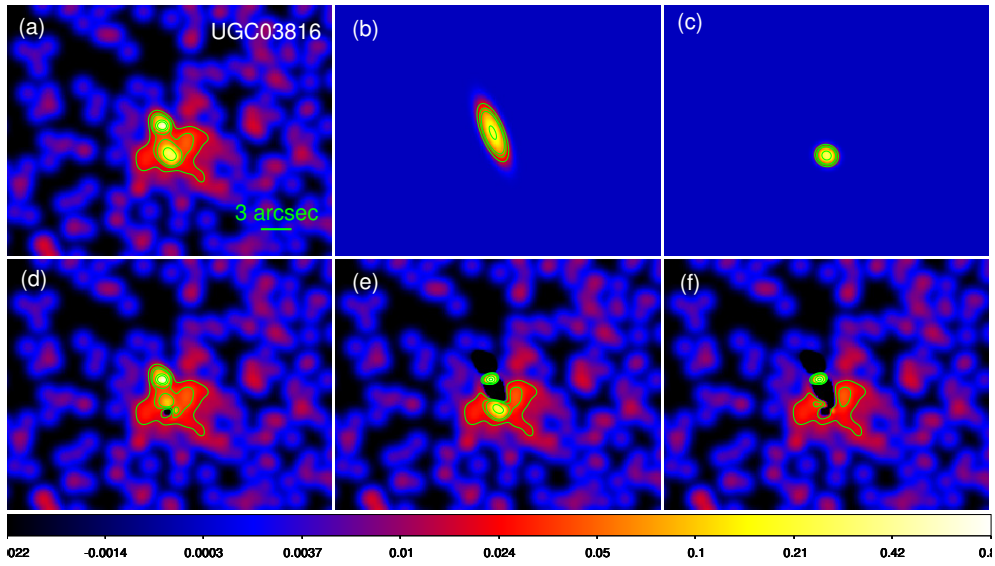


Figure 17: Morphological decomposition for UGC03816. Panels as in the Figure 2 of the paper.

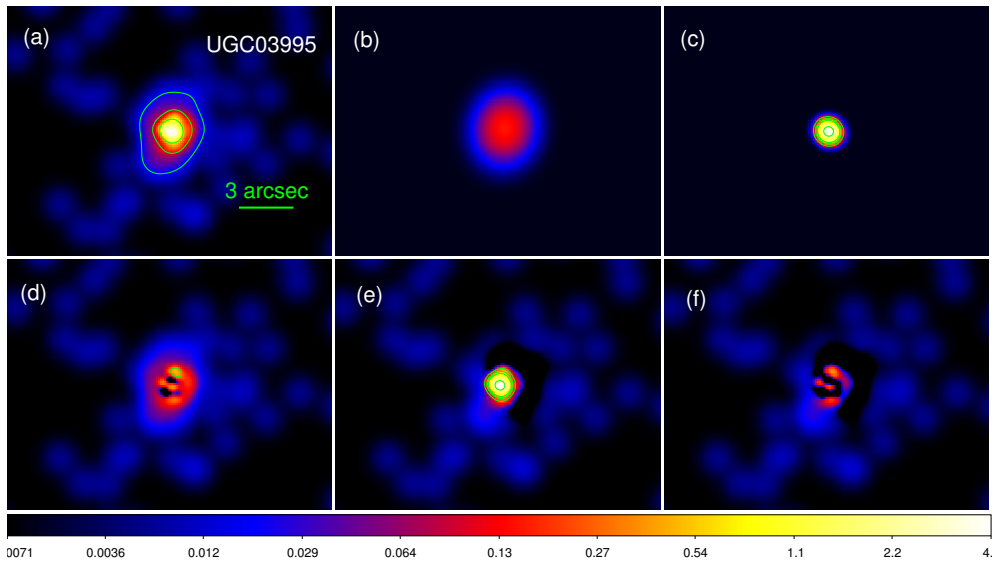


Figure 18: Morphological decomposition for UGC03995. Panels as in the Figure 2 of the paper.

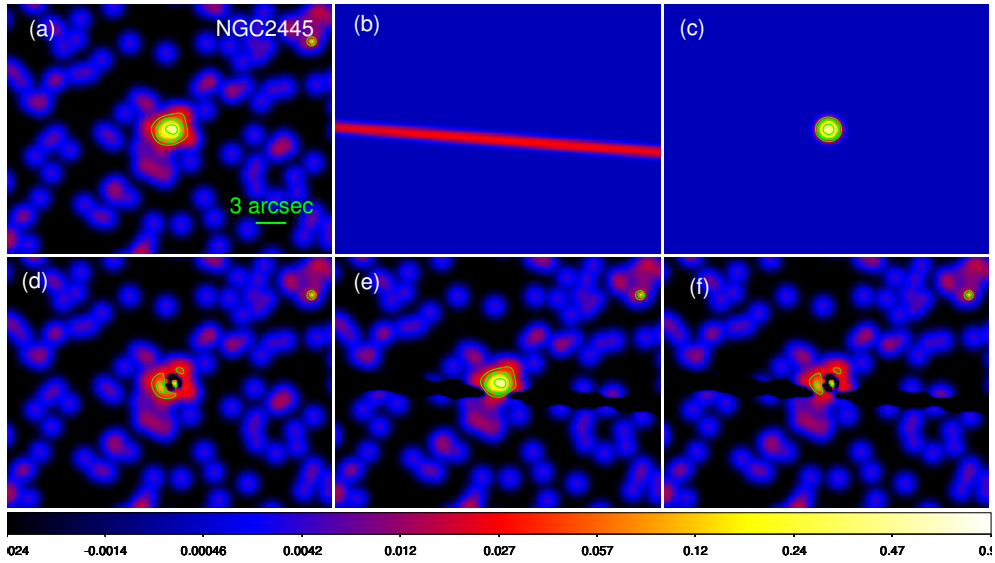


Figure 19: Morphological decomposition for NGC2445. Panels as in the Figure 2 of the paper.

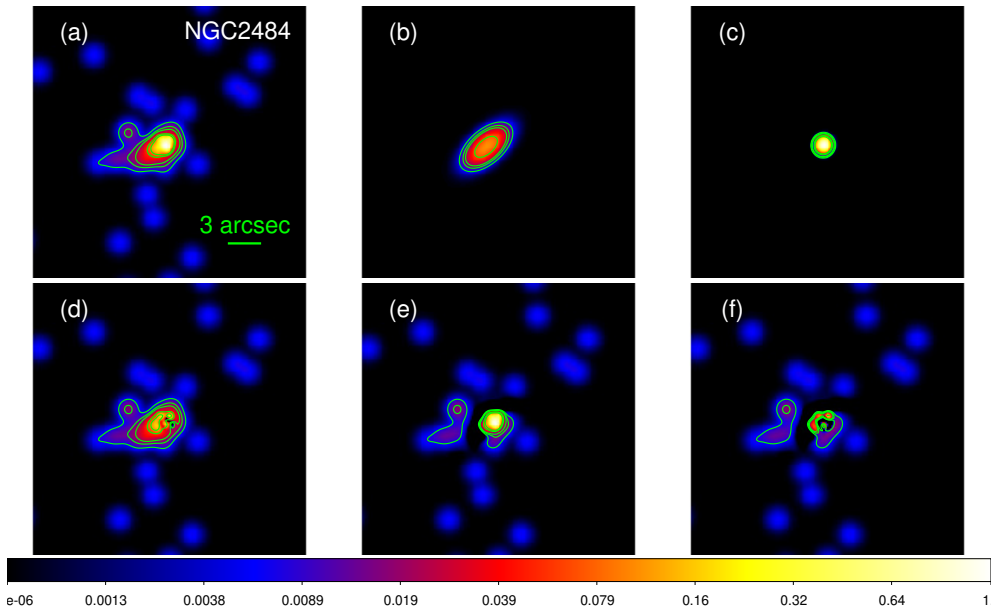


Figure 20: Morphological decomposition for NGC2484. Panels as in the Figure 2 of the paper.

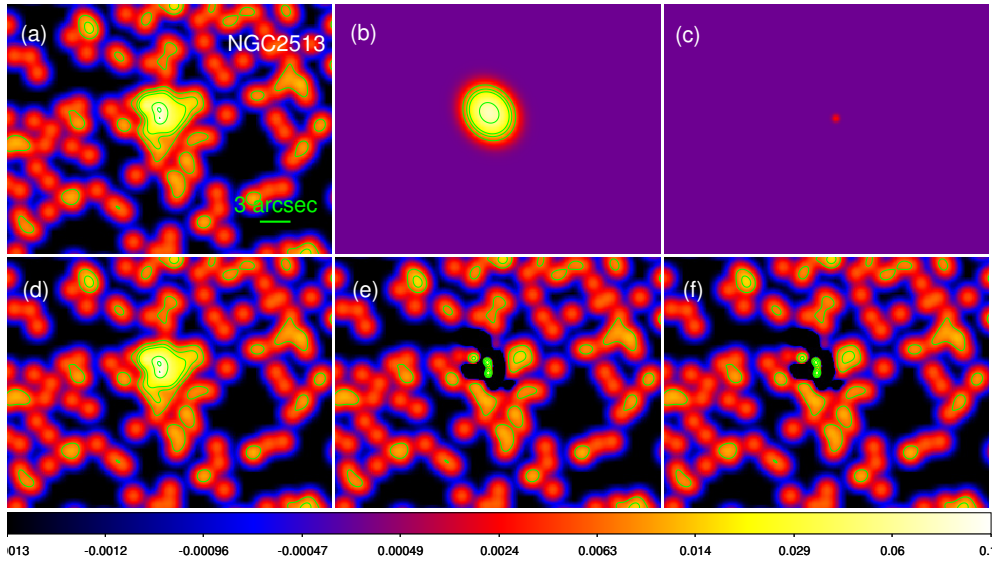


Figure 21: Morphological decomposition for NGC2513. Panels as in the Figure 2 of the paper.

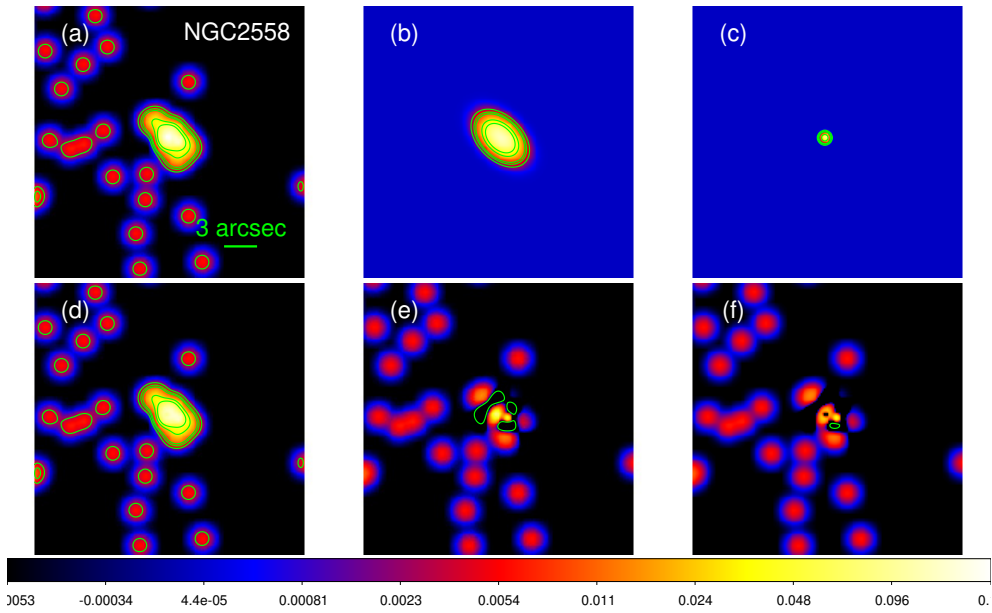


Figure 22: Morphological decomposition for NGC2558. Panels as in the Figure 2 of the paper.

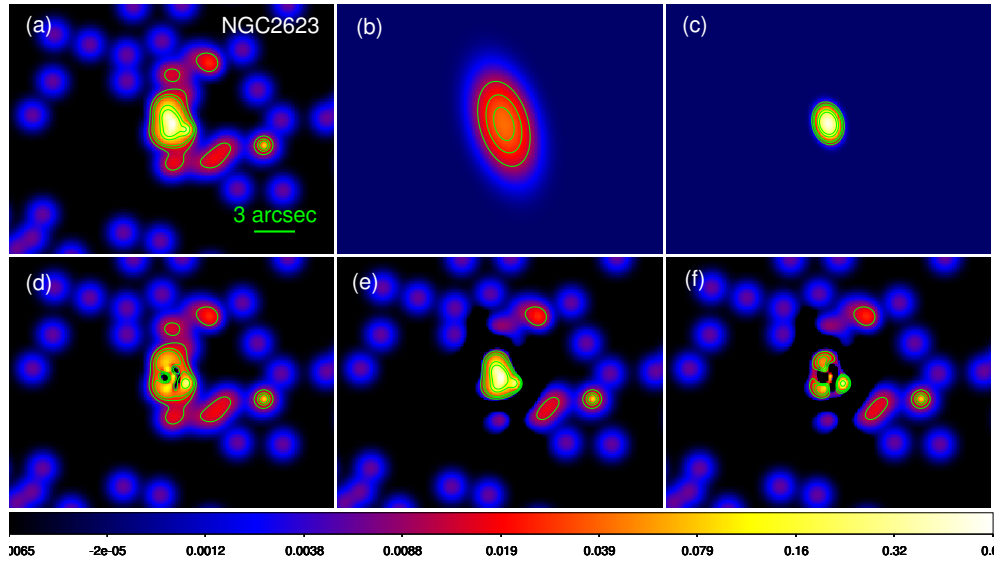


Figure 23: Morphological decomposition for NGC2623. Panels as in the Figure 2 of the paper.

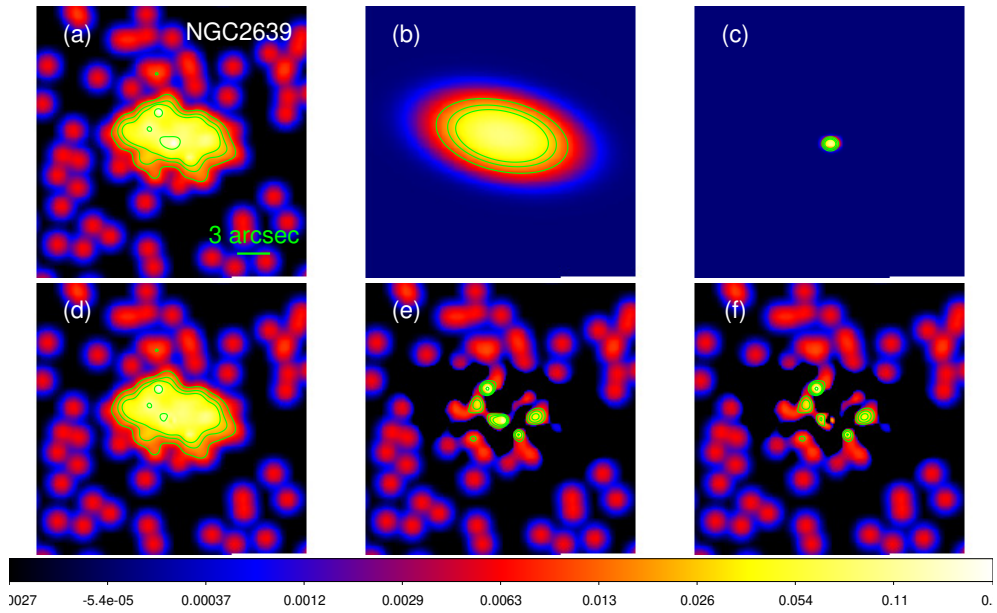


Figure 24: Morphological decomposition for NGC2639. Panels as in the Figure 2 of the paper.

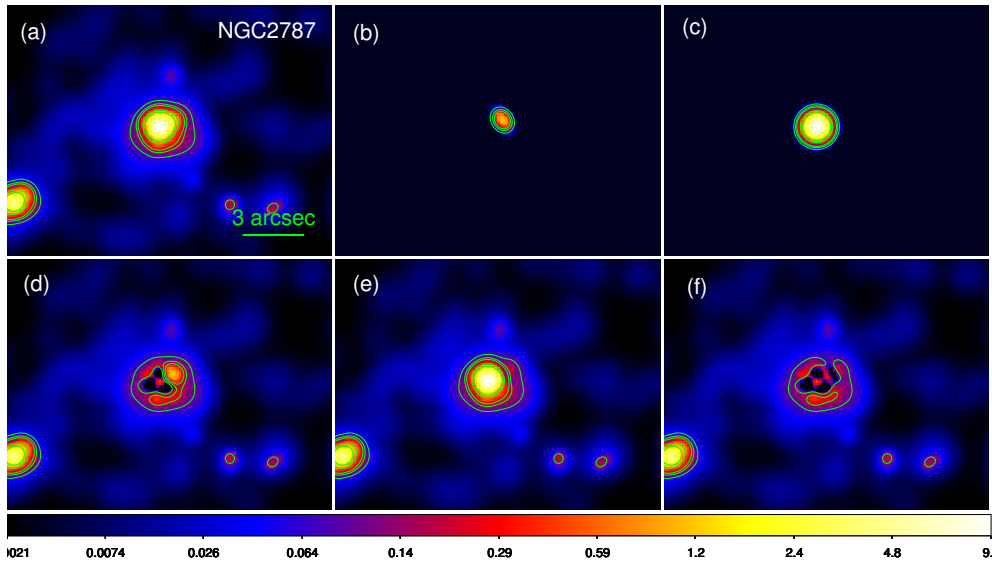


Figure 25: Morphological decomposition for NGC2787. Panels as in the Figure 2 of the paper.

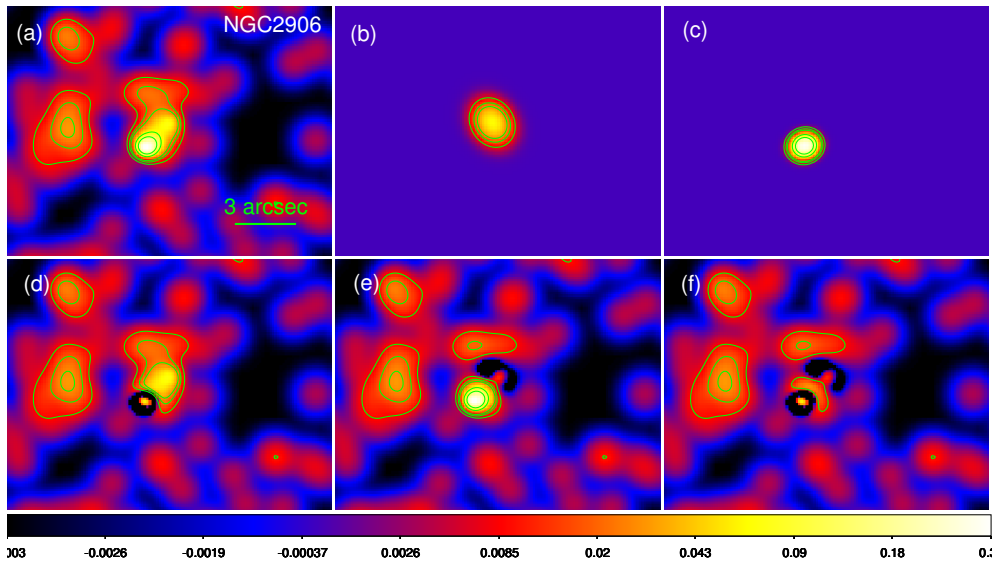


Figure 26: Morphological decomposition for NGC2906. Panels as in the Figure 2 of the paper.

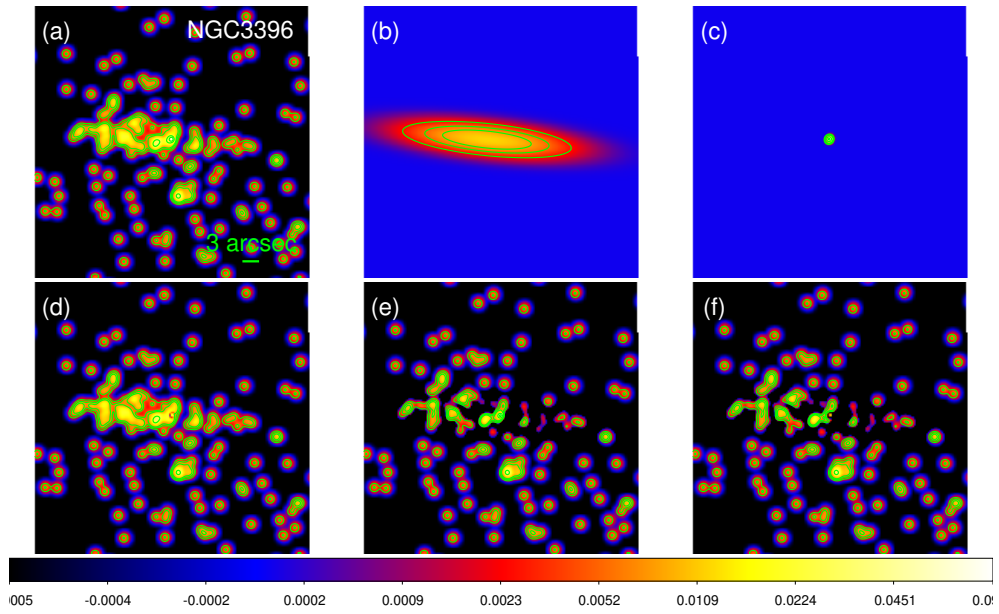


Figure 27: Morphological decomposition for NGC3396. Panels as in the Figure 2 of the paper.

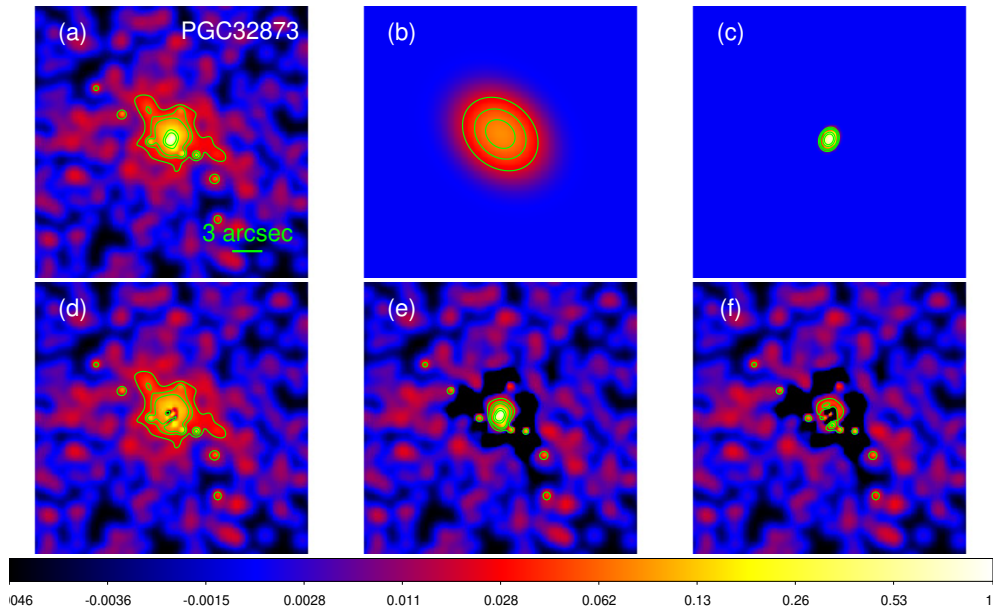


Figure 28: Morphological decomposition for PGC32873. Panels as in the Figure 2 of the paper.

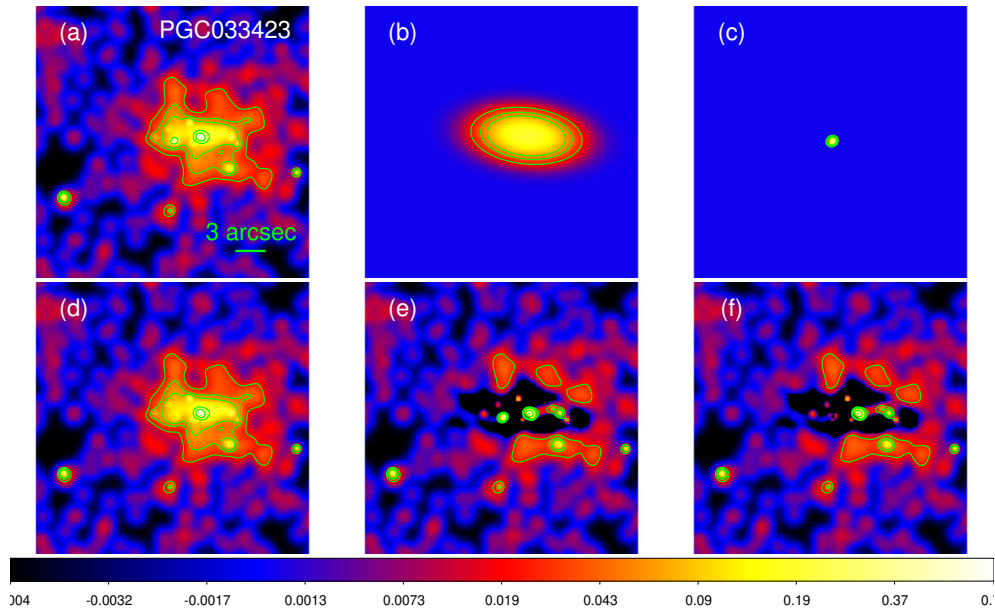


Figure 29: Morphological decomposition for PGC033423. Panels as in the Figure 2 of the paper.

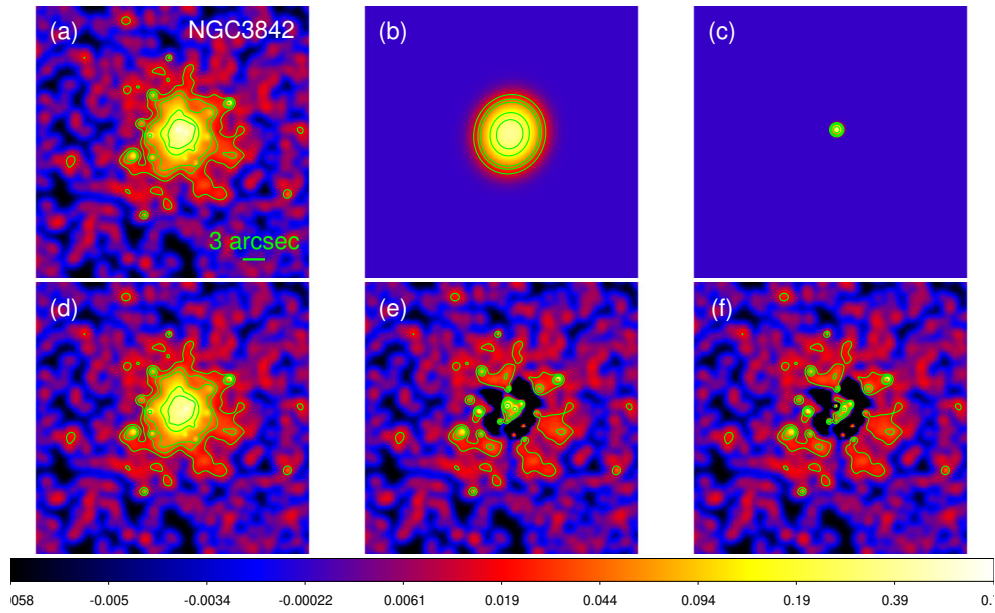


Figure 30: Morphological decomposition for NGC3842. Panels as in the Figure 2 of the paper.

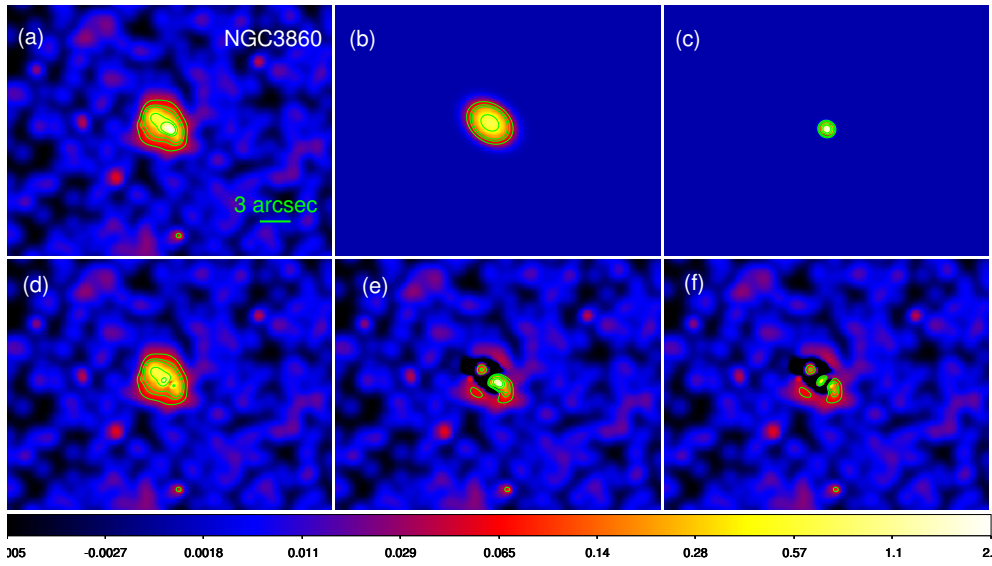


Figure 31: Morphological decomposition for NGC3860. Panels as in the Figure 2 of the paper.

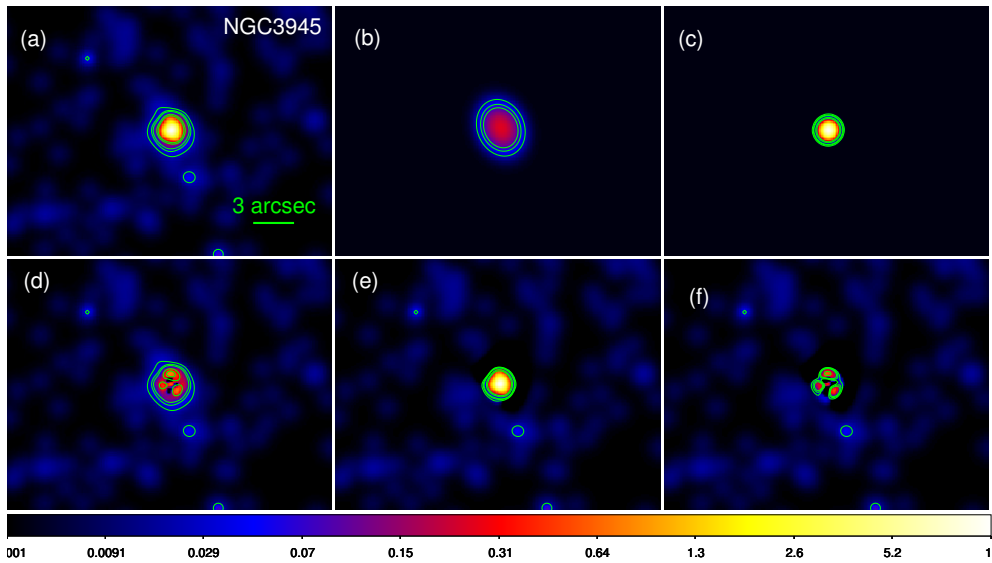


Figure 32: Morphological decomposition for NGC3945. Panels as in the Figure 2 of the paper.

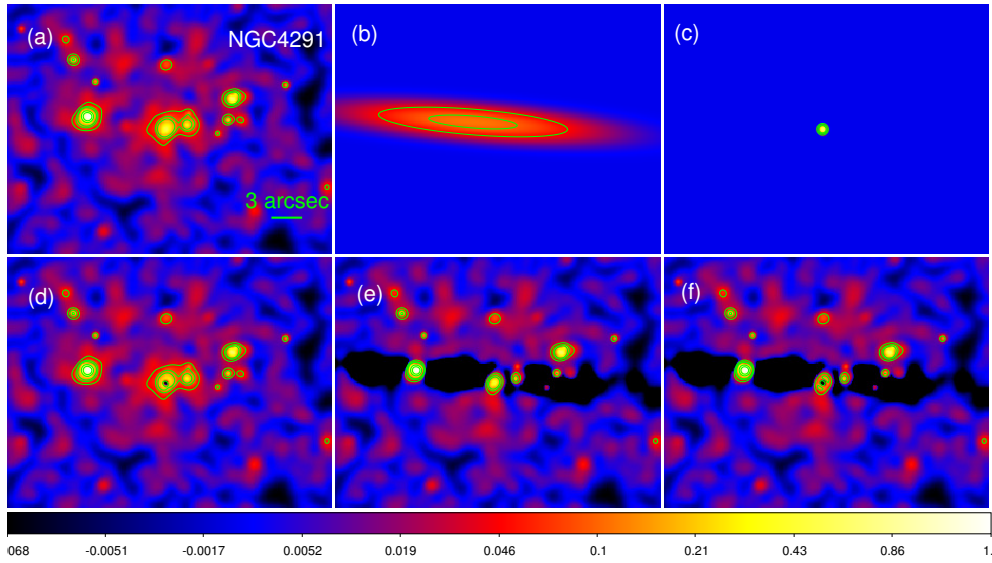


Figure 33: Morphological decomposition for NGC4291. Panels as in the Figure 2 of the paper.

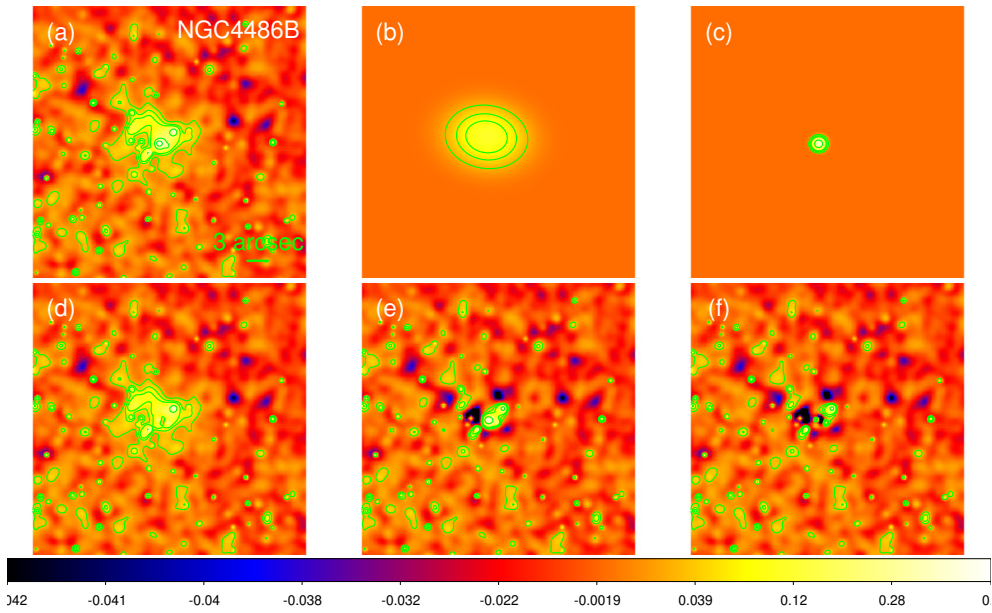


Figure 34: Morphological decomposition for NGC4486B. Panels as in the Figure 2 of the paper.

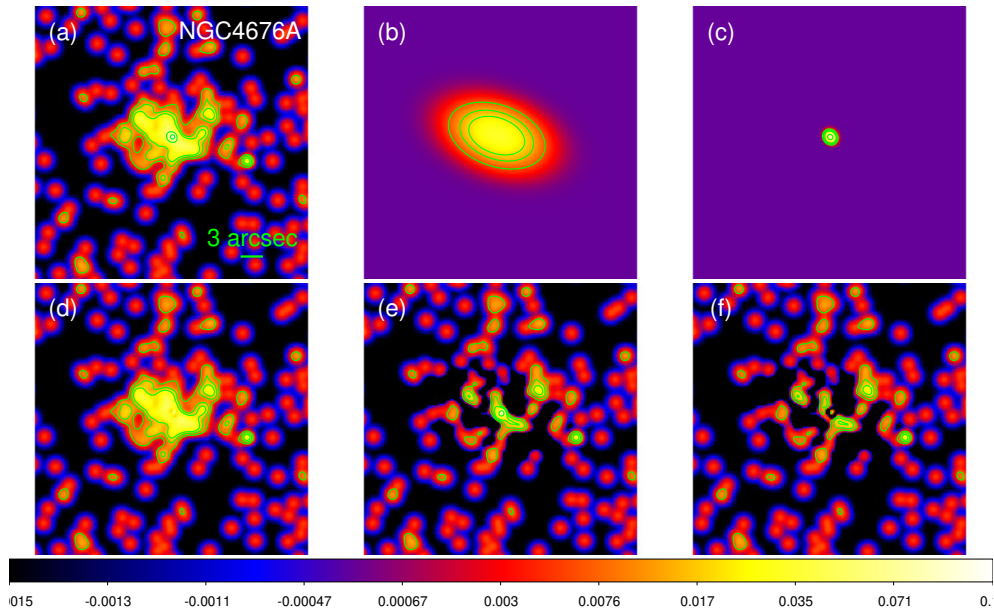


Figure 35: Morphological decomposition for NGC4676A. Panels as in the Figure 2 of the paper.

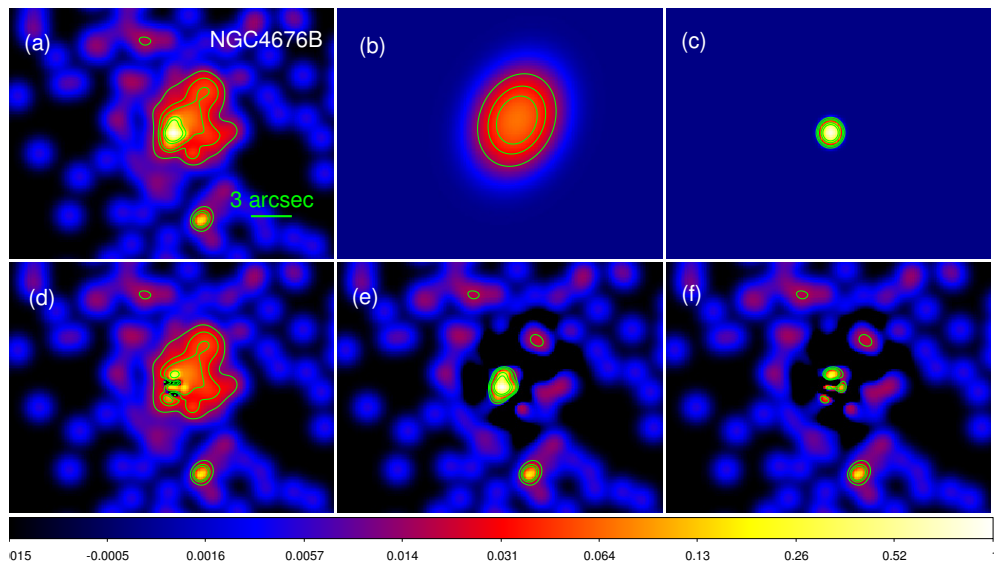


Figure 36: Morphological decomposition for NGC4676B. Panels as in the Figure 2 of the paper.

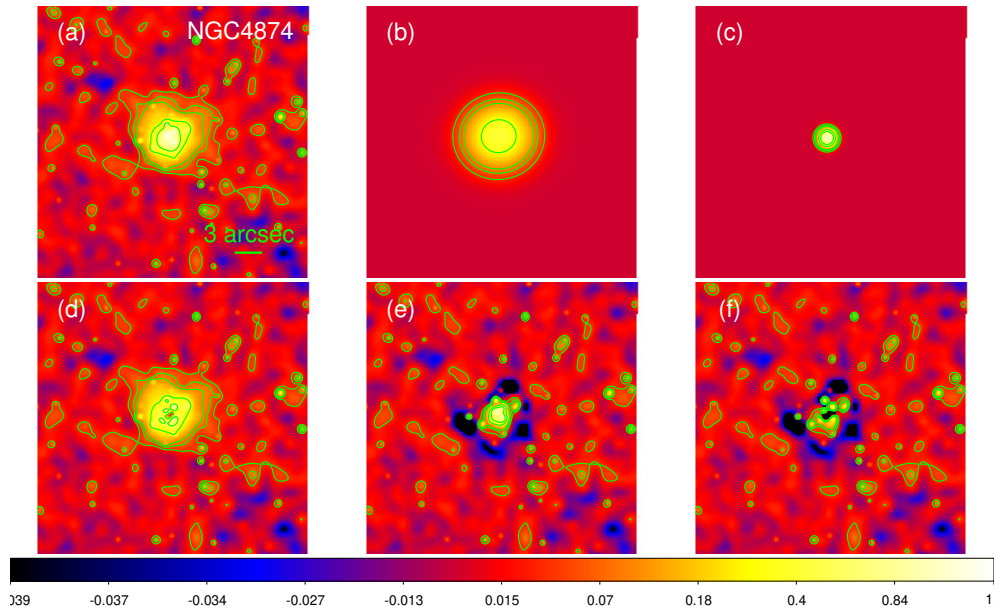


Figure 37: Morphological decomposition for NGC4874. Panels as in the Figure 2 of the paper.

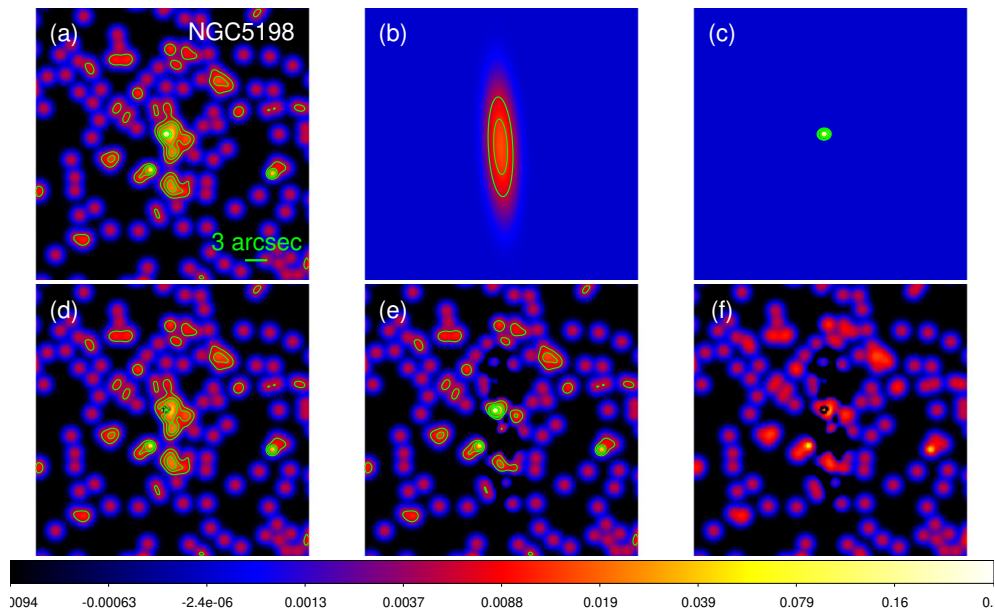


Figure 38: Morphological decomposition for NGC5198. Panels as in the Figure 2 of the paper.

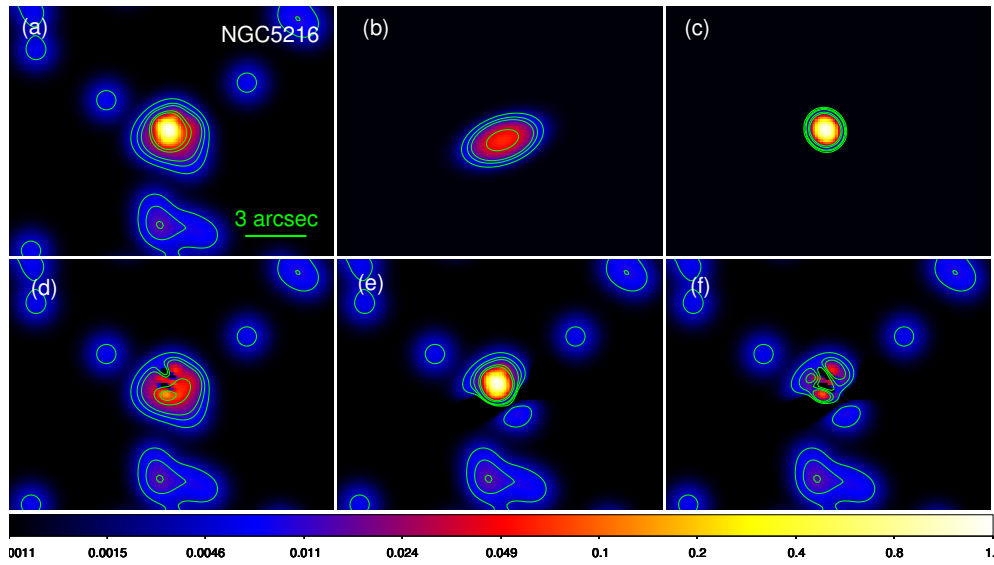


Figure 39: Morphological decomposition for NGC5216. Panels as in the Figure 2 of the paper.

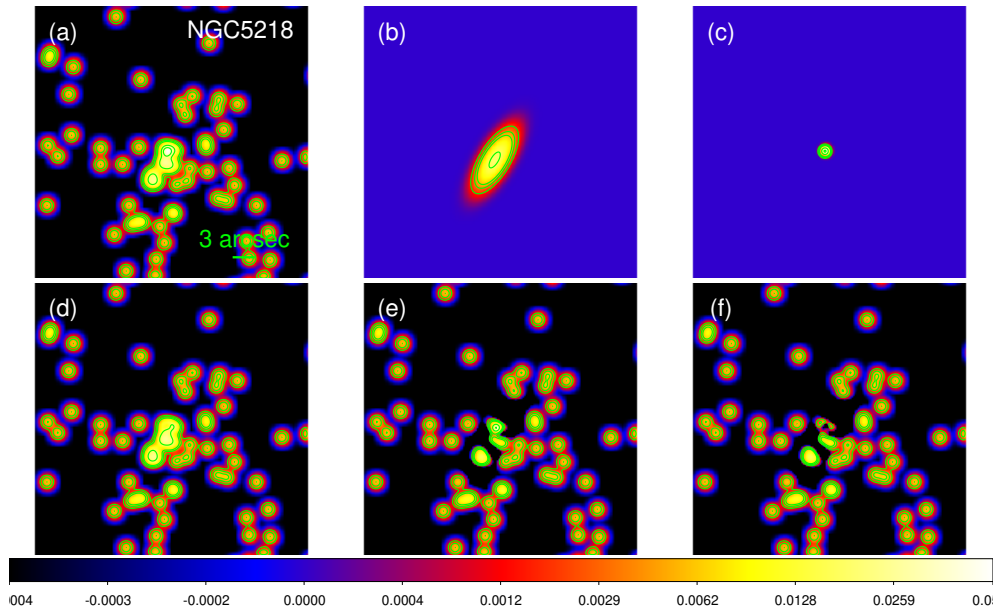


Figure 40: Morphological decomposition for NGC5218. Panels as in the Figure 2 of the paper.

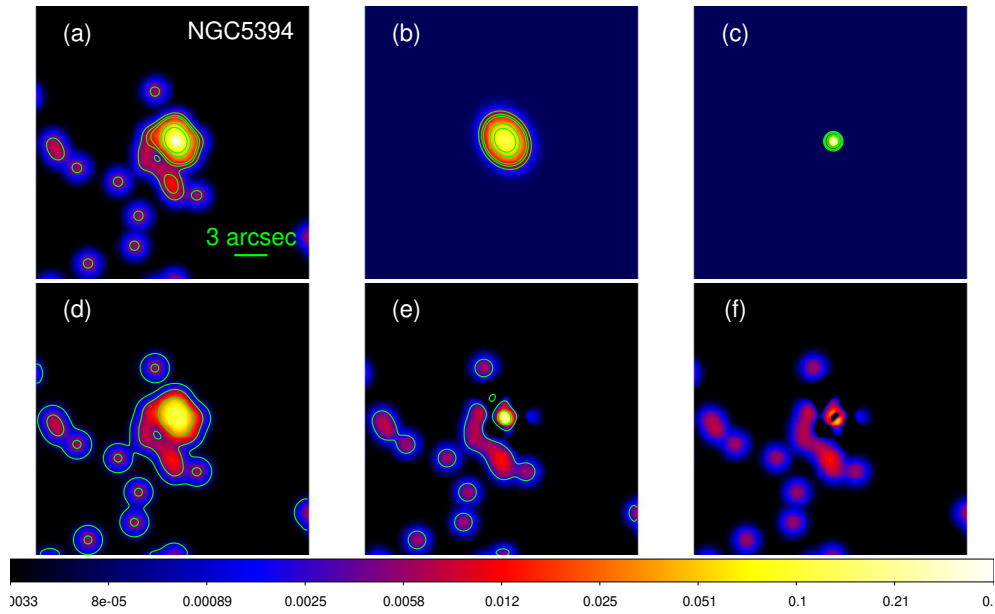


Figure 41: Morphological decomposition for NGC5394. Panels as in the Figure 2 of the paper.

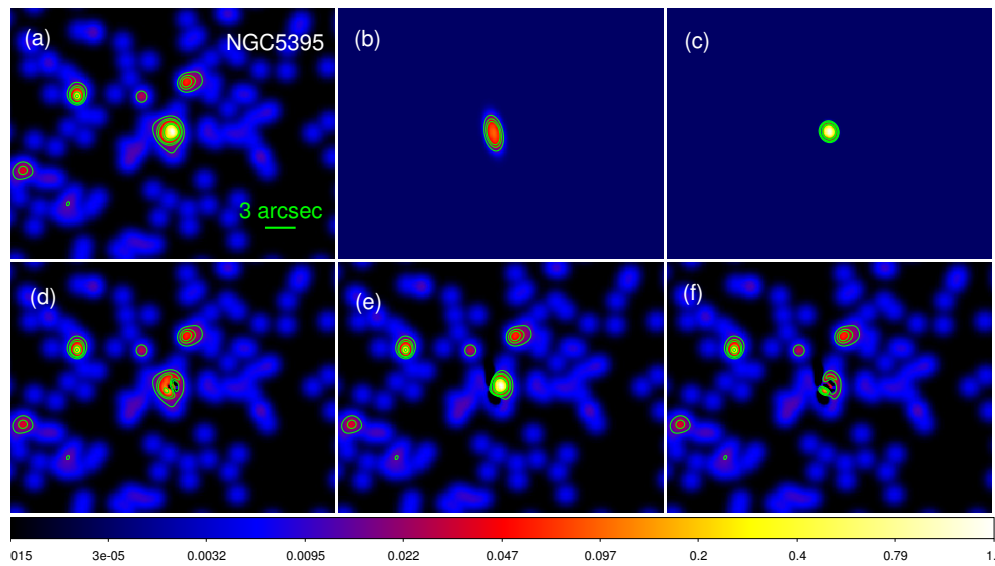


Figure 42: Morphological decomposition for NGC5395. Panels as in the Figure 2 of the paper.

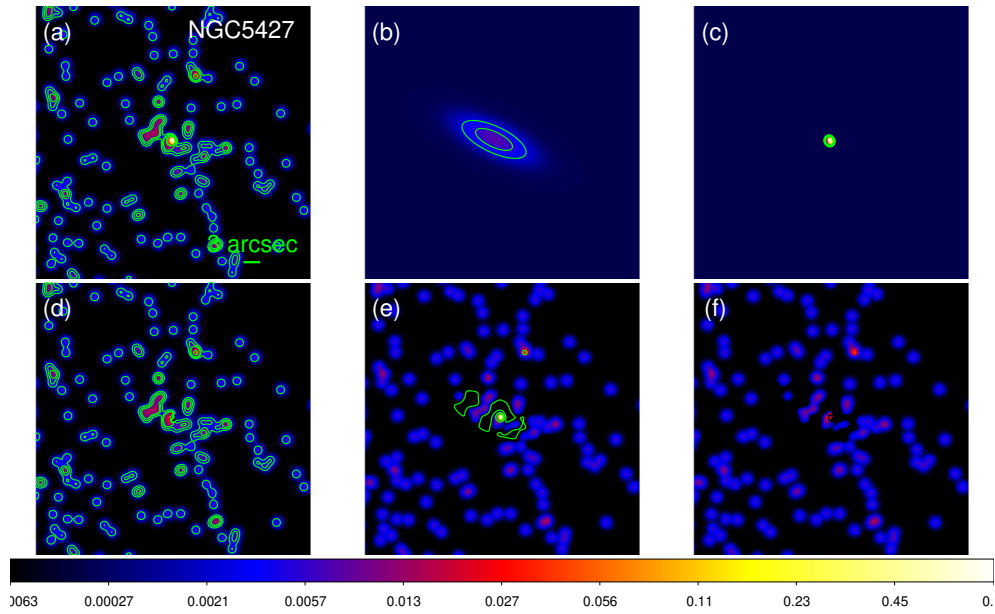


Figure 43: Morphological decomposition for NGC5427. Panels as in the Figure 2 of the paper.

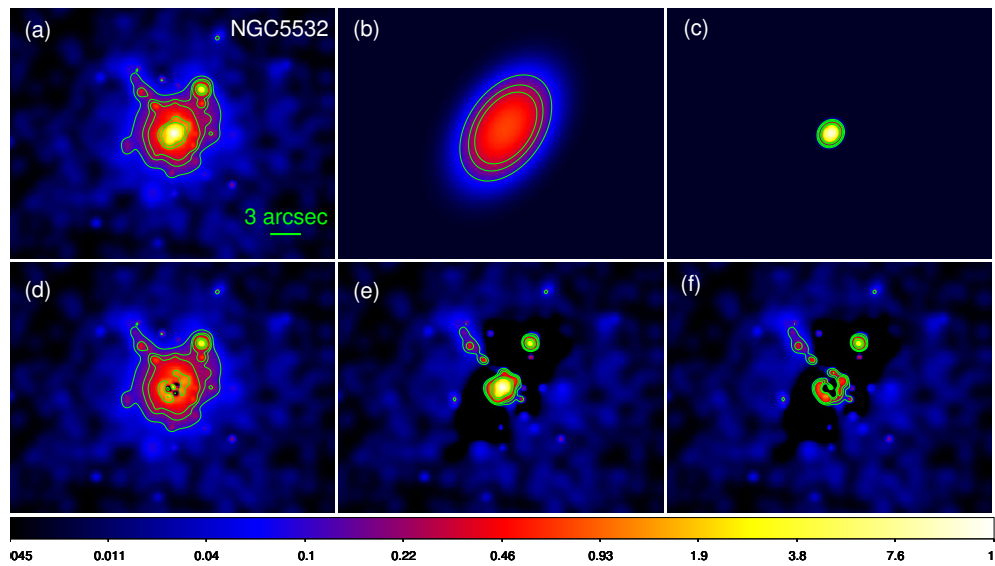


Figure 44: Morphological decomposition for NGC5532. Panels as in the Figure 2 of the paper.

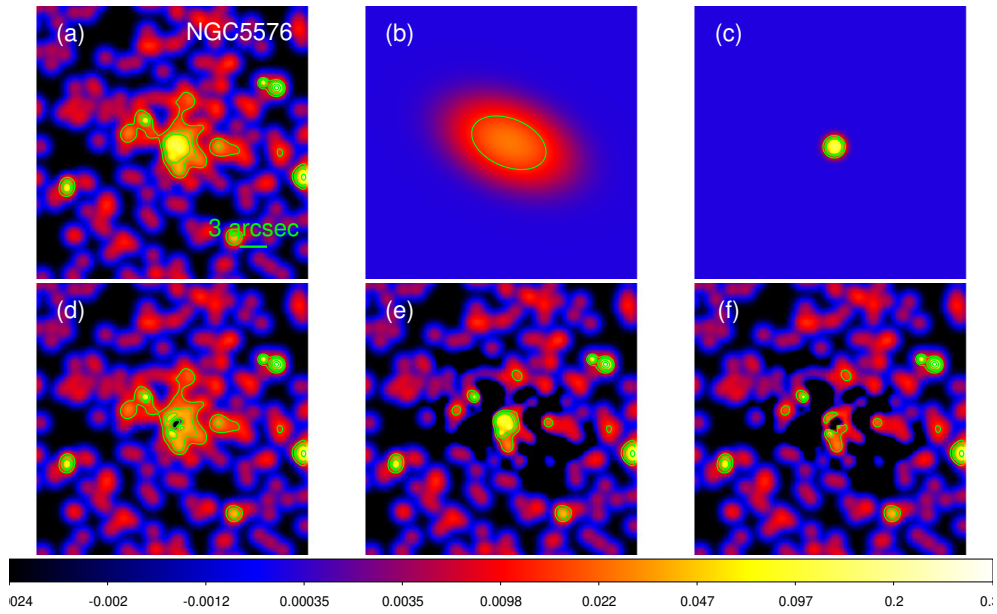


Figure 45: Morphological decomposition for NGC5576. Panels as in the Figure 2 of the paper.

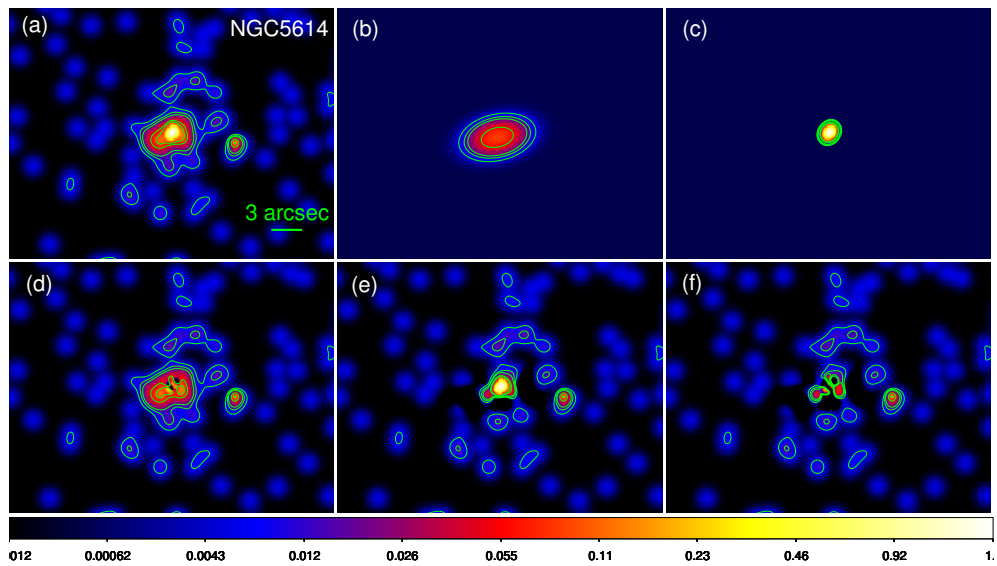


Figure 46: Morphological decomposition for NGC5614. Panels as in the Figure 2 of the paper.

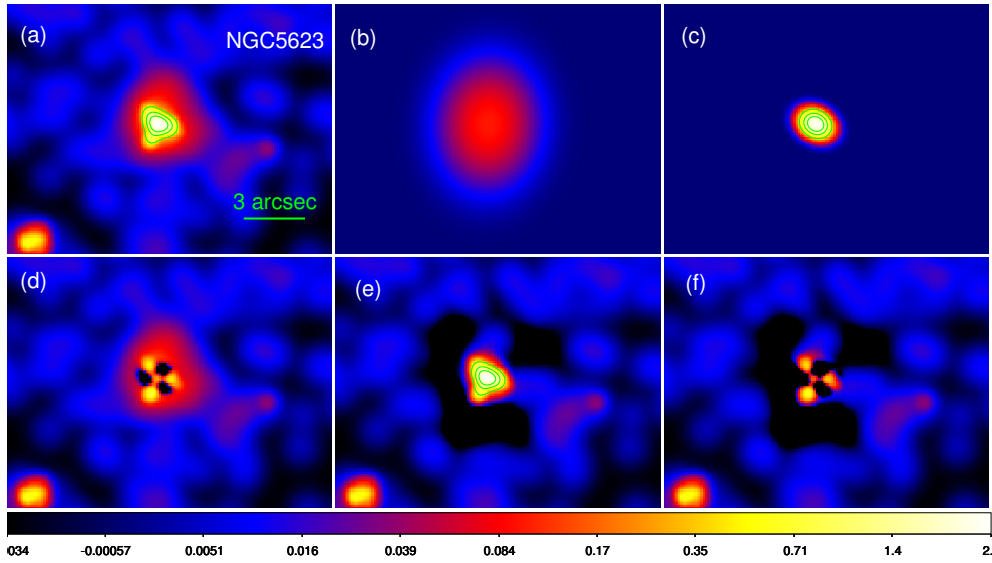


Figure 47: Morphological decomposition for NGC5623. Panels as in the Figure 2 of the paper.

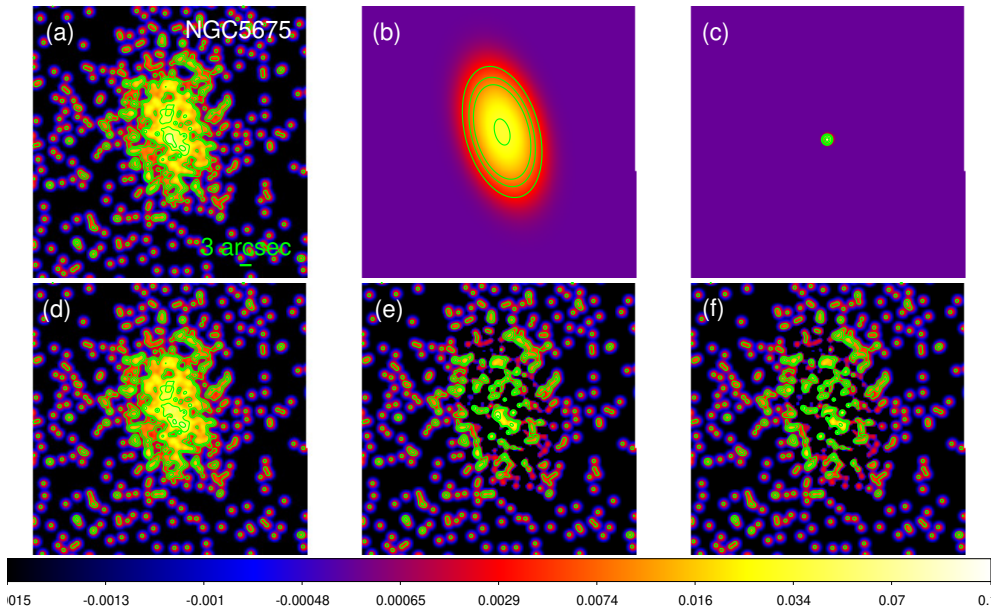


Figure 48: Morphological decomposition for NGC5675. Panels as in the Figure 2 of the paper.

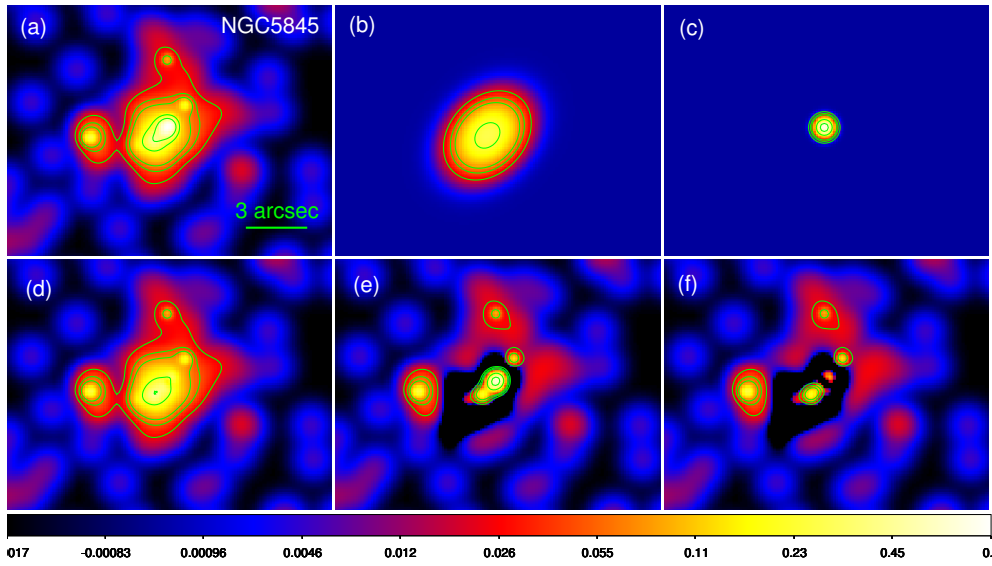


Figure 49: Morphological decomposition for NGC5845. Panels as in the Figure 2 of the paper.

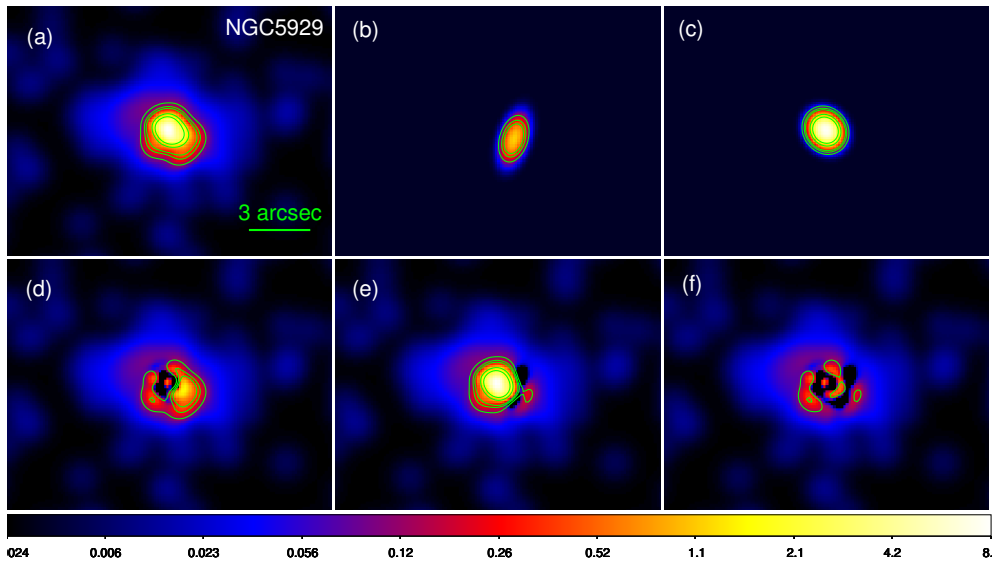


Figure 50: Morphological decomposition for NGC5929. Panels as in the Figure 2 of the paper.

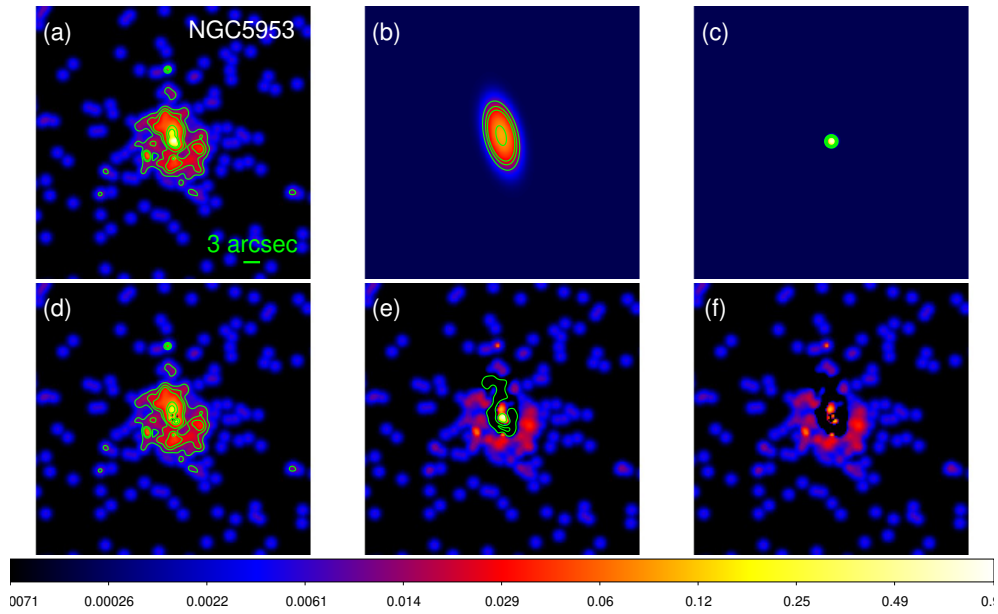


Figure 51: Morphological decomposition for NGC5953. Panels as in the Figure 2 of the paper.

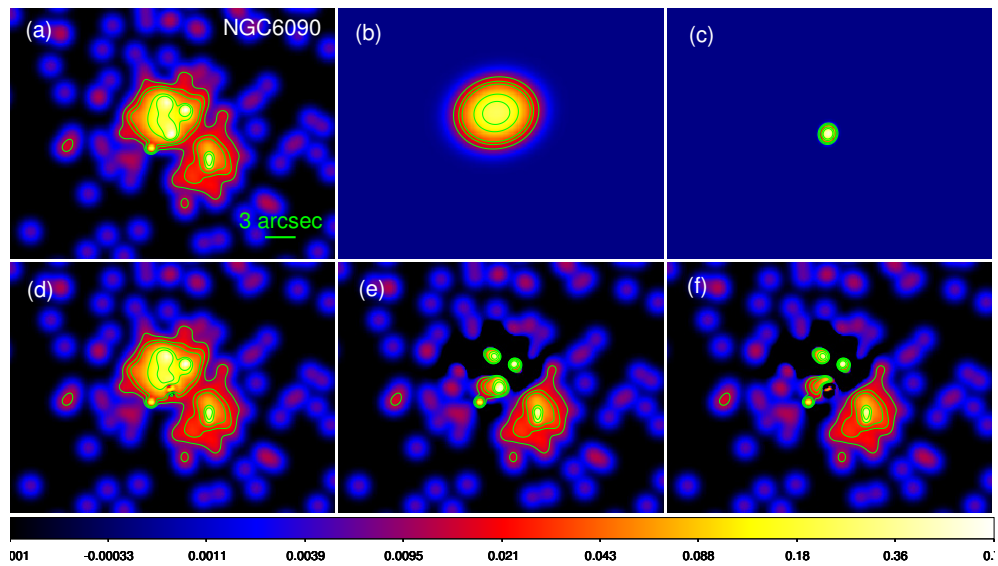


Figure 52: Morphological decomposition for NGC6090. Panels as in the Figure 2 of the paper.

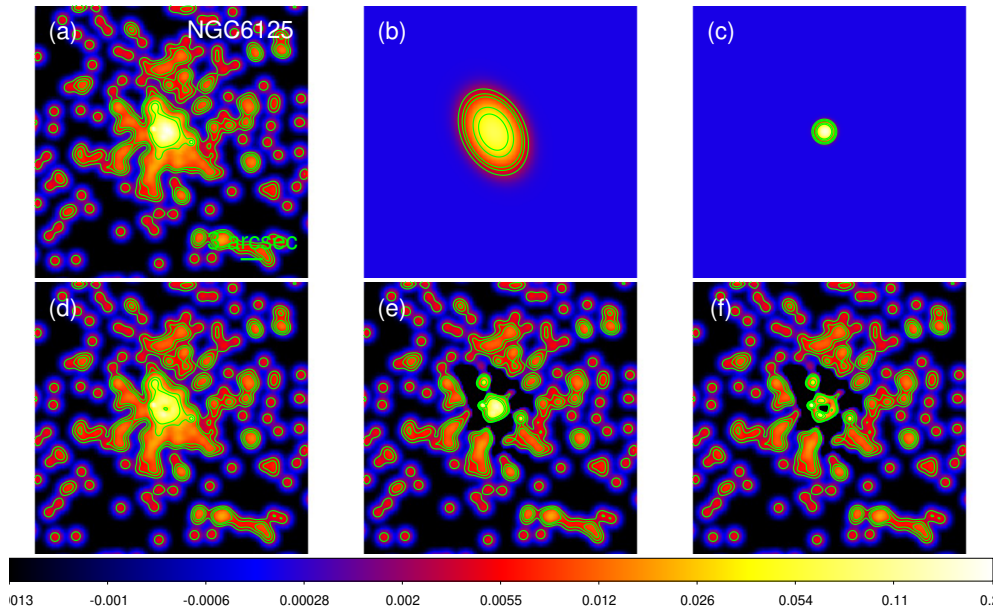


Figure 53: Morphological decomposition for NGC6125. Panels as in the Figure 2 of the paper.

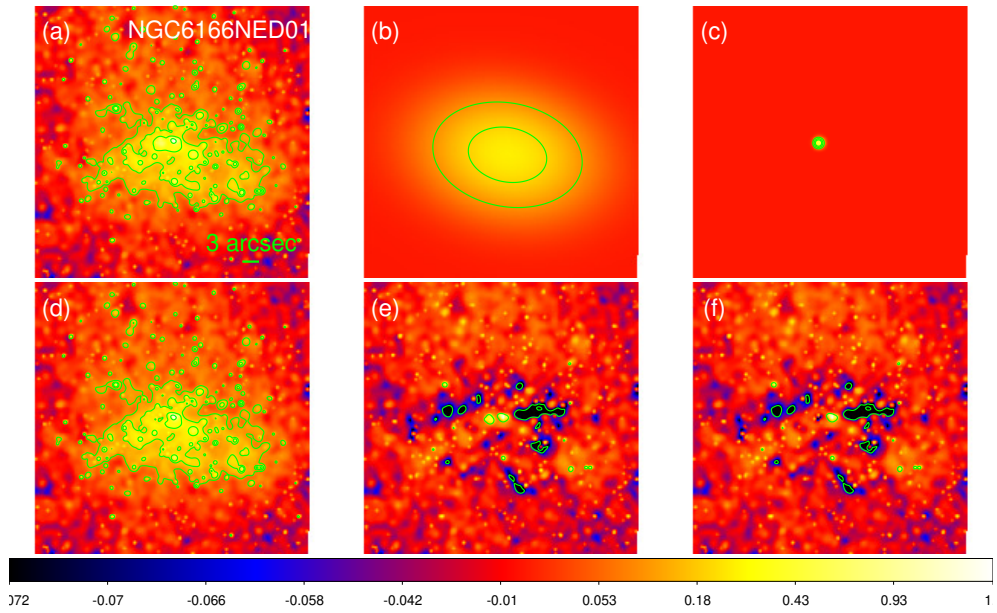


Figure 54: Morphological decomposition for NGC6166NED01. Panels as in the Figure 2 of the paper.

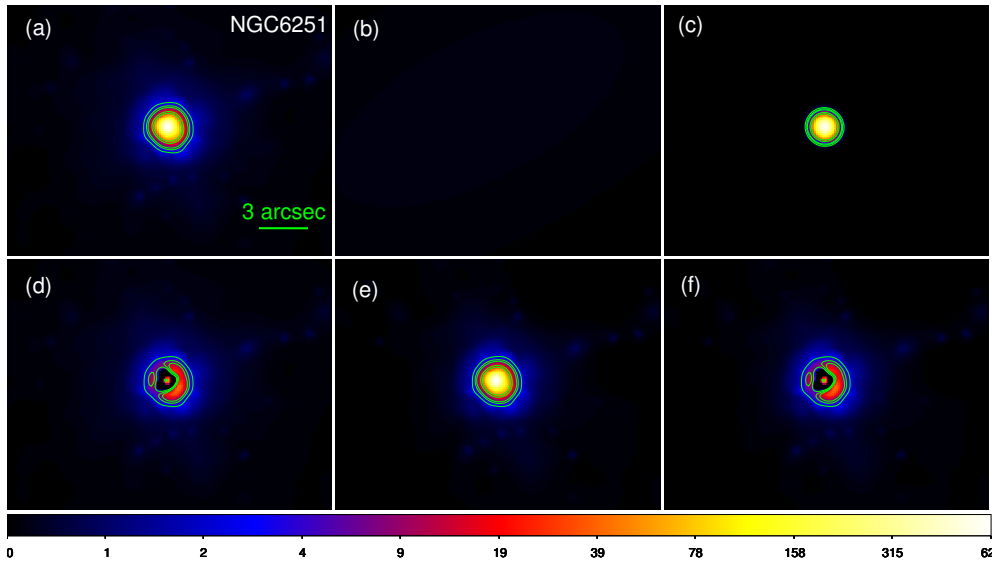


Figure 55: Morphological decomposition for NGC6251. Panels as in the Figure 2 of the paper.

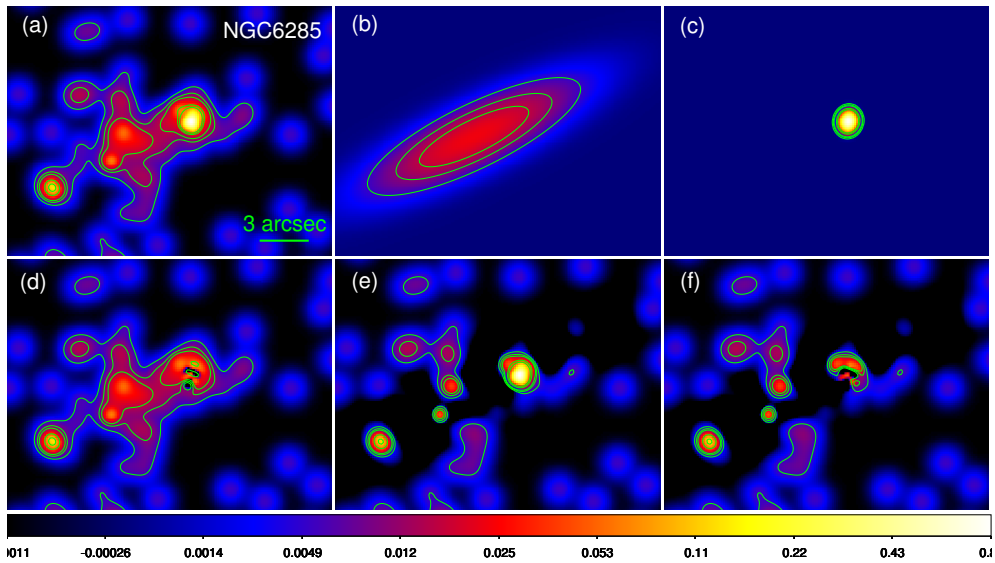


Figure 56: Morphological decomposition for NGC6285. Panels as in the Figure 2 of the paper.

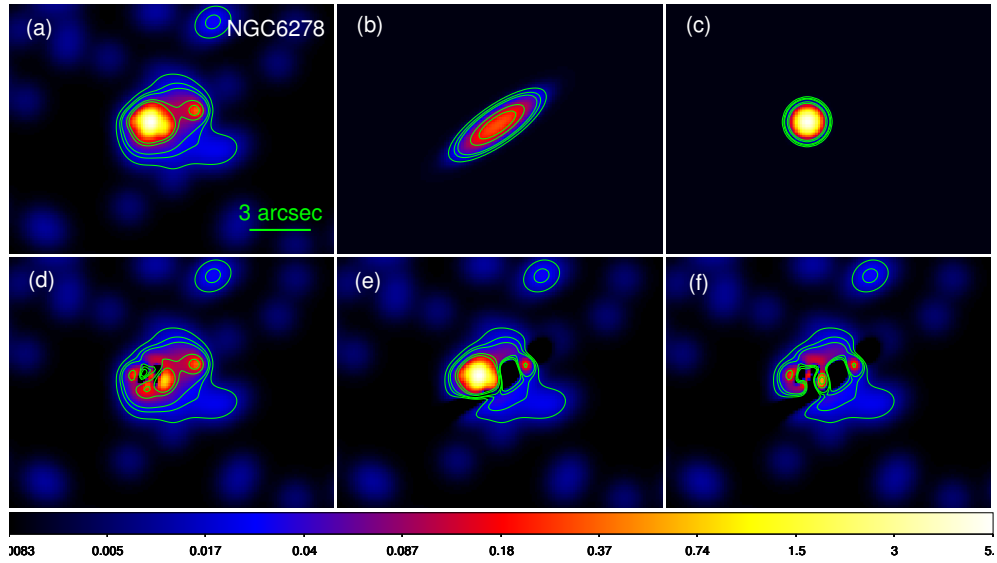


Figure 57: Morphological decomposition for NGC6278. Panels as in the Figure 2 of the paper.

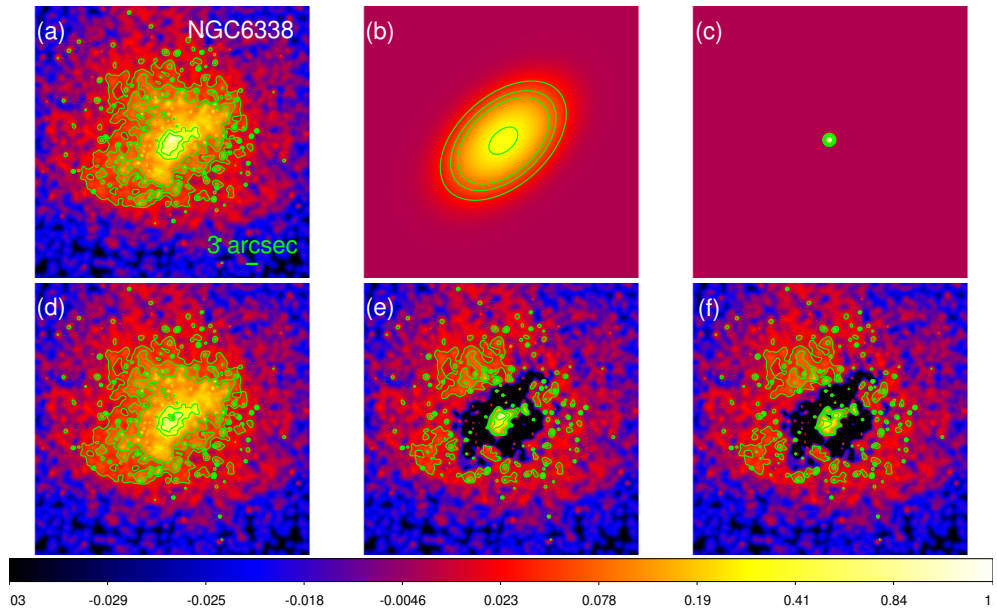


Figure 58: Morphological decomposition for NGC6338. Panels as in the Figure 2 of the paper.

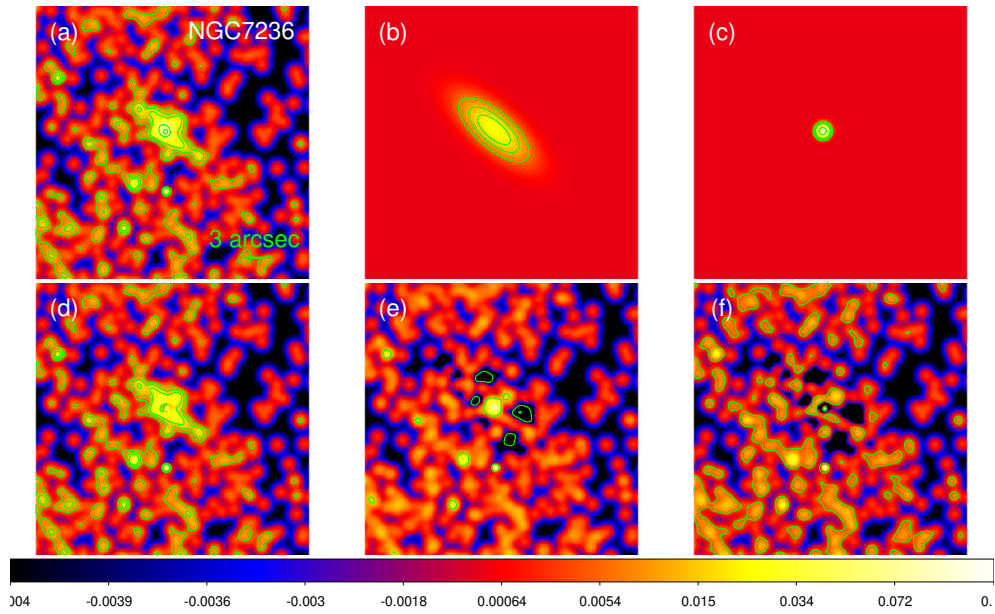


Figure 59: Morphological decomposition for NGC7236. Panels as in the Figure 2 of the paper.

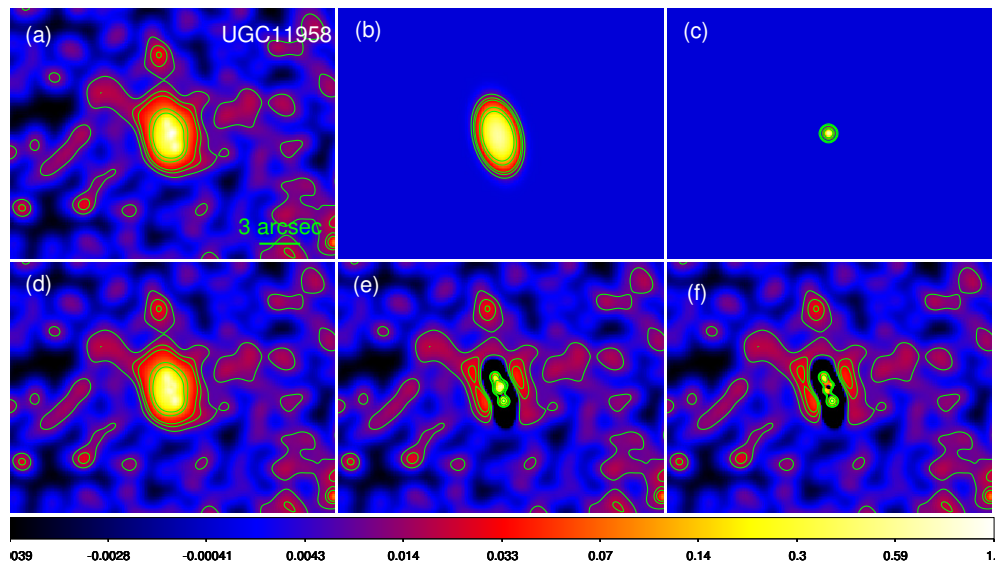


Figure 60: Morphological decomposition for UGC11958. Panels as in the Figure 2 of the paper.

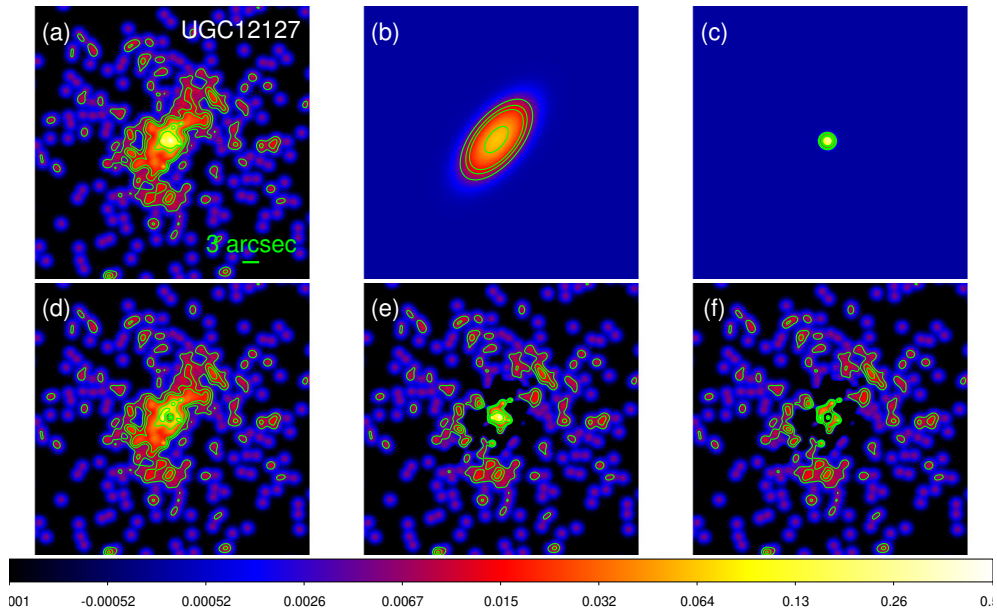


Figure 61: Morphological decomposition for UGC12127. Panels as in the Figure 2 of the paper.

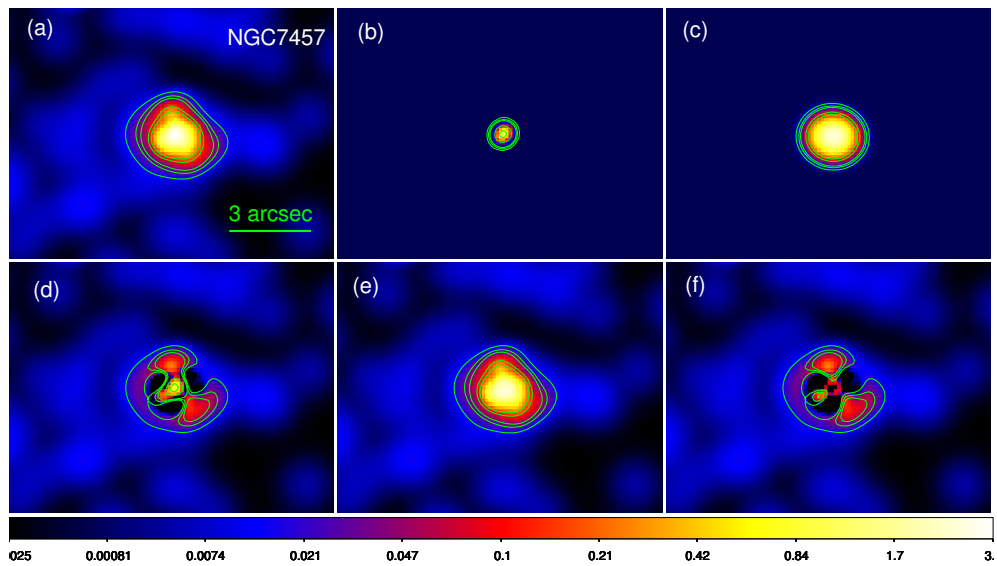


Figure 62: Morphological decomposition for NGC7457. Panels as in the Figure 2 of the paper.

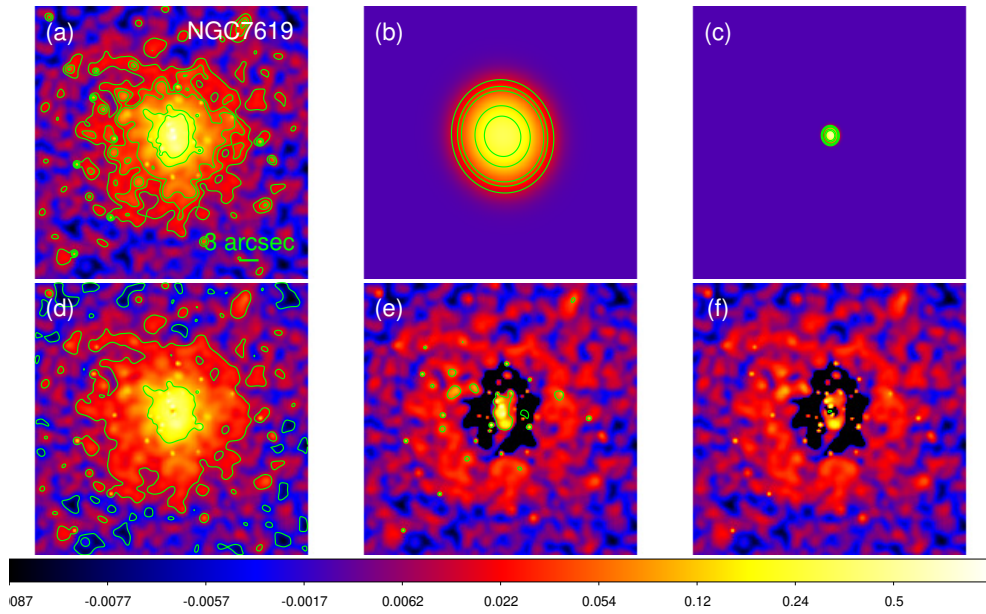


Figure 63: Morphological decomposition for NGC7619. Panels as in the Figure 2 of the paper.

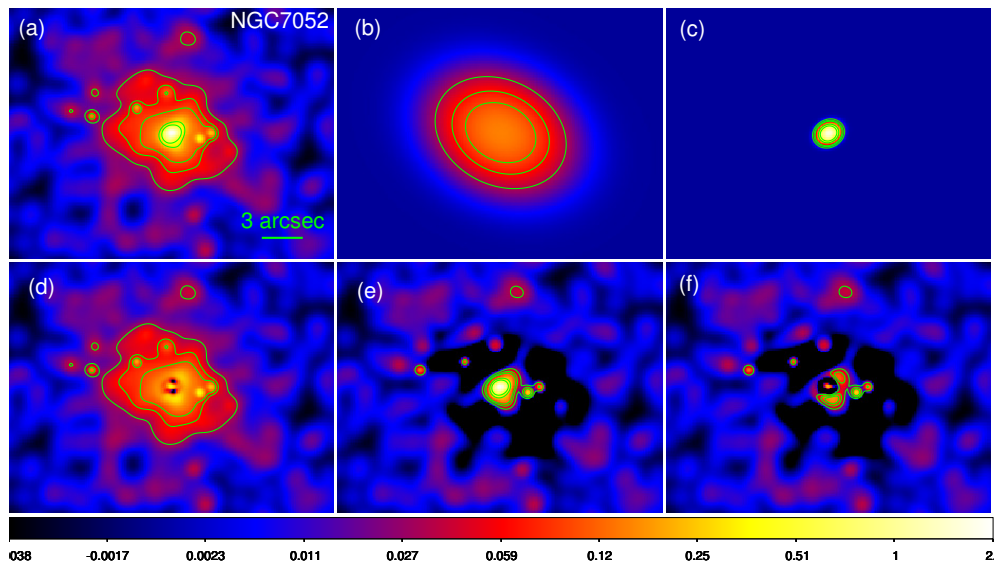


Figure 64: Morphological decomposition for NGC7052. Panels as in the Figure 2 of the paper.

8.4 Catalogue of spectral fittings: AGN in the CALIFA survey

survey

In this section, we show the figures of the corresponding spectral fits performed for the sources in the CALIFA survey with nuclear detection in the *Chandra* spectra. Each panel represents a model version with its corresponding residual panel.

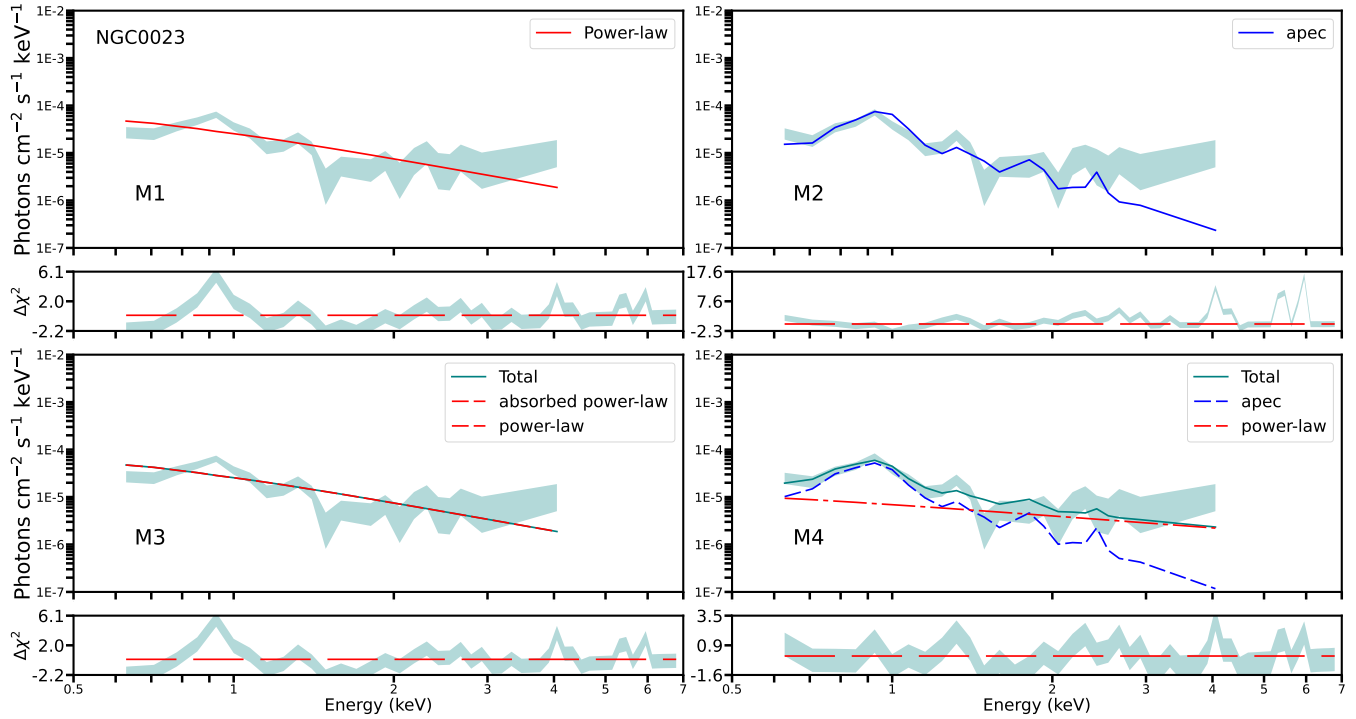


Figure 8.3: *Chandra* spectrum of the nuclear region of NGC 0023. The green area corresponds to the spectra, while the red and blue lines correspond to a power-law and thermal models, respectively. The bottom panels represent the residuals of the fits for each model version.

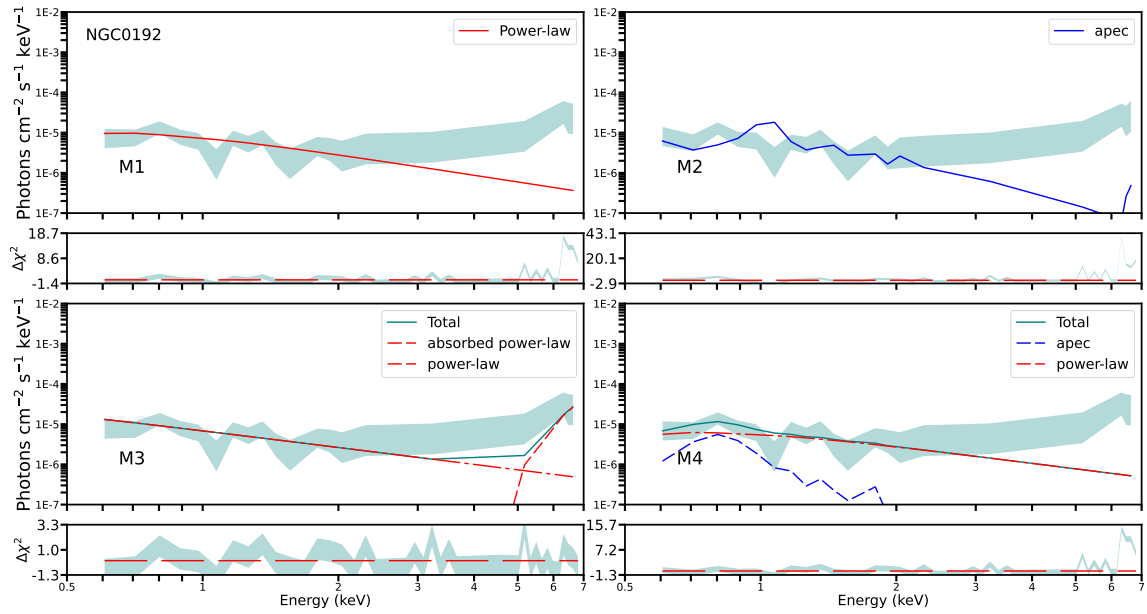


Figure 2: *NuSTAR* X-ray spectra of NGC0192. Labels as in Fig. 8.3.

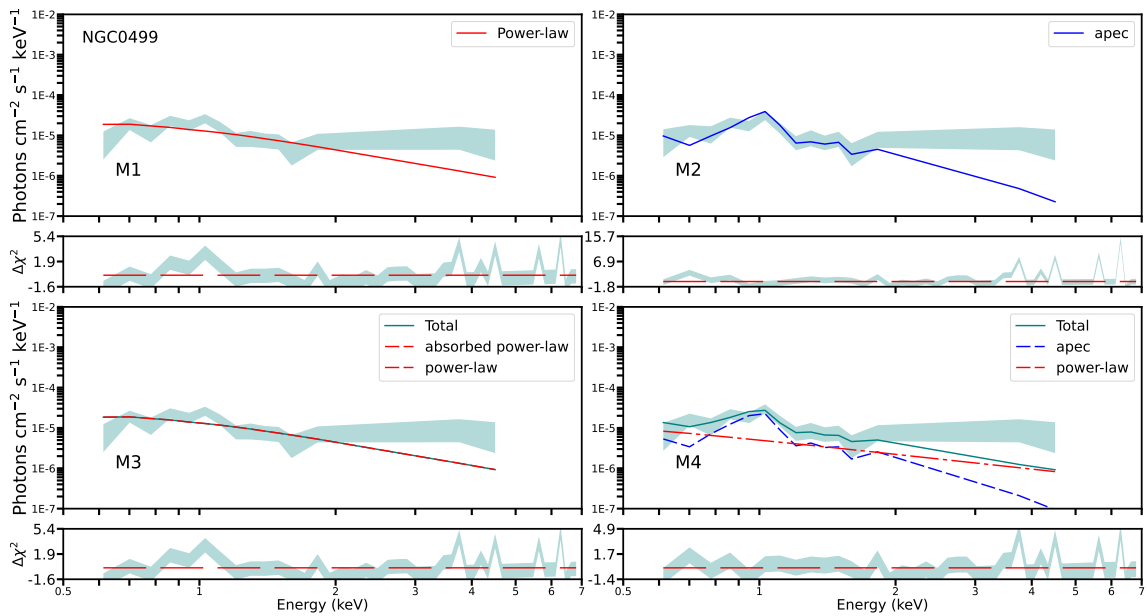


Figure 3: *NuSTAR* X-ray spectra of NGC0499. Labels as in Fig. 8.3.

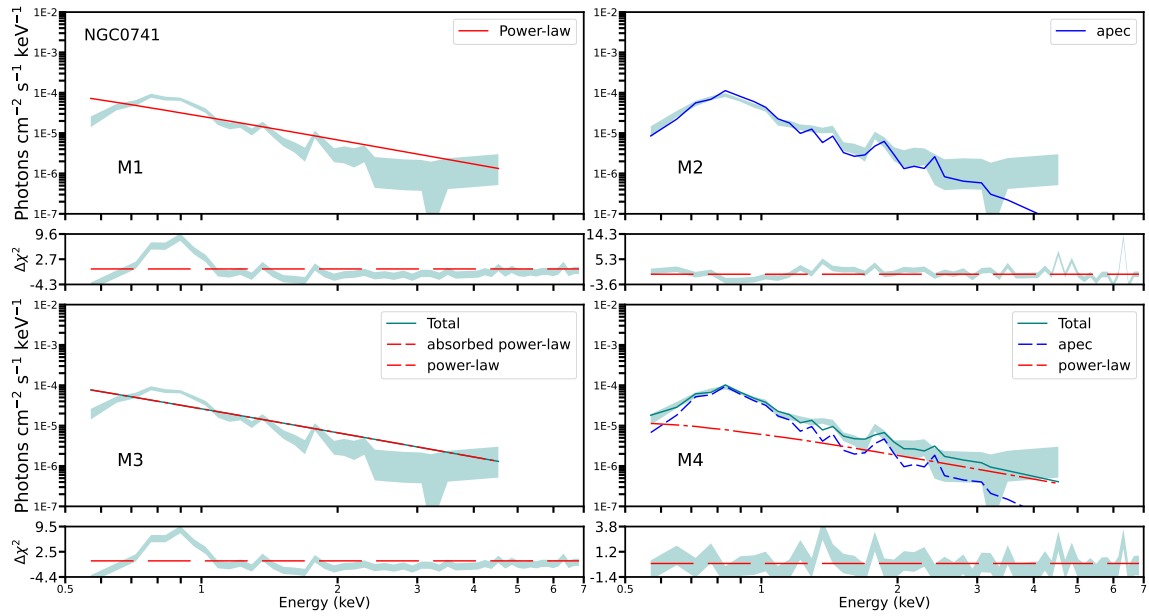


Figure 4: *NuSTAR* X-ray spectra of NGC0741. Labels as in Fig. 8.3.

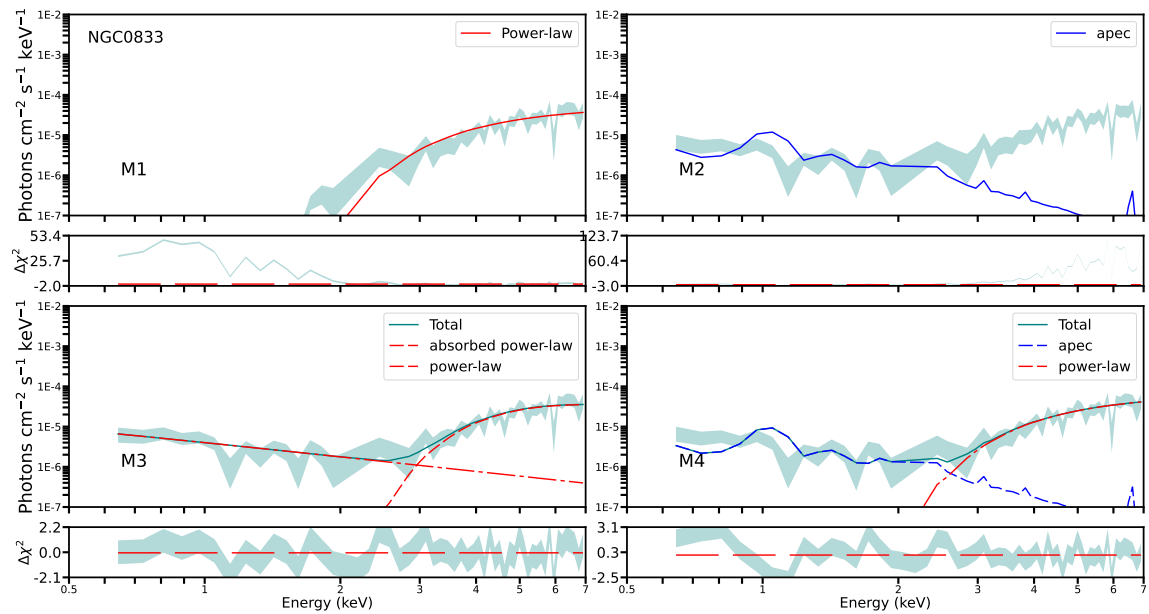


Figure 5: *NuSTAR* X-ray spectra of NGC0833. Labels as in Fig. 8.3.

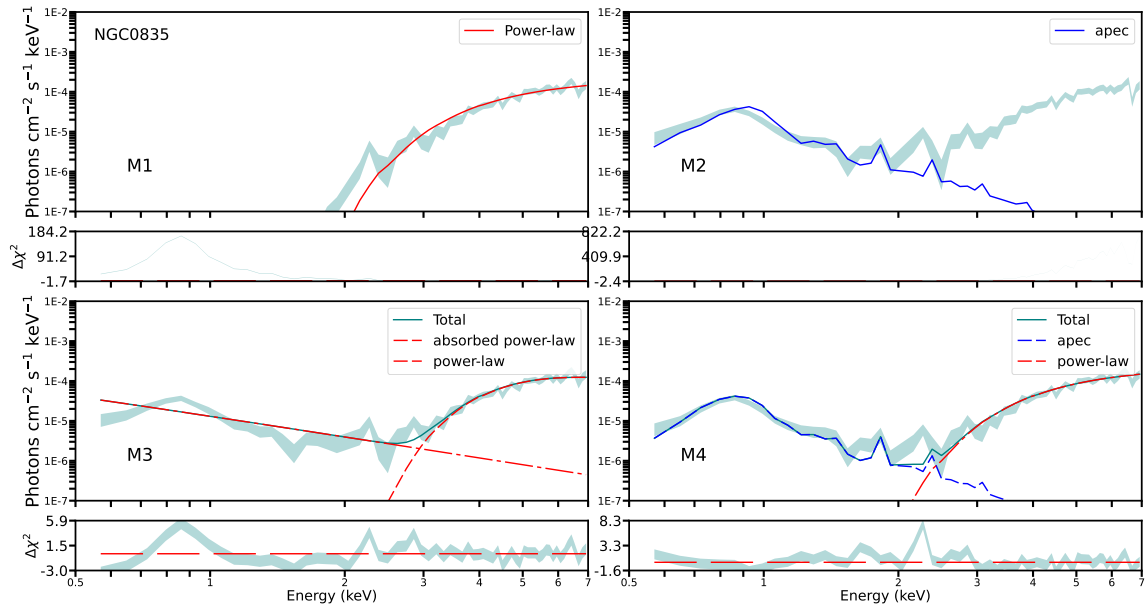


Figure 6: *NuSTAR* X-ray spectra of NGC0835. Labels as in Fig. 8.3.

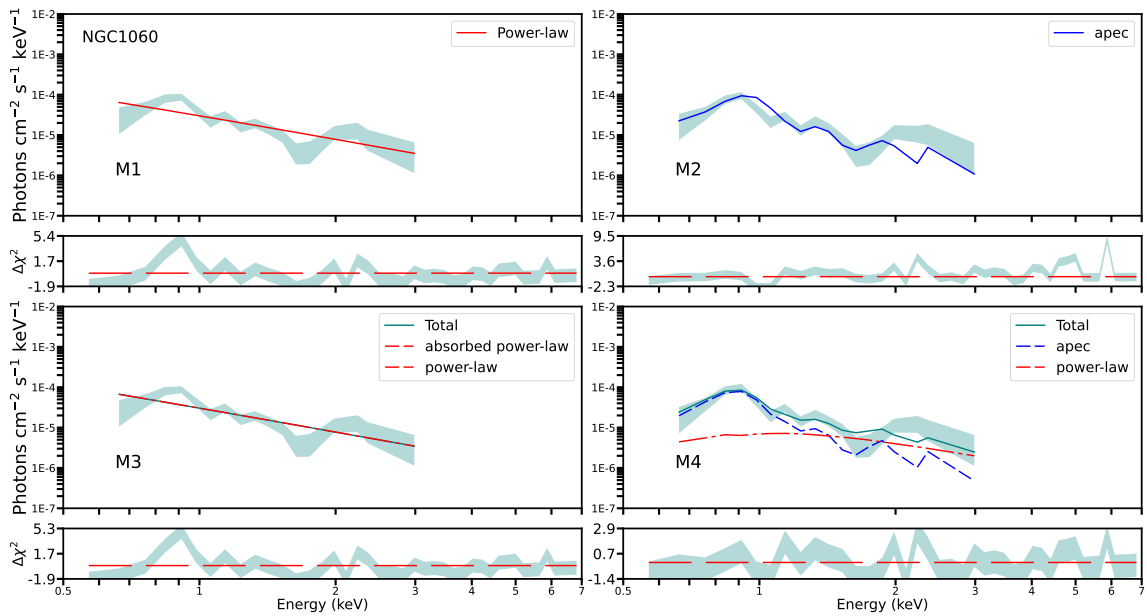


Figure 7: *NuSTAR* X-ray spectra of NGC1060. Labels as in Fig. 8.3.

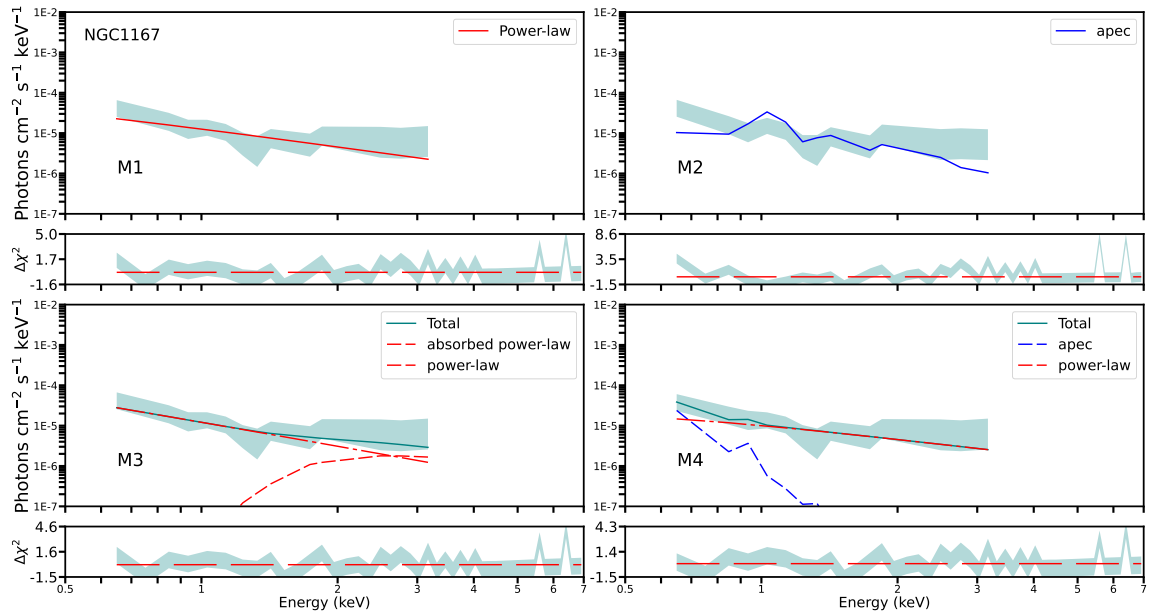


Figure 8: *NuSTAR* X-ray spectra of NGC1167. Labels as in Fig. 8.3.

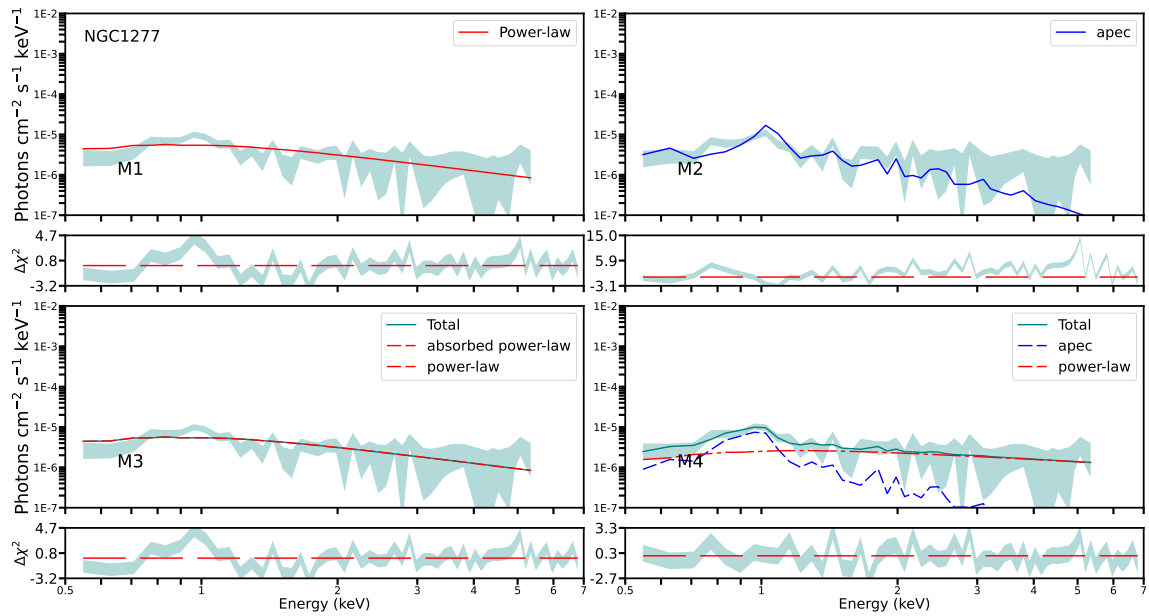


Figure 9: *NuSTAR* X-ray spectra of NGC1277. Labels as in Fig. 8.3.

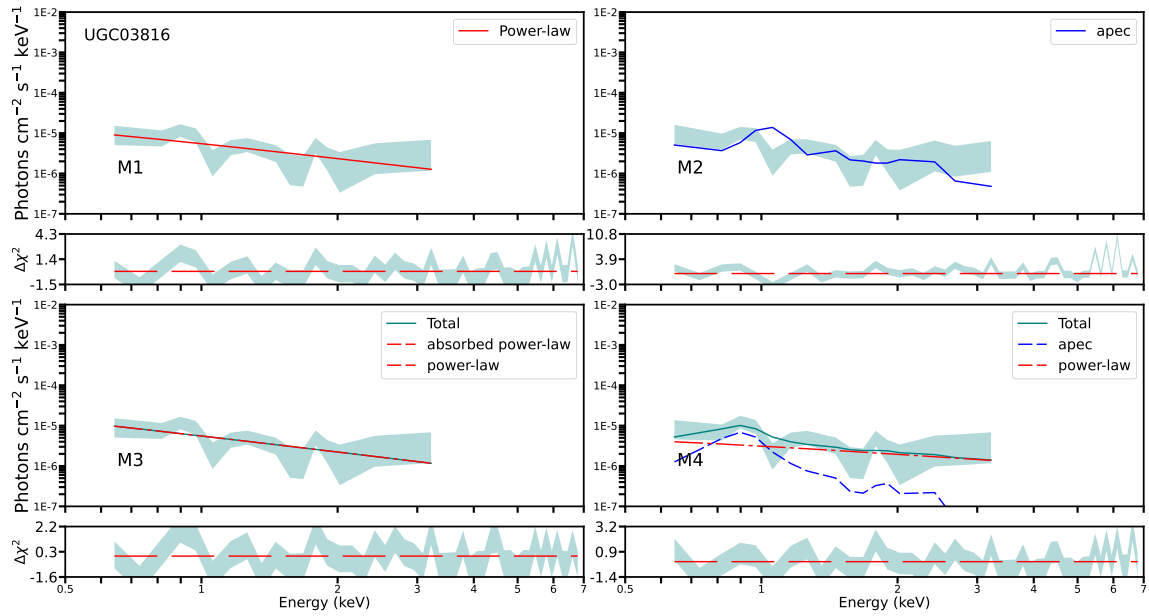


Figure 10: *NuSTAR* X-ray spectra of UGC03816. Labels as in Fig. 8.3.

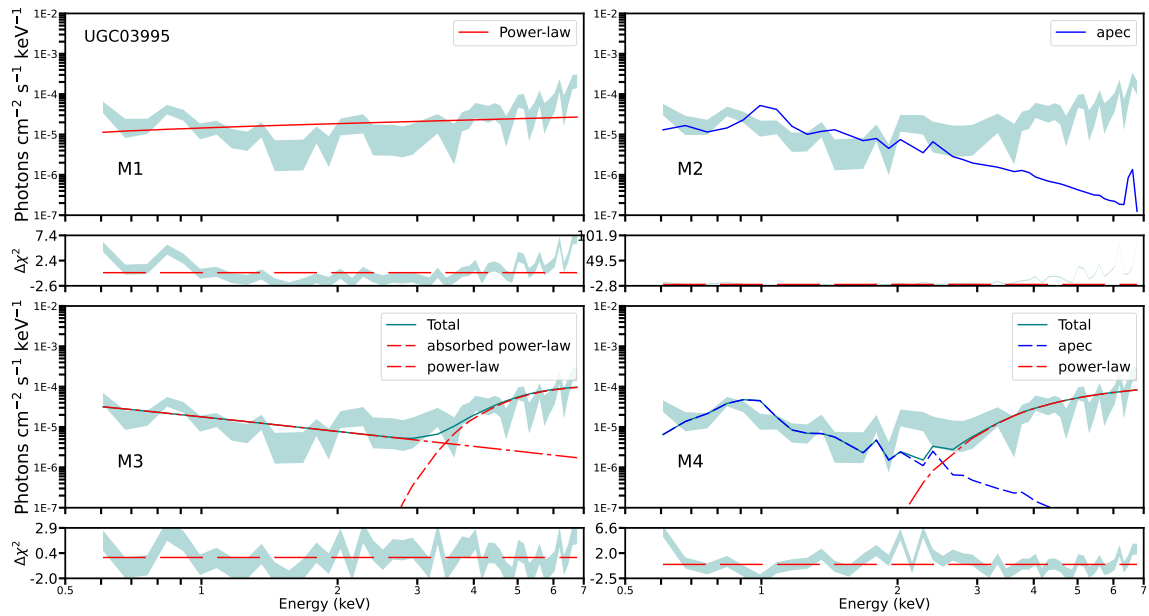


Figure 11: *NuSTAR* X-ray spectra of UGC03995. Labels as in Fig. 8.3.

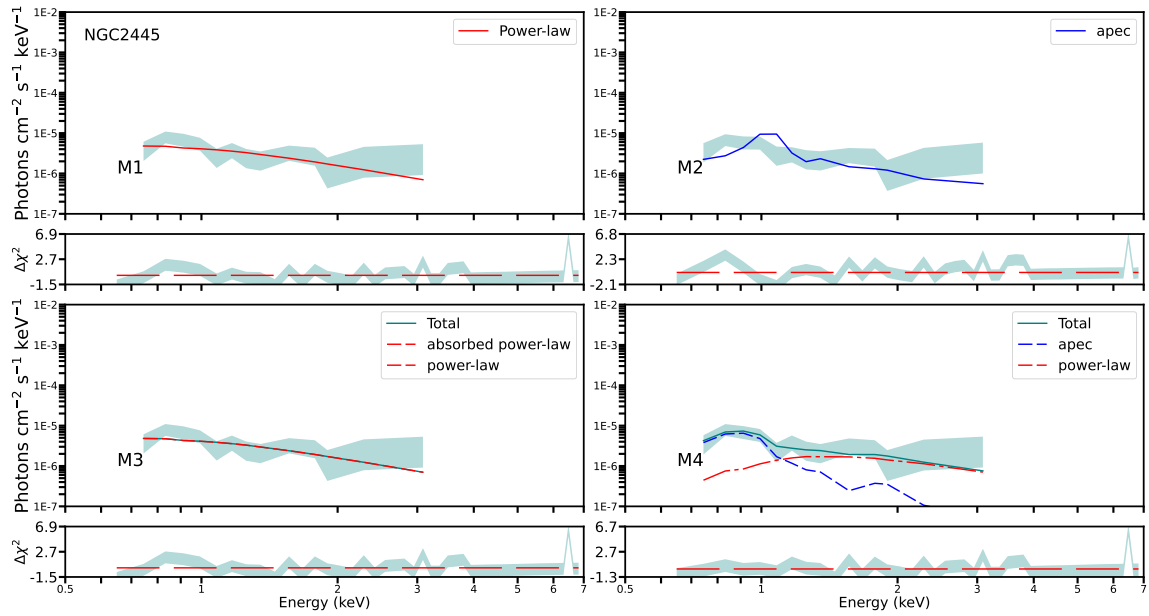


Figure 12: *NuSTAR* X-ray spectra of NGC2445. Labels as in Fig. 8.3.

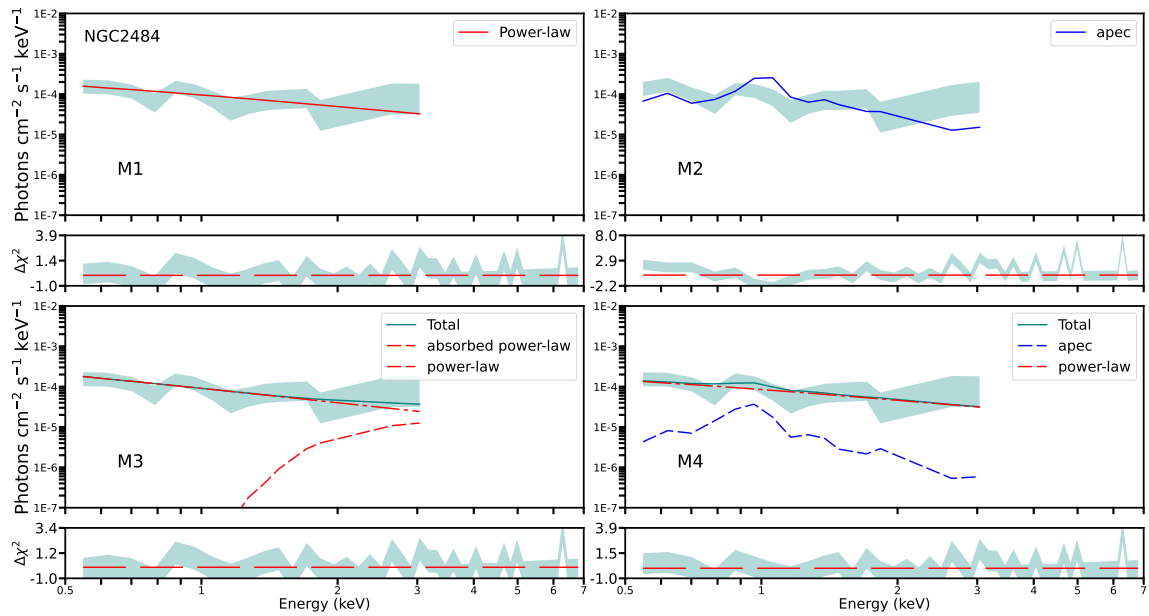


Figure 13: *NuSTAR* X-ray spectra of NGC2484. Labels as in Fig. 8.3.

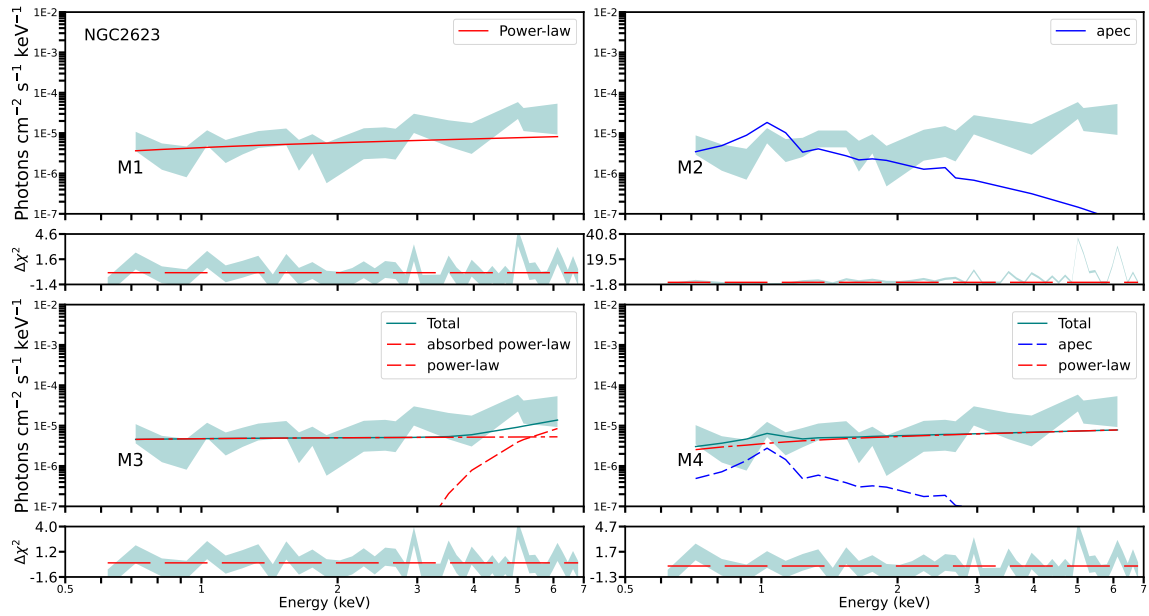


Figure 14: *NuSTAR* X-ray spectra of NGC2623. Labels as in Fig. 8.3.

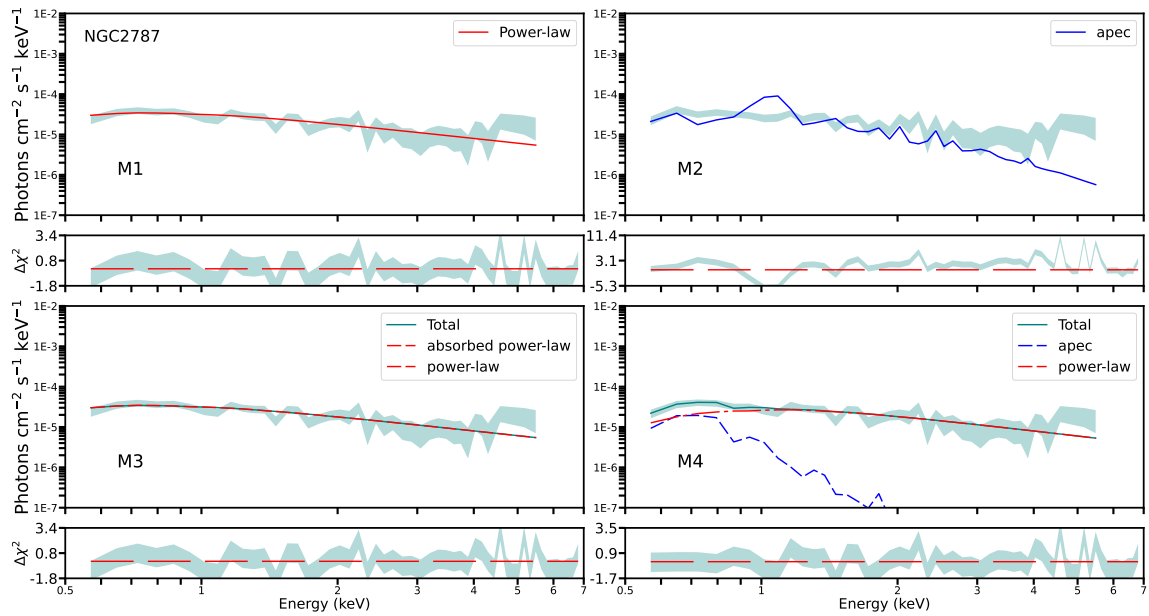


Figure 15: *NuSTAR* X-ray spectra of NGC2787. Labels as in Fig. 8.3.

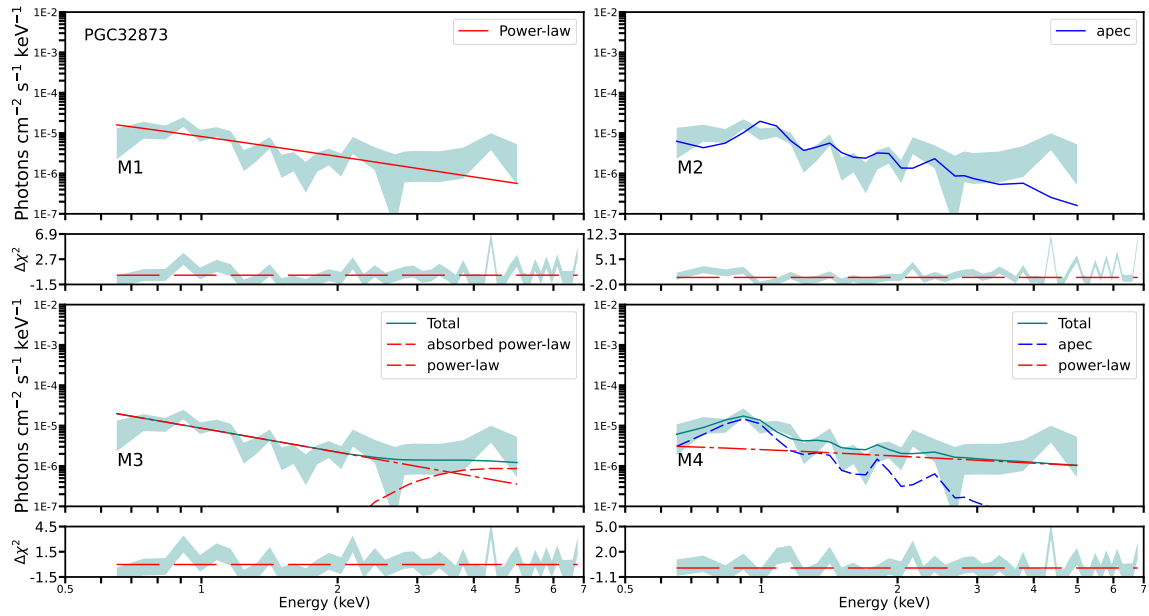


Figure 16: *NuSTAR* X-ray spectra of PGC32873. Labels as in Fig. 8.3.

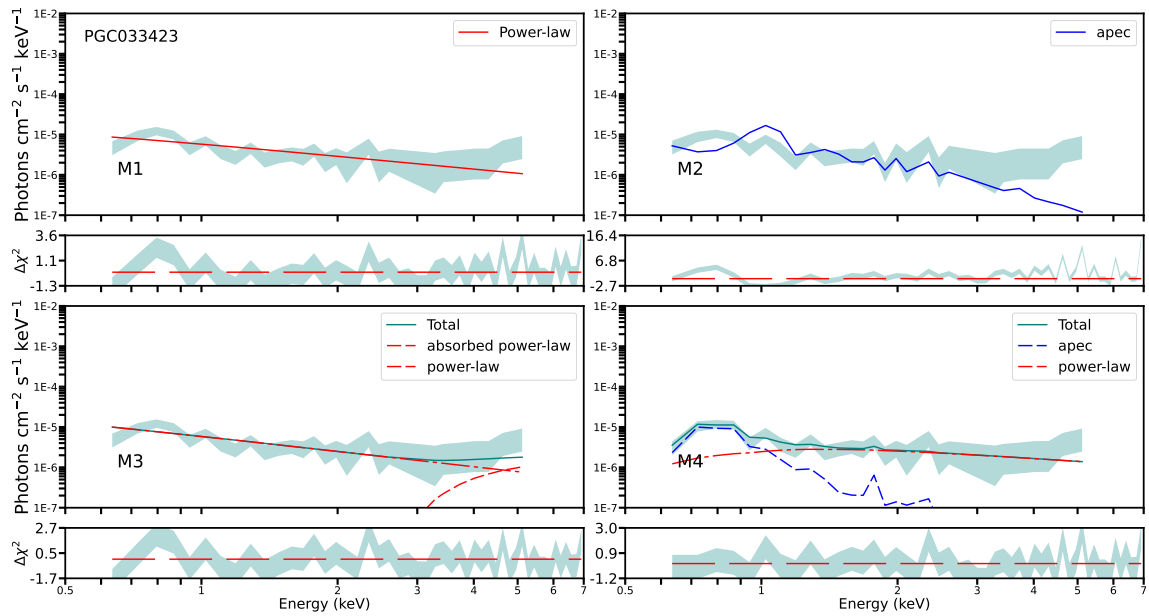


Figure 17: *NuSTAR* X-ray spectra of PGC033423. Labels as in Fig. 8.3.

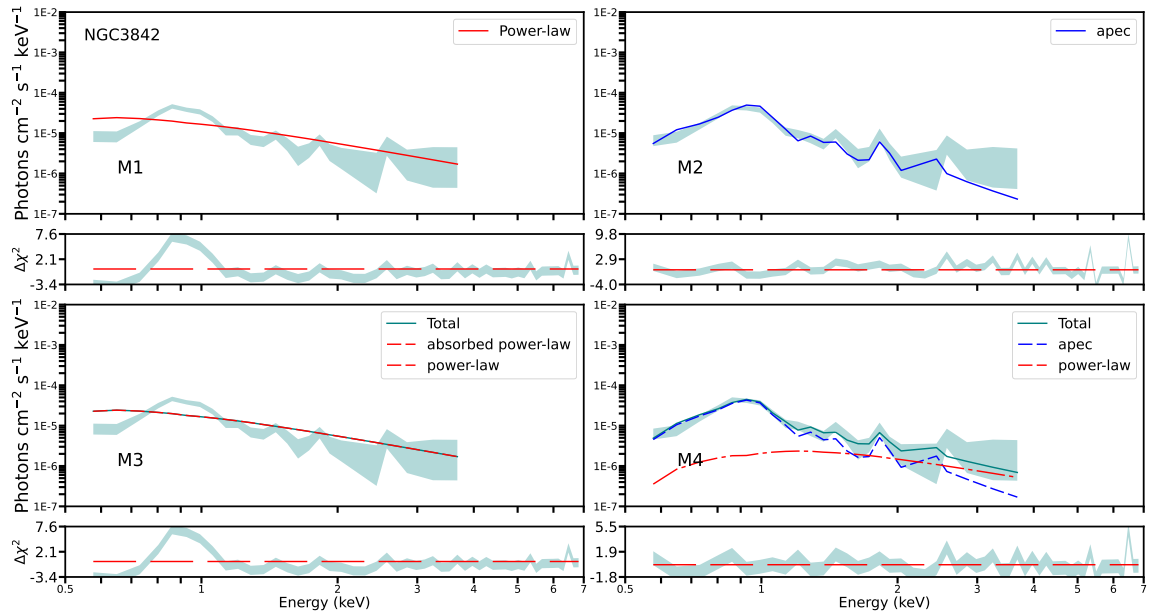


Figure 18: *NuSTAR* X-ray spectra of NGC3842. Labels as in Fig. 8.3.

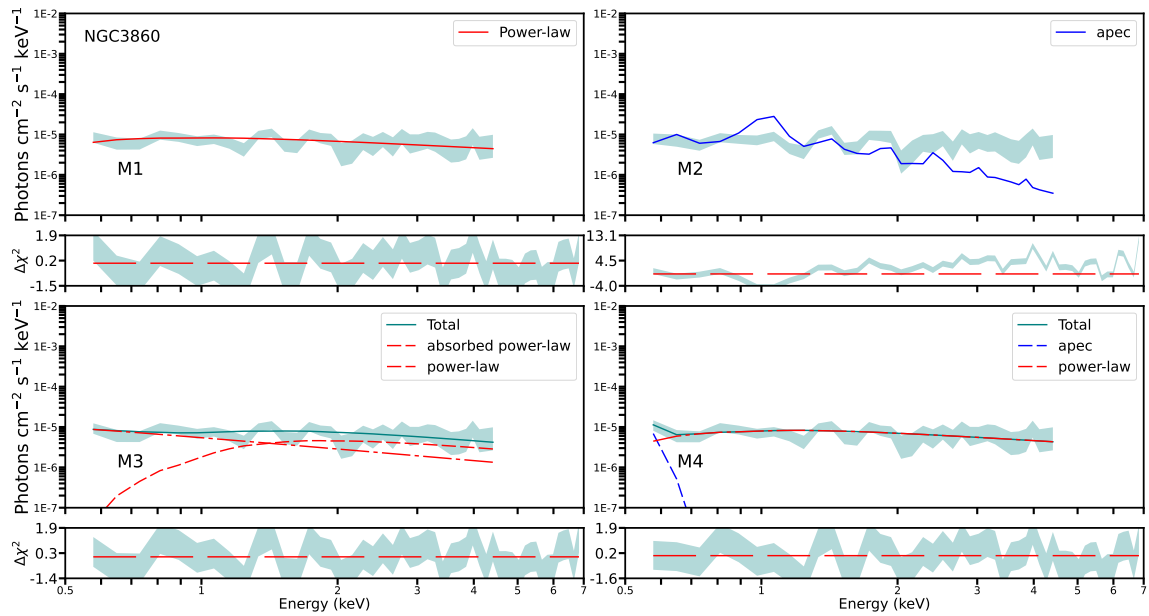


Figure 19: *NuSTAR* X-ray spectra of NGC3860. Labels as in Fig. 8.3.

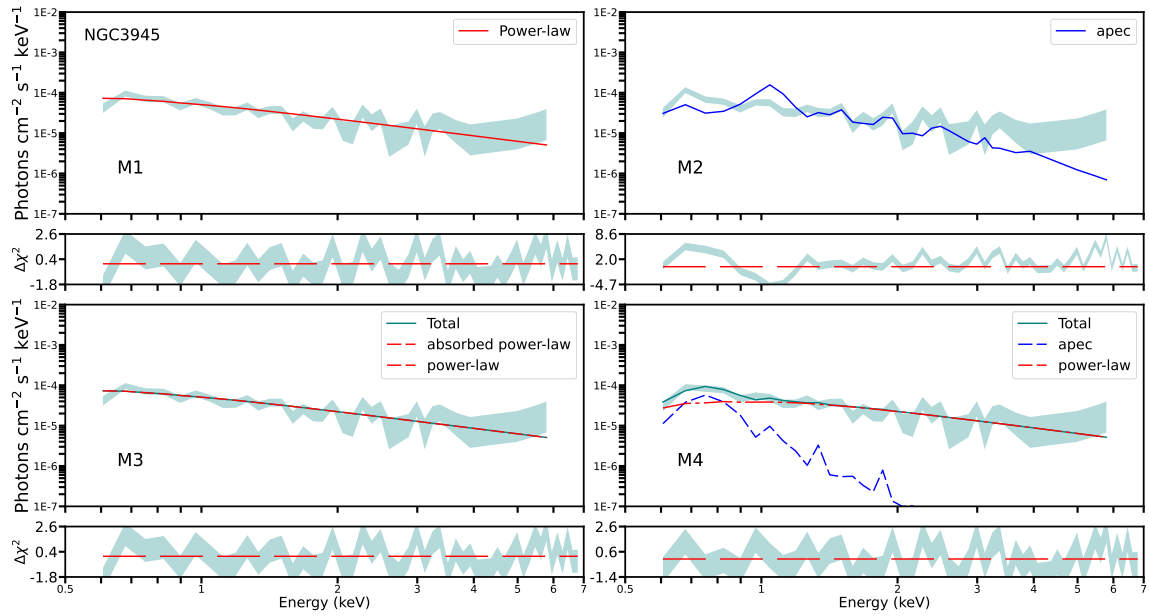


Figure 20: *NuSTAR* X-ray spectra of NGC3945. Labels as in Fig. 8.3.

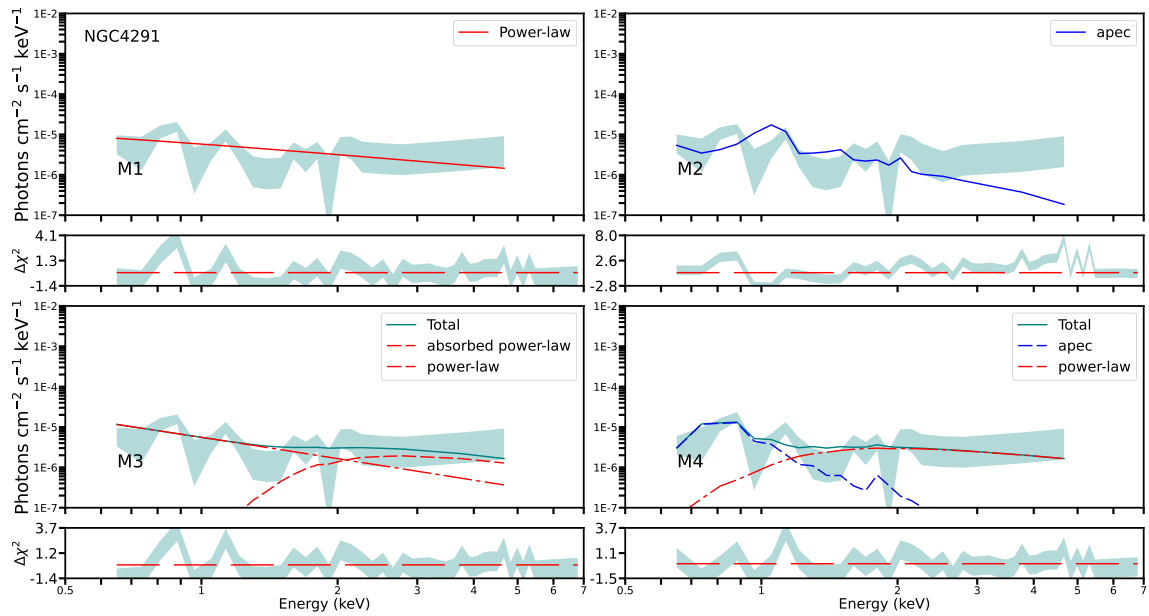


Figure 21: *NuSTAR* X-ray spectra of NGC4291. Labels as in Fig. 8.3.

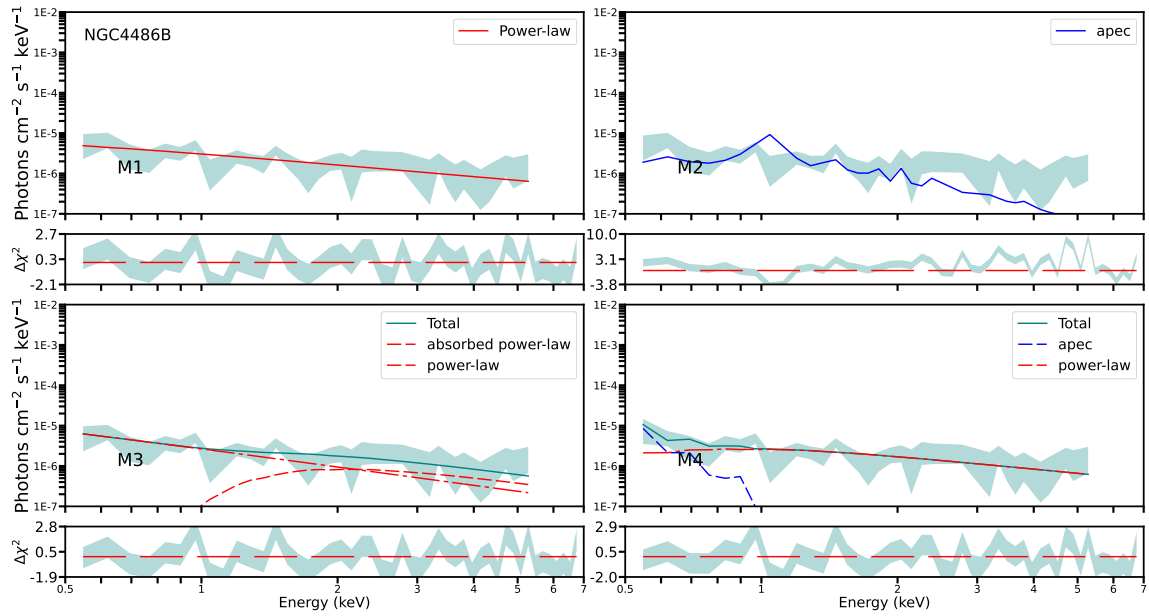


Figure 22: *NuSTAR* X-ray spectra of NGC4486B. Labels as in Fig. 8.3.

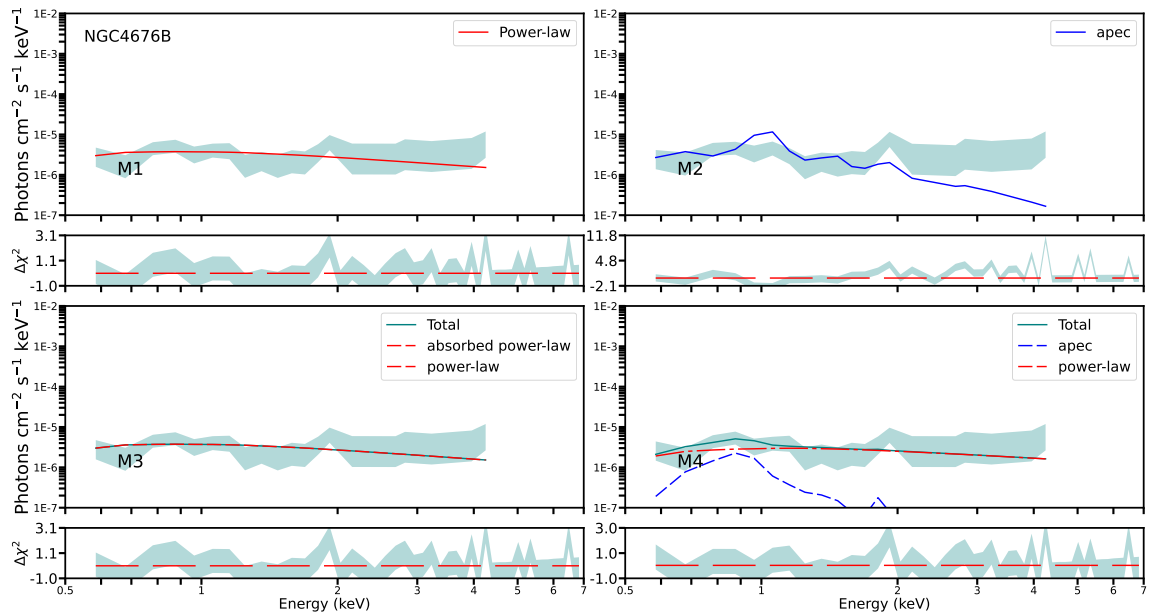


Figure 23: *NuSTAR* X-ray spectra of NGC4676B. Labels as in Fig. 8.3.

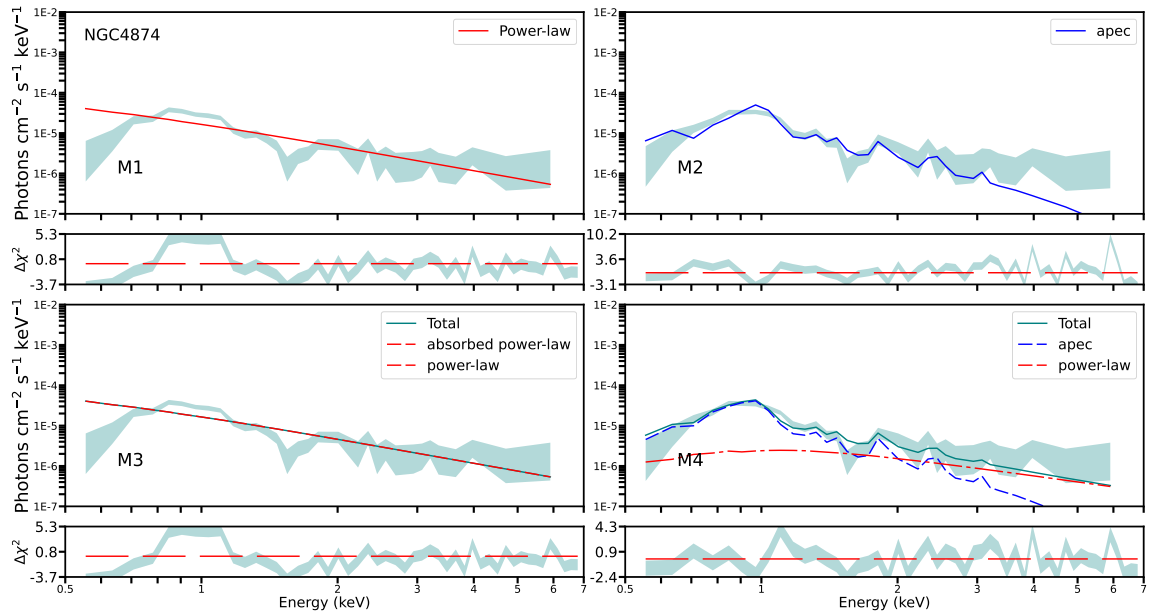


Figure 24: *NuSTAR* X-ray spectra of NGC4874. Labels as in Fig. 8.3.

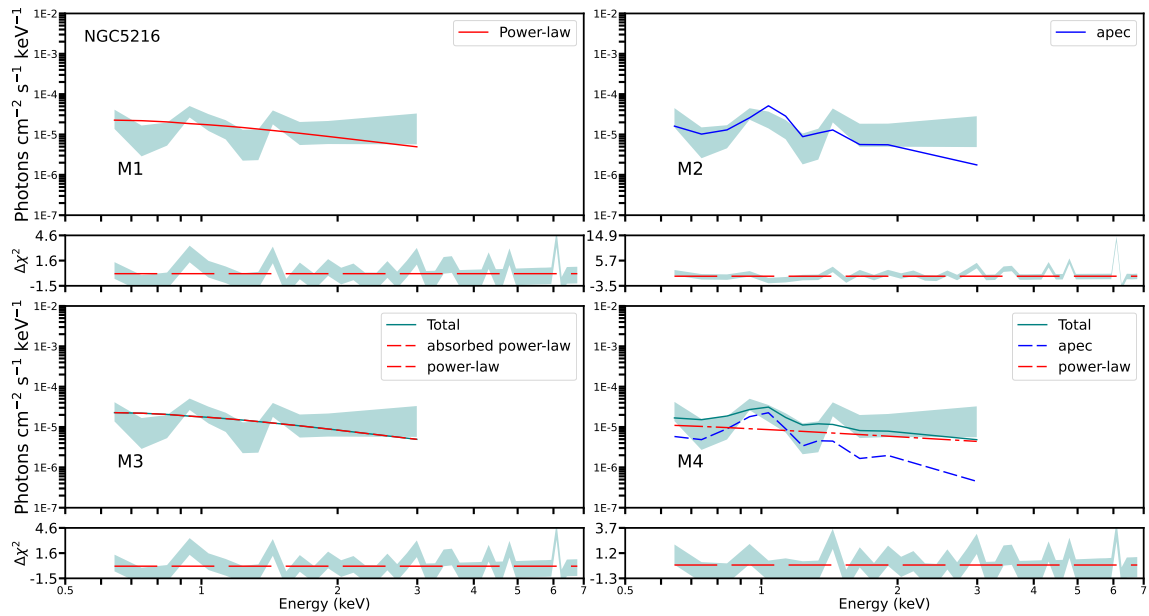


Figure 25: *NuSTAR* X-ray spectra of NGC5216. Labels as in Fig. 8.3.

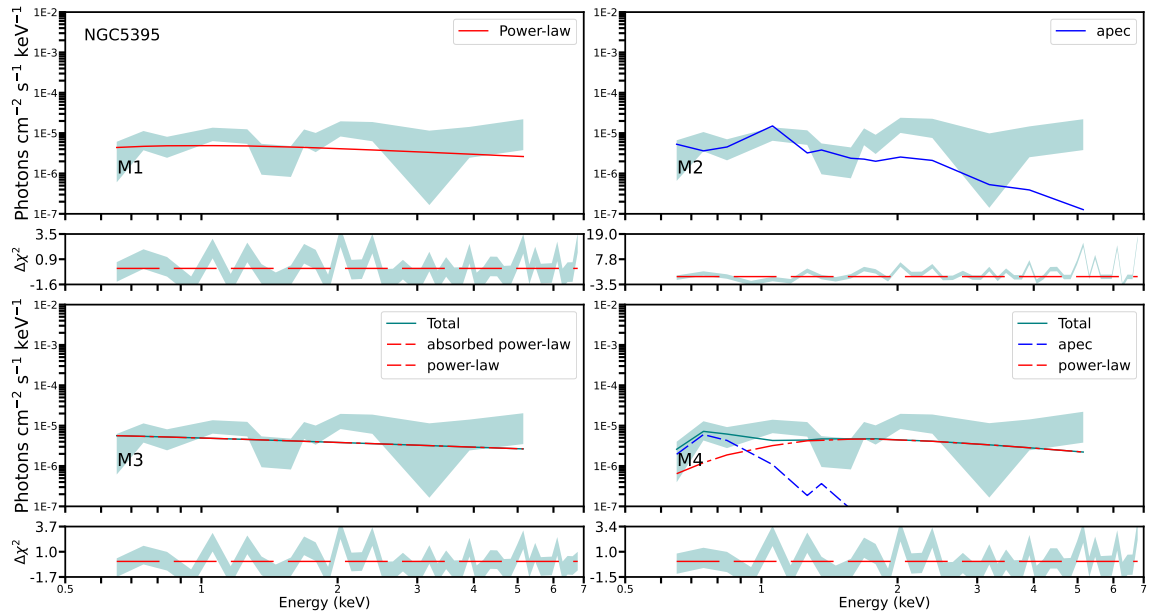


Figure 26: *NuSTAR* X-ray spectra of NGC5395. Labels as in Fig. 8.3.

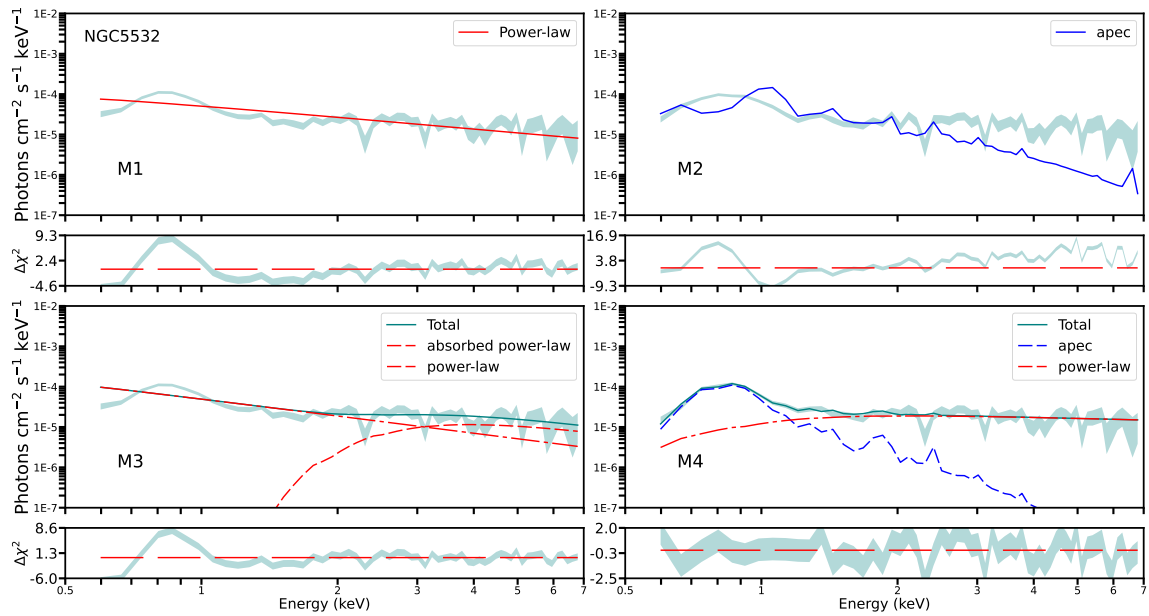


Figure 27: *NuSTAR* X-ray spectra of NGC5532. Labels as in Fig. 8.3.

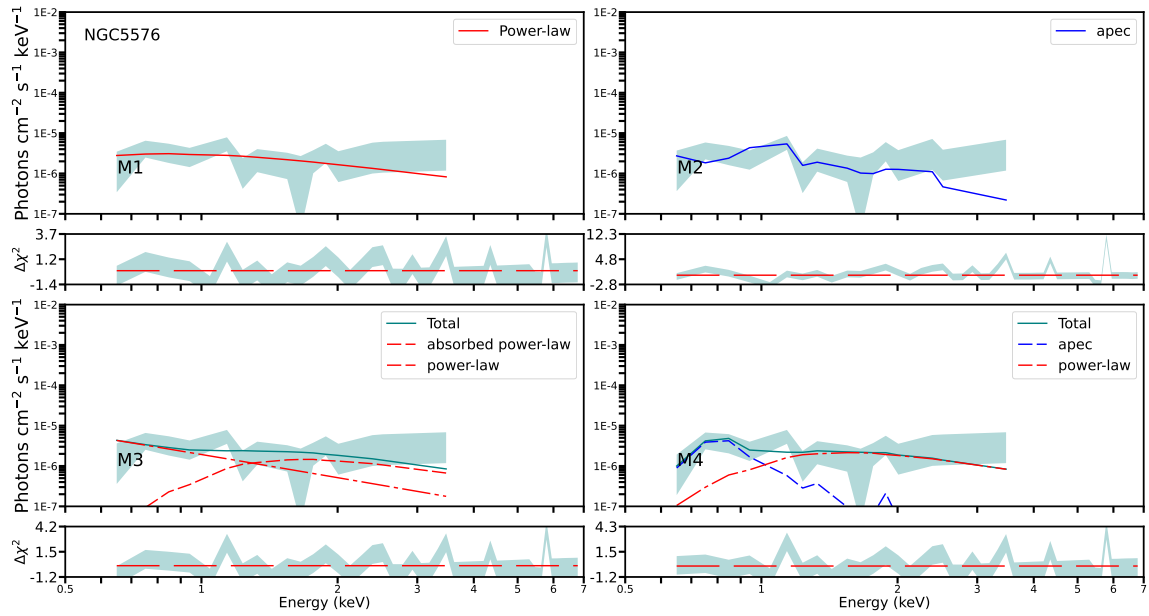


Figure 28: *NuSTAR* X-ray spectra of NGC5576. Labels as in Fig. 8.3.

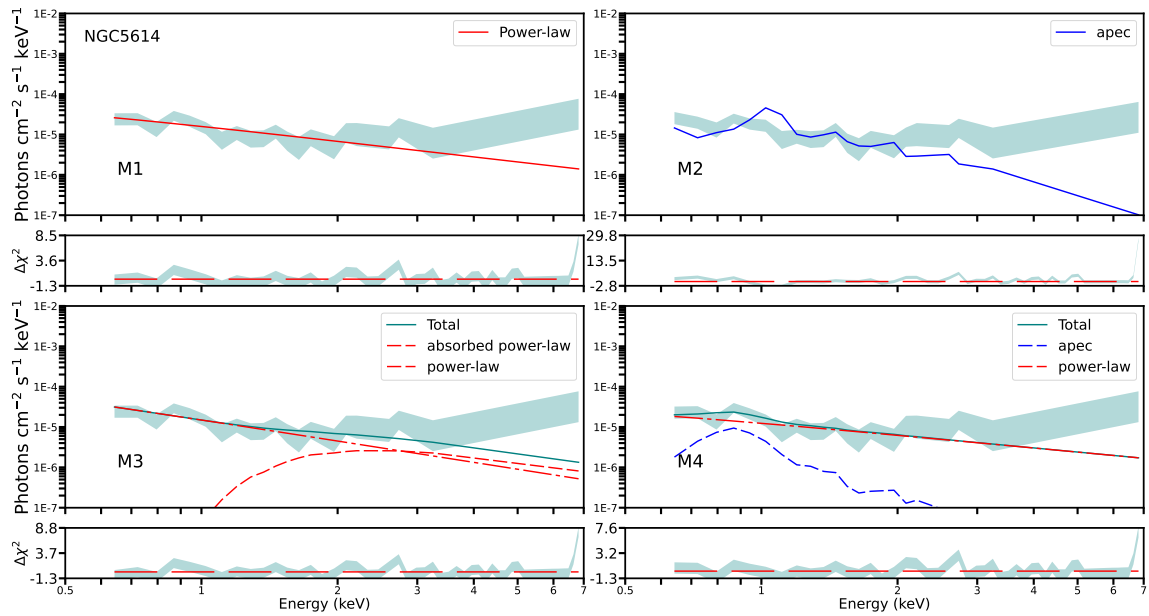


Figure 29: *NuSTAR* X-ray spectra of NGC5614. Labels as in Fig. 8.3.

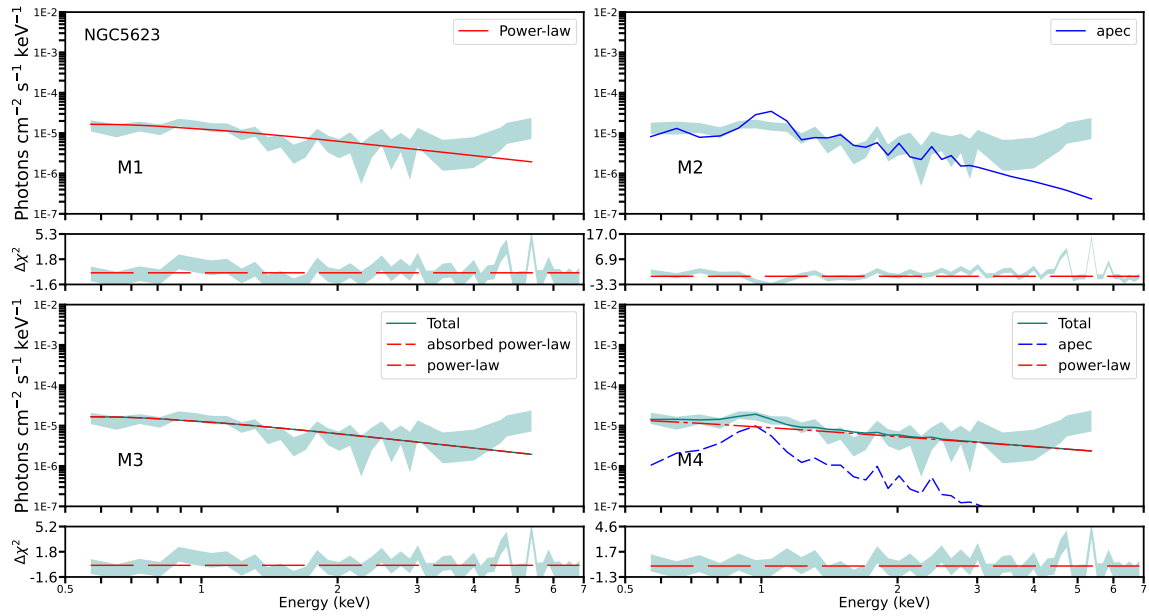


Figure 30: *NuSTAR* X-ray spectra of NGC5623. Labels as in Fig. 8.3.

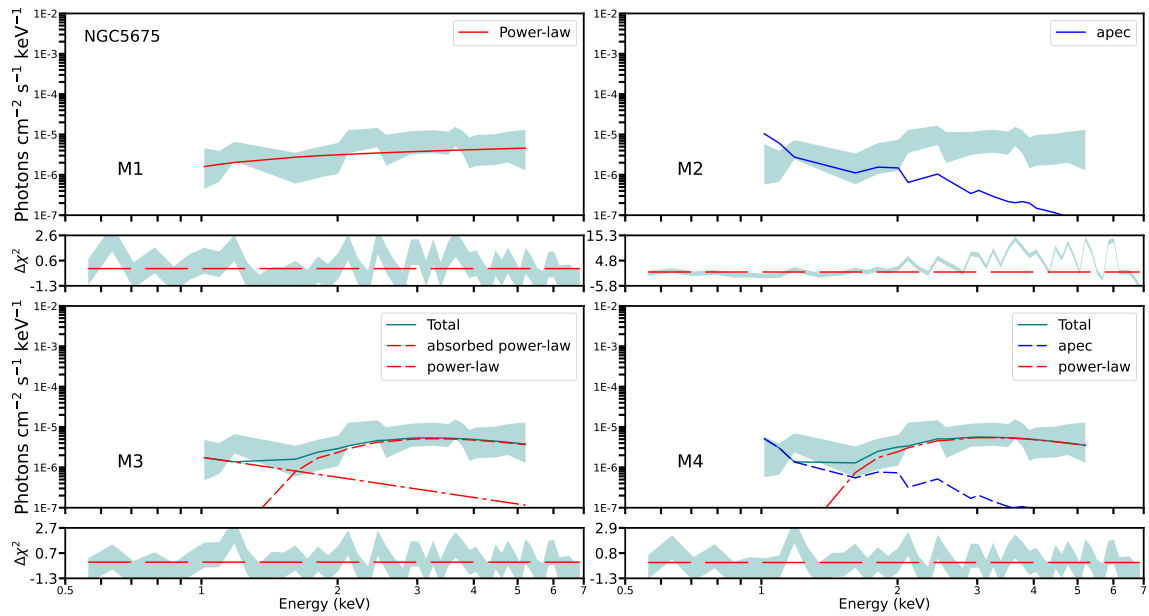


Figure 31: *NuSTAR* X-ray spectra of NGC5675. Labels as in Fig. 8.3.

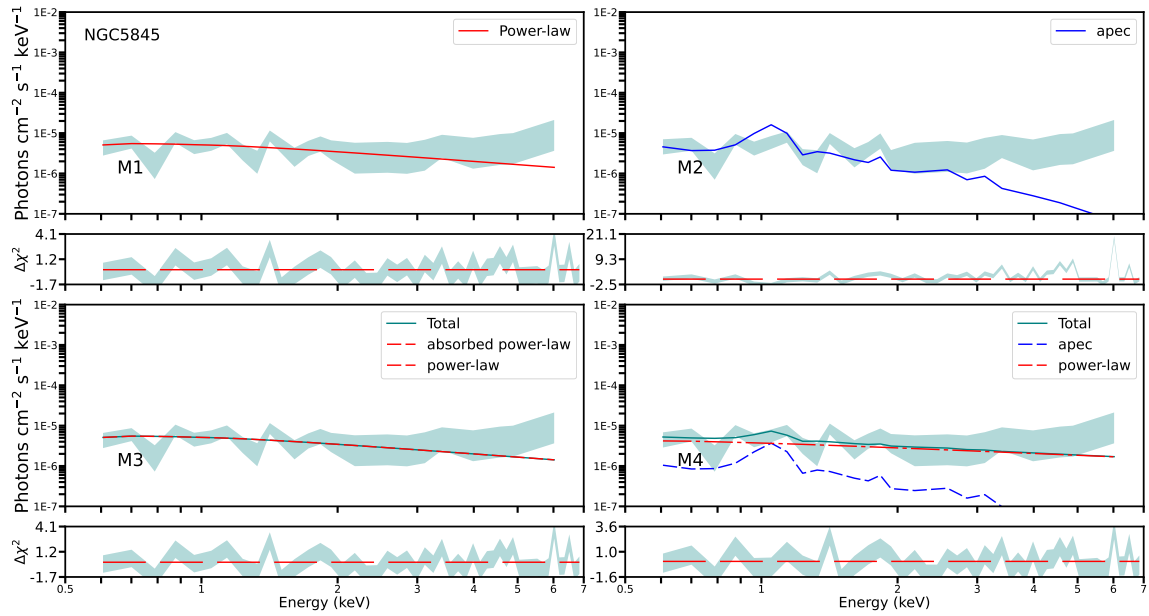


Figure 32: *NuSTAR* X-ray spectra of NGC5845. Labels as in Fig. 8.3.

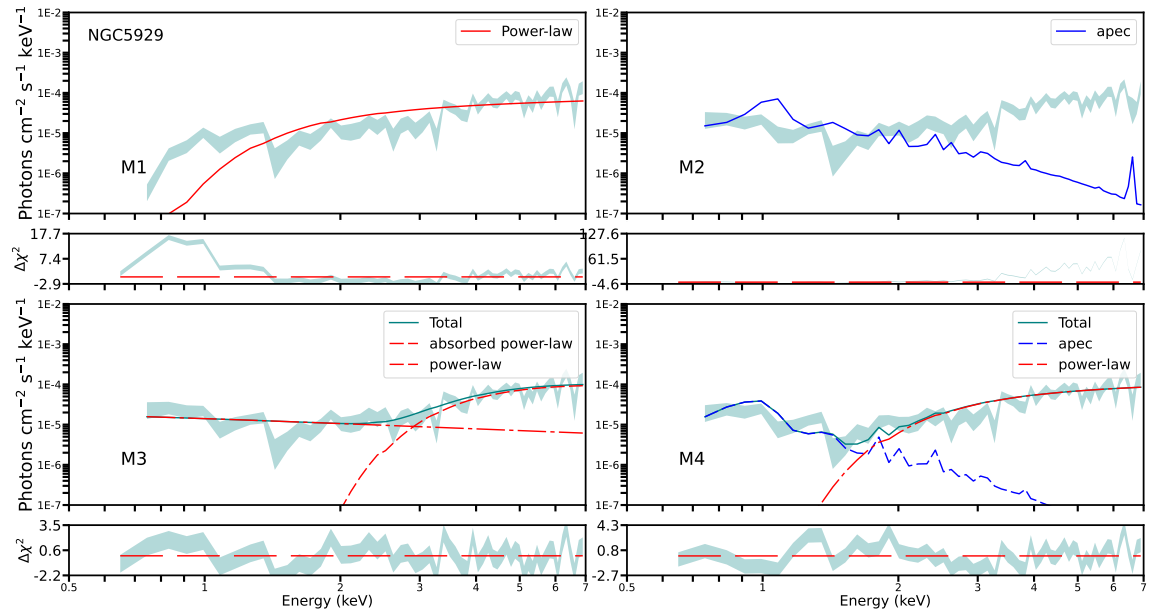


Figure 33: *NuSTAR* X-ray spectra of NGC5929. Labels as in Fig. 8.3.

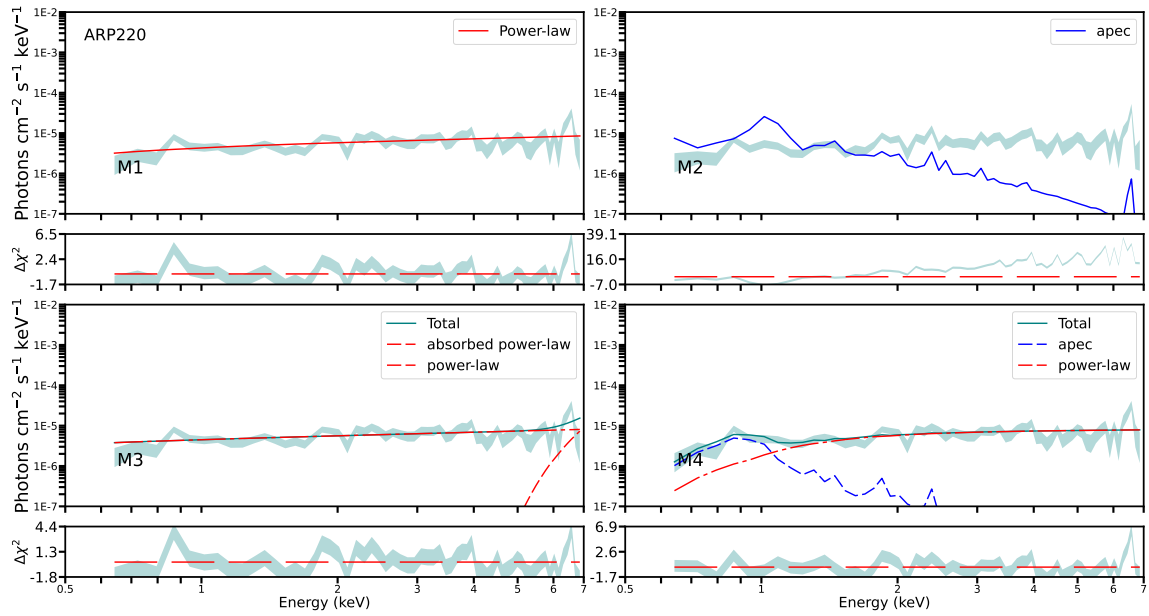


Figure 34: *NuSTAR* X-ray spectra of ARP220. Labels as in Fig. 8.3.

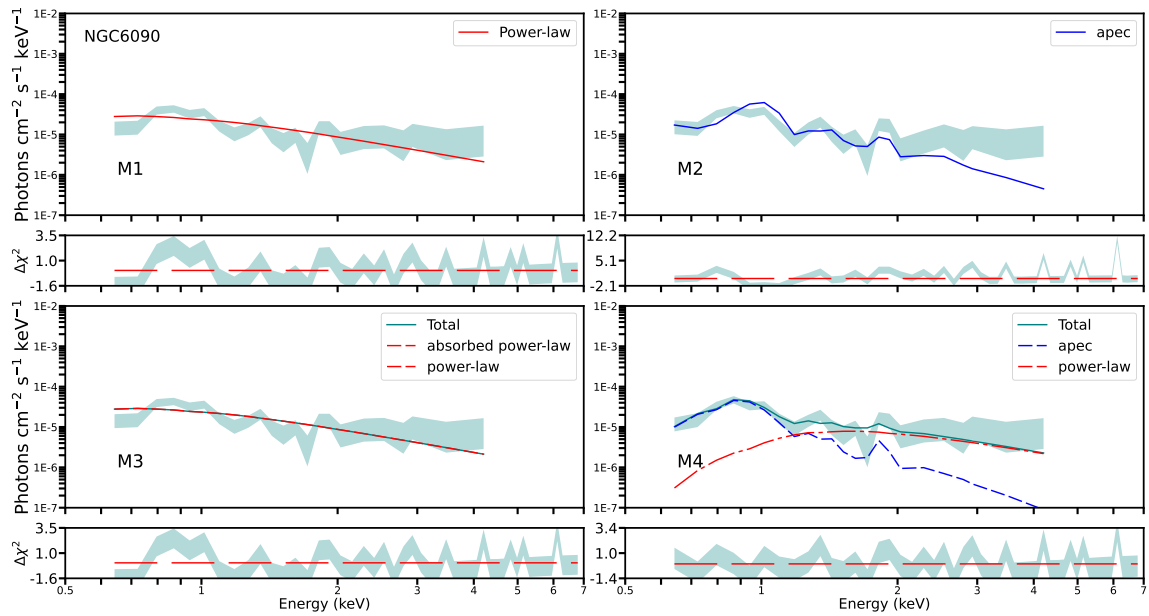


Figure 35: *NuSTAR* X-ray spectra of NGC6090. Labels as in Fig. 8.3.

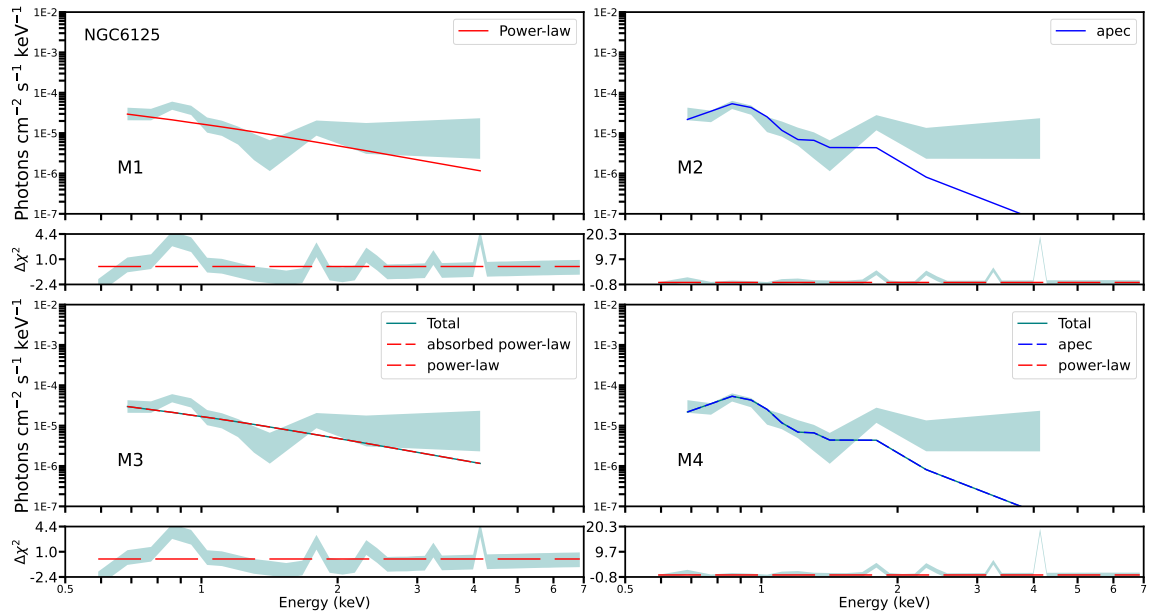


Figure 36: *NuSTAR* X-ray spectra of NGC6125. Labels as in Fig. 8.3.

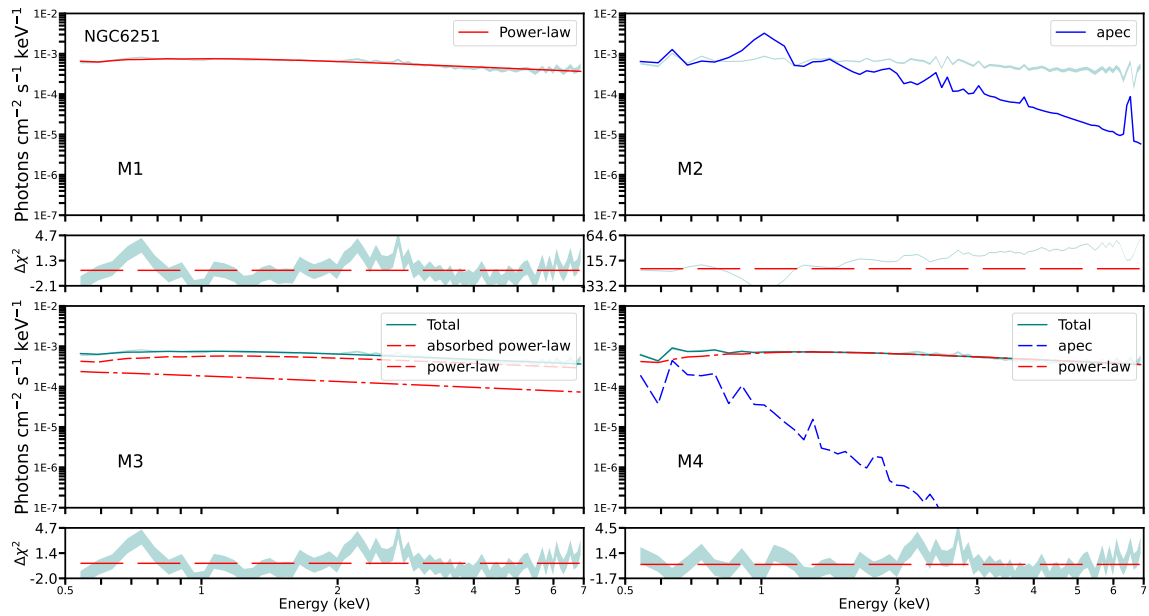


Figure 37: *NuSTAR* X-ray spectra of NGC6251. Labels as in Fig. 8.3.

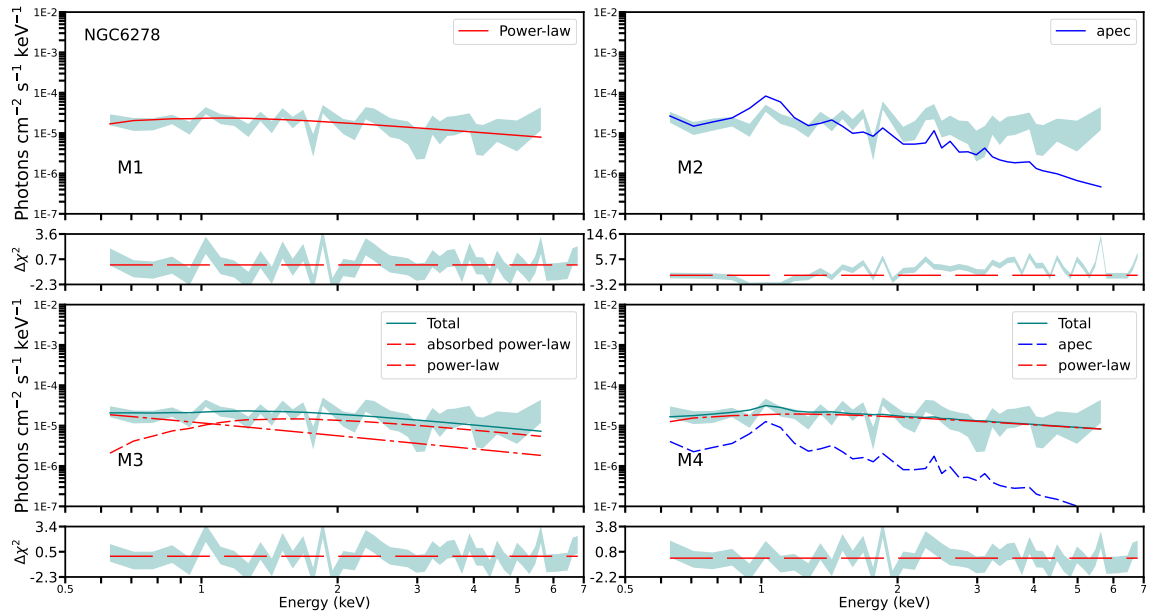


Figure 38: *NuSTAR* X-ray spectra of NGC6278. Labels as in Fig. 8.3.

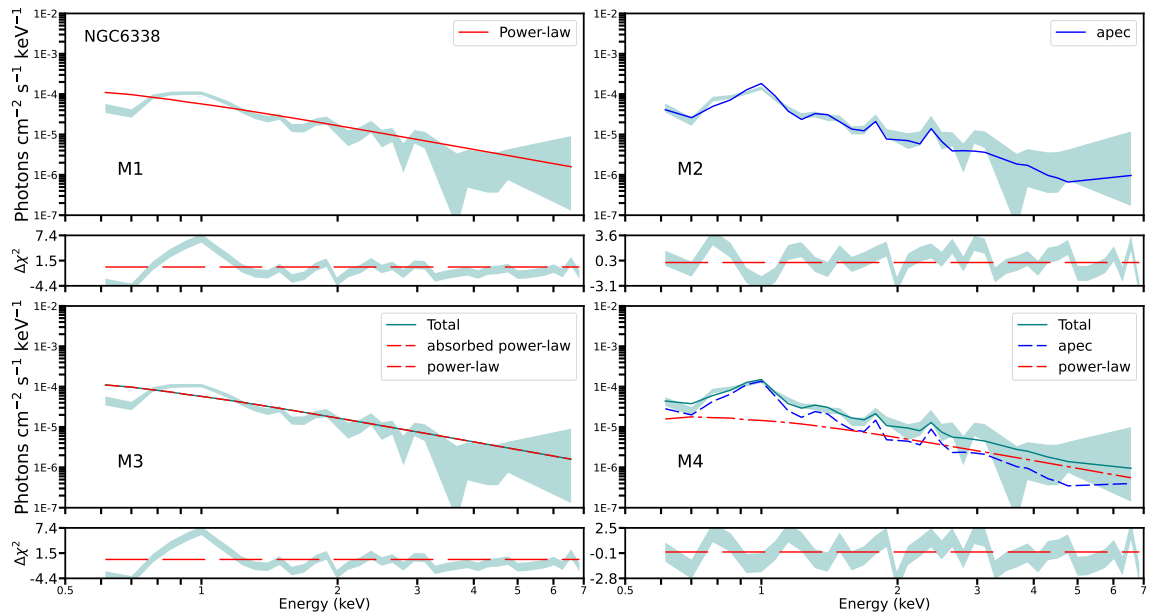


Figure 39: *NuSTAR* X-ray spectra of NGC6338. Labels as in Fig. 8.3.

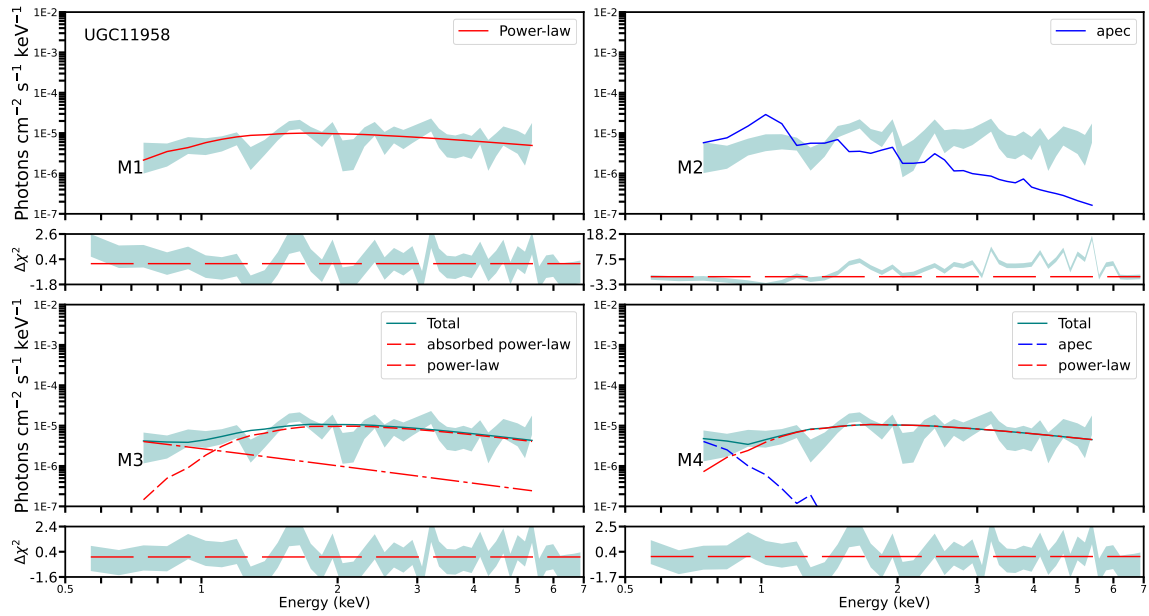


Figure 40: *NuSTAR* X-ray spectra of UGC11958. Labels as in Fig. 8.3.

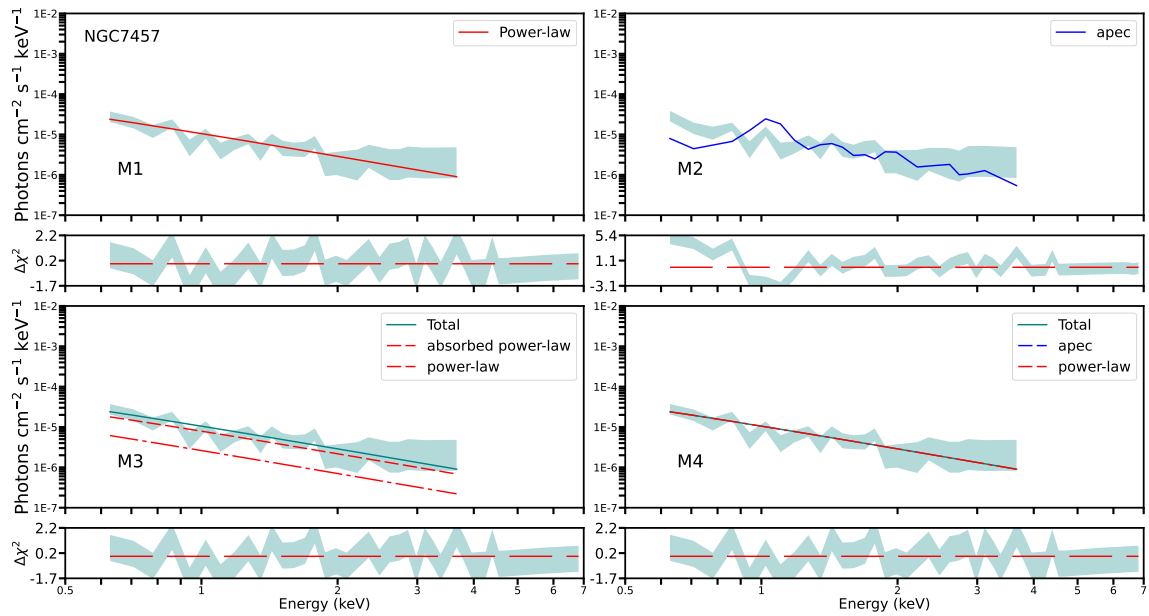


Figure 41: *NuSTAR* X-ray spectra of NGC7457. Labels as in Fig. 8.3.

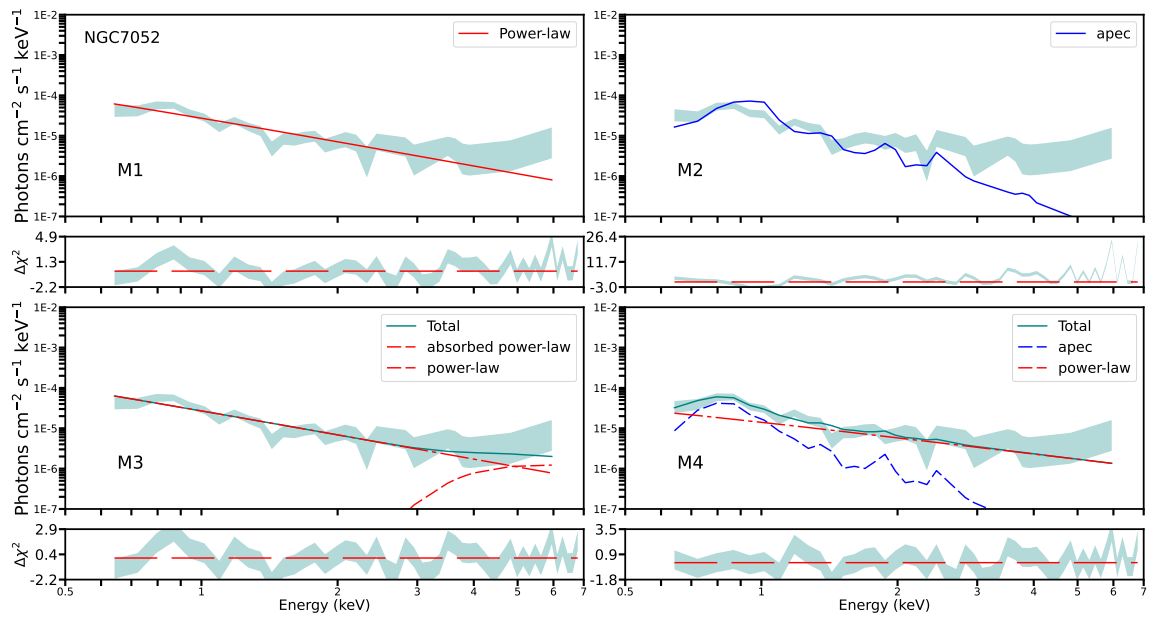


Figure 42: *NuSTAR* X-ray spectra of NGC7052. Labels as in Fig. 8.3.

Bibliography

- Abramowicz M. A., Czerny B., Lasota J. P., Szuszkiewicz E., 1988, *ApJ* , 332, 646
- Agostino C. J., Salim S., 2019, *ApJ* , 876, 12
- Agostino C. J., Salim S., Ellison S. L., Bickley R. W., Faber S. M., 2023, *ApJ* , 943, 174
- Albán M., Wylezalek D., 2023, *A&A* , 674, A85
- Allen J. T., et al., 2015, *MNRAS* , 446, 1567
- Allington-Smith J., 2006, *New Astronomy Reviews* , 50, 244
- Allington-Smith J., Content R., 1998, *PASP* , 110, 1216
- Alonso-Herrero A., et al., 2011, *ApJ* , 736, 82
- Alonso-Herrero A., et al., 2018, *ApJ* , 859, 144
- Antonucci R., 1993, *ARA&A* , 31, 473
- Arnaud K. A., 1996, in Jacoby G. H., Barnes J., eds, *Astronomical Society of the Pacific Conference Series Vol. 101, Astronomical Data Analysis Software and Systems V*. p. 17
- Awaki H., Koyama K., Inoue H., Halpern J. P., 1991, *Publications of the Astronomical Society of Japan* , 43, 195
- Azadi M., et al., 2017, *ApJ* , 835, 27
- Bacon R., et al., 2010, in *SPIE Conf. Series.* , doi:10.1117/12.856027

- Baldry I. K., Glazebrook K., Brinkmann J., Ivezić Ž., Lupton R. H., Nichol R. C., Szalay A. S., 2004, *ApJ* , 600, 681
- Baldwin J. A., Phillips M. M., Terlevich R., 1981, *PASP* , 93, 5
- Baloković M., et al., 2018, *ApJ* , 854, 42
- Baloković M., Cabral S. E., Brenneman L., Urry C. M., 2021, *ApJ* , 916, 90
- Bassani L., Dadina M., Maiolino R., Salvati M., Risaliti G., Della Ceca R., Matt G., Zamorani G., 1999, *ApJS* , 121, 473
- Belfiore F., et al., 2016, *MNRAS* , 461, 3111
- Benn C. R., Vigotti M., Carballo R., Gonzalez-Serrano J. I., Sanchez S. F., 1998, *MNRAS* , 295, 451
- Bennett A. S., 1962, *MmRAS* , 68, 163
- Berney S., et al., 2015, *MNRAS* , 454, 3622
- Bevington P., Robinson D., 2003, *Data Reduction and Error Analysis for the Physical Sciences*. McGraw-Hill Education, <https://books.google.com.mx/books?id=0poQAQAIAAJ>
- Bian W., Gu Q., 2007, *ApJ* , 657, 159
- Bianchi S., Matt G., Balestra I., Guainazzi M., Perola G. C., 2004, *A&A* , 422, 65
- Bianchi S., Guainazzi M., Chiaberge M., 2006, *A&A* , 448, 499
- Bianchi S., Bonilla N. F., Guainazzi M., Matt G., Ponti G., 2009, *A&A* , 501, 915
- Binette L., Magris C. G., Stasińska G., Bruzual A. G., 1994, *A&A* , 292, 13
- Blandford R., Meier D., Readhead A., 2019, *ARA&A* , 57, 467
- Bower R. G., Benson A. J., Malbon R., Helly J. C., Frenk C. S., Baugh C. M., Cole S., Lacey C. G., 2006, *MNRAS* , 370, 645

- Bregman J. N., 1990, *A&A Rev.* , 2, 125
- Brightman M., Nandra K., 2011, *MNRAS* , 413, 1206
- Brinchmann J., Charlot S., White S. D. M., Tremonti C., Kauffmann G., Heckman T., Brinkmann J., 2004, *MNRAS* , 351, 1151
- Bundy K., et al., 2015, *ApJ* , 798, 7
- Caccianiga A., Severgnini P., Della Ceca R., Maccacaro T., Carrera F. J., Page M. J., 2007, *A&A* , 470, 557
- Cackett E. M., Bentz M. C., Kara E., 2021, *iScience*, 24, 102557
- Capellupo D. M., Netzer H., Lira P., Trakhtenbrot B., Mejía-Restrepo J., 2015, *MNRAS* , 446, 3427
- Cappellari M., et al., 2011, *MNRAS* , 413, 813
- Cappi M., et al., 1999, *A&A* , 344, 857
- Carballo R., González-Serrano J. I., Benn C. R., Sánchez S. F., Vigotti M., 1999, *MNRAS* , 306, 137
- Cash W., 1979, *ApJ* , 228, 939
- Cid Fernandes R., Stasińska G., Schlickmann M. S., Mateus A., Vale Asari N., Schoenell W., Sodré L., 2010, *MNRAS* , 403, 1036
- Cid Fernandes R., et al., 2013, *A&A* , 557, A86
- Comastri A., 2004, in Barger A. J., ed., *Astrophysics and Space Science Library Vol. 308, Supermassive Black Holes in the Distant Universe*. p. 245 ([arXiv:astro-ph/0403693](https://arxiv.org/abs/astro-ph/0403693)), doi:10.1007/978-1-4020-2471-9_8
- Comastri A., et al., 2002, *ApJ* , 571, 771
- Comastri A., et al., 2011, *A&A* , 526, L9

- Comerford J. M., Negus J., Barrows R. S., Wylezalek D., Greene J. E., Müller-Sánchez F., Nevin R., 2022, *ApJ* , 927, 23
- Cortes-Suárez E., Negrete C. A., Hernández-Toledo H. M., Ibarra-Medel H., Lacerna I., 2022, *MNRAS* , 514, 3626
- Croft S., et al., 2006, *ApJ* , 647, 1040
- Crummy J., Fabian A. C., Gallo L., Ross R. R., 2006, *MNRAS* , 365, 1067
- Czerny B., Elvis M., 1987, *ApJ* , 321, 305
- Davies R. L., et al., 2016, *MNRAS* , 462, 1616
- Diaz Y., et al., 2020, *MNRAS* , 496, 5399
- Diaz Y., et al., 2023, *A&A* , 669, A114
- Done C., Gierliński M., Kubota A., 2007, *A&A Rev.* , 15, 1
- Donley J. L., et al., 2012, *ApJ* , 748, 142
- Dopita M. A., Sutherland R. S., 1995, *ApJ* , 455, 468
- Dubois Y., Peirani S., Pichon C., Devriendt J., Gavazzi R., Welker C., Volonteri M., 2016, *MNRAS* , 463, 3948
- Dultzin-Hacyan D., Marziani P., Negrete C. A., Sulentic J. W., 2007, in Karas V., Matt G., eds, Vol. 238, *Black Holes from Stars to Galaxies – Across the Range of Masses*. pp 83–86, doi:10.1017/S1743921307004735
- Edge D. O., Shakeshaft J. R., McAdam W. B., Baldwin J. E., Archer S., 1959, *MmRAS* , 68, 37
- Efstathiou A., Rowan-Robinson M., 1995, *MNRAS* , 273, 649
- Elitzur M., Ho L. C., 2009, *ApJL* , 701, L91
- Elitzur M., Netzer H., 2016, *MNRAS* , 459, 585

- Elitzur M., Shlosman I., 2006, *ApJL* , 648, L101
- Elitzur M., Ho L. C., Trump J. R., 2014, *MNRAS* , 438, 3340
- Elvis M., 2000, *ApJ* , 545, 63
- Esin A. A., McClintock J. E., Narayan R., 1997, *ApJ* , 489, 865
- Esparza-Arredondo D., et al., 2019, *ApJ* , 886, 125
- Esparza-Arredondo D., Osorio-Clavijo N., González-Martín O., Victoria-Ceballos C., Haro-Corzo S. A. R., Reyes-Amador O. U., López-Sánchez J., Pasetto A., 2020, *ApJ* , 905, 29
- Esparza-Arredondo D., Gonzalez-Martín O., Dultzin D., Masegosa J., Ramos-Almeida C., García-Bernete I., Fritz J., Osorio-Clavijo N., 2021, *A&A* , 651, A91
- Fabbiano G., 2006, *ARA&A* , 44, 323
- Fabian A. C., 2012, *ARA&A* , 50, 455
- Fabian A. C., Iwasawa K., 2000, *Advances in Space Research*, 25, 471
- Fanaroff B. L., Riley J. M., 1974, *MNRAS* , 167, 31P
- Fath E. A., 1909, PhD thesis, University of California System
- Ferland G. J., Osterbrock D. E., 1986, *ApJ* , 300, 658
- Fernández-Ontiveros J. A., Prieto M. A., Acosta-Pulido J. A., Montes M., 2012, in *Journal of Physics Conference Series*. p. 012006 ([arXiv:1206.0777](https://arxiv.org/abs/1206.0777)), doi:10.1088/1742-6596/372/1/012006
- Ferrarese L., Merritt D., 2000, *ApJL* , 539, L9
- Fritz J., Franceschini A., Hatziminaoglou E., 2006, *MNRAS* , 366, 767
- Furui S., Fukazawa Y., Odaka H., Kawaguchi T., Ohno M., Hayashi K., 2016, *ApJ* , 818, 164

- Gallimore J. F., et al., 2016, *ApJL* , 829, L7
- Gallo E., Fender R. P., Pooley G. G., 2003, *MNRAS* , 344, 60
- García-Bernete I., et al., 2022, *A&A* , 667, A140
- García-Burillo S., et al., 2014, *A&A* , 567, A125
- García-Burillo S., et al., 2021, *A&A* , 652, A98
- Gebhardt K., et al., 2000, *ApJL* , 539, L13
- Genzel R., Eckart A., Ott T., Eisenhauer F., 1997, *MNRAS* , 291, 219
- Genzel R., et al., 1998, *ApJ* , 498, 579
- Georgantopoulos I., Akylas A., 2010, *A&A* , 509, A38
- Ghez A. M., Klein B. L., Morris M., Becklin E. E., 1998, *ApJ* , 509, 678
- Ghisellini G., Haardt F., Matt G., 1994, *MNRAS* , 267, 743
- Gilli R., Comastri A., Hasinger G., 2007, *A&A* , 463, 79
- Gomes J. M., et al., 2016, *A&A* , 585, A92
- Gómez-Guijarro C., González-Martín O., Ramos Almeida C., Rodríguez-Espinosa J. M., Gallego J., 2017, *MNRAS* , 469, 2720
- González-Martín O., Masegosa J., Márquez I., Guerrero M. A., Dultzin-Hacyan D., 2006, *A&A* , 460, 45
- González-Martín O., Masegosa J., Márquez I., Guainazzi M., Jiménez-Bailón E., 2009, *A&A* , 506, 1107
- Gonzalez-Martin O., Acosta-Pulido J. A., Perez Garcia A. M., Ramos Almeida C., 2010, *ApJ* , 723, 1748
- González-Martín O., et al., 2017, *ApJ* , 841, 37

- González-Martín O., et al., 2019, *ApJ* , 884, 11
- Granato G. L., Danese L., 1994, *MNRAS* , 268, 235
- Grant C. E., Bautz M. W., Durham R. N., Plucinsky P. P., 2016, in den Herder J.-W. A., Takahashi T., Bautz M., eds, Vol. 9905, *Space Telescopes and Instrumentation 2016: Ultraviolet to Gamma Ray*. SPIE, p. 990545, doi:10.1117/12.2233424, <https://doi.org/10.1117/12.2233424>
- Guainazzi M., Antonelli L. A., 1999, *MNRAS* , 304, L15
- Guainazzi M., Bianchi S., 2007, *MNRAS* , 374, 1290
- Guainazzi M., Matt G., Perola G. C., 2005, *A&A* , 444, 119
- Gültekin K., Cackett E. M., Miller J. M., Di Matteo T., Markoff S., Richstone D. O., 2009, *ApJ* , 706, 404
- Haardt F., Maraschi L., 1991, *ApJL* , 380, L51
- Hao H., Elvis M., Civano F., Lawrence A., 2011, *ApJ* , 733, 108
- Hazard C., Mackey M. B., Shimmins A. J., 1963, *Nature* , 197, 1037
- Heckman T. M., 1980, *A&A* , 87, 152
- Heckman T. M., Best P. N., 2014, *ARA&A* , 52, 589
- Hickox R. C., Alexander D. M., 2018, *ARA&A* , 56, 625
- Ho L. C., 1999, *ApJ* , 516, 672
- Ho L. C., 2008, *ARA&A* , 46, 475
- Ho L. C., Filippenko A. V., Sargent W. L. W., 1996, *ApJ* , 462, 183
- Ho L. C., Filippenko A. V., Sargent W. L. W., 1997a, *ApJ* , 487, 579
- Ho L. C., Filippenko A. V., Sargent W. L. W., 1997b, *ApJ* , 487, 568

- Hönig S. F., Kishimoto M., 2010, *A&A* , 523, A27
- Hopkins P. F., Richards G. T., Hernquist L., 2007, *ApJ* , 654, 731
- Hopkins P. F., et al., 2010, *ApJ* , 715, 202
- Ichikawa K., Tazaki R., 2017, *ApJ* , 844, 21
- Ishigaki M. N., Chiba M., Aoki W., 2012, *ApJ* , 753, 64
- Izumi T., Wada K., Fukushige R., Hamamura S., Kohno K., 2018, *ApJ* , 867, 48
- Jiang L., et al., 2010, *Nature* , 464, 380
- Kaasra J. S., Bleeker J. A. M., 2016, *A&A* , 587, A151
- Kartalpepe J. S., et al., 2012, *ApJ* , 757, 23
- Kaspi S., et al., 2001, *ApJ* , 554, 216
- Kauffmann G., et al., 2003, *MNRAS* , 346, 1055
- Kawamuro T., Ueda Y., Tazaki F., Terashima Y., Mushotzky R., 2016, *ApJ* , 831, 37
- Kelz A., et al., 2006, *PASP* , 118, 129
- Kennicutt Jr. R. C., 1998, *ApJ* , 498, 541
- Kewley L. J., Dopita M. A., Sutherland R. S., Heisler C. A., Trevena J., 2001, *ApJ* , 556, 121
- Kewley L. J., Groves B., Kauffmann G., Heckman T., 2006, *MNRAS* , 372, 961
- Kirkpatrick A., Pope A., Sajina A., Roebuck E., Yan L., Armus L., Díaz-Santos T., Stierwalt S., 2015, *ApJ* , 814, 9
- Kormendy J., Ho L. C., 2013, *ARA&A* , 51, 511
- Kormendy J., Richstone D., 1995, *ARA&A* , 33, 581
- Koss M., et al., 2017, *ApJ* , 850, 74

- Krongold Y., Dultzin-Hacyan D., Marziani P., 2002, *ApJ* , 572, 169
- LaMassa S. M., Heckman T. M., Ptak A., Hornschemeier A., Martins L., Sonnentrucker P., Tremonti C., 2009, *ApJ* , 705, 568
- Lacerda E. A. D., Sánchez S. F., Cid Fernandes R., López-Cobá C., Espinosa-Ponce C., Galbany L., 2020, *MNRAS* , 492, 3073
- Lacerda E. A., Sánchez S., Mejía-Narváez A., Camps-Fariña A., Espinosa-Ponce C., Barrera-Ballesteros J., Ibarra-Medel H., Lugo-Aranda A., 2022, *New Astronomy*, 97, 101895
- Laloux B., et al., 2023, *MNRAS* , 518, 2546
- Lamer G., McHardy I. M., Uttley P., Jahoda K., 2003, *MNRAS* , 338, 323
- Laor A., Netzer H., 1989, *MNRAS* , 238, 897
- Liu Y., Li X., 2014, *ApJ* , 787, 52
- Lusso E., et al., 2012, *MNRAS* , 425, 623
- Lyu B., Wu Q., Yan Z., Yu W., Liu H., 2022, *ApJ* , 927, 227
- Magdziarz P., Zdziarski A. A., 1995, *MNRAS* , 273, 837
- Magdziarz P., Blaes O. M., Zdziarski A. A., Johnson W. N., Smith D. A., 1998, *MNRAS* , 301, 179
- Magorrian J., et al., 1998, *AJ* , 115, 2285
- Makishima K., Iyomoto N., Ishisaki Y., Terashima Y., 1997, in Peterson B. M., Cheng F.-Z., Wilson A. S., eds, *Astronomical Society of the Pacific Conference Series Vol. 113, IAU Colloq. 159: Emission Lines in Active Galaxies: New Methods and Techniques*. p. 52
- Malizia A., Bassani L., Bazzano A., Bird A. J., Masetti N., Panessa F., Stephen J. B., Ubertini P., 2012, *MNRAS* , 426, 1750

- Maoz D., 2007, MNRAS , 377, 1696
- Marchesi S., Ajello M., Marcotulli L., Comastri A., Lanzuisi G., Vignali C., 2018, ApJ , 854, 49
- Marconi A., Risaliti G., Gilli R., Hunt L. K., Maiolino R., Salvati M., 2004, MNRAS , 351, 169
- Markarian B. E., 1967, Astrofizika, 3, 24
- Markowitz A., et al., 2003, ApJ , 593, 96
- Martínez-Paredes M., et al., 2017, MNRAS , 468, 2
- Matthews T. A., Sandage A. R., 1963, ApJ , 138, 30
- McConnell N. J., Ma C.-P., 2013, ApJ , 764, 184
- McHardy I. M., Gunn K. F., Uttley P., Goad M. R., 2005, MNRAS , 359, 1469
- Mehdipour M., et al., 2011, A&A , 534, A39
- Merritt D., Ferrarese L., 2001, MNRAS , 320, L30
- Middleton M., Done C., Ward M., Gierliński M., Schurch N., 2009, MNRAS , 394, 250
- Moran E. C., Filippenko A. V., Chornock R., 2002, ApJL , 579, L71
- Müller-Sánchez F., Prieto M. A., Mezcua M., Davies R. I., Malkan M. A., Elitzur M., 2013, ApJL , 763, L1
- Murphy K. D., Yaqoob T., 2009, MNRAS , 397, 1549
- Nandra K., Pounds K. A., 1994, MNRAS , 268, 405
- Nandra K., Pounds K. A., Stewart G. C., George I. M., Hayashida K., Makino F., Ohashi T., 1991, MNRAS , 248, 760
- Nandra K., O'Neill P. M., George I. M., Reeves J. N., 2007a, MNRAS , 382, 194

- Nandra K., et al., 2007b, *ApJL* , 660, L11
- Narayan R., Yi I., 1994a, *ApJL* , 428, L13
- Narayan R., Yi I., 1994b, *ApJL* , 428, L13
- Narayan R., Yi I., Mahadevan R., 1996, *A&AS* , 120, 287
- Nemmen R., 2013, arXiv e-prints, p. arXiv:1301.7719
- Nenkova M., Sirocky M. M., Ivezić Ž., Elitzur M., 2008, *ApJ* , 685, 147
- Netzer H., 1990, in Blandford R. D., Netzer H., Woltjer L., Courvoisier T. J. L., Mayor M., eds, *Active Galactic Nuclei*. pp 57–160
- Netzer H., 2013, *The Physics and Evolution of Active Galactic Nuclei*
- Netzer H., 2015, *ARA&A* , 53, 365
- Netzer H., Peterson B. M., 1997, in Maoz D., Sternberg A., Leibowitz E. M., eds, *Astrophysics and Space Science Library Vol. 218, Astronomical Time Series*. p. 85 (arXiv:astro-ph/9706039), doi:10.1007/978-94-015-8941-3_8
- Nikutta R., Elitzur M., Lacy M., 2009, *ApJ* , 707, 1550
- Nilson P., 1973, *Uppsala general catalogue of galaxies*
- Ohsuga K., Mineshige S., 2011, *ApJ* , 736, 2
- Orlandini M., Frontera F., Masetti N., Sguera V., Sidoli L., 2012, *ApJ* , 748, 86
- Ortega-Minakata R. A., 2015, PhD thesis, Universidad de Guanajuato
- Osorio-Clavijo N., González-Martín O., Papadakis I. E., Masegosa J., Hernández-García L., 2020, *MNRAS* , 491, 29
- Osorio-Clavijo N., González-Martín O., Sánchez S. F., Esparza-Arredondo D., Masegosa J., Victoria-Ceballos C., Hernández-García L., Díaz Y., 2022, *MNRAS* , 510, 5102

- Osorio-Clavijo N., Gonzalez-Martín O., Sánchez S. F., Guainazzi M., Cruz-González I., 2023, *MNRAS* , 522, 5788
- Osterbrock D. E., 1989, *Astrophysics of gaseous nebulae and active galactic nuclei*. University Science Books
- Osterbrock D. E., Ferland G. J., 2006, *Astrophysics of gaseous nebulae and active galactic nuclei*
- Padovani P., et al., 2017, *A&A Rev.* , 25, 2
- Paggi A., Wang J., Fabbiano G., Elvis M., Karovska M., 2012, *ApJ* , 756, 39
- Panagiotou C., Walter R., 2019, *A&A* , 626, A40
- Panagiotou C., Walter R., 2020, *A&A* , 640, A31
- Panessa F., Bassani L., Cappi M., Dadina M., Barcons X., Carrera F. J., Ho L. C., Iwasawa K., 2006, *A&A* , 455, 173
- Panessa F., Baldi R. D., Laor A., Padovani P., Behar E., McHardy I., 2019, *Nature Astronomy*, 3, 387
- Papadakis I. E., 2004, *MNRAS* , 348, 207
- Pearson K., 1900, *The London, Edinburgh, and Dublin Philosophical Magazine and Journal of Science*, 50, 157
- Peterson B. M., 1993, *PASP* , 105, 247
- Peterson B. M., 1997, *An Introduction to Active Galactic Nuclei*
- Petrucci P. O., et al., 2002, *A&A* , 388, L5
- Pier E. A., Krolik J. H., 1992, *ApJ* , 401, 99
- Pouliasis E., et al., 2019, *MNRAS* , 487, 4285
- Pović M., et al., 2012, *A&A* , 541, A118

- Protassov R., van Dyk D. A., Connors A., Kashyap V. L., Siemiginowska A., 2002, *ApJ* , 571, 545
- Raftery A. E., 1995, *Sociological methodology*, pp 111–163
- Ramos Almeida C., Ricci C., 2017a, *Nature Astronomy*, 1, 679
- Ramos Almeida C., Ricci C., 2017b, *Nature Astronomy*, 1, 679
- Ramos Almeida C., et al., 2009, *ApJ* , 702, 1127
- Ramos Almeida C., et al., 2011, *ApJ* , 731, 92
- Rees M. J., 1984, *ARA&A* , 22, 471
- Remillard R. A., McClintock J. E., 2006, *ARA&A* , 44, 49
- Renzini A., Peng Y.-j., 2015, *ApJL* , 801, L29
- Reynolds C. S., Nowak M. A., Markoff S., Tueller J., Wilms J., Young A. J., 2009, *ApJ* , 691, 1159
- Ricci C., Walter R., Courvoisier T. J. L., Paltani S., 2011, *A&A* , 532, A102
- Ricci C., Tazaki F., Ueda Y., Paltani S., Boissay R., Terashima Y., 2014, *ApJ* , 795, 147
- Ricci C., et al., 2017a, *ApJS* , 233, 17
- Ricci C., et al., 2017b, *Nature* , 549, 488
- Richard J., Jones T., Ellis R., Stark D. P., Livermore R., Swinbank M., 2011, *MNRAS* , 413, 643
- Richards G. T., et al., 2001, *AJ* , 121, 2308
- Risaliti G., Maiolino R., Salvati M., 1999, *ApJ* , 522, 157
- Roberts T. P., Warwick R. S., 2000, *MNRAS* , 315, 98
- Roberts C. A., Bentz M. C., Vasiliev E., Valluri M., Onken C. A., 2021, *ApJ* , 916, 25

Rosas-Guevara Y., Bower R. G., Schaye J., McAlpine S., Dalla Vecchia C., Frenk C. S., Schaller M., Theuns T., 2016, *MNRAS* , 462, 190

Roth M. M., et al., 2005, *PASP* , 117, 620

Salim S., et al., 2007, *ApJS* , 173, 267

Salpeter E. E., 1955, *ApJ* , 121, 161

Sánchez S. F., et al., 2004a, *ApJ* , 614, 586

Sánchez S. F., Garcia-Lorenzo B., Mediavilla E., González-Serrano J. I., Christensen L., 2004b, *ApJ* , 615, 156

Sánchez S. F., et al., 2012, *A&A* , 538, A8

Sánchez S. F., et al., 2016a, *RMxAA* , 52, 21

Sánchez S. F., et al., 2016b, *RMxAA* , 52, 171

Sánchez S. F., et al., 2016c, *A&A* , 594, A36

Sánchez S. F., et al., 2018, *RMxAA* , 54, 217

Sánchez S. F., Walcher C. J., Lopez-Cobá C., Barrera-Ballesteros J. K., Mejía-Narváez A., Espinosa-Ponce C., Camps-Fariña A., 2021, *RMxAA* , 57, 3

Sanders D. B., Phinney E. S., Neugebauer G., Soifer B. T., Matthews K., 1989, *ApJ* , 347, 29

Santoro F., Oonk J. B. R., Morganti R., Oosterloo T. A., Tadhunter C., 2016, *A&A* , 590, A37

Schartmann M., Meisenheimer K., Camenzind M., Wolf S., Henning T., 2005, *A&A* , 437, 861

Schawinski K., Thomas D., Sarzi M., Maraston C., Kaviraj S., Joo S.-J., Yi S. K., Silk J., 2007, *MNRAS* , 382, 1415

- Schawinski K., et al., 2010, *ApJ* , 711, 284
- Schawinski K., et al., 2014, *MNRAS* , 440, 889
- Schmidt M., 1963, *Nature* , 197, 1040
- Schwarz G., 1978, *The Annals of Statistics*, 6, 461
- Seyfert C. K., 1943, *ApJ* , 97, 28
- Shakura N. I., Sunyaev R. A., 1973, *A&A* , 500, 33
- Shankar F., Salucci P., Granato G. L., De Zotti G., Danese L., 2004, *MNRAS* , 354, 1020
- She R., Ho L. C., Feng H., 2017, *ApJ* , 842, 131
- Sijacki D., Vogelsberger M., Genel S., Springel V., Torrey P., Snyder G. F., Nelson D., Hernquist L., 2015, *MNRAS* , 452, 575
- Silk J., 2005, *MNRAS* , 364, 1337
- Silk J., 2013, *ApJ* , 772, 112
- Silk J., Rees M. J., 1998, *A&A* , 331, L1
- Singh R., et al., 2013, *A&A* , 558, A43
- Sobolewska M. A., Done C., 2007, *MNRAS* , 374, 150
- Strateva I., et al., 2001, *AJ* , 122, 1861
- Symeonidis M., et al., 2013, *MNRAS* , 433, 1015
- Tang Y., Gu Q. S., Huang J. S., Wang Y. P., 2009, *MNRAS* , 397, 1966
- Torres-Papaqui J. P., Coziol R., Andernach H., Ortega-Minakata R. A., Neri-Larios D. M., Plauchu-Frayn I., 2012, *RMxAA* , 48, 275
- Torres-Papaqui J. P., Coziol R., Plauchu-Frayn I., Andernach H., Ortega-Minakata R. A., 2013, *RMxAA* , 49, 311

- Trump J. R., et al., 2009, *ApJ* , 706, 797
- Trussler J., Maiolino R., Maraston C., Peng Y., Thomas D., Goddard D., Lian J., 2020, *MNRAS* , 491, 5406
- Turner T. J., Miller L., 2009, *A&A Rev.* , 17, 47
- Ueda Y., Akiyama M., Hasinger G., Miyaji T., Watson M. G., 2014, *ApJ* , 786, 104
- Urry C. M., Padovani P., 1995, *PASP* , 107, 803
- Ursini F., et al., 2015, *MNRAS* , 452, 3266
- Vanderriest C., Haddad B., Lemonnier J. P., 1987, in *L'Activite dans les Galaxies*. p. 207
- Vasudevan R. V., Fabian A. C., 2007, *MNRAS* , 381, 1235
- Vasudevan R. V., Fabian A. C., 2009, *MNRAS* , 392, 1124
- Veilleux S., Osterbrock D. E., 1987, *ApJS* , 63, 295
- Veilleux S., Cecil G., Bland-Hawthorn J., 2005, *ARA&A* , 43, 769
- Vestergaard M., Peterson B. M., 2006, *ApJ* , 641, 689
- Wada K., 2012, *ApJ* , 758, 66
- Wada K., 2015, *ApJ* , 812, 82
- Wada K., Norman C. A., 2002, *ApJL* , 566, L21
- Walcher C. J., et al., 2014, *A&A* , 569, A1 (W14)
- Walton D. J., Mackenzie A. D. A., Gully H., Patel N. R., Roberts T. P., Earnshaw H. P., Mateos S., 2022, *MNRAS* , 509, 1587
- Williams D. R. A., et al., 2022, *MNRAS* , 510, 4909
- Wyder T. K., et al., 2007, *ApJS* , 173, 293

- Wylezalek D., Zakamska N. L., Greene J. E., Riffel R. A., Drory N., Andrews B. H., Merloni A., Thomas D., 2018, *MNRAS* , 474, 1499
- Xue Y. Q., et al., 2010, *ApJ* , 720, 368
- Yan R., et al., 2011, *ApJ* , 728, 38
- Yaqoob T., George I. M., Nandra K., Turner T. J., Serlemitsos P. J., Mushotzky R. F., 2001, *ApJ* , 546, 759
- Younes G., Ptak A., Ho L. C., Xie F.-G., Terasima Y., Yuan F., Huppenkothen D., Yukita M., 2019, *ApJ* , 870, 73
- Young A. J., McHardy I., Emmanoulopoulos D., Connolly S., 2018, *MNRAS* , 476, 5698
- Yuan F., 2007, in Ho L. C., Wang J. W., eds, *Astronomical Society of the Pacific Conference Series Vol. 373, The Central Engine of Active Galactic Nuclei*. p. 95 ([arXiv:astro-ph/0701638](https://arxiv.org/abs/astro-ph/0701638)), doi:10.48550/arXiv.astro-ph/0701638
- Zackrisson E., 2005, PhD thesis, Department of Astronomy and Space Physics, Uppsala University, Sweden
- Zhang W. M., Soria R., Zhang S. N., Swartz D. A., Liu J. F., 2009, *ApJ* , 699, 281
- Zwicky I. F., 1964, *ApJ* , 140, 1467
- de Zeeuw P. T., et al., 2002, *MNRAS* , 329, 513
- van Bemmell I. M., Dullemond C. P., 2003, *A&A* , 404, 1